TWR-17542-1

SPACE SHUTTLE

Solid Rocket Motors
Thiokol Corporation

Flight Motor Set 360L003 (STS-29R) Final Report

Volume I (System Overview)

July 1989

Prepared for

National Aeronautics and Space Administration
George C. Marshall Space Flight Center
Marshall Space Flight Center, Alabama 35812

Contract No.	NAS8-30490
DR No.	3-5
WBS No.	4B601-03-08
ECS No.	SS-1011

Thiokol CORPORATION
SPACE OPERATIONS

P.O. Box 707, Brigham City, UT 84302-0707 (801) 863-3511

Publications No. 89857

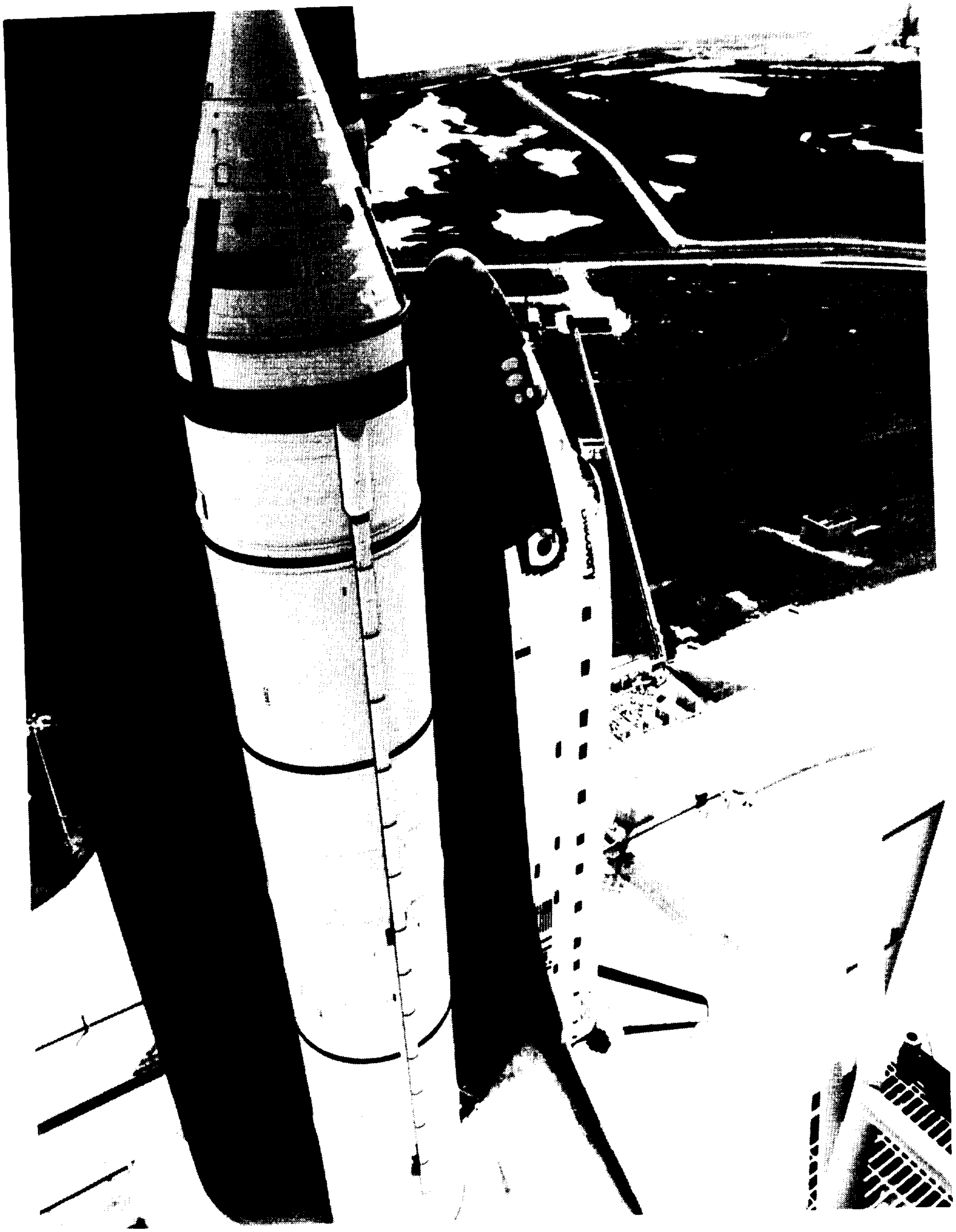

Flight motors 360L003A and 360L003B (not shown) provide the majority of thrust for the space shuttle Discovery ascent on 13 Mar 1989. Instrumentation data and postflight inspection results again verified exceptional solid rocket motor performance.

ORIGINAL PAGE
BLACK AND WHITE PHOTOGRAPH

Flight Motor Set 360L003 (STS-29R)
Final Report

Prepared by:

Test Planning and Reporting

Approved by:

Test Planning and Reporting Supervisor

Program Manager

Project Engineer

System Safety

17 July 89
Reliability

7-18-89
Data Management

89857-10.1

Listed below are the contributors to the major sections of the report, along with an acceptance signature from a section representative.

Mass Properties
C. Richards

Ballistics
K. Speas
B. Laubacher

7/12/89

Aero/Thermal
H. Huppi
J. Maw
R. Buttars

Structural Applications
(Ascent Loads and Seals)
D. Gurney
D. Rowsell

Nozzles
R. George
S. Meyer

Instrumentation
B. Baugh
J. Wright

Dynamics
V. Call
C. Chang

Insulation Design
S. Manz
S. Hicken

Case Components
R. Mackley

ORIGINAL PAGE IS
OF POOR QUALITY

ABSTRACT

Flight motor set 360L003 was launched at 9:57 a.m. eastern standard time on 13 Mar 1989 as part of NASA space shuttle mission STS-29R. As was the case with flight sets 360L001 and 360L002 (STS-26R and STS-27R), both motors performed in an excellent manner.

Evaluation of the ground environment instrumentation measurements again verified thermal model analysis data and showed agreement with predicted environmental effects (even though the historical March ambient temperature range was exceeded on both the warm and cold ends). The right-hand aft field joint primary heater failed during the countdown; the secondary heater was activated and performed as designed. All other field joint heaters and aft skirt thermal conditioning systems had no anomalies. Shuttle thermal imager infrared readings compared favorably with measured ground environment instrumentation data. No thermal launch commit criteria violations occurred at any time.

Evaluation of the development flight instrumentation showed exceptional propulsion performance. All ballistic parameters closely matched the predicted values and were well within the required contract end item specification levels. Girth and biaxial strain gage measurements compared closely with corresponding gages on previous flight motors, static tests, and with preflight predictions. Adequate safety factors were again verified. (Some ignition transient "spiking" was again noted in a few girth gages; the spiking was determined not to be representative of actual case behavior, but an instrumentation phenomena.) The accelerometers again measured high vibration amplitude levels during the ignition transient and the reentry Max Q phases.

Postflight inspection again showed that all combustion gas was contained by the insulation in the field and case-to-nozzle joints. No anomalous insulation erosion patterns were found, and the seals that did directly contain motor pressure showed no heat effects, erosion, or blowby. All anomalies identified were a result of splashdown damage, with the exception of fretting in the case field joint interference (nonsealing) surfaces and a prelaunch field joint heater failure.

It was again recommended to continue the use of development flight instrumentation on future flights (particularly accelerometers). The rationale for this recommendation, disposition of all anomalies, and complete result details are contained in this report.

CONTENTS

CONTENTS (Cont)

FIGURES

FIGURES (cont)

FIGURES (cont)

FIGURES (cont)

FIGURES (cont)

FIGURES (cont)

FIGURES (cont)

FIGURES (cont)

FIGURES (cont)

TABLES

TABLES (cont)

ACRONYMS

APU	auxiliary power unit
AT	action time
CCP	carbon-cloth phenolic
dc	direct current
DFI	development flight instrumentation
DWV	dielectric withstanding voltage
EPDM	ethylene-propylene-diene monomer
ET	external tank
ETA	external tank attach
FBMBT	flex bearing mean bulk temperature
FEWG	Flight Evaluation Working Group
FFT	fast Fourier transform
FMEA	failure mode effects analysis
FT	Fourier transform
GCP	glass-cloth phenolic
GEI	ground environment instrumentation
HOSC	Huntsville Operations Support Center
HPM	high performance motor
IFA	in-flight anomaly
IR	infrared
IVBC	integrated vehicle baseline configuration
JPS	joint protection system
KSC	Kennedy Space Center
LH	left hand
LRU	line replaceable unit
LSC	linear shaped charge
MED	maximum expected displacement
MLP	mobile launch platform
MSFC	Marshall Space Flight Center
OBR	outer boot ring
OMI	operational maintenance instructions
OMRSD	operations and maintenance requirements and specification document
OPT	operational pressure transducer
PIRN	preliminary interface revision notice
PMBT	propellant mean bulk temperature
RH	right hand
RSRM	redesigned solid rocket motor
RTD	resistance temperature detector
S&A	safety and arming device
SF	safety factor
sps	samples per second
SRB	solid rocket booster
SRM	solid rocket motor
SSME	space shuttle main engine
STI	shuttle thermal imager
STS	space transportation system
V	volt
VAB	vehicle assembly building
2-D	two dimensional
3-D	three dimensional

1

INTRODUCTION

The redesigned solid rocket motor (RSRM) flight set used for the 28th space shuttle mission (Space Transportation System-29R (STS-29R)) and third RSRM flight was composed of motors 360L003A (left) and 360L003B (right). Solid rocket booster (SRB) ignition command time was 89:72:14:57:00.017 Greenwich mean time (9:57 eastern standard time on 13 Mar 1989) at Kennedy Space Center (KSC), Florida. This volume (Volume I) of this report contains the Morton Thiokol Flight Evaluation Working Group (FEWG) inputs submitted to United Space Boosters, Inc. (USBI) for incorporation into the shuttle prime contractors' FEWG report (Document MSFC-RPT-1575). An executive summary of the entire RSRM flight set performance and a one-to-one correlation of conclusions by objectives (and CEI paragraphs) are also included herein. The detailed component volumes of this report (and the approximate timeline for volume release from the launch date) are as follows:

Volume	Component	Interim Release	Final Release
I	System overview	NA	Approximately 60 days after launch
II	Case	45 days after last field joint demate at KSC Hangar AF	45 days after washout of last segment at Clearfield H-7
III	Insulation	45 days after last field joint demate at KSC Hangar AF	45 days after last factory joint dis-assembly at Clearfield H-7
IV	Seals	45 days after last internal nozzle joint demate	45 days after last factory joint dis-assembly at Clearfield H-7
V	Nozzle	45 days after final nozzle joint dis-assembly	90 days after final nozzle liner char and erosion measurements
VI	Igniter	NA	30 days after igniter disassembly at Clearfield H-7
VII	Joint protection system (heater)	NA	60 days after launch

VIII	Systems tunnel	NA	60 days after launch
IX	Instrumentation	NA	60 days after launch
X	Performance and mass properties	NA	60 days after launch
XI	Dynamics (reconstructed loads evaluation)	NA	60 days after receipt of reconstructed loads

The subsections of this report volume that were submitted to USBI as part of the FEWG report are so designated with the FEWG report paragraph number.

2

OBJECTIVES

Test objectives for the third Morton Thiokol RSRM flight were derived from the Third Flight Test Summary Sheet of the D&V Plan (TWR-15723C) and are listed here as contained in the Engineering Requirements Document for RSRM Third Flight (TWR-18984). They are intended to satisfy the requirements of CPW1-3600A (including Addendum G) as listed in parenthesis below:

Qualification Test Objectives

A. Certify that the ignition interval is between 202 and 262 ms with a 40 ms environmental delay after ignition command (3.2.1.1.1.1, Morton Thiokol proposed).

B. Certify that the pressure rise rate meets specification requirements (3.2.1.1.1.2, Morton Thiokol proposed).

C. Certify that the thrust-time performance falls within the requirements of the nominal thrust-time curve (3.2.1.1.2.1, Table I).

D. Certify that the measured motor performance parameters, when corrected to a 60°F PMBT, fall within the nominal value, tolerance and limits for individual flight motors (3.2.1.1.2.2, Table II).

E. Certify that the thrust differential is within specified limits (3.2.1.1.2.3).

F. Certify that the thrust-time curve complies with impulse requirements (3.2.1.1.2.4).

G. Certify that specified temperatures are maintained in the case-to-nozzle joint region (3.2.1.2.1.f and subtier paragraphs).

H. Certify proper operation of the operational pressure transducer (OPT) during flight (3.2.1.6.2.1).

I. Certify proper operation of the igniter chamber pressure transducer during flight (3.2.1.6.2.4, Addendum G).

J. Certify the performance of the field joint heater and the sensor assembly so it maintains the case field joint at 75°F minimum. Field joints shall not exceed 130°F (3.2.1.11.a).

K. Certify the performance of the igniter heater so it maintains the igniter gasket rubber seals between 64° and 130°F during and after the motor has been exposed to the ground thermal environments (3.2.1.5.3).

L. Certify that each field joint heater assembly meets all performance requirements (3.2.1.11.1.2).

M. Demonstrate that the thermal protection insulates the systems tunnel floor plates and cables against overheating (3.2.1.10.2, Addendum G).

N. Demonstrate isolation of subsystem anomalies if required on third flight (360L003) hardware (3.2.3.3).

O. Demonstrate the RSRM capability of assembly/disassembly in both the vertical and horizontal positions (3.2.5.1).

P. Demonstrate assembly and verification of the SRB prior to external tank (ET) mating (3.2.5.4).

Q. Demonstrate that the RSRM and its components are capable of being transported to and from fabrication, test, operational launch, recovery/retrieval, and the refurbishment sites (3.2.8).

R. Demonstrate that the RSRM and components are protected against natural environments during postflight transportation (3.2.8.c).

S. Demonstrate the remove and replace capability of the functional line replaceable unit (3.4.1).

T. Demonstrate facilities and facility equipment (3.4.3).

U. Demonstrate that recovery procedures meet ICD specifications (3.6.2.e).

V. Demonstrate the void repair to joint protection system (JPS) with K5NA.

W. Demonstrate the operation of the igniter heater.

X. Conduct a backflow check of the JPS vent valves.

Y. Demonstrate the locking feature on exit cone leak check port plugs.

Test Objectives by Inspection

Perform the following required postflight inspections and demonstrations:

Z. Inspect all RSRM seals for performance (3.2.1.2).

AA. Inspect the seals for satisfactory operation within the specified temperature range that results from natural and induced environments (3.2.1.2.1.b).

AB. Inspect the factory joint insulation for accommodation to structural deflections and erosion (3.2.1.2.2.a).

AC. Inspect the factory joint insulation for operation within the specified temperature range (3.2.1.2.2.b, 3.2.1.2.3.b, 3.2.1.2.5.b, 3.2.1.2.4.b).

AD. Verify that at least one virgin ply of insulation exists over the factory joint at the end of motor operation (3.2.1.2.2.d).

AE. Verify that no leakage occurred through the insulation (3.2.1.2.2.e).

AF. Verify that no gas leaks occurred in the ignition system seals (3.2.1.2.4.d).

AG. Verify that no gas leaks occurred between the flex bearing internal components (3.2.1.2.3.d).

AH. Inspect the risers for damage or cracks that would degrade the pressure holding capability of the case (3.2.1.3.c).

AI. Inspect the case for tang alignment slots (3.2.1.3.f).

AJ. Inspect the case segment mating joints for the pin retention device (3.2.1.3.g).

AK. Demonstration and post-test inspection of exit cone severance (3.2.1.4.5).

AL. Inspect the flex bearing for damage due to water impact (3.2.1.4.6.a).

AM. Demonstrate the performance of the nozzle environmental protection (3.2.1.4.7.c).

AN. Verify the performance of the nozzle liner (3.2.1.4.13).

AO. Demonstrate that the exit cone severance ordnance ring performs correctly (3.2.1.4.12).

AP. Inspect the ignition system seals for evidence of hot gas leakage (3.2.1.5.a).

AQ. Demonstrate that the igniter and S&A are separable (3.2.1.5.b).

AR. Inspect the igniter for evidence of debris formation or damage (3.2.1.5.2).

AS. Inspect the internal insulation for degradation (3.2.1.8.1).

AT. Inspect the seals for visible degradation from motor combustion gas (3.2.1.8.1.1.d).

AU. Verify by inspection that the insulation met all performance requirements (3.2.1.8.1.1.e).

AV. Inspect insulation material for shedding of fibrous or particulate matter (3.2.1.8.1.1.f).

AW. Inspect the joint insulation for evidence of slag accumulation (3.2.1.8.1.1.g).

AX. Inspect the thermal protection system (TPS) to insure that there was no environmental damage to the RSRM components (3.2.1.8.2).

AY. Inspect for thermal damage to the igniter chamber or the adapter metal parts (3.2.1.8.3).

AZ. Verify that the case components are reusable (3.2.1.9.a).

BA. Verify that the nozzle metal parts are reusable (3.2.1.9.b).

BB. Verify through flight demonstration and a post-test inspection that the flex bearing is reusable (3.2.1.9.c).

BC. Verify that the igniter components are reusable (3.2.1.9.d).

BD. Verify by inspection that the S&A is reusable (3.2.1.9.e).

BE. Verify by inspection that the OPTs are reusable (3.2.1.9.f).

BF. Inspect the case factory joint external seal for moisture (3.2.1.12).

BG. Inspect the hardware for damage or anomalies as identified by the FMEAs (3.2.3).

BH. Determine the adequacy of the design safety factors (SF), relief provisions, fracture control, and safe-life and/or fail-safe characteristics (3.2.3.1).

BI. Determine the adequacy of subsystem redundancy and fail-safe requirements (3.2.3.2).

BJ. Inspect the RSRM and its subsystems for reuse following recovery and retrieval (3.2.5.7).

BK. Inspect the identification numbers of each reusable RSRM part and material for traceability (3.3.1.5).

BL. Verify the structural SF of the case-to-insulation bond (3.3.6.1.1.2.a).

BM. Verify the structural SF for all adhesive bonds (3.3.6.1.1.2.b)

BN. Verify by inspection the remaining thickness of the case insulation (3.3.6.1.2.2, 3.3.6.1.2.3, 3.3.6.1.2.4, 3.3.6.1.2.6).

BO. Verify by inspection the remaining nozzle ablative thicknesses (3.3.6.1.2.7).

BP. Verify the nozzle SFs (3.3.6.1.2.8).

BQ. Inspect the functional and physical interfaces between the SRBs and the retrieval station (3.6.2.e).

BR. Inspect metal parts for presence of stress corrosion (3.3.8.2.b).

3

RESULTS SUMMARY, CONCLUSIONS, AND RECOMMENDATIONS

3.1 RESULTS SUMMARY

This section contains an executive summary of the key results from the flight data evaluation and postflight inspection. Additional information and details can be found in the referenced report sections or in the separate component volumes of this report.

3.1.1 In-Flight Anomalies

Four in-flight anomalies (IFA) relating to RSRM motor set 360L003 were identified. They are summarized below.

MSFC IFA No.	Problem/Title/ Description	Corrective Action/ Closure
STS-29-M-1	Right-hand (RH) aft field joint heater malfunction/ circuit failed after approximately 11 hr of operation (at about T - 10 hr).	Redundant secondary heater activated for remainder of countdown. Additional circuit monitoring and protection safeguards implemented, as well as failure contingency guidelines.
STS-29-M-2	Left-hand (LH) aft center factory joint weatherseal unbonds/adhesive unbonds between case and Chemlock 205 primer in 11 separate areas circumferentially around the case.	Adhesive bond strength reduced by contamination--actual unbonding a result of splashdown loads (reuse issue only). Increased contamination control reduces chance of reoccurrence.
STS-29-M-3	Missing phenolic materials from LH nozzle aft exit cone/approximately 95 percent of glass-cloth phenolic (GCP) and carbon-cloth phenolic (CCP) missing from unsevered portion of LH aft exit cone.	Phenolic loss a result of splashdown loads. Analysis results indicate exit cone phenolics in compression throughout motor burn. Phenolic loss at splashdown has no effect on motor performance, flight safety, or reuse.

MSFC IFA No.	Problem/Title/ Description	Corrective Action/ Closure
STS-29-M-4	Fretting in field joints/small gouges, pits, or scratches on capture feature interference (nonsealing) surface.	No flight safety issue due to scratch size. RH aft field joints showed scars as deep as 0.13 in. Fracture mechanics allow 60 to 70 reuses before achieving critical scratch size. Refurbishment issue only.

The complete disposition and closeout statements of all the IFAs are contained in Section 4.1 of this volume. None were considered to be flight constraints.

3.1.2 Mass Properties

Excellent agreement was found between the postflight reconstructed data and predicted mass property values. Actual weights all varied less than 0.10 percent from the predicted values. As has previously been the case on motor sets 360L001 and 360L002, all RSRM weight values were also within the CEI specification limits. Complete mass property values are included in Section 4.3 of this volume and Volume X of this report.

3.1.3 Propulsion Performance (Ballistics)

3.1.3.1 Propellant Burn Rates/Specific Impulse. The delivered burn rate for flight motors 360L003A and 360L003B was 0.367 in./sec and 0.368 in./sec, respectively, which was 0.001 in./sec less than predicted for 360L003A and exactly as predicted for 360L003B. Reconstructed vacuum specific impulse values were 267.5 and 267.8 lbf-sec/lbm for the LH and RH motors, respectively, both within 0.27 percent of the predicted value of 268.2 lbf-sec/lbm.

3.1.3.2 CEI Specification Values. All time parameters, pressure and thrust levels, and impulse data (all corrected to 60°F) showed excellent agreement with the motor nominal performance values. Differences from the CEI specification limits were all significantly less than the allowable 3-sigma variation. Thrust imbalance data were also well within the specification limits for all required time periods.

Only the RH motor (360L003B) was equipped with an igniter pressure transducer. Evaluation revealed normal operation and that all parameters were within the limits of Morton Thiokol Specification STW3-3176. A complete ballistic evaluation is contained in Section 4.4 of this volume and Volume X of this report.

3.1.4 Ascent Loads

3.1.4.1 Girth Gage Response. The girth gage measurements from the field and case-to-nozzle joints compared closely to corresponding gages on previous flight motors (360L001 and 360L002), static tests, and pretest predictions. (As has been the case in the past, the predictions used a typical load case rather than actual loads, so they were only expected to predict within an order of magnitude.) The highest percentage differences from the predicted values on the field joints were 19.3 percent on the LH RSRM center field joint, 41 percent on the RH RSRM case-to-nozzle joint girth gages, and -13.3 percent on the LH RSRM case membrane (Station 611.5).

The data from the RH RSRM center and aft field joint girth gages and a few other girth gages on both motors contained a spike during the ignition transient at 0.25 sec (similar to the spiking reported on 360L002). Investigation has shown that this spiking is an instrumentation phenomenon. (The spike is believed to be an extremely small electrical pulse, the generation of which is inherit to the gage and electrical circuit configuration.)

Case movement (and thus girth gage response) follows internal motor pressure. However, girth gages on the RH RSRM forward field joint (all gages) and center joint (three most forward gages) showed up to a 0.25-sec response delay from motor pressure and the nearby biaxial strain gage readings. This delay is also believed to be due to the electrical circuit and gage configuration that caused the above-mentioned data spike. Additional information on the spiking and delay phenomena is contained in Section 4.9 of this volume.

3.1.4.2 Biaxial Gage (Hoop and Axial Strain) Response. The biaxial gage line/load measurements also compared well with predicted values. The biaxial strain gage data for each station were used to calculate a stress distribution, and this information was used to calculate bending moments, axial forces, and line loads as a function of time. The maximum measured hoop stress results in a SF of 1.61 (ultimate strength) and no local yielding.

A maximum bending moment of -264 x 10^6 in.-lb was recorded on the LH RSRM (Station 1797) during space shuttle main engine (SSME) buildup. The maximum axial force was -13.41 kip, and the maximum line load was -28.0 kip/in. (both on RH RSRM at Station 556).

Evaluation of the bending moment and axial force data during the flight envelopes also revealed a close correlation to past motors and predicted values. A complete evaluation of all ascent loads is contained in Section 4.6 of this volume.

3.1.5 Structural Dynamics

3.1.5.1 Vibration Amplitudes. Unexpected high vibration amplitude levels (up to 8g) around the center field joint area in the radial direction were detected during ignition transient. (Levels up to 5g had been observed on motor set 360L002 (STS-27R)). High-amplitude readings in the axial direction were also detected on the forward segment. All other amplitude readings were within the expected ranges.

As was also detected on 360L002, extremely high vibration amplitude levels lasting for a significant time duration were detected during reentry Max Q (approximately 300 sec after lift-off).

Frequency analysis indicates this is typical white-type aerodynamic wind loading. The relationship between this loading and the fretting observed in the field joints is being investigated.

3.1.5.2 Modal Frequencies. The expected trend of frequency levels increasing with time (due to the decrease of mass as the motor burns) that has been detected on the RSRM static test motors was not detected on 360L003. (Also, no frequency increase was detected on 360L002; 360L001 was not sufficiently instrumented to detect these frequency levels.)

3.1.5.3 Accelerometer Gage Limitations and Model Bounds. Identifying the SRB modal frequencies during flight and evaluation of the unexpected high vibration amplitudes (during both the ignition transient and reentry Max Q) is extremely difficult due to the current accelerometer gage ranging. Acceleration predictions are also limited due to the analysis model bounds. The recommended approach to resolve the unknown aspects of SRB flight dynamics is included in Section 3.3 of this volume. Additional detailed dynamic evaluation is in Section 4.7 of this volume.

3.1.6 External Thermal Protection System/Joint Heater Evaluation

3.1.6.1 Thermal Protection System Evaluation. Excellent external TPS performance was observed. No debris from any TPS component was noted, and evaluation showed typical flight heat effects and erosion.

3.1.6.2 Joint Heaters. After 11 hr of operation, the RH RSRM aft field joint heater failed at about the T - 10 hr point in the countdown (see IFA STS-29-M-1). The secondary heater was turned on; it performed nominally throughout the remainder of the countdown. All other heaters performed as expected. A detailed TPS and heater evaluation is contained in Section 4.8 of this volume.

3.1.7 Aero/Thermal Evaluation

3.1.7.1 On-Pad Local Environment Effects/Thermal Model Verification. The on-pad local environment predictions (assuming winds from the southeast) suggested a 1°F temperature suppression from cryogenic effects during ET loading. However, the winds were consistently from the west-southwest, and after assessing ground environment instrumentation (GEI) data only minor chilling (1° to 2°F) on the inboard region of the RH motor (360L003B) was noted.

Ambient temperature data (47° to 78°F) exceeded the range of the average March historical data (61° to 73°F) on both the warm and cool ends, with the lower or cooler side showing the greatest deviation. Windspeeds were also higher than the historical average (reaching 30 kn) a couple of days before launch, but fell within the historical average prior to launch.

3.1.7.2 Launch Commit Criteria/Infrared Readings. No launch commit criteria (LCC) thermal violations were noted. The joint heaters performed adequately and as expected, with the exception noted previously in Section 3.1.6.2. A 30°F temperature delta between the conditioning gas and solid rocket motor (SRM) hardware was noted in the aft skirt conditioning system (as had also been noticed on 360L002 (STS-27)), suggesting significant heat loss between the heater and aft skirt compartment. Infrared (IR) readings from shuttle thermal imager (STI) were taken at the T - 3 hr timeframe. The values were verbally reported to range between 59° and 61°F, which compared favorably with measured GEI data. No IR gun readings were taken during the ice team pad walkdown.

3.1.7.3 Development Flight Instrumentation Thermal Data Evaluation. Overall development flight instrumentation (DFI) data were well within the IVBC-3 design trajectory analysis. However, during reentry, design estimates were exceeded in the SRB aft skirt base region, probably due to nozzle severance at apogee and aft skirt hydrazine fires (which also have occurred in the past). The appropriate reuse criteria will be evaluated concerning this base region hardware. Measured data on the nozzle throat also exceeded the design estimate by a few degrees. This occurrence does not appear to be a problem, since actual hardware response is still well within the general reuse steel structure temperature criteria.

3.1.8 Instrumentation

Of the 417 SRM DFI measurements, 389 were operative at lift-off. Of those that were operative at lift-off, 375 (96 percent) performed properly throughout their respective mission phases. Of the 108 total GEI measurements, 105 (97 percent) performed properly throughout their respective mission phases. A complete discussion of all instrumentation is contained in Sections 4.10 and 4.11 of this volume and Volume IX of this report.

3.1.9 Postflight Hardware Assessment

3.1.9.1 Insulation. Postflight evaluation again showed excellent insulation performance. No evidence of motor combustion gas was found past the insulation in the six field joints or two case-to-nozzle joints. No gas paths or severe erosion was identified in any acreage insulation. All external insulation was in good condition, with the exception of the LH aft center segment factory joint, which was damaged at splashdown (IFA STS-29-M-2). A complete insulation evaluation is contained in Section 4.12.1 of this volume and Volume III of this report.

3.1.9.2 Case. Fretting was observed on five of the six field joints. Overall, this flight exhibited fretting comparable to 360L002 (STS-27). A few of the pits measured slightly deeper (as much as 0.013 in.) than those from 360L002. The 360L003 fretting was worse on the LH motor, whereas on 360L002 the RH motor fretting was worse. (On 360L001 (STS-26R) the fretting was relatively even.) Investigation of the fretting phenomenon is continuing.

All RH stiffener rings had cracks and buckles. There were a total of five outer ligament cracks on the boltholes of the corresponding stiffener case stubs. No metal damage was noted on the LH stiffener rings and stubs. The crack in the LH forward stiffener stub at 24 deg did not propagate during flight. A complete evaluation of the case components can be found in Section 4.12.2 of this volume and Volume II of this report.

3.1.9.3 Seals. All seals performed as expected and as designed. Postflight inspection verified that the insulation contained the motor pressure in the field and case-to-nozzle joints. All other seals that were exposed to motor pressure performed well, with no heat effects, erosion, or hot gas leakage evident. A complete seals evaluation is contained in Section 4.12.3 of this volume and Volume IV of this report.

3.1.9.4 Nozzle/Thrust Vector Control Performance. Postflight evaluation indicated that both nozzles performed as expected during flight, with typical smooth and uniform erosion profiles. The 360L003A (LH) nozzle aft exit cone and joint suffered excessive splashdown damage (IFA STS-29-M-3). Complete evaluation of both RSRM nozzles is contained in Section 4.12.4 of this volume and Volume V of this report.

3.2 CONCLUSIONS

Listed below are the conclusions as they relate specifically to the objectives and CEI paragraphs. Also included with each conclusion, in parenthesis, is the report section in which additional information can be found.

Objective	CEI Paragraph	Conclusion
Certify that the ignition interval is between 202 and 262 ms, with a 40-ms environmental delay after ignition command.	3.2.1.1.1.1 Ignition Interval. The ignition interval shall be between 202 and 262 ms...	Certified--The ignition interval for RSRMs 360L003A and 360L003B was 0.241 sec for both motors (Table 4.4-1).
Certify that the pressure rise rate meets specification requirements (Morton Thiokol proposed).	3.2.1.1.1.2 Pressure Rise Rate. The maximum rate of pressure buildup shall be 115.9 psi for any 10 ms interval.	Certified--The maximum pressure rise rate for RSRMs 360L003A and 360L003B was 82.7 and 89.9 psi/10 ms, respectively (Table 4.4-1).
Certify that the thrust-time performance falls within the requirements of the nominal thrust-time curve.	3.2.1.1.2.1 (See Nominal Thrust-Time Curve)	Certified--The thrust-time performance was within the nominal thrust-time curve (Figure 4.4.1).

Objective	CEI Paragraph	Conclusion
Certify that the measured motor performance parameters, when corrected to a 60°F propellant mean bulk temperature (PMBT), fall within the nominal value, tolerance, and limits for individual flight motors.	3.2.1.1.2.2 The delivered performance values for each individual motor when corrected to a 60°F PMBT shall not exceed the limits specified...	Certified--All motor performance values were well within the specification requirements (Tables 4.4-2 and 4.4-3).
Certify that the thrust differential is within specified limits.	3.2.1.1.2.3 Thrust Differential. ...the differential thrust between the two RSRMs shall not be greater than the values given...	Certified--All thrust differentials were well within the allowable limits (Table 4.4-2).
Certify that the thrust-time curve complies with impulse requirements.	3.2.1.1.2.4 Impulse Gates. Time (sec) / Total Impulse (10E6 lb-sec) 20 — 63.1 minimum 60 — 172.9 -1, +3% Action time (AT) = 293.8 minimum	Certified--The nominal thrust-time curve values are listed below. Time (sec) — Value LH / RH 20 — 63.98 / 63.94 60 — 172.11 / 172.29 AT — 295.58 / 296.10 (Table 4.4-1)
Certify that specified temperatures are maintained in the case-to-nozzle joint region.	3.2.1.2.1.f Case-to-nozzle joint O-rings shall be maintained within the temperature range as specified in ICD 2-0A002. (75° to 120°F)	Certified--Temperature ranges in the case-to-nozzle joint region are listed below. RH = 75°* - 88°F LH = 78° - 88°F (Table 4.9-4) *One sensor read consistently low
Certify proper operation of the operational pressure transducers (OPT) during flight.	3.2.1.6.2.1 The OPT shall monitor the chamber pressure of the RSRMs over the range from 0 to 1,050 ±/15 psi. They shall operate in accordance with ICD 3-44005...	Certified--The OPTs properly monitored the chamber pressure and operated in accordance with ICD 3-44005. (Recorded pressure data and values are discussed in Section 4.4 of this volume.)
Certify proper operation of the igniter chamber pressure transducer during flight.	3.2.1.6.2.4 (Addendum G) Developmental Flight Instrumentation. ...shall monitor in-flight SRM igniter and chamber pressure over the 0 to 3,000 psi range... 0 to 5 Vdc...response of 100 Hz.	Certified--Only 360L003B (RH) had an igniter chamber pressure transducer installed, and the transducer performed properly. (Complete data results are discussed in Section 4.4.5 of this volume.)

Objective	CEI Paragraph	Conclusion
Certify the performance of the field joint heater and the sensor assembly so it maintains the case field joint at 75°F minimum. Field joints shall not exceed 130°F.	3.2.11.a The case field joint external heater and sensor assembly shall maintain the case field joint O-ring seals between 75° and 120°F at launch...	Certified--The joint heaters maintained all field joints between 93° and 109°F during the prelaunch period (Table 4.8-5).
Certify the performance of the igniter heater so it maintains the igniter gasket rubber seals between 64° and 130°F during and after the motor has been exposed to the ground thermal environments.	3.2.1.5.3 Igniter Heater. The igniter heater shall maintain the igniter gasket rubber seals between 64° and 130°F during and after the motor has been exposed to the ground thermal environments.	Certified--The igniter joint heaters maintained the igniter joints between 70° and 101°F during the pre-launch period (Table 4.8-5).
Certify that each field joint heater assembly meets all performance requirements.	3.2.1.11.1.2 Power Supply. Each field joint external heater assembly shall meet all performance requirements...as defined in ICD 3-44005.	Certified--The RH aft field joint heater failed at about T - 10 hr. Use of the secondary heater was initiated, which performed nominally for the remainder of the countdown. (Details are discussed in IFA STS-29-M-1 and Section 4.8.3.5 of this volume.)
Demonstrate that the thermal protection insulates the systems tunnel floor plates and cables against overheating.	3.2.1.10.2 (Addendum G) Grounding. The systems tunnel shall provide a low-resistance path which is electrically continuous...	No evidence of overheating or adverse thermal effects was observed on the systems tunnel floorplate and cables. (Details are discussed in Volume VIII of this report.)
Demonstrate isolation of subsystem anomalies if required on third flight (360L003) hardware.	3.2.3.3 Isolation of anomalies of time-critical functions shall be provided such that a faulty subsystem element can be deactivated without disrupting its own or other subsystems.	The 360L003A (LH) igniter pressure transducer was found to be defective and was replaced with a dual seal plug (Section 4.2.1). The 360L003B (RH) aft field joint heater failed during prelaunch; the redundant secondary joint heater was activated in its place (Section 4.1). Both subsystem anomalies were deactivated and replaced without subsystem disruption.

Objective	CEI Paragraph	Conclusion
Demonstrate capability of RSRM assembly/disassembly in both the vertical and horizontal positions.	3.2.5.1 The RSRM shall be capable of assembly/disassembly in both the vertical and horizontal positions. The RSRM shall be capable of vertical assembly in a manner to meet the alignment criteria of USBI-10183-0022 without a requirement of optical equipment.	RSRM vertical assembly, in accordance with USBI-10183-0022, was demonstrated in the vehicle assembly building (VAB) prior to pad rollout. No vertical disassembly was required. Postflight horizontal disassembly was accomplished at the Hangar AF facilities.
Demonstrate assembly and verification of the SRB prior to ET mating.	3.2.5.4 The RSRM assembly and verification on the mobile launch platform (MLP) shall be required prior to mating to the external tank.	The RSRMs were successfully assembled on the MLP prior to being mated to the ET.
Demonstrate that the RSRM and its components are capable of being transported to and from fabrication, test, operational launch, recovery/retrieval, and refurbishment sites.	3.2.8 The RSRM and its component parts...shall be capable of being handled and transported by rail or other suitable means to and from fabrication, test, operational launch, recovery/retrieval, and refurbishment sites.	The RSRM and its associated components demonstrated transportability from fabrication in Utah to launch in Florida, where the components were recovered, retrieved, and transported back to the refurbishment sites in Utah.
Demonstrate that the RSRM and its components are protected against environments during transportation and handling.	3.2.8.c The RSRM and its components...are adequately protected, by passive means, against natural environments during transportation and handling.	Post-test inspection results demonstrated no damage to the RSRM components as a result of environmental exposure during transportation.
Demonstrate remove-and-replace capability of the functional line replaceable unit.	3.4.1 The maintenance concept shall be to "remove and replace"...in a manner which will... prevent deterioration of inherent design levels of reliability and operating safety at minimum practical costs.	The 360L003A (LH) igniter pressure transducer was removed and replaced with a dual seal plug (Section 4.2.1) without deterioration of safety or reliability design levels.
Demonstrate facilities and facility equipment.	3.4.3 Facilities and Facility Equipment. Existing facilities and equipment must be used for the storage of spares and maintenance functions to the maximum possible extent.	No new facilities or equipment for spares storage was required for flight set 360L003.

Objective	CEI Paragraph	Conclusion
Demonstrate that recovery procedures meet ICD specifications.	3.6.2.e ICD 2-4A002 Solid Rocket Booster Retrieval Station.	All recovery procedures that violated ICD 2-4A002 were documented as preliminary interface revision notices (PIRN) and are currently being worked.
Demonstrate the void repair to JPS with K5NA.	Not applicable--No D&V plan impact. Repairs performed in accordance with FEC RSRM 039. All future configuration changes to be documented on applicable drawings.	All repaired JPS areas performed as designed, remaining intact (no debris) throughout flight and showing no significant reentry heating effects (Table 4.8-3).
Demonstrate the operation of the igniter heater. (New igniter heater element material used--per ECP RSRM 1919--to preclude repeat possibility of QM-8 igniter heater burn.)	Not applicable--Thermal performance of igniter heater addressed previously by paragraph 3.2.1.5.3.	Postflight inspection revealed no adverse effects from igniter heater operation (Section 4.8).
Conduct a backflow test of the JPS vent valves.	Not applicable--No D&V plan impact. Backflow test performed under operational maintenance instructions (OMI) requirements.	Vent valve backflow checks are performed per the OMI prior to rollout. No anomalies with the vent valves were noted.
Demonstrate the locking feature on exit cone leak check port plugs.	3.3.6.10 Locking Threaded Parts. All threaded fasteners shall be positively locked. Self-locking devices shall be used one time only...	The Nylok® patch locking feature was used on the exit cone port plugs (as well as other plugs throughout the motor). Postflight inspection verified no loose or backed-out plugs. (Details of the aft exit cone joint inspection are discussed in Section 4.11.4.)
Postflight inspection of all RSRM seals to verify seal performance.	3.2.1.2 Redundant, verifiable seals shall be provided for each pressure vessel leak path. Both the primary and secondary seals shall provide independent sealing capability through the entire ignition transient and motor burn without evidence of blowby or erosion.	No evidence of hot gas, heat effect, erosion, or blowby was evident on any of the seals (Section 4.11.3).

Objective	CEI Paragraph	Conclusion
Postflight inspection of factory joint insulation for accommodation of structural deflections and erosion.	3.2.1.2.2.a Sealing shall accommodate any structural deflections or erosion which may occur.	The factory joint insulation remained sealed and accommodated all deflection and erosion (Section 4.11.1).
Postflight inspection to verify at least one virgin ply of insulation over factory joint at end of motor operation.	3.2.1.2.2.d The insulation shall provide one or more virgin ply coverage at end of motor operation. The design shall perform the seal function throughout SRM operation.	Preliminary inspections indicate no anomalies with the factory joint insulation (Section 4.11.1). Postflight ply measurements are taken at the Clearfield H-7 facility. (Detailed results contained in Volume III of this report.)
Postflight inspection of seals for satisfactory operation within temperature range resulting from natural and induced environments.	3.2.1.2.1.b Field and Nozzle/Case Joint Seals... 3.2.1.2.2.b Factory Joint Insulation... 3.2.1.2.3.b Flex Bearing Seals... 3.2.1.2.4.b Ignition System Seals... 3.2.1.2.5.b Nozzle Internal Seals... ...shall be capable of operating within a temperature range resulting from all natural and induced environments...all manufacturing processes, and any motor-induced environments.	All field joint seals, case-to-nozzle joint seals, ignition system seals, and internal nozzle seals operated within all induced environments and showed no evidence of heat effects, erosion, or blowby (Section 4.11.3). Evaluation indicates no anomalies with the factory joint insulation (Section 4.11.1) or the flex bearing internal seals. (Flex bearing evaluation is contained in Volume V of this report.)
Postflight inspection to verify no leakage occurred through the insulation.	3.2.1.2.2.e The insulation used as a primary seal shall be adequate to preclude leaking through the insulation.	No evidence of hot gas penetration through the factory joint insulation or severe erosion was identified (Section 4.11.1).
Postflight inspection to verify no gas leaks occurred in the ignition system seals.	3.2.1.2.4.d Ignition System. Each seal shall maintain, without pressure assistance, sealing capability with a joint displacement of 1.4 x maximum expected displacement (MED). Displacement will be applied in direct ratio to applicable pressure-time relationship.	All ignition system seals performed as expected. No evidence of heat effect, erosion, or blowby was noted on any seals, gaskets, or sealing surfaces (Section 4.11.3).

Objective	CEI Paragraph	Conclusion
Postflight inspection to verify no gas leaks occurred between the flex bearing internal components.	3.2.1.2.3.d The flex bearing shall maintain a positive gas seal between its internal components.	Preliminary inspection indicates the flex bearing maintained positive seal within its internal components. Detailed inspection to be completed during flex bearing acceptance testing.
Postflight inspection of risers for damage or cracks that would degrade the pressure holding capability of the case.	3.2.1.3.c The case shall contain risers for attaching the ET/SRB aft attach ring as defined in ICD 3-44004. The risers shall be part of the pressurized section of the case and shall not degrade the integrity of the case.	No damage or adverse effects to the external tank attach (ETA) risers was noted during post-test inspection (Section 4.11.2). All noted stiffener ring stub damage and complete case evaluation is in Volume II of this report.
Postflight inspection of the case for tang alignment slots.	3.2.1.3.f The case segment mating joints shall incorporate provisions to insure proper segment orientation and alignment to facilitate joining, stacking, dis-assembly, and refurbishment for reuse.	Post-test case inspection revealed no damage in this area, indicating that the segment tang slots provided proper orientation and alignment (Section 4.11.2).
Postflight inspection of the case segment mating joints for the pin retention device.	3.2.1.3.g The case segment mating joints shall contain a pin retention device.	The 360L003A (LH) aft factory joint pin retainer band was slightly damaged during splashdown. However, all pins remained in place (Section 4.11.2). (Detailed results contained in Volume II of this report.)
Demonstration and postflight inspection of exit cone severance.	3.2.1.4.5 Exit Cone Severance. The nozzle assembly design shall provide a capability to jettison a portion of the aft exit cone assembly...	Severance of both nozzle exit cones occurred at apogee. (Nozzle inspection results are contained in Section 4.11.4 of this volume and Volume V of this report.)
Postflight inspection for flex bearing damage due to water impact.	3.2.1.4.6.a The nozzle assembly shall incorporate a nozzle snubbing device suitable for preventing flex bearing damage resulting from water impact...	Preliminary inspection indicates no water impact flex bearing damage occurred. Final evaluation to be included during flex bearing acceptance testing.

Objective	CEI Paragraph	Conclusion
Demonstrate the performance of the nozzle environmental protection.	3.2.1.4.7.c The plug shall be capable of being expelled without damaging any part of the Shuttle System or adversely affecting the SRM performance.	No debris or adverse propulsion effects from the nozzle plug expulsion were found (Section 4.11.4).
Postflight inspection to verify nozzle liner performance. Note: SCN 49 proposes to change the CEI paragraph wedgeout requirement from "greater than 0.250 in. deep" to "yield a positive margin of safety".	3.2.1.4.13 The nozzle flame front liners shall prevent the formation of: a. Pockets greater than 0.250 in. deep (as measured from the adjacent non-pocketed areas); b. Wedgeouts greater than 0.250 in. deep; c. Prefire anomalies except as allowed by TWR-16340.	No nozzle flame front liner erosion pockets greater than 0.25 in. were observed. All wedgeouts found greater than 0.25 in. occurred postburn and did not affect liner performance. No prefire anomalies were observed (Section 4.11.4).
Demonstrate performance of the exit cone severance ordnance ring.	3.2.1.4.12 Aft Exit Cone Severance Ordnance Ring. The aft exit cone severance ordnance ring shall sever a portion of the nozzle aft exit cone.	Successful severance of both nozzle exit cones at apogee was demonstrated. (Postflight nozzle inspection results are contained in Section 4.11.4 of this volume and Volume V of this report.)
Postflight inspection of ignition system seals for evidence of hot gas leakage.	3.2.1.5.a The ignition system shall preclude hot gas leakage during and subsequent to motor ignition.	All ignition system seals, gaskets, and sealing surfaces showed no evidence of heat effects, erosion, or blowby (Section 4.11.3).
Demonstrate that the igniter and safety and arming device (S&A) are separable.	3.2.1.5.b The igniter and the S&A shall be separable from each other.	The S&A and igniter were separated during postflight inspection. (Details contained in Volume VI of this report.)
Postflight inspection of igniter for evidence of debris formation or damage.	3.2.1.5.2 ...the igniter hardware and materials shall not form any debris...	Preliminary indications show no evidence of any igniter debris formation. (Complete evaluation contained in Volume VI of this report.)

Objective	CEI Paragraph	Conclusion
Post-test inspection of internal insulation for degradation.	3.2.1.8.1 Internal Insulation. ...shall be designed to ensure that the motor operational integrity and refurbishment capability is not degraded by assembly, storage in the assembled condition, flight, and/or subsequent thermal soak for thermal environments.	All internal insulation performed as designed and did not adversely affect motor operation during flight or during the subsequent thermal soak, or any refurbishment capability due to storage in the assembled condition. (Details contained in Section 4.11.1 of this volume and Volume III or this report.)
Postflight inspection of seals for protection of degradation from motor combustion gas.	3.2.1.8.1.1.d Insulation shall protect primary and secondary seals from visible degradation from motor combustion gas.	All motor combustion gas was contained by the insulation J-leg on the six field joints and the polysulfide adhesive on the two case-to-nozzle joints (Sections 4.11.1 and 4.11.3).
Postflight inspection of insulation for required performance.	3.2.1.8.1.1.e The insulation shall...meet all performance requirements under worst manufacturing tolerances and geometry changes during and after assembly and throughout motor operation.	Preliminary inspection indicates the insulation met all the performance requirements (Section 4.11.1). (Detailed results contained in Volume III of this report.)
Postflight inspection of shedding insulation material.	3.2.1.8.1.1.f Insulation materials shall not shed fibrous or particulate matter during assembly which could prevent sealing.	No shedding of fibrous or particulate matter during assembly was detected (Section 4.11.1 and Volume III).
Postflight inspection of joint insulation for evidence of slag accumulation damage.	3.2.1.8.1.1.g The joint insulation shall withstand slag accumulation during motor operation.	The insulation withstood all slag accumulation during motor operation (Section 4.11.1 and Volume III).
Postflight TPS inspection to insure no environmental damage to any RSRM components.	3.2.1.8.2 TPS shall insure that the mechanical properties of the RSRM components are not degraded when exposed to the environments...	Normal heat effects and discoloration noted on all TPS surfaces, with no significant areas of missing material. All weatherseal unbonds were a direct result of splashdown loads. (TPS performance contained in Section 4.8.3.1 of this volume.)

Objective	CEI Paragraph	Conclusion
Postflight inspection for thermal damage to igniter chamber or adapter metal parts.	3.2.1.8.3 The igniter insulation shall provide thermal protection for the main igniter chamber and adapter metal parts to ensure that RSRM operation does not degrade their functional integrity or make them unsuitable for refurbishment.	Preliminary investigation revealed no thermal damage to the igniter due to lack of insulation functionality. (Igniter details contained in Volume VI of this report).
Postflight inspection to verify that case components are reusable.	3.2.1.9.a Case--Cylindrical segments, stiffener segments, attach segments, forward and aft segments, stiffener rings, clevis joint pins.	Five outer ligament bolthole cracks on the RH stiffener case stubs were noted during preliminary investigation. Fretting observed on five of six field joints (Section 4.11.2). (Detailed inspection results are discussed in Volume II of this report.)
Postflight inspection to verify that nozzle metal parts are reusable.	3.2.1.9.b Nozzle metal parts--Boss attach bolts.	No damage or corrosion to any nozzle reusable metal parts was observed. (Section 4.11.4 of this volume and Volume V of this report.)
Flight demonstration followed by post-test inspection to verify that flex bearing is reusable.	3.2.1.9.c Flex bearing system--Reinforced shims and end rings, elastomer materials.	Post-test inspection results indicate no adverse flex bearing system problems. Complete evaluation to be done during acceptance testing.
Postflight inspection to verify that igniter components are reusable.	3.2.1.9.d Igniter--Chamber, adapter, igniter port, special bolts.	Preliminary postflight inspection revealed nothing that would adversely affect reuse of any igniter part. (Detailed inspection results contained in Volume VI of this report.)
Postflight inspection to verify that the S&A is reusable.	3.2.1.9.e Safe and Arm Device	Preliminary postflight inspection revealed nothing that would adversely affect reuse of any S&A part. (Detailed inspection results contained in Volume VI of this report.)

Objective	CEI Paragraph	Conclusion
Postflight inspection to verify that OPTs are reusable.	3.2.1.9.f Transducers	One OPT on 360L003B (RH) had some slight case damage which will be corrected during refurbishment. No other issues that would adversely effect OPT reuse were noted. (Details contained in Volume IX of this report.)
Postflight inspection of the case factory joint external seal for moisture.	3.2.1.12 The factory joint external seal shall prevent the prelaunch intrusion of rain into the factory joints from the time of assembly of the segment until launch...The factory joint seal shall remain intact through flight and, as a goal, through recovery.	The external weatherseal protected the case adequately from assembly until launch. Damage to the aft center segment weatherseal (IFA STA-29-M-2) and moisture penetration through development flight instrumentation (DFI) wire exit locations occurred at splashdown. (Detailed weatherseal evaluation is contained in Volume III of this report.)
Postflight inspection of hardware for damage or anomalies identified by failure modes and effects analyses (FMEA).	3.2.3 The design shall minimize the probability of failure, taking into consideration the potential failure modes identified and defined by failure modes effects analyses.	No hardware damage or anomalies that were identified by FMEAs were found. (Specific inspection results are contained in the individual component volumes of this report.)
Postflight inspections to determine adequacy of design SFs, relief provisions, fracture control, and safe-life and/or fail-safe characteristics.	3.2.3.1 The primary structure, thermal protection, and pressure vessel subsystems shall be designed to preclude failure by use of adequate design safety factors, relief provisions, fracture control, and safe-life and/or fail-safe characteristics.	Postflight inspections verified adequate design SFs, relief provisions, fracture control, and safe-life and/or fail-safe characteristics for the primary structure, thermal protection, and pressure vessel subsystems as documented in this volume and the component volumes of this report.
Postflight inspection to determine adequacy of subsystem redundancy and fail-safe requirements.	3.2.3.2 The redundancy requirements for subsystems...shall be established on an individual subsystem basis, but shall not be less than fail-safe...	The redundant heater on the RH aft field joint performed adequately after the primary heater failed during countdown (IFA STS-29-M-1). No other primary subsystem failure was noted.

Objective	CEI Paragraph	Conclusion
Postflight inspection for reuse of RSRM and its subsystems after recovery and retrieval.	3.2.5.7 Recovery and Refurbishment. The RSRM and its subsystems shall be capable of reuse following recovery and retrieval...	Preliminary inspection after recovery and retrieval indicated no damage that would prevent reuse of any RSRM subsystem. (Details are contained in the individual component volumes of this report.)
Postflight inspection of identification numbers of reusable components for traceability.	3.3.1.5 Traceability shall be provided by assigning a traceability identification to each RSRM part and material and providing a means of correlating each to its historical records...	Inspection numbers for traceability of each RSRM part and material are provided and maintained in the Automatic Data Collection and Retrieval (ADCAR) computer system. (The past history of all RSRM parts used is contained in Section 4.2 of this volume.)
Postflight inspection of case-to-insulation bonds structural SF.	3.3.6.1.1.2.a Case/Insulation Bonds. 3.3.6.1.1.2.b Adhesive Bonds. The structural safety factor for the...bonds shall be 2.0 minimum during the life of the RSRM.	Verification of a 2.0 SF cannot be done by inspection; however, flight performance verified a bond of at least 1. Case-to-insulation bond and adhesive bond 2.0 SF are verified by analysis and documented in TWR-16961.
Postflight inspection of adhesive bonds.	3.3.6.1.2.2 The case insulation shall have a minimum design safety factor of 1.5, assuming normal motor operation, and 1.2 assuming loss of a castable inhibitor.	Detailed postflight insulation inspections are performed at the Clearfield H-7 facility. (Results are contained in Volume III of this report.)
Postflight inspection of case insulation to verify remaining insulation thickness.	3.3.6.1.2.3 Case insulation adjacent to metal part field joints, nozzle/case joints, and extending over factory joints shall have a minimum safety factor of 2.0.	See above statement.
Postflight inspection of case insulation to verify remaining insulation thickness.	3.3.6.1.2.4 Case insulation in sandwich construction regions (aft dome and center segment aft end) shall have a minimum safety factor of 1.5.	See above statement.

Objective	CEI Paragraph	Conclusion
Postflight inspection of case insulation to verify remaining insulation thickness.	3.3.6.1.2.6 Insulation performance shall be calculated using actual pre- and post-motor operation insulation thickness measurements.	Standard measurement techniques were used for final evaluation, as discussed in Volume III of this report.
Postflight inspection to verify remaining nozzle ablative thickness.	3.3.6.1.2.7 The minimum design safety factors for the nozzle assembly primary ablative material shall be as listed below...(Values not included here, as detailed results are not available at this writing.)	Preliminary inspections indicate nozzle ablative thicknesses were within design SFs (Section 4.11.4). (Detailed results are contained in Volume V of this report.)
Postflight inspection to verify nozzle SFs.	3.3.6.1.2.8 The nozzle performance margins of safety shall be zero or greater...	The nozzle performance margins of safety are discussed in Volume V of this report.
Postflight inspection of functional and physical interfaces between SRBs and retrieval station.	3.6.2.e Interface Requirements. The RSRM shall meet the interface requirements of ICD 2-4A002 and the Solid Rocket Booster Retrieval Station.	Both RSRMs were successfully recovered and returned to the Clearfield facility for refurbishment. All recovery procedures that violated ICD 2-4A002 were documented as PIRNs and are being worked.
Postflight inspection for presence of stress corrosion.	3.3.8.2.b The criteria for material selection in the design to prevent stress corrosion failure of fabricated components shall be in accordance with MSFC-SPEC-522 and SE-019-094-2H.	No evidence of stress corrosion was found during post-test case inspection. (Details are contained in Volume II of this report.

3.3 RECOMMENDATIONS

Following are the recommendations made concerning flight set 360L003.

3.3.1 Structural Applications (Ascent Loads) Recommendations

To gain additional information concerning the girth gage spiking phenomena, it is recommended that the cases which had the spiking gages be inspected (during refurbishment) for out of roundness, case thickness, and any other abnormalities. Also, during the hydrotest a series of girth and biaxial gages should be installed to measure case strain.

Since this phenomenon (spiking) is not completely understood, it is also recommended that DFI be applied to future flights to help determine positively that this is not a real event. These are the same recommendations given for flight set 360L002.

3.3.2 Structural Dynamics Recommendations

It is recommended that accelerometers be mounted at or near the center area on at least four additional RSRM flights to monitor and further understand the SRB vibrations. Additional confidence and knowledge of the extreme vibrations detected in the center area must be gained through additional measurements and analyses.

3.3.3 Aerothermal Recommendations

3.3.3.1 Flight Thermal Design Environments. It is recommended that NASA consider incorporating additional body points and environments for hydrazine fire data into the next revision of the reentry thermal design environment data book. It is evident, based upon STS-29R nozzle region DFI response, that these additional body points and environments for hydrazine fires need to be incorporated for the SRB base region.

3.3.3.2 GEI Prediction. Additional model development is recommended for modeling regions that require more emphasis and detail in order to improve predictions. (Submodels of the ETA ring, field joint, factory joint, systems tunnel, igniter, and nozzle regions are anticipated to be incorporated into the global thermal effort.)

It is also recommended that all these models, including the three-dimensional (3-D) SRM model, be made available for use at Marshall Space Flight Center (MSFC). This would allow Morton Thiokol thermal personnel the opportunity to support launch countdowns at the Huntsville Operations Support Center (HOSC) with real-time PMBT, GEI, and component prediction updates as well as allow MSFC thermal personnel the same modeling capabilities for their needs.

3.3.3.3 Aft Skirt Conditioning. It is recommended that the aft skirt conditioning gas temperature be monitored as it enters the aft skirt compartment. It is apparent, based on the STS-29R GEI sensor steady state response, that substantial gas cooling occurs in the ducting system before the gas enters the aft skirt. During cold weather monitoring this would allow the use of a higher operating temperature and at the same time not violate the 115°F maximum within the compartment.

3.3.3.4 GEI Accuracy. It is recommended that GEI data collection accuracy be increased by reducing the gage range and increasing the digital word length.

3.3.3.5 Real-Time Data Acquisition. It is recommended that near-real-time on-pad GEI and environmental data be available to Morton Thiokol after pad validation. These data, collected hourly, need to be transmitted electronically at weekly intervals until 2 weeks prior to scheduled launch dates. From this point until launch, daily transmittals are necessary. These data are necessary to help meet the requirement of PMBT updates prior to launch and to aid in predicting the local SRM environment by building a variable conditions data base.

3.3.3.6 Nozzle Severance

Based on the severe reentry heating environments of STS-29R, it is recommended that nozzle severance occur just prior to splashdown rather than at apogee. Reentry nozzle flame heating was significant for this flight, exceeding the 95-percent design environments.

It is also recommended that Thiokol obtain formal contract direction concerning hydrazine fires before the redesign of the nozzle severance cable.

4

FLIGHT EVALUATION RESULTS AND DISCUSSION

4.1 RSRM IN-FLIGHT ANOMALIES (FEWG REPORT SECTION 2.1.2)

The summary sheets for the four IFAs identified during evaluation of flight set 360L003 follow. These summary sheets contain the description, discussion, conclusions, and corrective actions for each anomaly. All IFAs have been closed, as indicated by the approval signature of the Level II PRCB chairman. None was considered to be a flight constraint.

4.2 RSRM CONFIGURATION SUMMARY (FEWG REPORT SECTION 2.1.3.2)

4.2.1 RSRM Reuse Hardware

Figures 4.2-1 through 4.2-3 detail the reuse hardware for the 360L003 case segments, LH igniter, and RH igniter, respectively. Figure 4.2-4 and Table 4.2-1 show the reuse history of the LH nozzle, while Figure 4.2.5 and Table 4.2-2 show the reuse history for the RH nozzle. The stiffener ring components are shown in Figure 4.2-6 and the respective reuse history is explained in Table 4.2-3.

4.2.2 SRM Hardware Changes

Below is a summary of the hardware changes made since 360L002 (STS-27R). A complete description of these hardware changes is included in Morton Thiokol document TWR-19001a, Redesigned Solid Rocket Motor Flight Readiness Review--MSFC Level III.

Nine Class I Hardware Changes Since 360L002 (STS-27R):

a. Vent port plug installation, ECP SRM 1632--Added custom vent port plug with redundant, verifiable seals to satisfy CEI paragraphs in RH aft center segment and self-locking nylon patch leak check port plug on both case-to-nozzle joints.
b. Vent port plug nylon patch locking feature, ECP SRM 1725R1--Added nylon patch to leak check port plugs in both nozzle exit cone joints to comply with CEI requirements.
c. New O-rings on barrier-booster rotor shaft, ECP SRM 11744R1--Provide adequate O-ring squeeze values
d. Revise DFI wire routing, ECP SRM 1716R2--Allow for changes to igniter heater, nozzle instrumentation, and TPS configuration drawings.
e. Replace heater cable cork lids with K5NA, FEC RSRM 039--Eliminate potential debris by replacing TPS cork lids over heater cables with K5NA.
f. Drill side holes on pin retainer buckle Kevlar® strap, FEC RSRM 046R1--Alleviate possibility of pressure differential in suspected voids.

ORIGINAL PAGE IS
OF POOR QUALITY

PCIN 44960	NSTS PROGRAM REQUIREMENTS CONTROL BOARD DIRECTIVE - LEVEL II	PAGE 01 OF 03
PRCBD S44960		PRCB DATE 04/13/89

CHANGE TITLE
RSRM RIGHT HAND AFT FIELD JOINT PRIMARY HEATER CIRCUIT MALFUNCTION (IFA)

CHANGE PROPOSAL(S) NO. AND SOURCE STS-29 ANOMALY TRACKING LIST FLIGHT PR#STS-29-M-1	DOCUMENTS AFFECTED (NO.,TITLE,PARA)
INITIATED BY: MSFC-SA41/G. SMITH	SUBMITTED BY: MSFC-SA01/W. MARSHALL

LEVEL II BASELINE CHANGE DIRECTION: OPR: WA SJ/AR BOARD: DAILY

THIS PRCBD IS ISSUED TO AUTHORIZE THE CLOSEOUT OF STS-29 SRB ANOMALY NUMBER STS-29-M-1 PER THE FOLLOWING RATIONALE:

STATEMENT OF PROBLEM:

. RSRM RIGHT HAND AFT FIELD JOINT PRIMARY HEATER CIRCUIT
. CEASED FUNCTIONING AFTER APPROXIMATELY 11 HOURS OF OPERATION.
. REDUNDANT HEATER WAS ACTIVATED FOR REMAINDER OF THE COUNTDOWN.

DISCUSSION:

. FOLLOWING THE HEATER MALFUNCTION, HEATER MONITORS SHOWED NO
. VOLTAGE TO THE CIRCUIT AND A TEMPERATURE GRADIENT DECREASE.
. THE REDUNDANT HEATER WAS POWERED-UP AND FUNCTIONED UNTIL
. LAUNCH. POST FLIGHT INSPECTIONS/MEASUREMENTS AT THE TO
. (TAKEOFF) UMBILICAL SHOWED AN OPEN CIRCUIT IN THE PRIMARY
. HEATER. OTHER HEATER ELEMENT MEASUREMENTS WERE NOMINAL.
. REMOVAL OF FOAM AND K5NA FROM THE PRIMARY HEATER CABLE
. CONNECTOR AND BACKSHELL REVEALED ARCING DAMAGE AND BURN
. THROUGH OF POWER LEADS. RECOVERED HEATER CONNECTOR PARTS
. WERE REMOVED AND SUBMITTED TO KSC MALFUNCTION ANALYSIS LAB
. FOR FAILURE ANALYSIS. RESULTS OF THE ANALYSIS INDICATOR
. TWO POSSIBLE FAILURE SCENARIOS.

AUTHORIZATION:

[signature]

CHAIRMAN, LEVEL II PRCB

04/~~13~~ 14/89

DATE

BARS RPT B020 BARS NSTS FORM 4003

PCIN 44960	NATIONAL SPACE SHUTTLE PROGRAM DOCUMENT CONTINUATION SHEET	PAGE 02 OF 03
S44960		OFFICE:
DOCUMENT: S44960		DATE 04/13/89

HEATER FAILURE SCENARIOS

1. THE FAILURE WAS INSIDE THE BACK SHELL OF THE CONNECTOR AS A RESULT OF STRANDS OF THE ELECTRICAL CABLE SHIELDING WHICH WERE INSIDE THE BACKSHELL AND AGAINST THE CONDUCTOR INSULATION AT THE TIME OF POTTING. THE INSULATION WAS DAMAGED AT THIS POINT. OVER A PERIOD OF TIME AN ELECTRICAL PATH WAS GENERATED BY CARBONIZATION OF THE KAPTON INSULATION BY THE 208 VAC HEATER POWER. A CATASTROPHIC FAILURE OCCURRED WHEN THE CARBONIZED PATH WAS COMPLETED.

2. THE FAILURE WAS IN THE ELECTRICAL INSULATION OF THE CONDUCTORS JUST OUTSIDE THE BACKSHELL OF THE CONNECTOR. THE KAPTON INSULATION WAS NICKED AND REPEATED BENDING CAUSED THE INSULATION TO BREAK OPEN. WHEN THE 208 VAC POWER WAS APPLIED TO THE HEATER, A CARBONIZED BATH WAS GRADUALLY FORMED THROUGH THE BREAK IN THE INSULATION. A CATASTROPHIC FAILURE OCCURRED WHEN THE CARBONIZED PATH WAS COMPLETED.

CONCLUSIONS:
THE 25 AMP CIRCUIT BREAKER WAS INEFFECTIVE IN SENSING THE FAILURE OR BREAKING THE CIRCUIT PRIOR TO DAMAGE. AN ELECTRICAL SHORT CIRCUIT OCCURRED BETWEEN THE PRIMARY HEATER POWER CONDUCTOR AND THE CABLE CONNECTOR BACKSHELL (SEE ATTACHED FIGURE 1). THE ELECTRICAL SHORT-CIRCUIT AND SUBSEQUENT ARCING RESULTED IN HEATER CONNECTOR DAMAGE THAT INTERRUPTED POWER TO PRIMARY HEATER ELEMENT. 25.0 AMP CIRCUIT BREAKER WAS INEFFECTIVE. REMOVAL AND INSTALLATION OF A NEW AFT CENTER SEGMENT HEATER POWER CABLE MAY HAVE DAMAGED THE HEATER CONNECTOR AND CONTRIBUTED TO THE SHORT CIRCUIT. SYSTEM DIELECTRIC WITHSTANDING VOLTAGE (DWV) TEST WAS NOT PERFORMED AFTER POWER CABLE REPLACEMENT.

PCIN 44960	NATIONAL SPACE SHUTTLE PROGRAM DOCUMENT CONTINUATION SHEET	PAGE 03 OF 03
S44960		OFFICE:
DOCUMENT: S44960		DATE 04/13/89

CORRECTIVE ACTION:
CORRECTIVE ACTION IS BEING IMPLEMENTED IN A TWO PHASE FASHION. IMMEDIATE CORRECTIVE ACTIONS TO ASSURE STS-30 SAFETY-OF-FLIGHT FOR THE EXISTING HEATER DESIGN INCLUDES IMPLEMENTATION OF THE INDIVIDUAL DWV TESTS FOR ALL INSTALLED STS-30 RSRM FIELD JOINT HEATERS. ADDITIONALLY IN THE UNLIKELY EVENT THAT AN ANOMALOUS CONDITION ESCAPES DETECTION, TWO OPERATIONAL SAFEGUARDS HAVE BEEN INCORPORATED: (1) FAST ACTING 20.0 AMP CIRCUIT BREAKERS HAVE BEEN TESTED AND INSTALLED FOR STS-30. THESE WILL DEACTIVATE HEATER SYSTEM IF AN STS-29 TYPE ANOMALY OCCURS. (2) A NEW CIRCUIT MONITORING AND PROTECTION SYSTEM COMPUTER SOFTWARE PACKAGE HAS BEEN TESTED AND INSTALLED FOR STS-30. SOFTWARE FEATURES HEATER SHUTDOWN AT 19.5 AMPS WITH 40-60 MILLISECONDS RESPONSE TIME. RCN 8865 HAS BEEN INITIATED TO REDUCE THE HEATER ACTIVATION TIME FROM L-24 HOURS TO L-8 HOURS. ALL HEATER/CABLES (EXCEPT LEFT FORWARD FIELD JOINT REDUNDANT HEATER) HAVE PASSED INDIVIDUAL AND END-TO-END SYSTEM DWV TESTS. IF THE LEFT FORWARD FIELD JOINT PRIMARY HEATER FAILS, A CONTINGENCY LCC CHANGE (ECP SRM 2071/ECS 3082) IS BEING INITIATED TO CONTINUE LAUNCH COUNTDOWN PROVIDED THE MONITORED JOINT TEMPERATURE DOES NOT GO BELOW 73 DEGREES. THIS ACTION MINIMIZES THE POTENTIAL FOR LCC VIOLATION IN THE UNLIKELY EVENT OF PRIMARY HEATER FAILURE.

IN ADDITION TO THE NOTED STS-30 CORRECTIVE ACTIONS, SUBSEQUENT FLIGHT DESIGN MODIFICATIONS ARE CURRENTLY BEING EVALUATED. A RE-ASSESSMENT OF THE CURRENT DESIGN IS UNDERWAY, AND CURRENT CONSIDERATIONS INCLUDE POSSIBLE MODIFICATIONS TO CONDUCTOR WIRE INSULATION, CONNECTOR POTTING MATERIAL AND CHOICE OF CONNECTOR, ELIMINATION OF 2 CONDUCTOR WIRES, AND RE-EVALUATION OF ASSEMBLY TECHNIQUES AND SAFEGUARDS.

EFFECTIVITY: STS-29

LEVEL II IMPACTS AUTHORIZED BY THIS DIRECTION: --WEIGHT: NONE, --SCHEDULE: NONE, --COST: NONE.

PCIN 44961 PRCBD S44961	NSTS PROGRAM REQUIREMENTS CONTROL BOARD DIRECTIVE - LEVEL II	PAGE 01 OF 02 PRCB DATE 04/12/89

CHANGE TITLE
LEFT HAND AFT CENTER FACTORY JOINT WEATHERSEAL UNBOND (IFA)

CHANGE PROPOSAL(S) NO. AND SOURCE STS-29 ANOMALY TRACKING LIST FLIGHT PR #STS-29-M-2	DOCUMENTS AFFECTED (NO.,TITLE,PARA)
INITIATED BY: MSFC-SA41/G. SMITH	SUBMITTED BY: MSFC-SA01/W. MARSHALL

LEVEL II BASELINE CHANGE DIRECTION: OPR: WA SJ/LS BOARD: DAILY

THIS PRCBD IS ISSUED TO AUTHORIZE THE CLOSEOUT OF STS-29 SRB ANOMALY NUMBER STS-29-M-2 PER THE FOLLOWING RATIONALE:

STATEMENT OF PROBLEM:
. STS-29 LEFT HAND AFT CENTER FACTORY JOINT WEATHERSEAL UNBOND.

DISCUSSION:
. POST FLIGHT INSPECTION REVEALED THE LEFT HAND (LH) AFT CENTER FACTORY JOINT OF RSRM-3A HAD SEVERAL SEPARATE UNBONDS ON THE AFT EDGE OF THE FACTORY JOINT WEATHERSEAL. THE UNBONDS WERE ALL ADHESIVE FAILURES BETWEEN THE CASE AND THE CHEMLOK 205 PRIMER. UNBONDS OCCURRED IN 11 SEPARATE AREAS. VISUAL INSPECTION OF JOINT SHOWED PIN RETAINER BAND TO BE RAISED IN ONE UNBOND AREA. FURTHER INSPECTION REVEALED THE PIN RETAINER BAND WAS STRETCHED BUT NOT BROKEN. PRELIMINARY EVALUATIONS INDICATE UNBONDS ARE THE RESULT OF SPLASHDOWN LOADS AS DAMAGE WAS OBSERVED TO OCCUR ON THE AFT EDGE OF WEATHERSEAL. THE LOCATION OF DAMAGE WOULD PRECLUDE ANY SCENARIO ASSOCIATED WITH AN ASCENT OCCURRENCE. REVIEW OF FABRICATION LOGS (RSRM-1 THRU RSRM-5) REVEALS A CONTAMINATION PROBLEM ON THIS PARTICULAR FACTORY JOINT (VIA CONSCAN). SURFACE FINISH READINGS INDICATE THIS JOINT WAS THE SMOOTHEST FACTORY JOINT TO DATE. WEATHERSEAL SAMPLES REMOVED FROM THE LH CENTER AFT SEGMENT DO NOT INDICATE SHEAR OR STRESS FAILURE, FURTHER SUPPORTING CONTAMINATION THEORY.

AUTHORIZATION

CHAIRMAN, LEVEL II PRCB — 04/12/89 DATE

RARS RPT 8020 — RARS NSTS FORM 4003

PCIN 44961	NATIONAL SPACE SHUTTLE PROGRAM DOCUMENT CONTINUATION SHEET	PAGE 02 OF 02
S44961		OFFICE:
DOCUMENT: S44961		DATE 04/12/89

CONCLUSIONS:
. WEATHERSEAL DAMAGE RESULTED FROM SPLASHDOWN IMPACT,
. ALTHOUGH THE FACTORY JOINT SURFACE CONTAMINATION AND
. SMOOTHNESS MAY HAVE CONTRIBUTED TO A REDUCED BOND STRENGTH.
. FACTORY JOINT DAMAGE OF THIS TYPE IS NOT CONSIDERED TO BE
. A FLIGHT SAFETY ISSUE. IT IS A REUSE CONCERN BECAUSE OF
. THE WATER INTRUSION INTO THE JOINT (METAL CORROSION CONCERN).

CORRECTIVE ACTION:
. CONSCAN LIMITS THAT HAVE BEEN IMPOSED ON ALL FACTORY
. JOINTS AND SURFACE FINISH REQUIREMENTS ARE CURRENTLY
. BEING REVIEWED.

EFFECTIVITY: STS-29

LEVEL II IMPACTS AUTHORIZED BY THIS DIRECTION: --WEIGHT: NONE, --SCHEDULE: NONE, --COST: NONE.

PCIN 44962	NSTS PROGRAM REQUIREMENTS CONTROL BOARD DIRECTIVE - LEVEL II	PAGE 01 OF 02
PRCBD S44962		PRCB DATE 04/13/89

CHANGE TITLE
. L/H EXIT CONE EXHIBITED MISSING CCP AND GCP (IFA)

CHANGE PROPOSAL(S) NO. AND SOURCE STS-29 ANOMALY TRACKING LIST FLIGHT PR #STS-29-M-3	DOCUMENTS AFFECTED (NO., TITLE, PARA)
INITIATED BY: MSFC-SA41/G. SMITH	SUBMITTED BY: MSFC-SA01/W. MARSHALL

LEVEL II BASELINE CHANGE DIRECTION: OPR: WA SJ/LS BOARD:DAILY

THIS PRCBD IS ISSUED TO AUTHORIZE THE CLOSEOUT OF STS-29 SRB ANOMALY NUMBER STS-29-M-3 PER THE FOLLOWING RATIONALE:

STATEMENT OF PROBLEM:
. STS-29 LEFT HAND EXIT CONE EXHIBITED MISSING CARBON CLOTH PHENOLIC (CCP) LINER AND GLASS CLOTH PHENOLIC (GCP) INSULATOR MATERIALS.

DISCUSSION:
. POST FLIGHT INSPECTION REVEALED MISSING CARBON CLOTH PHENOLIC LINER AND GLASS CLOTH PHENOLIC INSULATOR OVER APPROXIMATELY 95 PERCENT OF THE FORWARD (UNSEVERED) PORTION OF THE AFT EXIT CONE SHELL. FIVE SMALL 'SPOTS' OF ADHESIVE REMAINED BONDED TO THE SHELL AND EXHIBITED A GLOSSY FINISH AT THE GLASS CLOTH PHENOLIC INTERFACE, INDICATING THAT BONDLINE VOIDS WERE PRESENT. STS-29 AFT EXIT CONE(S) SEVERANCE OCCURRED AT APOGEE AND MAY HAVE CONTRIBUTED TO LOSS OF PHENOLICS DUE TO INCREASED HEATING OF THE SHELL EXTERIOR AND ADHESIVE BONDLINES.

AUTHORIZATION: [signature]
CHAIRMAN, LEVEL II PRCB

04/13/89
DATE

BARS RPT 8020 BARS NSTS FORM 4003

PCIN 44962	NATIONAL SPACE SHUTTLE PROGRAM DOCUMENT CONTINUATION SHEET	PAGE 02 OF 02
S44962		OFFICE:
DOCUMENT: S44962		DATE 04/13/89

- REVIEW OF STS-29 INSTRUMENTATION DATA SHOWS THAT THE LINER AND INSULATOR WERE LOST DUE TO LOADS RESULTING FROM SPLASHDOWN. THE EXPOSED ALUMINUM SHELL SHOWED NO SIGNS OF ANY HEAT EFFECTS, FURTHER INDICATING THIS EVENT OCCURRED AT SPLASHDOWN. A REVIEW OF THE STS-29 AFT EXIT CONE BONDING LOG SHOWS THAT NO DISCREPANCY REPORTS OR PROCESS DEPARTURES WERE INITIATED DURING PROCESSING. ONE EDGE VOID WAS REPAIRED PER STANDARD SHOP PLANNING.

CONCLUSIONS:

- SHELL EXTERIOR TEMPERATURES WERE SIGNIFICANTLY HIGHER BETWEEN 300 SECONDS (RE-ENTRY INTO ATMOSPHERE) AND 400 SECONDS (SPLASHDOWN). SEVERING AT APOGEE CAUSED INCREASED HEATING OF THE SHELL, LOSS OF BOND AND LOSS OF THE EXIT CONE PHENOLICS AT SPLASHDOWN. STRUCTURAL ANALYSIS RESULTS (MTI TWR-16975) SHOW AFT EXIT CONE PHENOLICS ARE IN COMPRESSION AND WILL REMAIN IN THE SHELL THROUGHOUT MOTOR BURN, WITH CONSERVATIVE ASSUMPTIONS, INCLUDING NO ADHESIVE BOND STRENGTH. NO PROCESSING PROBLEMS ARE KNOWN TO HAVE AFFECTED THE AFT EXIT CONE COMPONENT BONDING/ FABRICATION.

CORRECTIVE ACTION:

- STS-30 AFT EXIT CONE SEVERANCE WILL NOT OCCUR AT APOGEE. KSC POST FLIGHT ENGINEERING EVALUATION LIMITS DOCUMENT (TWR 18860, VOL. 5) WILL BE REVISED TO SHOW THAT POST-FLIGHT INSPECTION FINDINGS OF: 1. EXIT CONE GCP LINER AND GCP INSULATOR DAMAGE AT SPLASHDOWN, AND 2. SMALL AFT EXIT CONE SHELL BONDLINE VOIDS ARE BOTH ACCEPTABLE AND SHOULD BE EXPECTED.

EFFECTIVITY: STS-29

LEVEL II IMPACTS AUTHORIZED BY THIS DIRECTION: --WEIGHT: NONE, --SCHEDULE: NONE, --COST: NONE.

PCIN 44963	NSTS PROGRAM REQUIREMENTS CONTROL BOARD DIRECTIVE - LEVEL II	PAGE 01 OF 02
PRCBD S44963		PRCB DATE 04/13/89

CHANGE TITLE
FRETTING CORROSION PITS/SCRATCHES/GOUGES ON RSRM LH AND RH CASE FIELD JOINT CAPTURE FEATURE INTERFERENCE SURFACES (IFA)

CHANGE PROPOSAL(S) NO. AND SOURCE STS-29 ANOMALY TRACKING LIST FLIGHT PR# STS-29-M-4	DOCUMENTS AFFECTED (NO.,TITLE,PARA)
INITIATED BY: MSFC-SA41/G. SMITH	SUBMITTED BY: MSFC-SA01/W. MARSHALL

LEVEL II BASELINE CHANGE DIRECTION: OPR: WA SRJ/MLB BOARD:DAILY

THIS PRCBD IS ISSUED TO AUTHORIZE THE CLOSEOUT OF STS-29 SRB ANOMALY NUMBER STS-29-M-4 PER THE FOLLOWING RATIONALE:

STATEMENT OF PROBLEM:
FRETTING CORROSION PITS/SCRATCHES/GOUGES ON STS-29 RSRM LH AND RH CASE FIELD JOINT CAPTURE FEATURE INTERFERENCE SURFACES.

DISCUSSION:
INITIAL STS-29 POST FLIGHT HARDWARE INSPECTIONS IDENTIFIED THAT 4 OF 6 CASE FIELD JOINTS HAD TYPICALLY FRETTED AREAS ON INTERFERENCE FIT SURFACES. ANOTHER WAS FRETTED VERY LIGHTLY AND A SIXTH JOINT EXHIBITED NO FRETTING. THE RH AFT FIELD JOINT FRETTING SCARS WERE DEEPER (0.013") AND MORE SEVERE THAN ANY SENT TO DATE (STS-26 & 27R). AS IN PREVIOUS FRETTING INSPECTIONS, THE FRETTING SCARS (SCRATCHES/SMALL PITS/ GOUGES) OBSERVED ON INNER CLEVIS LEG JOINT SURFACES ARE MATCHED WITH CORRESPONDING PITTED AREAS ON THE CAPTURE FEATURE SURFACE. THIS IS THE FIRST INSTANCE OF A FRETTING SCAR EXCEEDING THE 0.010" DEPTH LIMIT ALLOWED BY THE CASE REFURBISHMENT SPECIFICATION STW7-2744. FRACTURE MECHANICS ANALYSIS IS BEING UTILIZED TO DETERMINE/PREDICT EXPECTED REUSE LIFE OF SUCH FRETTED CASE HARDWARE.

AUTHORIZATION

CHAIRMAN, LEVEL II PRCB

04/13/89
DATE

BARS RPT 8020 BARS NSTS FORM 4003

PCIN 44963	NATIONAL SPACE SHUTTLE PROGRAM DOCUMENT CONTINUATION SHEET	PAGE 02 OF 02
S44963		OFFICE:
DOCUMENT: S44963		DATE 04/13/89

CONCLUSIONS:

FRETTING OCCURS AT METAL-TO-METAL CONTACT SURFACES UNDER LOAD AND SUBJECTED TO VIBRATION AND SLIP. RSRM CASE FRETTING CAUSED BY HIGHLY LOCALIZED FRICTION WELDING BETWEEN CLOSELY-FITTING INTERFERENCE PORTION OF THE MATCHED FIELD JOINT CAPTURE FEATURE SURFACES. TIME OF OCCURRENCE REMAINS UNCLEAR. STS-29 RH AFT FIELD JOINT FRETTING SCARS (0.013") EXCEED CURRENT REFURBISHMENT SPECIFICATIONS LIMITS (0.010") MAXIMUM DEPTH AND WILL RESULT IN A DISCREPANCY REPORT DURING REFURBISHMENT INSPECTION. FRETTING IS NOT CONSIDERED TO BE A FLIGHT SAFETY ISSUE.

CORRECTIVE ACTION:

CONTINUE WITH POST FLIGHT REFURBISHMENT ACTIVITY OF HAND REMOVAL OF ALL BURRS AND SMOOTHING OF ANY RAISED METAL ON BOTH CAPTURE FEATURE COMPONENT SURFACES. STUDY/EVALUATE METHODS TO PINPOINT TIME OF OCCURRENCE. CONTINUE SUBSCALE MODELING/TESTING ACTIVITIES AND JOINT SURFACE COATING AND LUBRICATION STUDIES. CONDUCT FRACTURE MECHANICS ANALYSIS TO PREDICT USEFUL LIFE.

EFFECTS ON SUBSEQUENT MISSIONS:

FRACTURE MECHANICS CALCULATIONS INDICATE FLAWS OF THIS MAGNITUDE (0.013" DEPTH X 0.33" LENGTH X 0.22" WIDTH) WOULD ALLOW AN ESTIMATED 60-70 HARDWARE USES BEFORE ACHIEVING A CRITICAL SIZE. FRETTING IS CURRENTLY CONSIDERED TO BE A REFURBISHMENT ISSUE WITH NO FLIGHT SAFETY EFFECTS.

EFFECTIVITY: STS-29

LEVEL II IMPACTS AUTHORIZED BY THIS DIRECTION: --WEIGHT: NONE, --SCHEDULE: NONE, --COST: NONE.

Hydroproofs	Previous Use	LH (360L003A)	Case Segment	RH (360L003B)	Previous Use	Hydroproofs
4	SRM-21B, DM-9	S/N 0000028R2	Case Segment—Fwd Dome P/N 1U51473-01	S/N 0000047	New	3
6	QM-1, SRM-3B, 10B, 20A	S/N 0000057R4	Case Segment—Cylinder P/N 1U50131-11	S/N 0000079R3	SRM-2A, 9B, 20B	6
3	New	S/N 0000009	Case Segment—Capture Cylinder, Standard Weight P/N 1U52983-01	S/N 0000011	New	3
4	SRM-20B	S/N 0000093R1	Case Segment—Cylinder, Lightweight P/N 1U50717-03	S/N 0000070R2	SRM-14A, 24A	4
3	New	S/N 0000030	Case Segment—Capture Cylinder, Lightweight P/N 1U52982-02	S/N 0000005R1	DM-8	4
4	SRM-14B, 24B	S/N 0000071R2	Case Segment—Cylinder, Lightweight P/N 1U50717-03	S/N 0000118	New	3
3	New	S/N 0000029	Case Segment—Capture Cylinder, Lightweight P/N 1U52982-02	S/N 0000032	New	3
4	SRM-8B, HI	S/N 0000008R2	Case Segment, Attach—Lightweight P/N 1U50716-06	S/N 0000005R2	SRM-7B, 16B	4
3	SRM-21B	S/N 0000033R1	Case Segment—Stiffener, Lightweight P/N 1U50715-03	S/N 0000054	New	5
3	New	S/N 0000039	Case Segment—Stiffener, Lightweight P/N 1U50715-03	S/N 0000050	New	5
3	ETM-1A	S/N 0000041R1	Case Segment—Aft Dome P/N 1U50129-11	S/N 0000048	New	4

Note: No fleet leader hardware on 360L003 case

A022453a

Figure 4.2-1. Previous Use History—Case (pressure vessel)

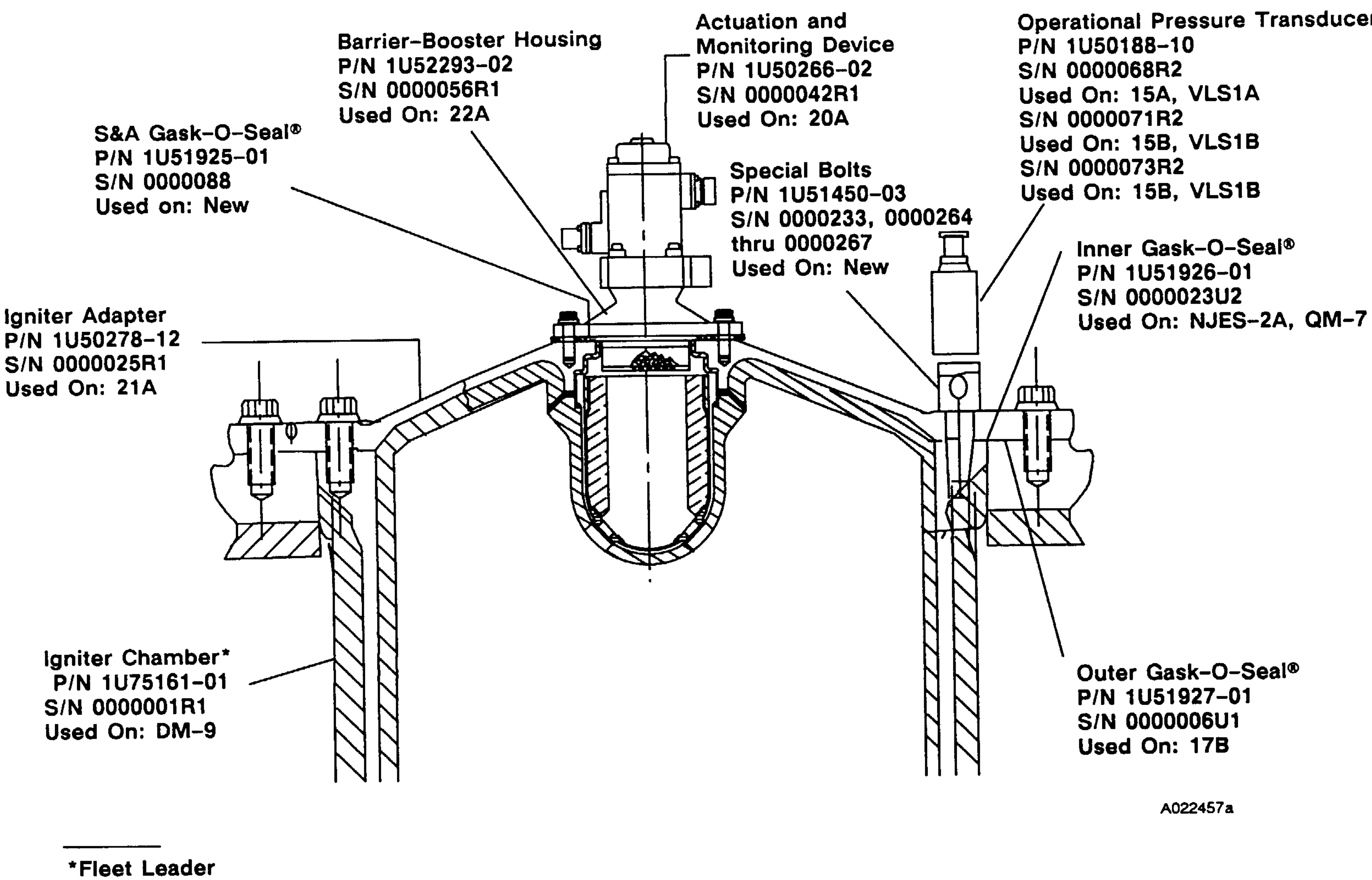

Figure 4.2-2. Previous Use History—LH Igniter

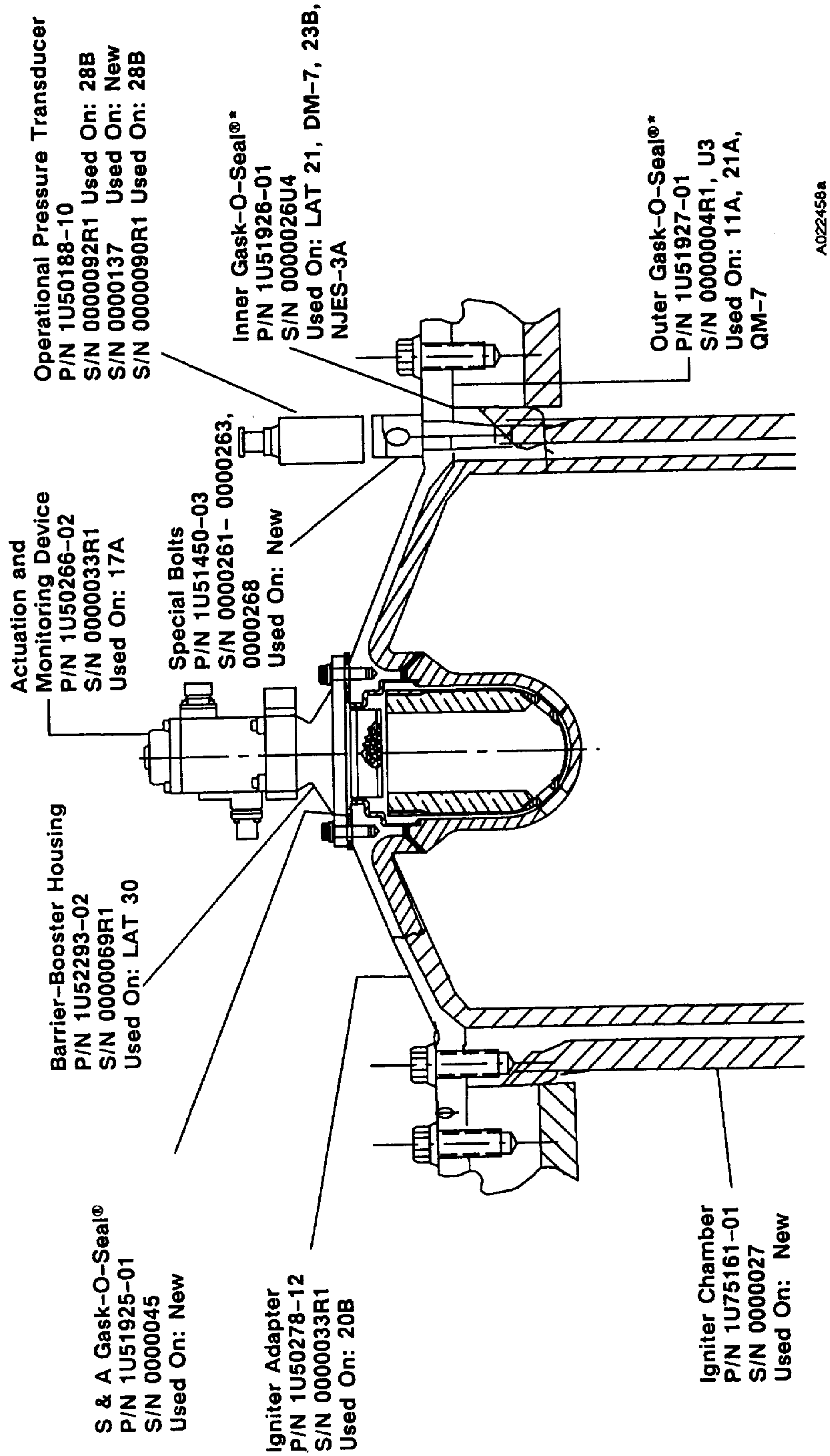

*Fleet Leader

Figure 4.2-3. Previous Use History—RH Igniter

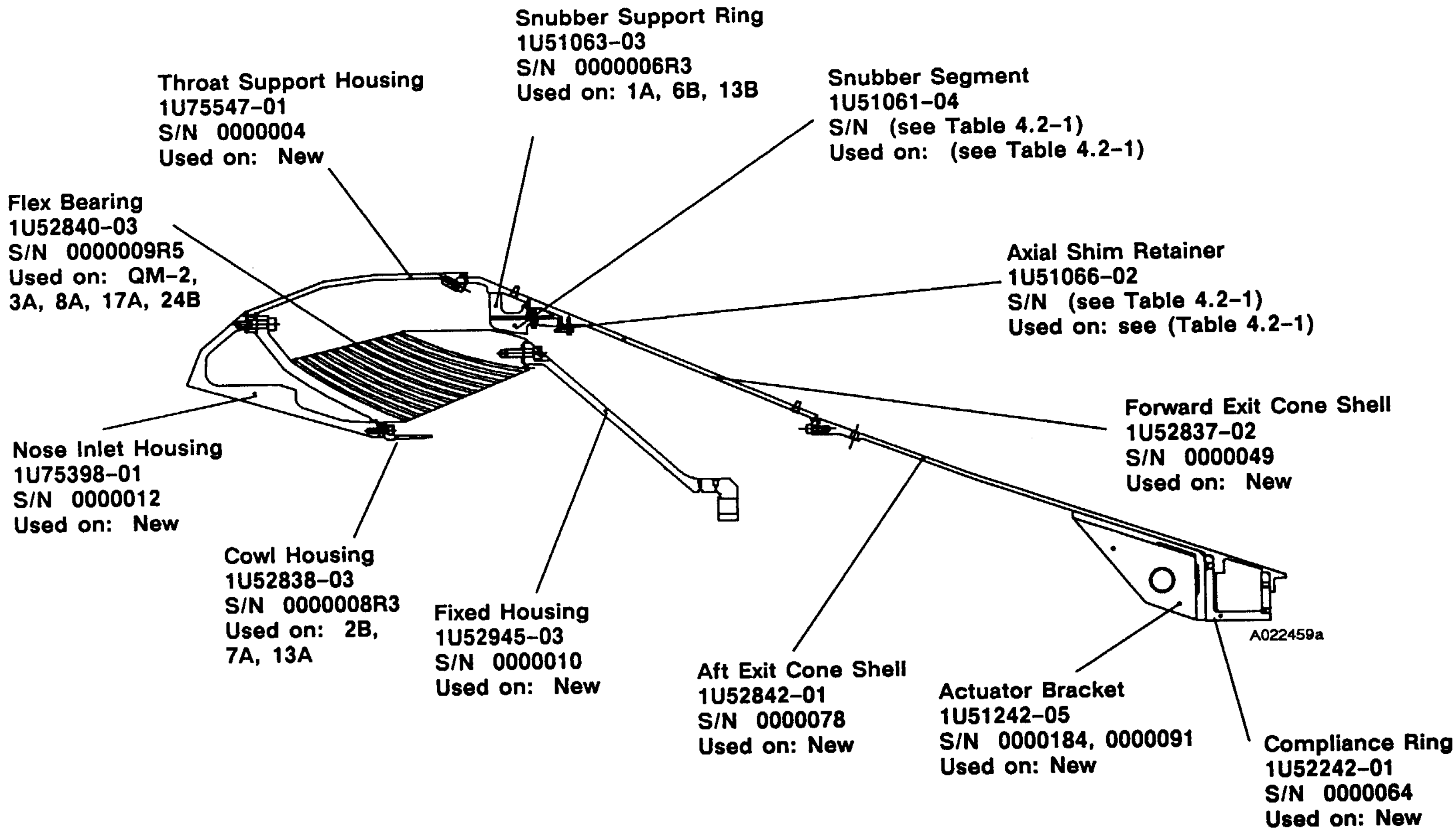

Note: No fleet leader hardware on LH nozzle

Figure 4.2-4. Previous Use History—LH Nozzle

Table 4.2-1. Previous Use History--LH Nozzle (360L003A)

Part No.	Serial No.	Previous Use
1U51061-04, Snubber Segment	0000106R1	SRM-5A
	0000107R1	SRM-5A
	0000108R2	SRM-5A, 19A
	0000109R1	SRM-5A
	0000110R2	SRM-5A, 19A
	0000111R2	SRM-5A, 19A
	0000112R2	SRM-5A, 19A
	0000113R2	SRM-5A, 19A
	0000114R2	SRM-5A, 19A
	0000115R2	SRM-5A, 19A
	0000116R2	SRM-5A, 19A
	0000117R2	SRM-5A, 19A
	0000118R2	SRM-5A, 19A
	0000119R1	SRM-5A
	0000120R1	SRM-5A
	0000121R2	SRM-5A, 19A
	0000122R2	SRM-5A, 19A
	0000123R1	SRM-5A
	0000124R1	SRM-5A
	0000125R2	SRM-5A, 19A
	0000126R2	SRM-5A, 19A
	0000127R2	SRM-5A, 19A
	0000135R2	SRM-5A, 19A
	0000139R2	SRM-5A, 19A
	0000141R1	SRM-5A
	0000144R1	SRM-5A
	0000155R1	SRM-5A
	0000159R2	SRM-5A, 19A
	0000162R2	SRM-5A, 19A
	0000941R1	SRM-19A
	0000942R1	SRM-19A
	0000943R1	SRM-19A
1U51066-02, Axial Shim Retainer	0001122 through	New
	0001313	New
	0001314	New

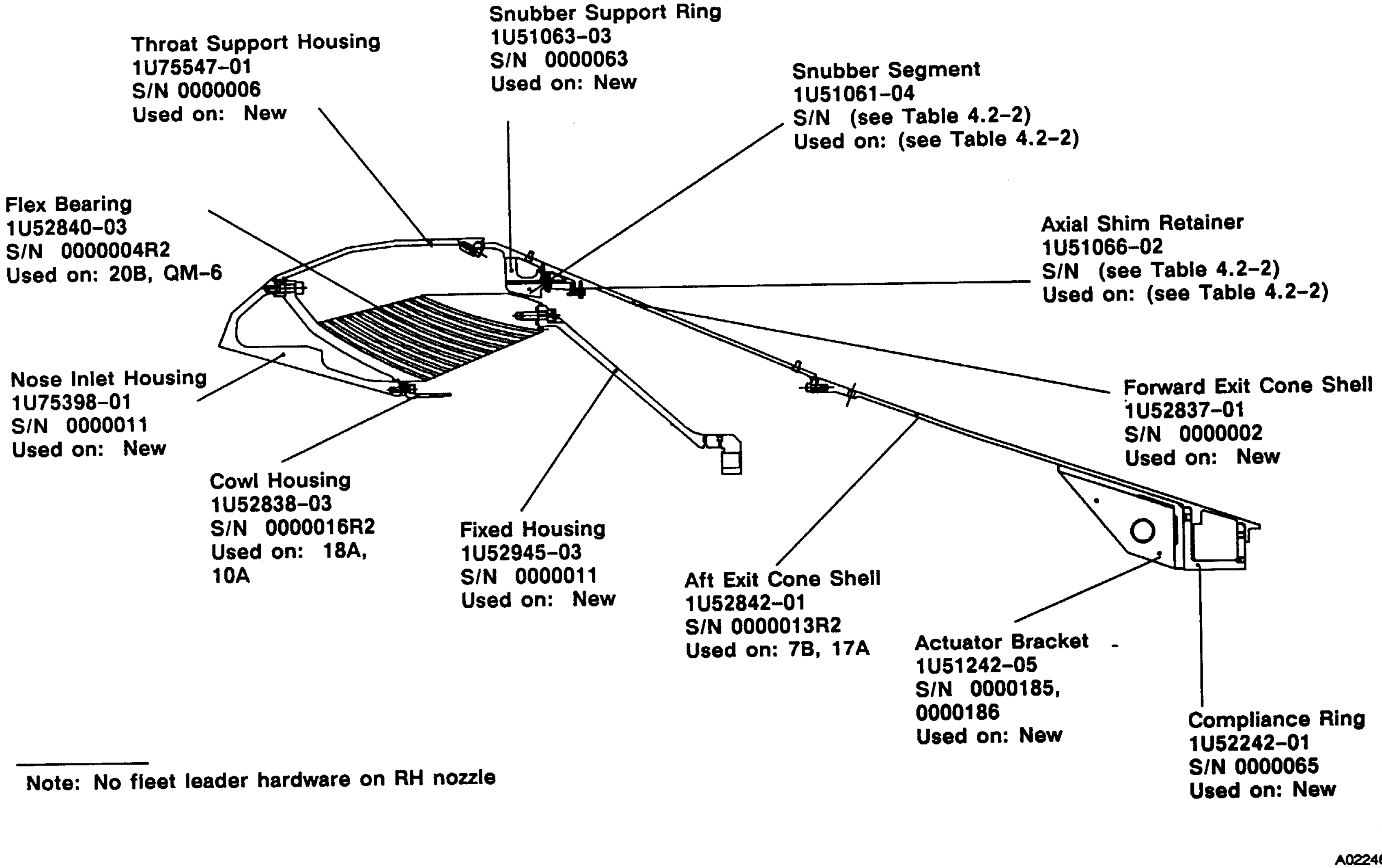

Figure 4.2-5. Previous Use History—RH Nozzle

Table 4.2-2. Previous Use History--RH Nozzle (360L003B)

Part No.	Serial No.	Previous Use
1U51061-04, Snubber Segment	0001601 through 0001632	New
1U50166-02, Axial Shim Retainer	0001315 through 0001339, 0001341, 0001342, 0001344, 0001345, 0001346, 0001347, 0001348	New

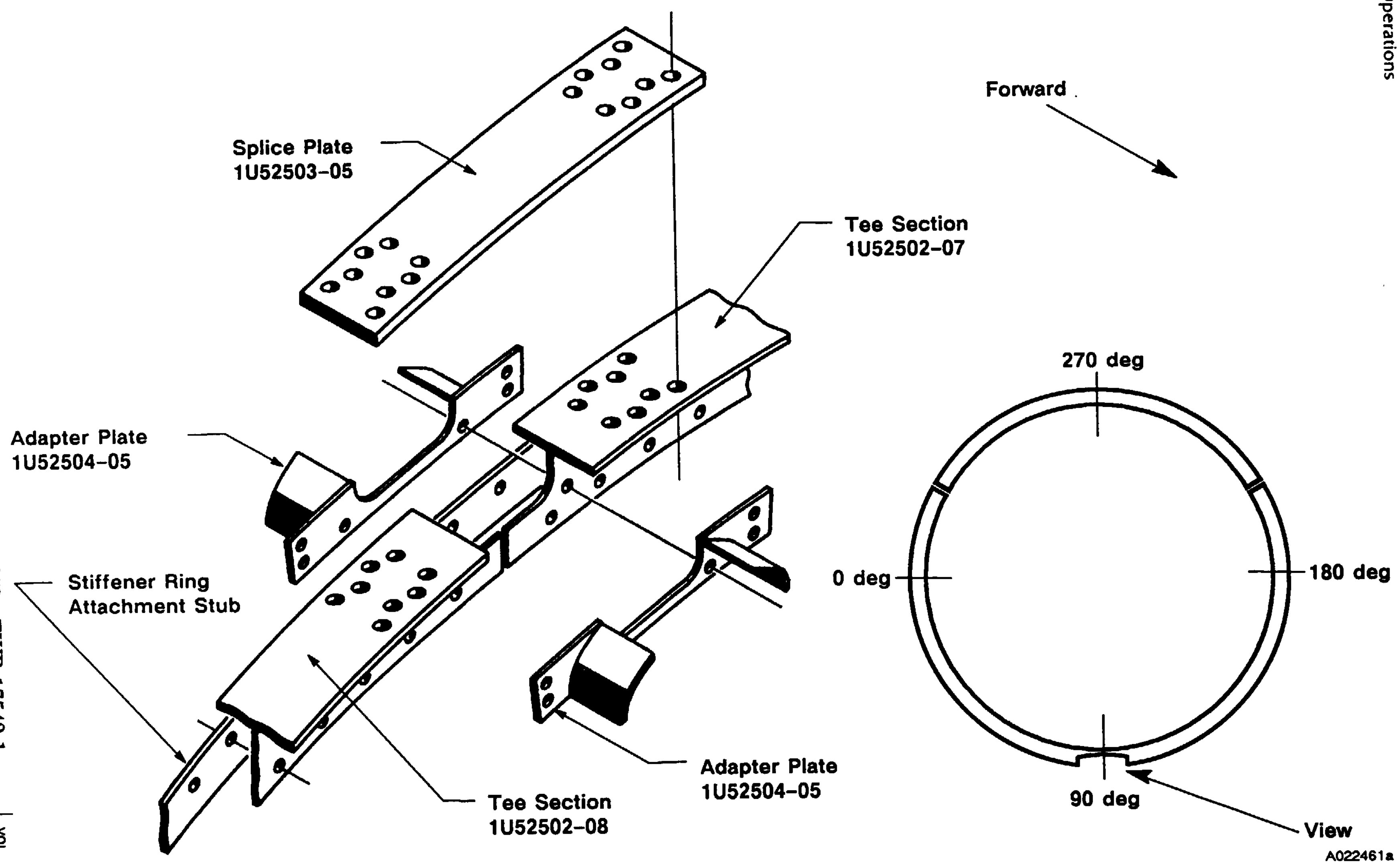

Figure 4.2-6. Previous Use History—Stiffener Rings

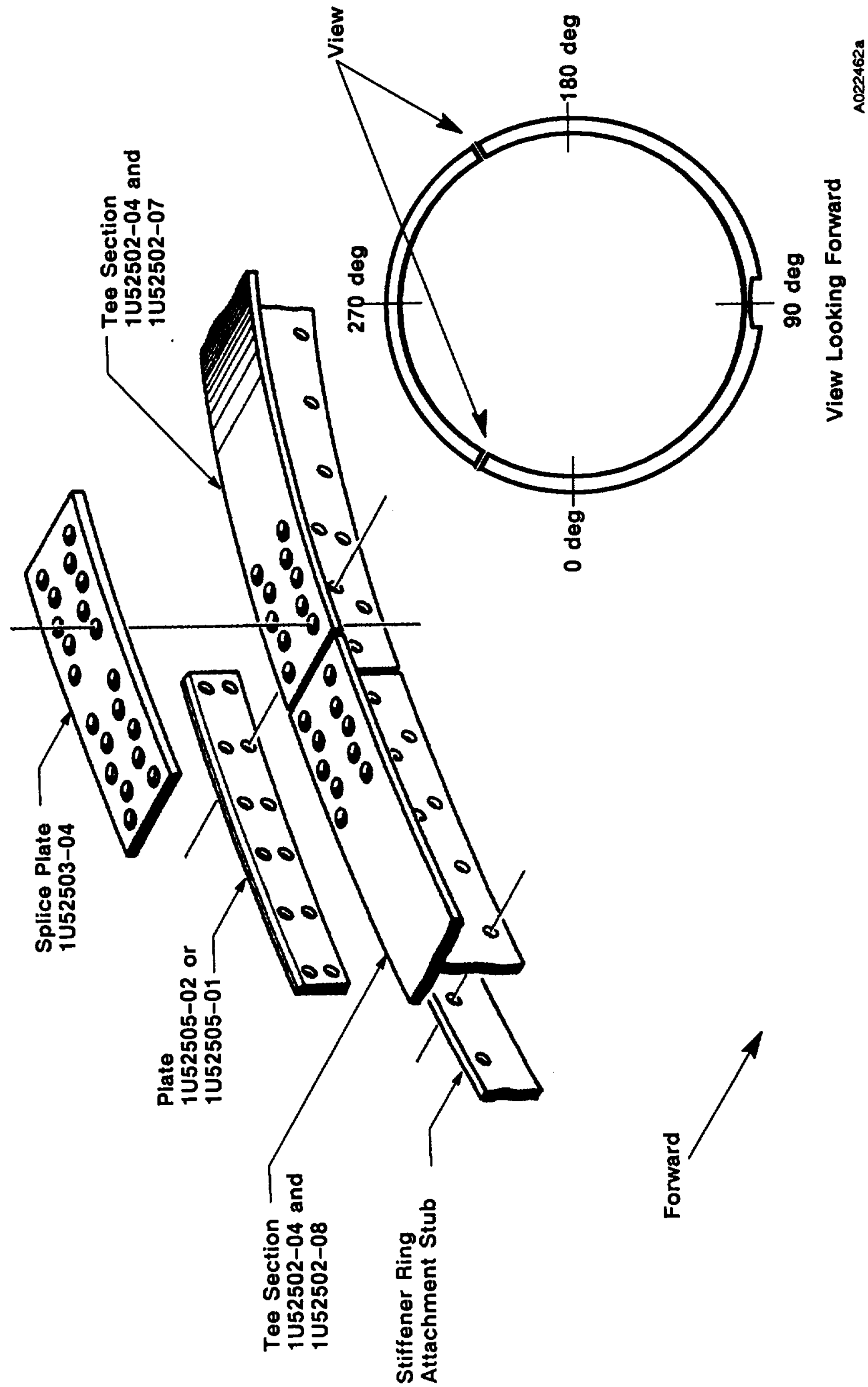

Figure 4.2-6. Previous Use History—Stiffener Rings (cont)

Table 4.2-3. Previous Use History--Stiffener Rings

Part No.	Serial No.	Previous Use
1U52502-04, Stiffener Ring	0000065R1	SRM-24
	0000066R1	SRM-24
	0000067R1	SRM-24
	0000068R1	SRM-24
	0000079R1	SRM-19
	0000083R1	SRM-21
1U52502-07, Stiffener Ring	0000001R2	SRM-14, 23
	0000002R2	SRM-14, 23
	0000005R2	SRM-15, 23
	0000055R1	SRM-22
	0000056R1	SRM-22
	0000062	New
1U52502-08, Stiffener Ring	0000008R2	SRM-15, 24
	0000009R2	SRM-15, 24
	0000044R1	SRM-20
	0000045R1	SRM-20
	0000046R1	SRM-20
	0000052R1	SRM-21
1U52503-04, Splice Plate	0000111	New
	0000112	New
	0000149	New
	0000085R1	SRM-19
	0000086R1	SRM-19
	0000087R1	SRM-19
	0000088R1	SRM-19
	0000090R1	SRM-19
	0000091R1	SRM-20
	0000092R1	SRM-20
	0000093R1	SRM-20
	0000094R1	SRM-20
1U52503-05, Splice Plate	0000001	New
	0000002	New
	0000005	New
	0000015	New
	0000020	New
	0000022	New

Table 4.2-3. Previous Use History--Stiffener Rings (cont)

Part No.	Serial No.	Previous Use
1U52504-05, Adapter Plate	0000019R2	SRM-15, 23
	0000027R2	SRM-16, 24
	0000028R2	SRM-16, 24
	0000086R1	SRM-18
	0000087R1	SRM-19
	0000089R1	SRM-19
	0000090R1	SRM-19
	0000094R1	SRM-19
	0000099R1	SRM-20
	0000103R1	SRM-23
	0000104R1	SRM-23
	0000106R1	SRM-23
1U52505-02, Plate, Stiffener Ring	0000079R1	SRM-18
	0000080R1	SRM-18
	0000081R1	SRM-18
	0000082R1	SRM-18
	0000139	New
	0000140	New
	0000141	New
	0000142	New
1U52505-01, Plate, Stiffener Ring	0000001R3 (fleet leader)	SRM-8, 13, 19
	0000002R3 (fleet leader)	SRM-8, 13, 19
	0000004R3 (fleet leader)	SRM-8, 13, 19
	0000008R3 (fleet leader)	SRM-8, 12, 19

g. New igniter heater element material, ECP RSRM 1919--Precludes repeat possibility of QM-8 igniter heater burn.
h. Removed and reinstalled resistance temperature detectors (RTD) and strain gages from igniter adapter and forward dome, FEC RSRM 045--Allowed igniter heater element to be installed flush on igniter adapter.
i. Hardware Changeout--Replace LH igniter pressure transducer with dual seal plug, FEC RSRM 050--DFI transducer did not meet refurbishment specification; no replacement part available.

4.3 SRB MASS PROPERTIES (FEWG REPORT SECTION 2.2.0)

4.3.1 Sequential Mass Properties

Tables 4.3-1 and 4.3-2 provide 360L003 (STS-29) LH and RH reconstructed sequential mass properties, respectively.

4.3.2 Predicted Data Versus Postflight Reconstructed Data

Tables 4.3-3 and 4.3-4 compare RSRM predicted sequential weight and center of gravity (cg) data with postflight reconstructed data. Prefire mass properties data are based on average actual data presented in the 5 Sep 1988 Mass Properties Quarterly Status Report (TWR-10211-88) for a lightweight case configuration with DFI. Actual 360L003 mass properties may be obtained from Mass Properties History Log Space Shuttle 360L003-LH (TWR-17338, dated 25 Oct 1988) and 360L003-RH (TWR-17339, dated 25 Oct 1988). Postflight reconstructed data reflect ballistics mass flow data from the 320 sample per second (sps) measured pressure traces and a predicted slag weight of 1,518 lb. Those mass properties reported after separation reflect delta times from separation and nose cap separation previously used on earlier flights.

4.3.3 CEI Specification Requirements

Tables 4.3-5 and 4.3-6 present CEI specification requirements and predicted and actual weight comparisons. Mass properties data for both RSRMs comply with the CEI specification requirements.

4.4 RSRM PROPULSION PERFORMANCE (FEWG REPORT SECTION 2.3.0)

4.4.1 High Performance Motor (HPM)/RSRM Performance Comparisons

The reconstructed thrust-time traces of flight motor set 360L003 at standard conditions were averaged with the HPM/RSRM population and compared to the CEI specification limits. The results are shown in Figure 4.4-1.

4.4.2 SRM Propulsion Performance Comparisons

The reconstructed RSRM propulsion performance is compared to the predicted performance in Table 4.4-1. The RSRM ignition interval is to be between 202 and 302 ms after ignition command

Table 4.3-1. Sequential Mass Properties (LH motor)

Event Time (sec)	Weight (lb)	Center of Gravity (in.)			Moment of Inertia		
		Long	Lat	Vert	Pitch	Roll	Yaw
Prelaunch = 0.00	1,255,040.6	1171.588	0.072	0.008	42391.866	878.095	42392.895
Lift-Off = 0.24	1,254,345.7	1171.724	0.072	0.008	42348.459	876.758	42349.488
Intermediate Burn = 20.00	1,016,525.6	1207.942	0.089	0.010	30830.782	761.675	30831.809
Intermediate Burn = 40.00	796,537.3	1231.709	0.112	0.013	21792.256	627.629	21793.278
Max Q = 54.00	666,485.7	1229.527	0.134	0.015	18079.433	550.529	18080.447
Intermediate Burn = 60.00	611,980.3	1227.097	0.145	0.017	16688.611	515.470	16689.622
Intermediate Burn = 80.00	420,936.3	1215.124	0.209	0.024	12011.826	381.793	12012.826
Max G = 87.00	356,591.9	1213.719	0.247	0.029	10609.358	331.180	10610.352
Intermediate Burn = 100.00	251,397.2	1225.183	0.348	0.041	8605.563	242.987	8606.549
Web Burn = 111.44	174,250.5	1266.459	0.499	0.059	7272.103	173.124	7273.080
End of Action Time = 124.08	144,582.6	1313.361	0.600	0.071	6568.299	146.845	6569.271
Separation = 125.83	144,008.7	1314.840	0.603	0.070	6542.600	146.436	6543.575
Nozzle Jettison = 195.83	141,429.0	1305.149	0.604	0.070	6323.230	141.664	6324.185
Max Reentry Q = 320.83	141,211.1	1305.045	0.605	0.070	6311.820	141.471	6312.776
Nose Cap Deployment = 350.83	141,158.8	1305.022	0.605	0.070	6309.031	141.425	6309.987

89857-7.1

Table 4.3-1. Sequential Mass Properties (LH motor) (cont)

Event Time (sec)	Weight (lb)	Center of Gravity (in.)			Moment of Inertia		
		Long	Lat	Vert	Pitch	Roll	Yaw
Drogue Chute Deployment = 351.43	141,157.8	1305.022	0.605	0.070	6308.976	141.424	6309.931
Frustum Release = 372.53	141,121.0	1305.006	0.605	0.070	6307.001	141.391	6307.957
Main Chute Line Stretch = 373.83	141,118.7	1305.005	0.605	0.070	6306.880	141.389	6307.835
Main Chute First Disreefing = 383.93	141,101.1	1304.998	0.605	0.070	6305.930	141.374	6306.885
Main Chute Second Disreefing = 389.83	141,090.8	1304.994	0.605	0.070	6305.376	141.365	6306.331
Splashdown = 415.83	141,046.6	1304.974	0.605	0.070	6302.947	141.326	6303.903

89857-7.2

Table 4.3-2. Sequential Mass Properties (RH motor)

Event Time (sec)	Weight (lb)	Center of Gravity (in.)			Moment of Inertia		
		Long	Lat	Vert	Pitch	Roll	Yaw
Prelaunch = 0.00	1,255,967.6	1171.614	0.072	0.007	42439.683	877.956	42440.705
Lift-Off = 0.24	1,255,262.7	1171.753	0.072	0.007	42395.714	876.621	42396.736
Intermediate Burn = 20.00	1,017,869.0	1207.998	0.089	0.009	30903.479	761.890	30904.499
Intermediate Burn = 40.00	797,566.8	1231.878	0.113	0.011	21854.650	627.715	21855.664
Max Q = 54.00	667,488.4	1229.801	0.135	0.013	18140.952	550.484	18141.958
Intermediate Burn = 60.00	612,997.9	1227.476	0.146	0.015	16756.976	515.980	16757.980
Intermediate Burn = 80.00	421,936.0	1215.855	0.211	0.021	12077.750	381.788	12078.742
Max G = 87.00	357,146.9	1214.734	0.249	0.025	10665.221	330.832	10666.209
Intermediate Burn = 100.00	251,180.6	1227.119	0.352	0.035	8644.564	241.953	8645.543
Web Burn = 111.36	174,637.2	1267.562	0.503	0.051	7313.501	172.451	7314.471
End of Action Time = 123.84	144,862.4	1314.842	0.605	0.061	6591.180	146.265	6592.145
Separation = 125.83	144,235.5	1316.690	0.608	0.061	6559.568	145.837	6560.535
Nozzle Jettison = 195.83	141,679.1	1306.972	0.609	0.061	6373.431	141.125	6374.385
Max Reentry Q = 320.83	141,461.2	1306.870	0.610	0.061	6362.032	140.932	6362.987
Nose Cap Deployment = 350.83	141.408.9	1306.848	0.610	0.061	6359.244	140.886	6360.199

89857-7.3

Table 4.3-2. Sequential Mass Properties (RH motor) (cont)

Event Time (sec)	Weight (lb)	Center of Gravity (in.)			Moment of Inertia		
		Long	Lat	Vert	Pitch	Roll	Yaw
Drogue Chute Deployment = 351.43	141,407.9	1306.847	0.610	0.061	6359.190	140.885	6360.143
Frustum Release = 372.53	141,371.1	1306.832	0.610	0.060	6357.216	140.852	6358.171
Main Chute Line Stretch = 373.83	141,368.9	1306.831	0.610	0.060	6357.095	140.850	6358.049
Main Chute First Disreefing = 383.93	141,351.2	1306.824	0.610	0.060	6356.145	140.835	6357.100
Main Chute Second Disreefing = 389.83	141,341.0	1306.820	0.610	0.060	6355.592	140.826	6356.547
Splashdown = 415.83	141,296.7	1306.801	0.610	0.060	6353.165	140.787	6354.120

89857-7.4

Table 4.3-3. Sequential Mass Properties--Predicted Versus Actual Comparisons (LH motor)

Event	Weight (lb) Predicted*	Actual	Delta	Error (%)	Longitudinal cg (in.) Predicted*	Actual	Delta	Error (%)
Preignition	1,255,041	1,255,041	0	0.00	1,171.588	1,171.588	0.000	0.00
Lift-off	1,254,412	1,254,346	-66	0.01	1,171.715	1,171.724	+0.009	0.00
Action Time	144,707	144,583	-124	0.09	1,312.994	1,313.361	+0.367	0.03
Separation**	143,974	144,009	+35	0.02	1,314.957	1,314.840	-0.117	0.01
Nozzle Jettison	141,420	141,429	+9	0.01	1,305.146	1,305.149	+0.003	0.00
Nose Cap Deployment	141,161	141,159	-2	0.00	1,305.022	1,305.022	0.000	0.00
Drogue Chute Deployment	141,146	141,158	+12	0.01	1,305.015	1,305.022	+0.007	0.00
Main Chute Line Stretch	141,119	141,119	0	0.00	1,305.004	1,305.005	+0.001	0.00
Main Chute First Disreefing	141,107	141,101	-6	0.00	1,304.999	1,304.998	-0.001	0.00
Main Chute Second Disreefing	141,100	141,091	-9	0.01	1,304.996	1,304.994	-0.002	0.00
Splashdown	141,047	141,047	0	0.00	1,304.974	1,304.974	0.000	0.00

*Based on Mass Properties History Log Space Shuttle 360L003--LH, 25 Oct 1988 (TWR-17338)
**The separation longitudinal cg of 1,314.840 is 60 percent of the vehicle length

89857-7.5

Table 4.3-4. Sequential Mass Properties--Predicted Versus Actual Comparisons (RH motor)

Event	Weight (lb) Predicted*	Weight (lb) Actual	Weight (lb) Delta	Weight (lb) Error (%)	Longitudinal cg (in.) Predicted*	Longitudinal cg (in.) Actual	Longitudinal cg (in.) Delta	Longitudinal cg (in.) Error (%)
Preignition	1,255,968	1,255,968	0	0.00	1,171.614	1,171.614	0.000	0.00
Lift-off	1,255,339	1,255,263	-76	0.01	1,171.740	1,171.753	+0.013	0.00
Action Time	144,964	144,862	-102	0.07	1,314.570	1,314.842	+0.272	0.02
Separation**	143,230	144,235	+5	0.00	1,316.539	1,316.690	+0.151	0.01
Nozzle Jettison	141,670	141,679	+9	0.01	1,306.969	1,306.972	+0.003	0.00
Nose Cap Deployment	141,411	141,409	-2	0.00	1,306.848	1,306.848	0.000	0.00
Drogue Chute Deployment	141,396	141,408	+12	0.01	1,306.841	1,306.847	+0.006	0.00
Main Chute Line Stretch	141,369	141,369	0	0.00	1,306.830	1,306.831	+0.001	0.00
Main Chute First Disreefing	141,357	141,351	-6	0.00	1,306.825	1,306.824	-0.001	0.00
Main Chute Second Disreefing	141,350	141,341	-9	0.01	1,306.822	1,306.820	-0.002	0.00
Splashdown	141,297	141,297	0	0.00	1,306.801	1,306.801	0.000	0.00

*Based on Mass Properties History Log Space Shuttle 360L003--RH, 25 Oct 1988 (TWR-17339)
**The separation longitudinal cg of 1,316.690 is 67 percent of the vehicle length

89857-7.6

Table 4.3-5. Predicted Versus Actual Weight Comparisons (lb) (LH motor)

Item	Minimum	Maximum	Predicted***	Actual	Delta	Error (%)
Inerts						
Prefire, Controlled*		150,076	148,968	148,968	0	0.00
Propellant*	1,104,714		1,104,894	1,104,894	0	0.00
Usable**			1,104,037	1,104,157	+120	0.01
To Lift-off			533	597	+64	10.72
Lift-off to Action			1,103,504	1,103,560	+56	0.01
Unusable			857	737	-120	16.28
Action to Separation			667	508	-159	31.30
After Separation			190	229	+39	17.03
Slag**			1,518	1,518	0	0.00

*Requirement per CPW1-3600A, Addendum G, Part I, RSRM CEI specification
**Slag included in usable propellant, lift-off to action
***Based on Mass Properties History Log Space Shuttle 360L003--LH, 25 Oct 1988 (TWR-17338)

89857-7.7

Table 4.3-6. Predicted Versus Actual Weight Comparisons (lb) (RH motor)

Item	Minimum	Maximum	Predicted***	Actual	Delta	Error (%)
Inerts						
Prefire, Controlled*		150,076	149,231	149,231	0	0.00
Propellant*	1,104,714		1,105,565	1,105,565	0	0.00
Usable**			1,104,707	1,104,804	+97	0.01
To Lift-off			534	607	+73	12.03
Lift-off to Action			1,104,173	1,104,197	+24	0.00
Unusable			858	761	-97	12.75
Action to Separation			668	561	-107	19.07
After Separation			190	200	+10	5.00
Slag**			1,518	1,518	0	0.00

*Requirement per CPW1-3600A, Addendum G, Part I, RSRM CEI specification
**Slag included in usable propellant, lift-off to action
***Based on Mass Properties History Log Space Shuttle 360L003--RH, 25 Oct 1988 (TWR-17339)

89857-7.8

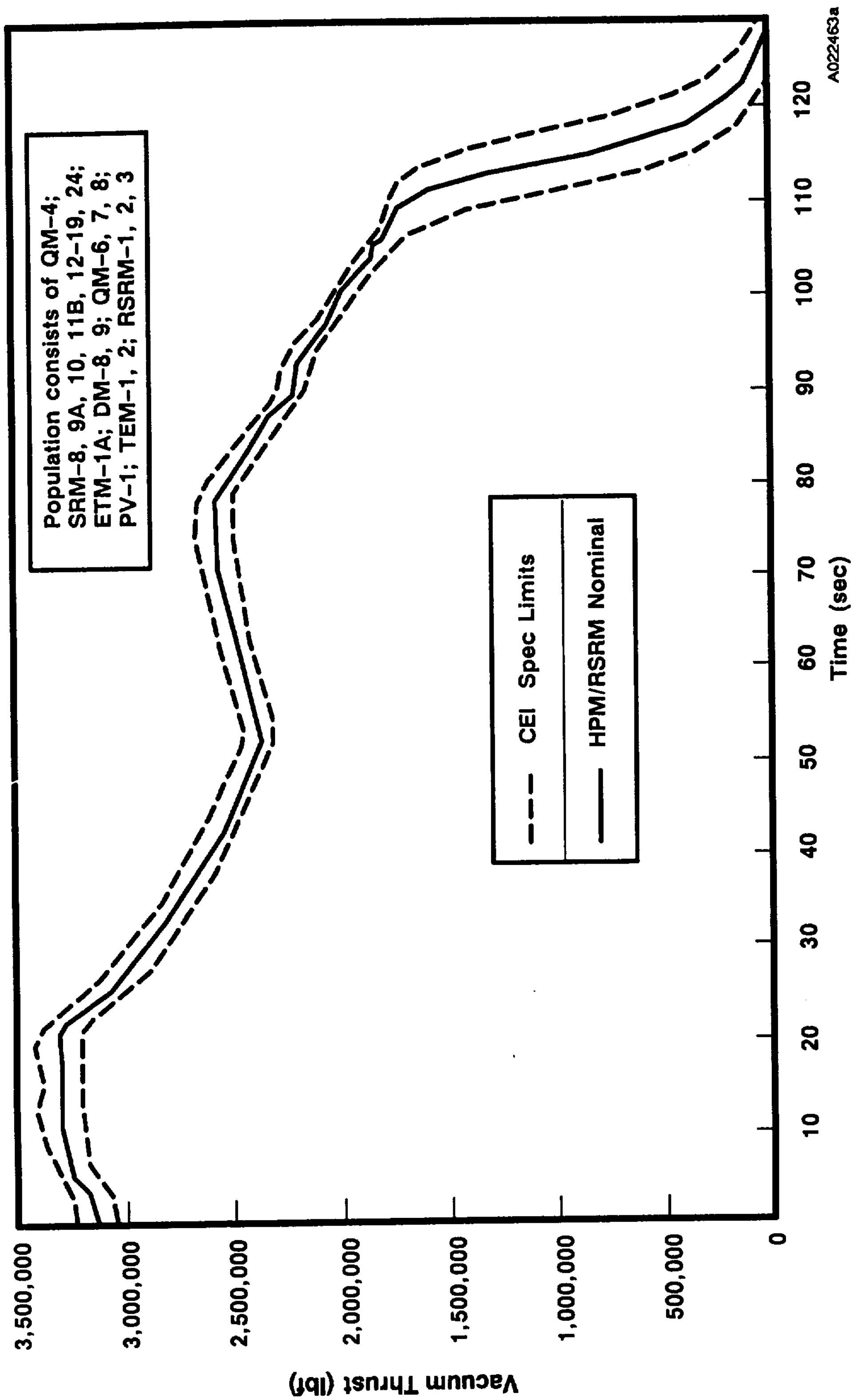

Figure 4.4-1. Reconstructed Thrust-Time Traces

Table 4.4-1. RSRM Propulsion Performance Assessment

	LH Motor (62°F)		RH Motor (62°F)	
	Predicted	Actual	Predicted	Actual
Impulse Gates				
I-20 (10^6 lbf-sec)	64.73	63.98	64.80	63.94
I-60 (10^6 lbf-sec)	172.52	172.11	172.68	172.29
I-AT (10^6 lbf-sec)	296.33	295.58	296.51	296.10
Vacuum I_{sp} (lbf*sec/lbm)	268.2	267.5	268.2	267.8
Burn Rate (in./sec) (600°F, 625 psia)	0.368	0.367	0.368	0.368
Event Times (sec)				
Ignition Interval	0.232	0.241	0.232	0.241
Web Time	111.1	111.4	111.1	111.4
Time of 50-psia Cue	120.8	120.8	120.7	120.9
Action Time	123.1	124.1	123.1	123.8
Separation Command (sec)	125.7	125.8	125.7	125.8
PMBT (°F)	62.0	62.0	62.0	62.0
Maximum Ignition Rise Rate (psia/10 ms)	91.9	82.7	91.9	89.9
Decay Time (sec) (59.4 psia to 85 K)	2.9	4.0	2.8	3.5

	Predicted	Actual
Tailoff Imbalance Impulse Differential (lbf-sec)	+47 K	+61 K

Note: Impulse imbalance = LH motor - RH motor to the NASA standard initiators in the S&A. The ignition interval ends when the headend chamber pressure has increased to a value of 563.5 psia. The maximum rate of headend chamber pressure buildup during the ignition transient is required to be less than 115.9 psia for any 10-ms interval.

Separation is based upon the 50-psia cue from the last RSRM, plus 4.9 sec, plus a time delay between the receipt and execution of the command to separate. No time delay is assumed in the prediction. The decay time intervals are measured from the time motor headend chamber pressure has decayed to 59.4 psia to the time corresponding to 85,000 lb of thrust.

4.4.3 Matched Pair Thrust Differential

Table 4.4-2 shows the thrust differential during ignition, steady state, and tailoff. All the thrust differential values were near the nominal values experienced by previous flight SRMs and were well within the CEI specification limits. The thrust values used for the assessment were reconstructed at the delivered conditions of each motor.

Table 4.4-2. RSRM Thrust Imbalance Assessment

Event	Imbalance Specification (lbf)	Maximum Imbalance (lbf)	Time of Maximum Imbalance (sec)
Ignition (0 to 1.0 sec, lbf)	300 K	-88.8 K	0.094
Steady State (1.0 sec to first web time minus 4.5 sec, lbf, 4-sec average)	85 K	-39.0 K	90.0
Transition (first web time minus 4.5 sec to first web time, lbf)	85 - 268 K linear	+30.8 K	111.0
Tailoff (first web time to last action time)	710 K	+46.1 K	112.0

Note: Thrust imbalance = LH motor - RH motor

4.4.4 Performance Tolerances

A comparison of the LH and RH motor calculated and reconstructed parameters at PMBT of 60°F with respect to the nominal values and the SRM CEI specification maximum 3-sigma requirements is shown in Table 4.4-3.

Table 4.4-3. RSRM Performance Comparisons

	SRM CEI (+/-) Max 3-Sigma Var (%)	Nominal Value**	LH SRM RSRM-3A (60°F)	RSRM-3A Var (%)**	RH SRM RSRM-3B (60°F)	RSRM-3B Var (%)**
Web Time (sec)	5.0	111.7	111.4	-0.27	111.4	-0.27
Action Time (sec)	6.5	123.4	124.1	0.57	123.8	0.32
Web Time Avg Pressure (psia)	5.3	660.8	659.8	-0.15	660.8	0.00
Max Headend Pressure (psia)	6.5	918.4	895	-2.55	890	-3.09
Max Sea Level Thrust (Mlbf)	6.2	3.06	3.04	-0.65	3.05	-0.33
Wet Time Avg Vac Thrust (Mlbf)	5.3	2.59	2.58	-0.39	2.59	0.00
Vac Del I_{sp} (lbf*sec/lbm)	0.7	267.1	267.5	0.15	267.8	0.26
Web Time Vac Total Impulse (Mlbf*sec)	1.0	288.9	287.8	-0.38	288.2	-0.24
Action Time Vac Total Impulse (Mlbf*sec)	1.0	296.3	295.4	-0.30	295.9	-0.13

*QM-4 static test and SRM-8A and B; SRM-9A; SRM-10A and B; SRM-11A; SRM-13A and B flight average at standard conditions
**Variation = [(RSRM-2A - nominal)/nominal] * 100
[(RSRM-2B - nominal)/nominal] * 100

4.4.5 360L003 Igniter Performance

Only one motor, 360L003B (RH), was equipped to measure igniter chamber pressure. Initial assessment of the performance of this igniter showed normal operation. The maximum pressure of 1,974 psia was exactly as predicted. The igniter operated within the limits of Morton Thiokol Specification STW3-3176.

4.5 RSRM NOZZLE PERFORMANCE (FEWG REPORT SECTION 2.4.3)

The maximum RSRM nozzle torque was 2.96×10^6 in.-lbf and 3.59×10^6 in.-lbf for the LH and RH motors, respectively. This compares well with previous flight data and to static test torque data. Nozzle char and erosion performance is discussed in Section 4.11.4 of this volume.

4.6 RSRM ASCENT LOADS--STRUCTURAL ASSESSMENT (FEWG REPORT SECTION 2.5.2)

4.6.1 Introduction

The 360L003 RSRMs were fully instrumented in order to evaluate motor performance during hold-down, lift-off, and ascent through separation. This section details the assessment of the case field joints, case-to-nozzle joints, and case metal components. Comparisons to flight envelopes and previous flights will also be presented.

4.6.2 Summary

4.6.2.1 Girth Gage Response. The girth gage measurements from the field and case-to-nozzle joints compare closely to corresponding gages on static tests as well as to pretest predictions. The predictions used a typical load case rather than actual loads, so they were only expected to predict the order of magnitude. The highest percentage difference from the predicted values on the field joints was -19.3 percent on the LH center field joint, 41 percent on the RH case-to-nozzle joint girth gages, and -13.3 percent on the LH RSRM case membrane (Station 611.5).

The data of the center and aft field joint girth gages on the RH SRB and a few others on both motors contained a spike during the ignition transient that was similar to that seen on 360L001 and 360L002. Girth gage data on the forward field joint and several on the center field joint of the RH SRB show a delay before movement occurs. Investigation has shown this spiking to be an instrumentation phenomena. (The spike is believed to be an extremely small electrical pulse, the generation of which is inherit to the gage and electrical circuit configuration.) Additional discussion of this instrumentation phenomenon is discussed in Section 4.9 of this volume.

4.6.2.2 Biaxial Gage Response. The biaxial gage line/load measurements compared well with predicted values. The biaxial strain gage data for each station were used to calculate a stress distribution; this information was used to calculate bending moments and axial force as a function of time. Evaluation of the results shows that the maximum measured bending moment occurred on the LH SRB at Station 1797 during SSME buildup, reaching a maximum value of -264 x 10^6 in-lb. The axial force reached a maximum of -13.41 kip at Station 556 on the RH motor and occurred at lift-off. The maximum line load was -28.0 kip/in., occurring at Station 556 on the RH motor. Good correlation was found when the flight data were compared with the flight envelopes and previous flight data.

4.6.3 Flight Results Assessment

4.6.3.1 Global Model Predictions and Methodology. In most cases, actual test data were compared to predicted values for each location. A detailed global model of the RSRM was used to predict joint and case structural responses. This finite element model uses superelement techniques to model all components of the RSRM in detail (except for the case-to-nozzle joint, which will be discussed in Section 4.6.3.6 of this volume). Rockwell International load case L02044R was chosen to represent the typical loading parameters that are imposed upon the RSRM during lift-off. This load case includes a timespan from 0 to 10 sec, with SRB ignition occurring at approximately 6.5 sec, and is expected to predict displacement and strain values to within an order of magnitude only. A detailed description of the model and analysis techniques used in predicting the structural response of the motor is found in TWR-19197. The predictions included in the tables are ratioed to the 360L003 pressure. The ratios were determined by multiplying the original prediction by the ratio of the estimated 360L003 pressure to the predicted pressure. By using the ratio of the predictions to 360L003 values, a more accurate comparison can be made.

The calculation of the pressure ratio works as follows: Maximum radial growth (and the time at which it occurred), e.g., girth strain, for a particular location is found from test data. The headend pressure at this time is next determined. Also, the predicted pressure drop (from headend pressure) is found at this time. For 360L003, the predicted pressure drops were given in TWR-19092. Therefore, the pressure ratio is:

$$\frac{\text{headend pressure - predicted pressure drop}}{\text{predicted pressure}} = \text{pressure ratio}$$

The percent difference between analysis and measured data is given by:

$$\left[\frac{\text{(pressure ratio x prediction) - measured}}{\text{measured}}\right] \text{x } 100$$

Biaxial strain gages were placed in the aft field joint, ETA ring regions, and around the case-to-nozzle joints. These gages were used to calculate the corresponding hoop and axial stresses. These stresses illustrate the effects of the ETA ring on the aft field joint and of vectoring on the case-to-nozzle joint. The maximum experienced hoop stress and corresponding axial stress were compared to the predicted values. Since the hoop stress is much larger than axial stress, this represents the maximum stress for each of the areas; thus, a SF can be determined.

The predictions (with the exception of those for the case-to-nozzle joint) are the maximum expected values for the first 3 sec of flight. The maximum experienced axial and hoop stresses for the duration of the flight were also tabulated.

The strain gages were zeroed after SRB stacking but before mating with the orbiter and ET, so the strain gages report some initial strain before launch which is caused by the weight and induced bending of the orbiter and ET. Because they were zeroed after stacking, the strain gages do not show any strain resulting from the weight of the segments above them. However, it would be ideal to know the actual strain experienced by the case at every instrumented location for every flight event. After separation, and before chute deployment, the SRBs are essentially in a free state (free fall), with very little (if any) motor pressure and very small external loads. For this reason, all of the strain gages were adjusted to end at zero strain at this point in time. This shifting of the data shows, as near as possible, the actual strain level at any point during flight. Because the data are shifted at every time, it also shows the strain caused by the weight of the case segments prior to SSME buildup. It should be noted, however, that when comparing strain values with predicted values, the data have been adjusted to start at zero rather than end at zero. The reason is that the predictions represent a delta change from the state before SSME ignition to the state after full SRB motor pressure has been achieved. This is necessary to show a true comparison with predictions.

Once these strain adjustments have been made, the strain values are input into program SLB01, which calculates the stress distribution around the case. The output from this program is put into program SLB06, which calculates bending moment and axial force.

The results of this program are presented as a function of time, and were also plotted with previous flight data as a function of time and with the envelopes for specific flight events as a function of station. The average line load for each is calculated using the bending moment in each direction (MY and MZ) and the axial force (VX). The results are plotted as a function of time for Stations 556.6, 876.5, 1196, 1466, 1501, and 1797.

4.6.3.2 Instrumentation. Girth and biaxial strain gages were placed on and close to the field and case-to-nozzle joints to characterize joint performance. Following is a list of gages used and their function.

- Joint girth gages--measure the average hoop strain for the entire 360-deg circumference. From the hoop strain, radial deflections are determined from the product of measured (average) girth strain and the nominal hardware radii at the corresponding gage location.

- Biaxial gages--measure local axial and hoop strain (rather than average) incurred in the case during flight. From these strains, stress can be calculated.
- Pressure transducer--installed in the igniter to measure headend chamber pressure.

4.6.3.3 Field Joint Girth Gage Performance. The instrumentation on both the LH and RH RSRMs consisted of six girth gages per field joint. Tables 4.6-1 through 4.6-6 list the girth gage response from 0 to 3 sec and the maximum strain for -10 through 120 sec for the forward, center, and aft field joints for both the LH and RH motors. Tables 4.6-5 and 4.6-6 have a time range from 0.6 to 3 sec because several of these gages show a spike before maximum headend pressure (at about 0.6 sec); adjusting the predictions at this point gives incorrect results.

The above-mentioned tables also compare the maximum measured strain and corresponding radial growth with the predicted values for the forward, center, and aft field joints. The results show a good correlation between analysis and test data. All field joint predictions are within -19.3 percent of measured values. The maximum measured radial growth was 0.181 in., which occurred on the center field joint at Location 6 (Station 1177.3) of the RH SRB.

Tables 4.6-7 through 4.6-9 compare 360L003 with several static motors, 360L001, 360L002, and predictions. It can be seen from these tables that the correlation is good. Close study of the field joint growth behavior shows that the joint is rotating outward, as can be seen from the higher radial growth values at the forward and aft ends of each joint and the lower values closer to the pin centerline.

The center and aft field joint girth gages of the RH SRB had spikes in the data during the ignition transient. There were a few other gages on both the LH and RH motor that showed some degree of spiking. It is believed that this is an instrumentation problem. The values in Tables 4.6-5 and 4.6-6 (center and aft field joints, respectively) contain the maximum values found after the data spiking occurred (after 0.6 to 3.0 sec) and the maximum value found for the full time duration (time range of -10 to 120 sec).

Another interesting event occurred on the forward (all gages) and center (three most forward gages) of the RH SRB. In these gages there was a time delay of approximately 0.25 sec before these gages showed an increase in magnitude. A girth gage is normally linear with pressure, but these show no response until the headend pressure is approximately 600 psi. It is also of significance to note that the biaxial gages in the membrane just aft of each of these joints respond normally, with no time delay. The center field joint is the most interesting of all since three of the girth gages show a time delay, two gages show spiking, and one gage is bad. All of these gages experienced the same motor pressure but responded differently. For these reasons it is believed that the data delays are the result of an instrumentation problem. Additional discussion of the instrumentation is contained in Section 4.9 of this volume.

Table 4.6-1. LH Motor Forward Field Joint Girth Gage Measurements

TEST NAME: 360L003
JOINT: LEFT SRM FWD FIELD JOINT
DESCRIPTION: JOINT GIRTH GAGES
THE TIME RANGE IS 0.0 TO 3.0 SECONDS

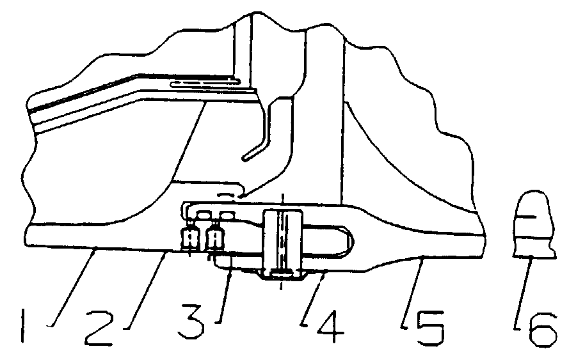

GIRTH GAGE LOCATION	GAGE NUMBER	STATION	RADIUS (IN)	RADIAL GROWTH (IN)	TEST STRAIN (UIN/IN)	ADJUSTED ANALYSIS STRAIN (UIN/IN)	ADJUSTED ANALYSIS RADIAL GROWTH (IN)	DIFF IN RADIAL GROWTH (% DIFF)	MAXIMUM RADIAL GROWTH -10 TO 120 SECONDS
1	B08G7273	847.0	73.1	0.172	2349	2212	0.162	-5.8	0.178
2	B08G7274	848.5	73.1	0.159	2168	1940	0.142	-10.5	0.164
3	B08G7275	850.2	73.5	0.140	1903	1874	0.138	-1.5	0.145
4	B08G7276	852.6	73.5	0.158	2148	1808	0.133	-15.8	0.164
5	B08G7277	855.0	73.1	0.168	2303	2075	0.152	-9.9	0.177
6	B08G7278	857.5	73.1	ND	ND	ND	ND	ND	ND

Table 4.6-2. LH Motor Center Field Joint Girth Gage Measurements

TEST NAME: 360L003
JOINT: LEFT SRM CTR FIELD JOINT
DESCRIPTION: JOINT GIRTH GAGES
THE TIME RANGE IS 0.0 TO 3.0 SECONDS

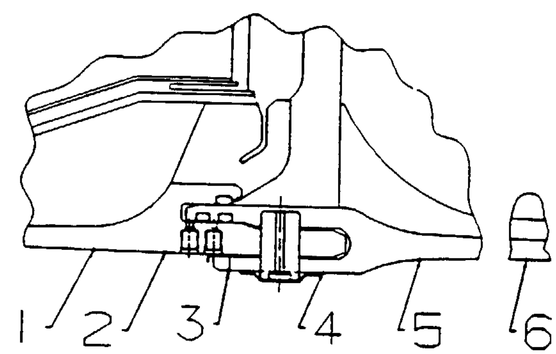

GIRTH GAGE LOCATION	GAGE NUMBER	STATION	RADIUS (IN)	RADIAL GROWTH (IN)	TEST STRAIN (UIN/IN)	ADJUSTED ANALYSIS STRAIN (UIN/IN)	ADJUSTED ANALYSIS RADIAL GROWTH (IN)	DIFF IN RADIAL GROWTH (% DIFF)	MAXIMUM RADIAL GROWTH -10 TO 120 SECONDS
1	B08G7283	1168.8	73.1	0.169	2308	2079	0.152	-9.9	0.177
2	B08G7284	1168.5	73.1	ND	ND	ND	ND	ND	ND
3	B08G7285	1170.2	73.5	0.138	1876	1768	0.130	-5.8	0.147
4	B08G7286	1172.6	73.5	0.155	2111	1705	0.125	-19.3	0.165
5	B08G7287	1175.0	73.1	ND	ND	ND	ND	ND	ND
6	B08G7288	1177.3	73.1	ND	ND	ND	ND	ND	ND

Table 4.6-3. LH Motor Aft Field Joint Girth Gage Measurements

TEST NAME: 360L003
JOINT: LEFT SRM AFT FIELD JOINT
DESCRIPTION: JOINT GIRTH GAGES
THE TIME RANGE IS 0.0 TO 3.0 SECONDS

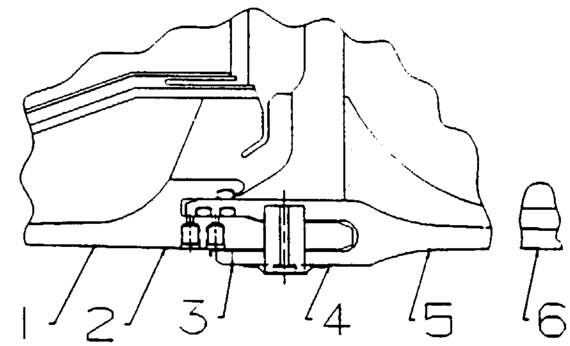

GIRTH GAGE LOCATION	GAGE NUMBER	STATION	RADIUS (IN)	RADIAL GROWTH (IN)	TEST STRAIN (UIN/IN)	ADJUSTED ANALYSIS STRAIN (UIN/IN)	ADJUSTED ANALYSIS RADIAL GROWTH (IN)	DIFF IN RADIAL GROWTH (% DIFF)	MAXIMUM RADIAL GROWTH -10 TO 120 SECONDS
1	B08G7293	1487.0	73.1	0.157	2144	2050	0.150	-4.4	0.178
2	B08G7294	1488.5	73.1	ND	ND	1818	0.133	ND	ND
3	B08G7295	1490.2	73.5	ND	ND	1726	0.127	ND	ND
4	B08G7296	1492.6	73.5	ND	ND	1659	0.122	ND	ND
5	B08G7297	1495.0	73.1	0.139	1897	1833	0.134	-3.4	0.157
6	B08G7298	1497.5	73.1	0.143	1955	1994	0.146	2.0	0.164

Table 4.6-4. RH Motor Forward Field Joint Girth Gage Measurements

TEST NAME: 360L003
JOINT: RIGHT SRM FWD FIELD JOINT
DESCRIPTION: JOINT GIRTH GAGES
THE TIME RANGE IS 0.0 TO 3.0 SECONDS

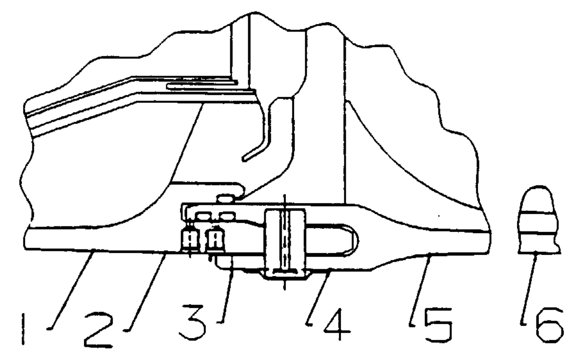

GIRTH GAGE LOCATION	GAGE NUMBER	STATION	RADIUS (IN)	RADIAL GROWTH (IN)	TEST STRAIN (UIN/IN)	ADJUSTED ANALYSIS STRAIN (UIN/IN)	ADJUSTED ANALYSIS RADIAL GROWTH (IN)	DIFF IN RADIAL GROWTH (% DIFF)	MAXIMUM RADIAL GROWTH -10 TO 120 SECONDS
1	B08G8273	847.0	73.1	0.170	2319	2211	0.162	-4.6	0.177
2	B08G8274	848.5	73.1	ND	ND	ND	ND	ND	ND
3	B08G8275	850.2	73.5	0.141	1921	1875	0.138	-2.4	0.145
4	B08G8276	852.6	73.5	0.158	2147	1811	0.133	-15.6	0.164
5	B08G8277	855.0	73.1	0.169	2316	2078	0.152	-10.3	0.178
6	B08G8278	857.5	73.1	ND	ND	ND	ND	ND	ND

Table 4.6-5. RH Motor Center Field Joint Girth Gage Measurements

TEST NAME: 360L003
JOINT: RIGHT SRM CTR FIELD JOINT
DESCRIPTION: JOINT GIRTH GAGES
THE TIME RANGE IS 0.6 TO 3.0 SECONDS

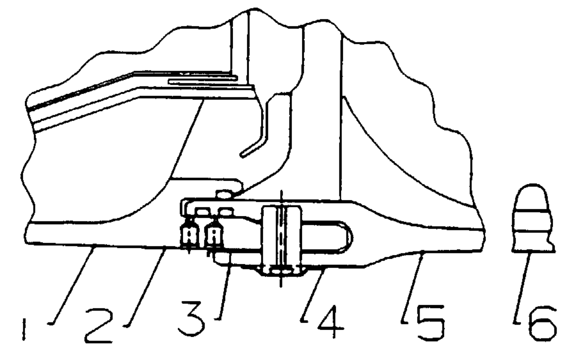

GIRTH GAGE LOCATION	GAGE NUMBER	STATION	RADIUS (IN)	RADIAL GROWTH (IN)	TEST STRAIN (UIN/IN)	ADJUSTED ANALYSIS STRAIN (UIN/IN)	ADJUSTED ANALYSIS RADIAL GROWTH (IN)	DIFF IN RADIAL GROWTH (% DIFF)	MAXIMUM RADIAL GROWTH -10 TO 120 SECONDS
1	B08G8283	1168.8	73.1	0.167	2278	2049	0.150	-10.0	0.176
2	B08G8284	1168.5	73.1	ND	ND	ND	ND	ND	ND
3	B08G8285	1170.2	73.5	0.134	1828	1747	0.128	-4.4	0.140
4	B08G8286	1172.6	73.5	0.151	2051	1680	0.123	-18.1	0.158
5	B08G8287	1175.0	73.1	0.163	2231	1917	0.140	-14.1	0.183
6	B08G8288	1177.3	73.1	0.181	2472	2277	0.166	-7.9	0.196

Table 4.6-6. RH Motor Aft Field Joint Girth Gage Measurements

TEST NAME: 360L003
JOINT: RIGHT SRM AFT FIELD JOINT
DESCRIPTION: JOINT GIRTH GAGES
THE TIME RANGE IS 0.6 TO 3.0 SECONDS

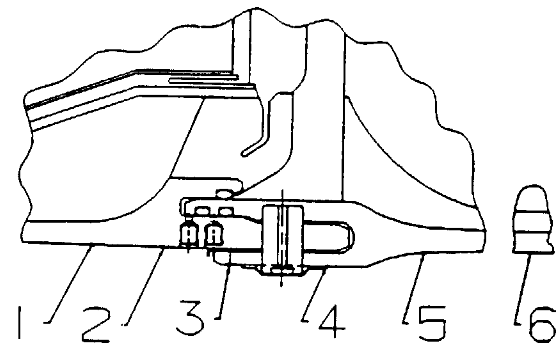

GIRTH GAGE LOCATION	GAGE NUMBER	STATION	RADIUS (IN)	RADIAL GROWTH (IN)	TEST STRAIN (UIN/IN)	ADJUSTED ANALYSIS STRAIN (UIN/IN)	ADJUSTED ANALYSIS RADIAL GROWTH (IN)	DIFF IN RADIAL GROWTH (% DIFF)	MAXIMUM RADIAL GROWTH -10 TO 120 SECONDS
1	B08G8293	1487.0	73.1	ND	ND	ND	ND	ND	ND
2	B08G8294	1488.5	73.1	ND	ND	ND	ND	ND	ND
3	B08G8295	1490.2	73.5	0.126	1718	1712	0.126	-0.3	0.139
4	B08G8296	1492.6	73.5	0.139	1888	1619	0.119	-14.3	0.154
5	B08G8297	1495.0	73.1	0.146	2002	1789	0.131	-10.7	0.163
6	B08G8298	1497.5	73.1	0.154	2111	1948	0.142	-7.7	0.173

Table 4.6-7. Forward Field Joint Radial Growth--Previous Motors Compared to 360L003

Forward Field Joint Radial Growth Comparisons to STS-29

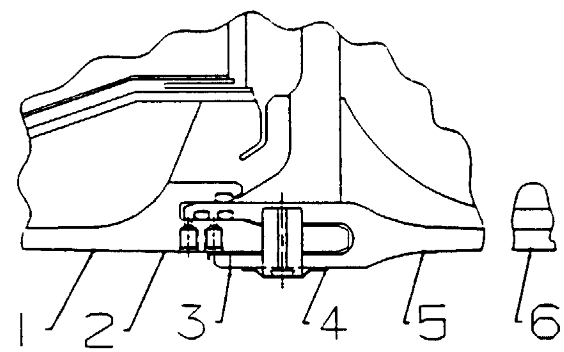

Fwd Field Girths

LOC.	STS-29 GAGE	STS-29 RIGHT	STS-29 LEFT	STS-27 RIGHT	STS-27 LEFT	STS-26 RIGHT	STS-26 LEFT	PV-1	QM-7	RADIAL GROWTH (Inches) QM-6	DM-9	DM-8	PRED	NOMINAL RADIUS (INCHES)
1	B08GX273	0.170	0.172	0.170	0.174	ND	ND	ND	ND	0.162	0.167	0.170	0.162	73.1
2	B08GX274	ND	0.159	ND	ND	ND	ND	ND	0.186	0.152	0.155	0.158	0.142	73.1
3	B08GX275	0.141	0.140	ND	0.147	ND	0.187	ND	0.143	0.132	0.148	0.142	0.138	73.5
4*	B08GX276	0.158	0.158	ND	0.163	ND	0.164	ND	0.161	0.155	ND	0.155	0.133	73.5
5	B08GX277	0.169	0.168	0.179	0.175	ND	0.180	ND	0.178	0.174	0.169	0.177	0.152	73.1
6	B08GX278	ND	ND	0.198	0.194	ND	ND	ND	ND	0.200	ND	0.202	ND	73.1

* QM-7, QM-6, and DM-9 Locations are 1/3 Inch Aft of DM-8 Location.
Note: All Test Radial Growths Are Ratios of STS-29 Test Pressure

Table 4.6-8. Center Field Joint Radial Growth--Previous Motors Compared to 360L003

Center Field Joint Radial Growth Comparisons to STS-29

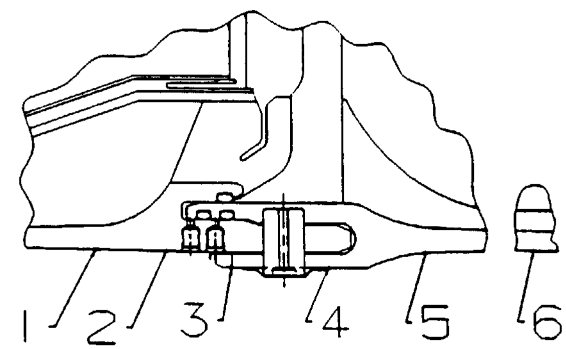

Ctr Field Girths

LOC.	STS-29 GAGE	STS-29 RIGHT	STS-29 LEFT	STS-27 RIGHT	STS-27 LEFT	STS-26 RIGHT	STS-26 LEFT	PV-1	QM-7	RADIAL GROWTH (Inches) QM-6	DM-9	DM-8	PRED	NOMINAL RADIUS (INCHES)
1	B08GX283	0.167	0.169	0.166	0.167	ND	ND	ND	ND	0.160	ND	0.172	0.151	73.1
2	B08GX284	ND	ND	ND	ND	ND	ND	ND	ND	ND	0.153	0.158	ND	73.1
3	B08GX285	0.134	0.138	0.136	0.139	ND	0.138	ND	0.141	0.131	0.149	0.140	0.129	73.5
4*	B08GX286	0.151	0.155	ND	0.154	0.156	ND	0.152	0.156	0.148	0.134	0.155	0.124	73.5
5	B08GX287	0.163	ND	0.166	0.165	ND	ND	0.170	0.172	0.165	0.164	0.176	0.140	73.1
6	B08GX288	0.181	ND	ND	0.187	ND	ND	ND	ND	0.186	ND	0.211	0.166	73.1

* QM-7, QM-6, and DM-9 Locations are 1/3 Inch Aft of DM-8 Location.
Note: All Test Radial Growths Are Ratios of STS-29 Test Pressure
Note: Locations 1, 3, and 4 on the right SRB contain negative spikes at 0.225 seconds
Note: Locations 5 and 6 on the right SRB contain spikes at 0.275 seconds

Table 4.6-9. Aft Field Joint Radial Growth--Previous Motors Compared to 360L003

Aft Field Joint Radial Growth Comparisons to STS-29

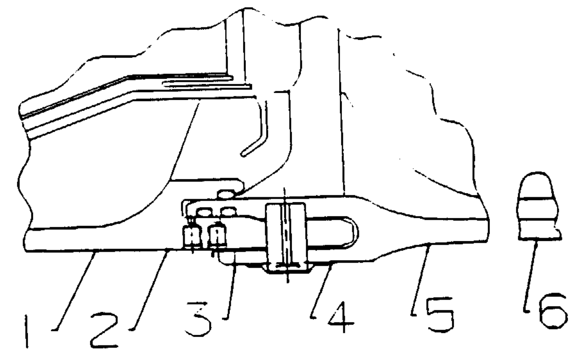

Aft Field Girths

LOC.	STS-29 GAGE	STS-29 RIGHT	STS-29 LEFT	STS-27 RIGHT	STS-27 LEFT	STS-26 RIGHT	STS-26 LEFT	PV-1	QM-7	RADIAL GROWTH (Inches) QM-6	DM-9	DM-8	PRED	NOMINAL RADIUS (INCHES)
1	B08GX293	ND	0.157	0.155	0.160	ND	ND	ND	ND	0.153	0.156	0.159	0.150	73.1
2	B08GX294	ND	ND	ND	0.146	ND	ND	ND	0.168	0.141	0.144	0.150	0.133	73.1
3	B08GX295	0.126	ND	ND	0.131	0.132	0.142	ND	0.133	0.118	0.125	0.132	0.126	73.5
4*	B08GX296	0.139	ND	ND	0.138	0.141	0.139	0.137	0.140	0.134	0.133	0.140	0.121	73.5
5	B08GX297	0.146	0.139	0.148	0.140	ND	0.151	0.143	0.140	0.141	0.138	0.148	0.133	73.1
6	B08GX298	0.154	0.143	0.140	0.146	ND	ND	ND	ND	ND	0.145	0.157	0.144	73.1

* QM-7, QM-6, and DM-9 Locations are 1/3 Inch Aft of DM-8 Location.
Note: All Test Radial Growths Are Ratios of STS-29 Test Pressure
Note: All Right SRB Gages Spike at 0.2875 seconds

It is recommended that the cases which had the spiking gages be inspected during refurbishment for out of roundness, case thickness, and any other abnormalities. It is also recommended that, during the hydrotest, a series of girth and biaxial gages be installed to measure case strain. Since this phenomenon is not completely understood, it is also recommended that DFI be installed on future flights to help determine positively that this is not a real event. These are the same recommendations given for flight set 360L002.

4.6.3.4 Case Membrane Girth Gage Response. Flight set 360L003 instrumentation on both the LH and RH RSRMs consisted of seven girth gages on the case membrane. Tables 4.6-10 and 4.6-11 list the girth gage response from 0 to 3 sec and compare the measured strain and calculated radial growth with predicted values. (These predicted values are for the first 3 sec only.) Every prediction is within -13.3 percent of the measured test data. Also listed is the maximum radial growth for -10 to 120 sec. The maximum girth strains for the duration of the flight are slightly larger than those found from 0 to 3 sec. The maximum radial growth occurred at Station 611.5 on the LH SRB and has a value of 0.279 inch.

Table 4.6-12 shows the comparison of 360L003 with several static tests, 360L001, 360L002, and predictions (from -10 to 120 sec). This table shows a good correlation with these tests. The values for Station 1637.5 (Location 7) exclude the spiking event (discussed in Section 4.6.3.3 of this volume).

4.6.3.5 Case Biaxial Stresses (Case Line Loads, Aft Field/ETA Joint). The 360L003 instrumentation consisted of biaxial gages at seven locations along the case (four pairs at Stations 556.5, 876.5, 1196.5, 1466, and 1797 and nine pairs at Stations 1497 and 1501). Tables 4.6-13 and 4.6-14 illustrate the hoop and axial strain values with their corresponding predictions for the first 3 sec of flight. These tables show a good correlation between measured and predicted values, with the exception of Station 1330 in the axial direction. This station is located on the outer leg of the clevis and forward of the pins. This location is not as constrained as other areas on the joint, so the behavior is different and less predictable--especially in the axial direction.

Table 4.6-15 lists the maximum hoop and axial stresses measured from biaxial gages for the total 120-sec burn time. These tables do not provide a comparison between test data and analysis. An analysis was performed for the initial 3-sec burn time only, which does not necessarily correspond to maximum stress occurrence. The maximum measured hoop stress occurred at Station 670 at 98 deg on the RH SRB, measuring a local stress of 137.4 ksi. The ultimate strength of D6AC steel is 214 ksi with biaxial improvement. The maximum measured hoop stress results in a SF of 1.56 with the ultimate strength. The yield strength of D6AC steel is 180 ksi. Therefore, no local yielding was measured in this area.

Table 4.6-10. LH Motor Case Radial Deflection

TEST NAME: 360L003
JOINT: LEFT SRM CASE RADIAL DEFLECTION
DESCRIPTION: CASE GIRTH GAGES
THE TIME RANGE IS 0.0 TO 3.0 SECONDS

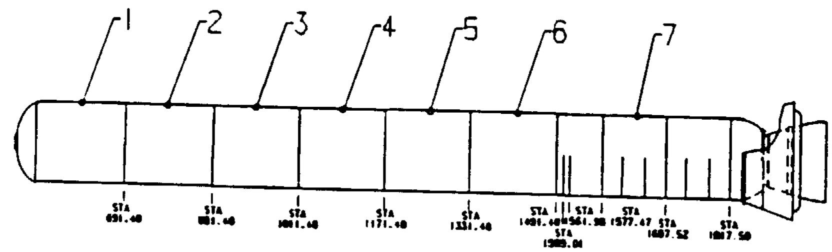

GIRTH GAGE LOCATION	GAGE NUMBER	STATION	RADIUS (IN)	RADIAL GROWTH (IN)	TEST STRAIN (UIN/IN)	ADJUSTED ANALYSIS STRAIN (UIN/IN)	ADJUSTED ANALYSIS RADIAL GROWTH (IN)	DIFF IN RADIAL GROWTH (% DIFF)	MAXIMUM RADIAL GROWTH -10 TO 120 SECONDS
1	B08G7269	611.5	73.0	0.279	3816	3294	0.241	-13.3	0.279
2	B08G7272	771.5	73.0	0.261	3567	3225	0.236	-9.6	0.264
3	B08G7279	931.5	73.0	0.267	3651	3319	0.242	-9.1	0.275
4	B08G7282	1091.5	73.0	0.264	3618	3235	0.236	-10.6	0.274
5	B08G7289	1251.5	73.0	0.258	3534	ND	ND	ND	0.271
6	B08G7292	1411.5	73.0	0.227	3112	3077	0.225	-1.1	0.241
7	B08G7301	1637.5	73.0	0.230	3143	3152	0.230	0.3	0.260

Table 4.6-11. RH Motor Case Radial Deflection

TEST NAME: 360L003
JOINT: RIGHT SRM CASE RADIAL DEFLECTION
DESCRIPTION: CASE GIRTH GAGES
THE TIME RANGE IS 0.0 TO 3.0 SECONDS

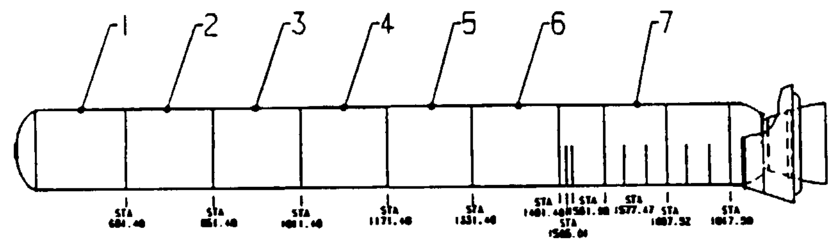

GIRTH GAGE LOCATION	GAGE NUMBER	STATION	RADIUS (IN)	RADIAL GROWTH (IN)	TEST STRAIN (UIN/IN)	ADJUSTED ANALYSIS STRAIN (UIN/IN)	ADJUSTED ANALYSIS RADIAL GROWTH (IN)	DIFF IN RADIAL GROWTH (% DIFF)	MAXIMUM RADIAL GROWTH -10 TO 120 SECONDS
1	B08G8269	611.5	73.0	0.275	3764	3302	0.241	-12.3	0.277
2	B08G8272	771.5	73.0	0.258	3532	3172	0.232	-10.2	0.263
3	B08G8279	931.5	73.0	0.264	3620	3327	0.243	-8.1	0.276
4	B08G8282	1091.5	73.0	0.265	3634	3242	0.237	-10.8	0.278
5	B08G8289	1251.5	73.0	0.258	3531	ND	ND	ND	0.267
6	B08G8292	1411.5	73.0	0.251	3433	3086	0.225	-10.1	0.266
7	B08G8301	1637.5	73.0	0.260	3558	3084	0.225	-2.8	0.265

Table 4.6-12. Case Membrane Radial Growth--Previous Motors Compared to 360L003

Case Membrane Radial Growth Comparisons to STS-29

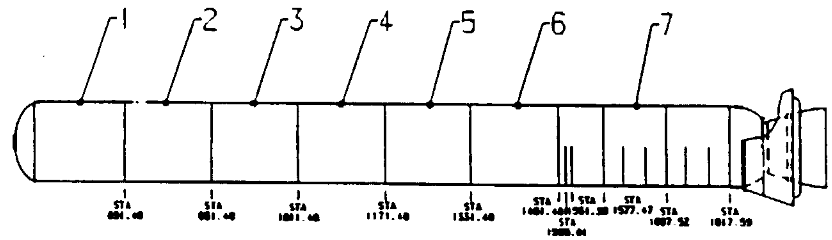

Case Membrane Girths

LOC.	·STS-29 GAGE	STS-29 RIGHT	STS-29 LEFT	STS-27 RIGHT	STS-27 LEFT	STS-26 RIGHT	STS-26 LEFT	PV-1	QM-7	RADIAL GROWTH (Inches) QM-6	DM-9	DM-8	PRED	NOMINAL RADIUS (INCHES)
1	B08GX269	0.275	0.279	0.280	0.279	ND	ND	ND	0.289	0.275	0.268	0.284	0.241	73.04
2	B08GX272	0.258	0.261	0.265	0.270	ND	0.275	ND	0.275	0.262	0.271	0.282	0.234	73.04
3	B08GX279	0.264	0.267	0.273	ND	ND	ND	ND	0.287	0.279	0.283	0.291	0.243	73.04
4	B08GX282	0.265	0.264	0.270	ND	0.281	0.279	ND	0.288	0.273	0.279	0.292	0.237	73.04
5	B08GX289	0.258	0.258	0.268	0.268	ND	ND	ND	0.279	0.264	ND	0.285	ND	73.04
6	B08GX292	0.251	0.227	0.265	0.258	0.276	ND	ND	0.278	0.268	ND	ND	0.225	73.04
7	B08GX301	0.260	0.230	0.244	ND	0.261	0.260	ND	0.266	0.253	0.253	0.260	0.227	73.04

* QM-7, QM-6, and DM-9 Locations are 1/3 Inch Aft of DM-8 Location.
Note: Only the Predicted Radial Growths Are Ratios of STS-29 Test Pressure
Note: Location 1 contains small spike on the way up at 0.2625 seconds
Note: Location 7 contains a double spike at 0.2875 and 0.3125 seconds which exceeds overall maximum

Table 4.6-13. Comparison of Maximum Predicted Versus Measured Biaxial Strain Values--RH Motor (0 to 3 sec)

		Maximum Hoop Strain (μ in/in)			Maximum Axial Strain (μ in/in)		
Station	Deg.	Gage Name	Predicted	Measured	Gage Name	Predicted	Measured
556.5	0.	B08G8323A	3586.	3490.	B08G8322A	736.	788.
"	82.	B08G8321A	3583.	3573.	B08G8320A	731.	821.
"	180.	B08G8319A	3568.	3486.	B08G8318A	791.	850.
"	270.	B08G8325A	3580.	3596.	B08G8324A	765.	885.
670.0	0.	B08G8252A	2680.	3690.	B08G8251A	985.	1102.
"	85.	B08G8254A	2661.	3827.	B08G8253A	1059.	1041.
"	180.	B08G8256A	2670.	3277.	B08G8255A	1111.	885.
"	270.	B08G8258A	2668.	3481.	B08G8257A	971.	867.
876.5	0.	B08G8331A	3688.	3680.	B08G8330A	1114.	787.
"	82.	B08G8329A	3685.	3552.	B08G8328A	1139.	898.
"	180.	B08G8327A	3668.	3609.	B08G8326A	1371.	1006.
"	270.	B08G8333A	3685.	3576.	B08G8332A	955.	806.
1196.5	0.	B08G8339A	3408.	3281.	B08G8338A	1567.	791.
"	82.	B08G8337A	3286.	3415.	B08G8336A	1266.	896.
"	180.	B08G8335A	3302.	3148.	B08G8334A	1130.	1076.
"	270.	B08G8341A	3353.	3378.	B08G8340A	888.	618.
1330.0	0.	B08G8264A	2654.	1136.	B08G8263A	1084.	-223.
"	85.	B08G8266A	2516.	1532.	B08G8265A	1303.	-405.
"	180.	B08G8260A	2553.	2699.	B08G8259A	1574.	-1086.
"	270.	B08G8262A	2590.	2581.	B08G8261A	886.	ND
1466.0	0.	B08G8347A	3381.	3244.	B08G8346A	1264.	646.
"	82.	B08G8345A	3199.	3147.	B08G8344A	1516.	902.
"	180.	B08G8343A	3216.	3180.	B08G8342A	1829.	1128.
"	270.	B08G8349A	3267.	3205.	B08G8348A	1029.	654.

Table 4.6-13. Comparison of Maximum Predicted Versus Measured Biaxial Strain Values--RH Motor (0 to 3 sec) (cont)

		Maximum Hoop Strain (μ in/in)			Maximum Axial Strain (μ in/in)		
Station	Deg.	Gage Name	Predicted	Measured	Gage Name	Predicted	Measured
1497.0	0.	B08G8369A	2104.	2143.	B08G8368A	2223.	1266.
"	82.	B08G8371A	1925.	1970.	B08G8370A	2284.	1718.
"	180.	B08G8373A	1925.	1927.	B08G8372A	2658.	1754.
"	220.	B08G8375A	1934.	1859.	B08G8374A	2259.	1321.
"	240.	B08G8377A	1973.	2025.	B08G8376A	2078.	1030.
"	255.	B08G8379A	1945.	1871.	B08G8378A	1980.	1298.
"	270.	B08G8381A	1987.	1903.	B08G8380A	2039.	1228.
"	285.	B08G8383A	2032.	1962.	B08G8382A	2083.	1175.
"	320.	B08G8385A	2071.	1996.	B08G8384A	2132.	1416.
1501.0	0.	B08G8387A	2104.	1929.	B08G8386A	1190.	598.
"	82.	B08G8389A	1851.	1914.	B08G8388A	1270.	981.
"	180.	B08G8391A	1864.	1737.	B08G8390A	1535.	1034.
"	220.	B08G8393A	1729.	1711.	B08G8392A	1238.	911.
"	240.	B08G8395A	1881.	1870.	B08G8394A	1073.	800.
"	255.	B08G8397A	1840.	1721.	B08G8396A	1005.	ND
"	270.	B08G8399A	1930.	1803.	B08G8398A	1048.	819.
"	285.	B08G8401A	1933.	1920.	B08G8400A	1063.	732.
"	320.	B08G8403A	1917.	1957.	B08G8402A	1145.	842.
1797.0	0.	B08G8409A	3548.	2968.	B08G8408A	1960.	634.
"	82.	B08G8407A	3585.	3184.	B08G8406A	1161.	533.
"	180.	B08G8405A	3383.	2658.	B08G8404A	2924.	1054.
"	270.	B08G8411A	3628.	3074.	B08G8410A	906.	440.

Table 4.6-14. Comparison of Maximum Predicted Versus Measured Biaxial Strain Values--LH Motor (0 to 3 sec)

		Maximum Hoop Strain (μ in/in)			Maximum Axial Strain (μ in/in)		
Station	Deg.	Gage Name	Predicted	Measured	Gage Name	Predicted	Measured
556.5	0.	B08G7319A	3563.	3696.	B08G7318A	791.	821.
"	98.	B08G7321A	3583.	3409.	B08G7320A	731.	828.
"	180.	B08G7323A	3579.	3561.	B08G7322A	734.	774.
"	270.	B08G7325A	3577.	3570.	B08G7324A	765.	997.
876.5	0.	B08G7327A	3502.	3362.	B08G7326A	1371.	1058.
"	98.	B08G7329A	3472.	3430.	B08G7328A	1141.	972.
"	180.	B08G7331A	3555.	3460.	B08G7330A	1114.	828.
"	270.	B08G7333A	3513.	3526.	B08G7332A	957.	792.
1196.5	0.	B08G7335A	3165.	ND	B08G7334A	1580.	996.
"	98.	B08G7337A	3289.	3449.	B08G7336A	1266.	921.
"	180.	B08G7339A	3435.	3393.	B08G7338A	1129.	788.
"	270.	B08G7341A	3356.	3186.	B08G7340A	893.	803.
1330.0	0.	B08G7260A	2552.	861.	B08G7259A	1579.	-201.
"	95.	B08G7266A	2533.	1696.	B08G7265A	1313.	-432.
"	180.	B08G7264A	2652.	2398.	B08G7263A	1100.	-1035.
"	270.	B08G7262A	2041.	1943.	B08G7261A	864.	-1267.
1466.0	0.	B08G7343A	3172.	3006.	B08G7342A	1837.	941.
"	98.	B08G7345A	3199.	3497.	B08G7344A	1519.	957.
"	180.	B08G7347A	3383.	3346.	B08G7346A	1264.	690.
"	270.	B08G7349A	3239.	ND	B08G7348A	1029.	ND

C-2

Table 4.6-14. Comparison of Maximum Predicted Versus Measured Biaxial Strain Values--LH Motor (0 to 3 sec) (cont)

		Maximum Hoop Strain (μ in/in)			Maximum Axial Strain (μ in/in)		
Station	Deg.	Gage Name	Predicted	Measured	Gage Name	Predicted	Measured
1497.0	0.	B08G7373A	1919.	1926.	B08G7372A	2672.	1282.
"	98.	B08G7371A	1926.	1859.	B08G7370A	2284.	996.
"	180.	B08G7369A	2106.	1869.	B08G7368A	2223.	1139.
"	220.	B08G7385A	2070.	1883.	B08G7384A	2132.	945.
"	255.	B08G7383A	2030.	1817.	B08G7382A	2086.	1063.
"	270.	B08G7381A	1989.	1869.	B08G7380A	2034.	1012.
"	285.	B08G7379A	1943.	1823.	B08G7378A	1980.	1096.
"	300.	B08G7377A	1971.	1799.	B08G7376A	2059.	1226.
"	320.	B08G7375A	1933.	1763.	B08G7374A	2259.	1185.
1501.0	0.	B08G7391A	1864.	1737.	B08G7390A	1553.	1073.
"	98.	B08G7389A	1855.	1865.	B08G7388A	1273.	976.
"	180.	B08G7387A	2107.	1793.	B08G7386A	1191.	936.
"	220.	B08G7403A	1914.	1894.	B08G7402A	1140.	837.
"	255.	B08G7401A	1905.	ND	B08G7400A	1049.	ND
"	270.	B08G7399A	1907.	ND	B08G7398A	1041.	ND
"	285.	B08G7397A	1819.	ND	B08G7396A	1005.	ND
"	300.	B08G7395A	1888.	1788.	B08G7394A	1075.	1037.
"	320.	B08G7393A	1733.	1697.	B08G7392A	1239.	1010.
1797.0	0.	B08G7405A	3574.	ND	B08G7404A	2907.	1030.
"	98.	B08G7407A	3580.	3097.	B08G7406A	1171.	545.
"	180.	B08G7409A	3557.	3015.	B08G7408A	1960.	737.
"	270.	B08G7411A	3631.	2986.	B08G7410A	904.	449.

Table 4.6-15. Maximum Measured Biaxial Stress Values (0 to 120 sec)

		Left SRB Stress (KSI)			Right SRB Stress (KSI)	
Station	Degree	Max Hoop Measured	Corr. Axial Measured	Degree	Max Hoop Measured	Corr. Axial Measured
556.5	0.	129.9	61.6	0.	123.2	59.6
"	98.	120.4	62.3	82.	125.7	64.5
"	180.	124.8	59.2	180.	123.5	61.4
"	270.	126.0	47.2	270.	125.8	45.8
670.0	0.	-	-	0.	ND	ND
"	98.	-	-	82.	137.4	74.5
"	180.	-	-	180.	119.0	60.7
"	270.	-	-	270.	124.3	48.3
876.5	0.	124.7	59.6	0.	132.8	58.2
"	98.	124.5	64.8	82.	128.1	63.9
"	180.	125.7	57.4	180.	133.1	60.5
"	270.	127.3	49.6	270.	128.8	50.9
1196.5	0.	ND	ND	0.	121.6	54.1
"	98.	127.7	57.9	82.	126.9	58.4
"	180.	125.1	55.4	180.	120.7	56.4
"	270.	119.7	49.3	270.	125.5	46.2
1330.0	0.	-64.8	-21.1	0.	34.4	1.3
"	98.	54.6	4.2	82.	48.0	4.2
"	180.	73.4	-9.3	180.	74.9	-19.5
"	270.	55.7	-10.1	270.	ND	ND
1466.0	0.	115.0	57.2	0.	121.6	51.5
"	98.	133.2	58.9	82.	122.0	53.9
"	180.	124.6	52.4	180.	124.2	54.2
"	270.	ND	ND	270.	120.8	49.8

Table 4.6-15. Maximum Measured Biaxial Stress Values (0 to 120 sec) (cont)

		Left SRB Stress (KSI)			Right SRB Stress (KSI)	
Station	Degree	Max Hoop Measured	Corr. Axial Measured	Degree	Max Hoop Measured	Corr. Axial Measured
1497.0	0.	80.8	54.8	0.	89.1	63.4
"	98.	78.2	51.4	82.	87.9	74.0
"	180.	78.4	54.6	180.	83.9	63.4
"	220.	78.3	52.4	220.	82.1	58.4
"	255.	77.6	55.6	240.	84.4	54.8
"	270.	78.5	52.5	255.	81.1	60.4
"	285.	77.3	53.7	270.	81.5	59.9
"	300.	78.8	57.6	285.	83.3	59.9
"	320.	78.4	55.2	320.	86.9	69.9
1501.0	0.	73.5	45.4	0.	74.6	38.7
"	98.	75.7	46.9	82.	76.3	47.7
"	180.	74.4	47.6	180.	73.1	44.2
"	220.	76.9	48.5	220.	75.3	46.1
"	255.	ND	ND	240.	76.2	43.3
"	270.	ND	ND	255.	ND	ND
"	285.	ND	ND	270.	72.5	44.1
"	300.	75.8	49.7	285.	74.5	43.1
"	320.	75.3	49.7	320.	78.5	50.6
1797.0	0.	ND	ND	0.	114.5	45.4
"	98.	117.7	50.0	82.	120.3	51.3
"	180.	117.1	48.3	180.	112.9	43.3
"	270.	117.5	40.9	270.	121.0	41.3

4.6.3.6 Case-to-Nozzle Joint Performance. Instrumentation on the case-to-nozzle joint consisted of six girth gages and two stations of biaxial gages. Test results at these locations are compared to analytical results acquired from a 3-D finite element analysis. The analysis was performed with the finite element code ANSYS using a 1.8-deg model of the case-to-nozzle joint. Near the joint region the model was 3-D, transitioning to two dimensional (2-D) away from the joint. The following assumptions and parameters were included in the model:

a. Nominal values for material properties and hardware dimensions

b. Preload of 140 kip in the axial bolts and 47 kip in the radial bolts

c. Internal pressure of 920 psig applied up to the backside of the primary O-ring groove

d. Frictionless joint behavior

e. Zero vectoring nozzle condition

f. Propellant and insulation were not modeled

Because the model is cyclic-symmetric, any circumferential variation indicated by the test data will not be taken into account. The analysis was performed at 920 psig, and was linearly scaled to the estimated nozzle stagnation pressure, which involves approximately 5-percent error due to the nonlinear analysis.

Case-to-Nozzle Joint Girth Gages. Radial deflection is an important parameter to characterize since it is proportional to joint hoop stress. Tables 4.6-16 and 4.6-17 list the girth gage response during the flight and compare it to analysis. These tables show a good correlation with predicted values, with the exception of gage B08G8314, which is at Station 1875.5 on the RH SRB. The percent difference for this gage is 41 percent. The percent difference for the other gages ranges from 8.3 to 26.1. As expected, calculated radial growths indicated a prying open action and outward rotation of the joint. The maximum radial growth was 0.101 in. and occurred at Location 4 (Station 1875.5) on the LH SRB. Table 4.6-18 compares 360L003, several static test motors, 360L001, 360L002, and predictions. The correlation with 360L001 and 360L002 is very good and is slightly lower than with static motors.

Case-to-Nozzle Joint Biaxial Strain Gages. The case-to-nozzle biaxials measure local rather than average strains. Tables 4.6-19 and 4.6-20 show the maximum hoop stress value for the duration of the test (-10 to 120 sec). The maximum stress occurred in the hoop direction at Location 1 (90 deg on the RH SRB) and had a value of 66.6 ksi. This gives a SF of 3.21 with the ultimate strength. Tables 4.6-21 and 4.6-22 show a comparison with predicted values between -10 and 120 sec. The hoop direction compares very closely but the axial is somewhat off. Previous static fire tests have shown that the case-to-nozzle joint gages do not compare as well to analytical data in the meridional direction as in the hoop direction. Several possible reasons for this are:

Table 4.6-16. LH Motor Aft Dome Fixed Housing Girth Gage Measurements

TEST NAME: 360L003
JOINT: LEFT SRM AFT DOME, FIXED HOUSING
DESCRIPTION: NOZZLE CASE GIRTH GAGES
THE TIME RANGE IS -10.0 TO 120.0 SECONDS

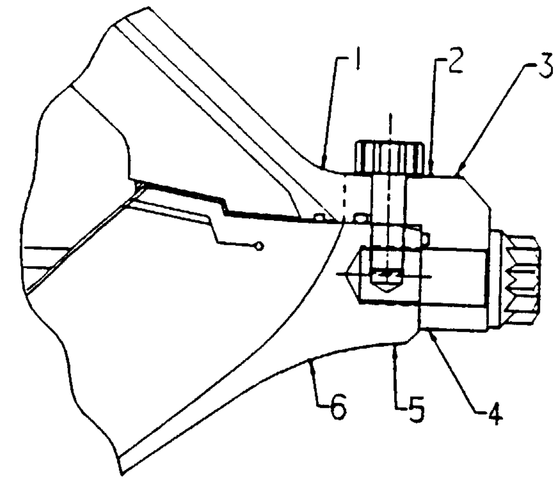

GIRTH GAGE LOCATION	GAGE NUMBER	STATION	RADIUS (IN)	RADIAL GROWTH (IN)	TEST STRAIN (UIN/IN)	ADJUSTED ANALYSIS STRAIN (UIN/IN)	ADJUSTED ANALYSIS RADIAL GROWTH (IN)	DIFF IN RADIAL GROWTH (% DIFF)
1	B08G7312	1873.0	50.4	0.059	1181	1476	0.074	25.0
2	B08G7310	1875.7	50.5	0.094	1868	2022	0.102	8.3
3	B08G7315	1876.0	50.5	0.100	1987	2440	0.123	22.8
4	B08G7314	1875.5	54.4	0.101	1859	2344	0.128	26.1
5	B08G7313	1874.0	54.8	0.085	1547	1860	0.102	20.2
6	B08G7311	1872.5	55.2	0.062	1118	1392	0.077	24.5

Table 4.6-17. RH Motor Aft Dome Fixed Housing Girth Gage Measurements

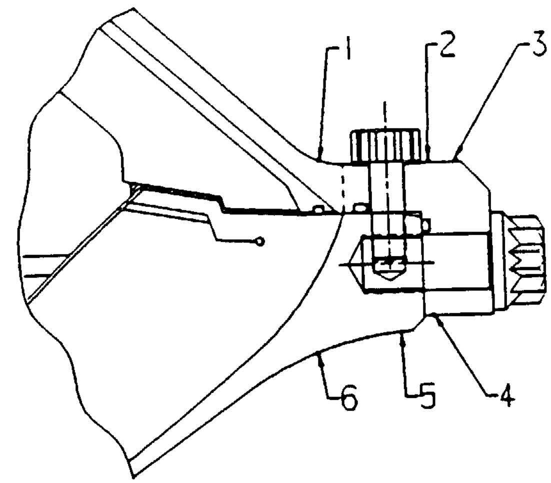

TEST NAME: 360L003
JOINT: RIGHT SRM AFT DOME, FIXED HOUSING
DESCRIPTION: NOZZLE CASE GIRTH GAGES
THE TIME RANGE IS -10.0 TO 120.0 SECONDS

GIRTH GAGE LOCATION	GAGE NUMBER	STATION	RADIUS (IN)	RADIAL GROWTH (IN)	TEST STRAIN (UIN/IN)	ADJUSTED ANALYSIS STRAIN (UIN/IN)	ADJUSTED ANALYSIS RADIAL GROWTH (IN)	DIFF IN RADIAL GROWTH (% DIFF)
1	B08G8312	1873.0	50.4	0.059	1174	1460	0.074	24.4
2	B08G8310	1875.7	50.5	0.092	1820	2014	0.102	10.7
3	B08G8315	1876.0	50.5	0.098	1934	2420	0.122	25.1
4	B08G8314	1875.5	54.4	0.091	1665	2348	0.128	41.0
5	B08G8313	1874.0	54.8	0.083	1515	1845	0.101	21.8
6	B08G8311	1872.5	55.2	0.066	1198	1383	0.076	15.4

Table 4.6-18. Case-to-Nozzle Joint Radial Growth--Previous Motors Compared to 360L003

Nozzle to Case Joint Radial Growth Comparisons to STS-29

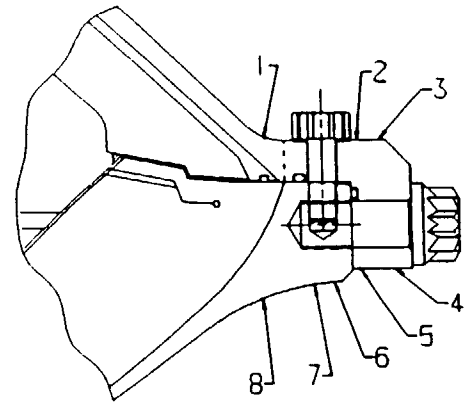

Nozzle to Case Girths

LOC.	STS-29 GAGE	STS-29 RIGHT	STS-29 LEFT	STS-27 RIGHT	STS-27 LEFT	STS-26 RIGHT	STS-26 LEFT	PV-1	QM-7	QM-6	DM-9	DM-8	PRED	NOMINAL RADIUS (INCHES)
								RADIAL GROWTH (Inches)						
1	B08GX312	0.059	0.059	0.057	0.059	ND	0.049	0.087	0.068	0.081	0.072	ND	0.074	50.4
2	B08GX310	0.092	0.094	0.090	ND	ND	ND	ND	ND	ND	ND	ND	0.102	50.5
3	B08GX315	0.098	0.100	0.095	0.094	0.093	0.093	0.127	0.128	0.130	0.115	ND	0.122	50.5
4	NO GAGE	ND	ND	ND	ND	ND	ND	0.118	0.126	0.126	ND	0.124	ND	54.4
5	B08GX314	0.091	0.101	0.088	0.088	0.097	0.097	0.124	0.120	0.119	0.114	ND	0.128	54.4
6	B08GX313	0.083	0.085	0.081	0.080	ND	ND	0.107	0.109	0.106	0.087	0.110	0.101	54.8
7	NO GAGE	ND	ND	ND	ND	0.087	0.084	0.100	0.101	0.102	0.102	0.103	ND	54.8
8	B08GX311	0.066	0.062	0.063	0.062	0.070	0.067	0.084	0.087	0.086	0.086	0.090	0.076	55.2

Note: All Test Radial Growths Are Ratios of STS-29 Test Pressure

Table 4.6-19. LH Motor Aft Dome Fixed Housing Biaxial Gage Measurements (-10 to 120 sec)

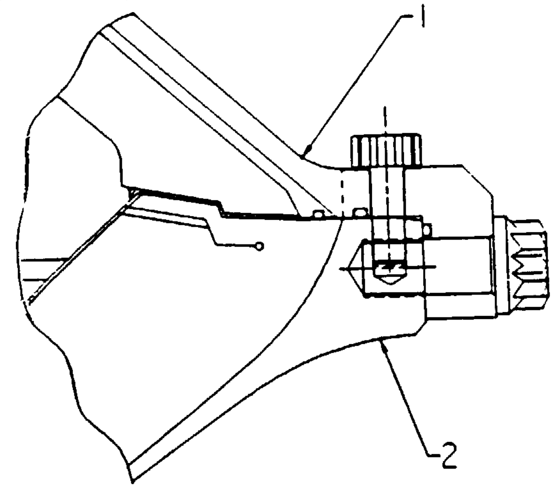

TEST NAME: 360L003
JOINT: LEFT SRM FIXED HOUSING, AFT DOME
DESCRIPTION: NOZZLE / CASE BIAXIAL GAGES
CORRECTED LOCAL PRESS:
THE TIME RANGE IS -10.0 TO 120.0 SECONDS

LOCAT	ANGULAR LOCATION	HOOP GAGE	MERID GAGE	MAX HOOP STRESS (KSI)	MERID STRESS (KSI)	TEST DATA HOOP STRAIN (UIN/IN)	TEST DATA MERID STRAIN (UIN/IN)
1	0.0	B08G7415	B08G7416	38.9	-17.6	1503	-1014
	90.0	B08G7420	B08G7421	32.2	-38.4	1504	-1646
	180.0	B08G7425	B08G7426	39.9	-16.9	1529	-1001
	270.0	B08G7430	B08G7431	39.2	-16.5	1504	-981
			AVERAGE:	37.6	-22.3	1510	-1161
2	0.0	B08G7413	B08G7412	ND	ND	ND	ND
	90.0	B08G7418	B08G7417	27.3	-32.7	1277	-1401
	180.0	B08G7423	B08G7422	ND	ND	ND	ND
	270.0	B08G7428	B08G7427	32.2	-18.4	1287	-969
			AVERAGE:	29.8	-25.5	1282	-1185

Table 4.6-20. RH Motor Aft Dome Fixed Housing Biaxial Gage Measurements (-10 to 120 sec)

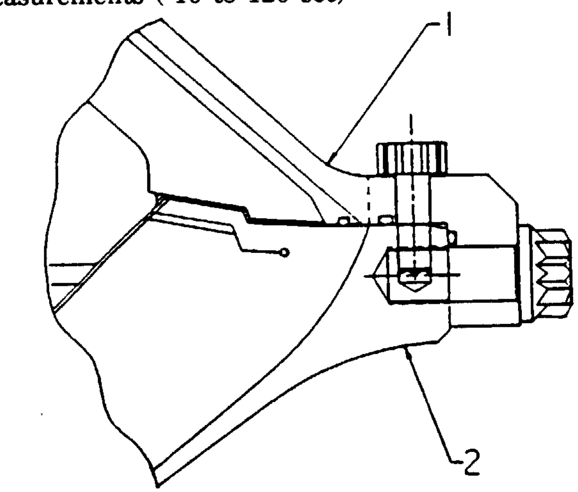

TEST NAME: 360L003
JOINT: RIGHT SRM FIXED HOUSING, AFT DOME
DESCRIPTION: NOZZLE / CASE BIAXIAL GAGES
THE TIME RANGE IS -10.0 TO 120.0 SECONDS

LOCAT	ANGULAR LOCATION	HOOP GAGE	MERID GAGE	MAX HOOP STRESS (KSI)	MERID STRESS (KSI)	TEST DATA HOOP STRAIN (UIN/IN)	TEST DATA MERID STRAIN (UIN/IN)
1	0.0	B08G8425	B08G8426	25.3	-22.3	1094	-1026
	90.0	B08G8420	B08G8421	66.6	-27.6	2547	-1651
	180.0	B08G8413	B08G8416	39.0	-20.8	1540	-1123
	270.0	B08G8430	B08G8431	38.3	-15.3	1459	-932
			AVERAGE:	42.3	-21.5	1660	-1183
2	0.0	B08G8423	B08G8422	30.8	-20.5	1263	-1027
	90.0	B08G8418	B08G8417	27.0	-29.6	1233	-1291
	180.0	B08G8413	B08G8412	25.4	-19.6	1068	-935
	270.0	B08G8428	B08G8427	31.4	-18.2	1257	-953
			AVERAGE:	28.6	-22.0	1205	-1052

Table 4.6-21. LH Motor Aft Dome Fixed Housing Biaxial Gage Measurements (-10 to 120 sec)

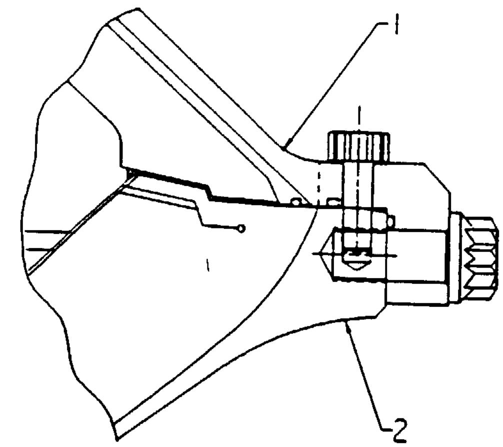

TEST NAME: 360L003
JOINT: LEFT SRM FIXED HOUSING, AFT DOME
DESCRIPTION: NOZZLE / CASE BIAXIAL GAGES
THE TIME RANGE IS -10.0 TO 120.0 SECONDS

				TEST DATA		ADJUSTED ANALYSIS			
LOCAT	ANGULAR LOCATION	HOOP GAGE	MERID GAGE	HOOP STRAIN (UIN/IN)	MERID STRAIN (UIN/IN)	HOOP STRAIN (UIN/IN)	MERID STRAIN (UIN/IN)	%DIFF HOOP	%DIFF MERID
1	0.0	B08G7415	B08G7416	1503	-1038	1363	-1336	-9.3	28.6
	90.0	B08G7420	B08G7421	1504	-1666	1371	-1337	-8.9	-19.7
	180.0	B08G7425	B08G7426	1529	-1013	1365	-1334	-10.7	31.6
	270.0	B08G7430	B08G7431	1504	-1001	1366	-1331	-9.2	32.9
			AVERAGE:	1510	-1180				
2	0.0	B08G7413	B08G7412	ND	-1054	ND	-659	ND	-37.5
	90.0	B08G7418	B08G7417	1277	-1477	1066	-659	-16.5	-55.4
	180.0	B08G7423	B08G7422	ND	-2142	ND	-657	ND	-69.3
	270.0	B08G7428	B08G7427	1295	-1013	1071	-659	-17.3	-34.9
			AVERAGE:	1286	-1422				

Table 4.6-22. RH Motor Aft Dome Fixed Housing Biaxial Gage Measurements (-10 to 120 sec)

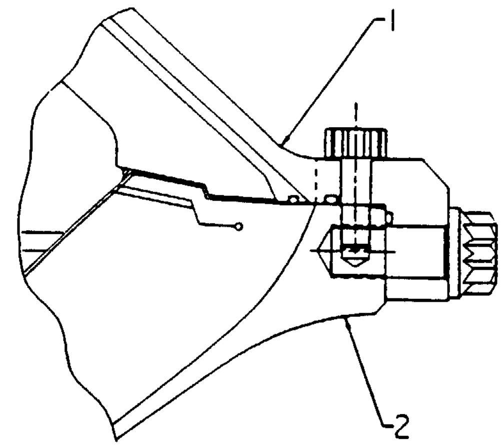

TEST NAME: 360L003
JOINT: RIGHT SRM FIXED HOUSING, AFT DOME
DESCRIPTION: NOZZLE / CASE BIAXIAL GAGES
THE TIME RANGE IS -10.0 TO 120.0 SECONDS

LOCAT	ANGULAR LOCATION	HOOP GAGE	MERID GAGE	TEST DATA HOOP STRAIN (UIN/IN)	TEST DATA MERID STRAIN (UIN/IN)	ADJUSTED ANALYSIS HOOP STRAIN (UIN/IN)	ADJUSTED ANALYSIS MERID STRAIN (UIN/IN)	%DIFF HOOP	%DIFF MERID
1	0.0	B08G8425	B08G8426	1094	-1050	1359	-1328	24.2	26.5
	90.0	B08G8420	B08G8421	2563	-2563	1309	-1292	-48.9	-49.6
	180.0	B08G8415	B08G8416	1540	-1131	1362	-1327	-11.6	17.3
	270.0	B08G8430	B08G8431	1459	-960	1362	-1328	-6.7	38.3
			AVERAGE:	1664	-1426				
2	0.0	B08G8423	B08G8422	1263	-1079	1062	-657	-15.9	-39.1
	90.0	B08G8418	B08G8417	1257	-1404	1066	-656	-15.2	-53.3
	180.0	B08G8413	B08G8412	1261	-1715	1064	-655	-15.6	-61.8
	270.0	B08G8428	B08G8427	1257	-1017	1058	-656	-15.8	-35.5
			AVERAGE:	1260	-1304				

a. Some gages are located in the neck of the fixed housing, where the 3-D model grid may not be fine enough to accurately predict circumferential strain.

b. Analytical data were linearly scaled to the test data.

c. Nozzle stagnation pressure was estimated to be 824 psig at 20 sec but was not measured.

d. Nominal materials were used for the finite element model.

4.6.3.7 Moment, Shear, and Strut Forces. Six stations along the full length of the SRM contained biaxial strain gages at four locations around the circumference (approximately 90 deg apart). From these, a stress plane at each station is generated; from the stress plane the Y and X axis bending moments and axial loads are computed. These results will be compared to both previous flights and predicted loads at all significant operational periods, including prelaunch, buildup, lift-off, shuttle roll maneuver, maximum acceleration, maximum dynamic pressure, and separation.

Bending About the Y Axis (MY). Figures 4.6-1 through 4.6-6 show the bending about the Y axis at both the LH and RH motors for Stations 556, 876, 1466, 1501, and 1797, respectively. Initially, the case is seen to be bending in the plus Y direction, which is caused by the orbiter weight. The magnitude increases linearly going down the case toward the hold-down point. During SSME buildup, every station experiences a change from positive to negative bending as the assembly bends over. The maximum value was -264×10^6 in.-lb at Station 1797 on the LH SRB (Figure 4.6-6). This value compares well with the design maximum of -304×10^6 in.-lb. Upon lift-off, the values reduce significantly, coming back to nearly zero for every station. During the shuttle roll maneuver, the LH SRB experiences an increase in bending, while the RH SRB experiences a decrease. This is because the nozzles are vectoring to cause the roll, the change of the LH and RH SRBs is opposite for the same reason. From this point on, the data are not very interesting and find their way to zero. The large spike seen at approximately 124 sec occurs at separation and is typical of other flights.

Figures 4.6-7 through 4.6-23 are plots of the first three flights (STS-1, STS-2, and STS-3), and the first three RSRM flights (360L001, 360L002, and 360L003). As shown in the figures, the correlation is very good. From these plots it can be seen that the roll maneuver of 360L003 is not similar to 360L001. The only notable difference is at Station 556 on the LH SRB. 360L001 is significantly higher and follows a different path than 360L002 and 360L003. (Data for 360L001 at Stations 556 and 876 on the RH motor are not included due to bad results.) Also, there was not instrumentation on the LH SRB near Station 556 for the first three flights, so no comparison can be made there either.

Bending About the Z Axis (MZ). Figures 4.6-24 through 4.6-29 show the bending about the Z axis for both the LH and RH motors for Stations 556, 876, 1196, 1466, 1501, and 1797, respectively.

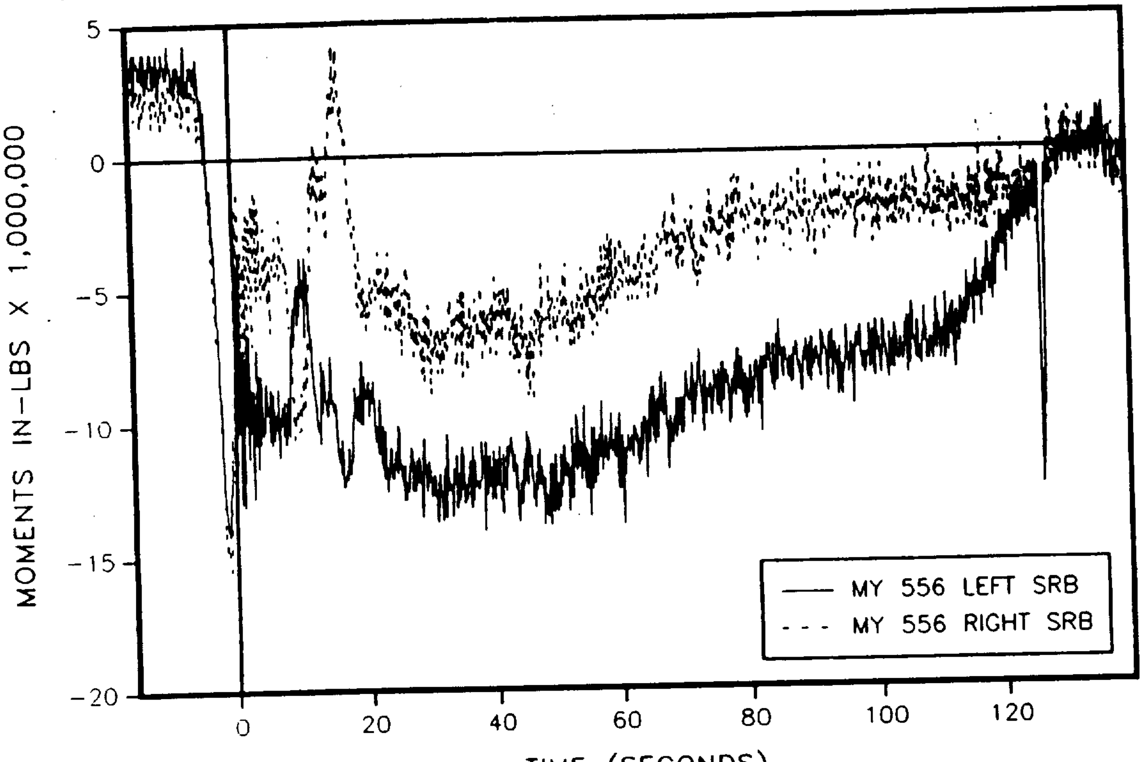

Figure 4.6-1. 360L003 Y Axis Bending Moment (Station 556)

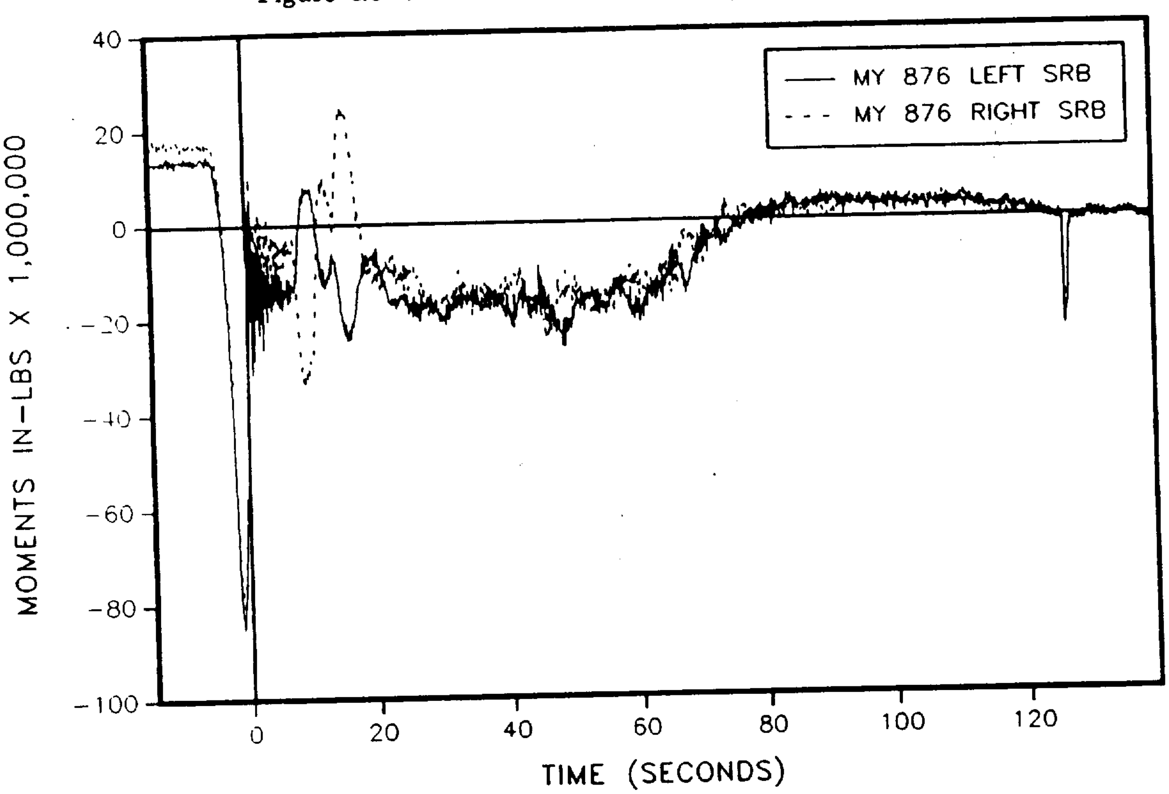

Figure 4.6-2. 360L003 Y Axis Bending Moment (Station 876)

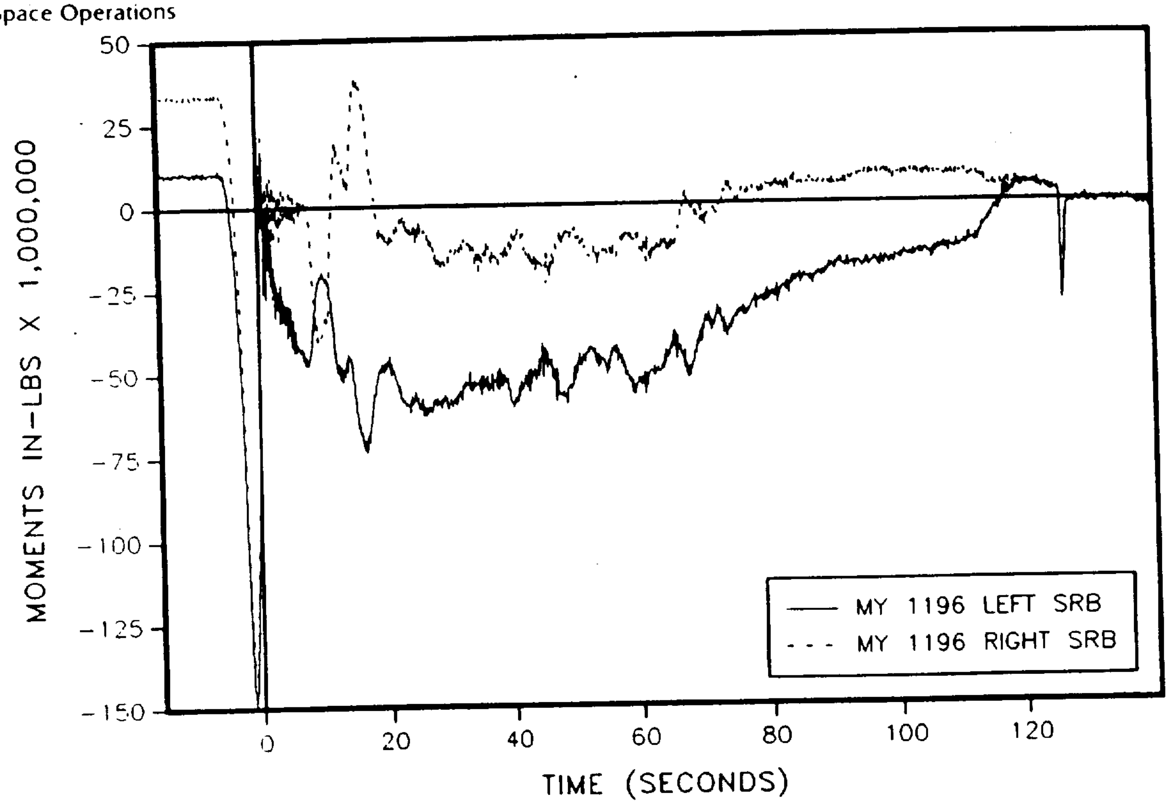

Figure 4.6-3. 360L003 Y Axis Bending Moment (Station 1196)

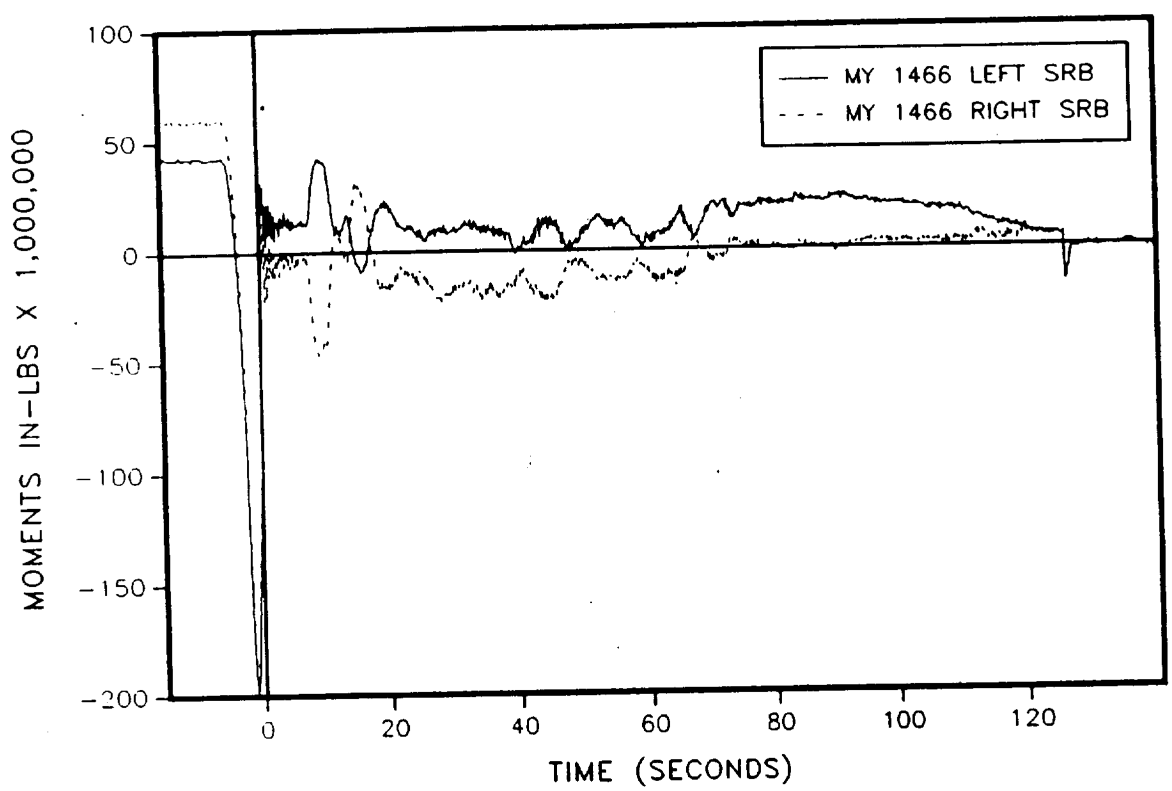

Figure 4.6-4. 360L003 Y Axis Bending Moment (Station 1466)

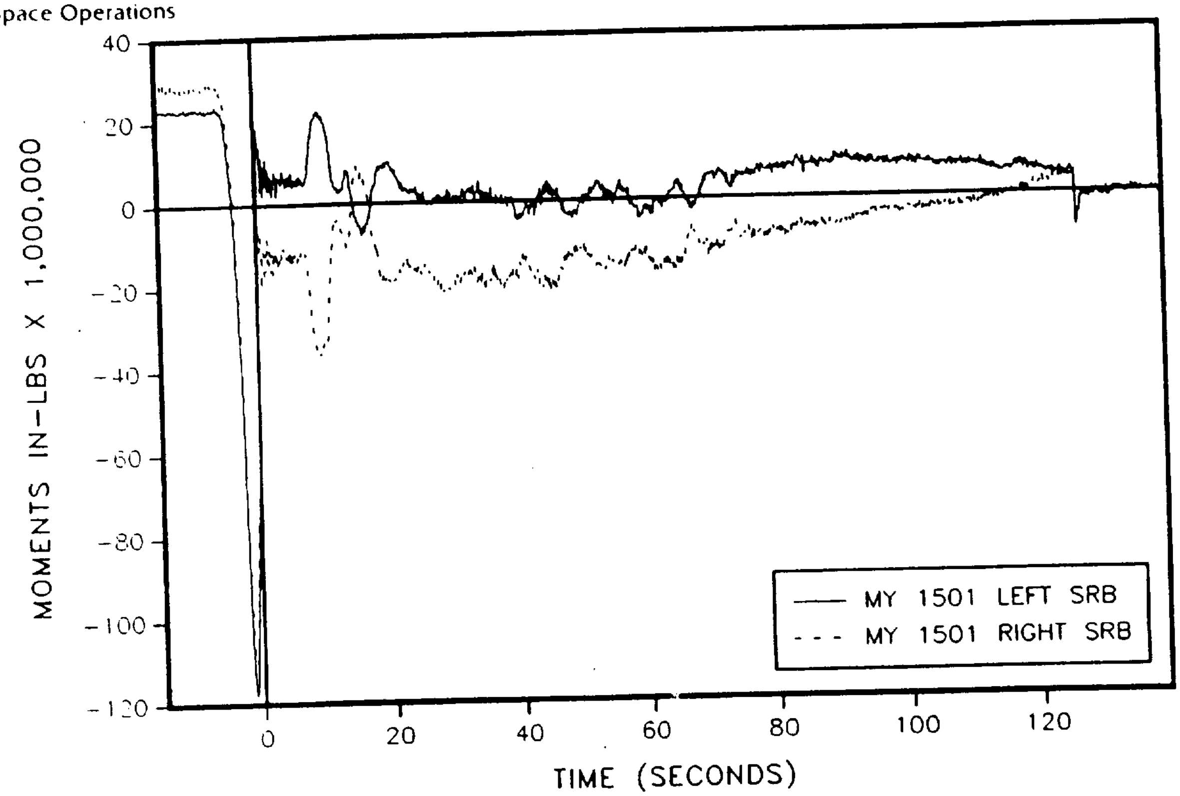

Figure 4.6-5. 360L003 Y Axis Bending Moment (Station 1501)

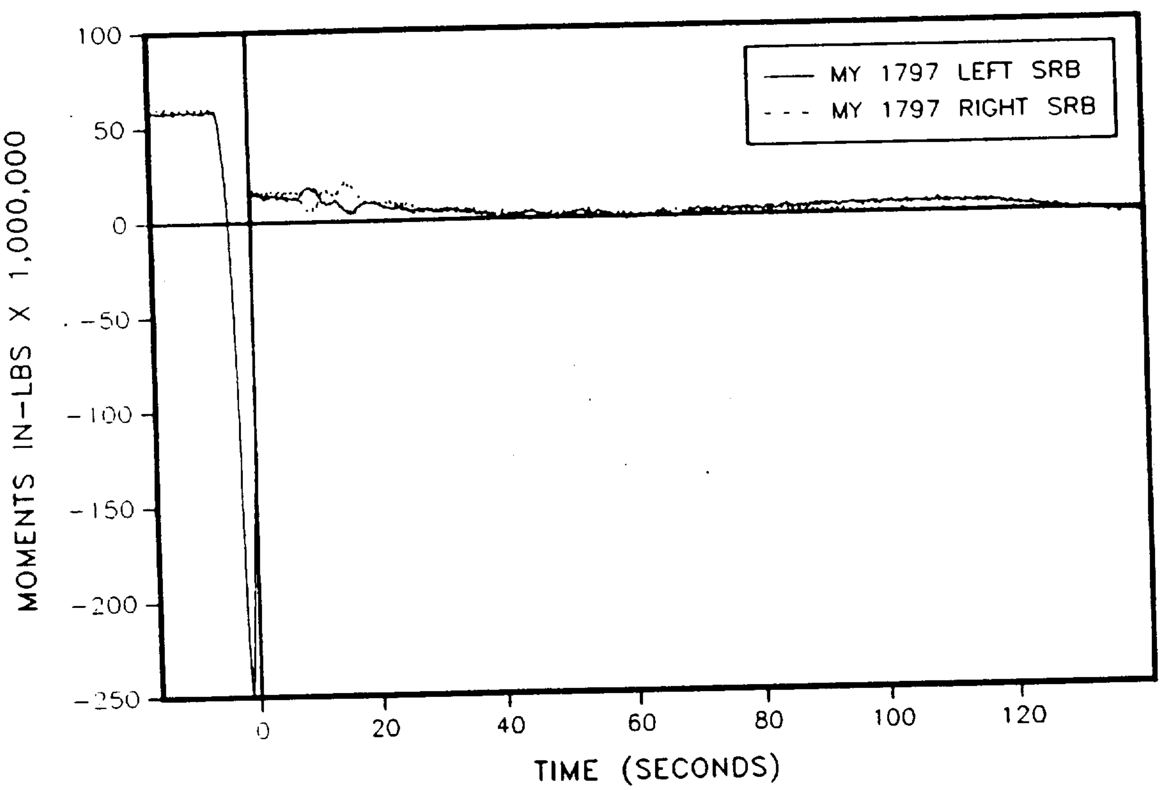

Figure 4.6-6. 360L003 Y Axis Bending Moment (Station 1797)

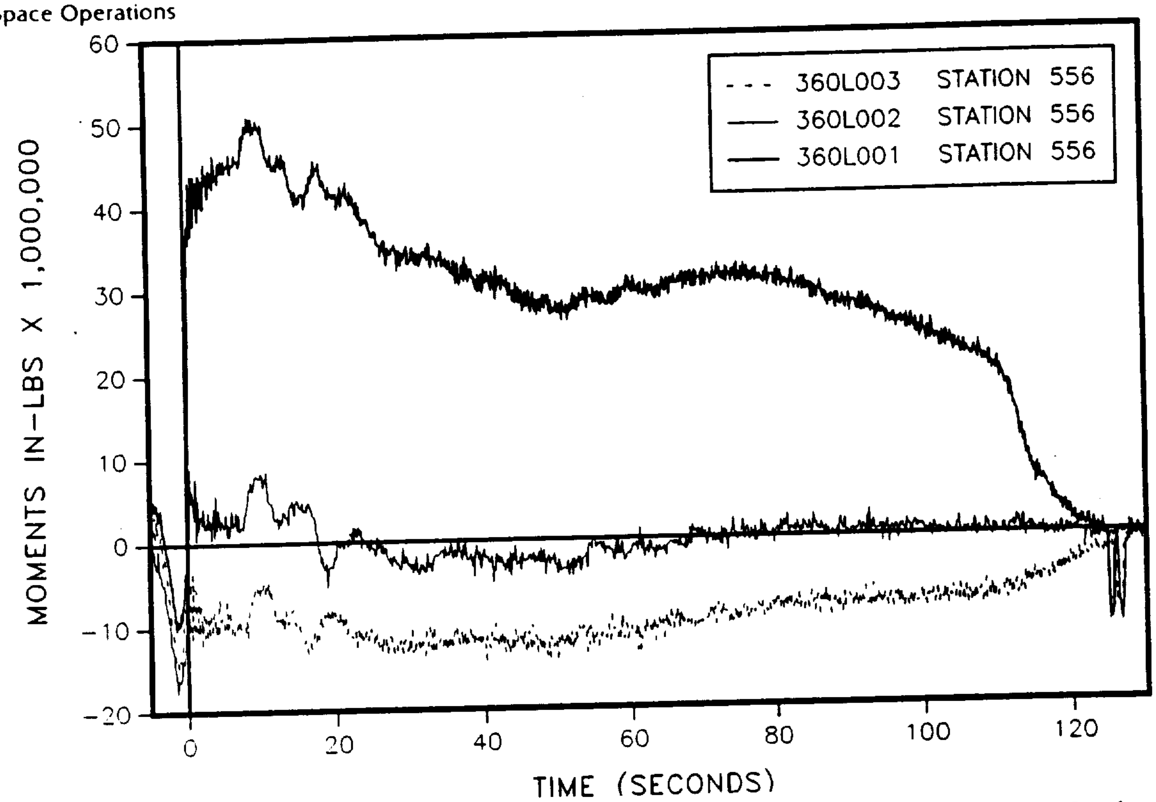

Figure 4.6-7. Y Axis Bending Moment--360L003 Versus 360L001, 360L002 (LH motor, Station 556)

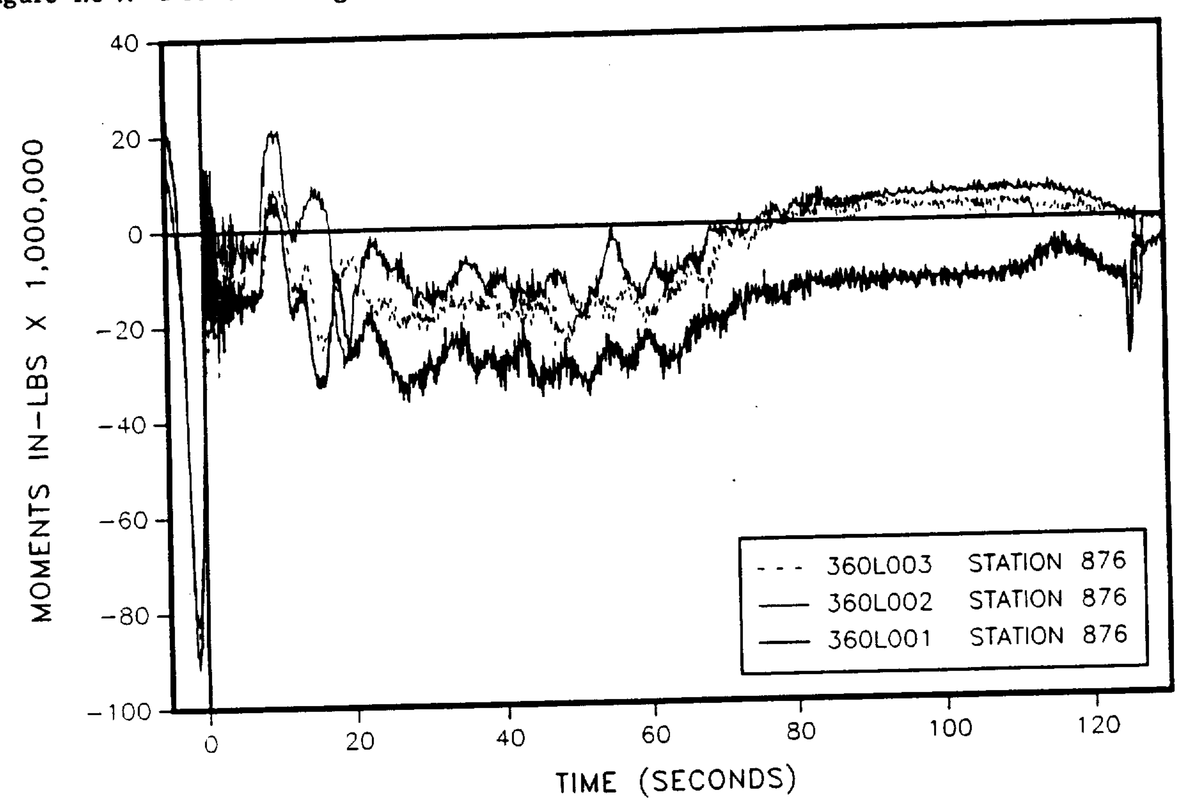

Figure 4.6-8. Y Axis Bending Moment--360L003 Versus 360L001, 360L002 (LH motor, Station 876)

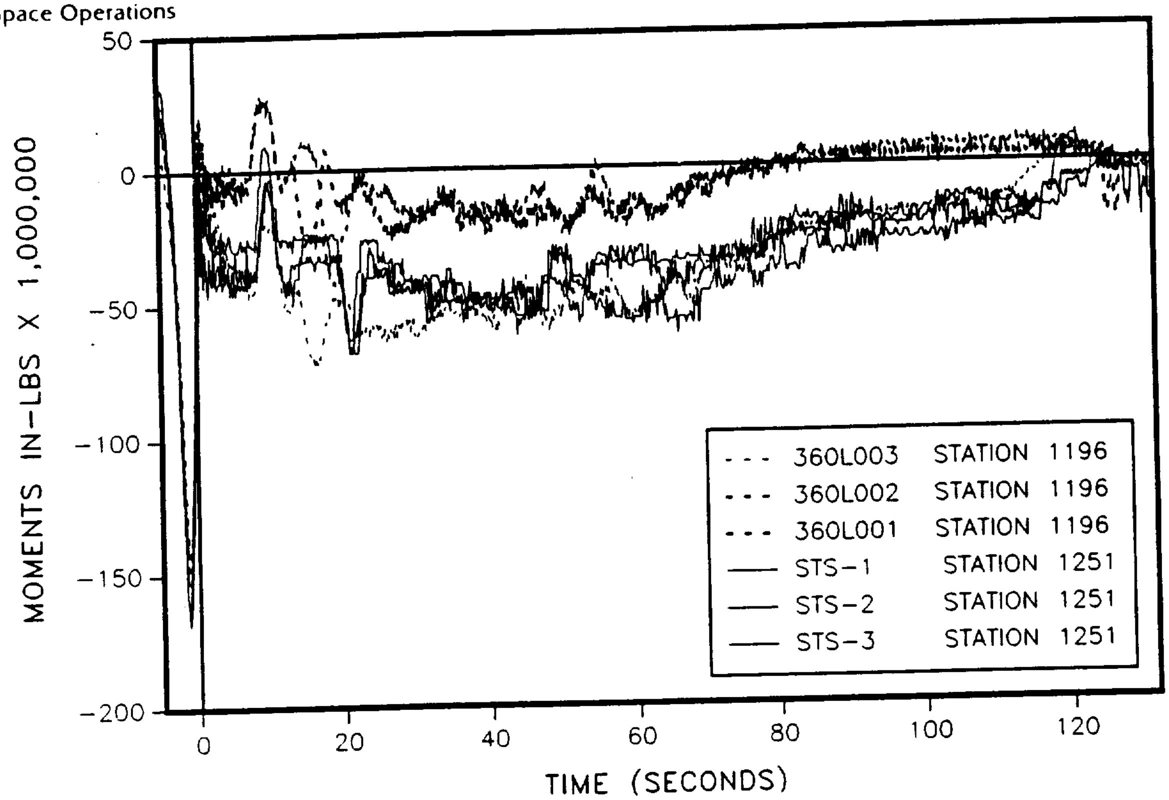

Figure 4.6-9. Y Axis Bending Moment--360L003 Versus 360L001, 360L002, and STS-1, 2, and 3 (LH motor, Stations 1196 and 1251)

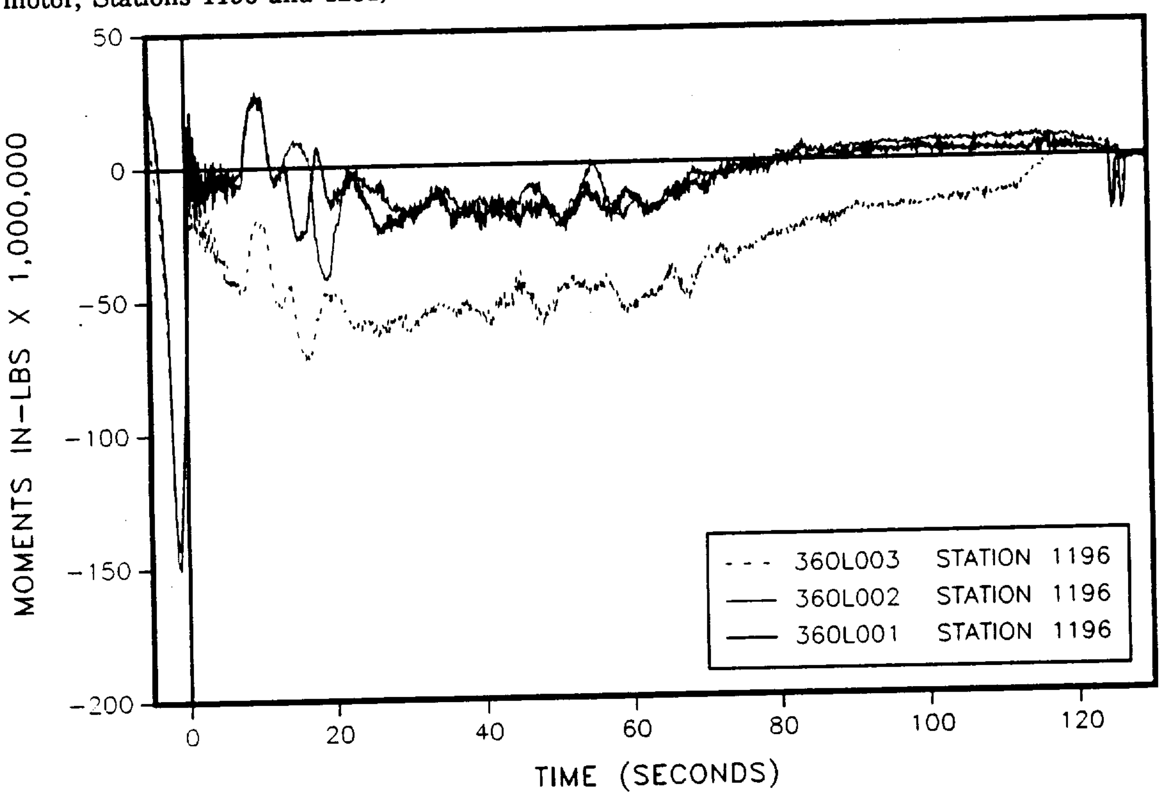

Figure 4.6-10. Y Axis Bending Moment--360L003 Versus 360L001, 360L002 (LH motor, Station 1196)

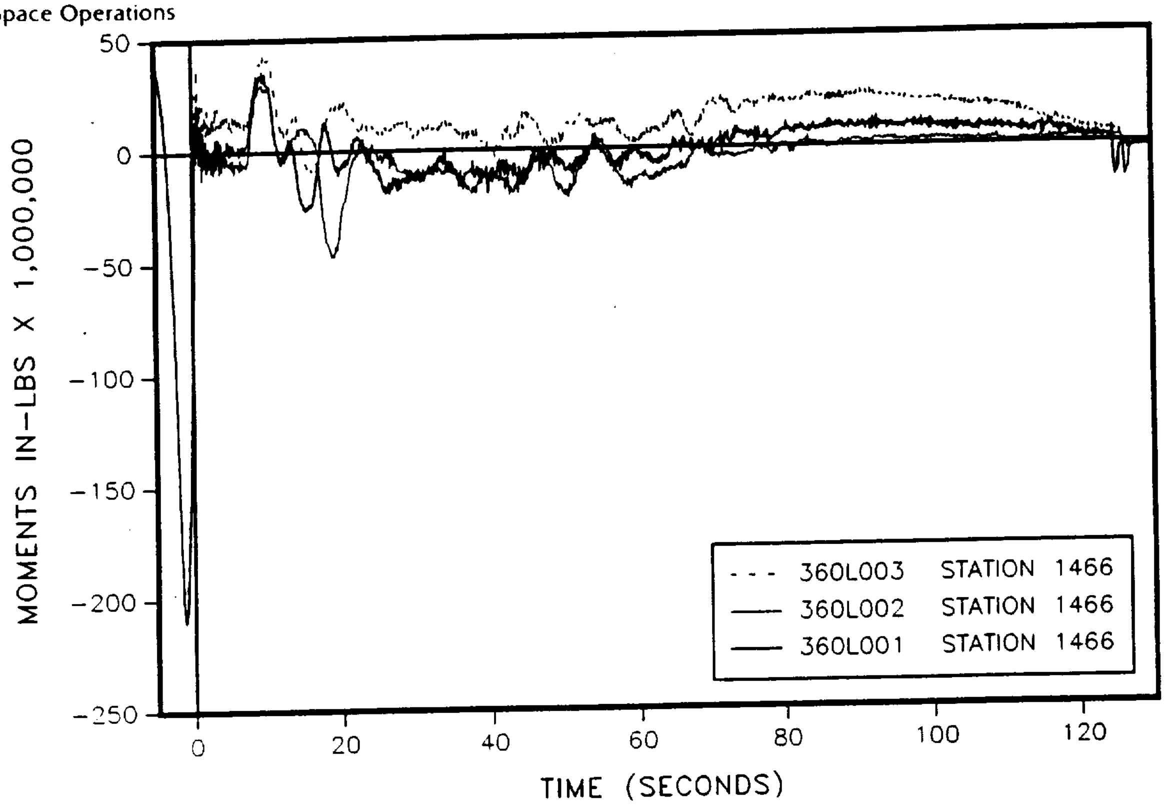

Figure 4.6-11. Y Axis Bending Moment--360L003 Versus 360L001, 360L002 (LH motor, Station 1466)

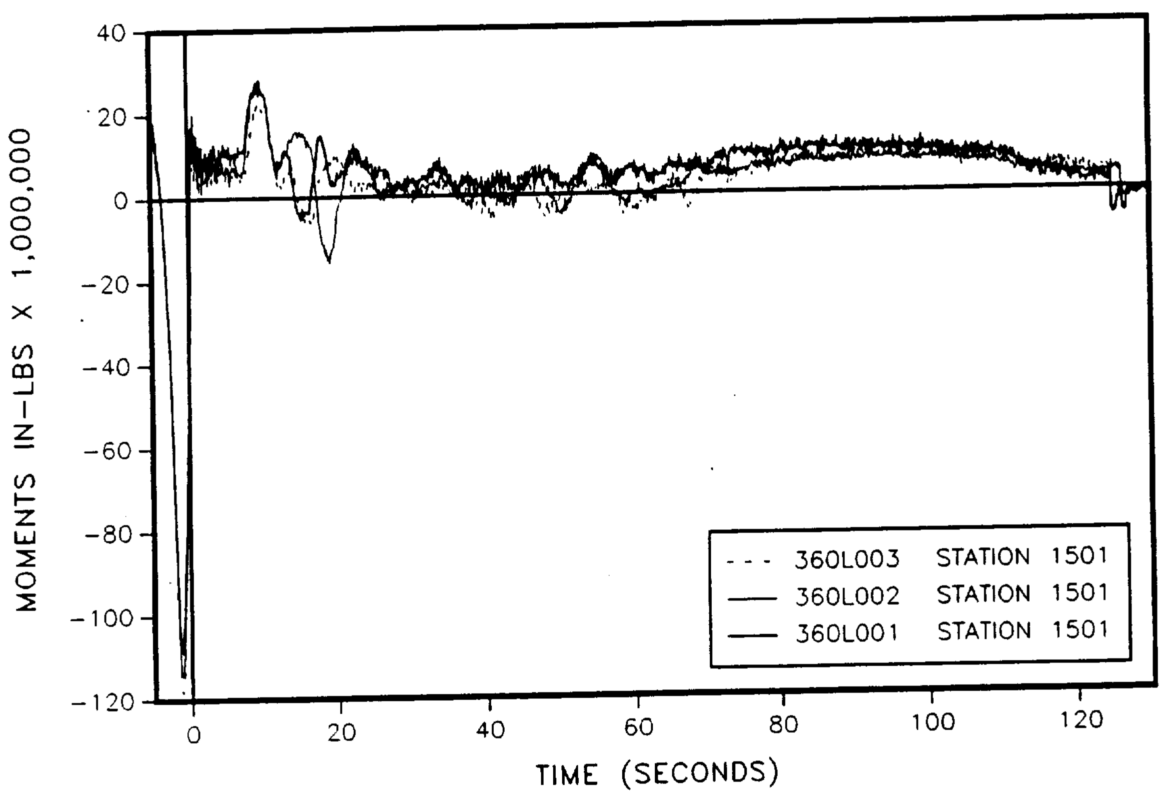

Figure 4.6-12. Y Axis Bending Moment--360L003 Versus 360L001, 360L002 (LH motor, Station 1501)

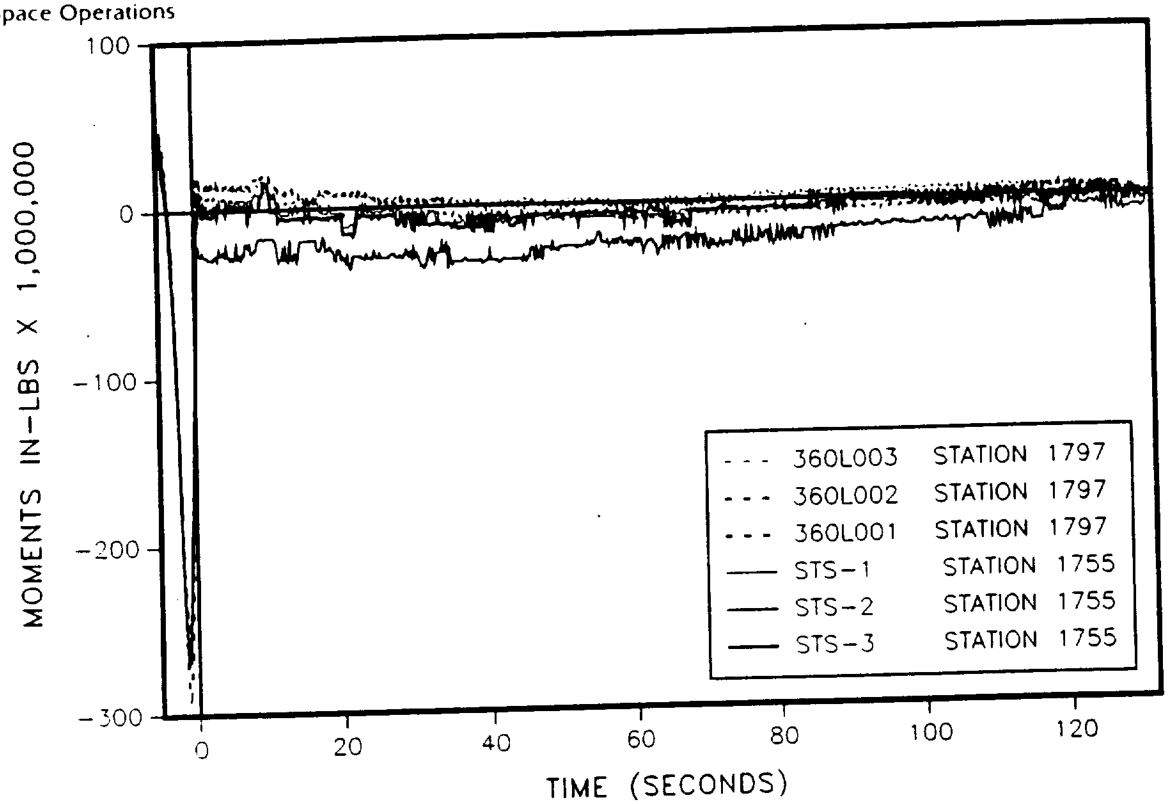

Figure 4.6-13. Y Axis Bending Moment--360L003 Versus 360L001, 360L002, and STS-1, 2, and 3 (LH motor, Stations 1797 and 1755)

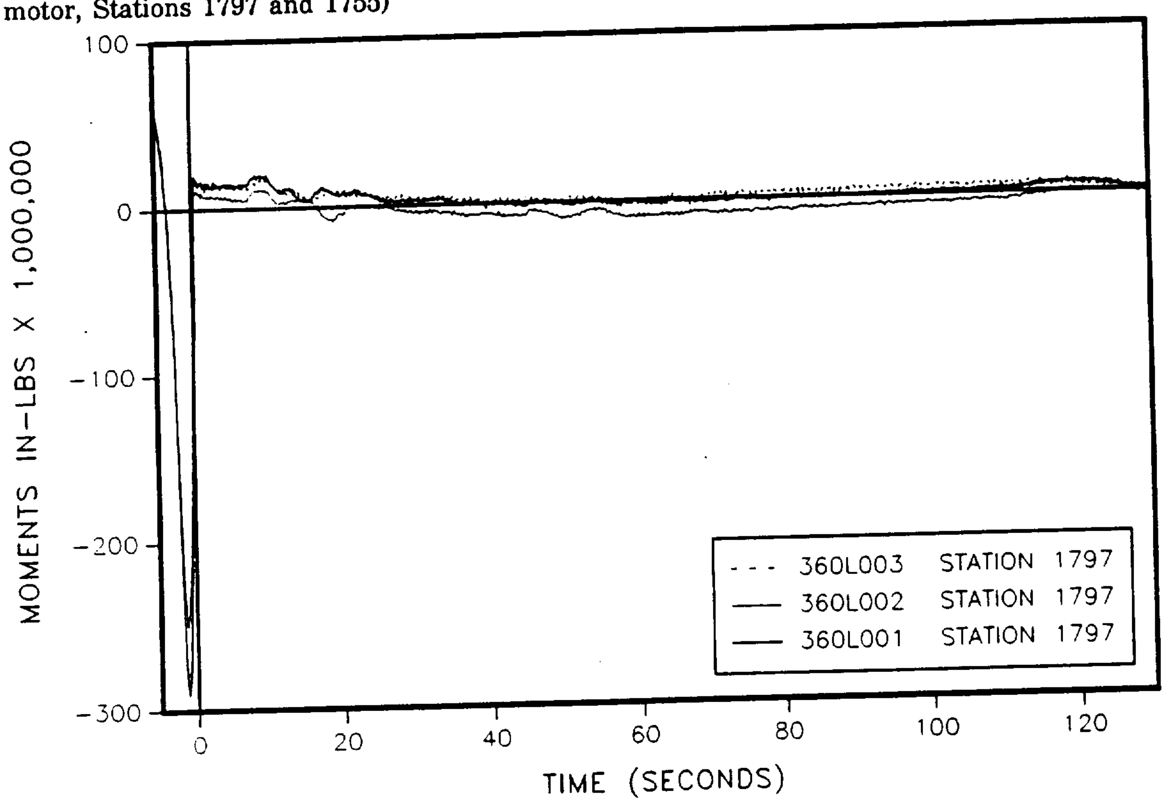

Figure 4.6-14. Y Axis Bending Moment--360L003 Versus 360L001, 360L002 (LH motor, Station 1797)

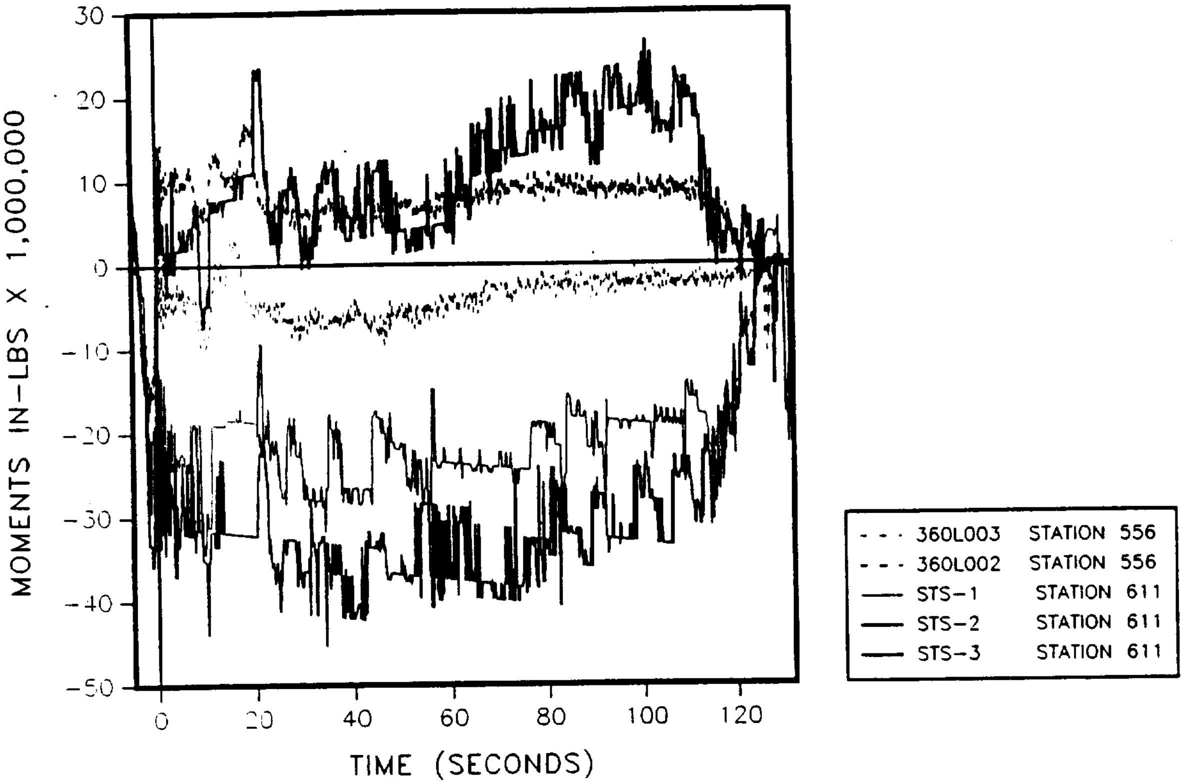

Figure 4.6-15. Y Axis Bending Moment--360L003 Versus 360L002 and STS-1, 2, and 3 (RH motor, Stations 556 and 611)

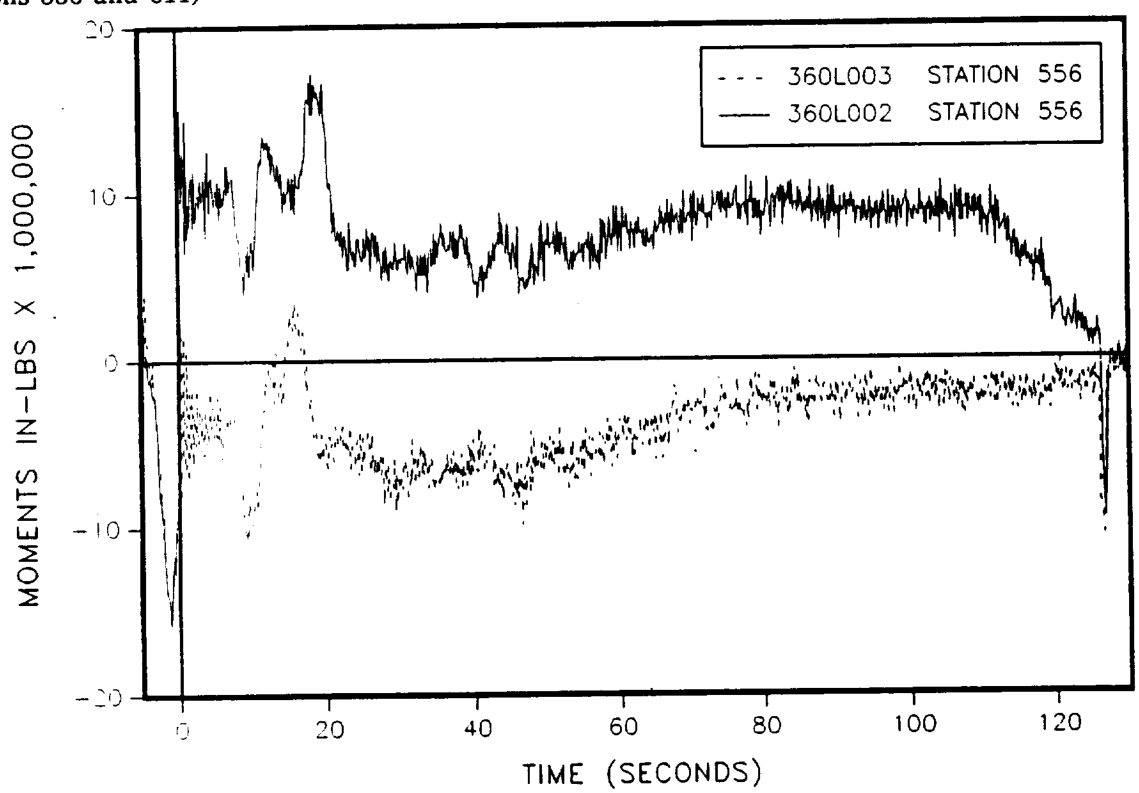

Figure 4.6-16. Y Axis Bending Moment--360L003 Versus 360L002 (RH motor, Station 556)

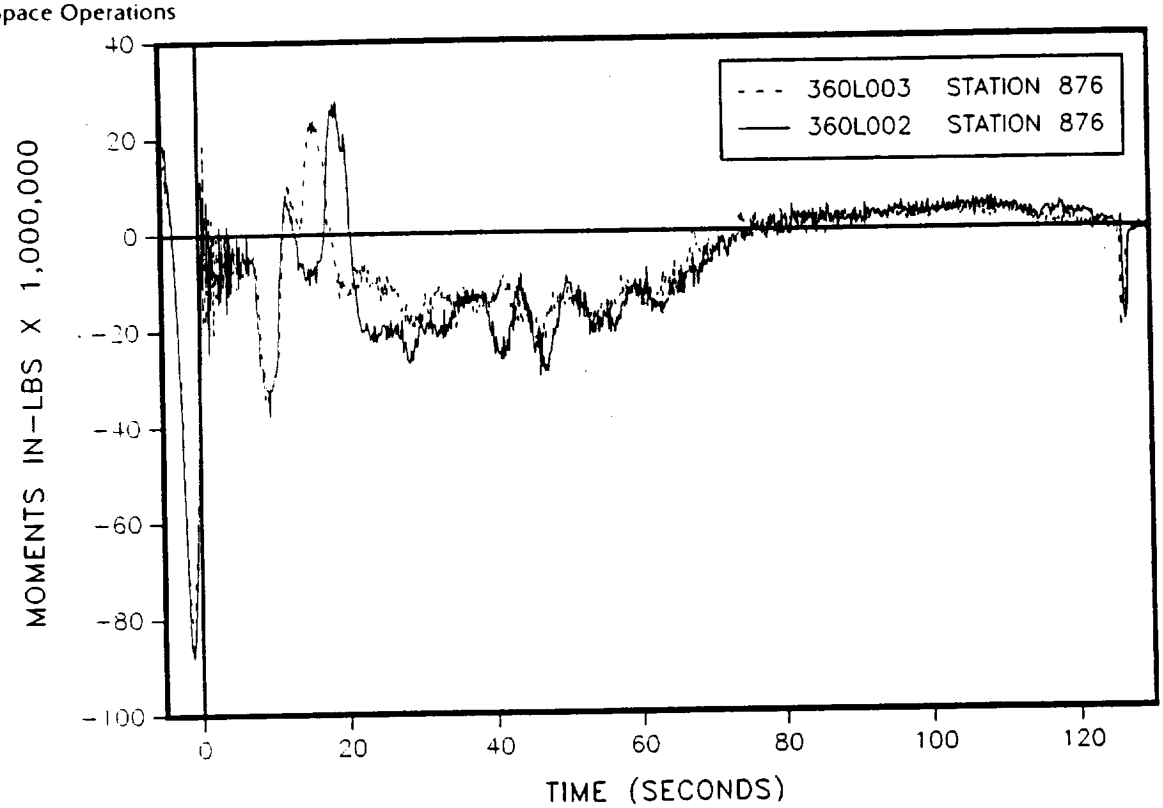

Figure 4.6-17. Y Axis Bending Moment--360L003 Versus 360L002 (RH motor, Station 876)

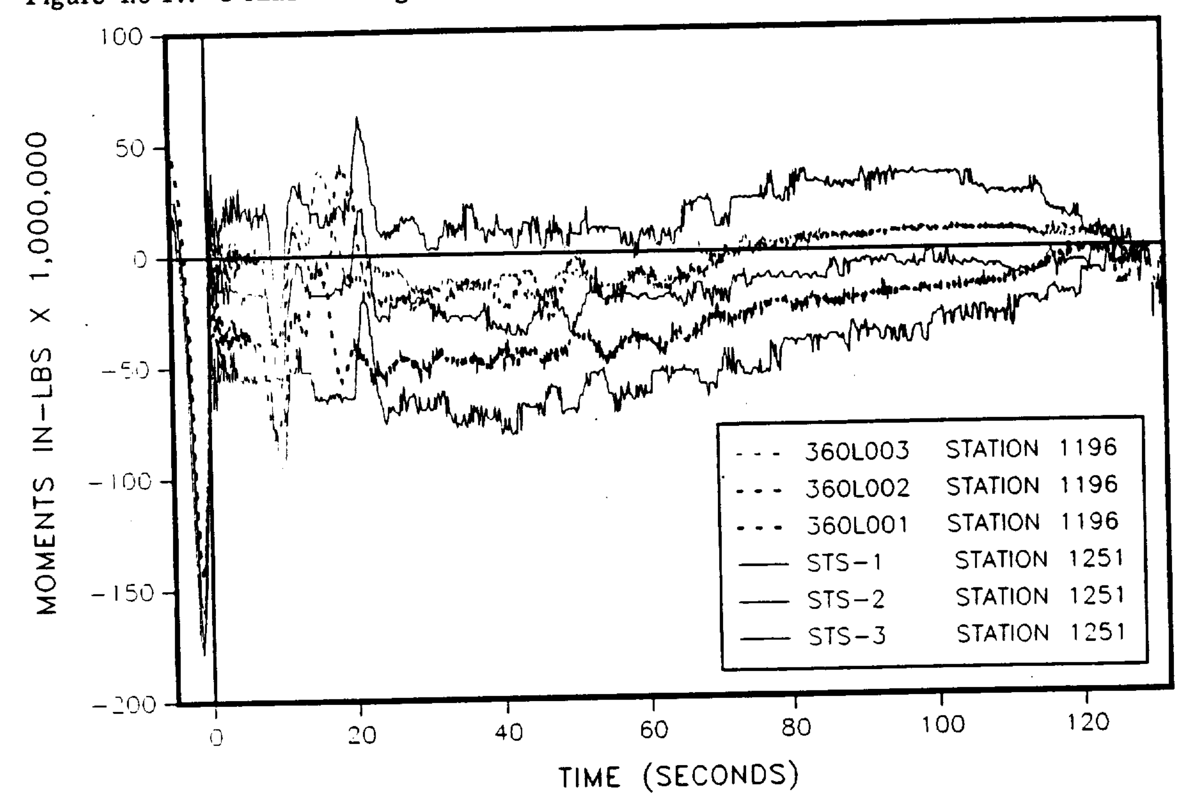

Figure 4.6-18. Y Axis Bending Moment--360L003 Versus 360L001, 360L002, and STS-1, 2, and 3 (RH motor, Stations 1196 and 1251)

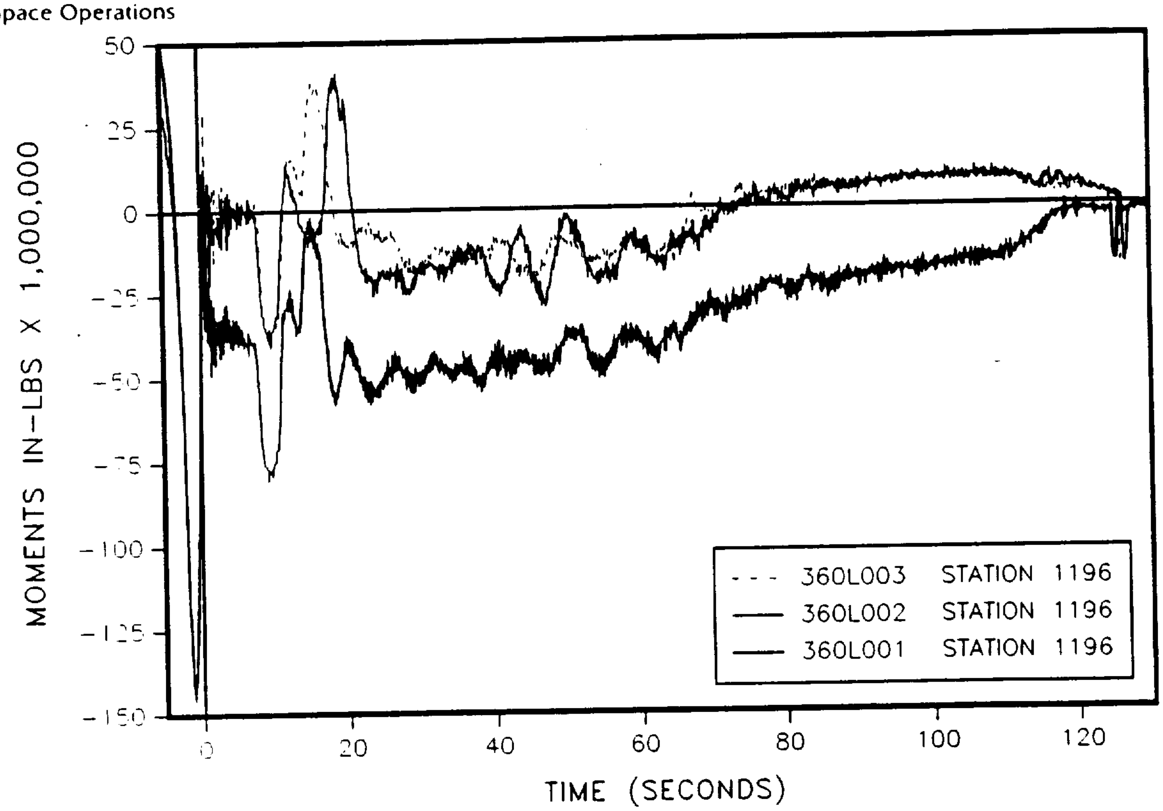

Figure 4.6-19. Y Axis Bending Moment--360L003 Versus 360L001, 360L002 (RH motor, Station 1196)

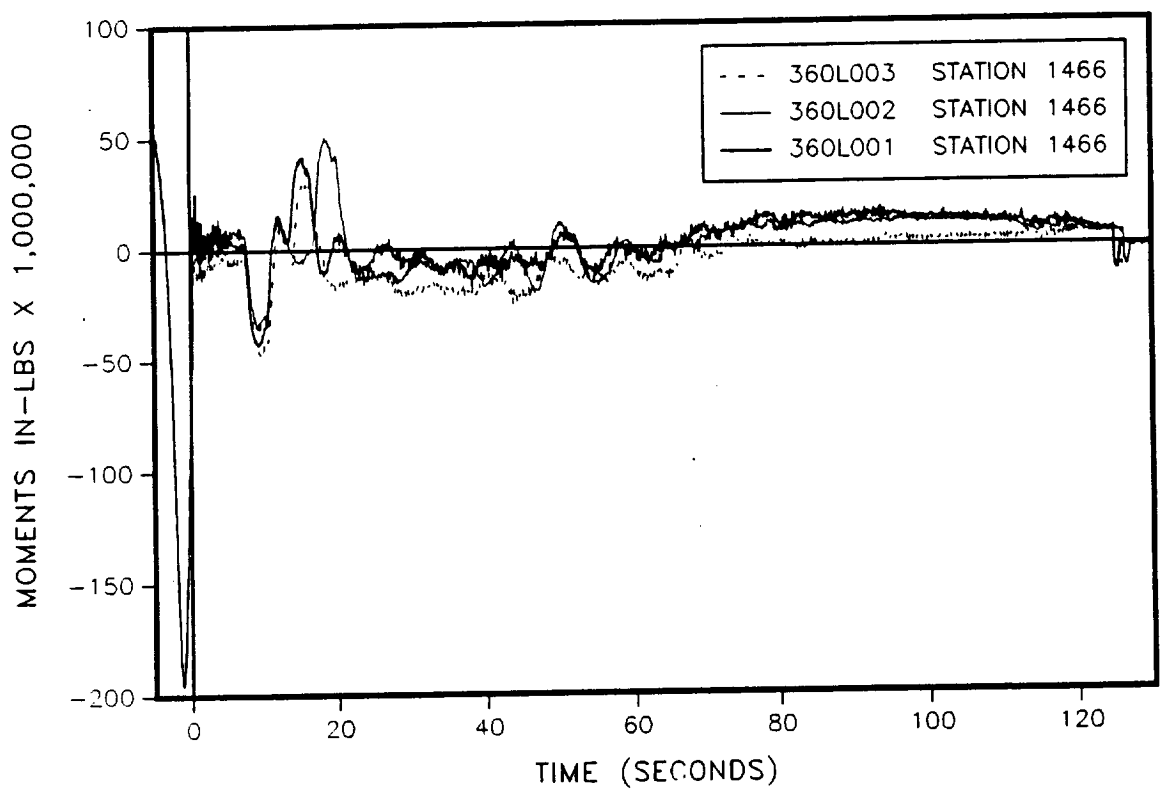

Figure 4.6-20. Y Axis Bending Moment--360L003 Versus 360L001, 360L002 (RH motor, Station 1466)

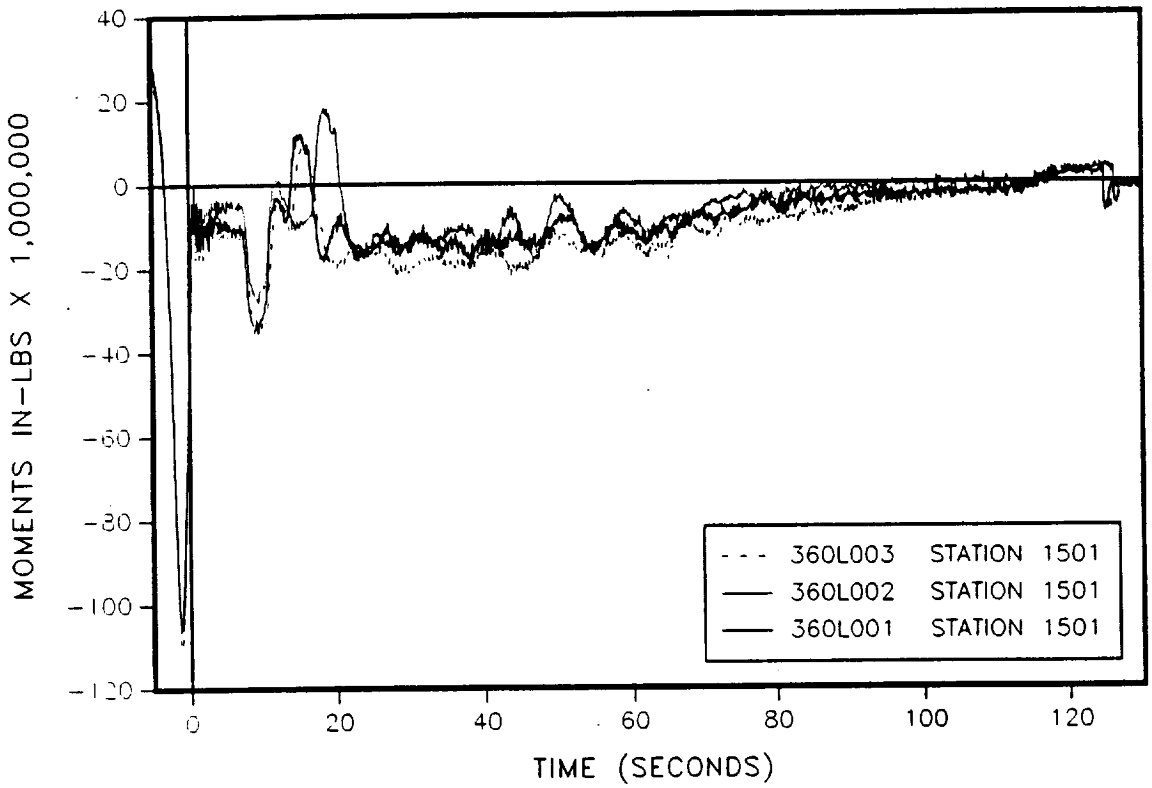

Figure 4.6-21. Y Axis Bending Moment--360L003 Versus 360L001, 360L002 (RH motor, Station 1501)

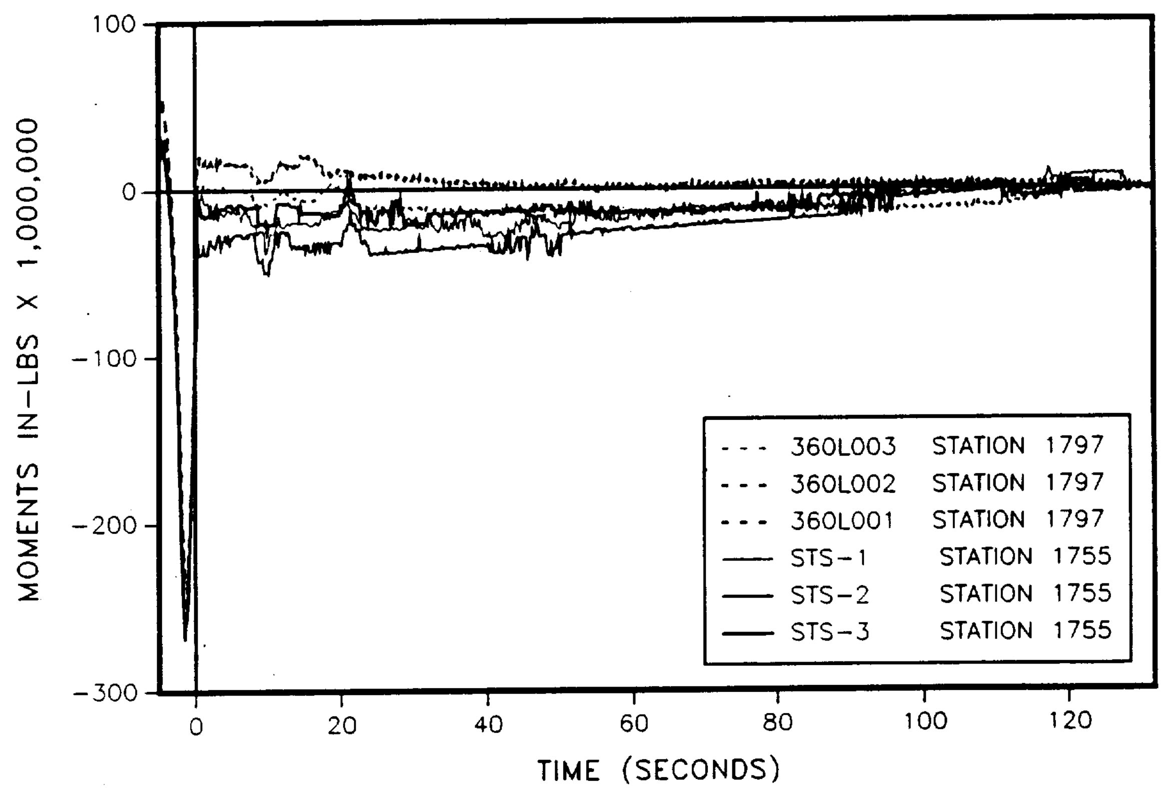

Figure 4.6-22. Y Axis Bending Moment--360L003 Versus 360L001, 360L002, and STS-1, 2, and 3 (RH motor, Stations 1797 and 1755)

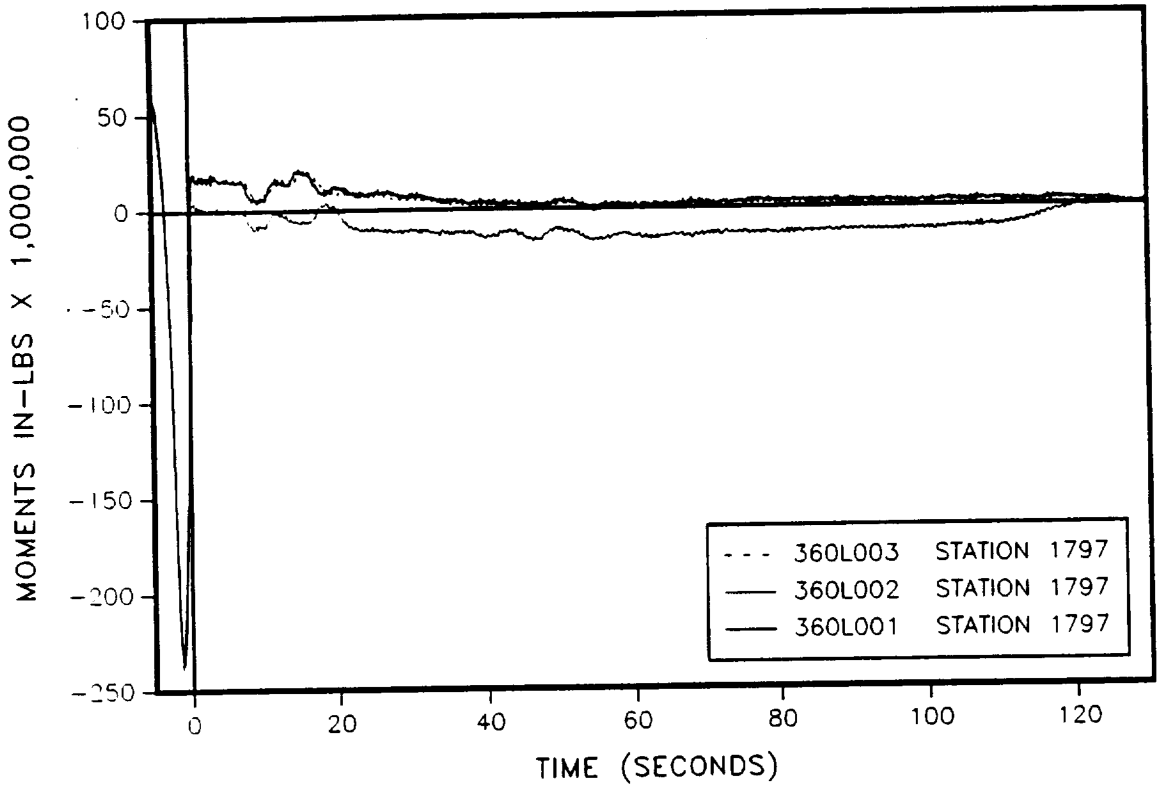

Figure 4.6-23. Y Axis Bending Moment--360L003 Versus 360L001, 360L002 (RH motor, Station 1797)

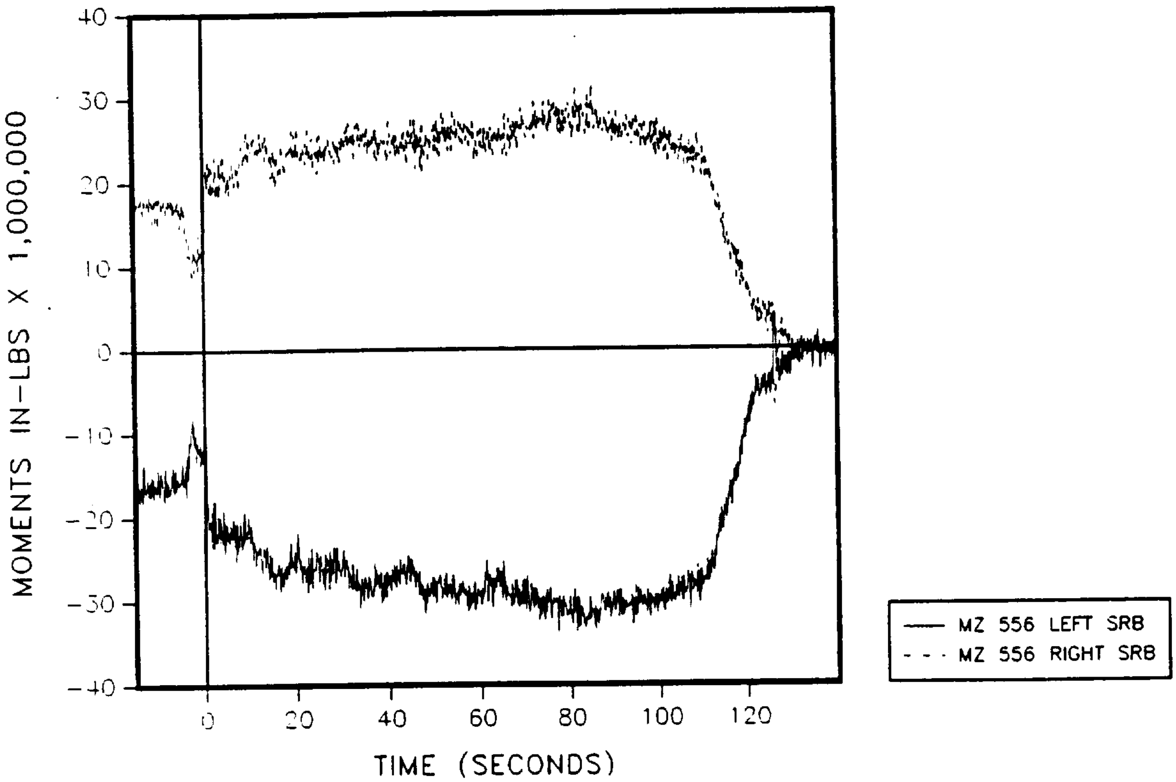

Figure 4.6-24. 360L003 Z Axis Bending Moment (Station 556)

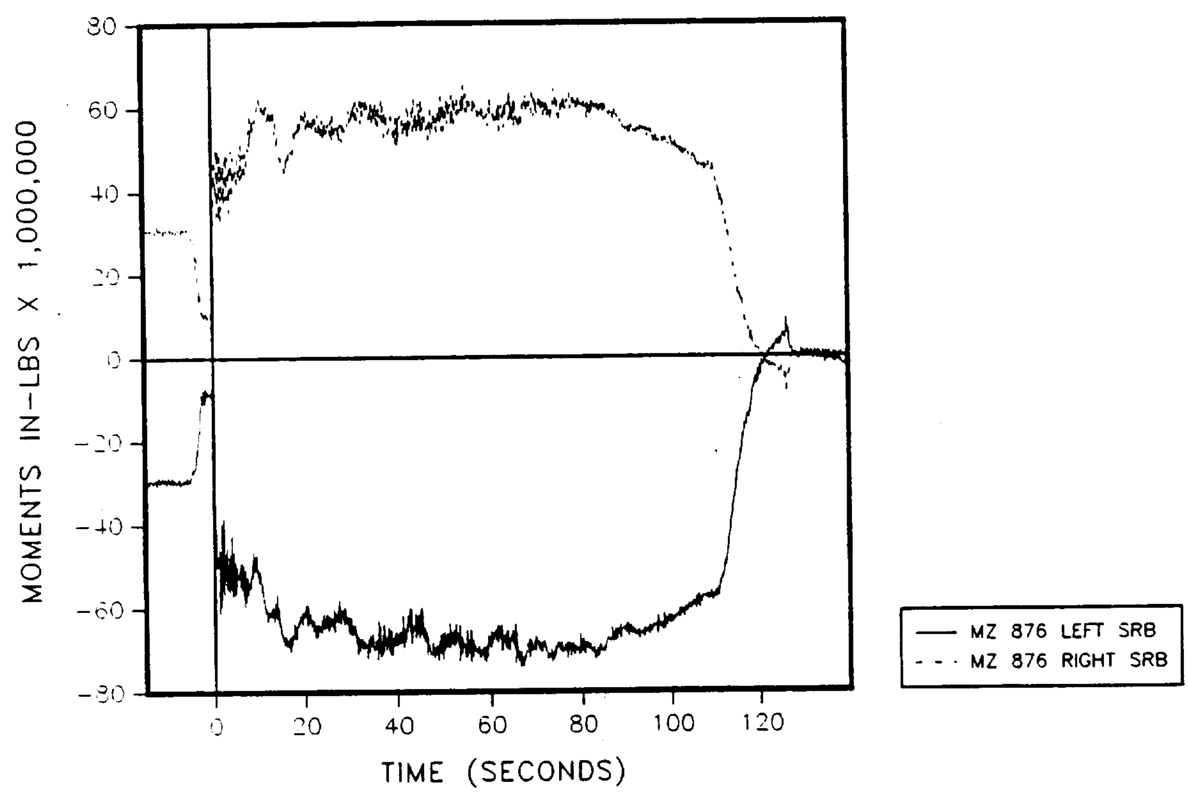

Figure 4.6-25. 360L003 Z Axis Bending Moment (Station 876)

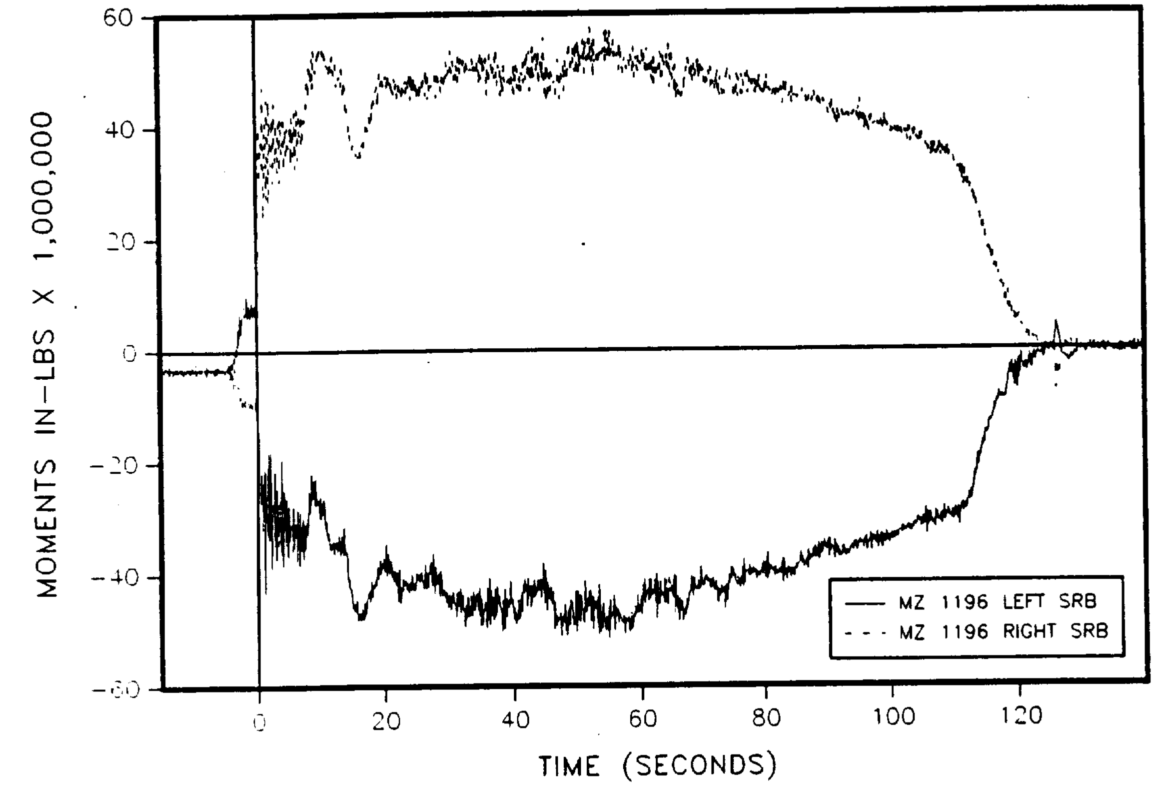

Figure 4.6-26. 360L003 Z Axis Bending Moment (Station 1196)

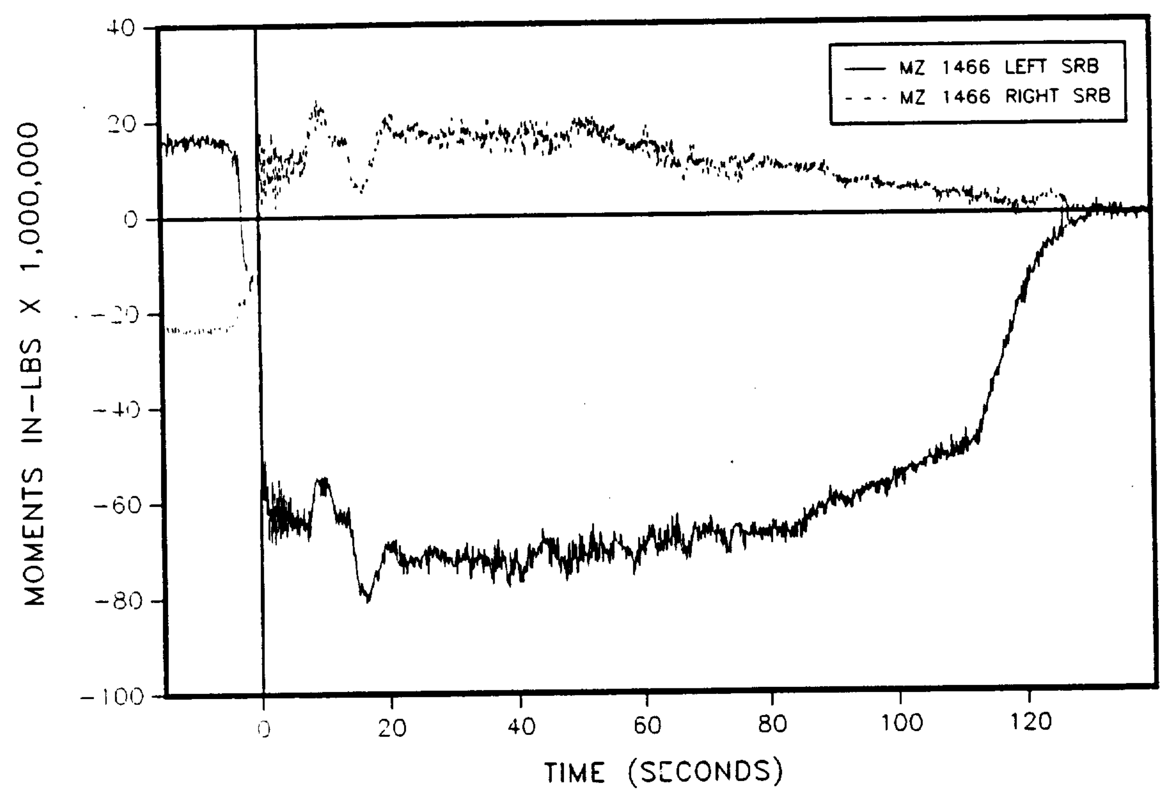

Figure 4.6-27. 360L003 Z Axis Bending Moment (Station 1466)

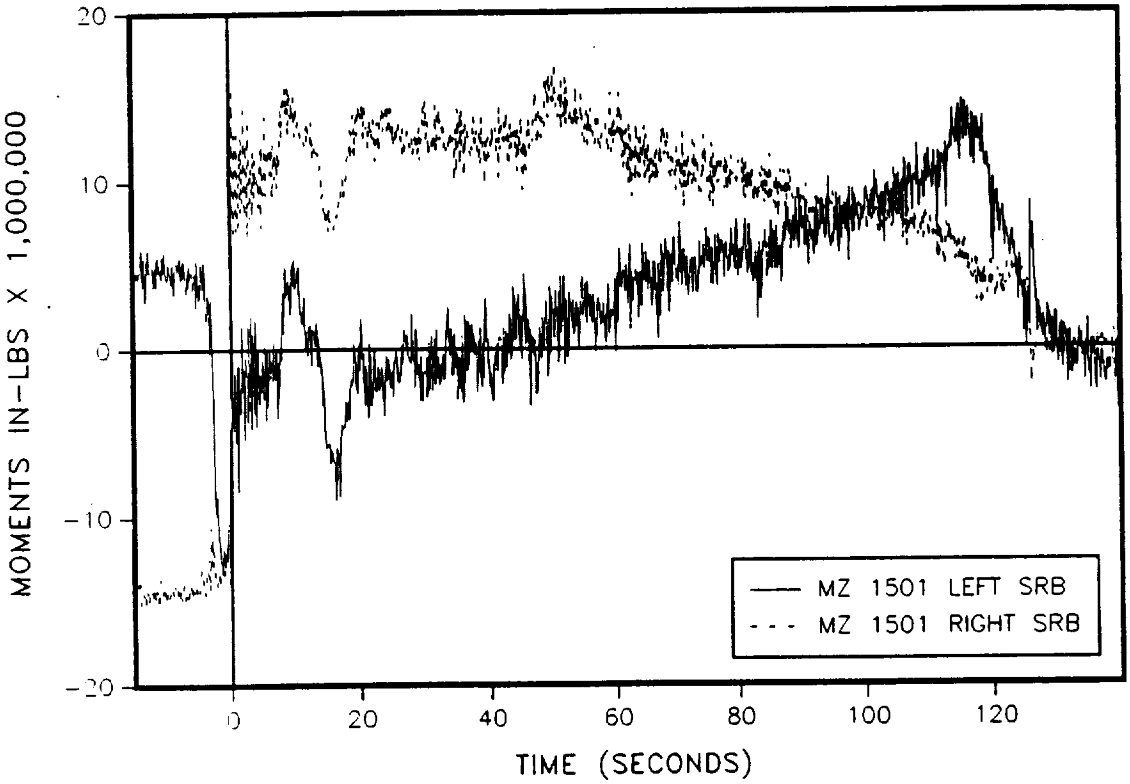

Figure 4.6-28. 360L003 Z Axis Bending Moment (Station 1501)

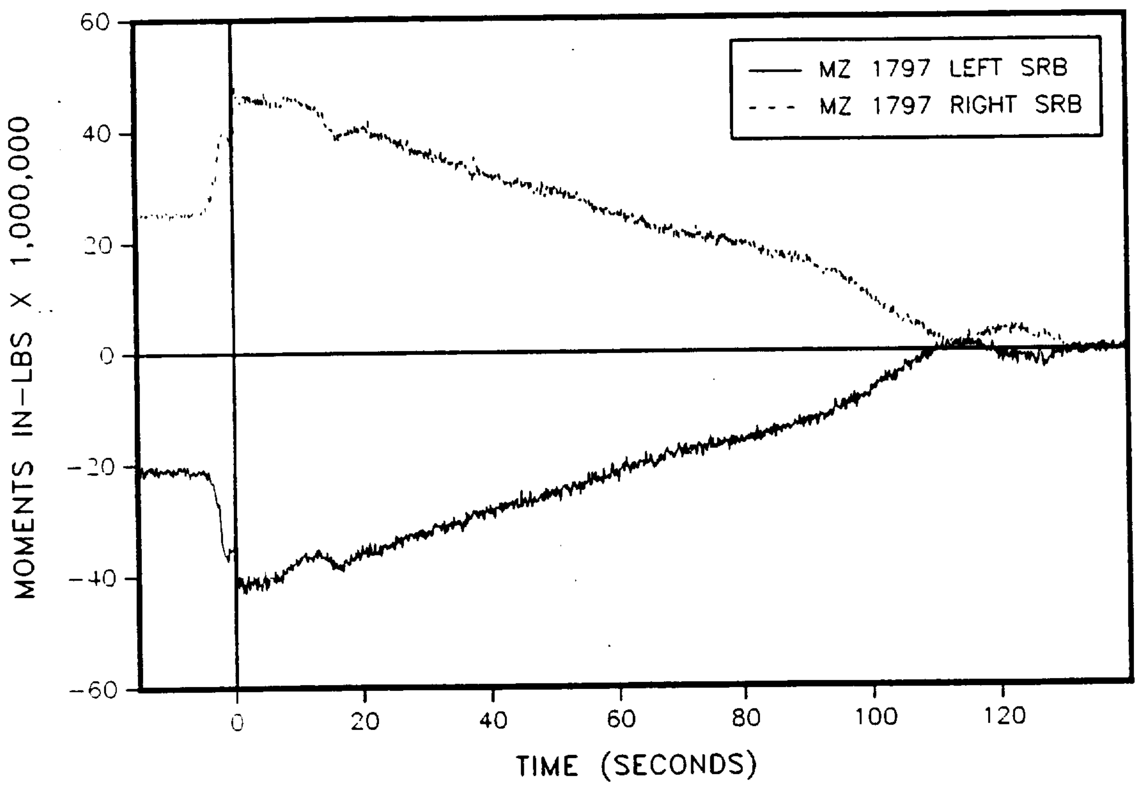

Figure 4.6-29. 360L003 Z Axis Bending Moment (Station 1797)

Initially, the tops of the motors are seen to be bending in toward the ET due to the weight of the ET and orbiter. Moving down the motor, the bending increases slightly for both motors at Station 876, then both values reduce to approximately the same value at Station 1196, changing sign at Station 1466 as expected. At Station 1797, it changes back to the same sign as at the top of the motor, as expected. Upon lift-off, the tops of the SRBs are moving toward the ET, and the bottoms of the SRBs are moving away from the ET. During the roll maneuver, Stations 1196 and 1466 show the same peaks as bending about the Y axis, with the exception that both the LH and RH motors move in the same direction. This is due to the sign convention. During the first phase of the roll, the LH motor is pushing away from the ET, and the RH motor is pushing toward the ET.

The opposite is true of the second part of the roll maneuver. Station 1797 is different from the other stations because after lift-off it follows a fairly linear path back to zero during the flight.

Figures 4.6-30 through 4.6-46 are plots of the first three flights and the first three RSRM flights as a function of time. As shown in the figures, the overall correlation is very good. Station 556 of 360L003 shows a much lower magnitude than 360L001 and 360L002 on both the LH and RH motors. Station 1466 of 360L003 shows a higher magnitude than the other flights. Comparisons at the other stations show a close correlation.

Axial Force, X Axis (VX). Figures 4.6-47 through 4.6-52 show the axial force for both the LH and RH motors for Stations 556, 876, 1196, 1466, 1501, 1797, respectively. In these figures, a positive value represents a compressive force and a negative value represents a tensile force. Initially the SRBs are subjected to the weight of the ET, orbiter, and segments above the particular station. Since these are the only forces acting axially, the result should increase linearly proceeding down the case. Station 1501 shows a slight decrease in measured strain due to the increased case thickness in this region. Upon SRB ignition, the cases immediately go into tension as the motors pressurize and lift off. The maximum value was 13,408 kip and occurred at Station 556.5 of the RH motor. After this point, the shape of the plot looks like the motor pressure plots. There is good agreement between the LH and RH motors. Some of the difference can be attributed to the fact that the gages were zeroed at the end of the flight, and the actual strain values experienced by the LH and RH motors, and each station, were probably not exactly zero.

Figures 4.6-53 through 4.6-69 are plots of the first three flight (STS-1, STS-2, and STS-3) and the first three RSRM flights (360L001, 360L002, and 360L003). As shown in the figures, the shapes of the curves are very similar. The higher magnitudes of 360L001, 360L002, and 360L003 can be explained by the fact that the redesigned boosters are HPMs and obtain a higher operating pressure than the older motors. The comparison between 360L001, 360L002, and 360L003 is very good.

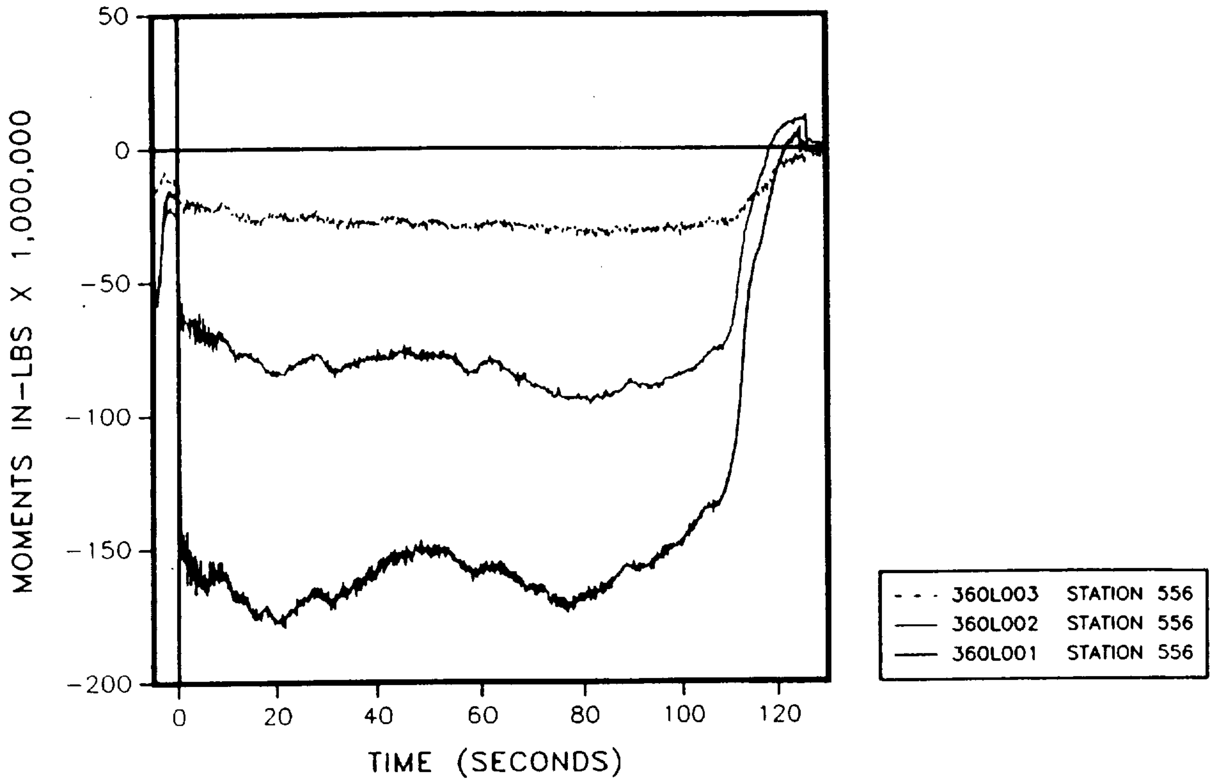

Figure 4.6-30. Z Axis Bending Moment--360L003 Versus 360L001, 360L002 (LH motor, Station 556)

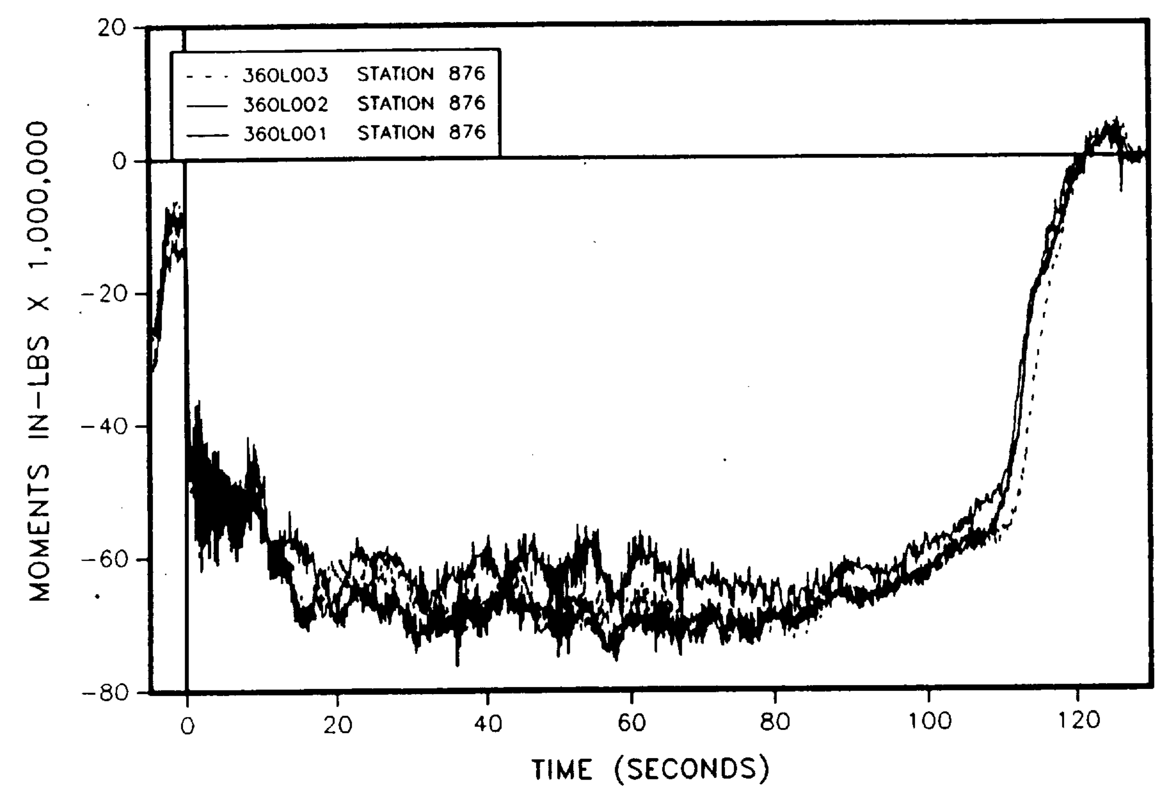

Figure 4.6-31. Z Axis Bending Moment--360L003 Versus 360L001, 360L002 (LH motor, Station 876)

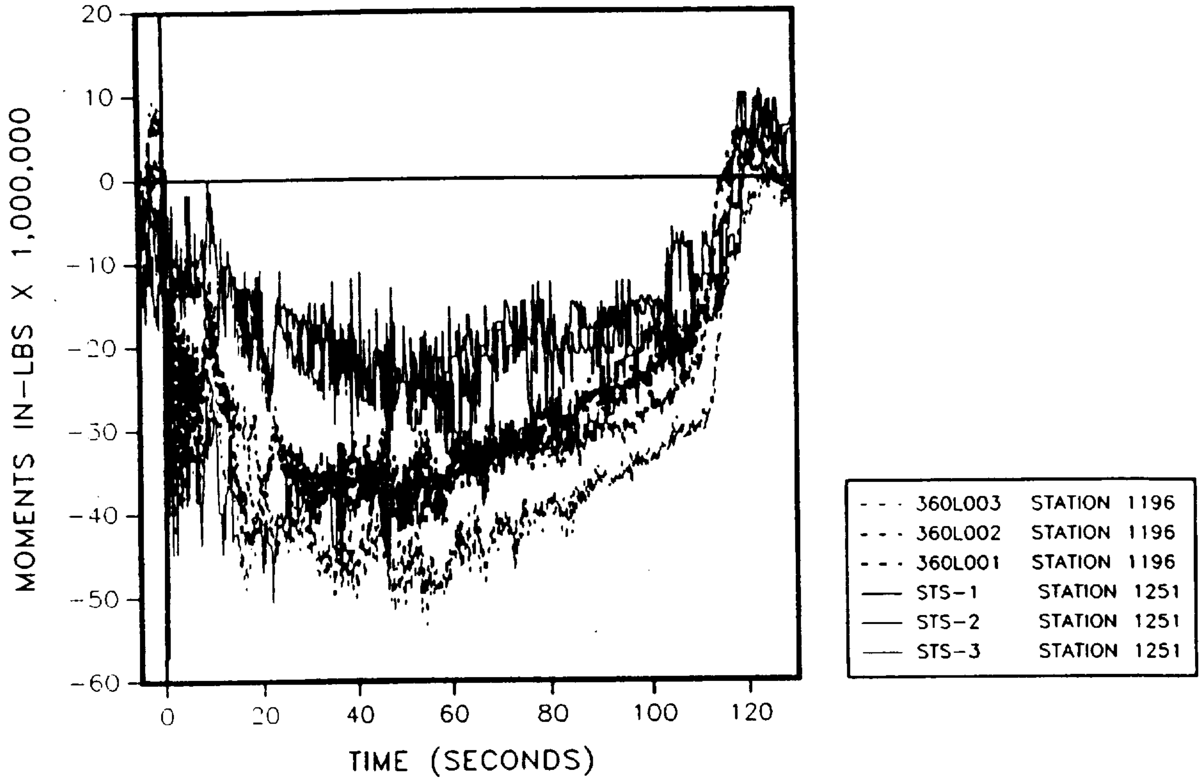

Figure 4.6-32. Z Axis Bending Moment--360L003 Versus 360L001, 360L002, and STS-1, 2, and 3 (LH motor, Stations 1196 and 1251)

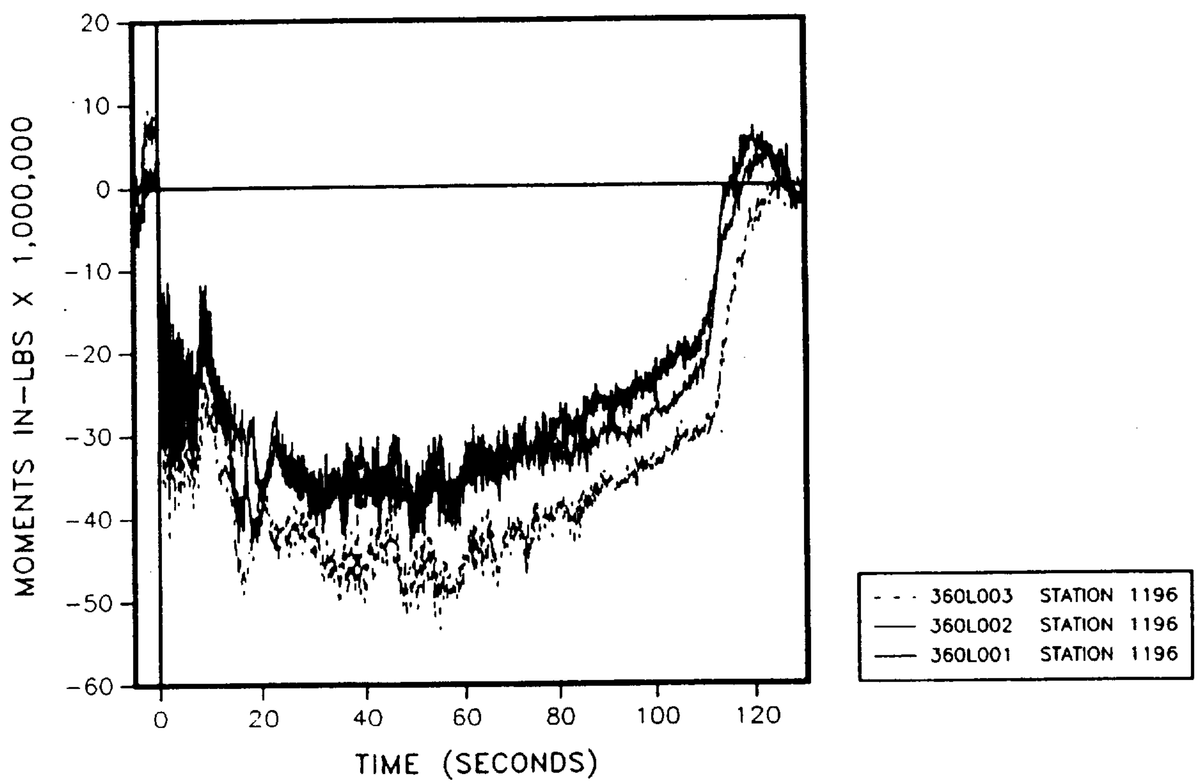

Figure 4.6-33. Z Axis Bending Moment--360L003 Versus 360L001, 360L002 (LH motor, Station 1196)

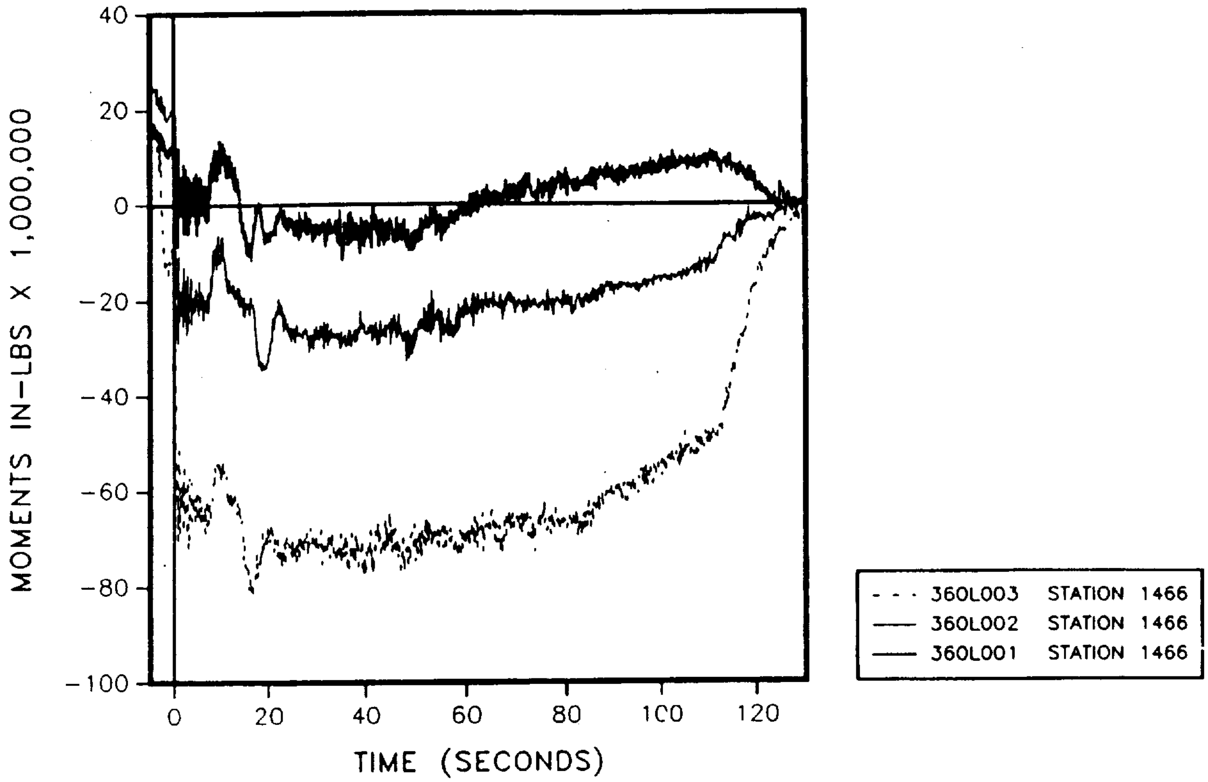

Figure 4.6-34. Z Axis Bending Moment--360L003 Versus 360L001, 360L002 (LH motor, Station 1466)

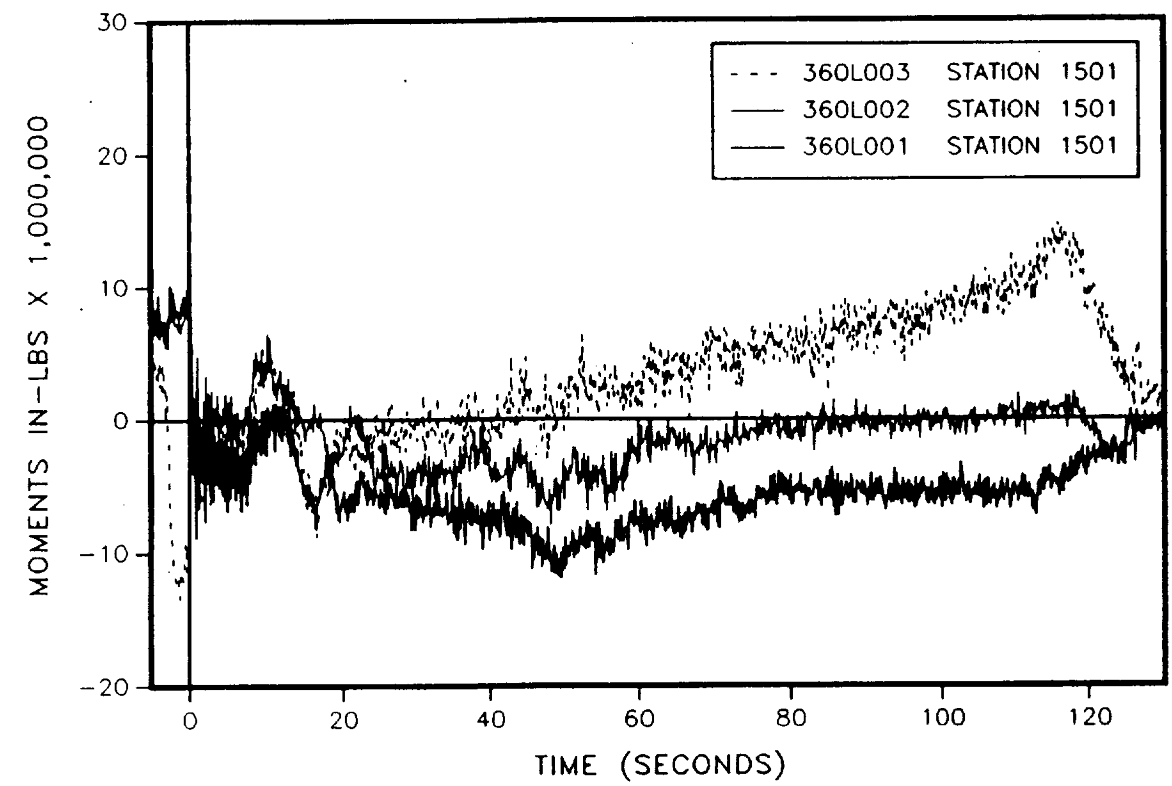

Figure 4.6-35. Z Axis Bending Moment--360L003 Versus 360L001, 360L002 (LH motor, Station 1501)

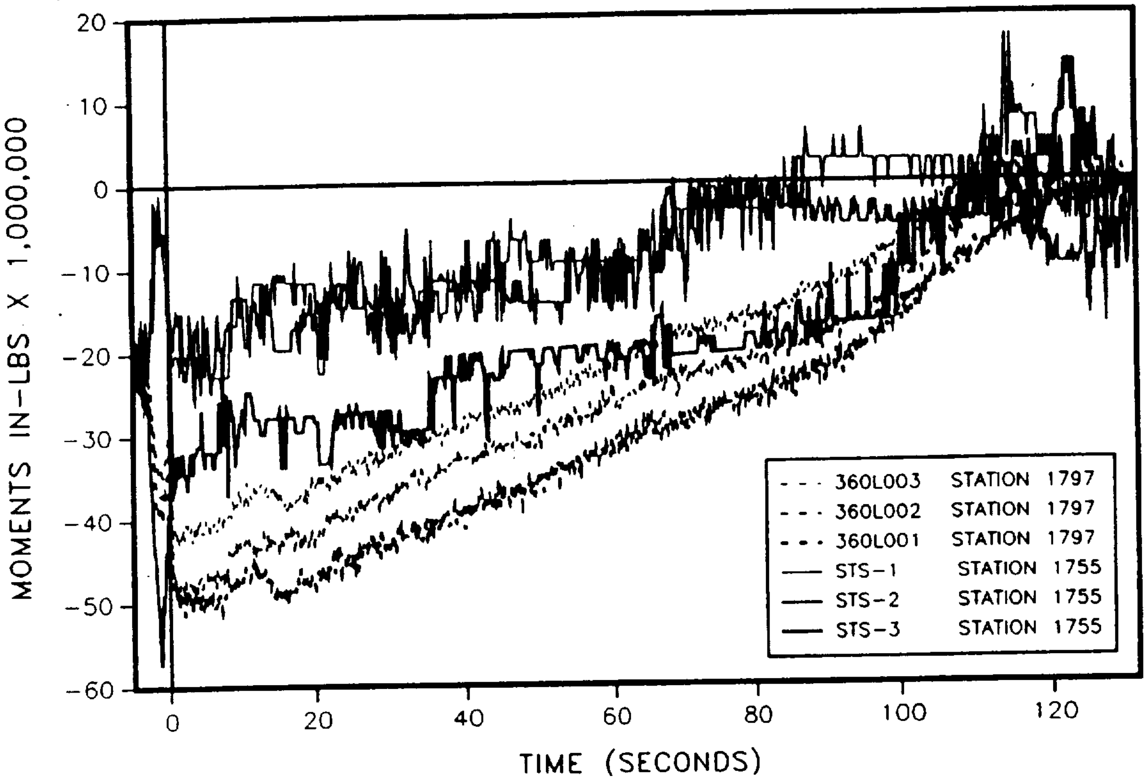

Figure 4.6-36. Z Axis Bending Moment--360L003 Versus 360L001, 360L002, and STS-1, 2, and 3 (LH motor, Stations 1797 and 1755)

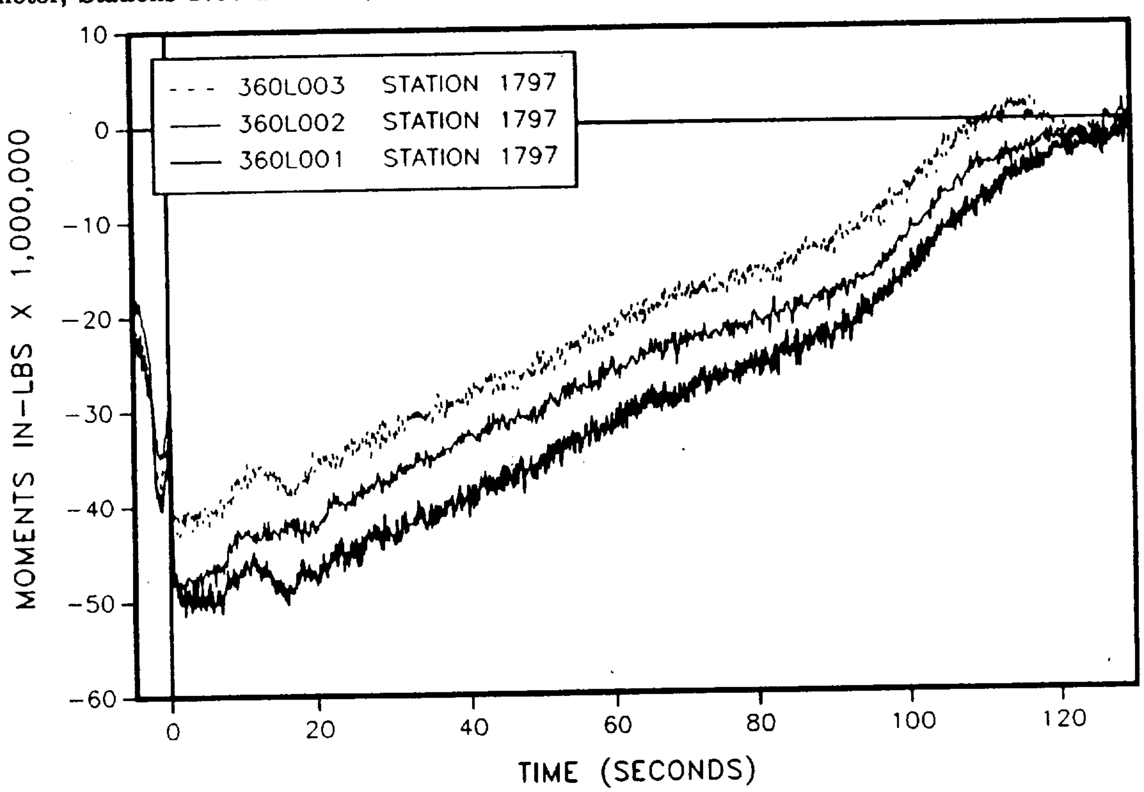

Figure 4.6-37. Z Axis Bending Moment--360L003 Versus 360L001, 360L002 (LH motor, Station 1797)

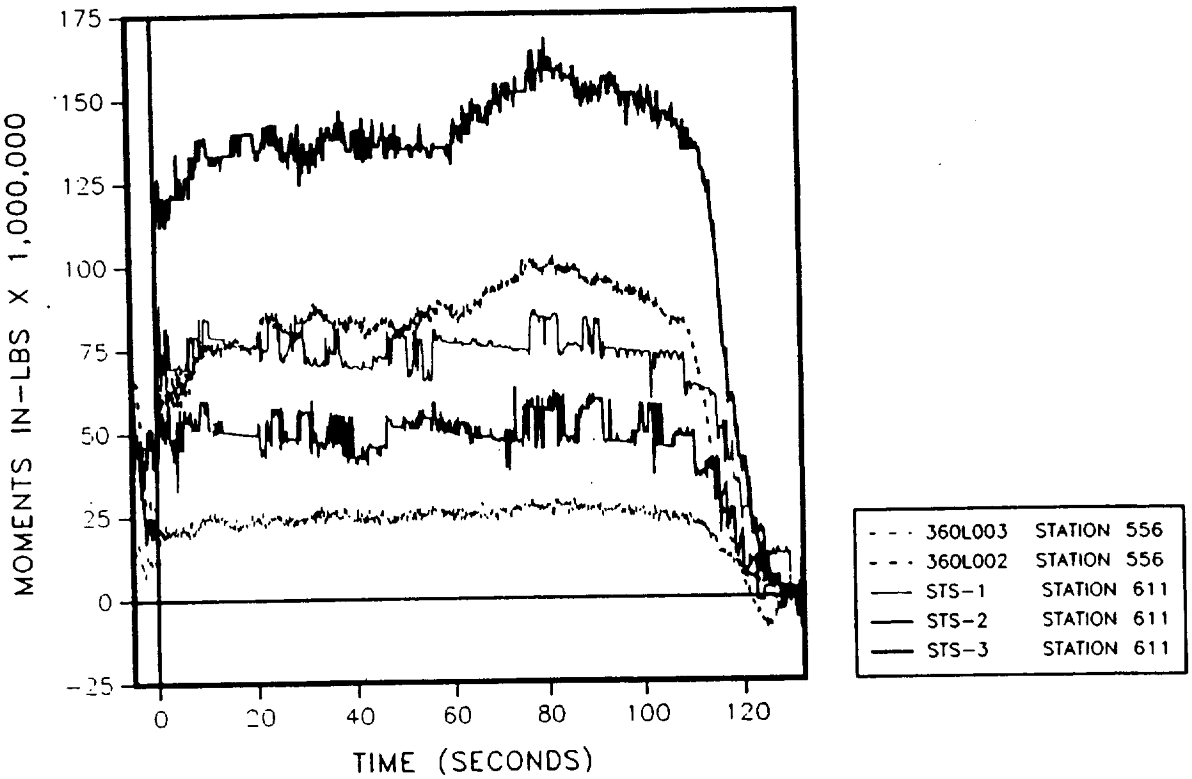

Figure 4.6-38. Z Axis Bending Moment--360L003 Versus 360L001, 360L002, and STS-1, 2, and 3 (RH motor, Stations 556 and 611)

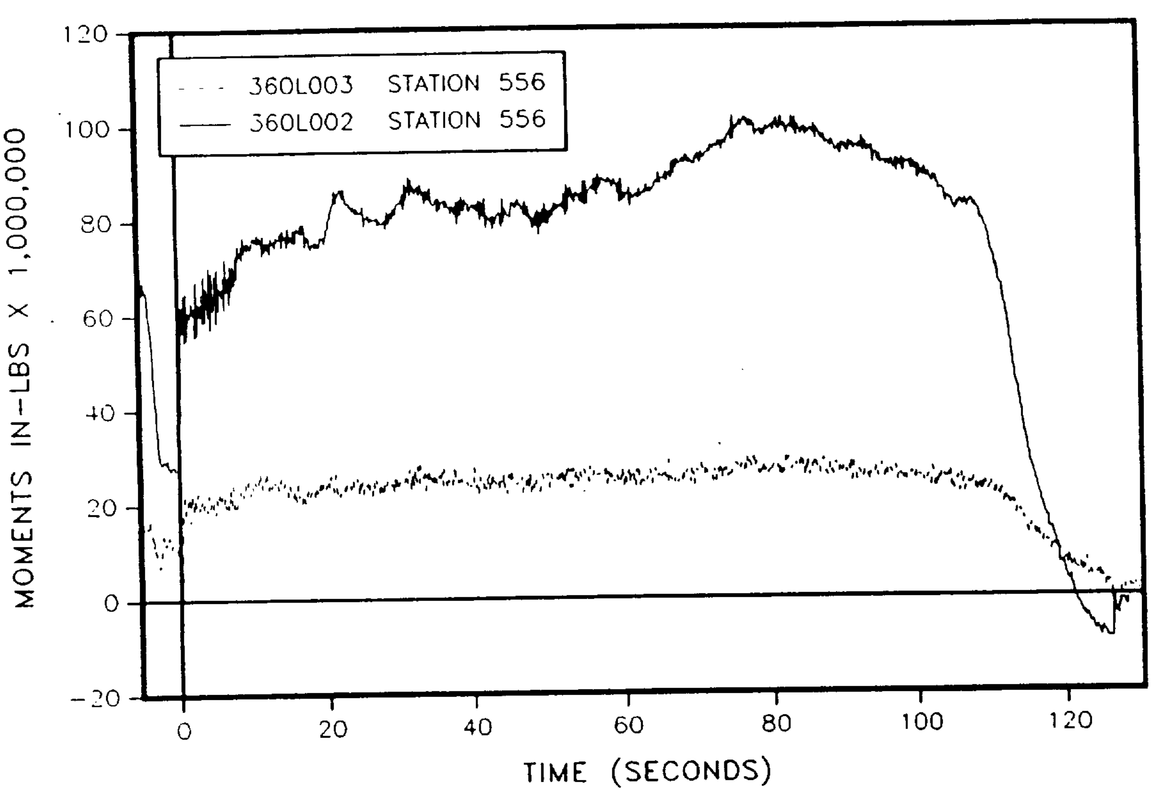

Figure 4.6-39. Z Axis Bending Moment--360L003 Versus 360L002 (RH motor, Station 556)

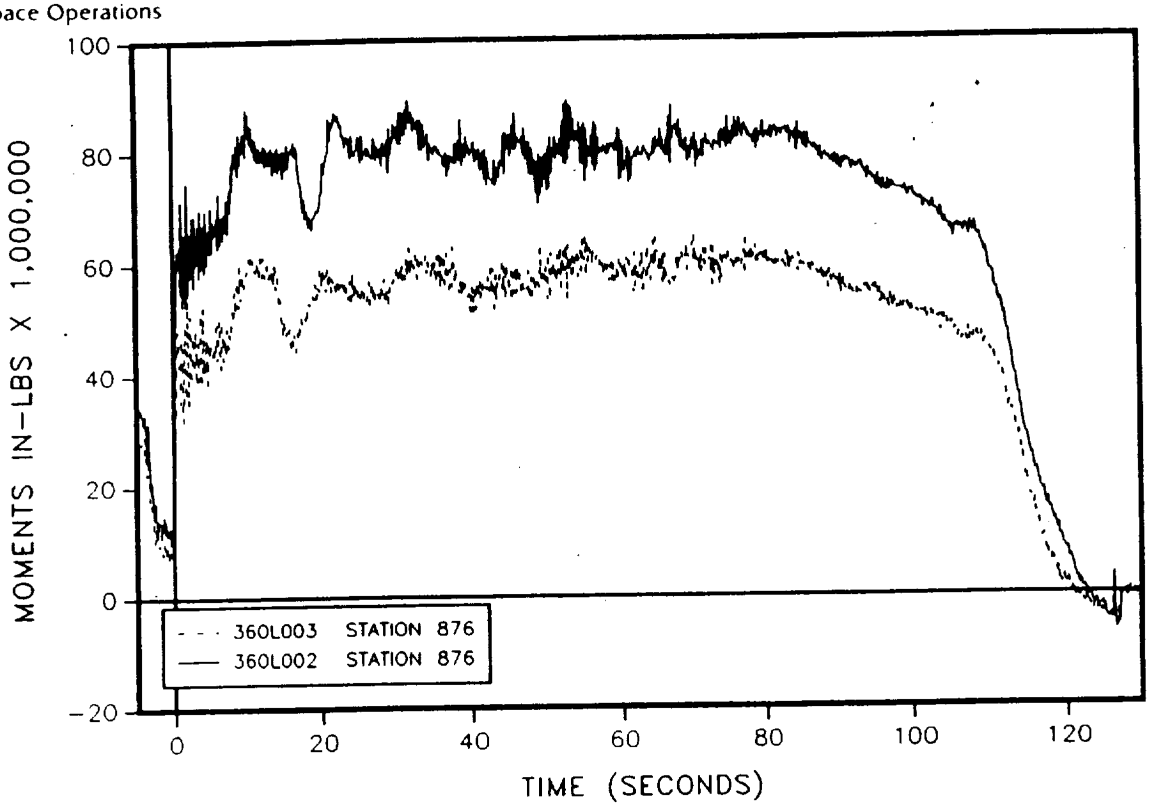

Figure 4.6-40. Z Axis Bending Moment--360L003 Versus 360L002 (RH motor, Station 876)

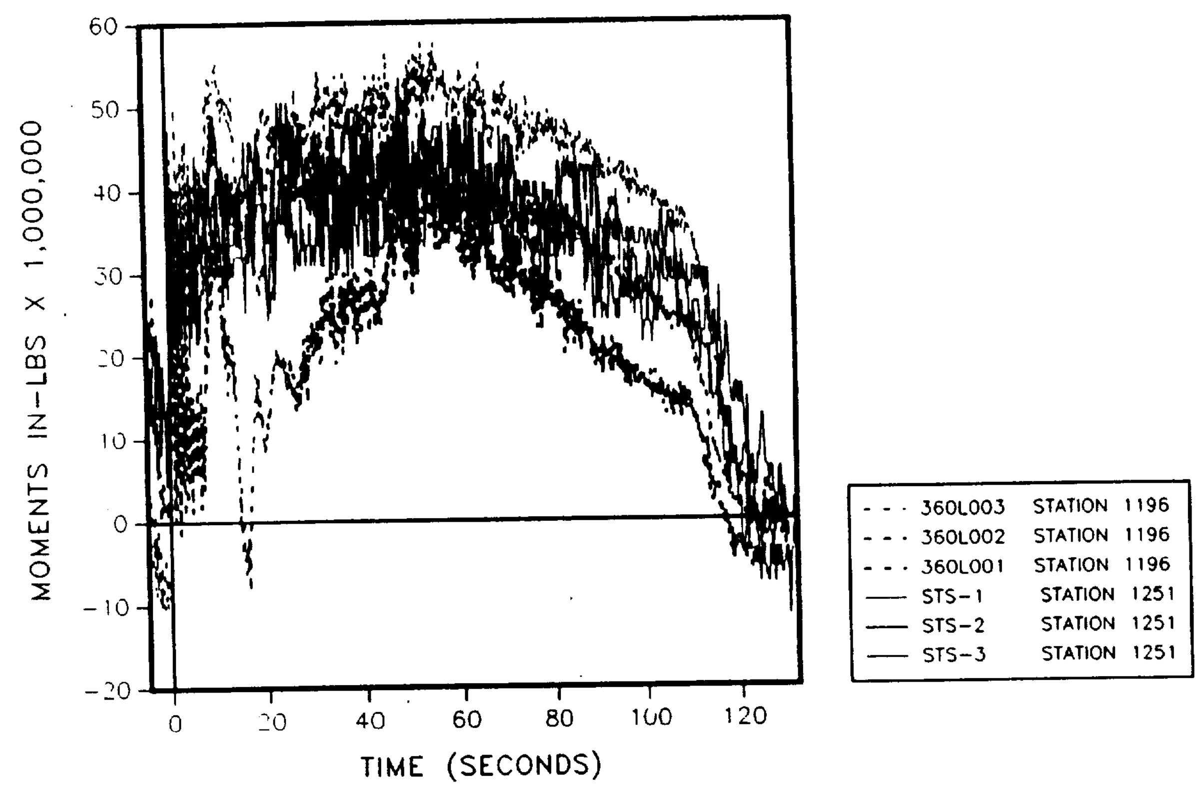

Figure 4.6-41. Z Axis Bending Moment--360L003 Versus 360L001, 360L002, and STS-1, 2, and 3 (RH motor, Stations 1196 and 1251)

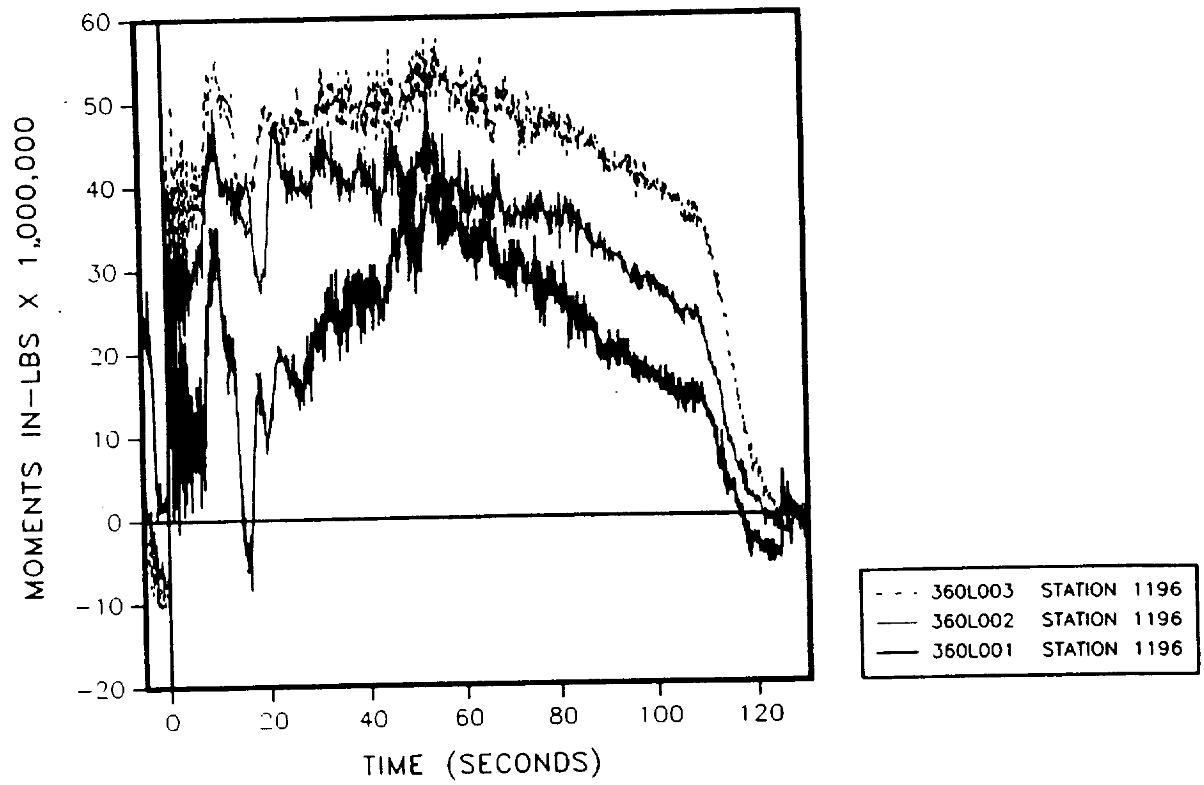

Figure 4.6-42. Z Axis Bending Moment--360L003 Versus 360L001, 360L002 (RH motor, Station 1196)

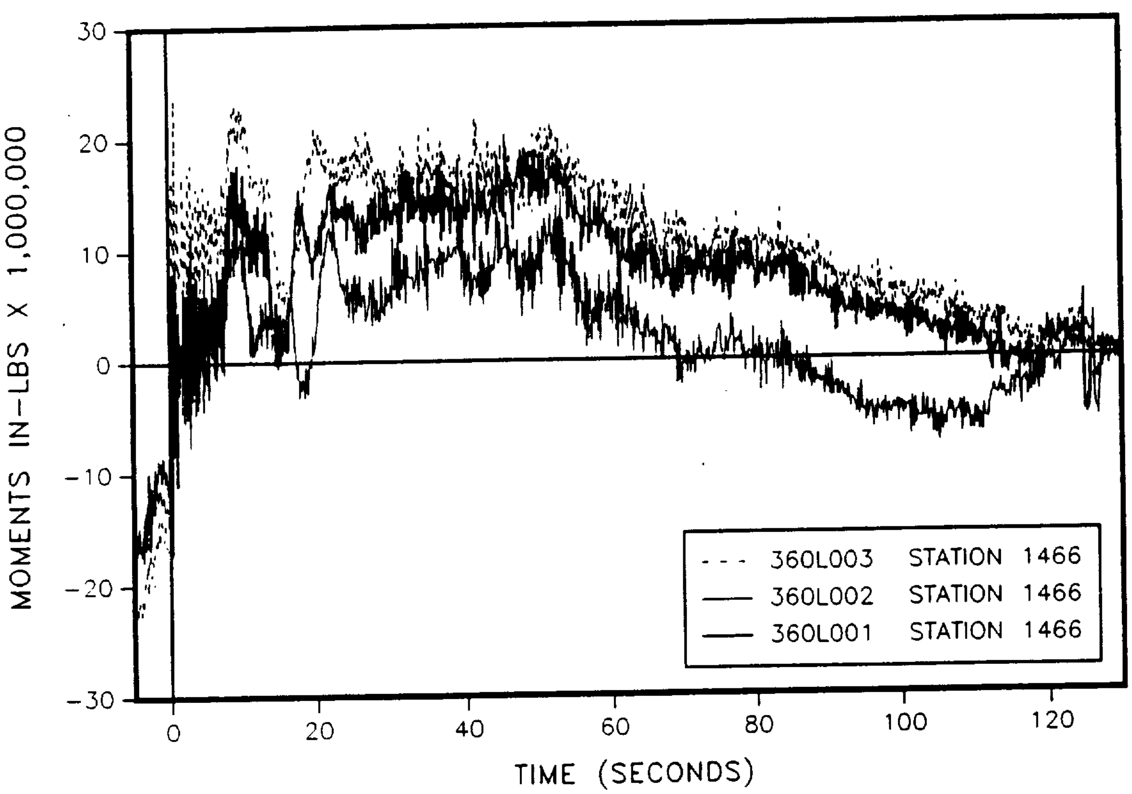

Figure 4.6-43. Z Axis Bending Moment--360L003 Versus 360L001, 360L002 (RH motor, Station 1466)

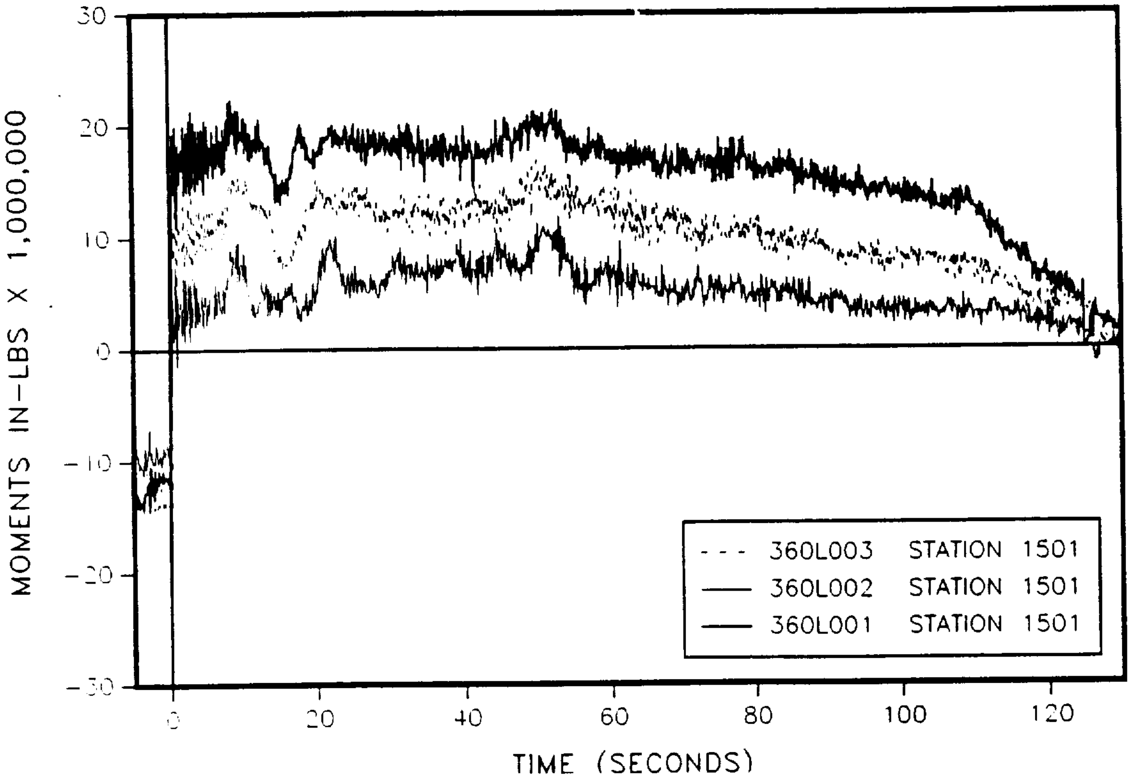

Figure 4.6-44. Z Axis Bending Moment--360L003 Versus 360L001, 360L002 (RH motor, Station 1501)

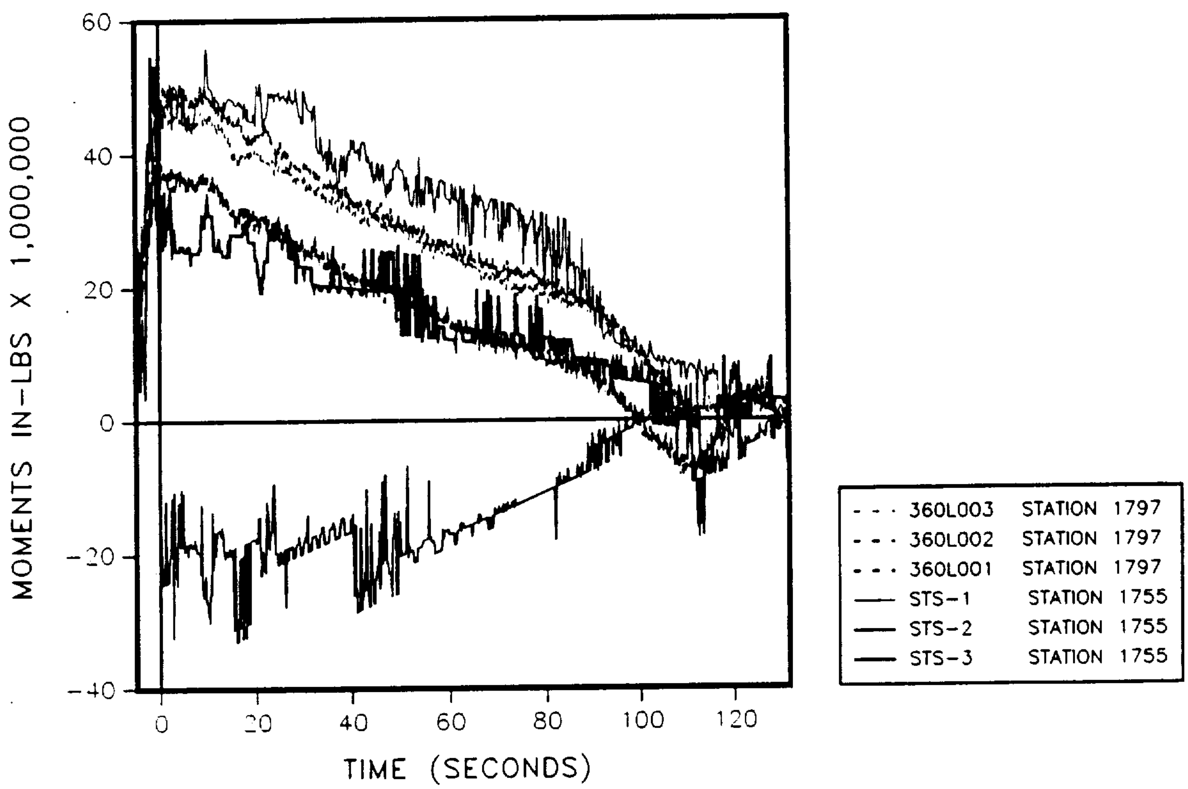

Figure 4.6-45. Z Axis Bending Moment--360L003 Versus 360L001, 360L002, and STS-1, 2, and 3 (RH motor, Stations 1797 and 1755)

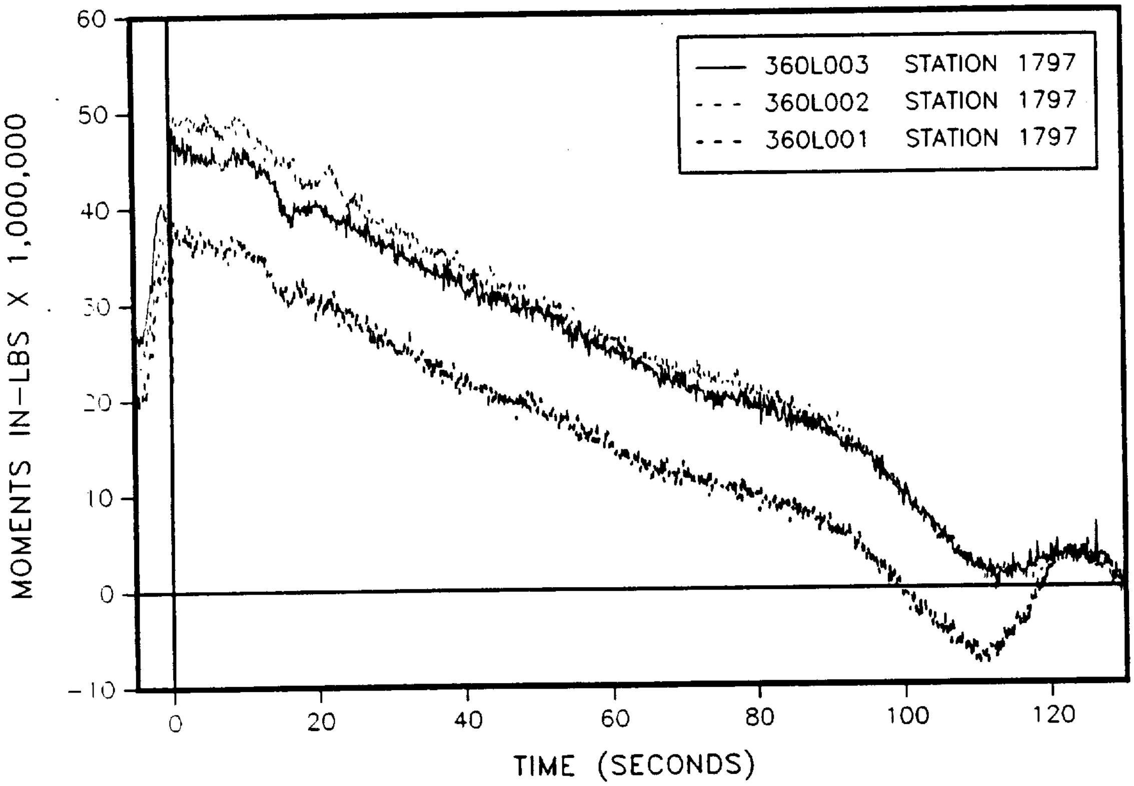

Figure 4.6-46. Z Axis Bending Moment--360L003 Versus 360L001, 360L002 (RH motor, Station 1797)

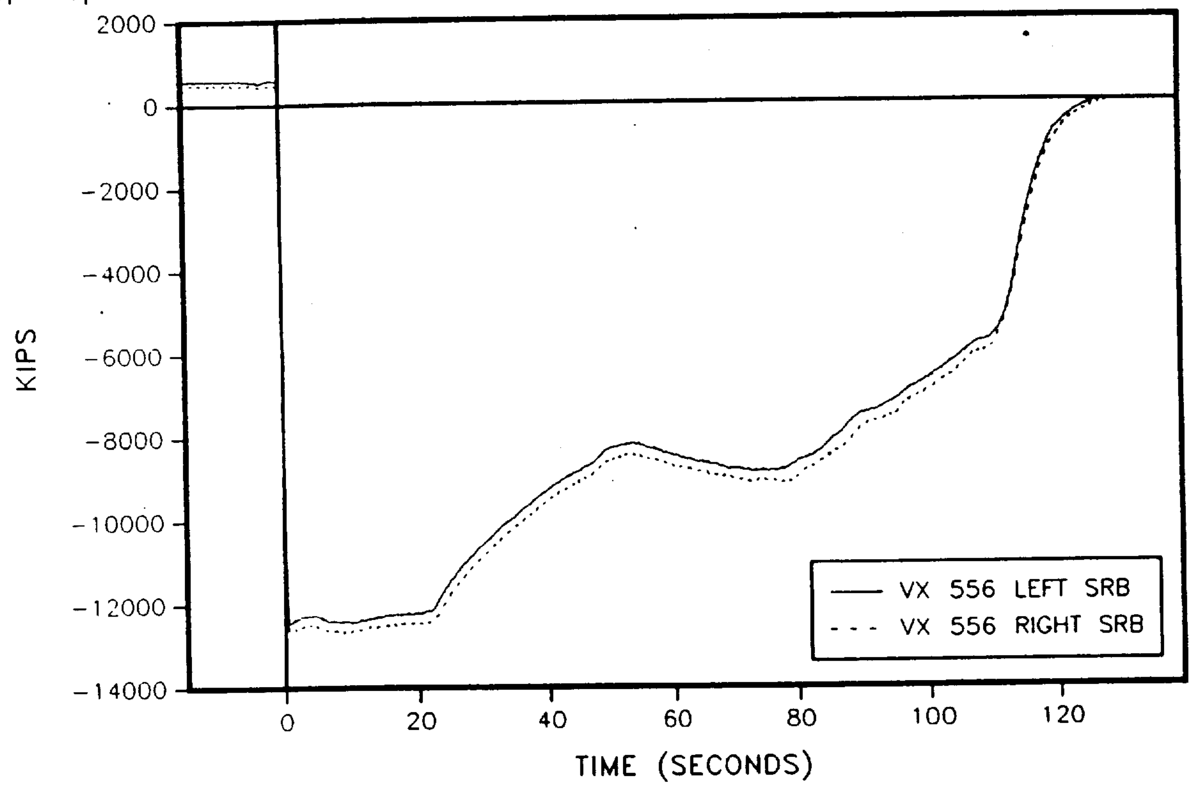

Figure 4.6-47. 360L003 Axial Force (Station 556)

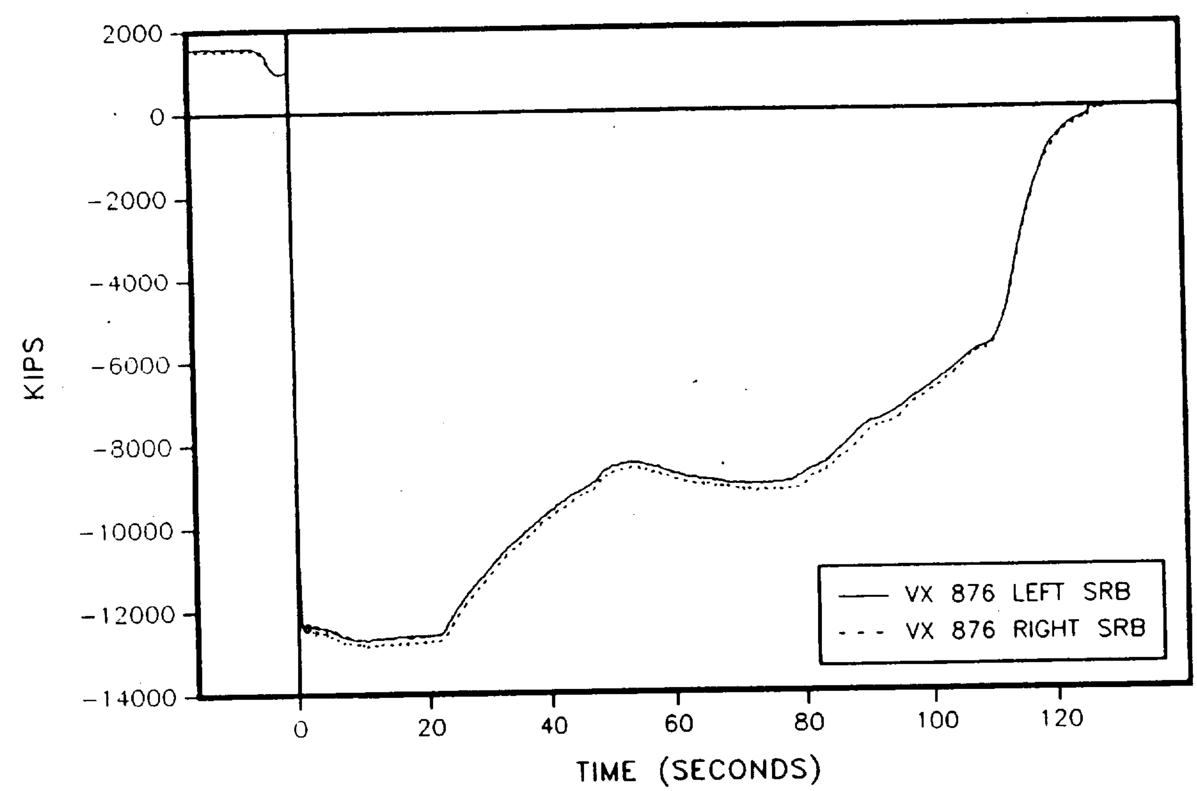

Figure 4.6-48. 360L003 Axial Force (Station 876)

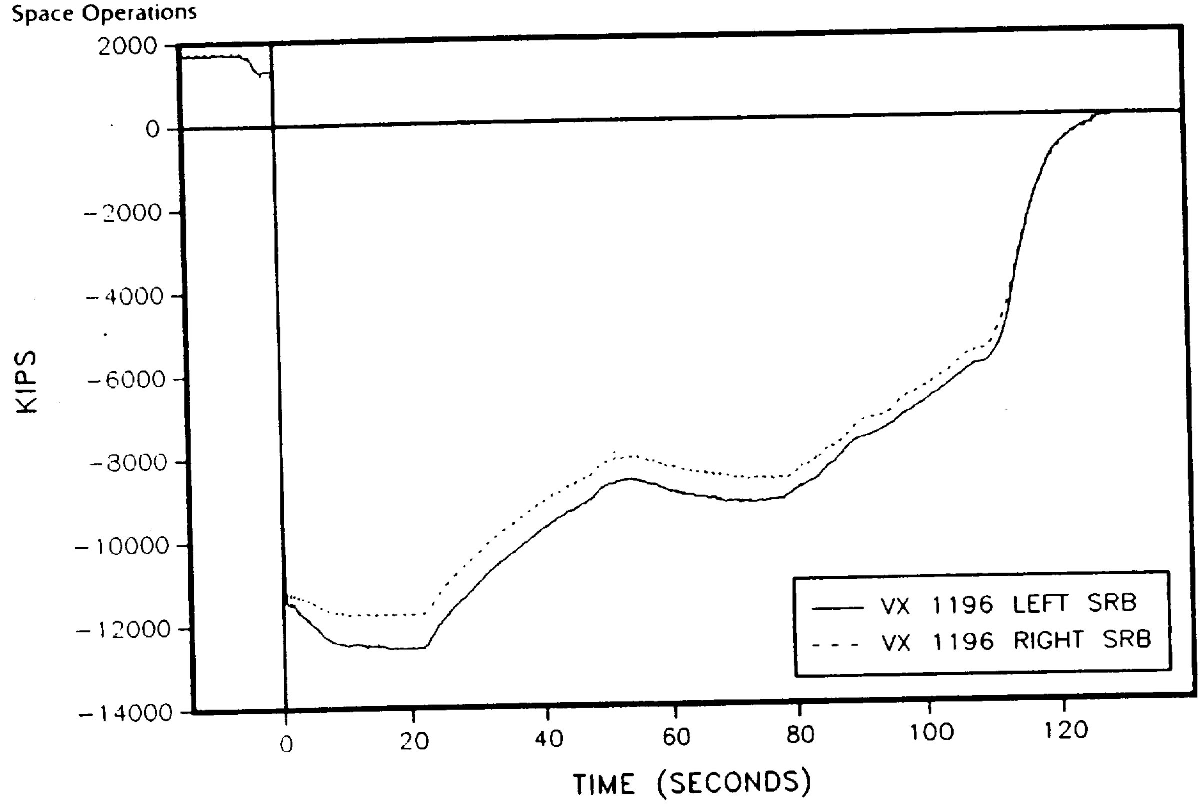

Figure 4.6-49. 360L003 Axial Force (Station 1196)

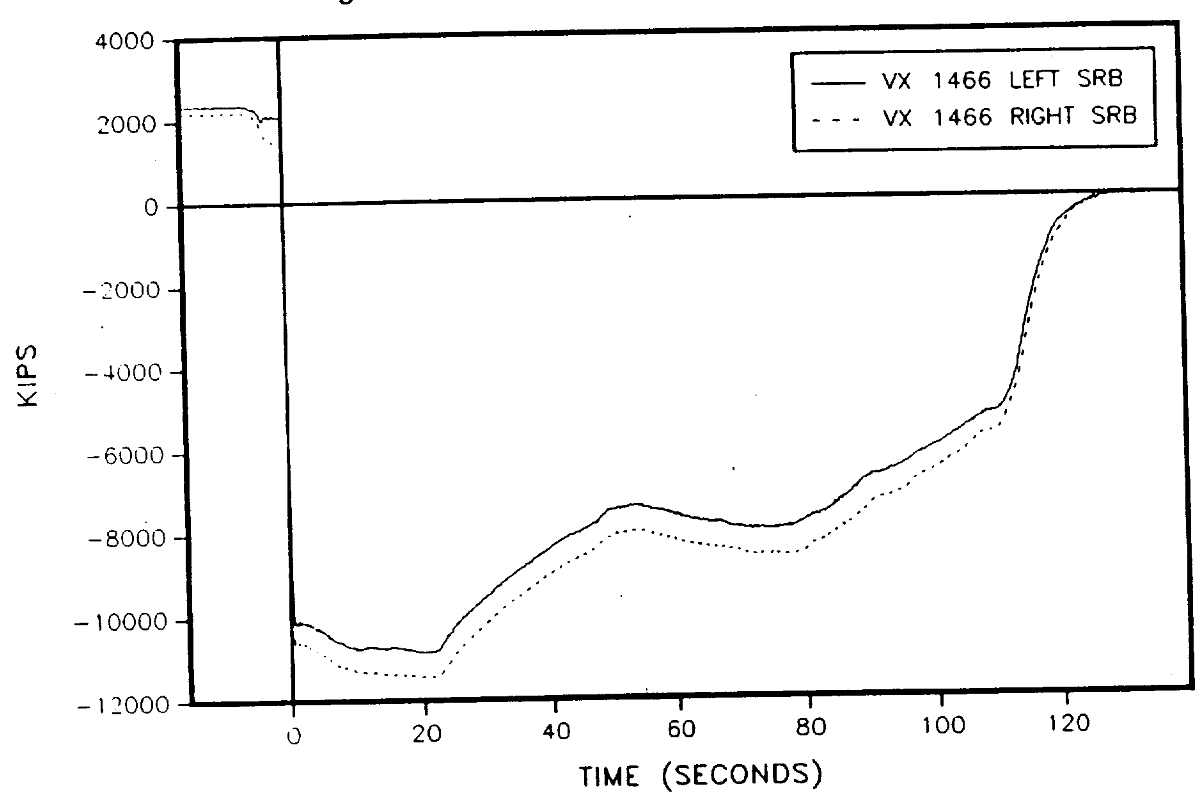

Figure 4.6-50. 360L003 Axial Force (Station 1466)

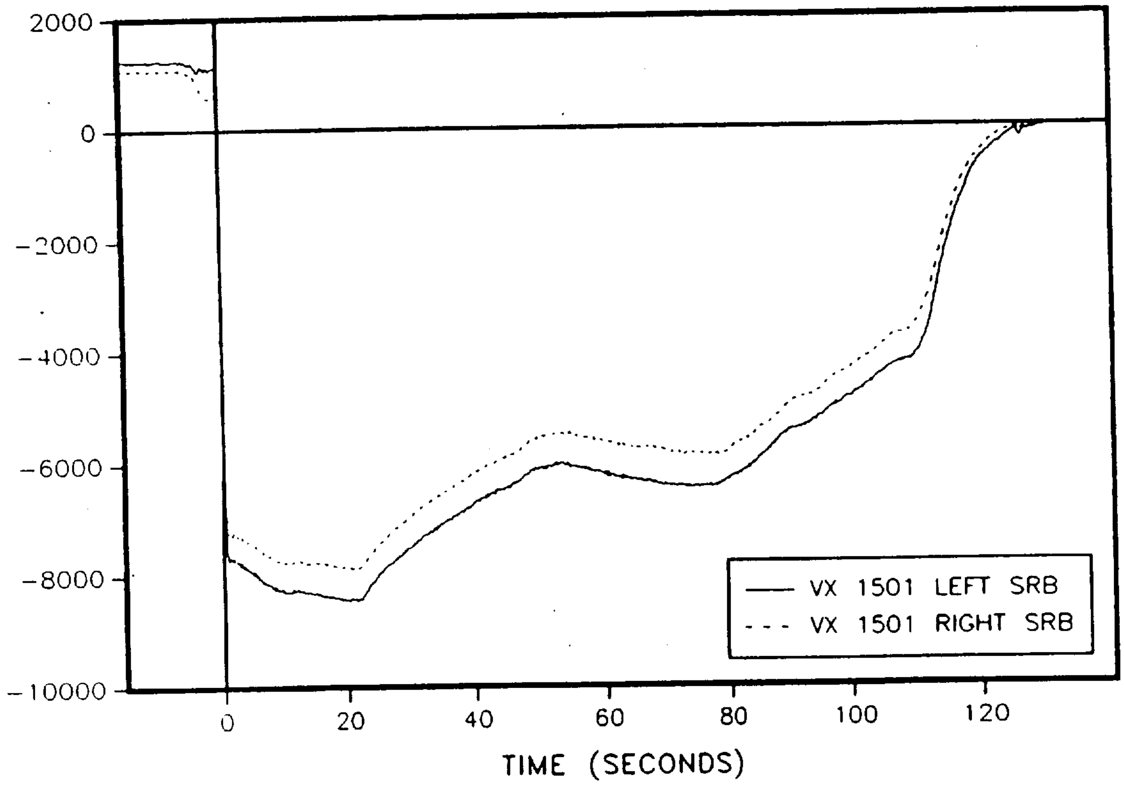

Figure 4.6-51. 360L003 Axial Force (Station 1501)

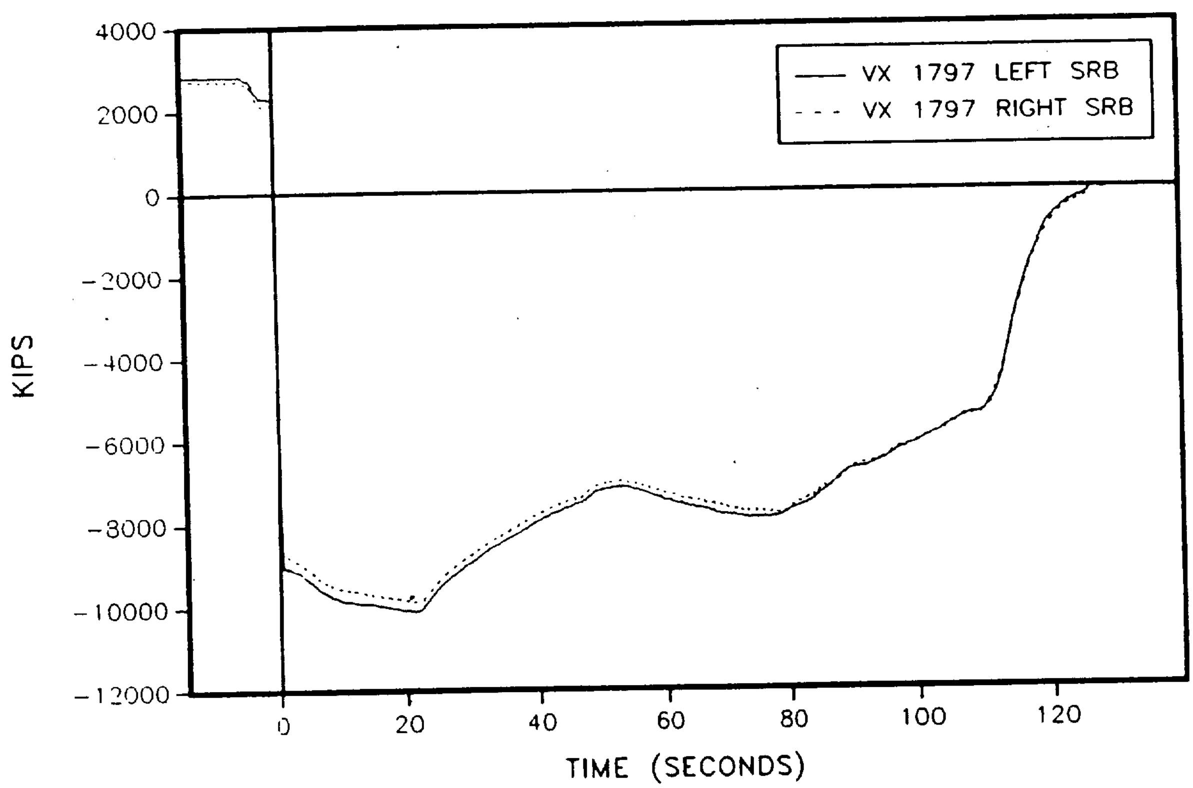

Figure 4.6-52. 360L003 Axial Force (Station 1797)

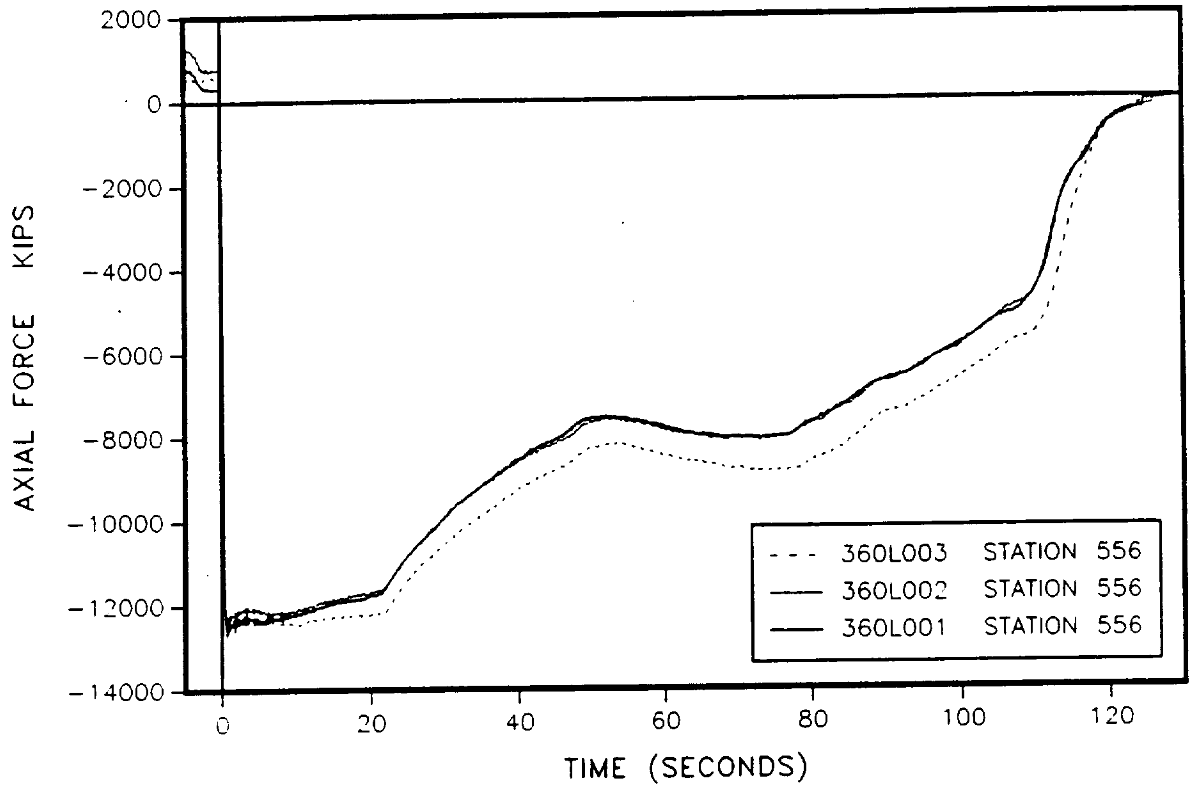

Figure 4.6-53. Axial Force--360L003 Versus 360L001, 360L002 (LH motor, Station 556)

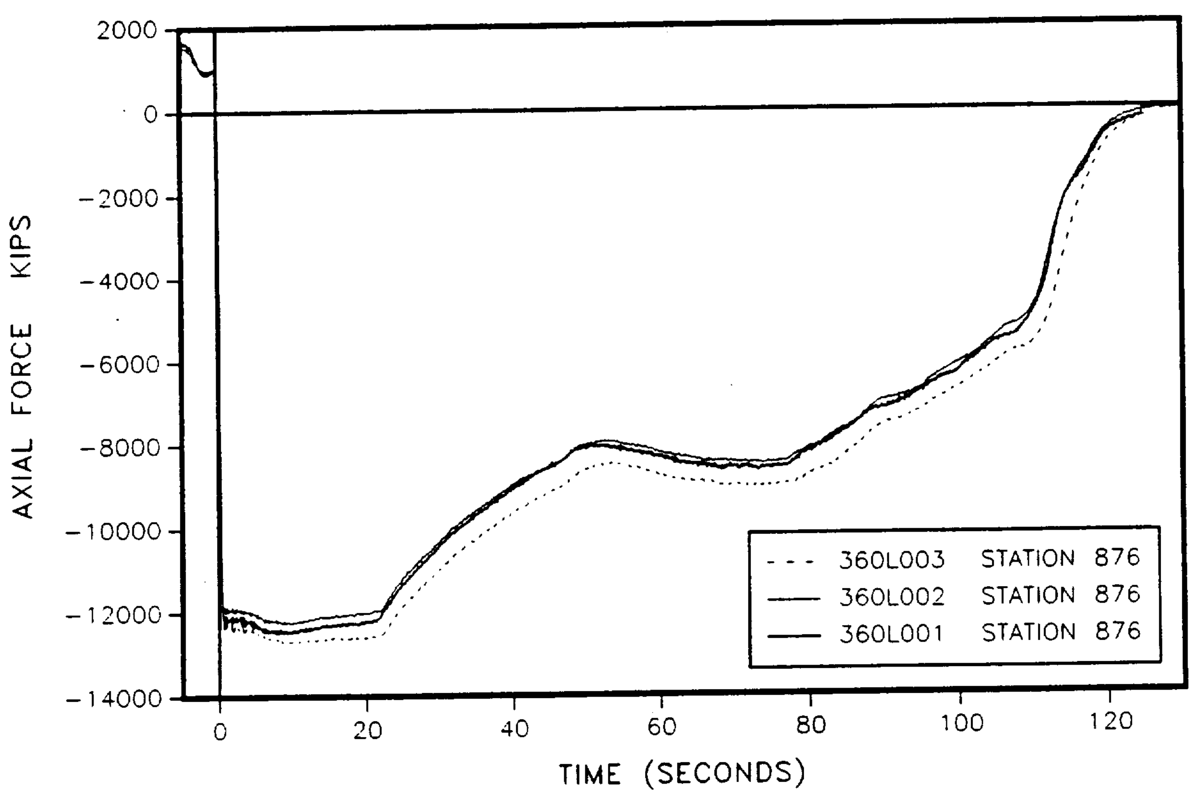

Figure 4.6-54. Axial Force--360L003 Versus 360L001, 360L002 (LH motor, Station 876)

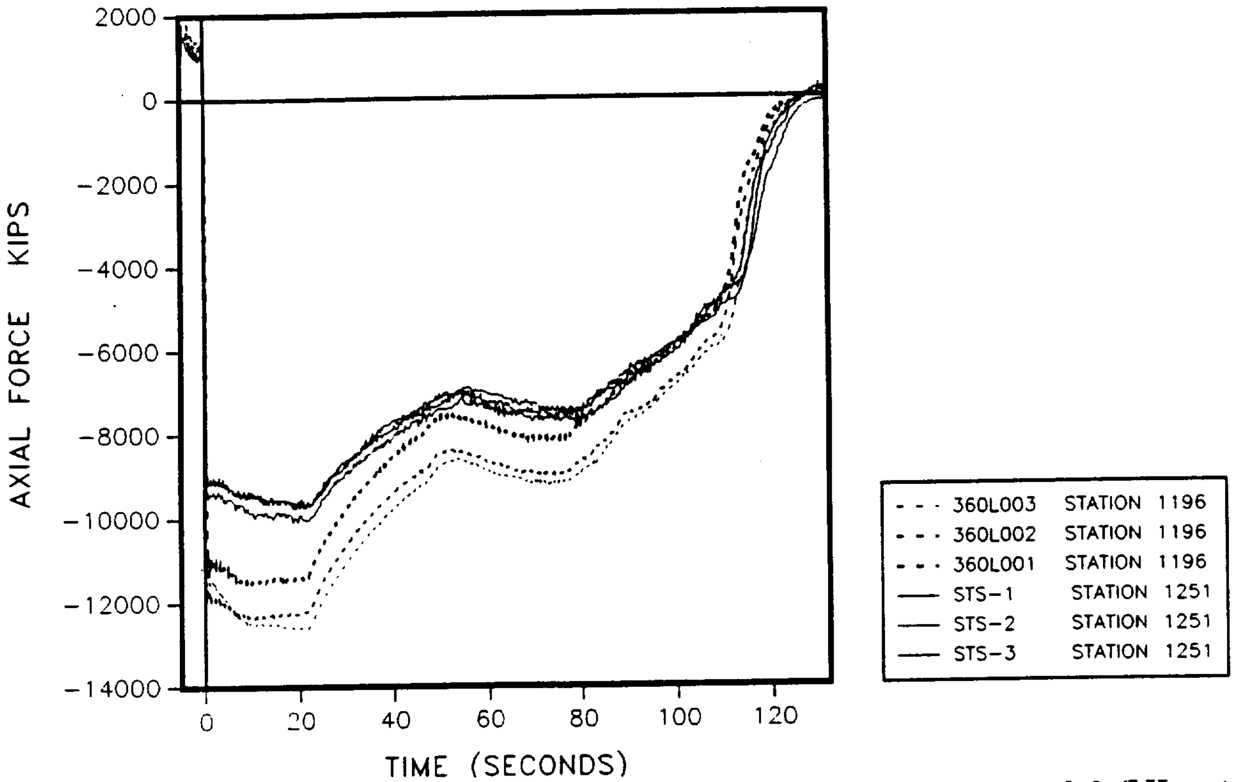

Figure 4.6-55. Axial Force--360L003 Versus 360L001, 360L002, and STS-1, 2, and 3 (LH motor, Stations 1196 and 1251)

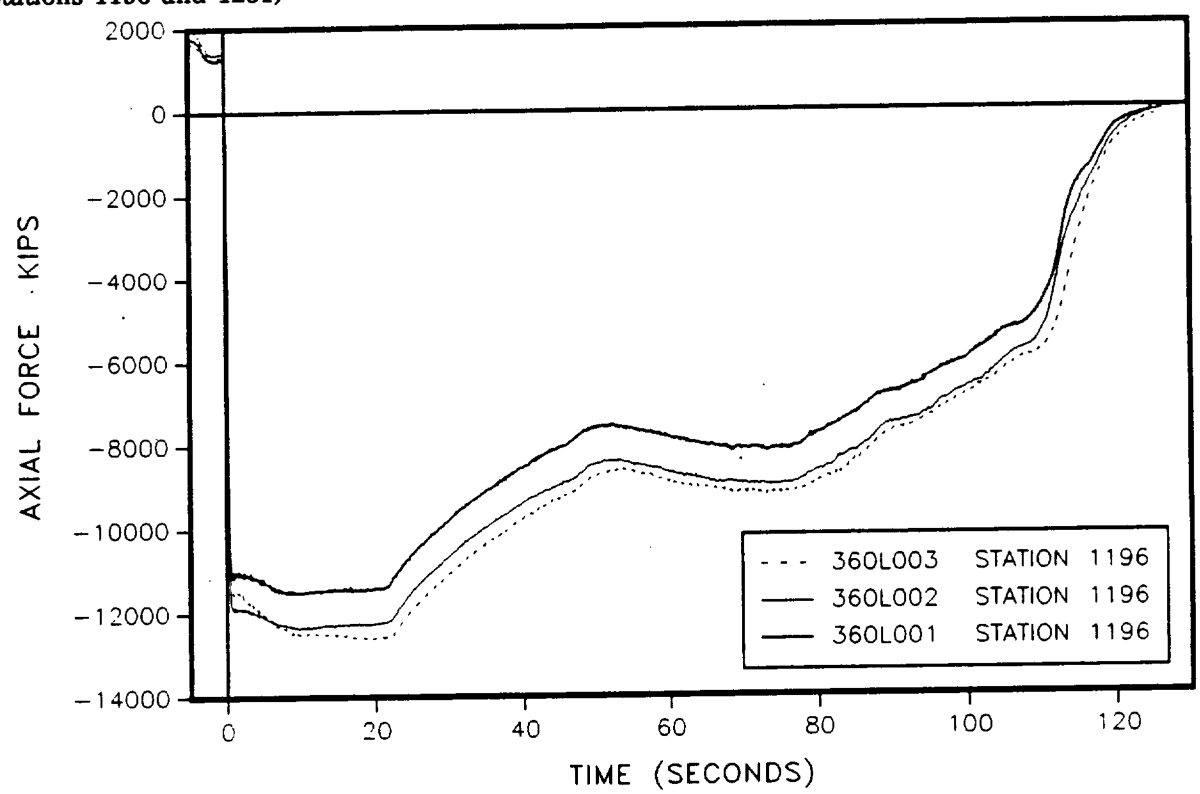

Figure 4.6-56. Axial Force--360L003 Versus 360L001, 360L002 (LH motor, Station 1196)

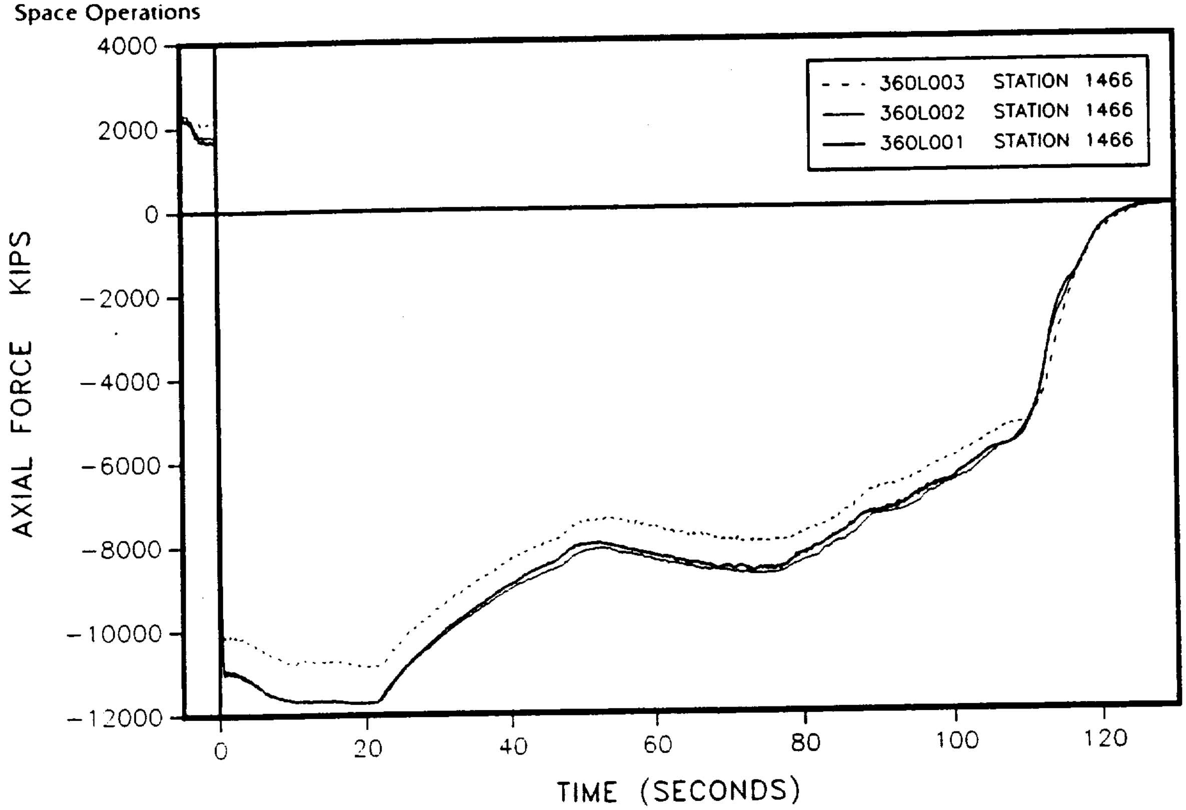

Figure 4.6-57. Axial Force--360L003 Versus 360L001, 360L002 (LH motor, Station 1466)

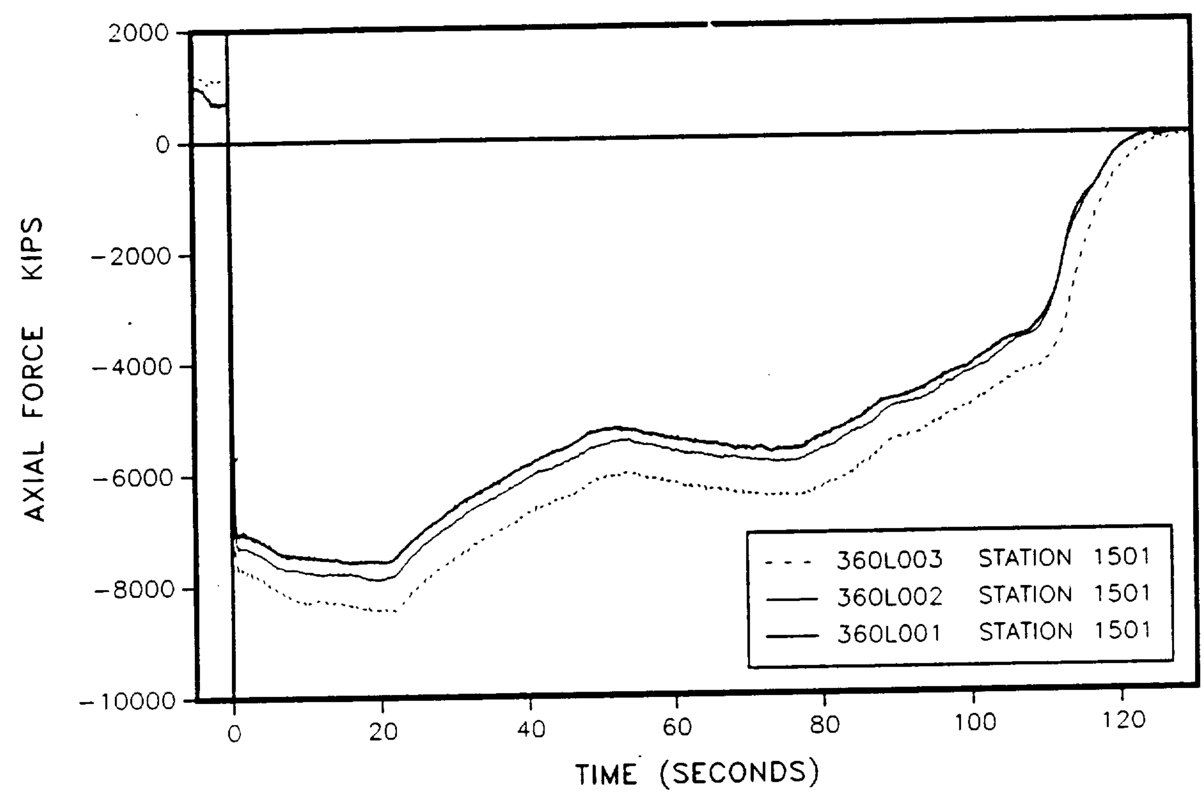

Figure 4.6-58. Axial Force--360L003 Versus 360L001, 360L002 (LH motor, Station 1501)

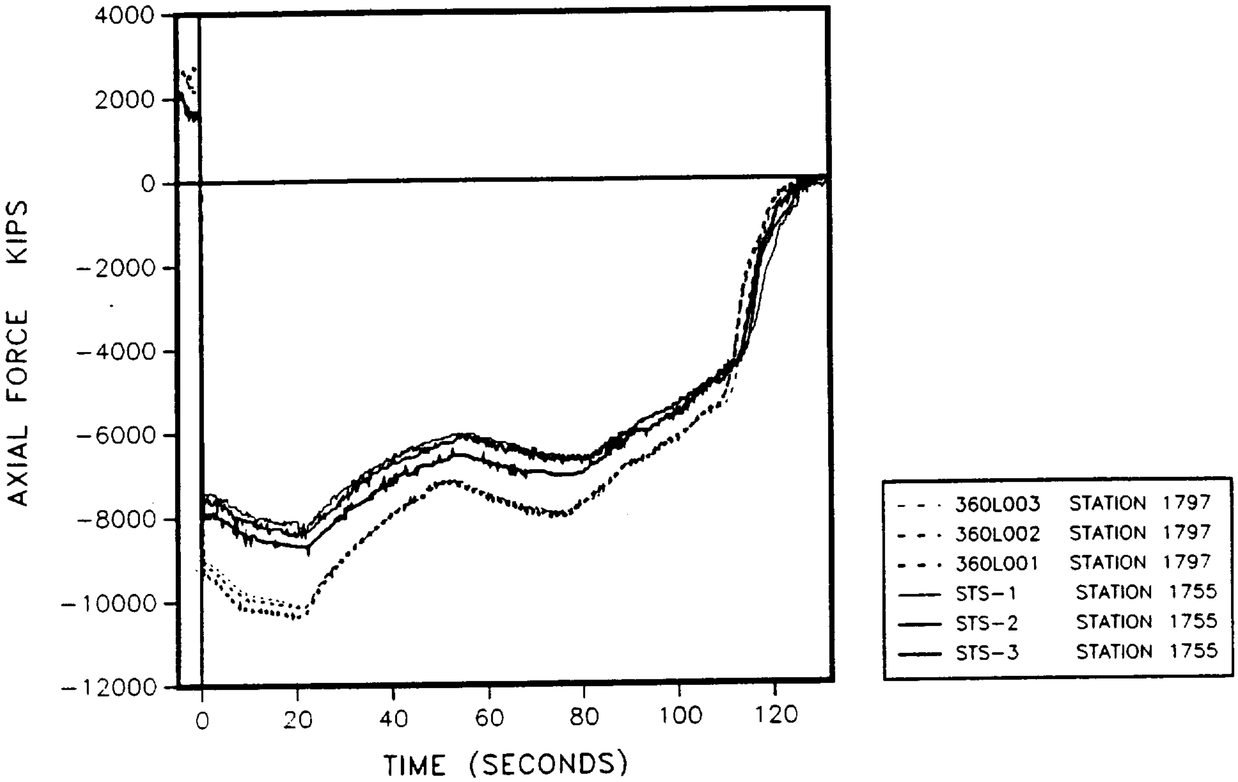

Figure 4.6-59. Axial Force--360L003 Versus 360L001, 360L002, and STS-1, 2, and 3 (LH motor, Stations 1797 and 1755)

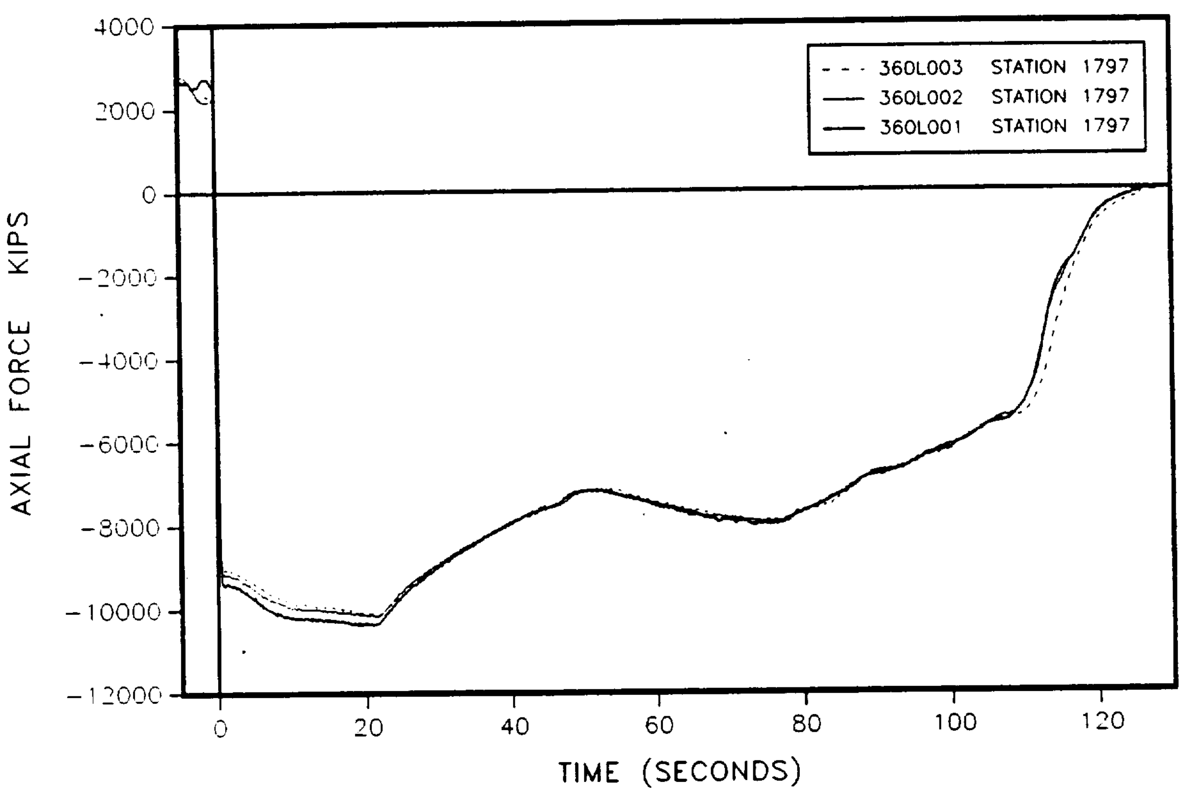

Figure 4.6-60. Axial Force--360L003 Versus 360L001, 360L002 (LH motor, Station 1797)

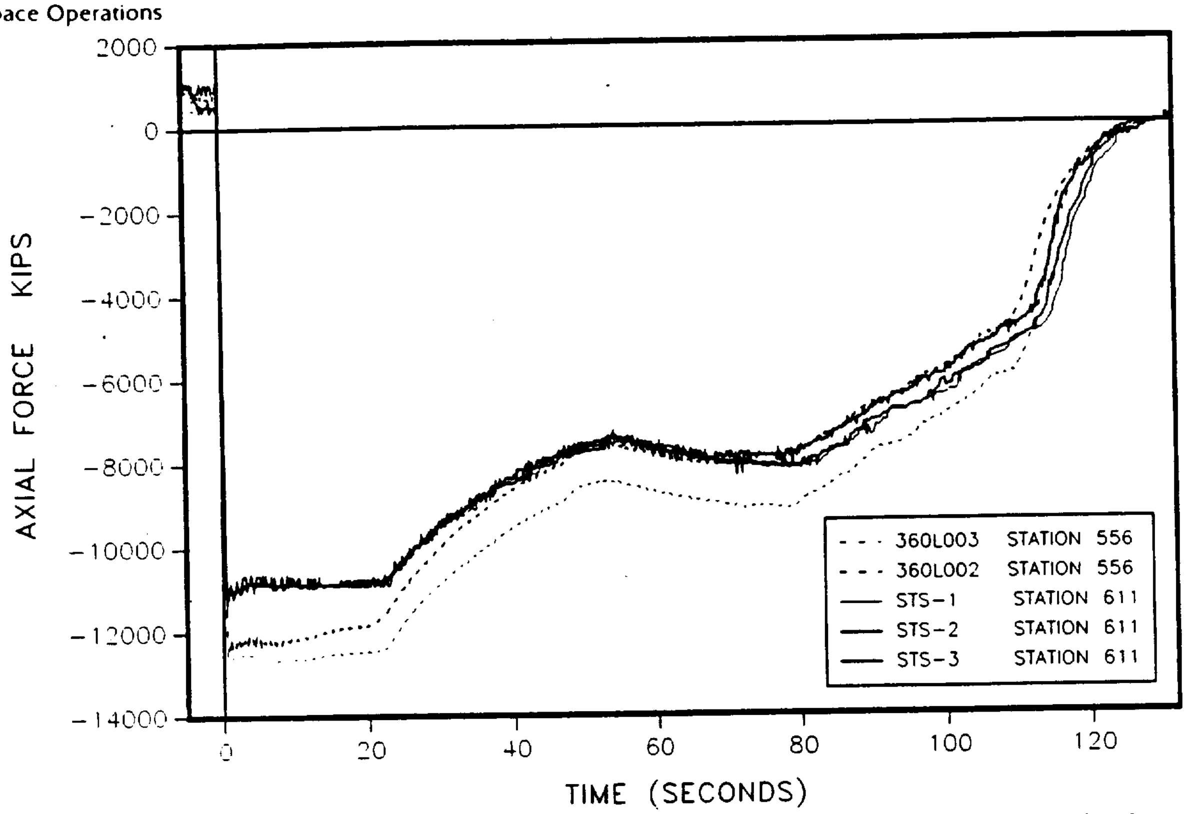

Figure 4.6-61. Axial Force--360L003 Versus 360L002 and STS-1, 2, and 3 (RH motor, Stations 556 and 611)

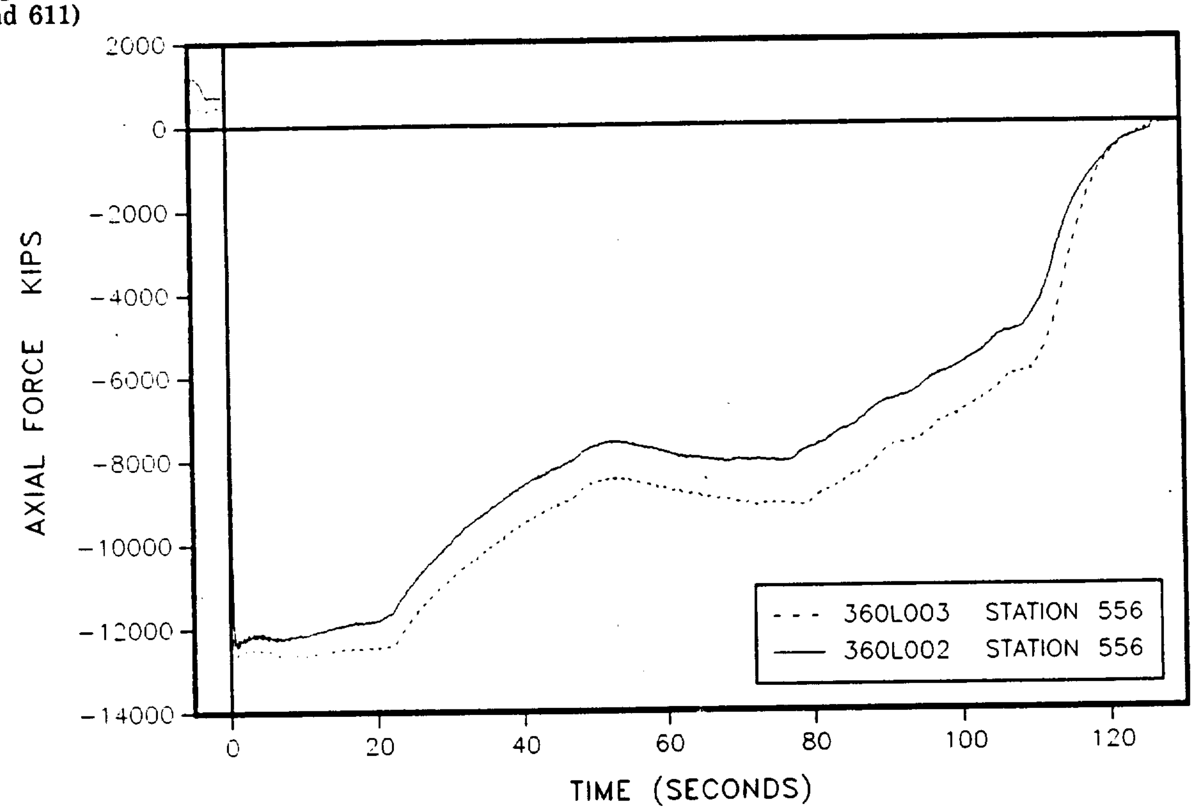

Figure 4.6-62. Axial Force--360L003 Versus 360L002 (RH motor, Station 556)

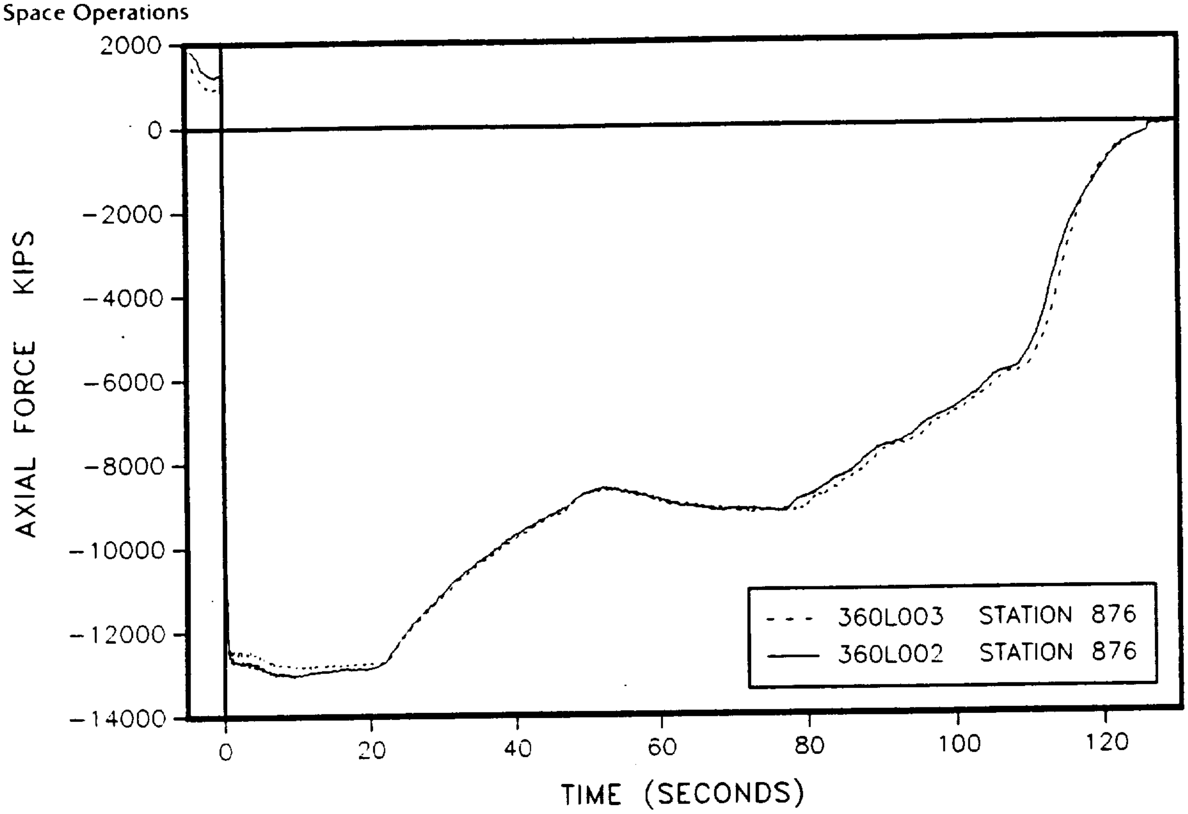

Figure 4.6-63. Axial Force--360L003 Versus 360L002 (RH motor, Station 876)

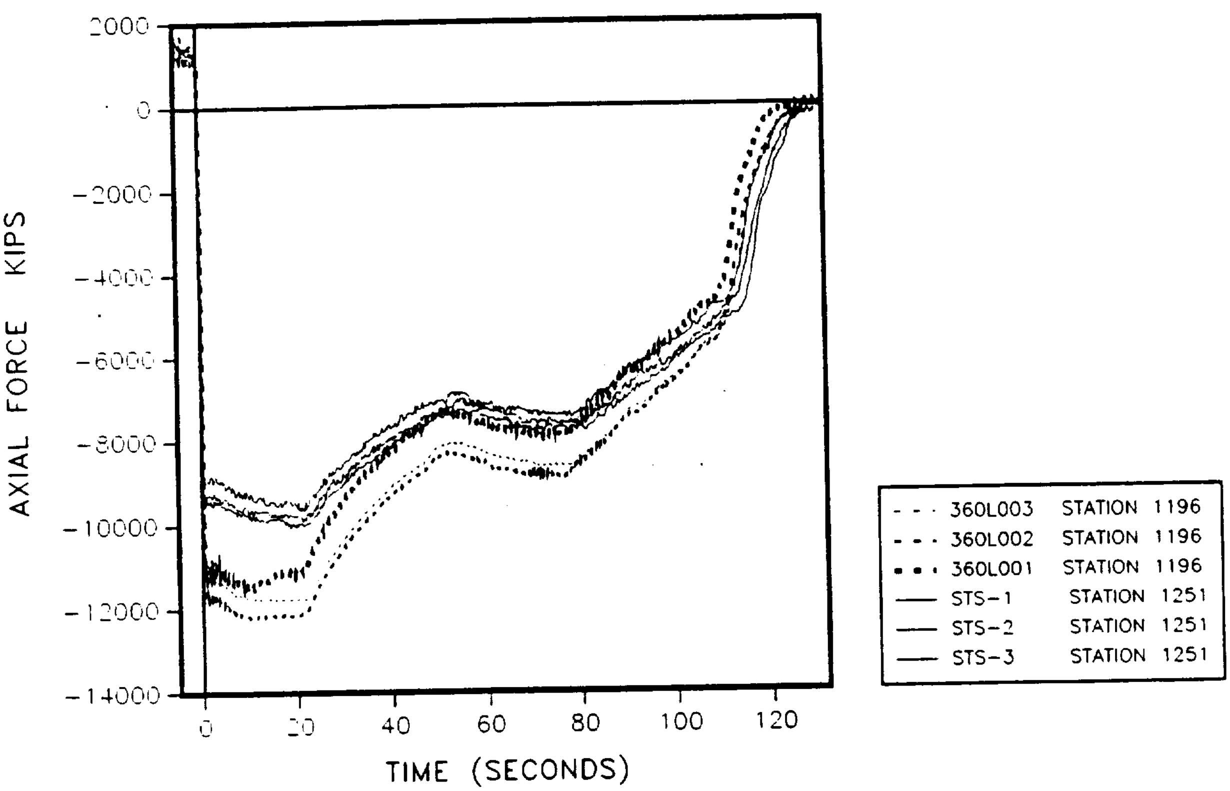

Figure 4.6-64. Axial Force--360L003 Versus 360L001, 360L002, and STS-1, 2, and 3 (RH motor, Stations 1196 and 1251)

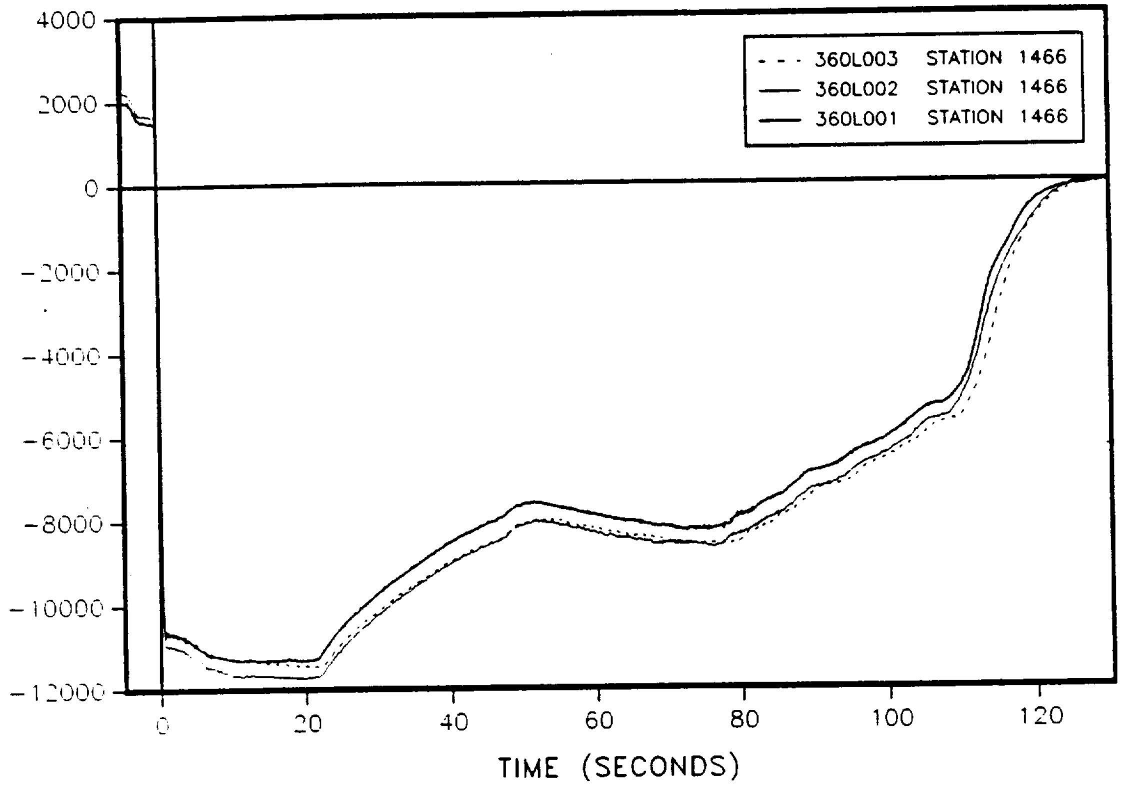

Figure 4.6-65. Axial Force--360L003 Versus 360L001, 360L002 (RH motor, Station 1196)

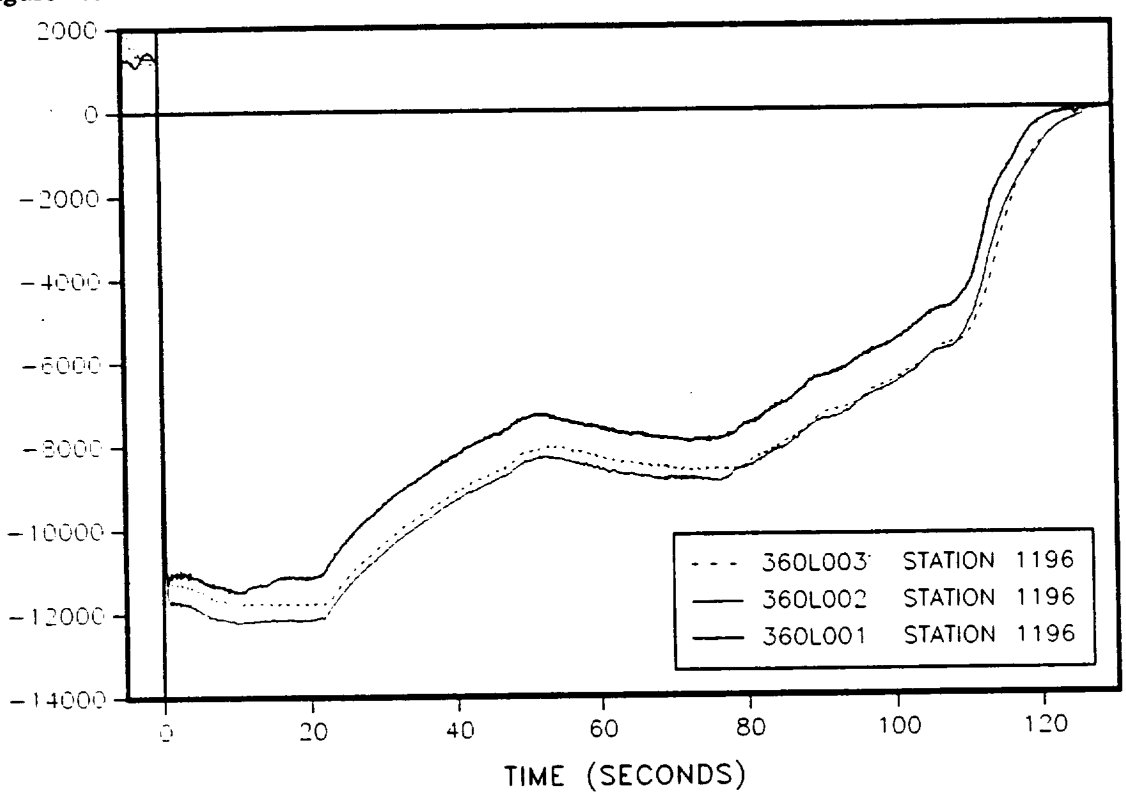

Figure 4.6-66. Axial Force--360L003 Versus 360L001, 360L002 (RH motor, Station 1466)

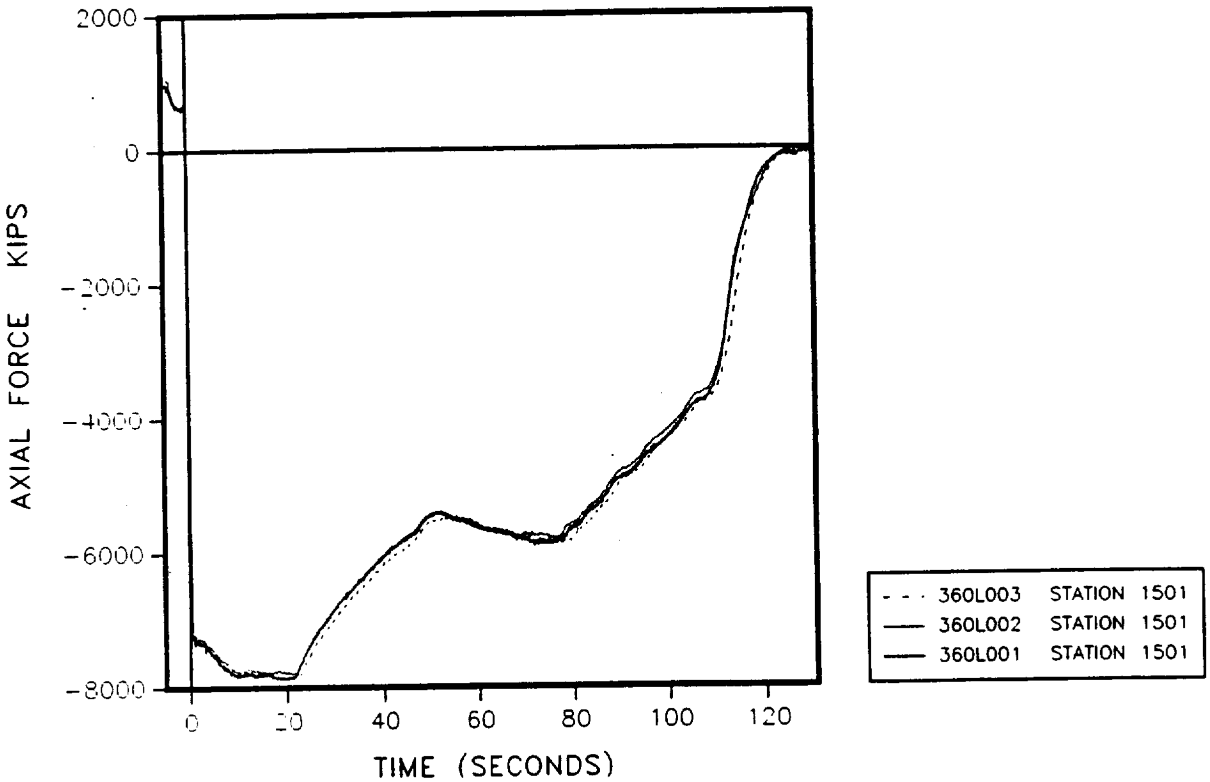

Figure 4.6-67. Axial Force--360L003 Versus 360L001, 360L002 (RH motor, Station 1501)

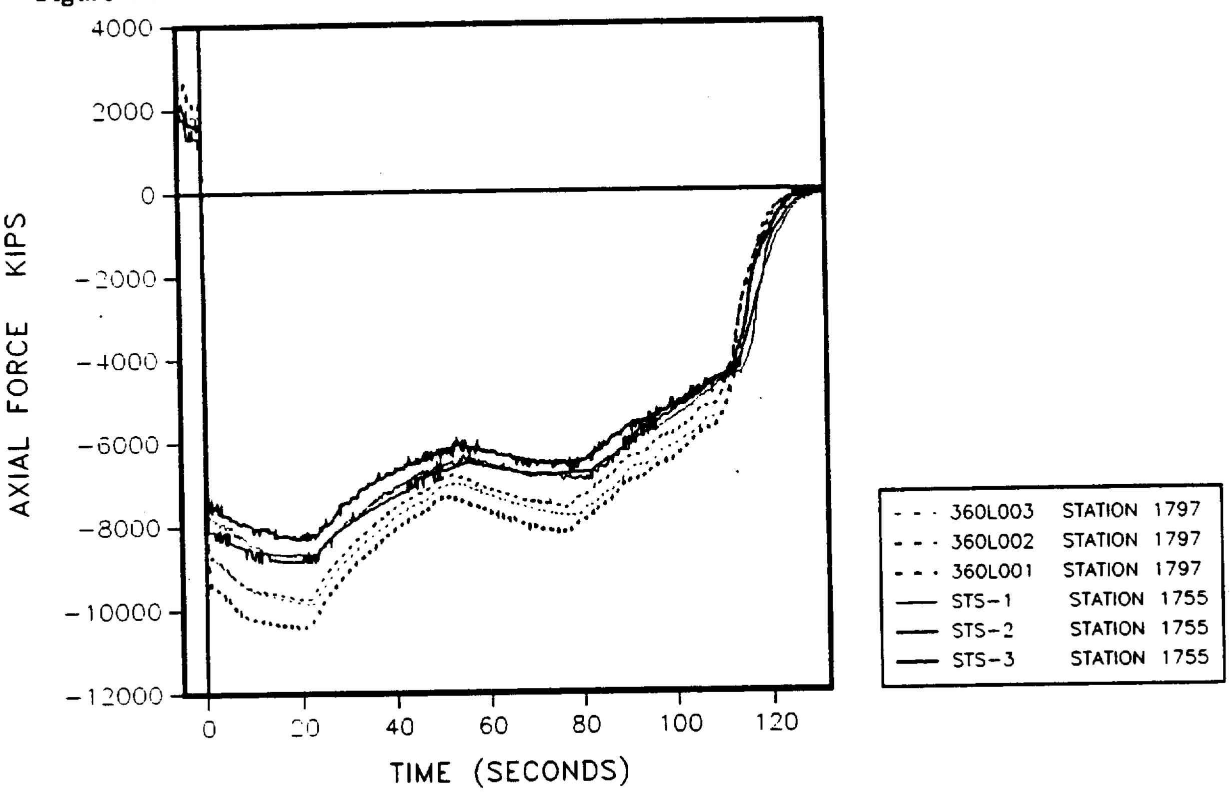

Figure 4.6-68. Axial Force--360L003 Versus 360L001, 360L002, and STS-1, 2, and 3 (RH motor, Stations 1797 and 1755)

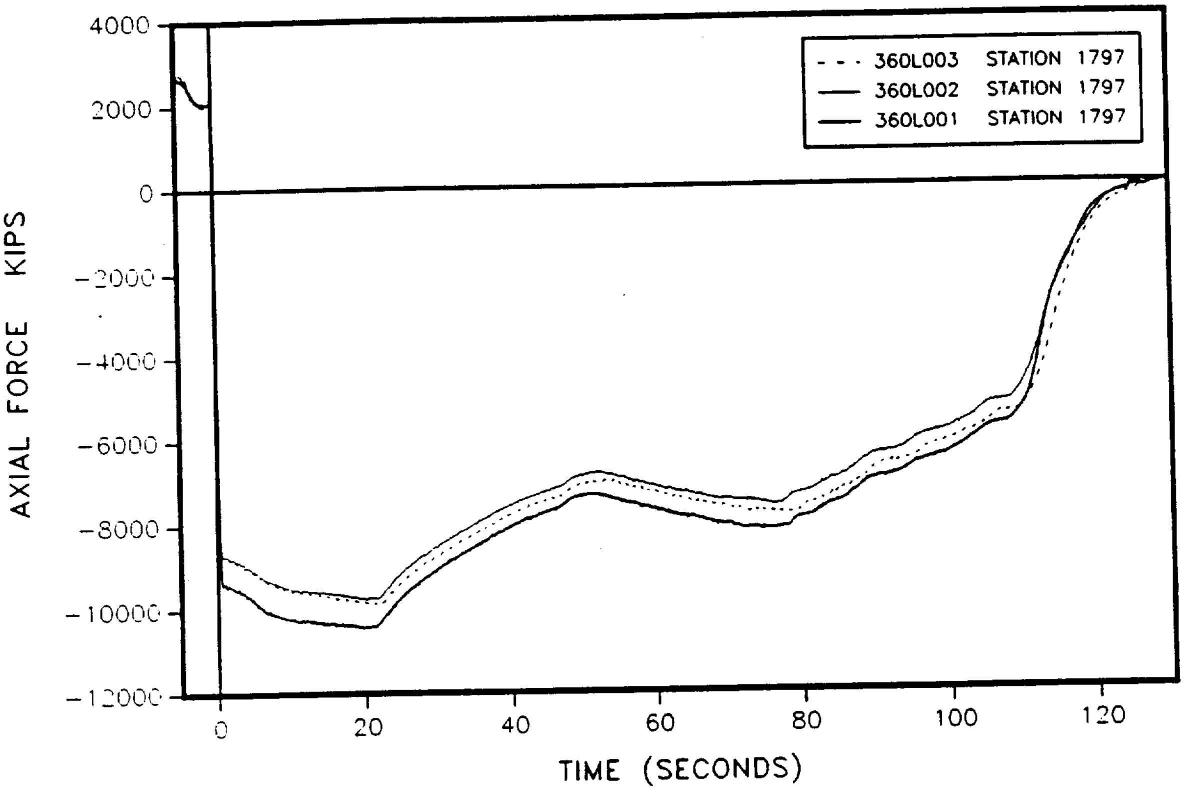

Figure 4.6-69. Axial Force--360L003 Versus 360L001, 360L002 (RH motor, Station 1797)

4.6.3.8 Line Loads. Using the bending moment and axial force data, the average line loads were calculated. Figures 4.6-70 through 4.6-75 show the line load as a function of time. These figures show a curve shape similar to axial force but with a different magnitude. The method of calculation of this line load produces only an average value around the case, so they are not directly comparable to maximum design line loads.

4.6.3.9 Strut Forces. Figures 4.6-76 and 4.6-77 show the resultant strut force in the Y and Z directions, respectively. The LH and RH motors are mirror images of each other in the resultant Y force direction. The RH SRB shows a positive value while the LH SRB shows a negative value.

4.6.3.10 Flight Envelopes. The bending moments and axial force experienced by 360L003 that were not within the envelopes were only slightly out. The following are some possible reasons why all of the loading did not fall within the envelopes.

1. Several strain gages went into the calculation of each load, and every gage has an uncertainty associated with the gage itself, plus some drift in each gage during the flight.
2. Adjusting the strain data to end at zero adds some uncertainty, since the exact strain experienced during free fall is not known.
3. The program calculates a linear stress distribution from the strain data, and the case does not necessarily behave linearly during flight. It should be noted that the data compare favorably with previous flight data, as expected. The time ranges used to find the maximum and minimum values for each event are defined in the table below.

Flight Event	Time Range
Prelaunch	-15.0 to -7.0
Buildup	-1.6 to -0.8
Lift-off	0.0 to 4.0
Roll Maneuver	5.0 to 22.0
Max Q	27.0 to 76.0
Max G	72.0 to 90.0
Preseparation	119.0 to 124.0

4.6.3.11 Bending About the Y Axis. Figures 4.6-78 through 4.6-91 are plots of the maximum and minimum values for 360L003 and the envelopes for specific flight events. These plots show that the data fit the envelopes quite well. Those stations that do fall outside the envelope are of a relatively small magnitude.

4.6.3.12 Bending About the Z Axis. Figures 4.6-92 through 4.6-105 are plots of the maximum and minimum values for 360L003 and the envelopes for specific flight events. These plots show that

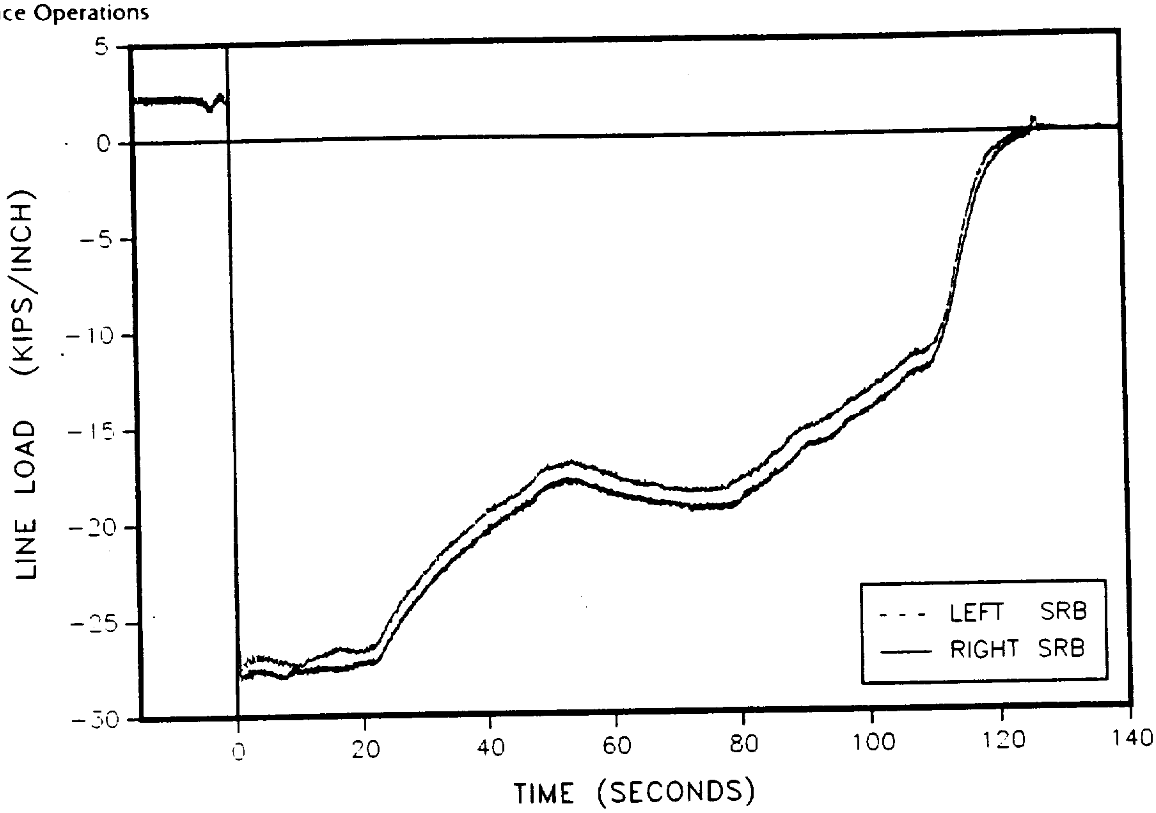

Figure 4.6-70. 360L003 Line Load Comparison (Station 556)

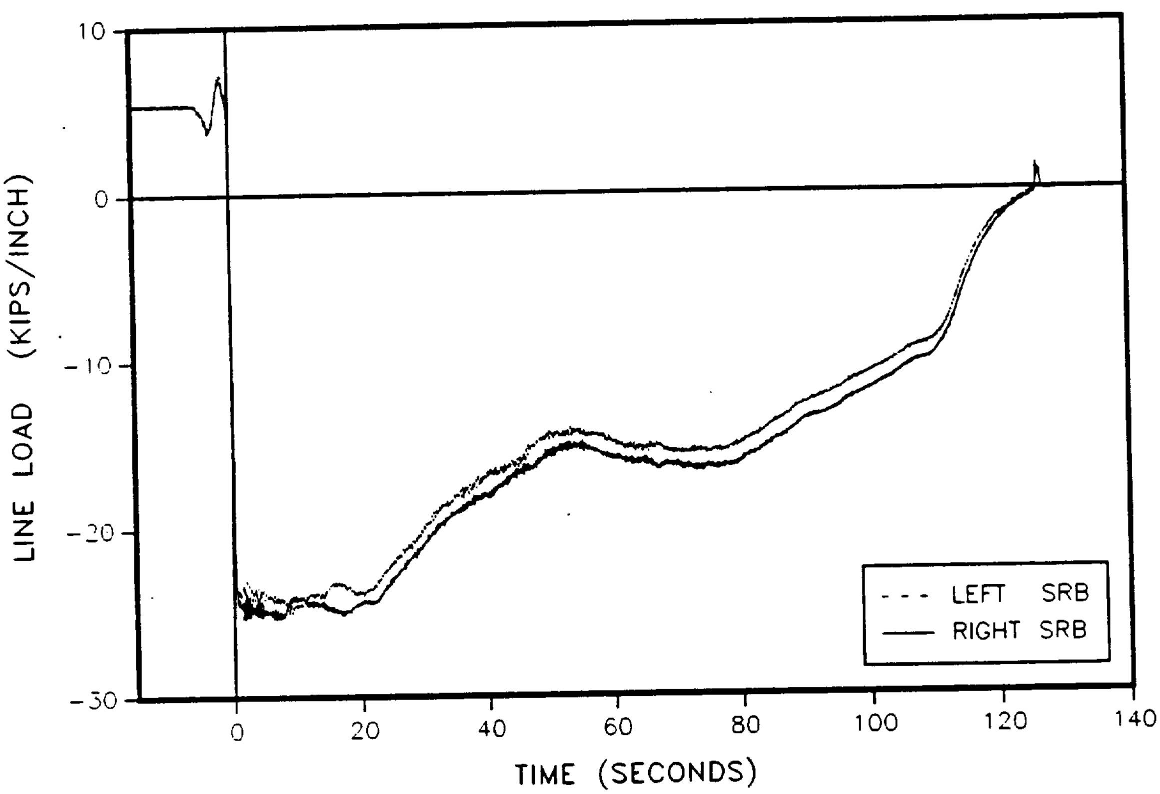

Figure 4.6-71. 360L003 Line Load Comparison (Station 876)

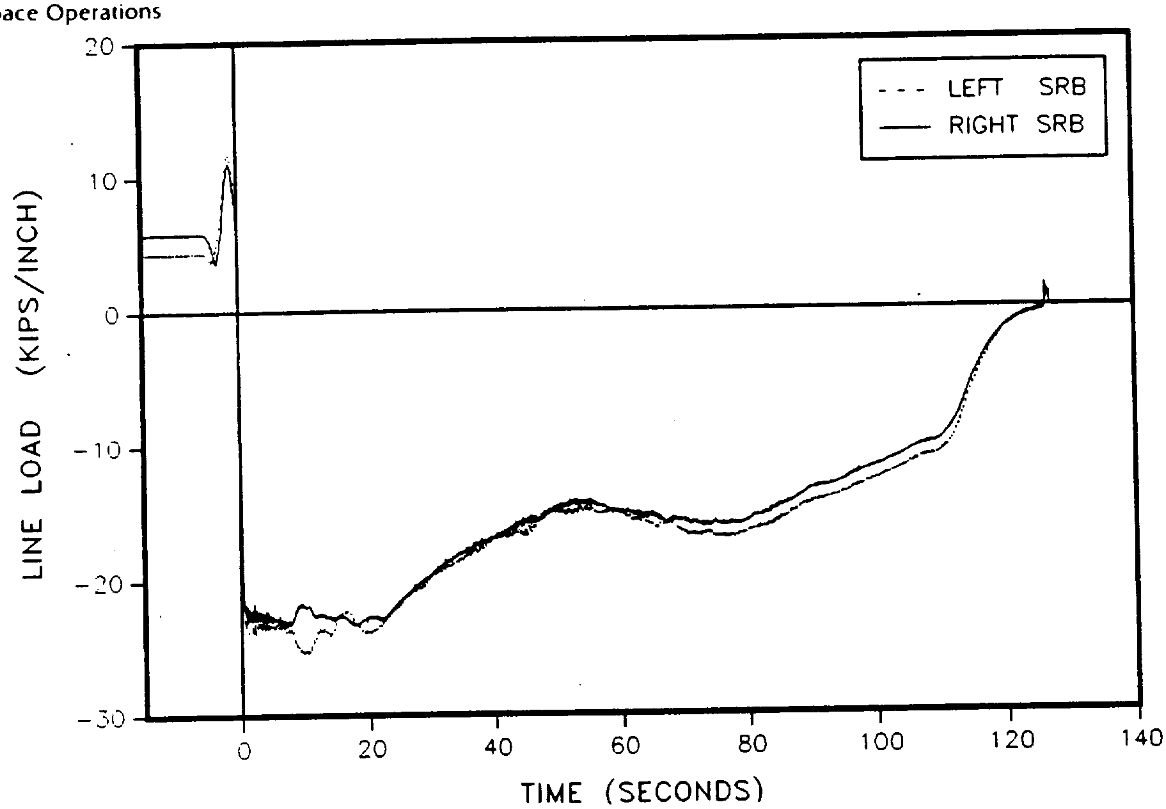

Figure 4.6-72. 360L003 Line Load Comparison (Station 1196)

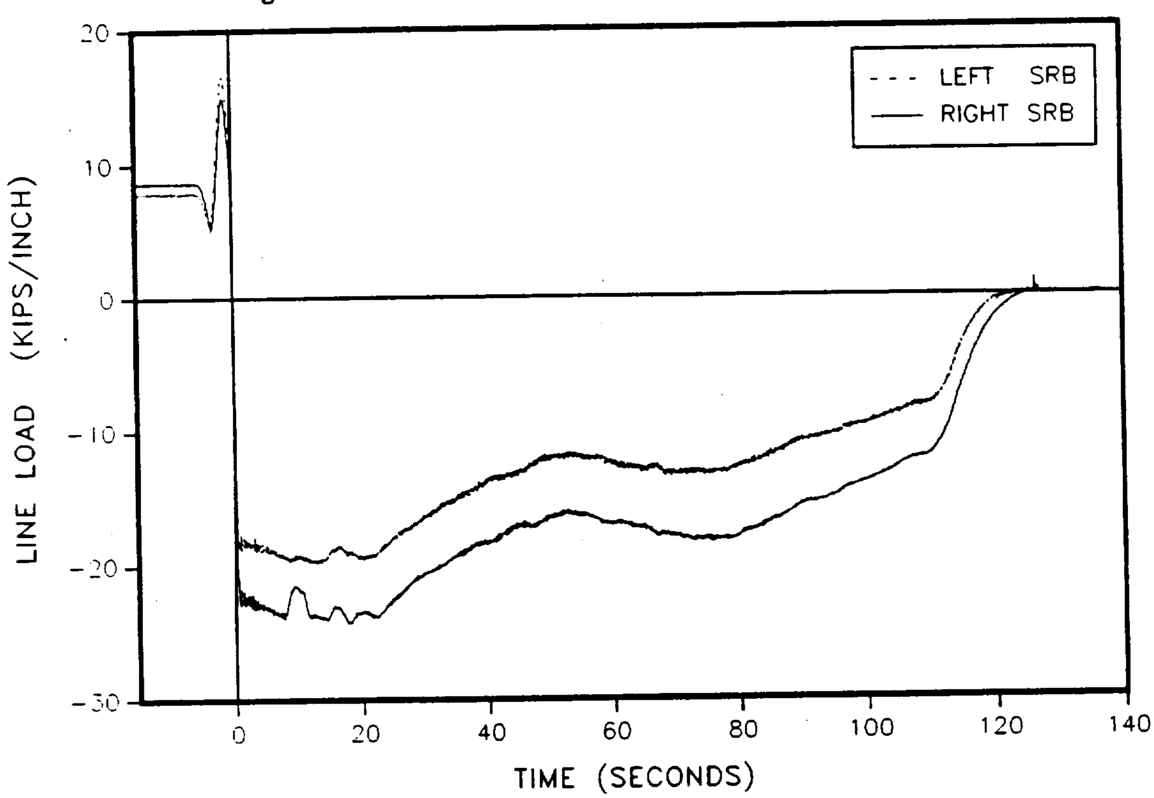

Figure 4.6-73. 360L003 Line Load Comparison (Station 1466)

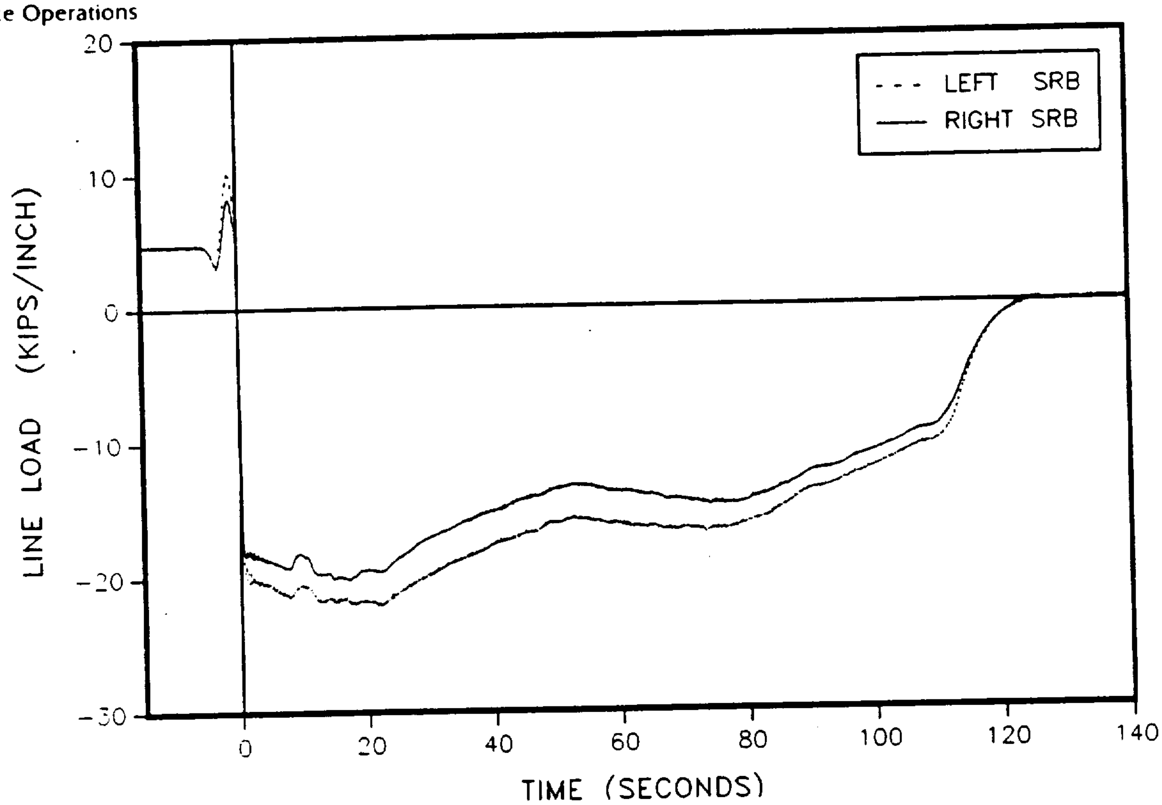

Figure 4.6-74. 360L003 Line Load Comparison (Station 1501)

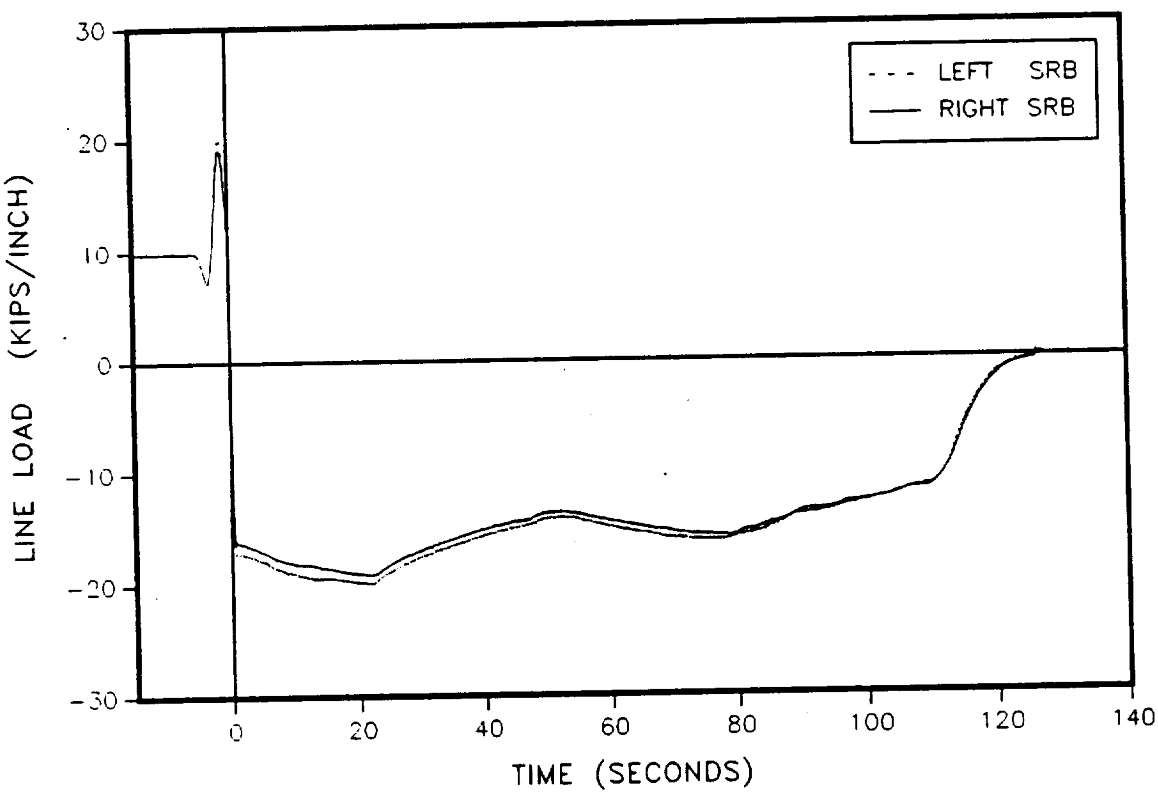

Figure 4.6-75. 360L003 Line Load Comparison (Station 1797)

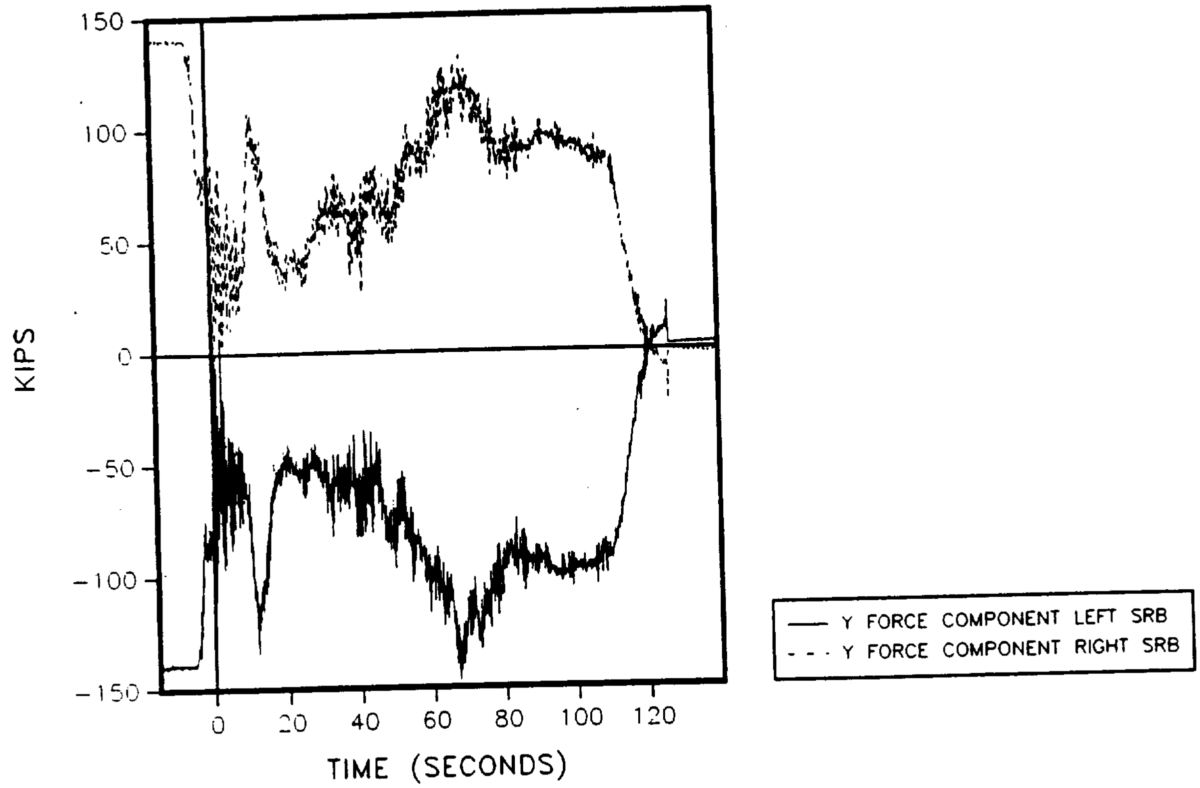

Figure 4.6-76. 360L003 Y Component Strut Forces

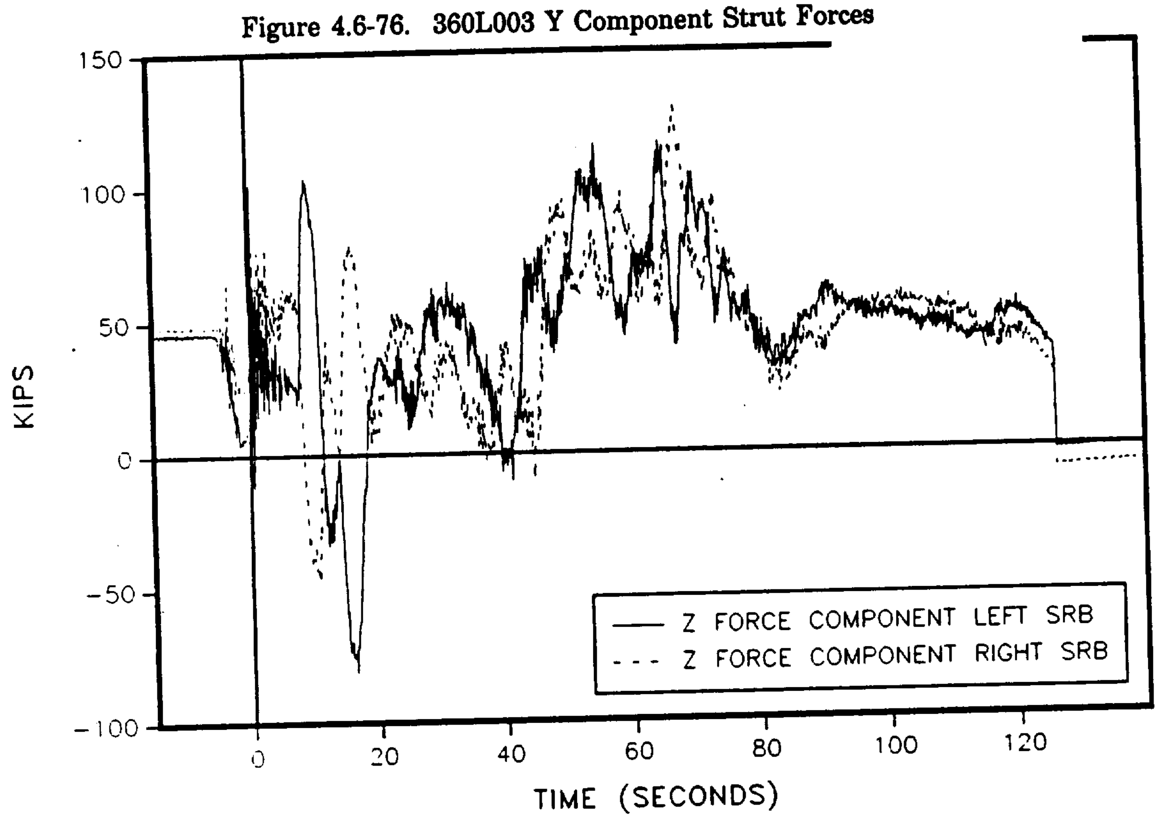

Figure 4.6-77. 360L003 Z Component Strut Forces

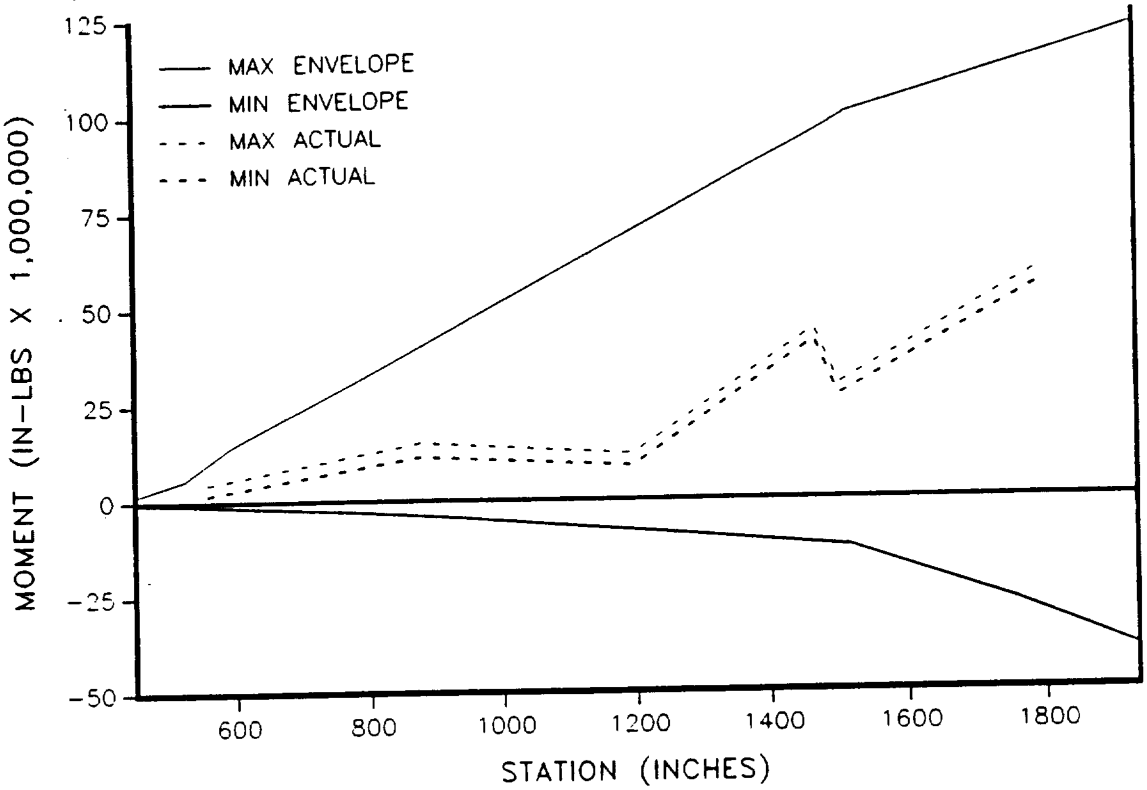

Figure 4.6-78. 360L003 Y Axis Bending Moment--Prelaunch Envelope (LH motor)

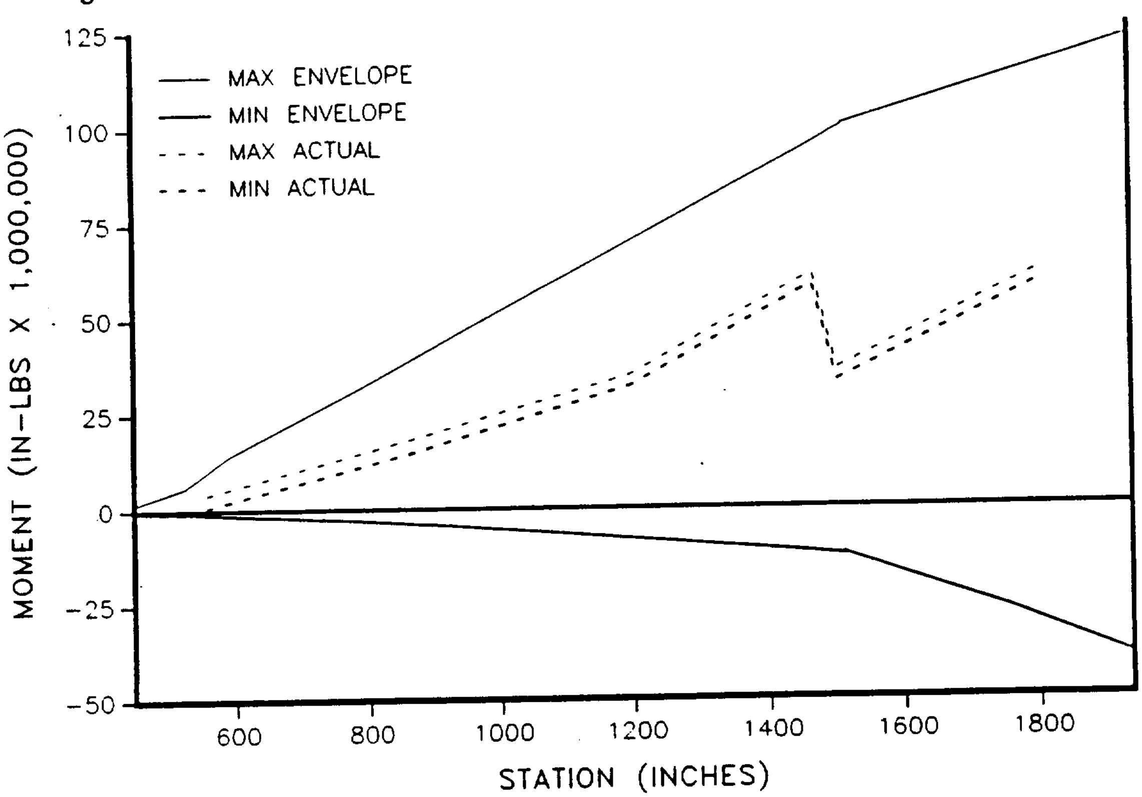

Figure 4.6-79. 360L003 Y Axis Bending Moment--Prelaunch Envelope (RH motor)

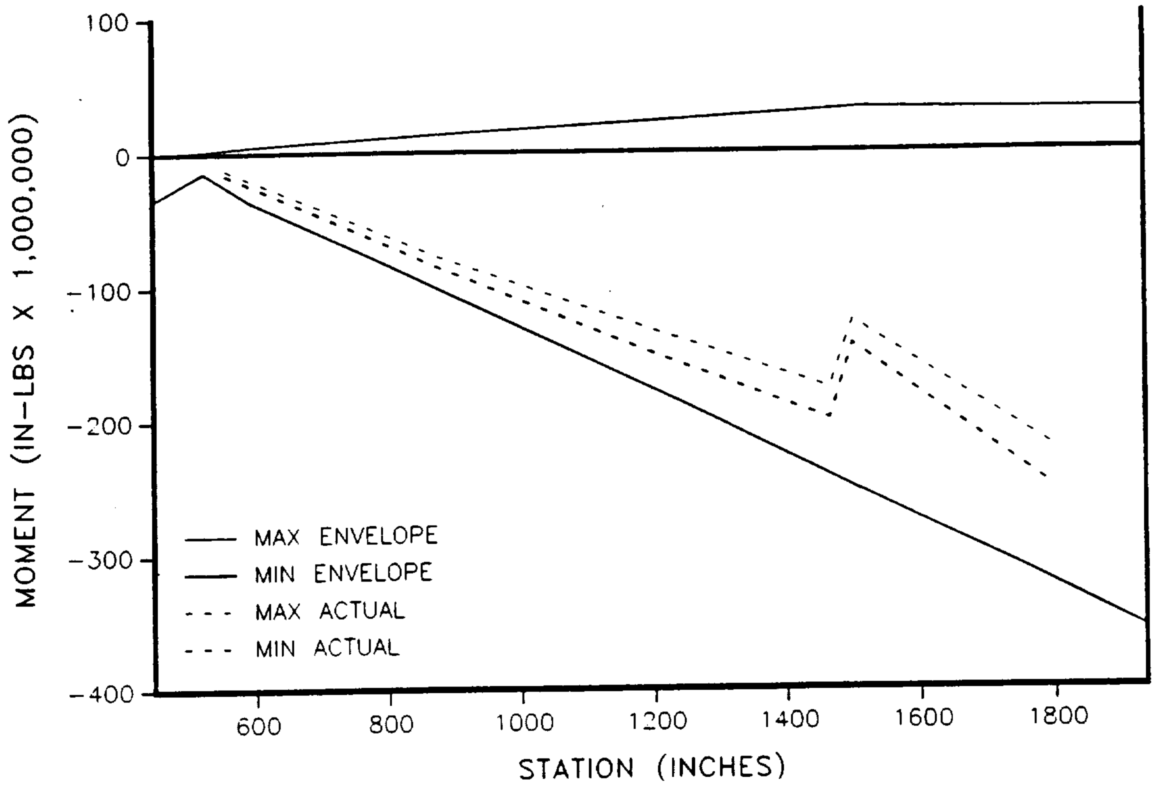

Figure 4.6-80. 360L003 Y Axis Bending Moment--Buildup Envelope (LH motor)

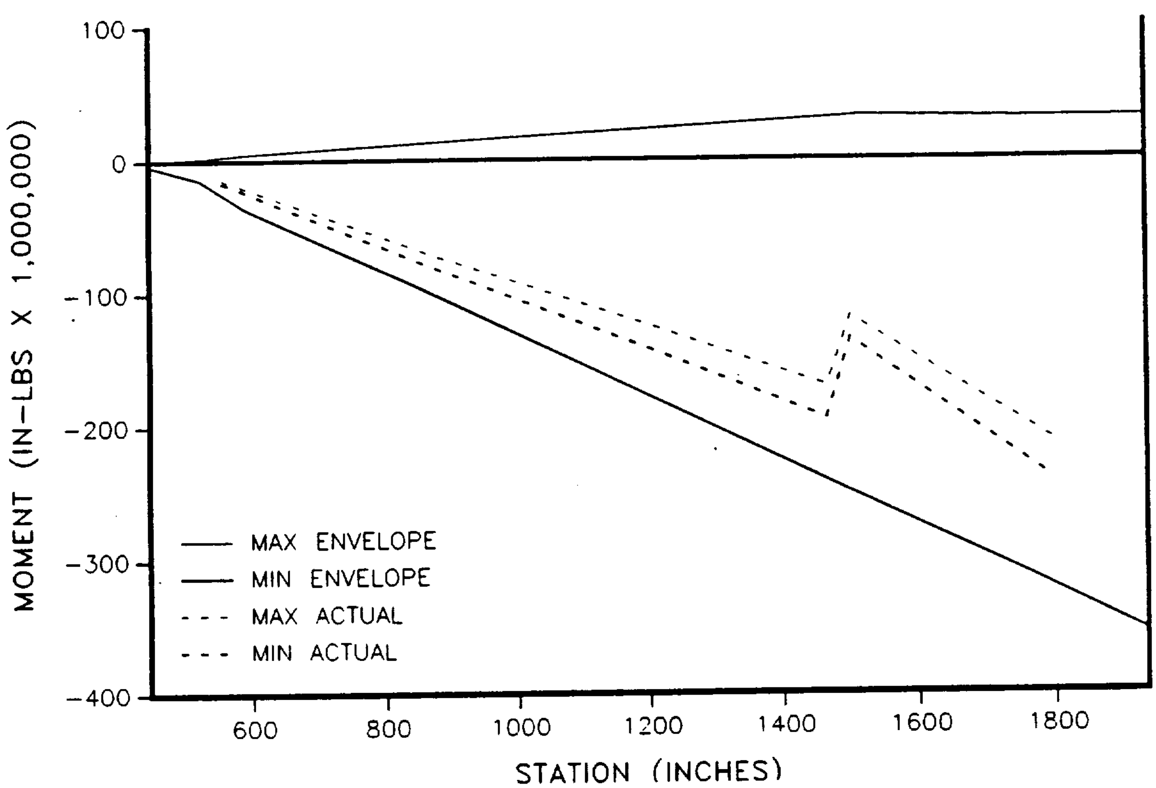

Figure 4.6-81. 360L003 Y Axis Bending Moment--Buildup Envelope (RH motor)

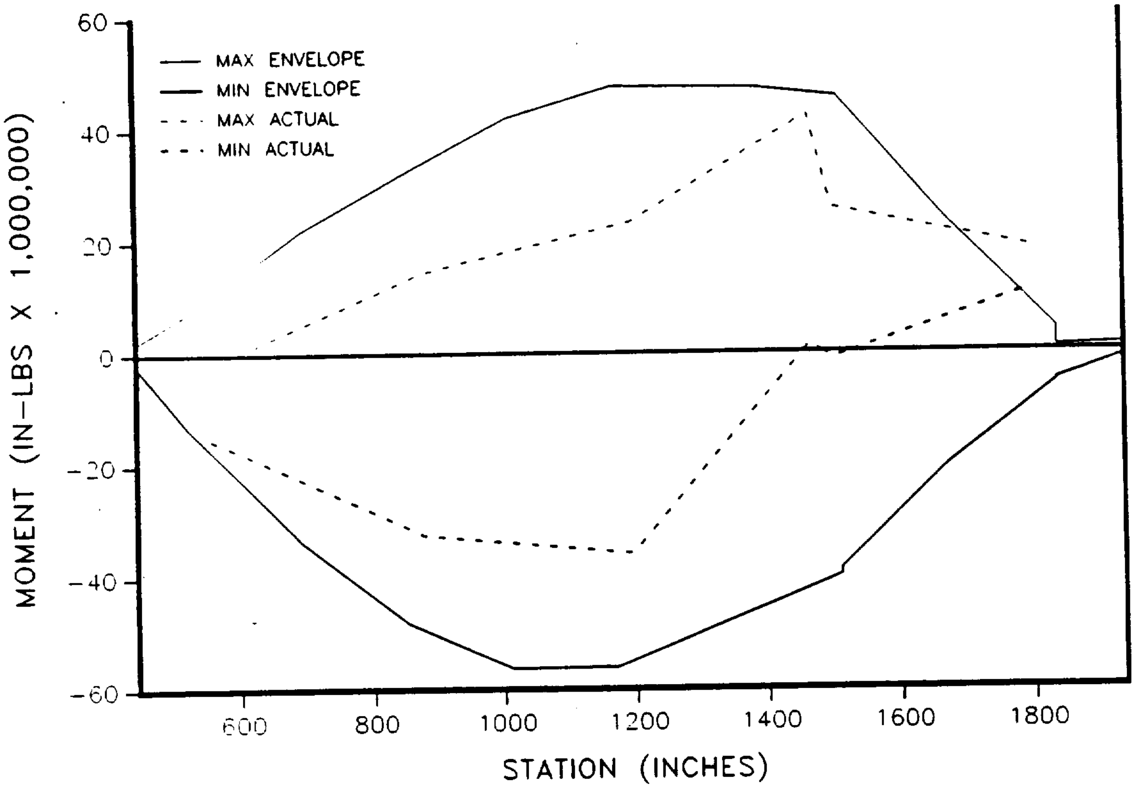

Figure 4.6-82. 360L003 Y Axis Bending Moment--Lift-off Envelope (LH motor)

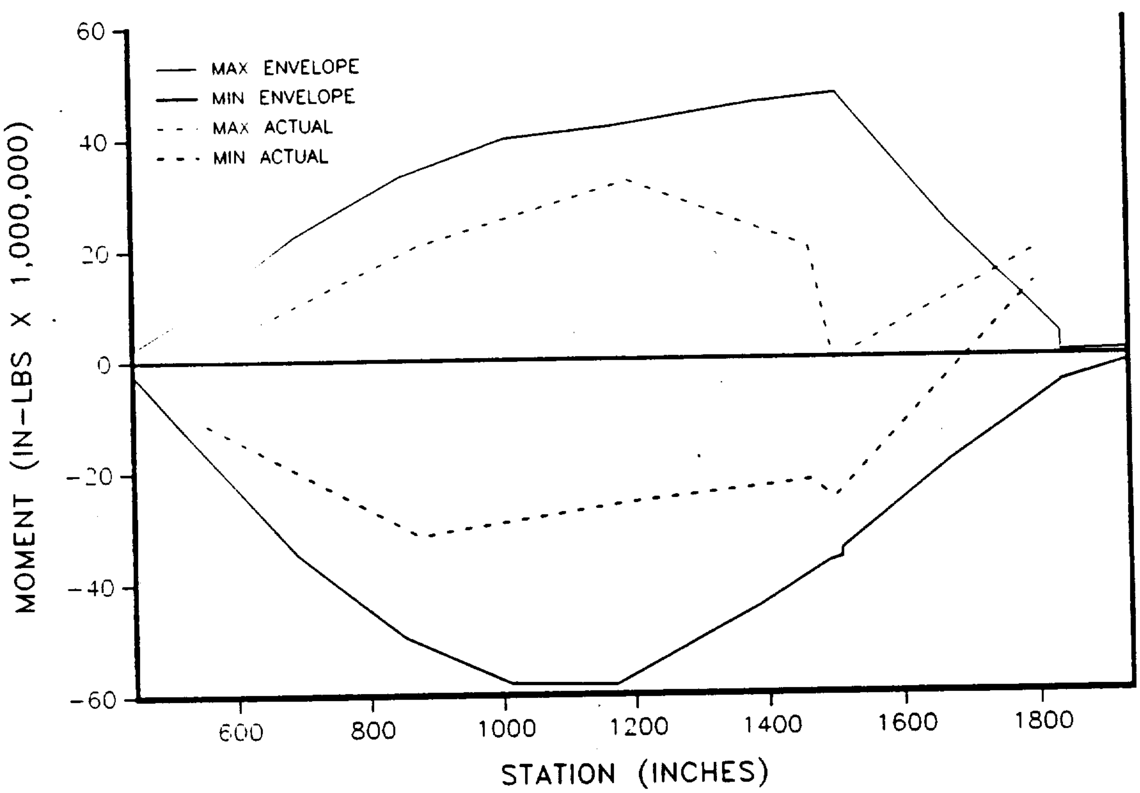

Figure 4.6-83. 360L003 Y Axis Bending Moment--Lift-off Envelope (RH motor)

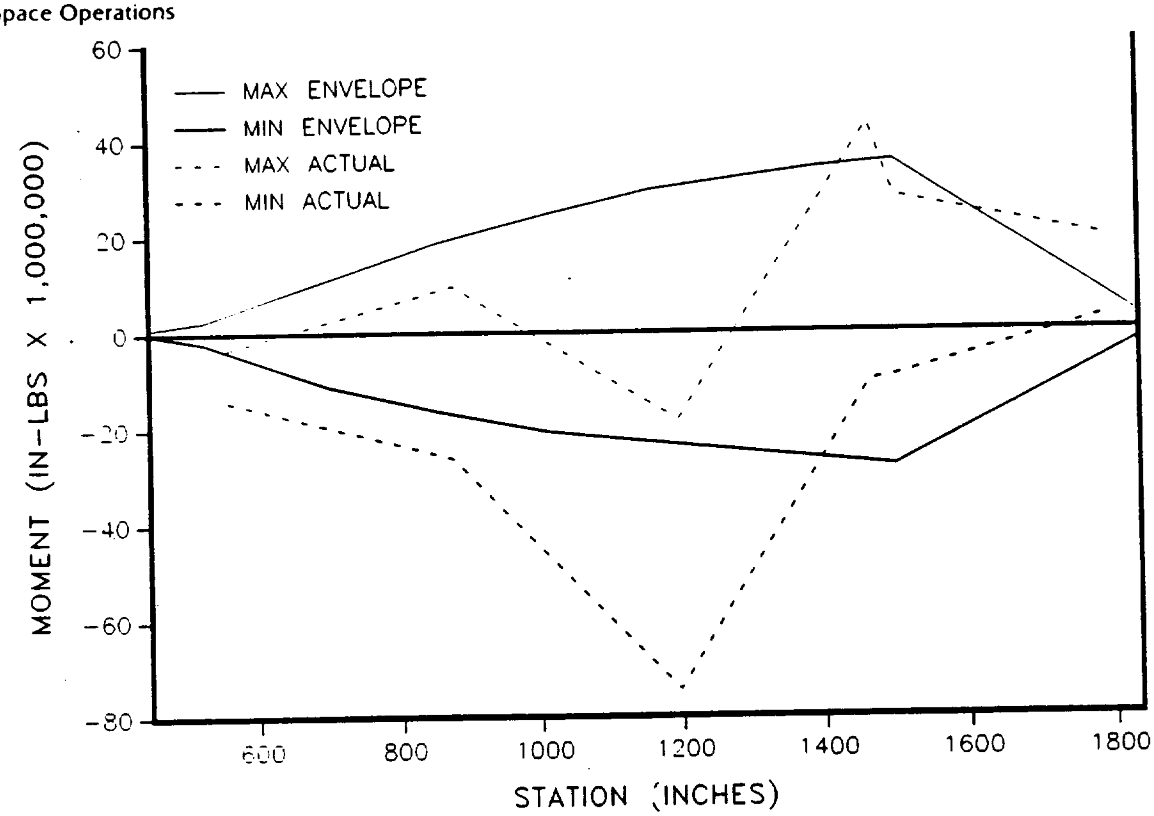

Figure 4.6-84. 360L003 Y Axis Bending Moment--Roll Envelope (LH motor)

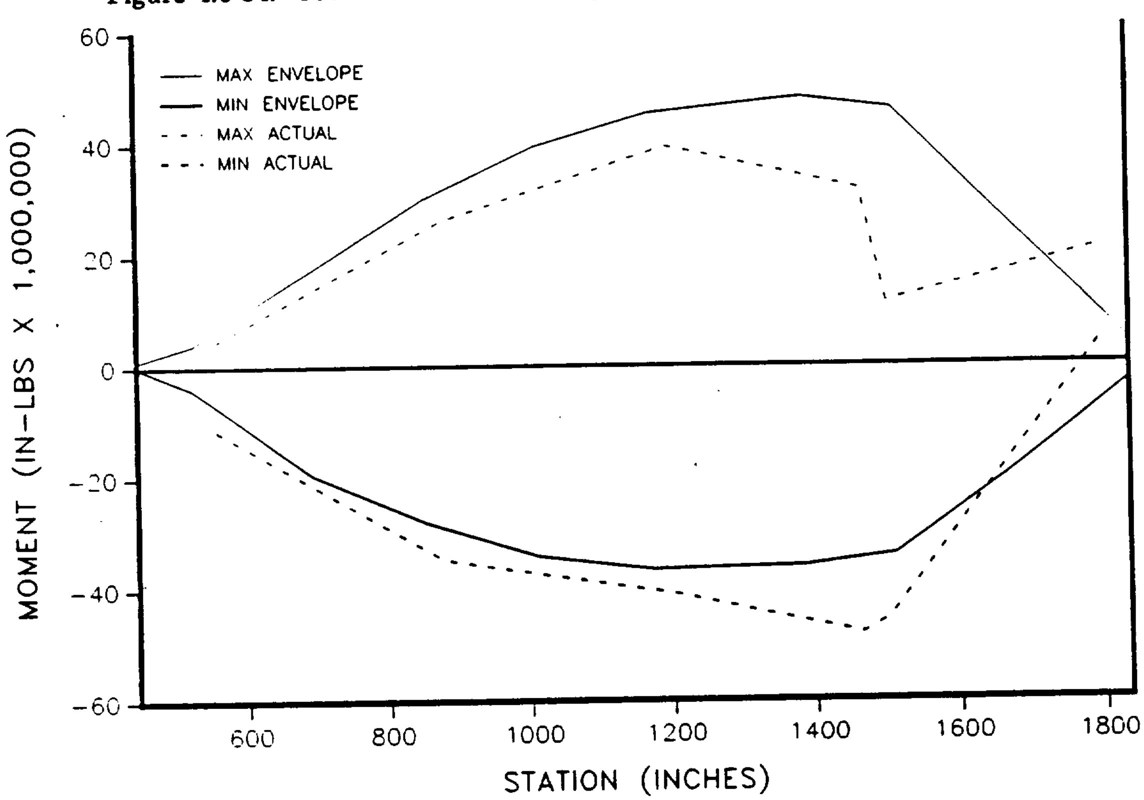

Figure 4.6-85. 360L003 Y Axis Bending Moment--Roll Envelope (RH motor)

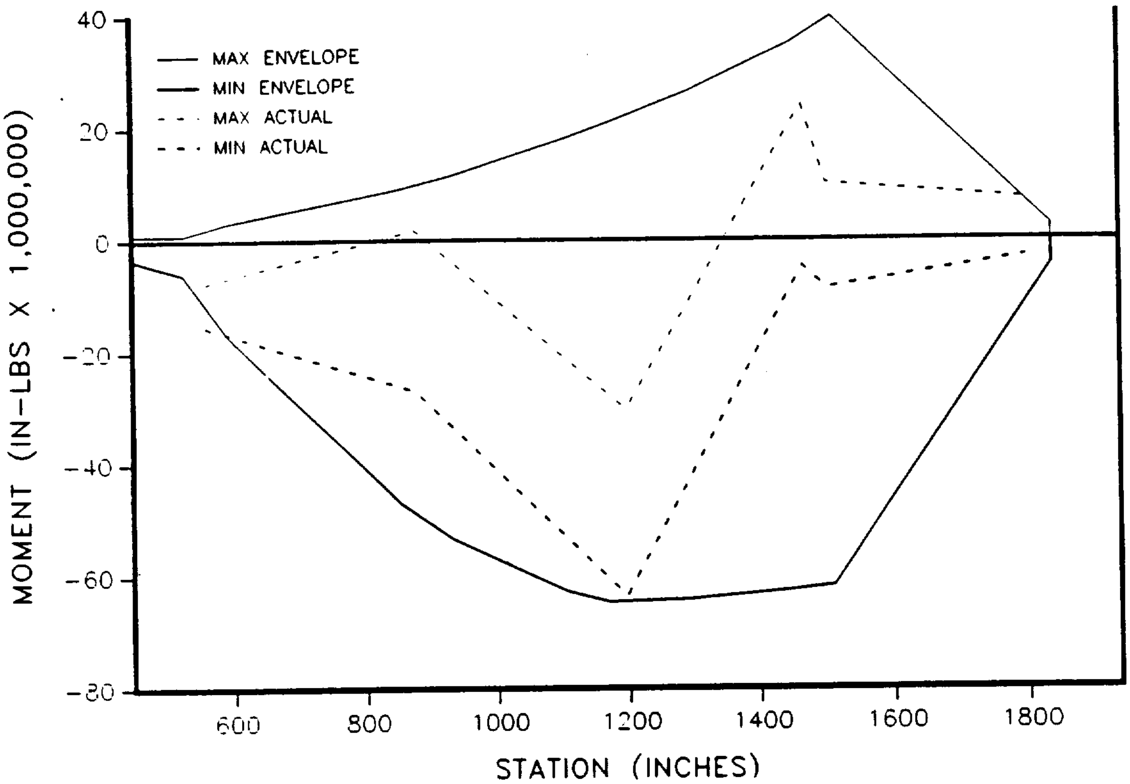

Figure 4.6-86. 360L003 Y Axis Bending Moment--Max Q Envelope (LH motor)

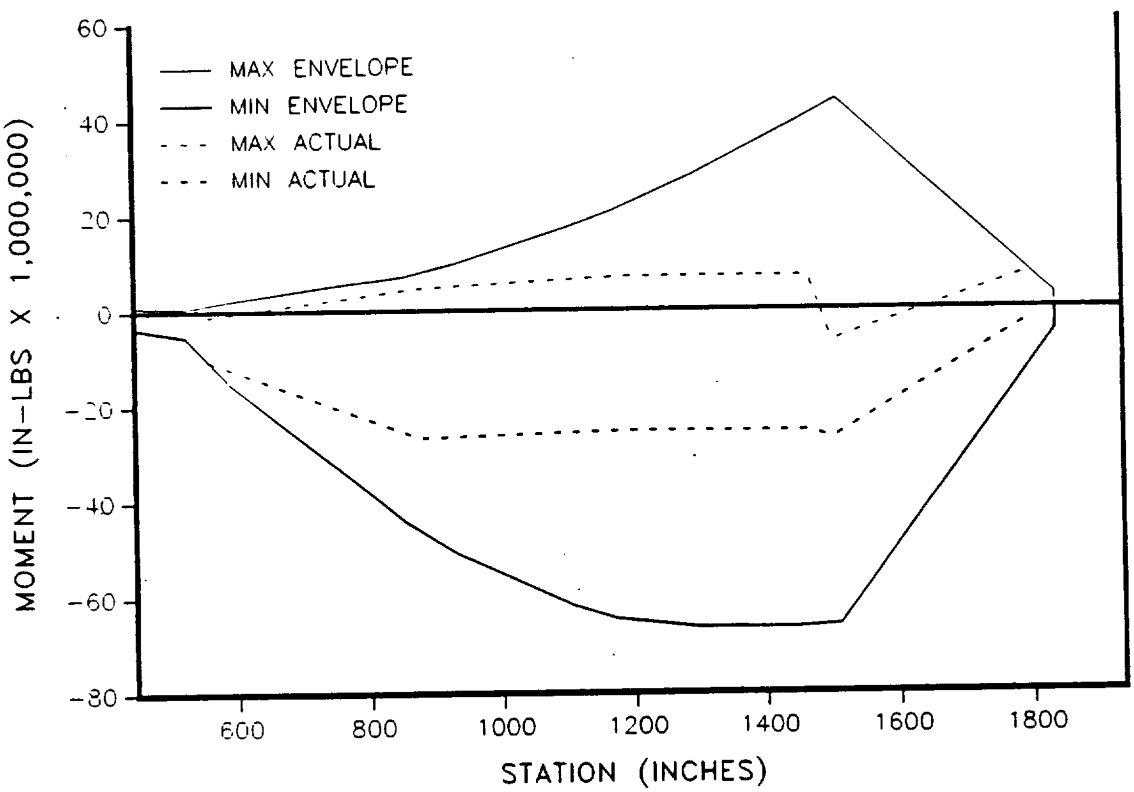

Figure 4.6-87. 360L003 Y Axis Bending Moment--Max Q Envelope (RH motor)

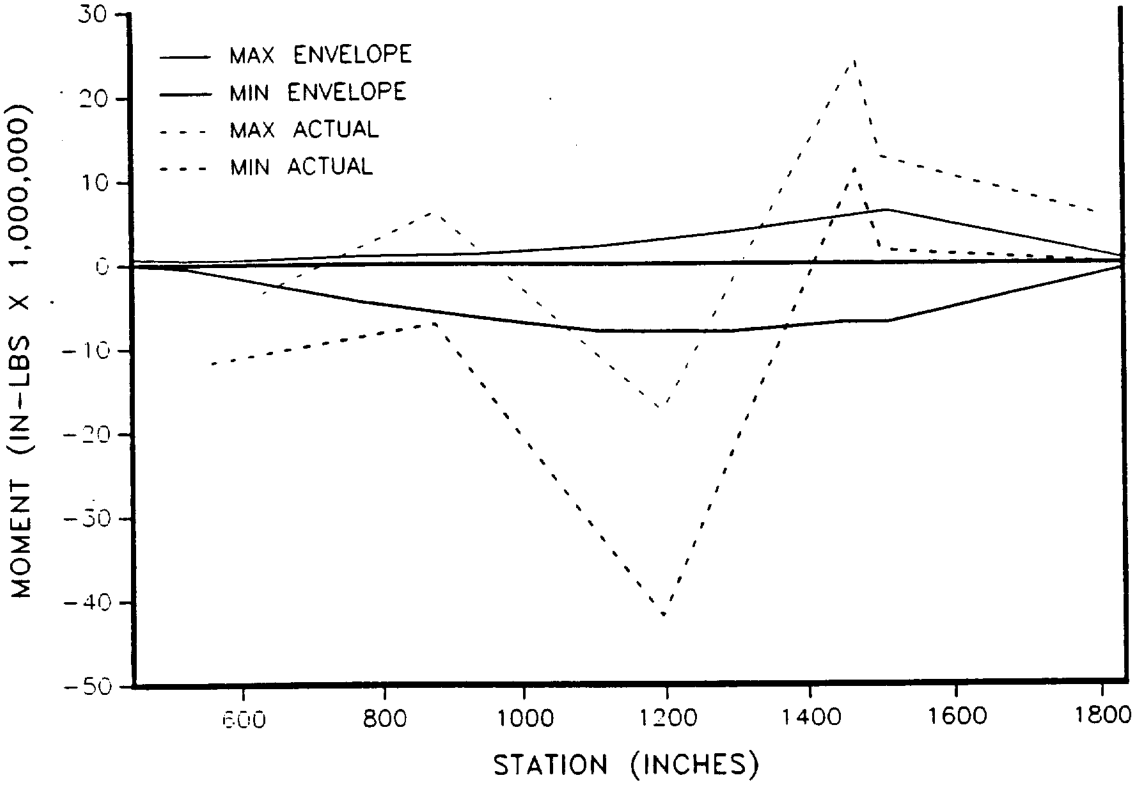

Figure 4.6-88. 360L003 Y Axis Bending Moment--Max G Envelope (LH motor)

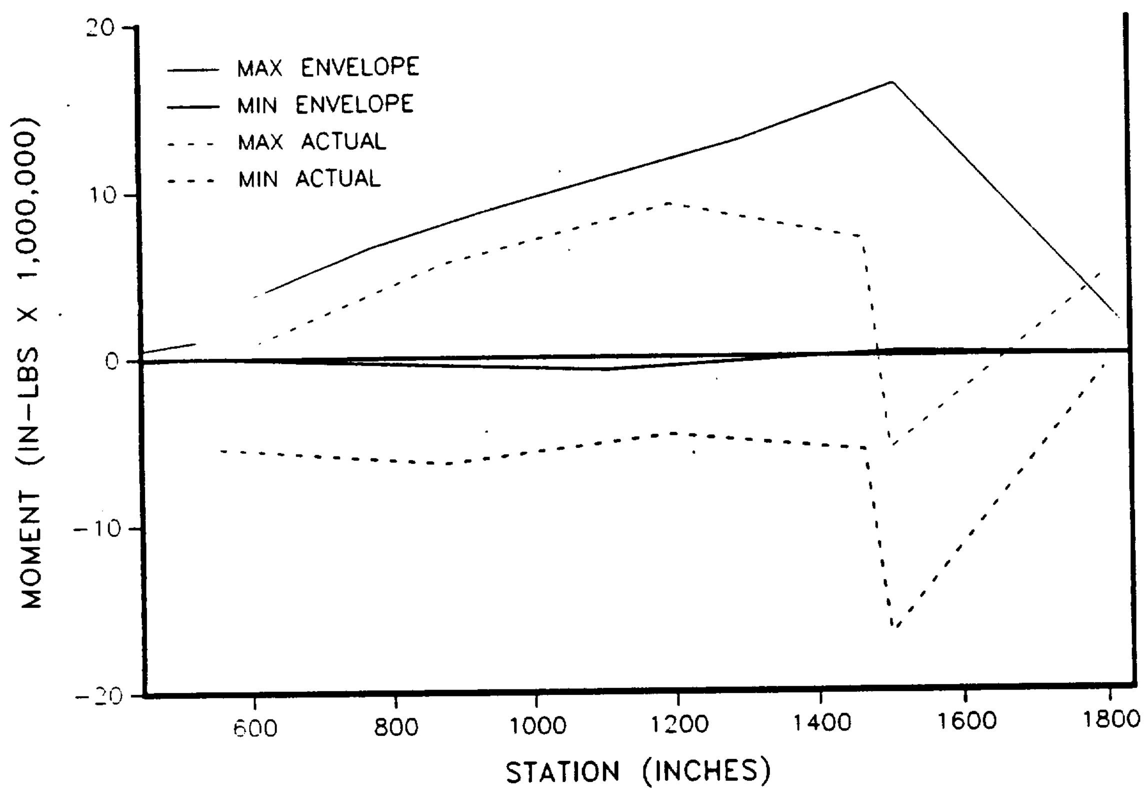

Figure 4.6-89. 360L003 Y Axis Bending Moment--Max G Envelope (RH motor)

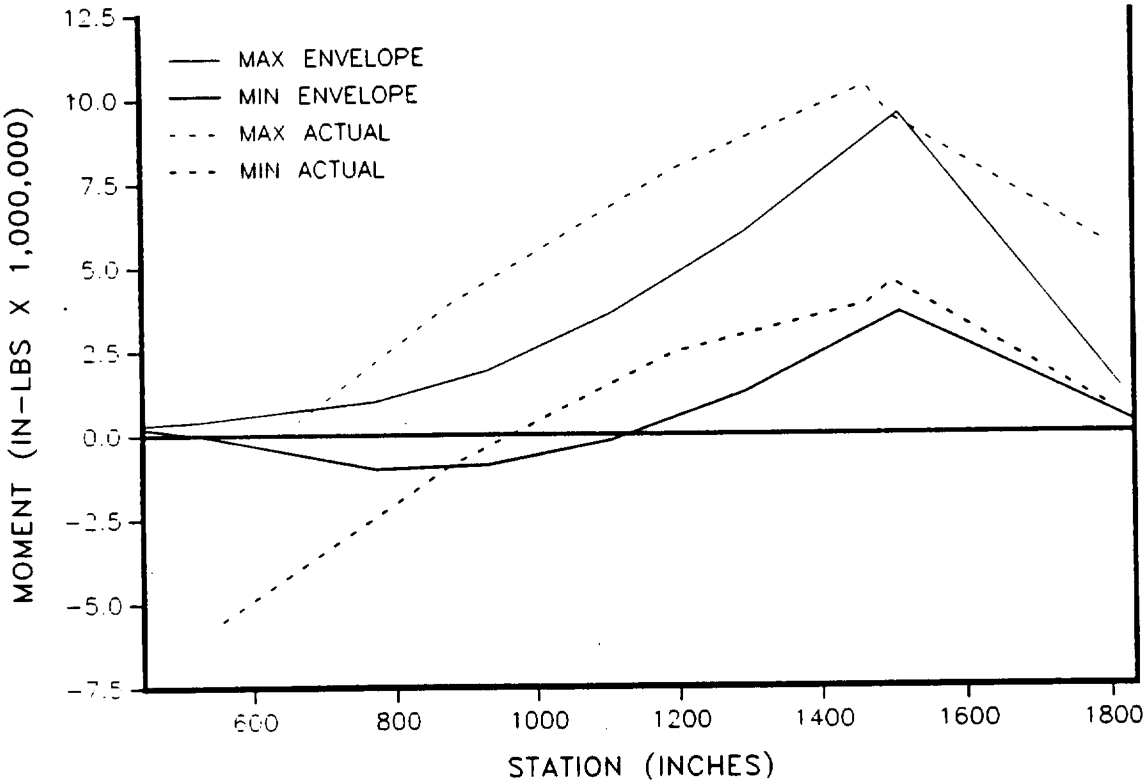

Figure 4.6-90. 360L003 Y Axis Bending Moment--Prestaging Envelope (LH motor)

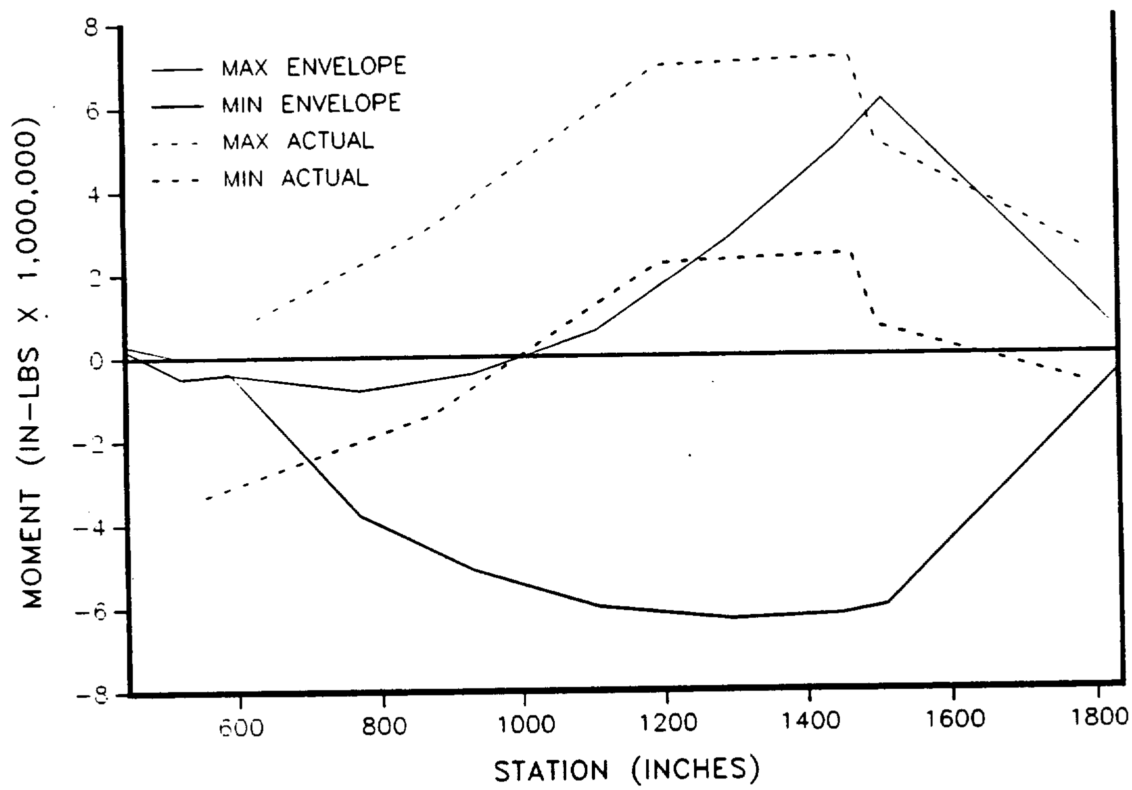

Figure 4.6-91. 360L003 Y Axis Bending Moment--Prestaging Envelope (RH motor)

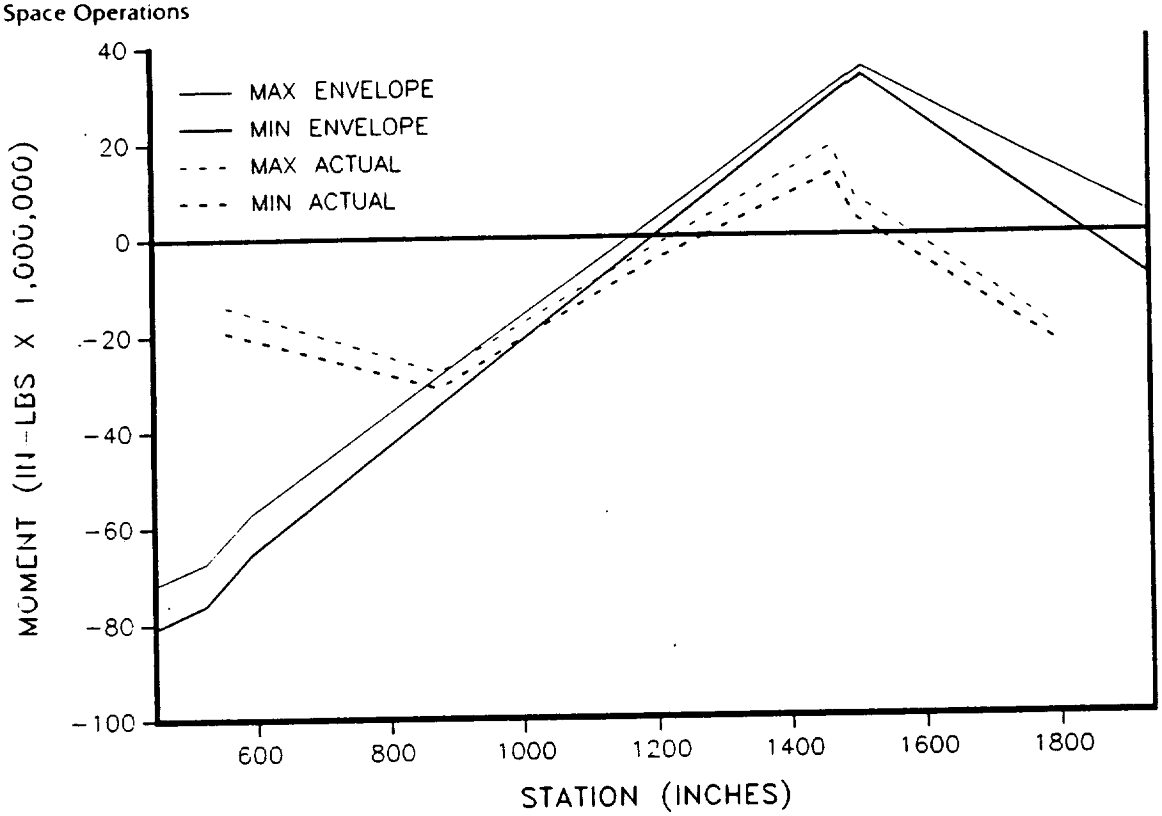

Figure 4.6-92. 360L003 Z Axis Bending Moment--Prelaunch Envelope (LH motor)

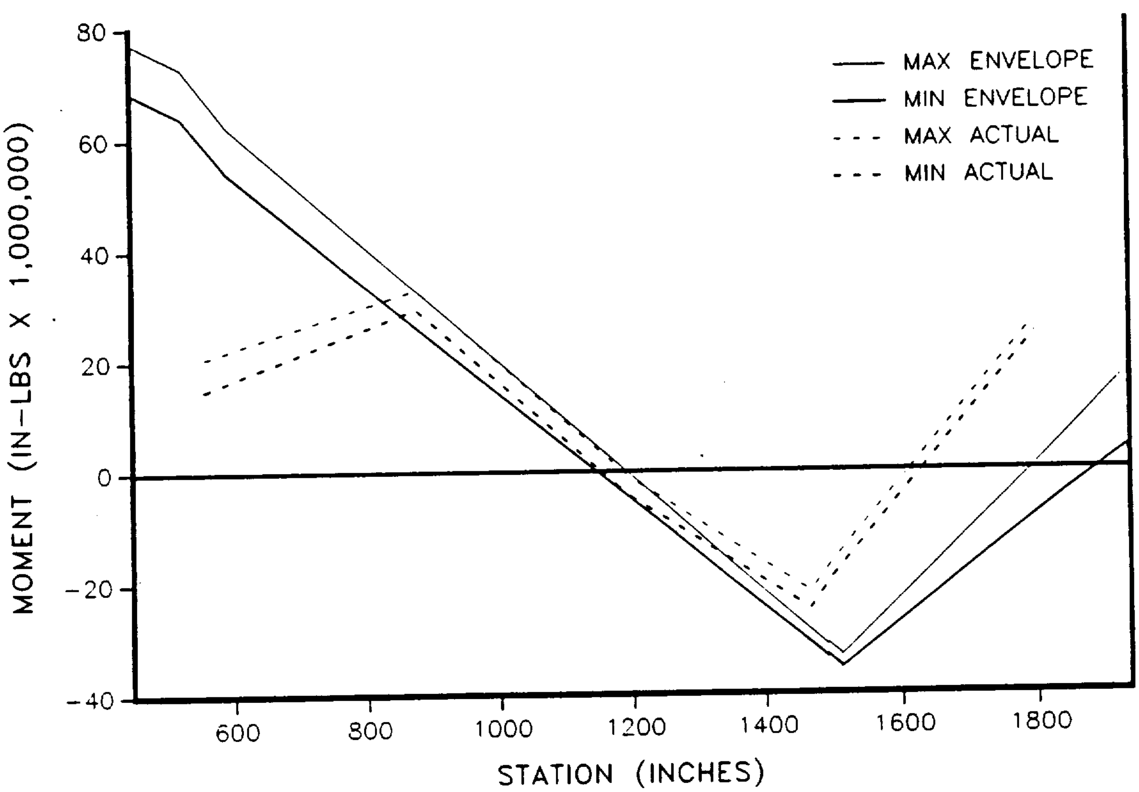

Figure 4.6-93. 360L003 Z Axis Bending Moment--Prelaunch Envelope (RH motor)

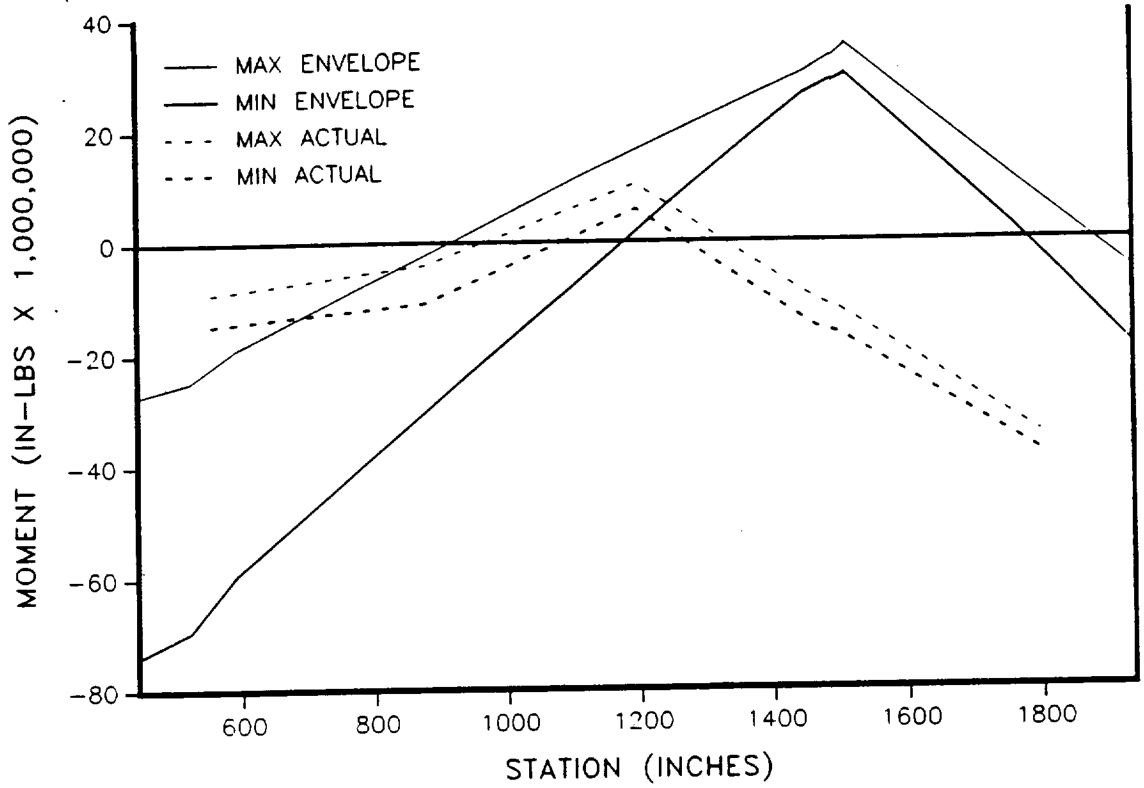

Figure 4.6-94. 360L003 Z Axis Bending Moment--Buildup Envelope (LH motor)

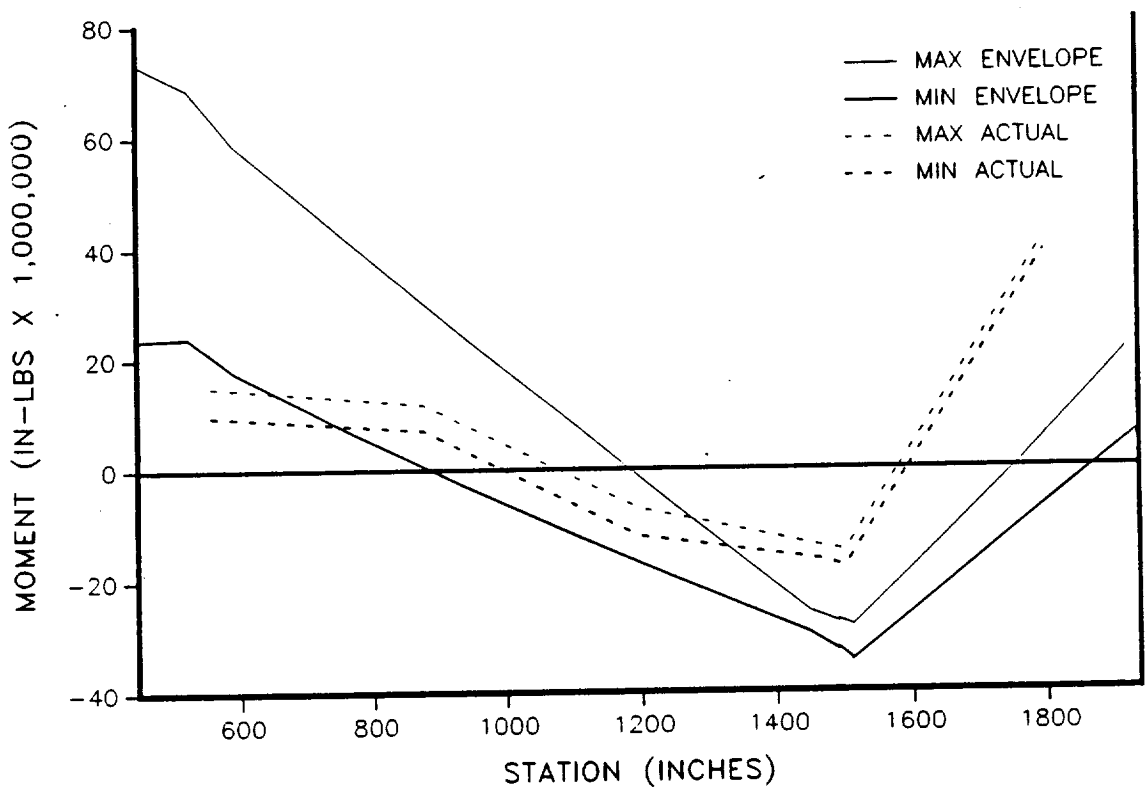

Figure 4.6-95. 360L003 Z Axis Bending Moment--Buildup Envelope (RH motor)

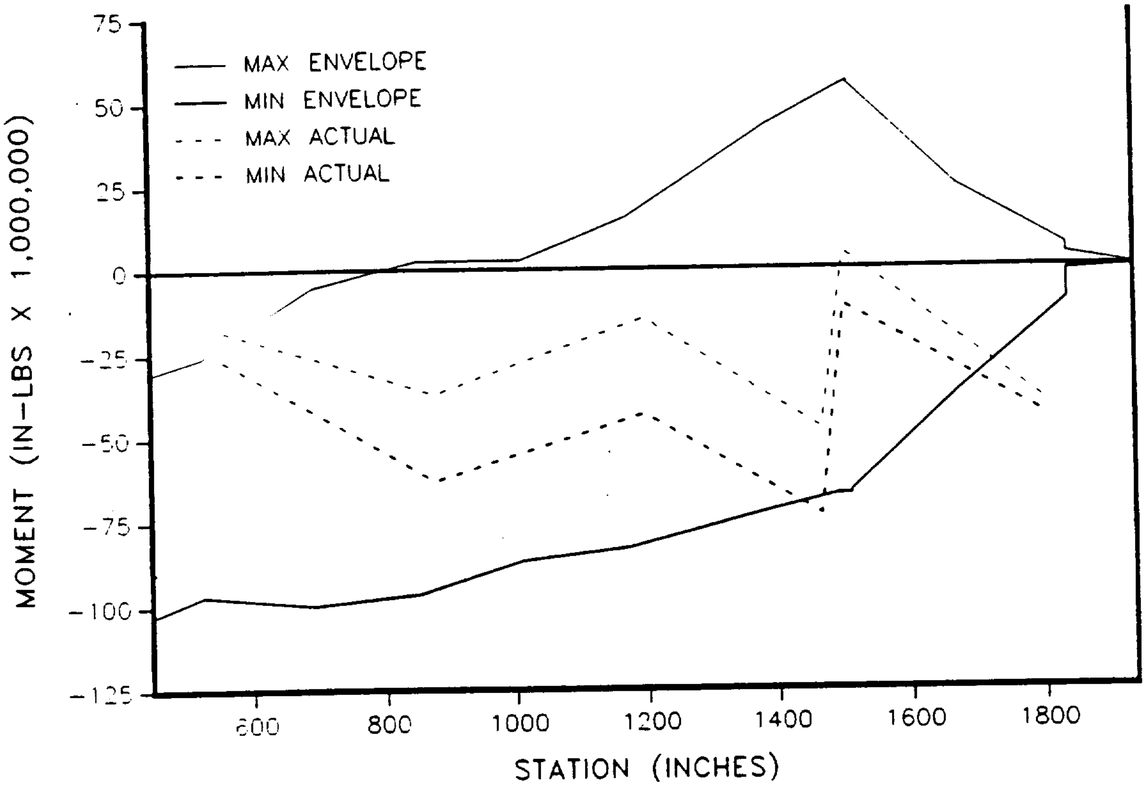

Figure 4.6-96. 360L003 Z Axis Bending Moment--Lift-off Envelope (LH motor)

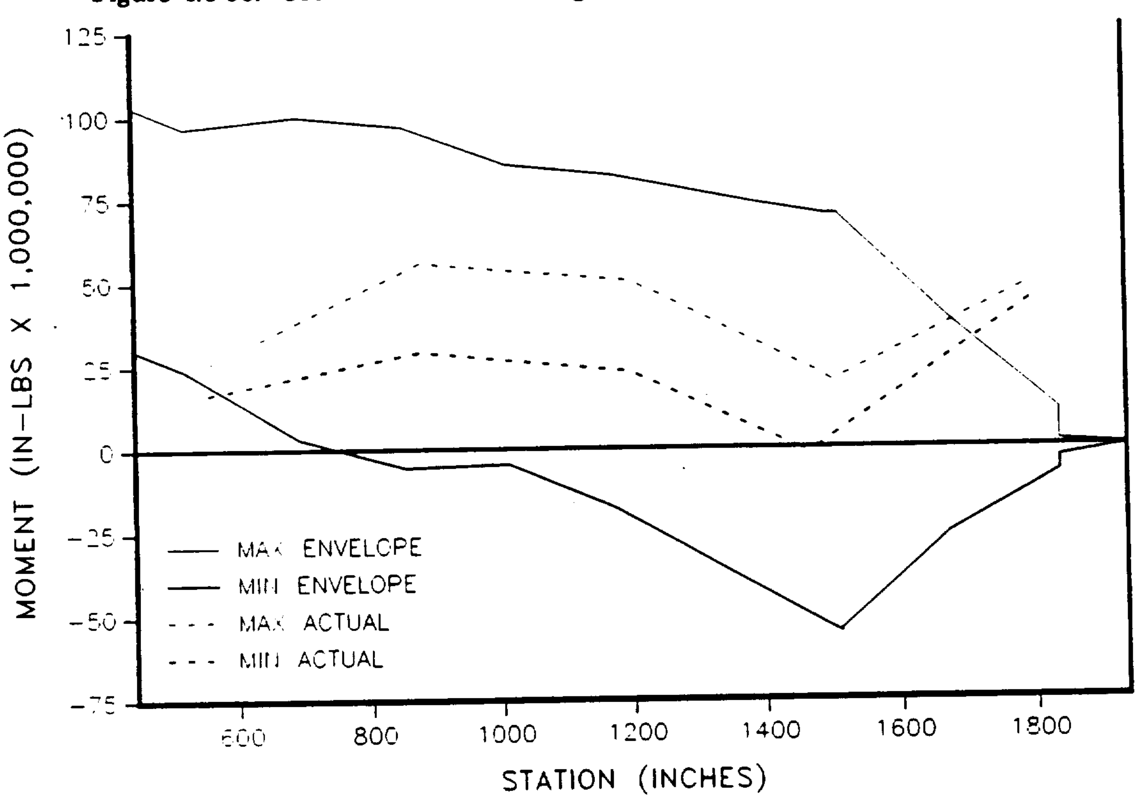

Figure 4.6-97. 360L003 Z Axis Bending Moment--Lift-off Envelope (RH motor)

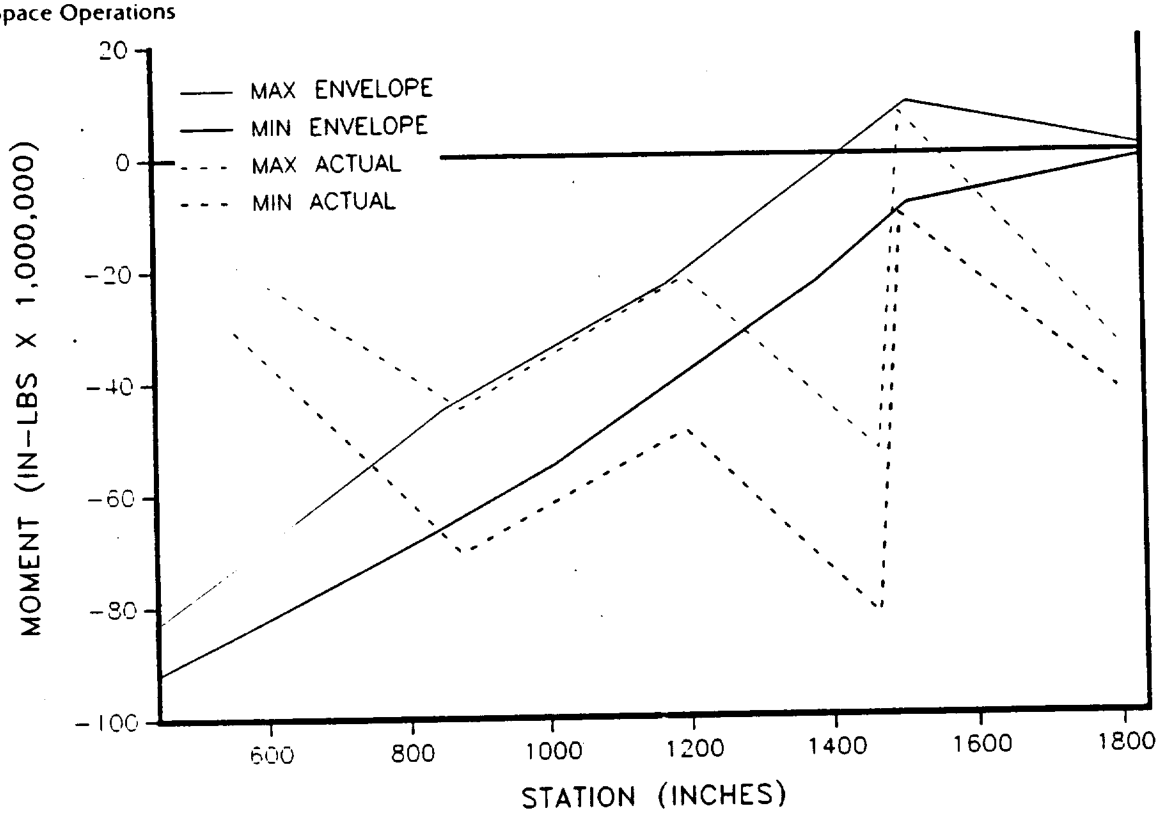

Figure 4.6-98. 360L003 Z Axis Bending Moment--Roll Envelope (LH motor)

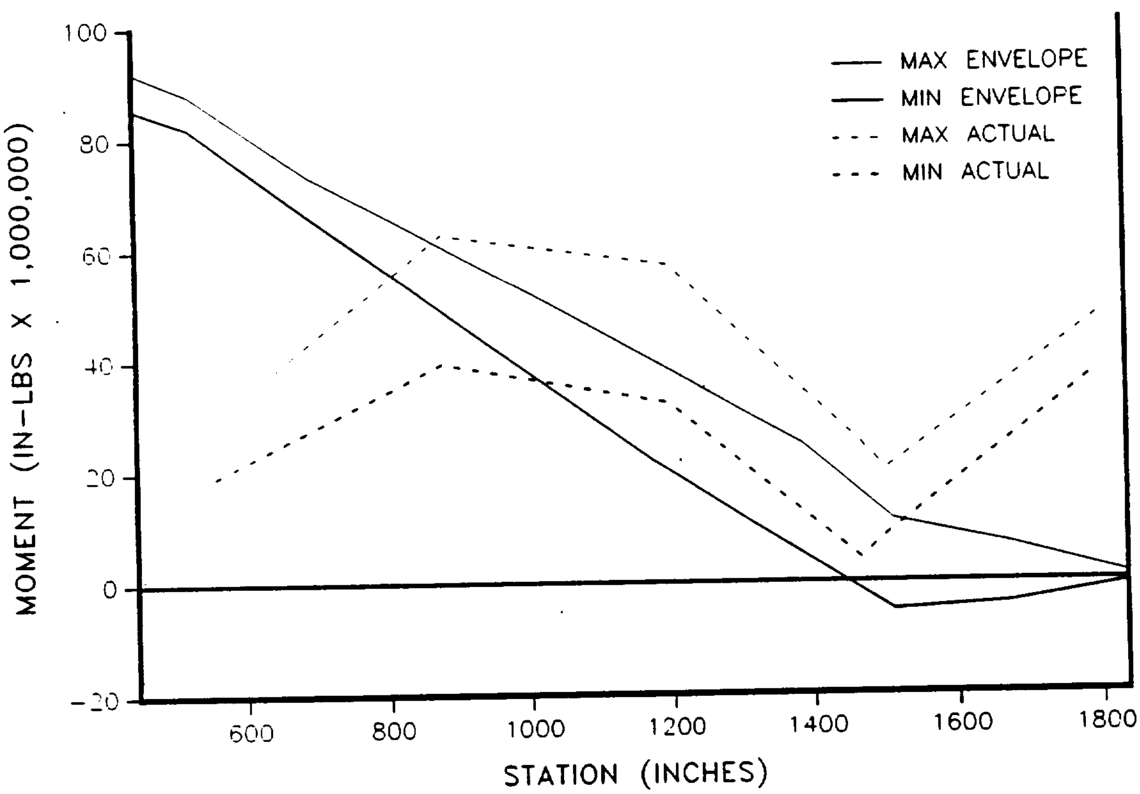

Figure 4.6-99. 360L003 Z Axis Bending Moment--Roll Envelope (RH motor)

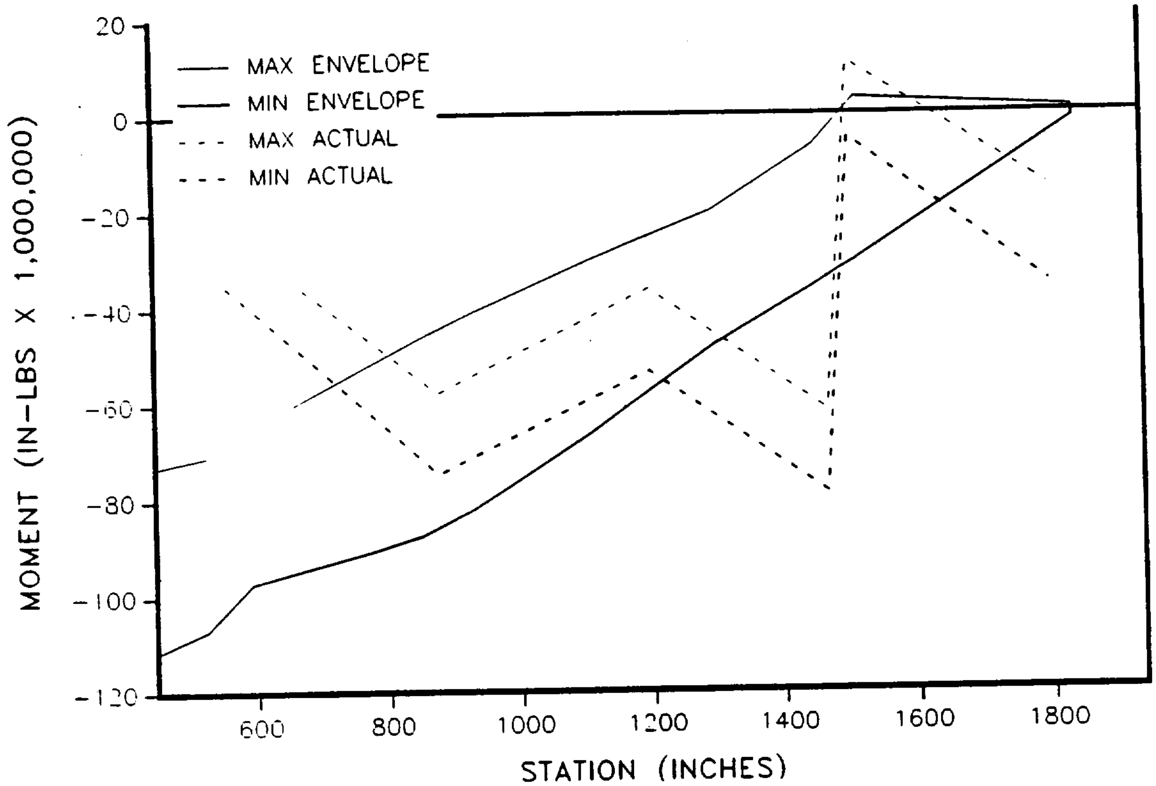

Figure 4.6-100. 360L003 Z Axis Bending Moment--Max Q Envelope (LH motor)

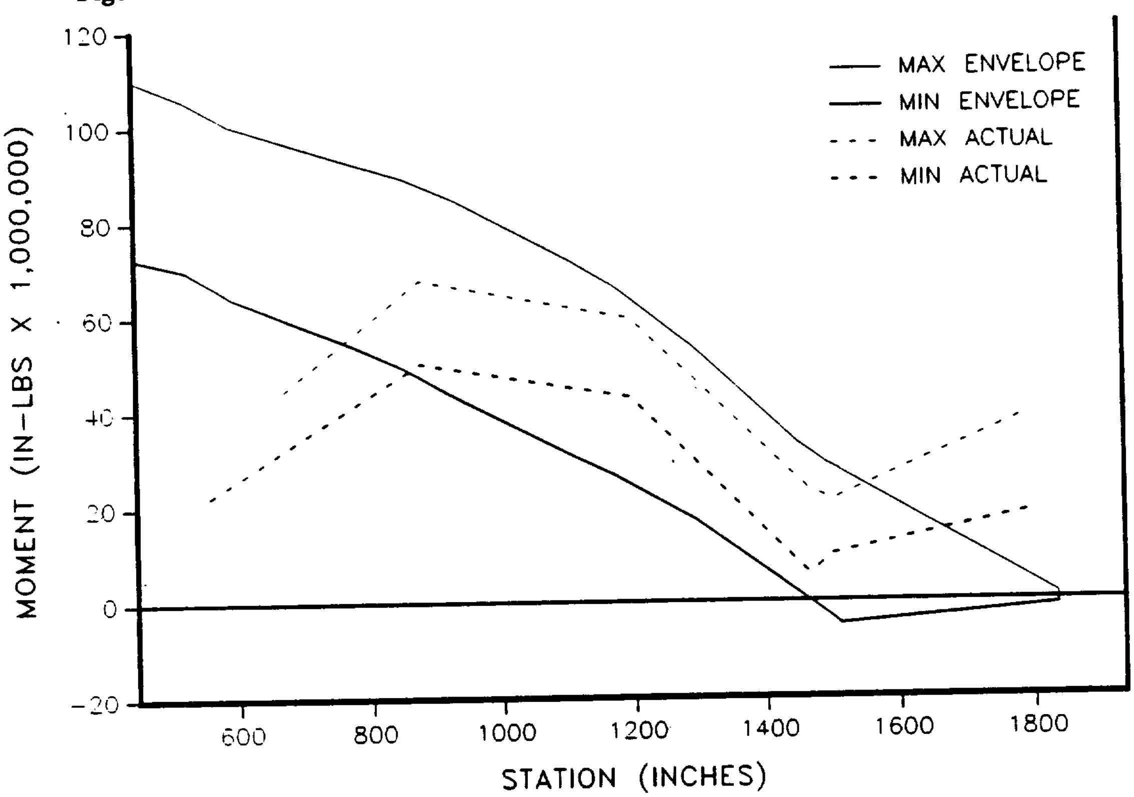

Figure 4.6-101. 360L003 Z Axis Bending Moment--Max Q Envelope (RH motor)

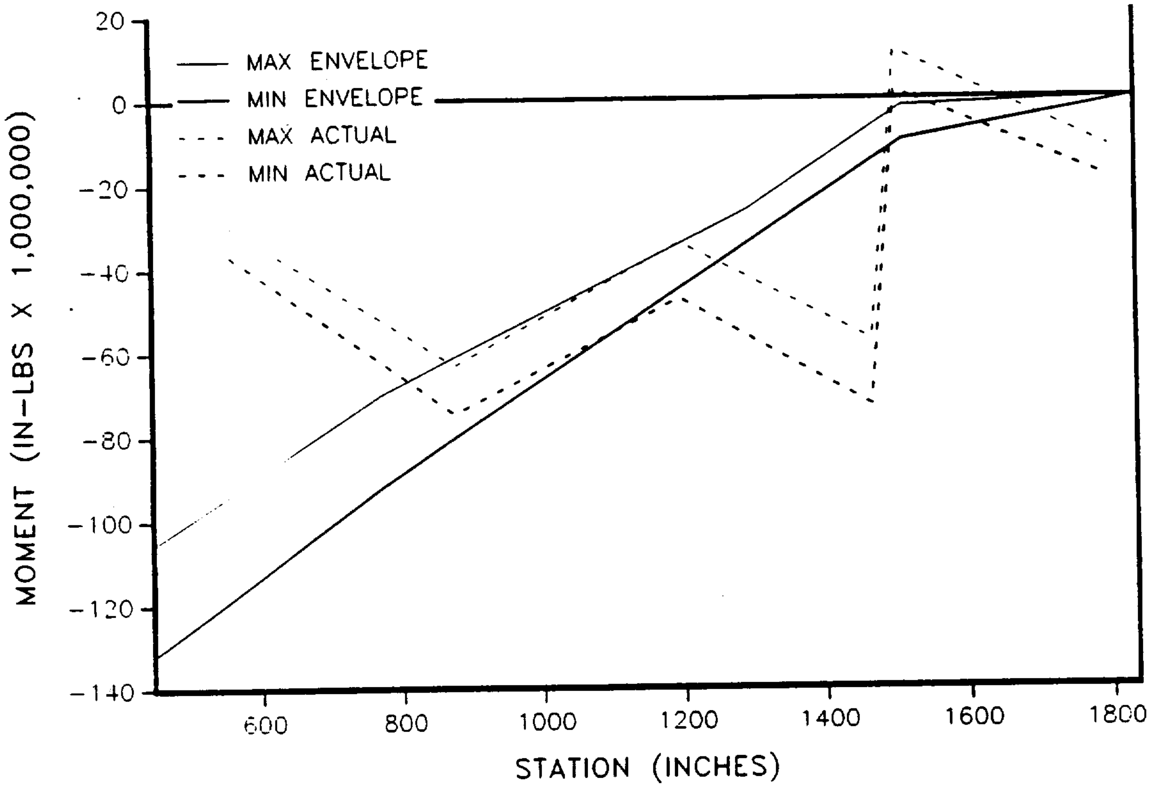

Figure 4.6-102. 360L003 Z Axis Bending Moment--Max G Envelope (LH motor)

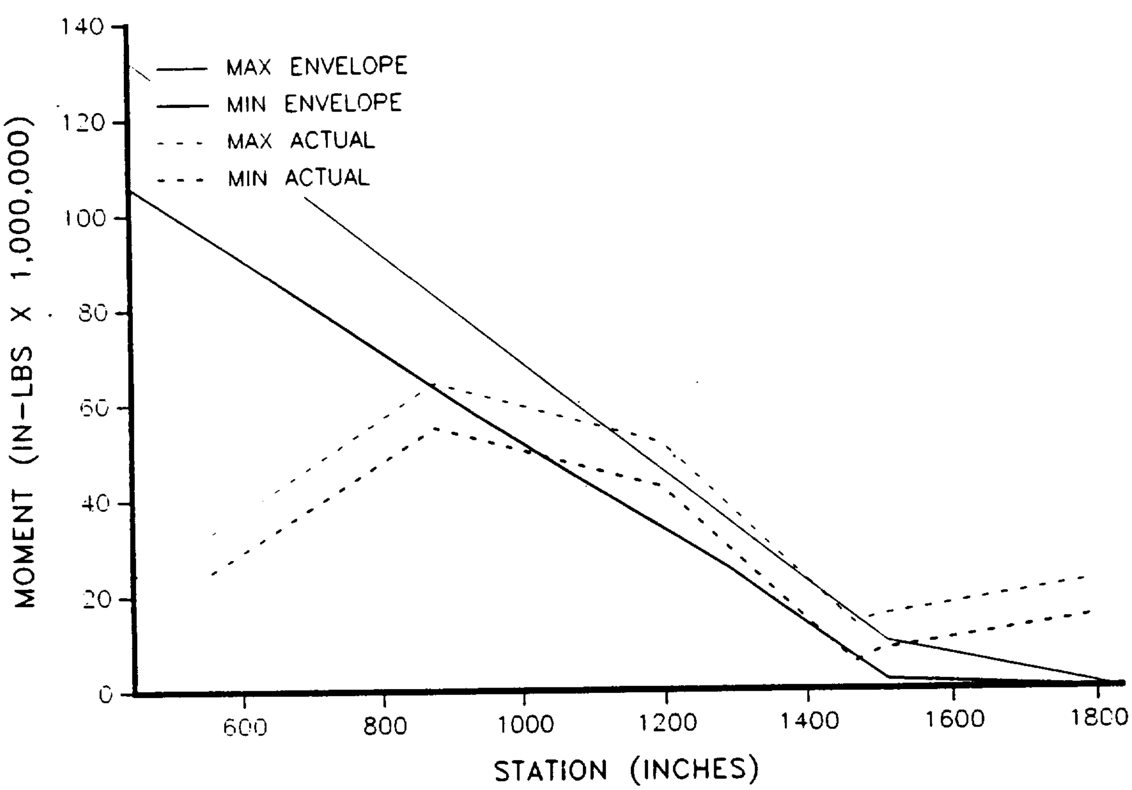

Figure 4.6-103. 360L003 Z Axis Bending Moment--Max G Envelope (RH motor)

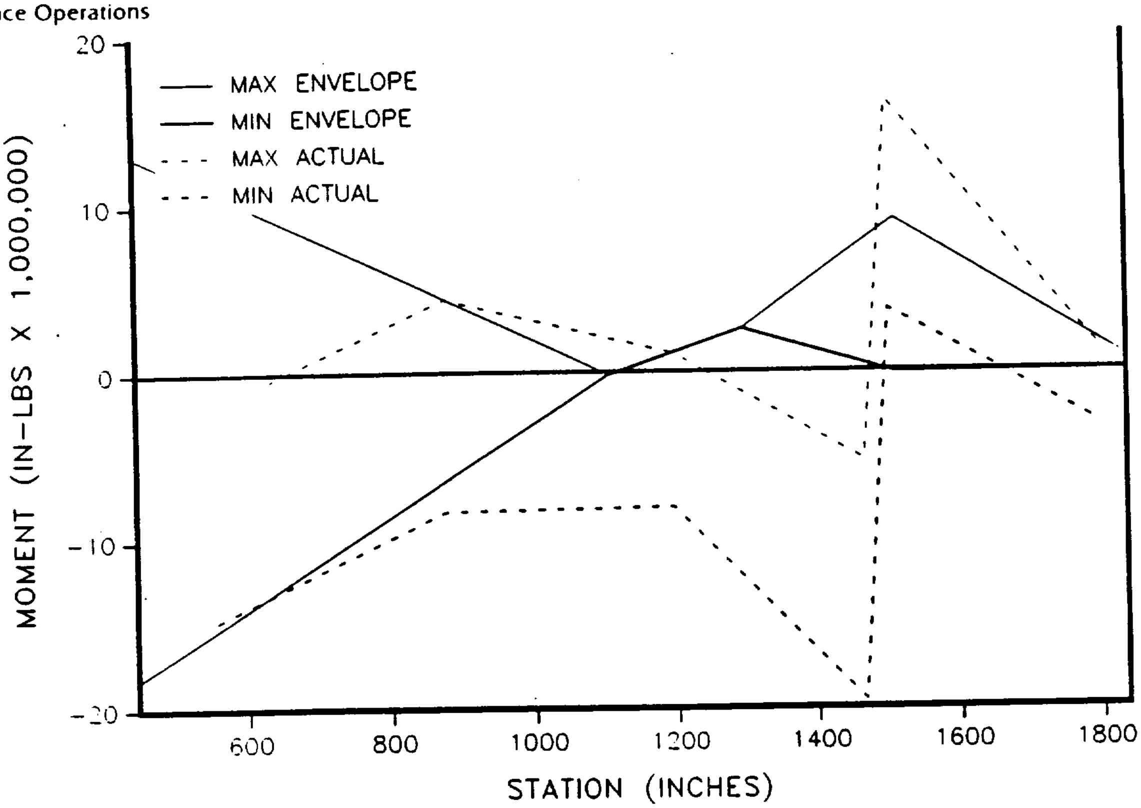

Figure 4.6-104. 360L003 Z Axis Bending Moment--Prestaging Envelope (LH motor)

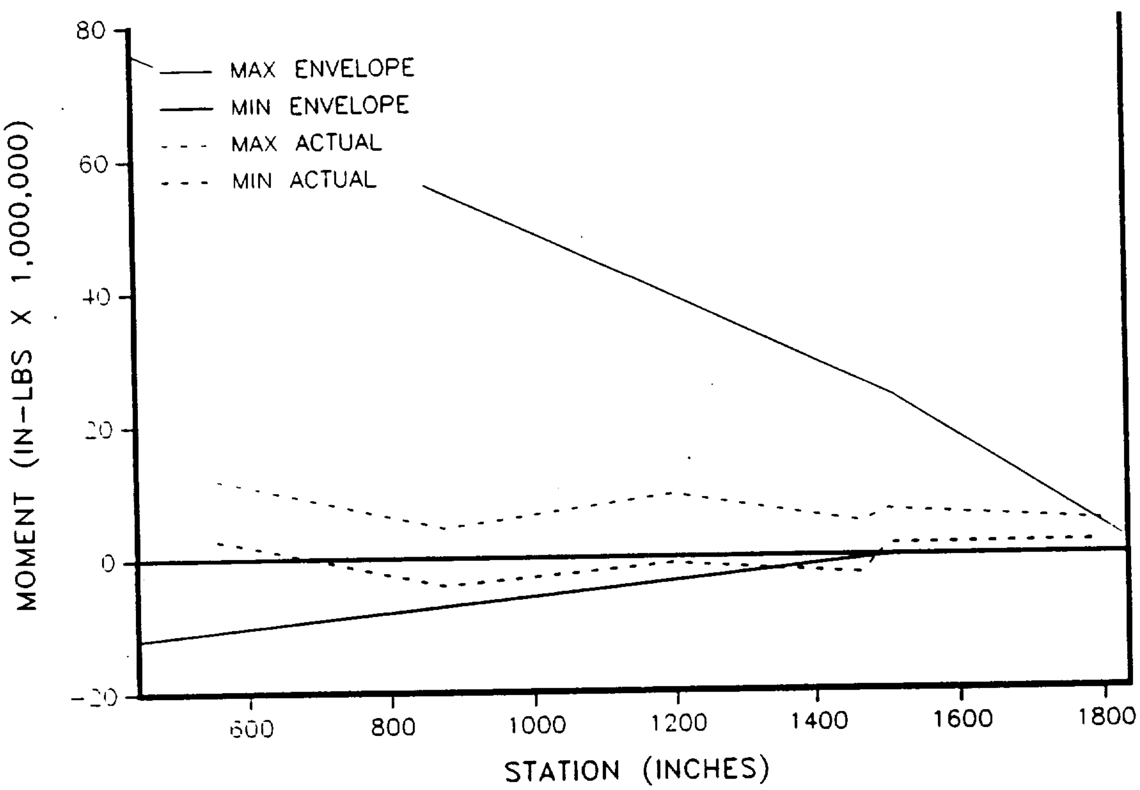

Figure 4.6-105. 360L003 Z Axis Bending Moment--Prestaging Envelope (RH motor)

the data follow the correct trend and are quite close to the envelopes. The tops and bottoms of the SRBs (Stations 556.5 and 1797, respectively) are the most outside of the envelopes.

4.6.3.13 Axial Force. Figures 4.6-106 through 4.6-119 are the axial force envelopes and the 360L003 data plotted as a function of station. These data are near the envelopes.

4.7 RSRM STRUCTURAL DYNAMICS (FEWG REPORT SECTION 2.6.2)

4.7.1 Introduction

Accelerometer data were evaluated to understand the SRM vibration level and frequency, and to verify predicted behavior of the preflight, lift-off, and flight envelopes. Tables 4.7-1 and 4.7-2 list the accelerometers used for data acquisition. Data from 360L003A (LH) (about 290 to 350 sec) were lost during Max Q reentry due to a recording system malfunction. Three channels were also bad (Table 4.7-1). Consequently, the number of available channels used for the RH and LH SRB dynamic evaluation was 17 and 16, respectively.

4.7.2 Vibration Amplitudes

The time history data were plotted using a sample rate of 320 sps. Generally, during SRM burn the vibration in the nozzle area is higher than that in the case, which was expected and is normal. As compared with 360L002 (STS-27), 360L003 (STS-29) has generally higher vibration amplitudes. For example, Channel B08D8175A (Station 839, axial direction) experiences a 12g amplitude. In the radial direction, the high-amplitude (5g) vibrations observed in 360L002 were exceeded by the recorded data for 360L003 and measured 8g, as shown in the B08D8166A and B08D7166A time history plots (Figures 4.7-1 and 4.7-2).

The dominant vibration frequency is 200 to 300 Hz for data from 0 to 1 sec after SRB ignition. This dominant frequency occurred for almost every channel, and the peak amplitudes of vibration occurred at approximately 0.2 to 0.4 sec (which is before the internal pressure is fully established). The resulting effects of these high-amplitude vibrations on the SRB, such as stress level, high cycle fatigue, etc., are still under investigation.

Time history plots were also used to identify the SRB loading events during reentry and can be seen in Figures 4.7-1 through 4.7-36. It is important to observe that, during reentry, the SRB is subjected to another extremely severe loading environment--Max Q reentry, which occurred from 300 to 340 sec. During this time period, the vibration level exceeded the 15g measurement limit. Not only is the vibration amplitude high, but the vibration duration is also long during this severe loading environment. The frequency content for Max Q reentry was computed to be flat-ranged from 10 to 200 Hz, which is very typical for white-type aerodynamic wind loads. The possible effects of Max Q reentry on the SRB (such as fretting) are still under investigation.

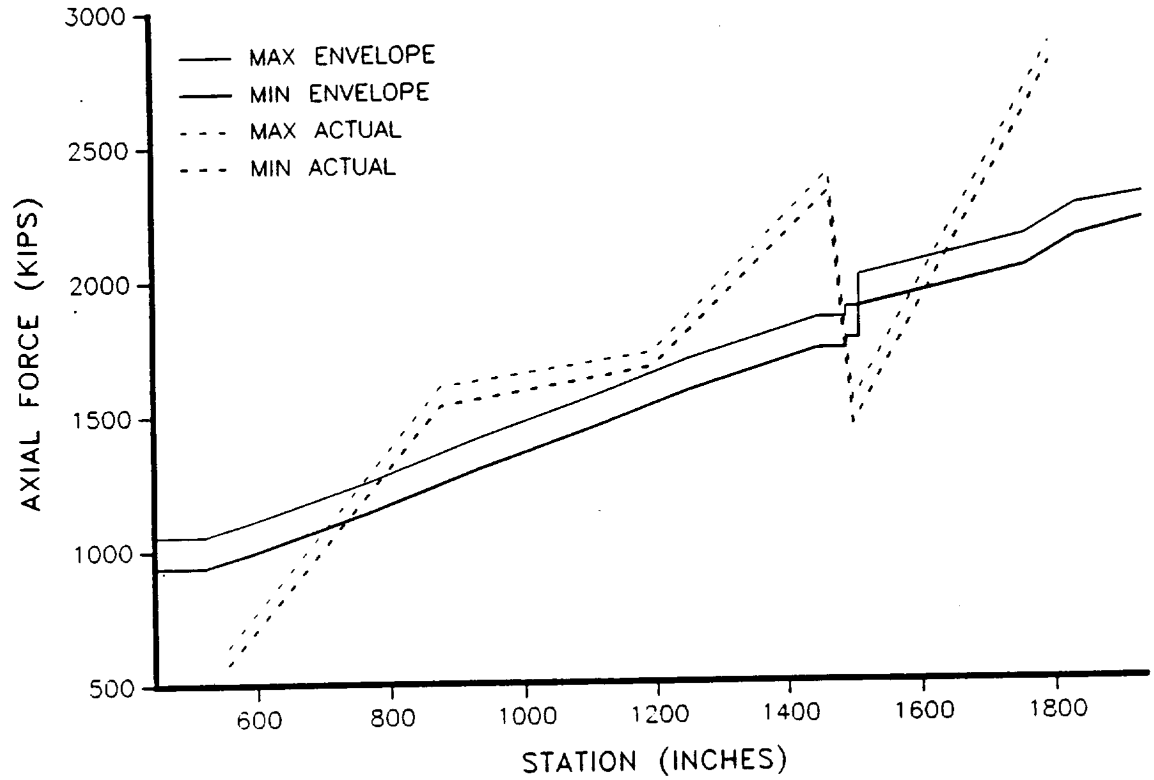

Figure 4.6-106. 360L003 Axial Force--Prelaunch Envelope (LH motor)

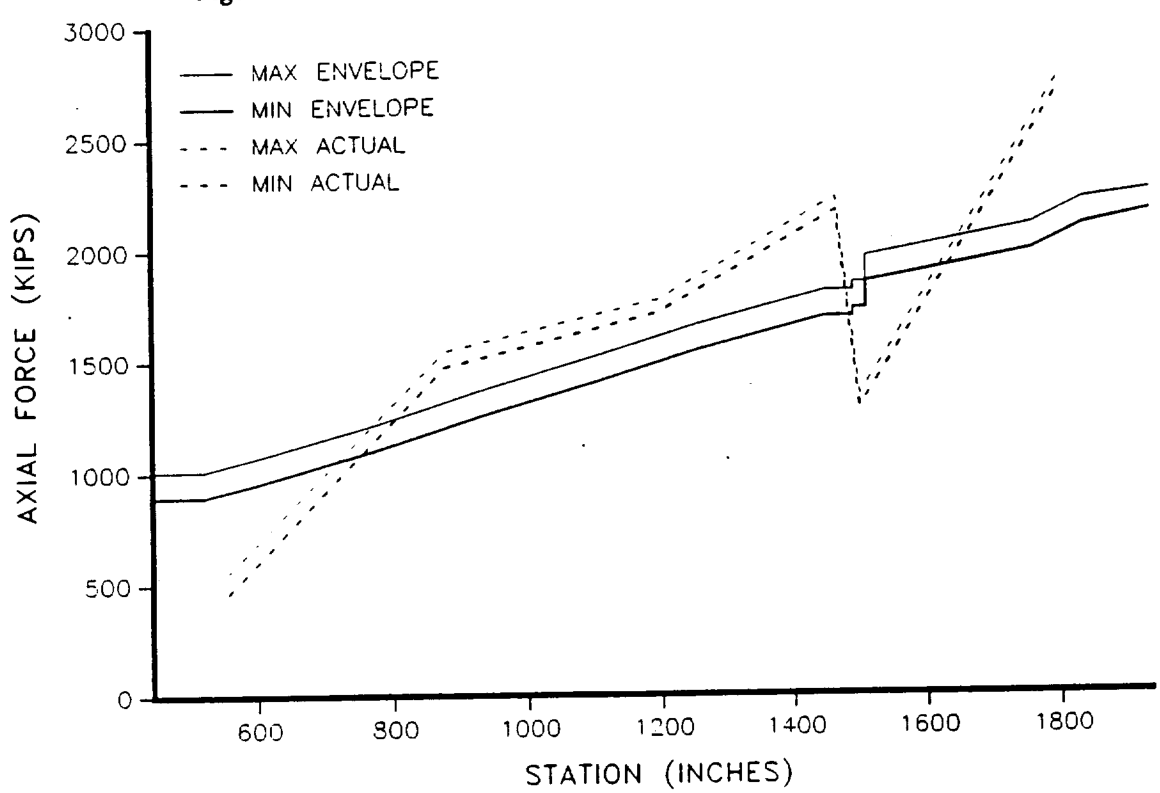

Figure 4.6-107. 360L003 Axial Force--Prelaunch Envelope (RH motor)

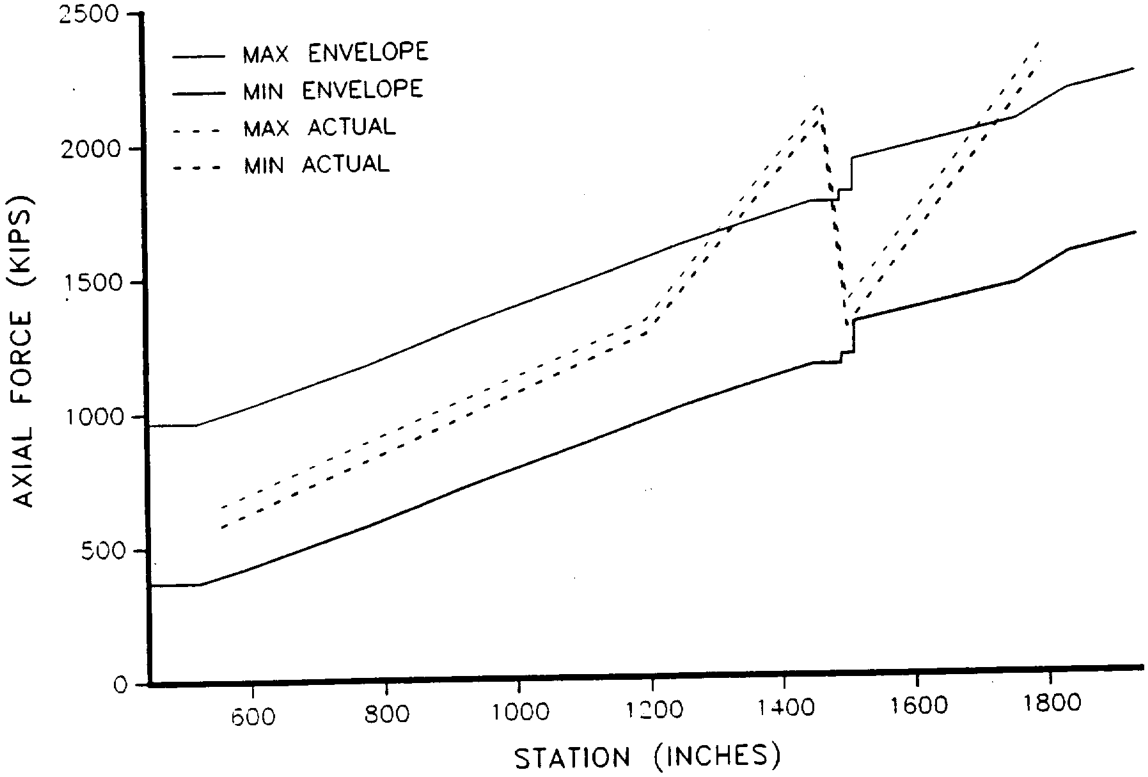

Figure 4.6-108. 360L003 Axial Force--Buildup Envelope (LH motor)

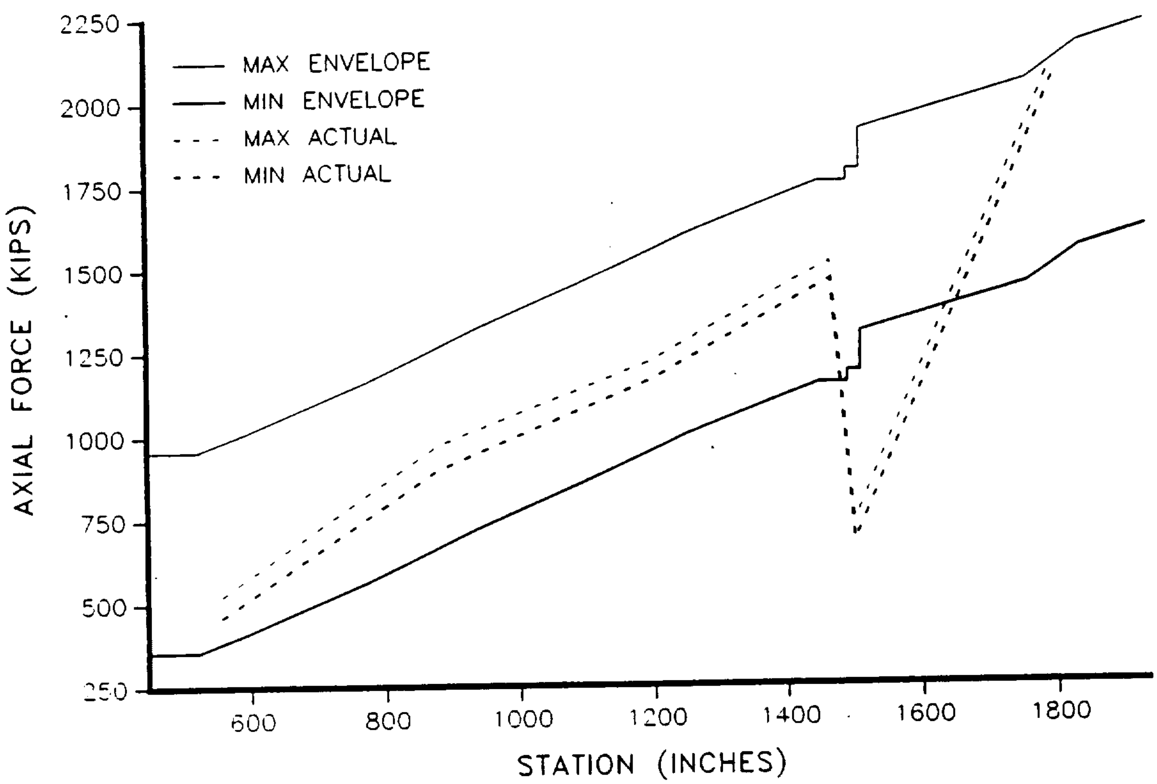

Figure 4.6-109. 360L003 Axial Force--Buildup Envelope (RH motor)

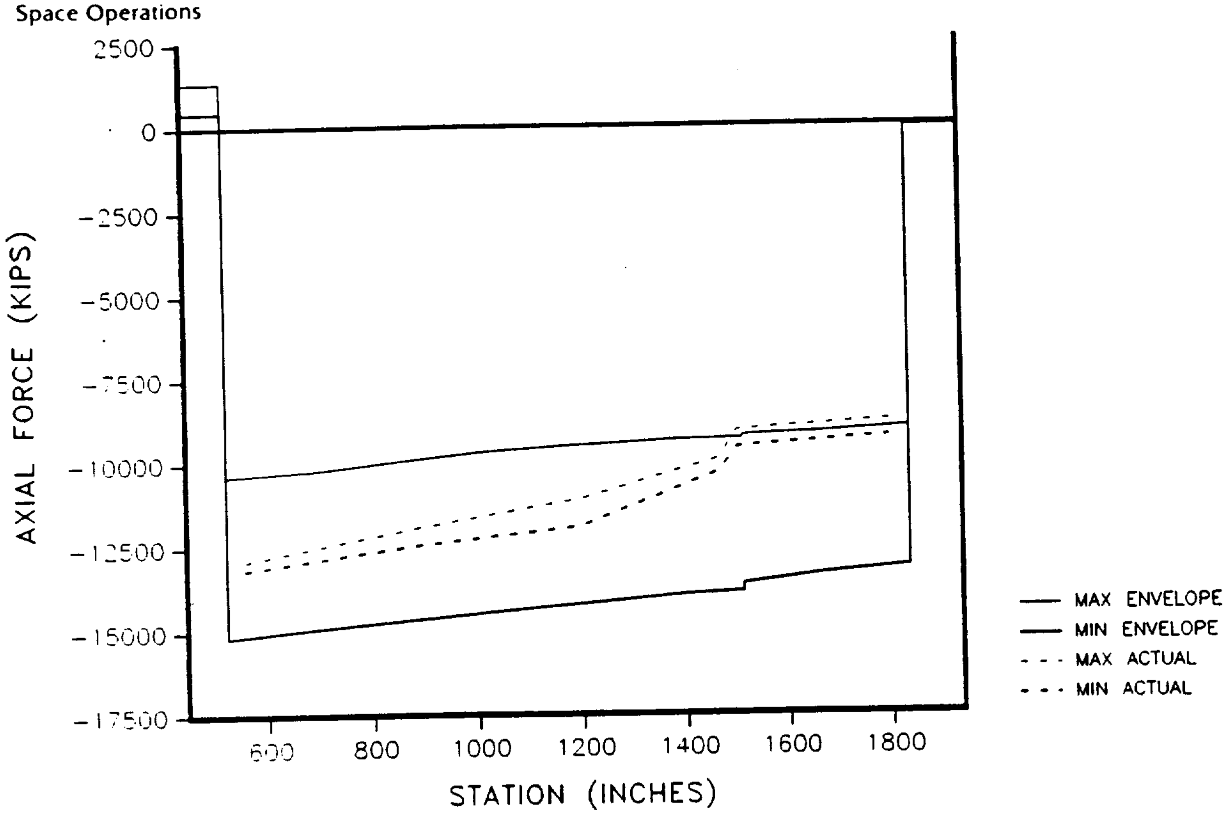

Figure 4.6-110. 360L003 Axial Force--Lift-off Envelope (LH motor)

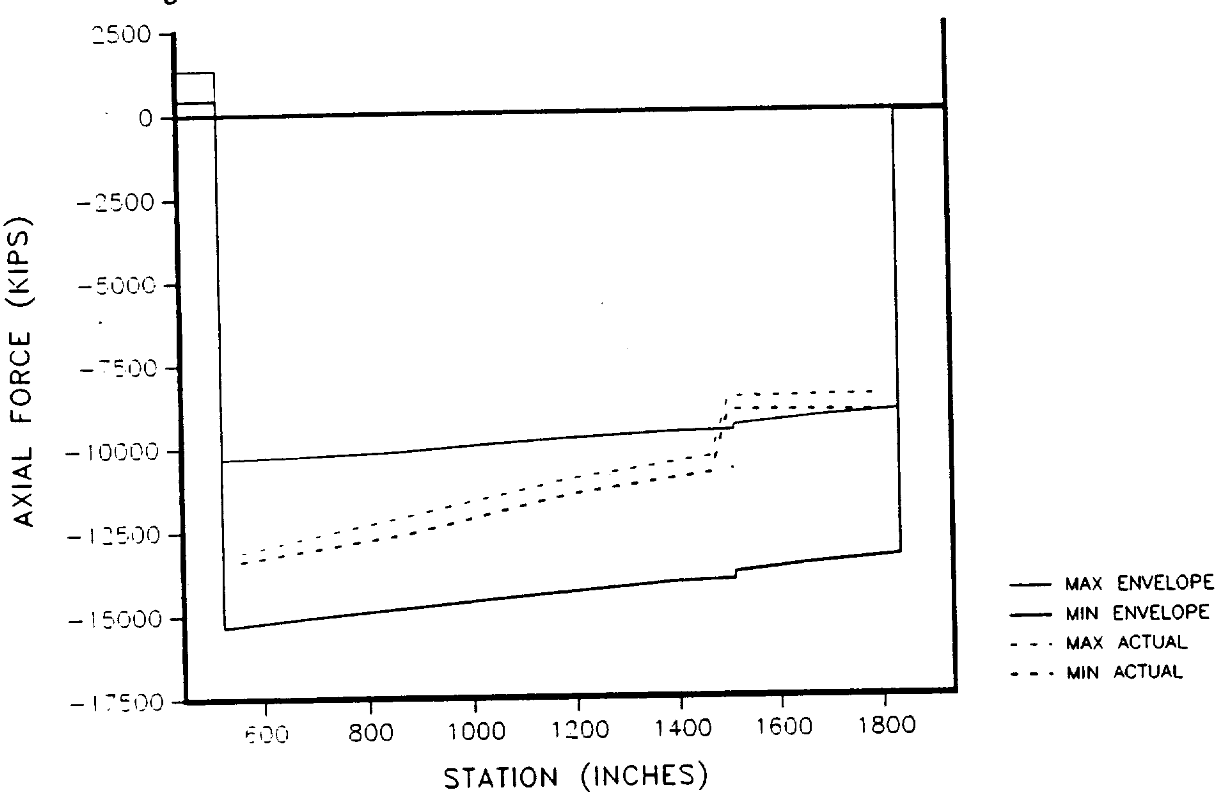

Figure 4.6-111. 360L003 Axial Force--Lift-off Envelope (RH motor)

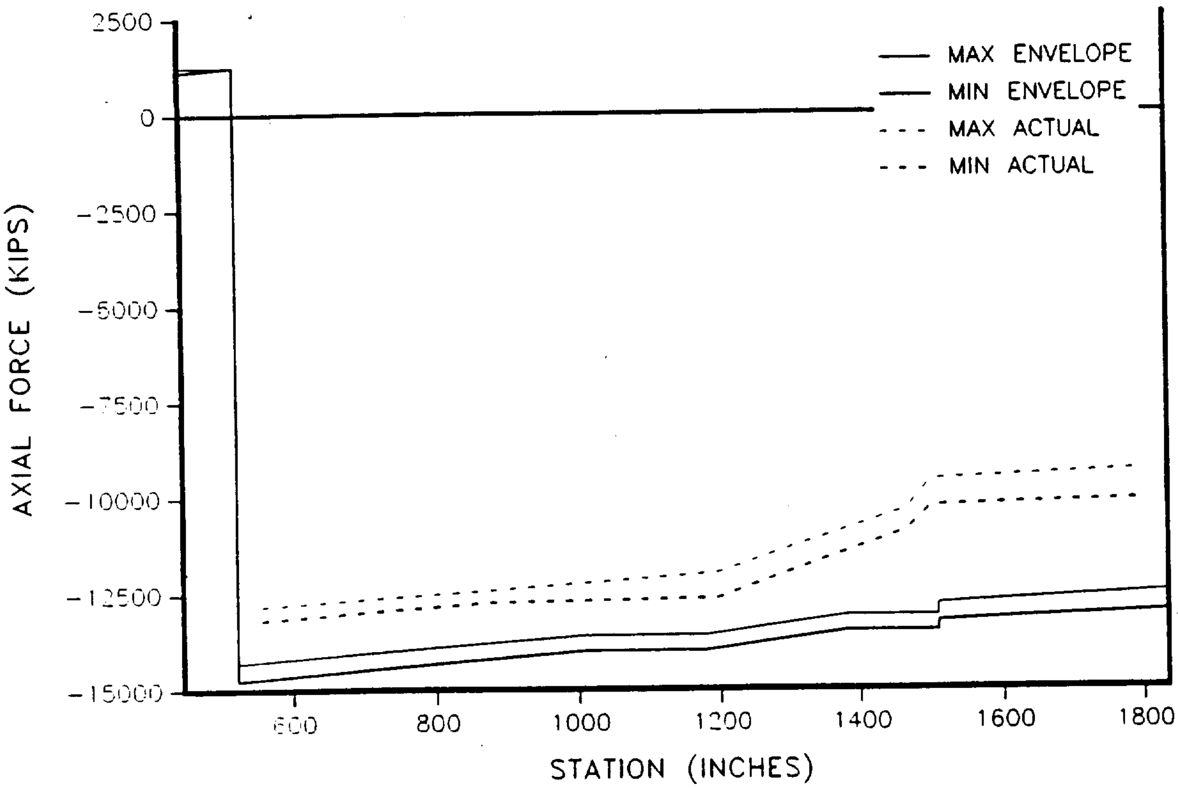

Figure 4.6-112. 360L003 Axial Force--Roll Envelope (LH motor)

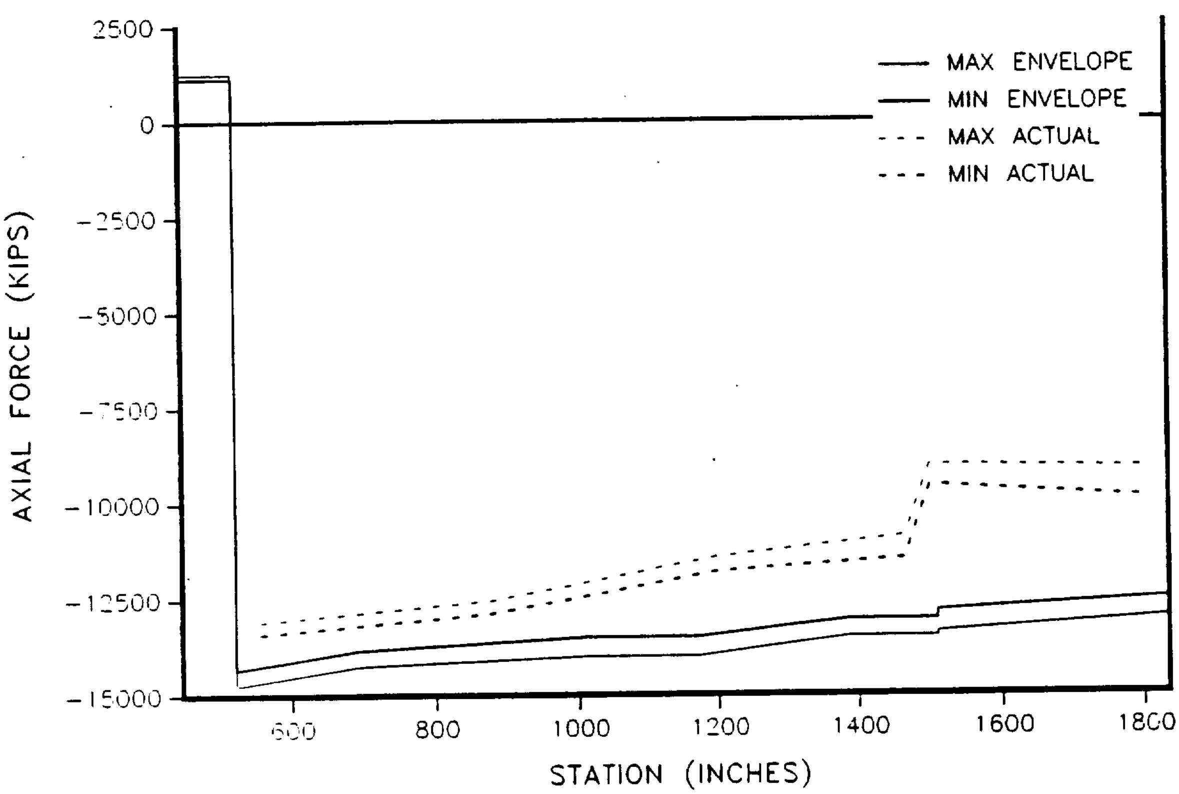

Figure 4.6-113. 360L003 Axial Force--Roll Envelope (RH motor)

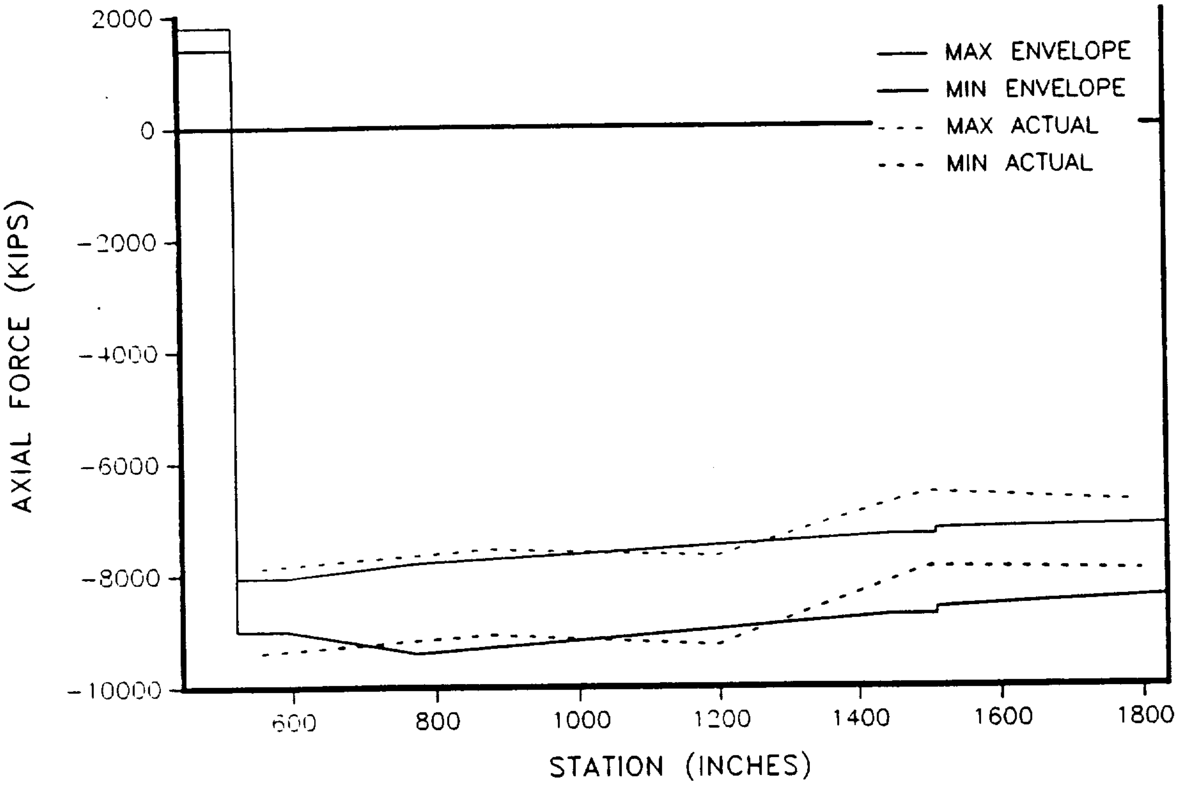

Figure 4.6-114. 360L003 Axial Force--Max G Envelope (LH motor)

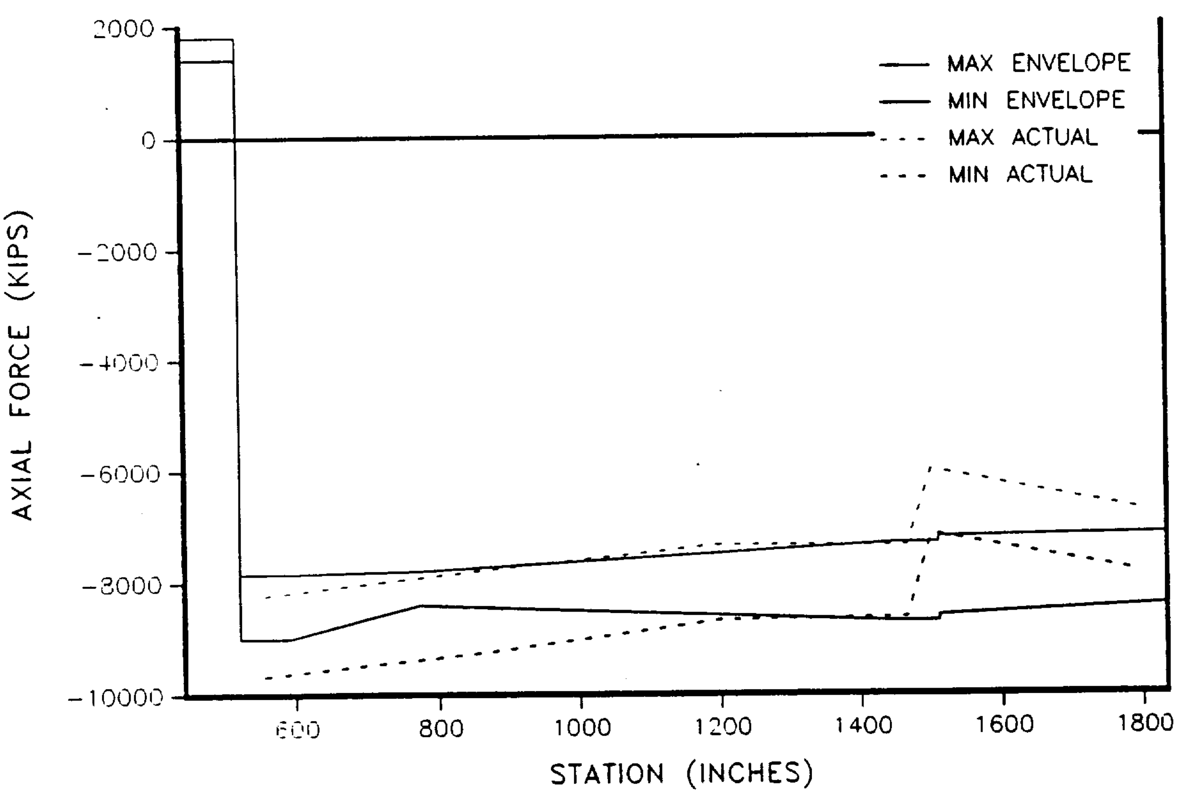

Figure 4.6-115. 360L003 Axial Force--Max G Envelope (RH motor)

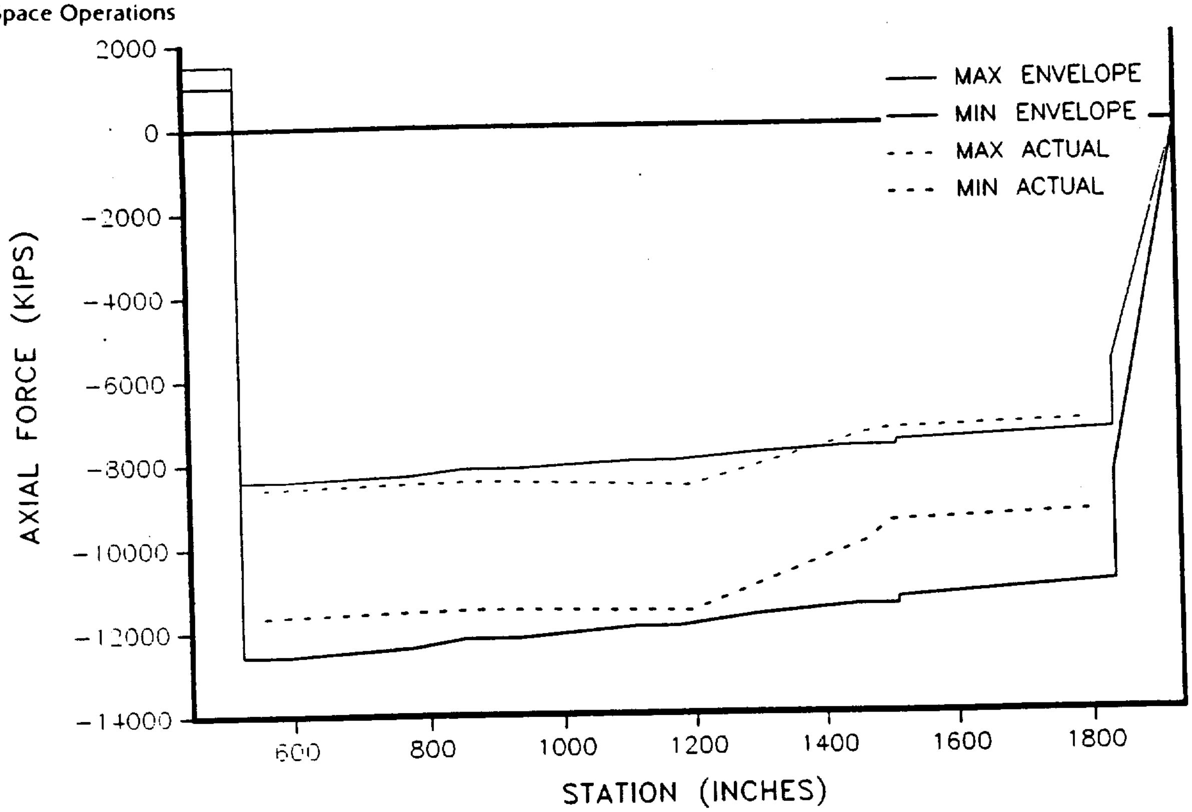

Figure 4.6-116. 360L003 Axial Force--Max Q Envelope (LH motor)

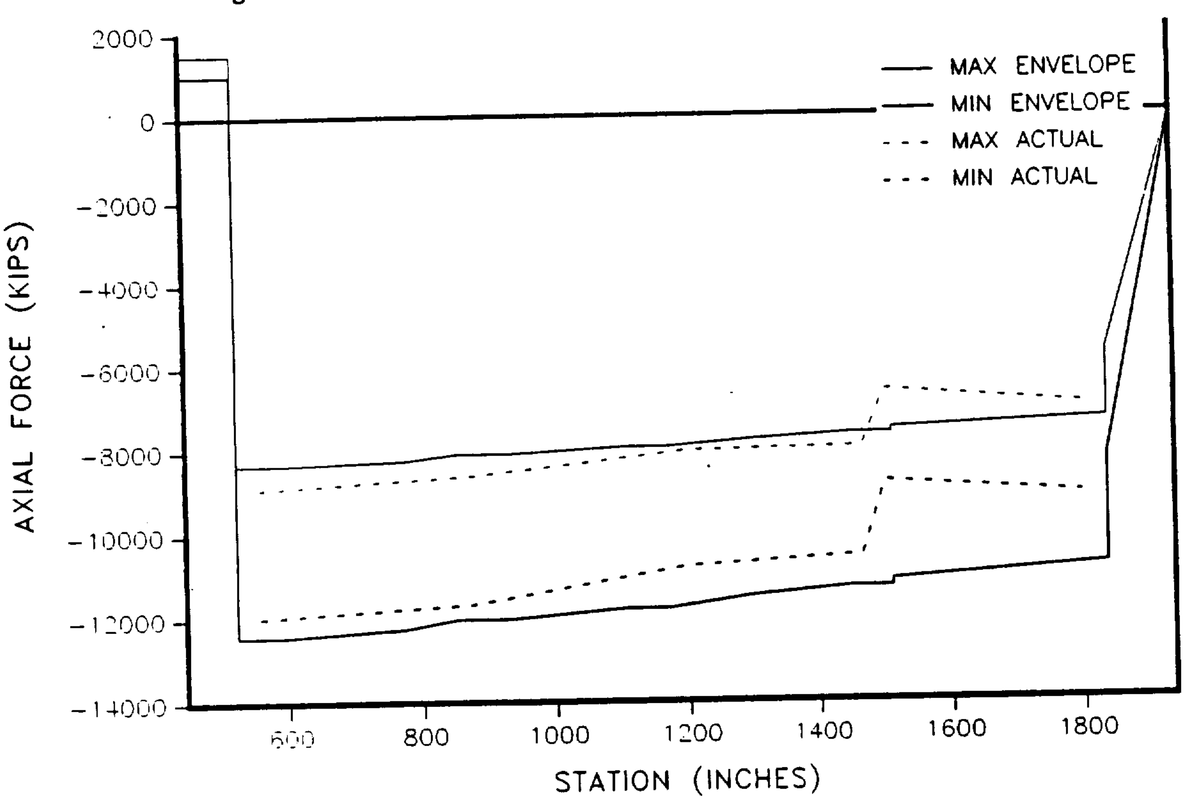

Figure 4.6-117. 360L003 Axial Force--Max Q Envelope (RH motor)

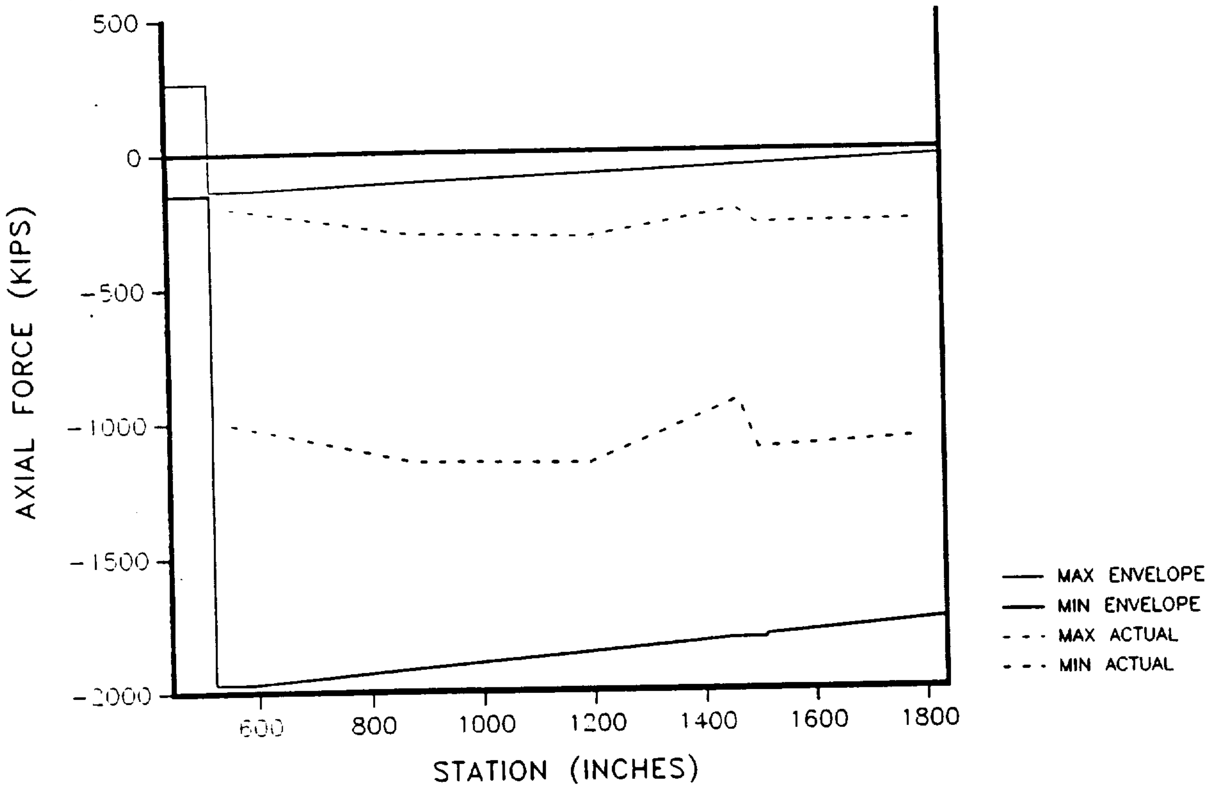

Figure 4.6-118. 360L003 Axial Force--Prestaging Envelope (LH motor)

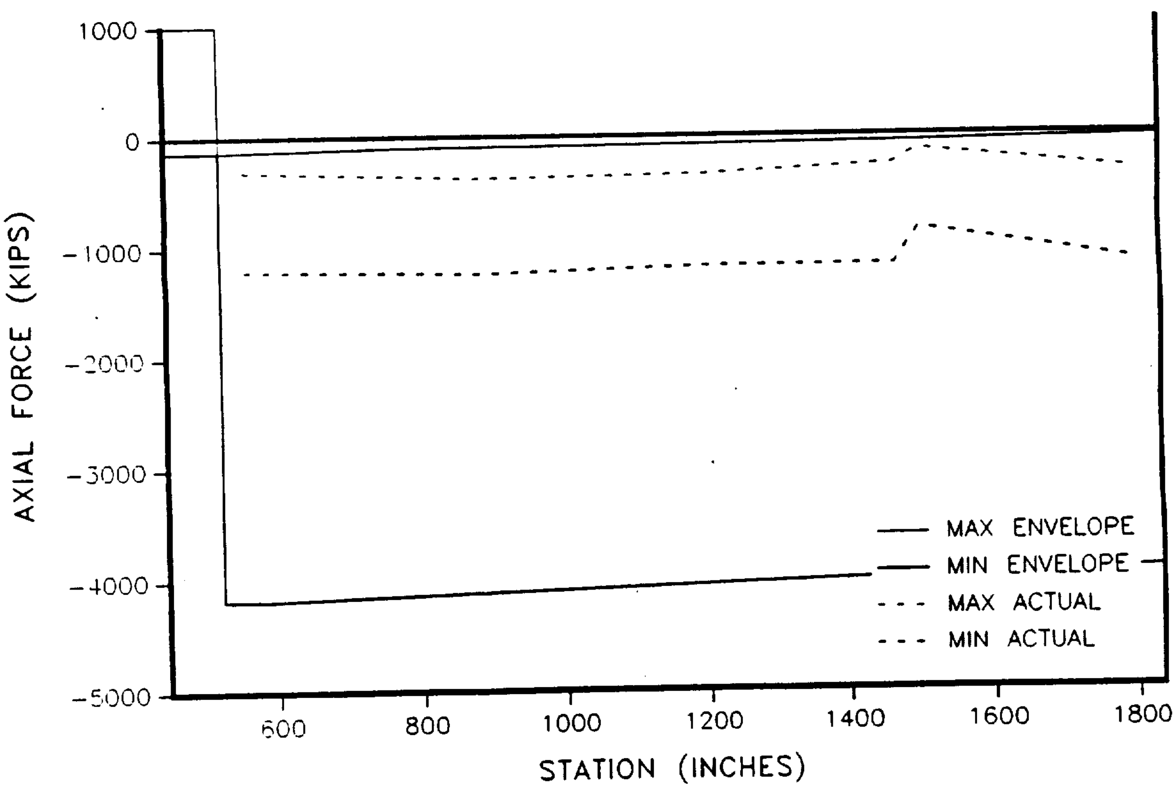

Figure 4.6-119. 360L003 Axial Force--Prestaging Envelope (RH motor)

Table 4.7-1. Maximum Accelerations (LH motor)

Gage	Station	Location (deg)	Direction	Peak Acceleration From NASTRAN Prediction (g)	Peak Acceleration From STS-29 (filter 40 Hz)	Peak Acceleration From STS-29 (filter 160 Hz)
B08D7160A	500.0	0	Axial	0.9	0.51	1.8
B08D7161A	500.0	0	Tang	1.2	0.27	0.8
B08D7162A	500.0	0	Radial	0.7	0.33	5.2
B08D7175A	839.5	0	Axial	0.9	0.66	2.0
B08D7176A	839.5	0	Tang	1.1	0.98	3.8
B08D7164A	1159.5	0	Axial	0.8	0.21	1.5
B08D7165A	1159.5	0	Tang	1.1	0.15	1.8
B08D7166A	1159.5	0	Radial	0.6	1.90	5.0
B08D7177A	1479.5	0	Axial	1.0	0.27	1.3
B08D7178A	1479.5	0	Tang	1.0	0.25	1.5
B08D7179A	1479.5	180	Tang	0.9	0.50	2.0
B08D7167A	1829.5	0	Axial	1.3	0.85	4.2
B08D7168A	1829.5	0	Tang	1.2	0.84	1.5
B08D7169A	1829.5	0	Radial	0.6	0.29	4.8
B08D7171A	1923	270	Axial	NA	3.60	9.5
B08D7172A	1923	270	Tang	NA	Bad gage	Bad gage
B08D7173A	1923	270	Radial	NA	Bad gage	Bad gage
B08D8174A	1923	90	Tang	NA	0.23	3.8

Table 4.7-2. Maximum Accelerations (RH motor)

Gage	Station	Location (deg)	Direction	Peak Acceleration From NASTRAN Prediction (g)	Peak Acceleration From STS-29 (filter 40 Hz)	Peak Acceleration From STS-29 (filter 160 Hz)
B08D8160A	500.0	0	Axial	0.9	0.22	1.5
B08D8161A	500.0	0	Tang	1.3	0.26	0.5
B08D8163A	500.0	180	Tang	1.2	0.31	2.0
B08D8175A	839.5	0	Axial	0.8	9.00	12.0
B08D8176A	839.5	0	Tang	0.8	0.21	2.5
B08D8164A	1159.5	0	Axial	0.8	0.31	1.0
B08D8165A	1159.5	0	Tang	0.8	1.00	11.0
B08D8166A	1159.5	0	Radial	0.6	2.00	7.5
B08D8177A	1479.5	0	Axial	1.0	0.33	2.0
B08D8178A	1479.5	0	Tang	0.9	0.84	4.0
B08D8179A	1479.5	180	Tang	1.0	0.31	1.8
B08D8167A	1829.5	0	Axial	1.3	0.73	4.1
B08D8168A	1829.5	0	Tang	1.0	0.38	1.8
B08D8170A	1829.5	180	Radial	0.6	0.38	4.0
B08D8171A	1923	90	Axial	NA	2.90	1.0
B08D8172A	1923	90	Tang	NA	1.40	4.0
B08D8173A	1923	90	Radial	NA	8.60	9.0
B08D8174A	1923	270	Tang	NA	Bad gage	Bad gage

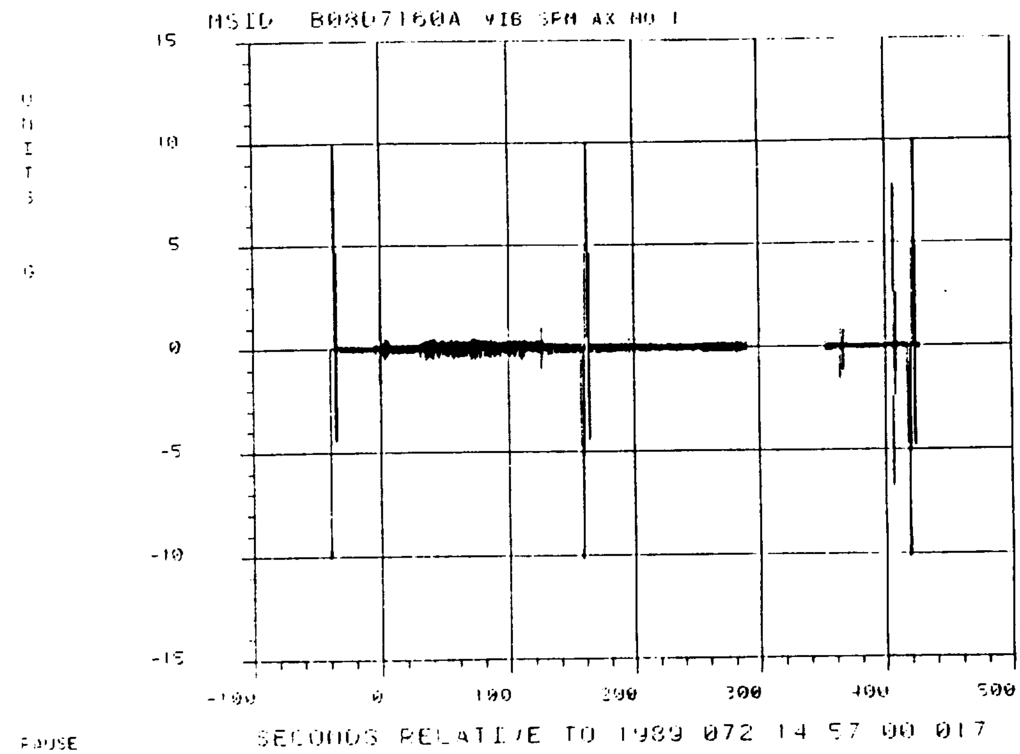

Figure 4.7-1. Acceleration Time History (Gage B08D7160A)

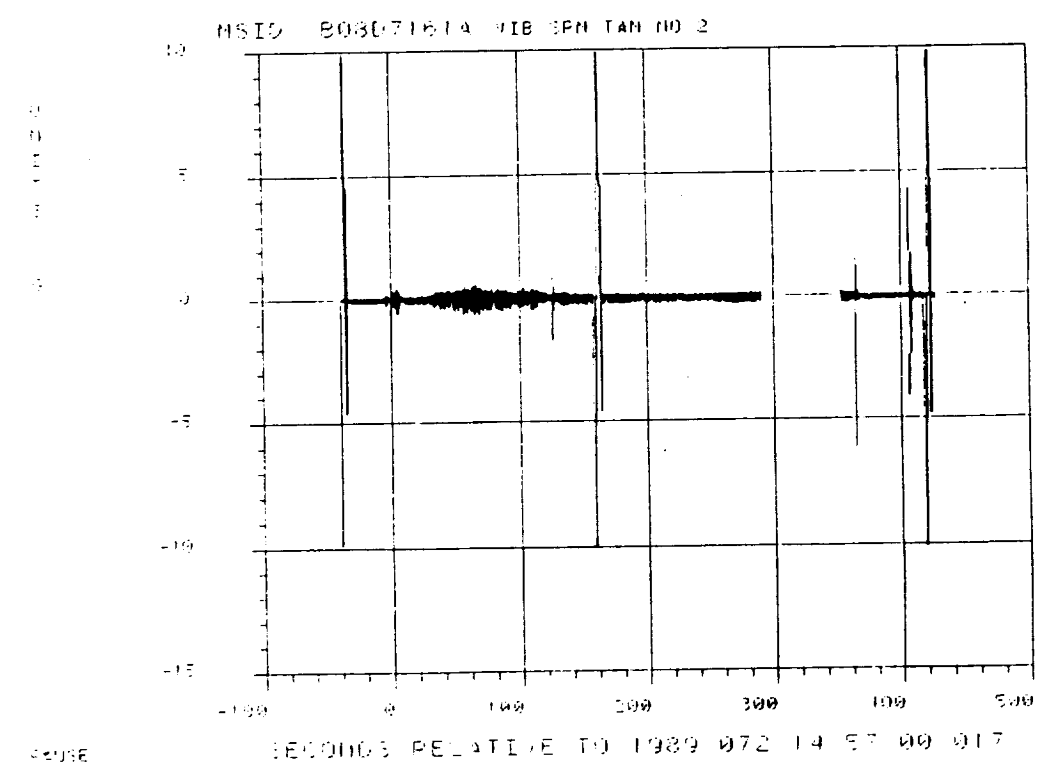

Figure 4.7-2. Acceleration Time History (Gage B08D7161A)

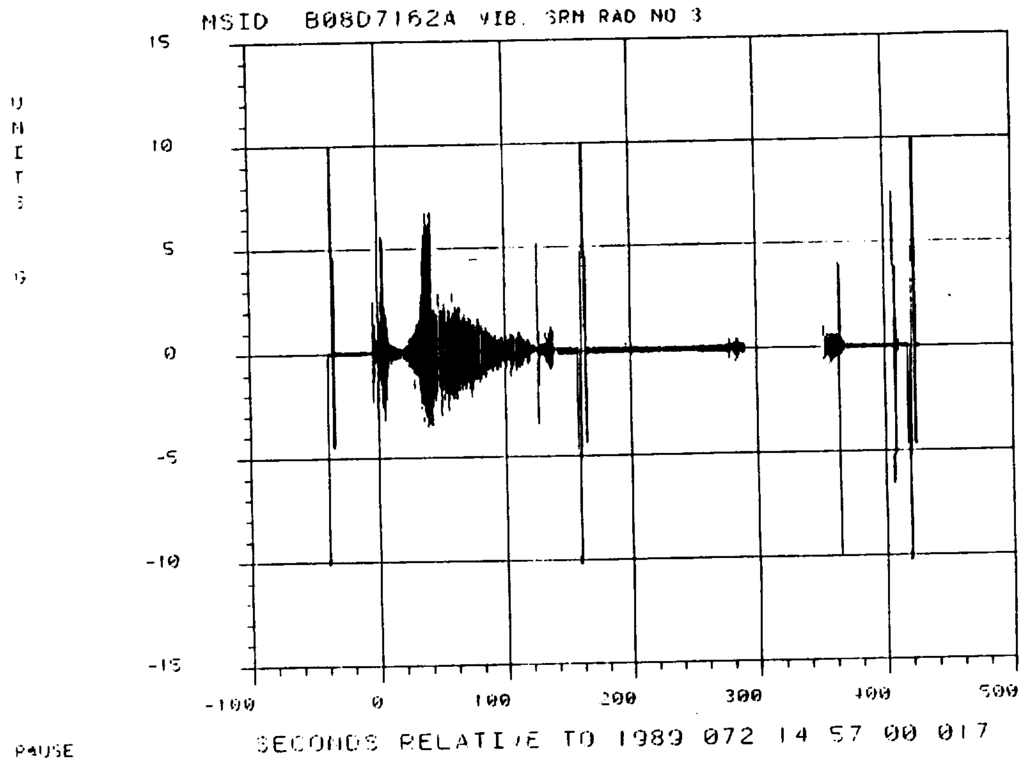

Figure 4.7-3. Acceleration Time History (Gage B08D7162A)

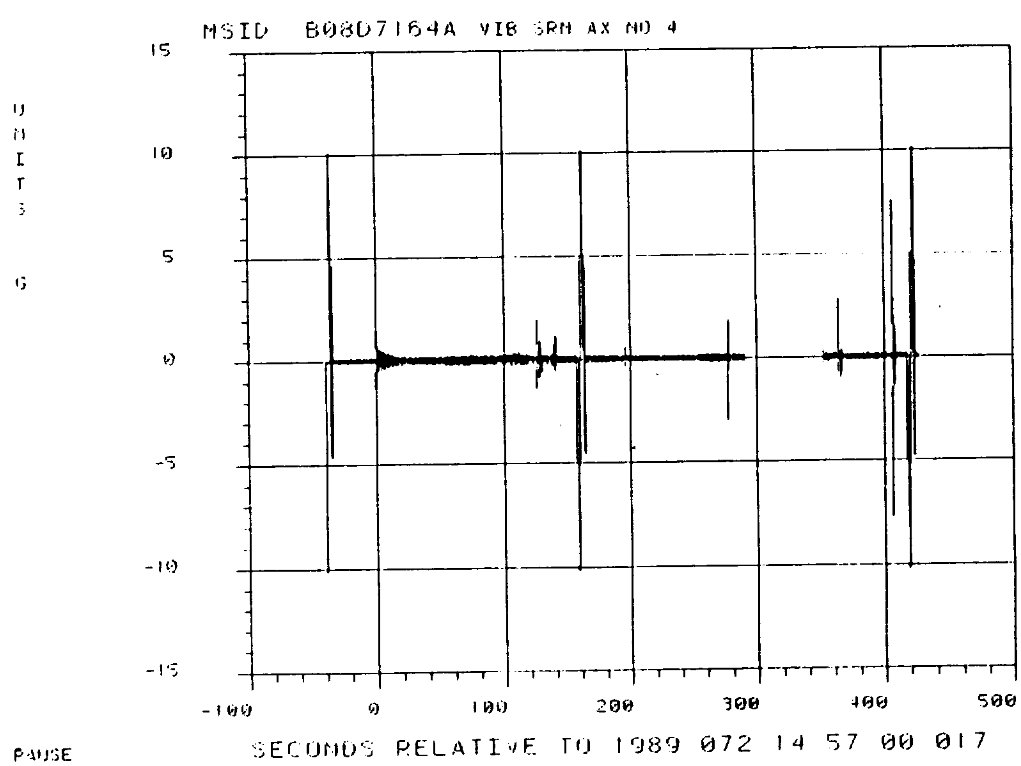

Figure 4.7-4. Acceleration Time History (Gage B08D7164A)

ORIGINAL PAGE IS
OF POOR QUALITY

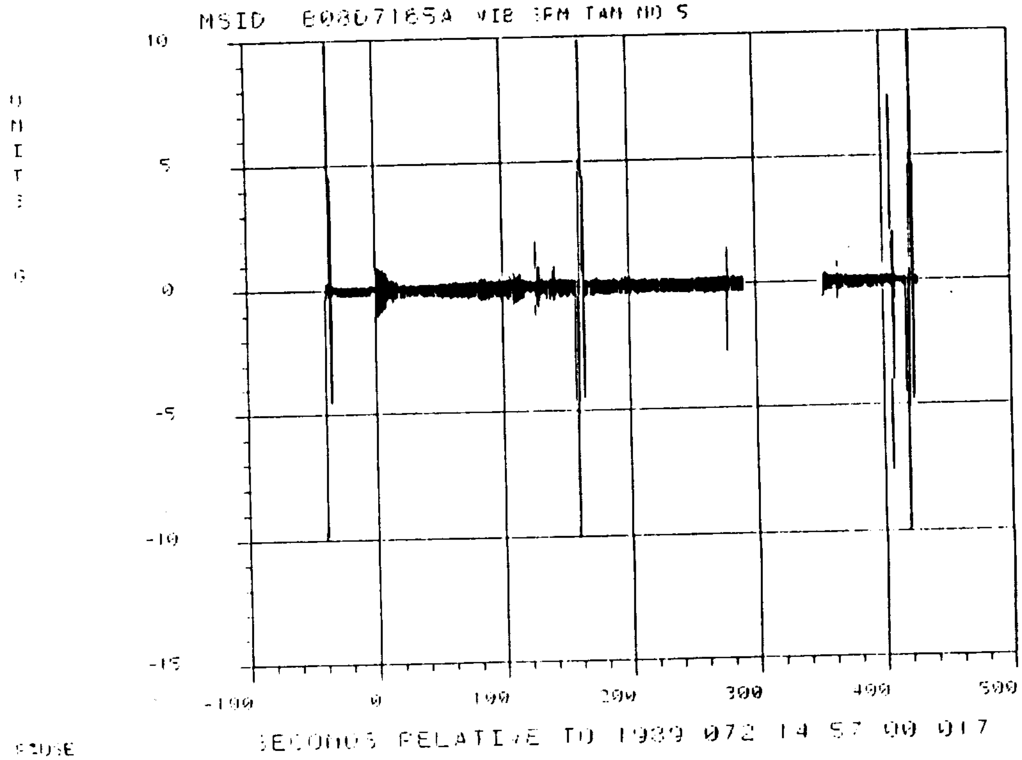

Figure 4.7-5. Acceleration Time History (Gage B08D7165A)

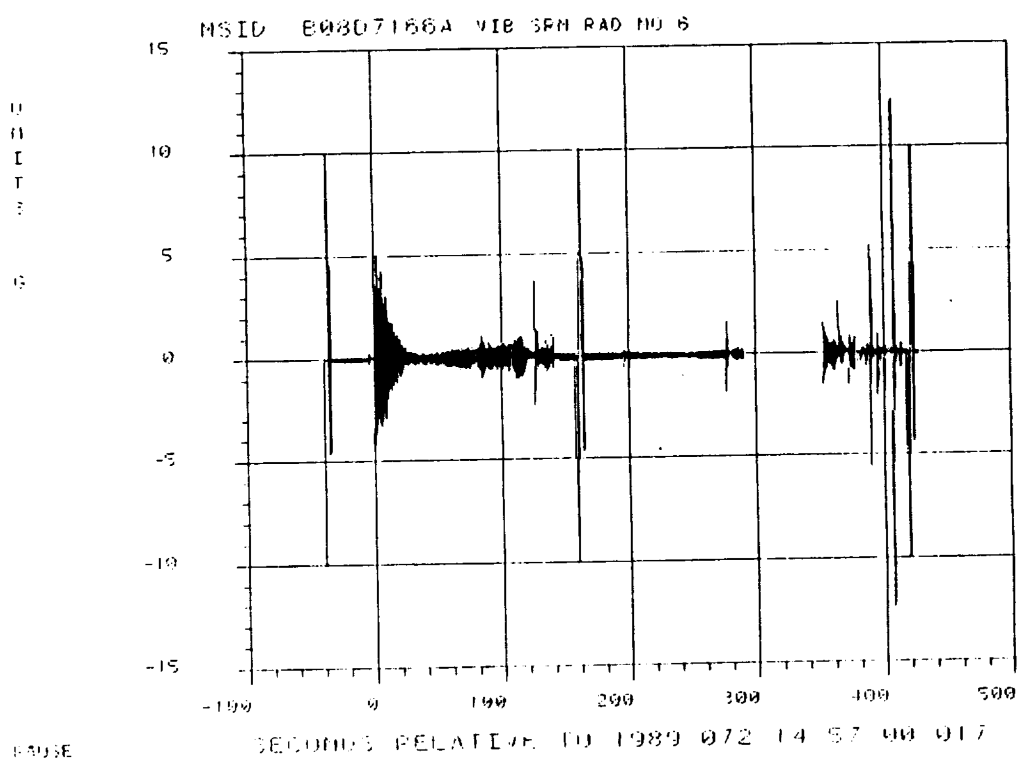

Figure 4.7-6. Acceleration Time History (Gage B08D7166A)

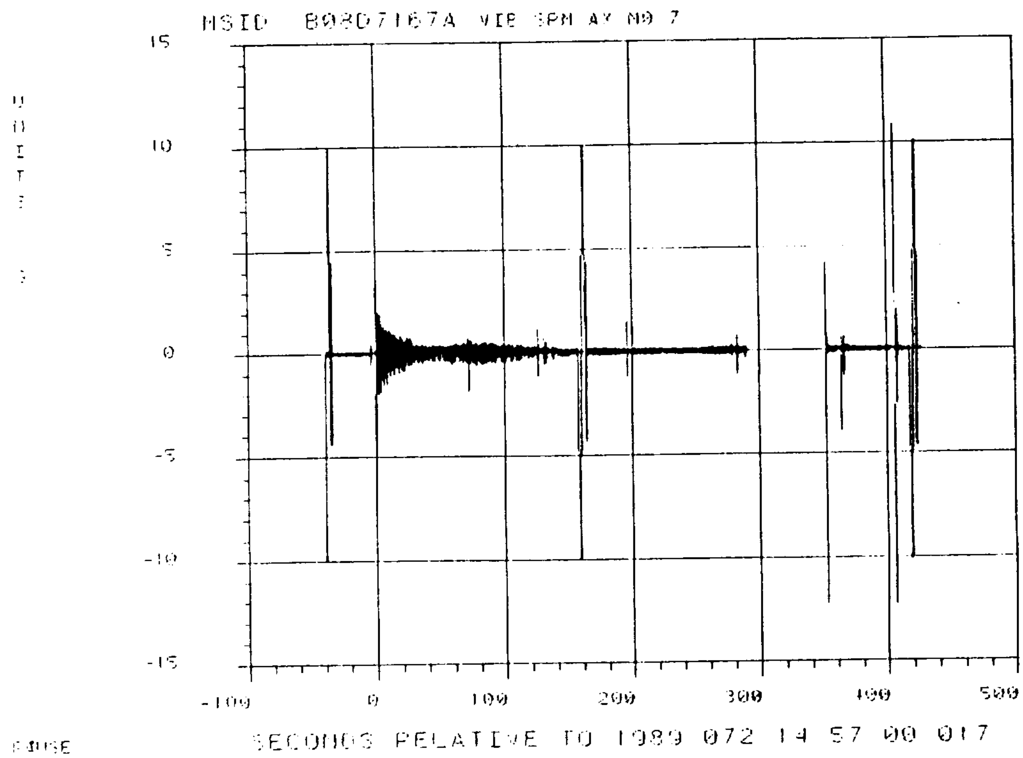

Figure 4.7-7. Acceleration Time History (Gage B08D7167A)

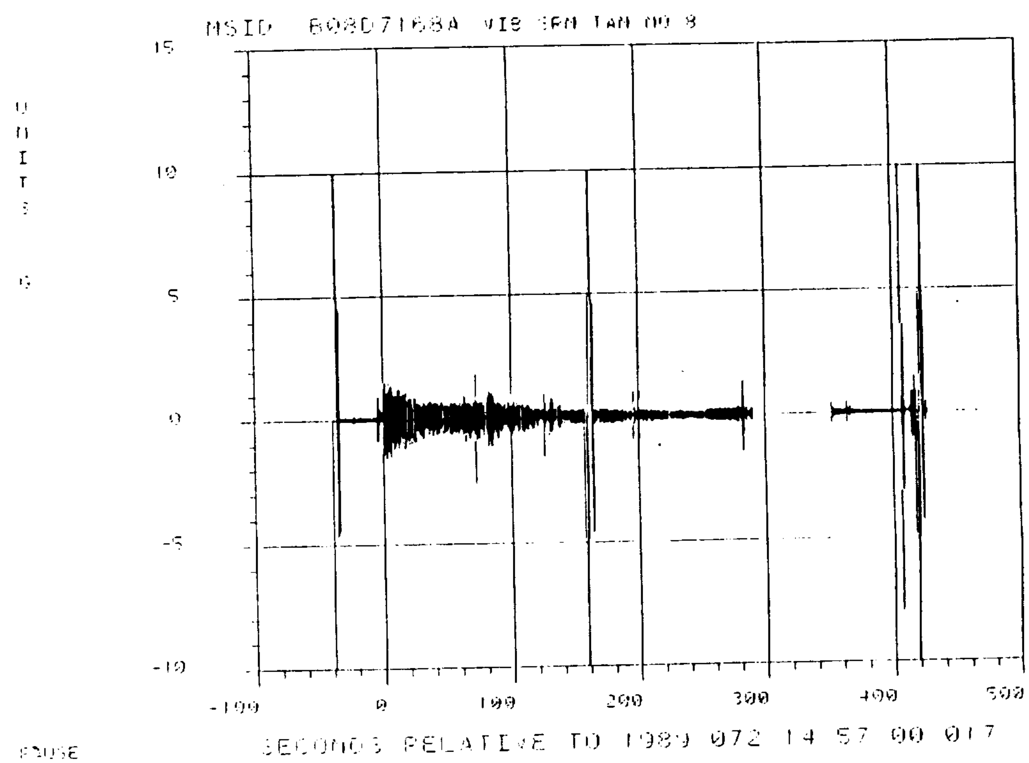

Figure 4.7-8. Acceleration Time History (Gage B08D7168A)

ORIGINAL PAGE IS
OF POOR QUALITY

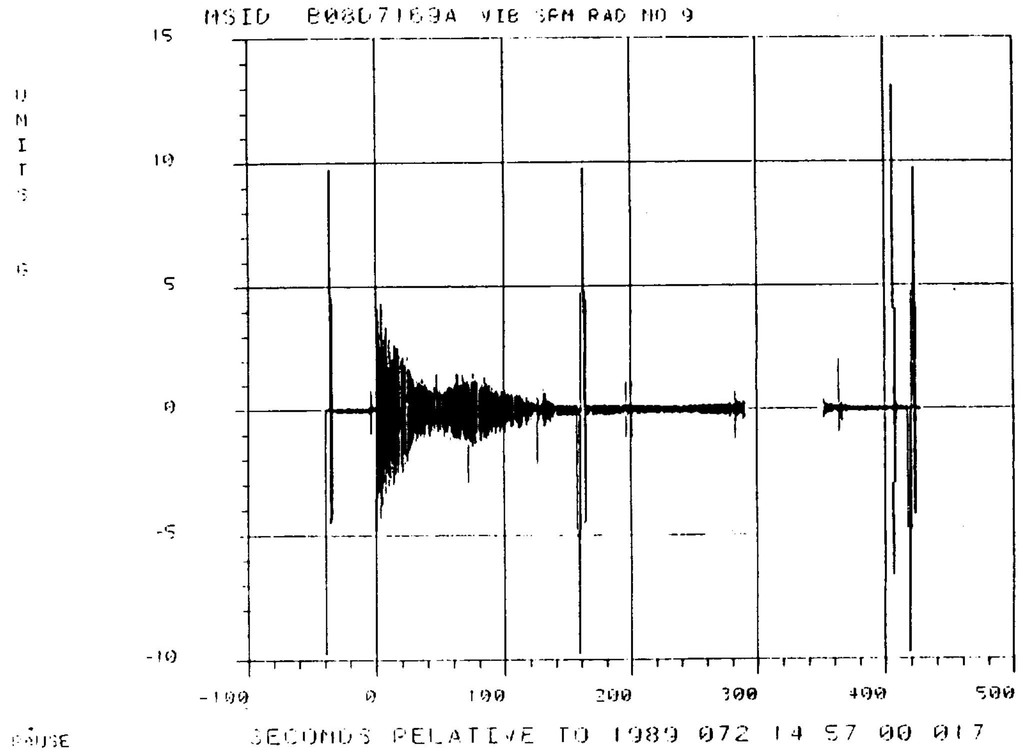

Figure 4.7-9. Acceleration Time History (Gage B08D7169A)

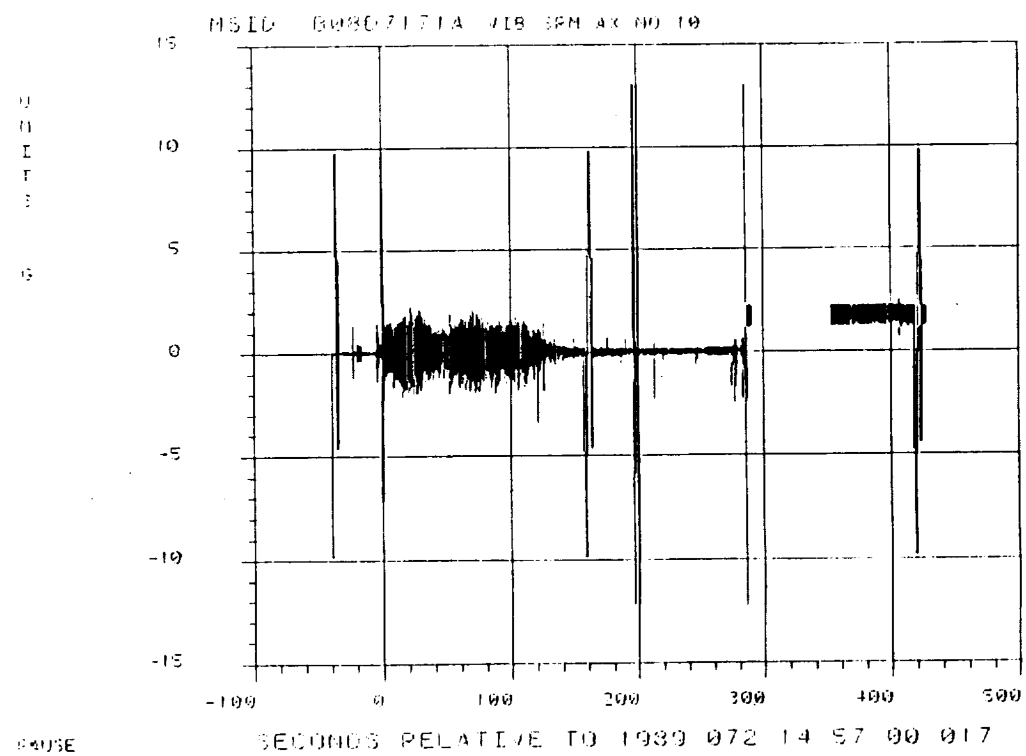

Figure 4.7-10. Acceleration Time History (Gage B08D7171A)

ORIGINAL PAGE IS
OF POOR QUALITY

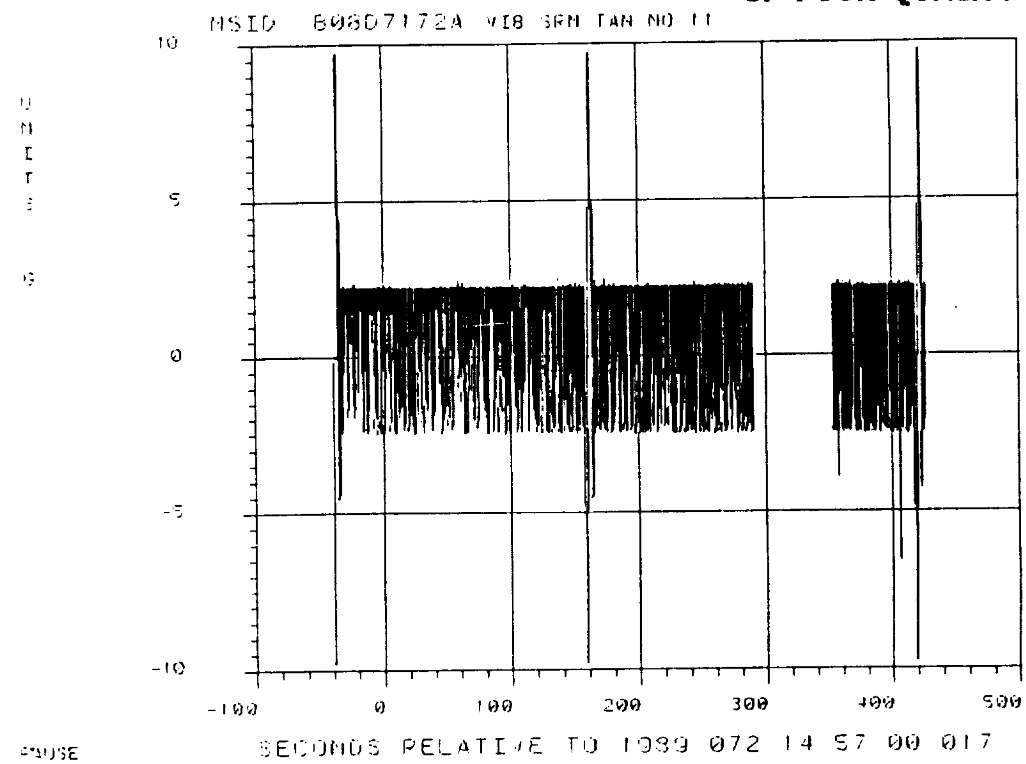

Figure 4.7-11. Acceleration Time History (Gage B08D7172A)

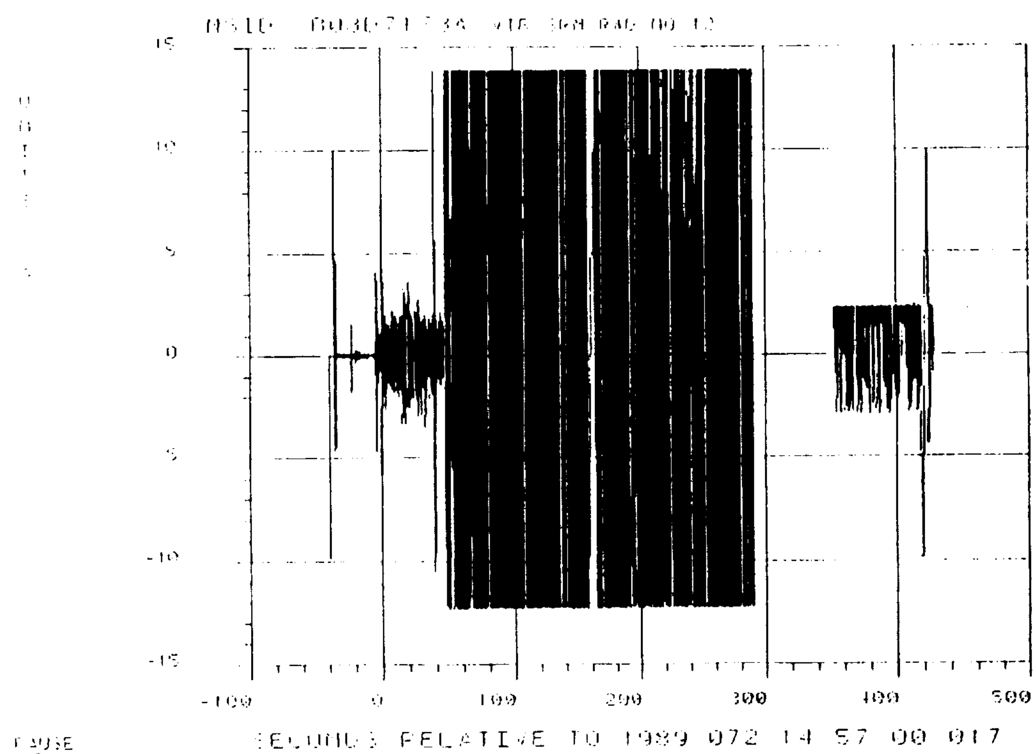

Figure 4.7-12. Acceleration Time History (Gage B08D7173A)

ORIGINAL PAGE IS
OF POOR QUALITY

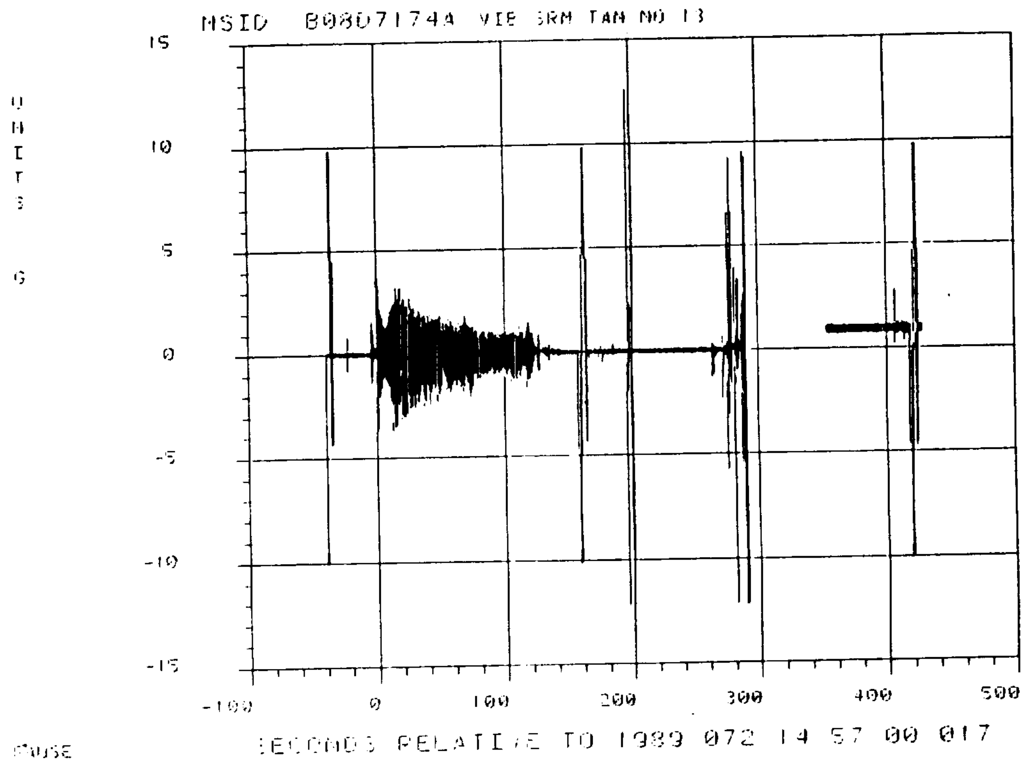

Figure 4.7-13. Acceleration Time History (Gage B08D7174A)

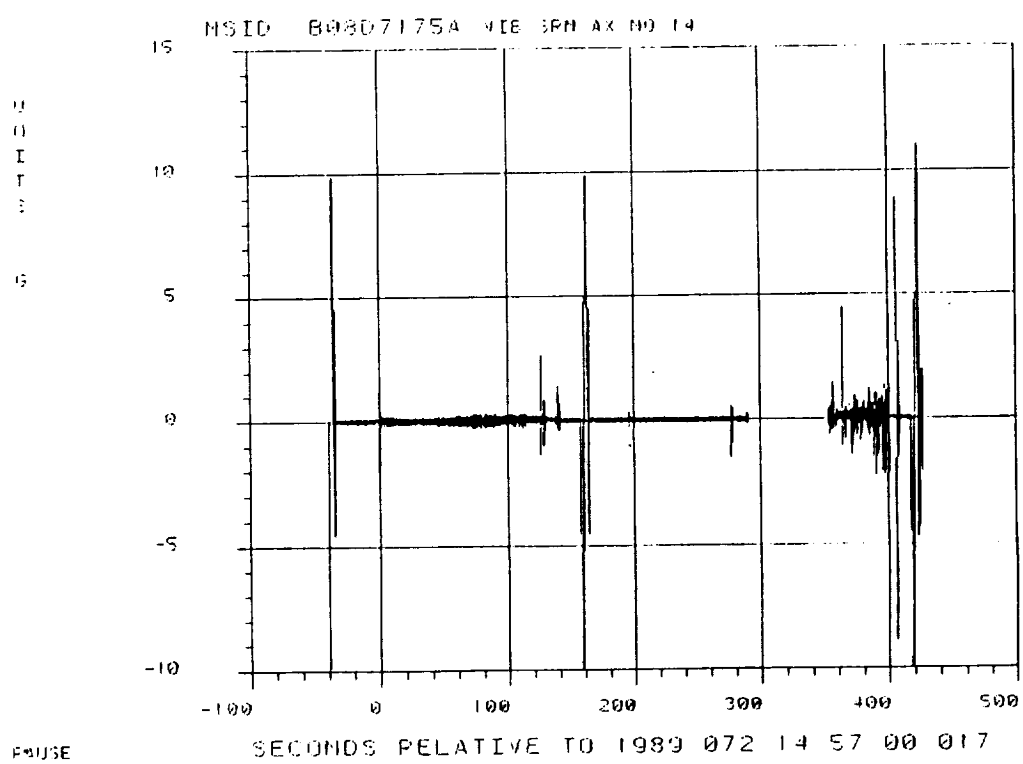

Figure 4.7-14. Acceleration Time History (Gage B08D7175A)

ORIGINAL PAGE IS
OF POOR QUALITY

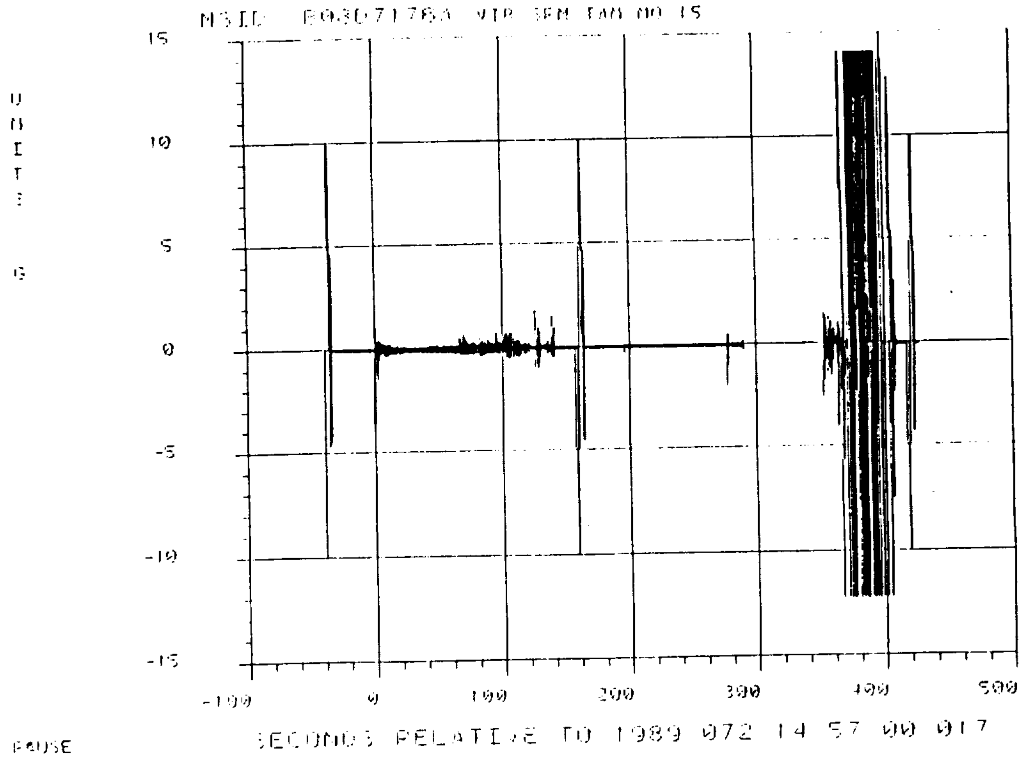

Figure 4.7-15. Acceleration Time History (Gage B08D7176A)

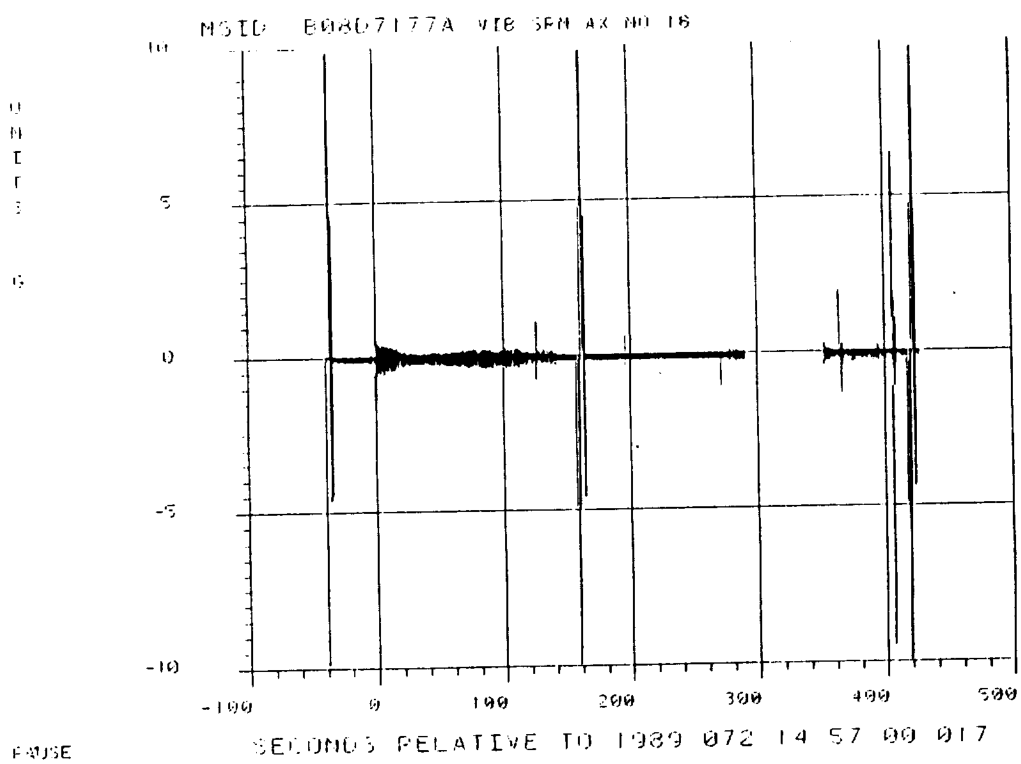

Figure 4.7-16. Acceleration Time History (Gage B08D7177A)

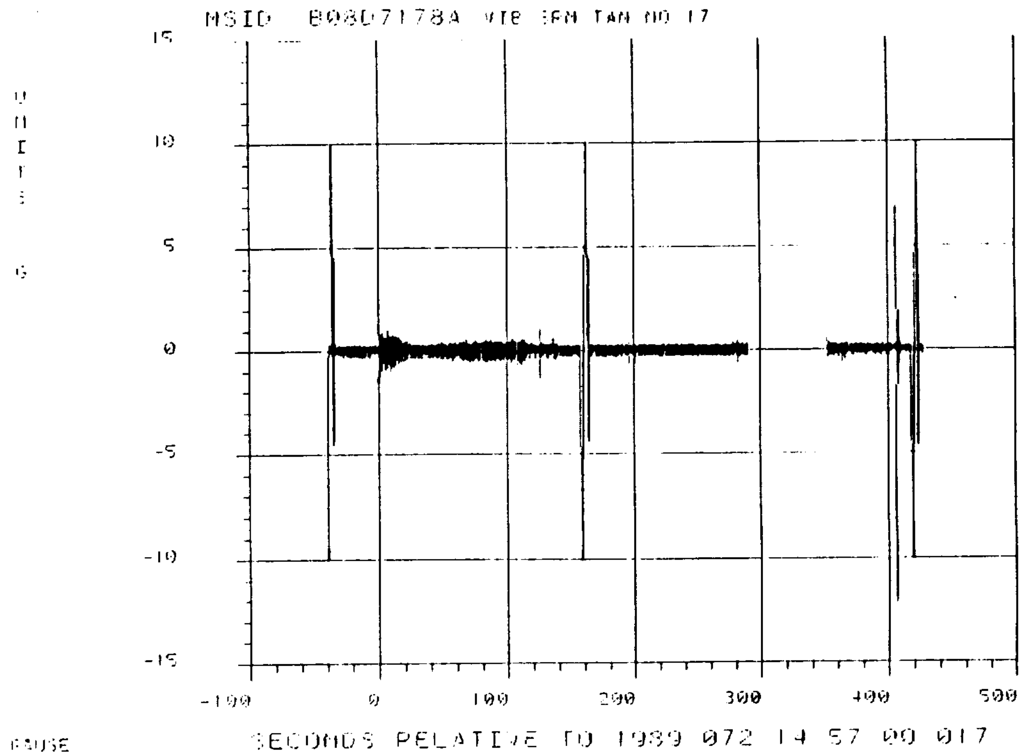

Figure 4.7-17. Acceleration Time History (Gage B08D7178A)

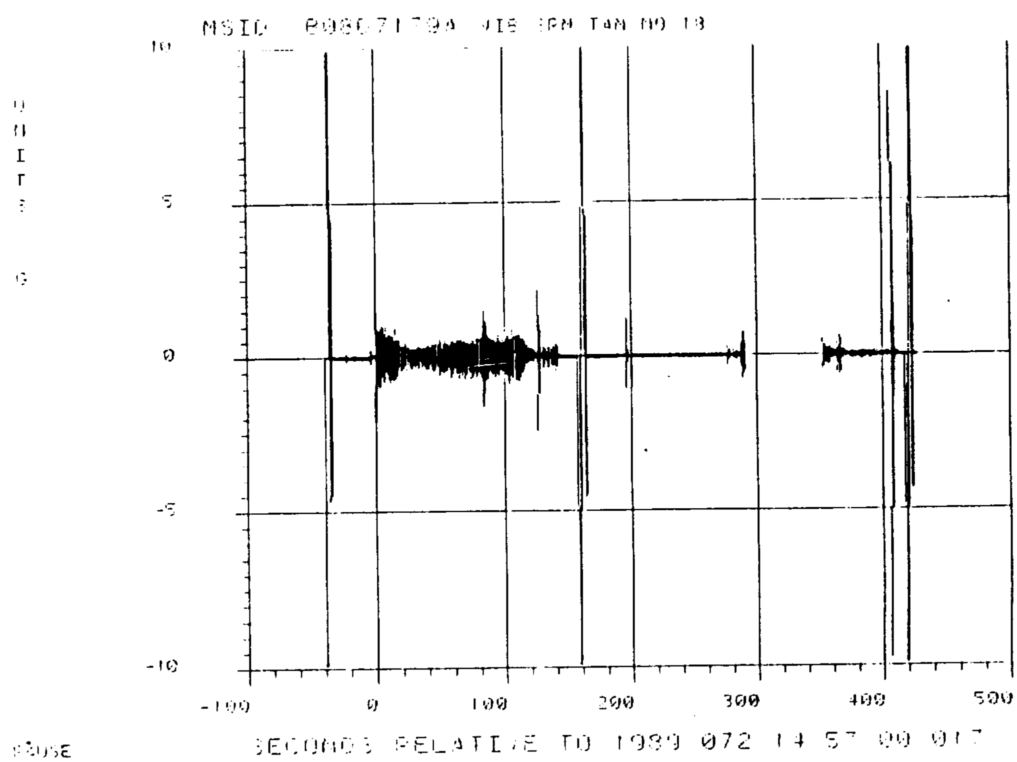

Figure 4.7-18. Acceleration Time History (Gage B08D7179A)

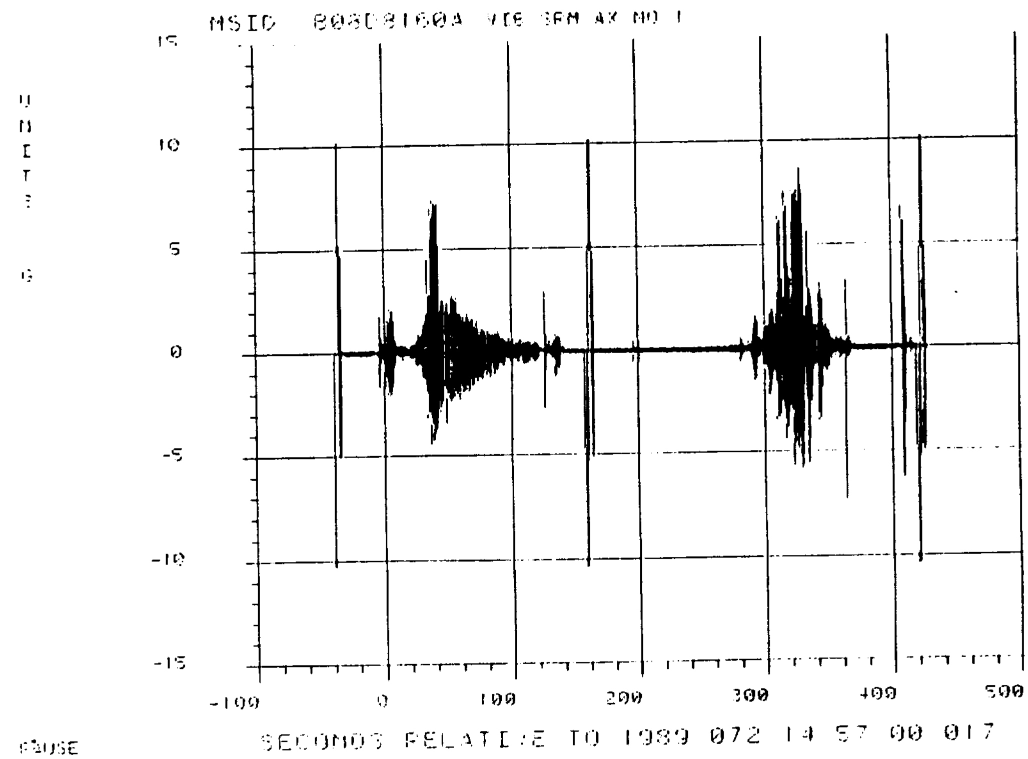

Figure 4.7-19. Acceleration Time History (Gage B08D8160A)

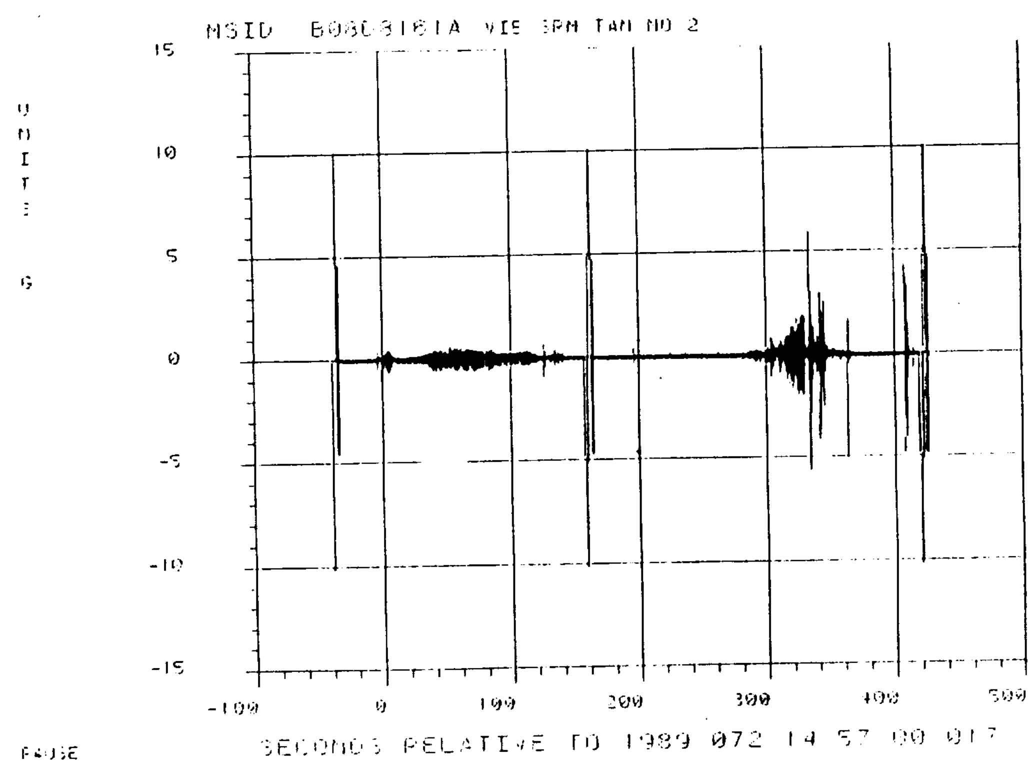

Figure 4.7-20. Acceleration Time History (Gage B08D8161A)

ORIGINAL PAGE IS
OF POOR QUALITY

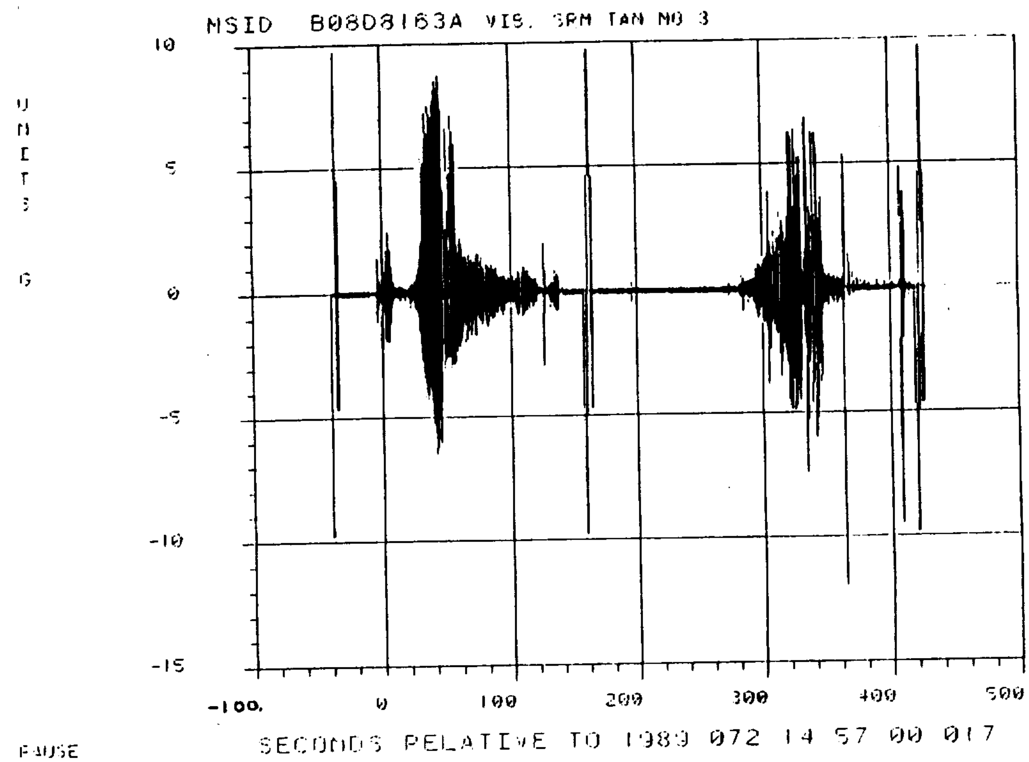

Figure 4.7-21. Acceleration Time History (Gage B08D8163A)

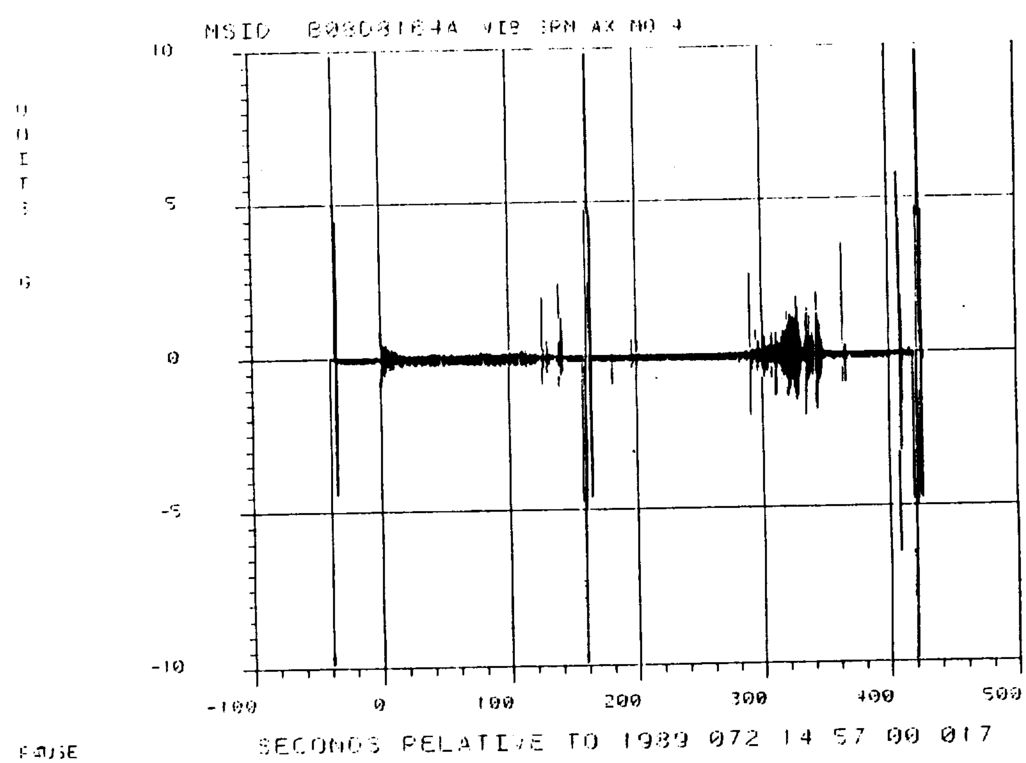

Figure 4.7-22. Acceleration Time History (Gage B08D8164A)

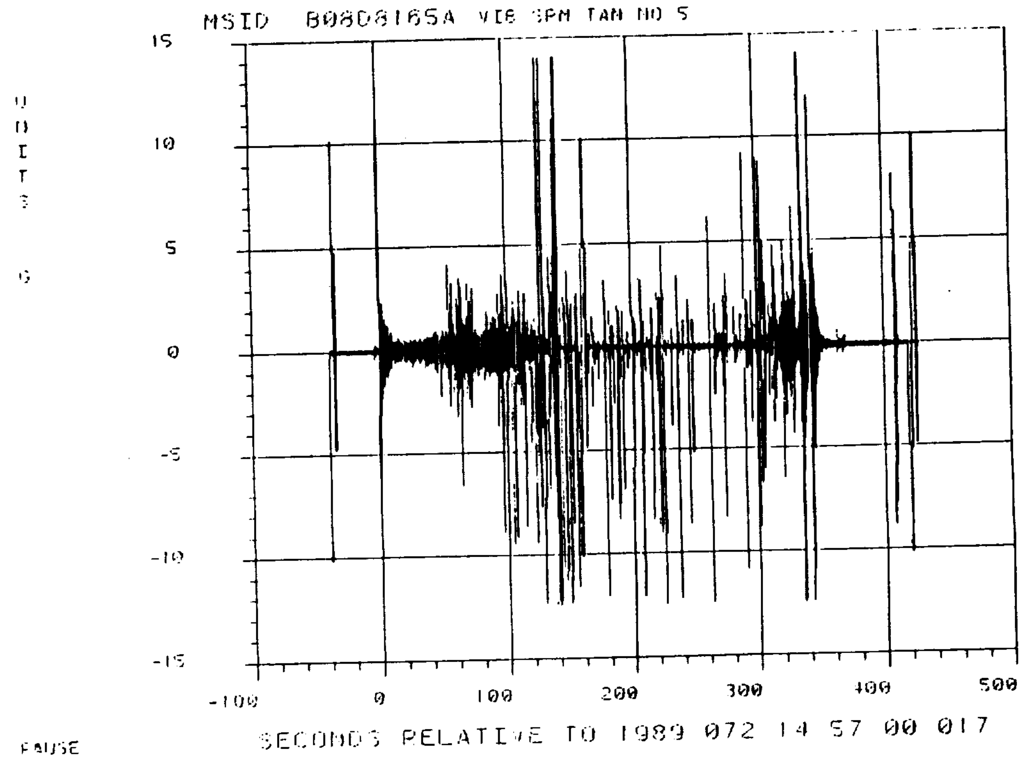

Figure 4.7-23. Acceleration Time History (Gage B08D8165A)

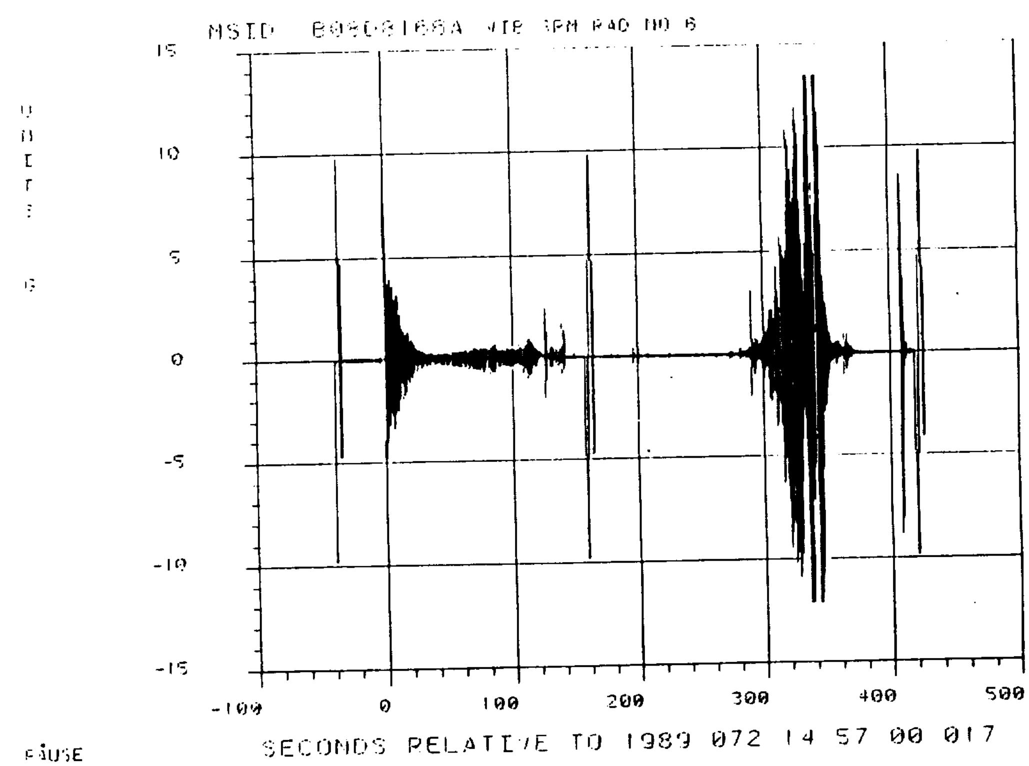

Figure 4.7-24. Acceleration Time History (Gage B08D8166A)

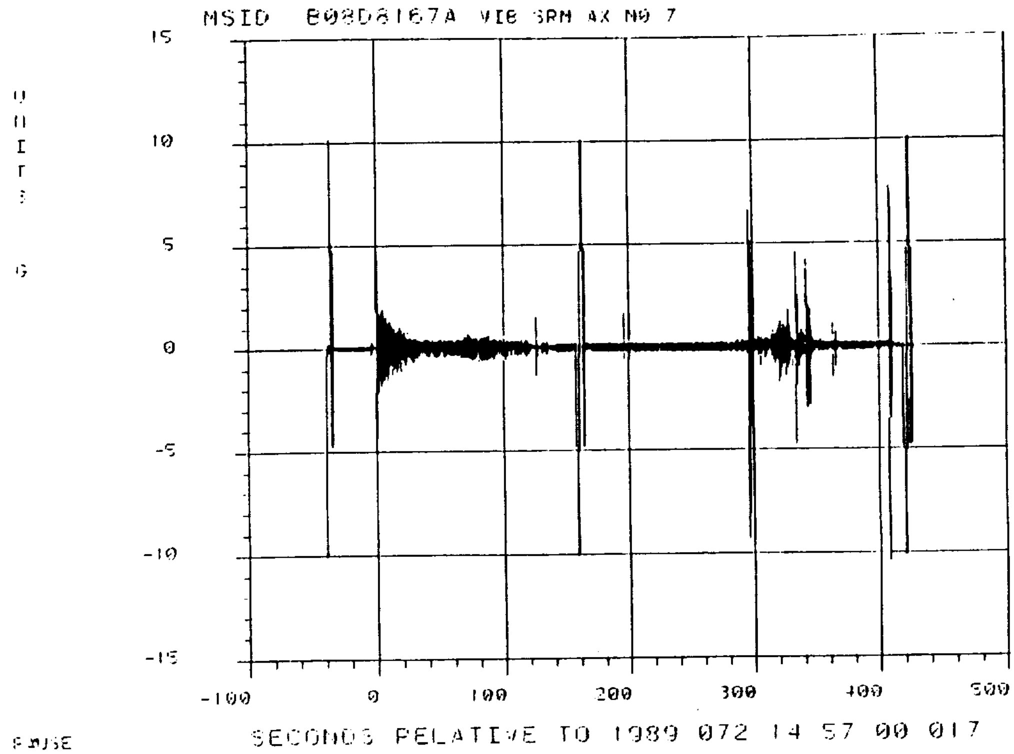

Figure 4.7-25. Acceleration Time History (Gage B08D8167A)

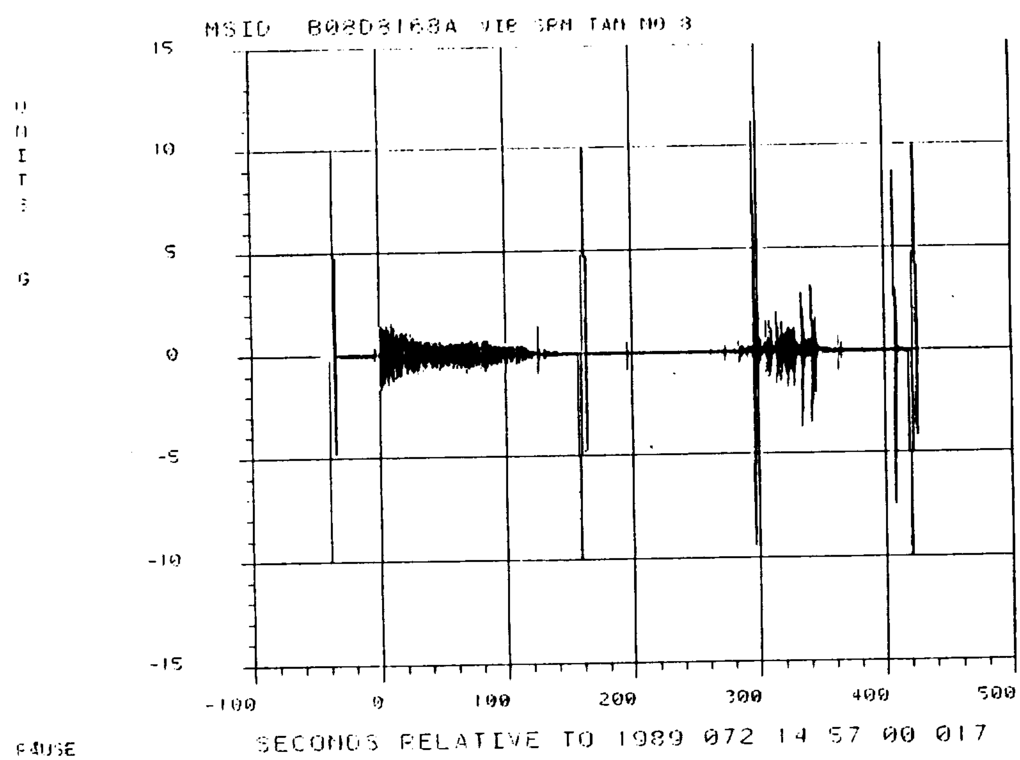

Figure 4.7-26. Acceleration Time History (Gage B08D8168A)

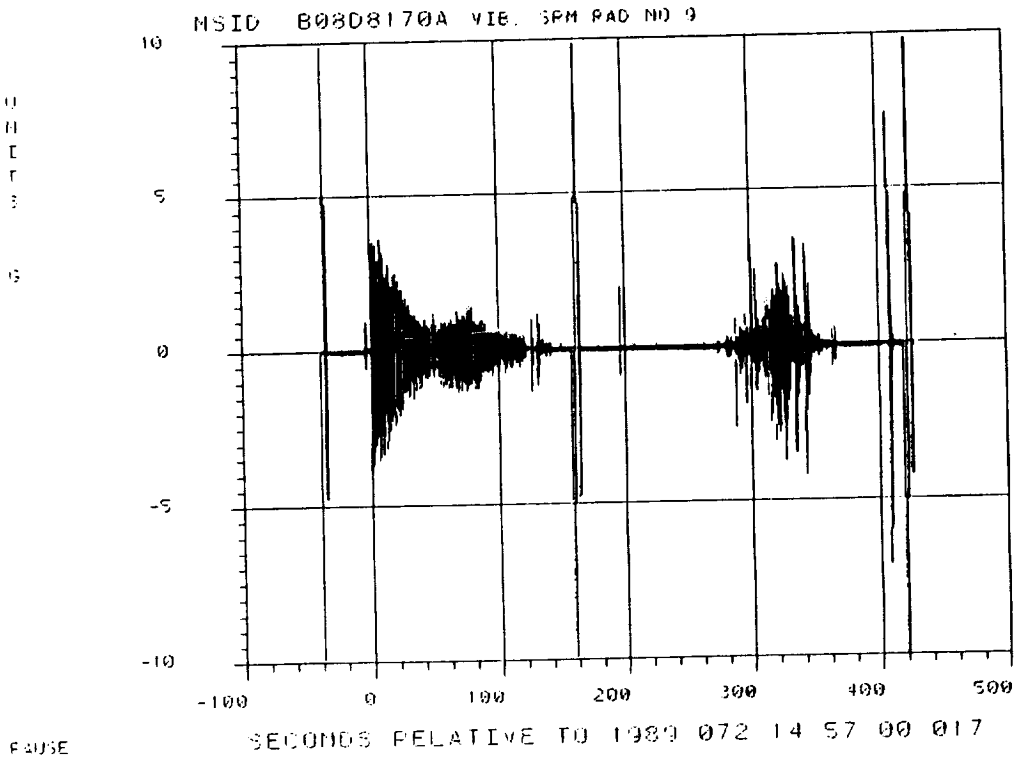

Figure 4.7-27. Acceleration Time History (Gage B08D8170A)

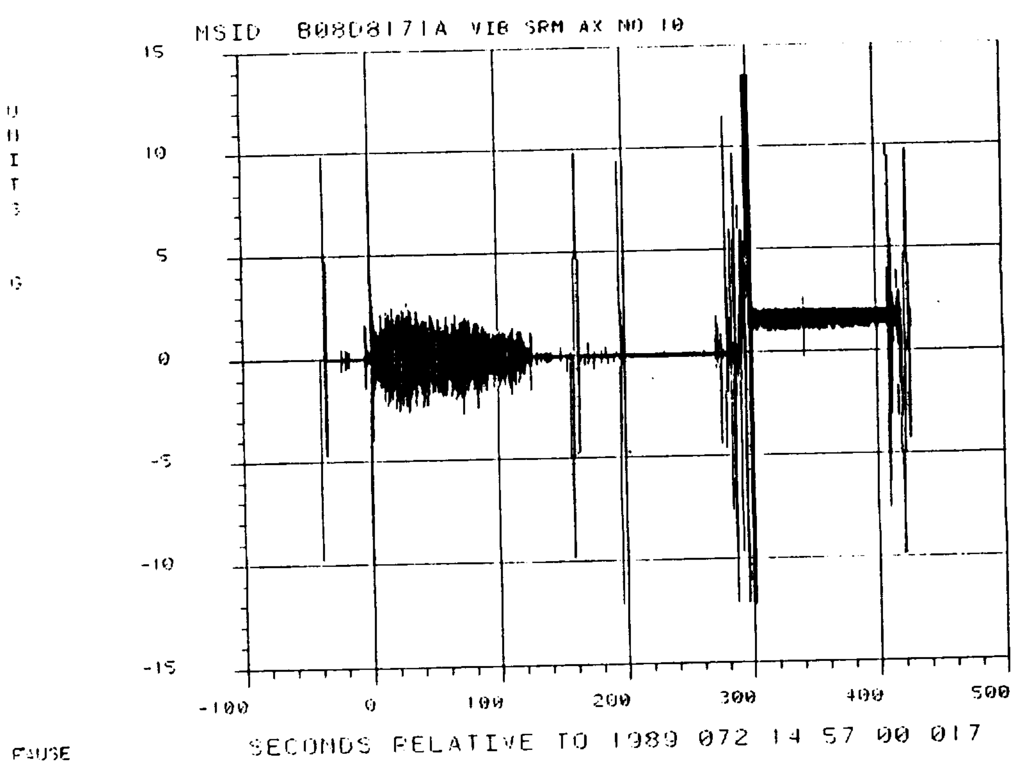

Figure 4.7-28. Acceleration Time History (Gage B08D8171A)

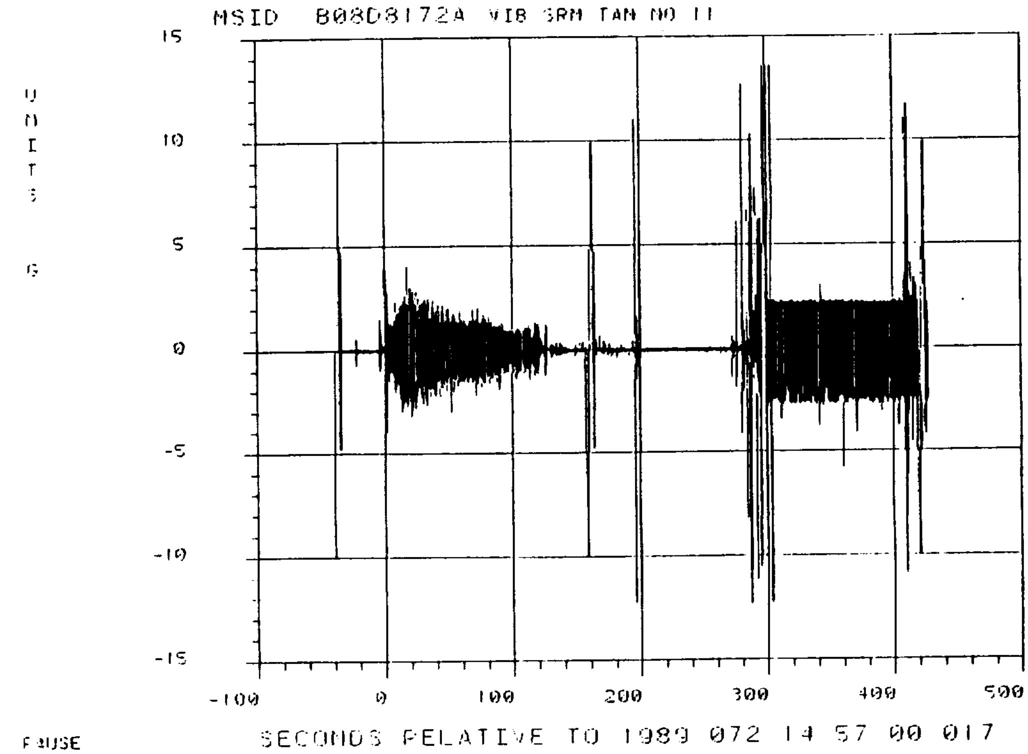

Figure 4.7-29. Acceleration Time History (Gage B08D8172A)

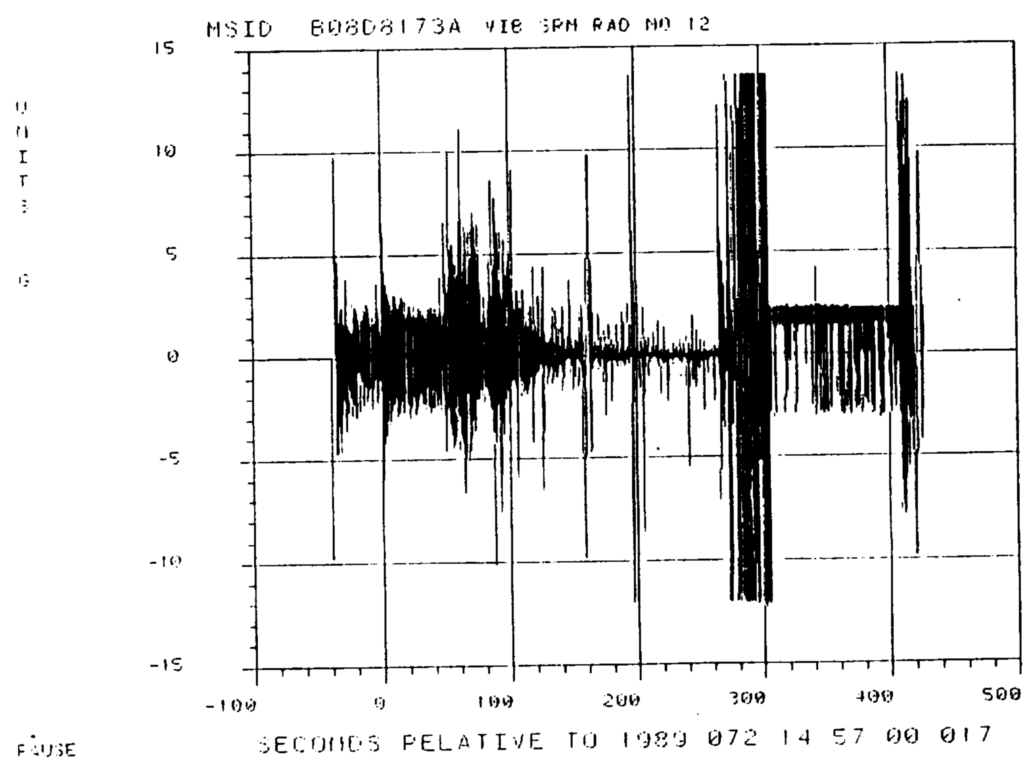

Figure 4.7-30. Acceleration Time History (Gage B08D8173A)

ORIGINAL PAGE IS
OF POOR QUALITY

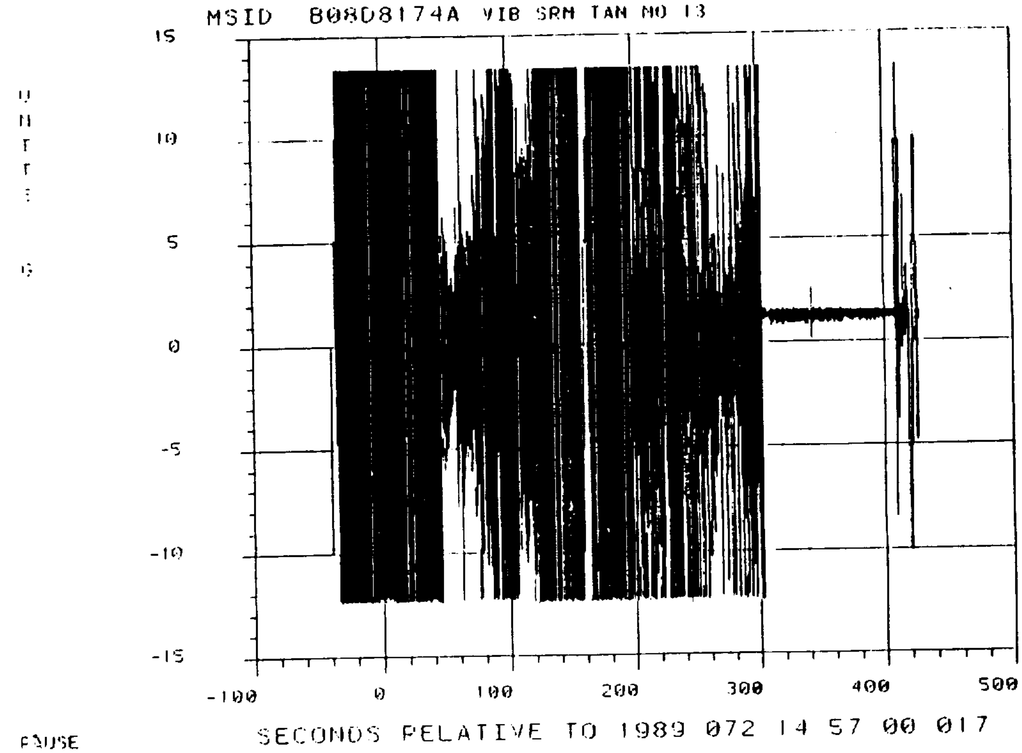

Figure 4.7-31. Acceleration Time History (Gage B08D8174A)

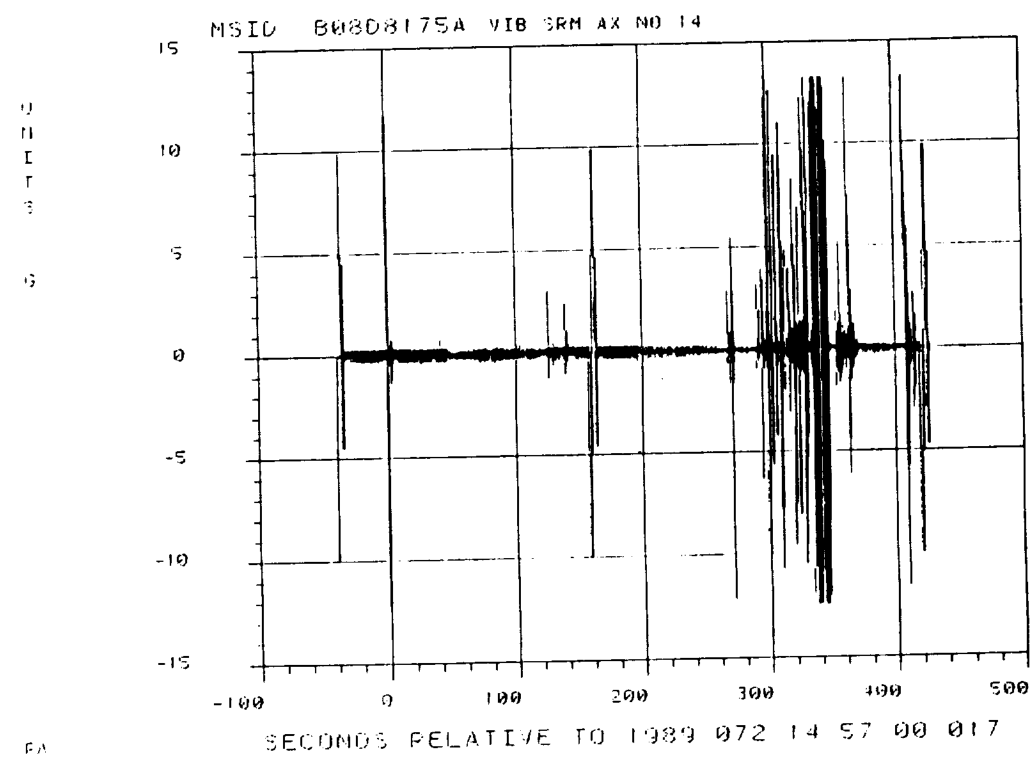

Figure 4.7-32. Acceleration Time History (Gage B08D8175A)

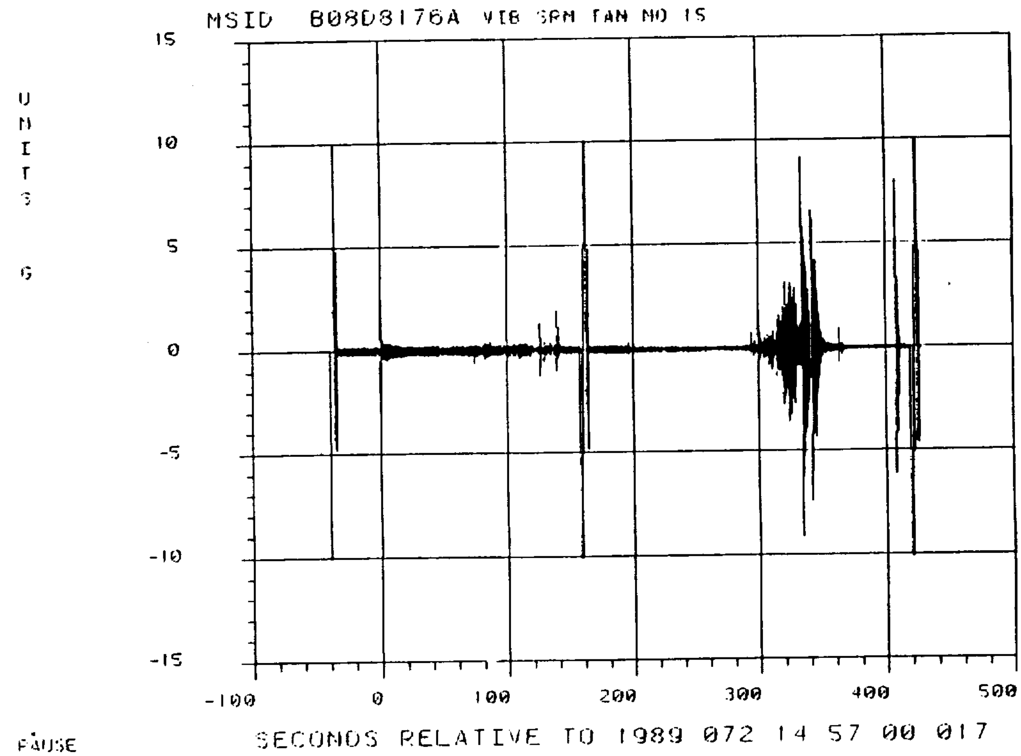

Figure 4.7-33. Acceleration Time History (Gage B08D8176A)

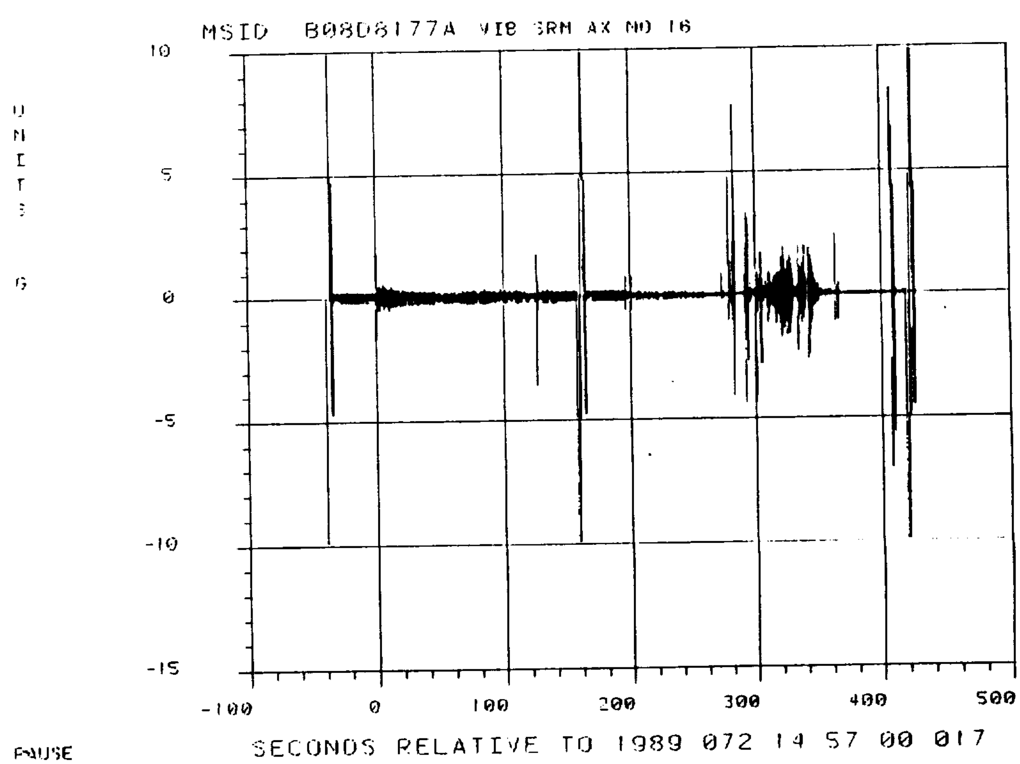

Figure 4.7-34. Acceleration Time History (Gage B08D8177A)

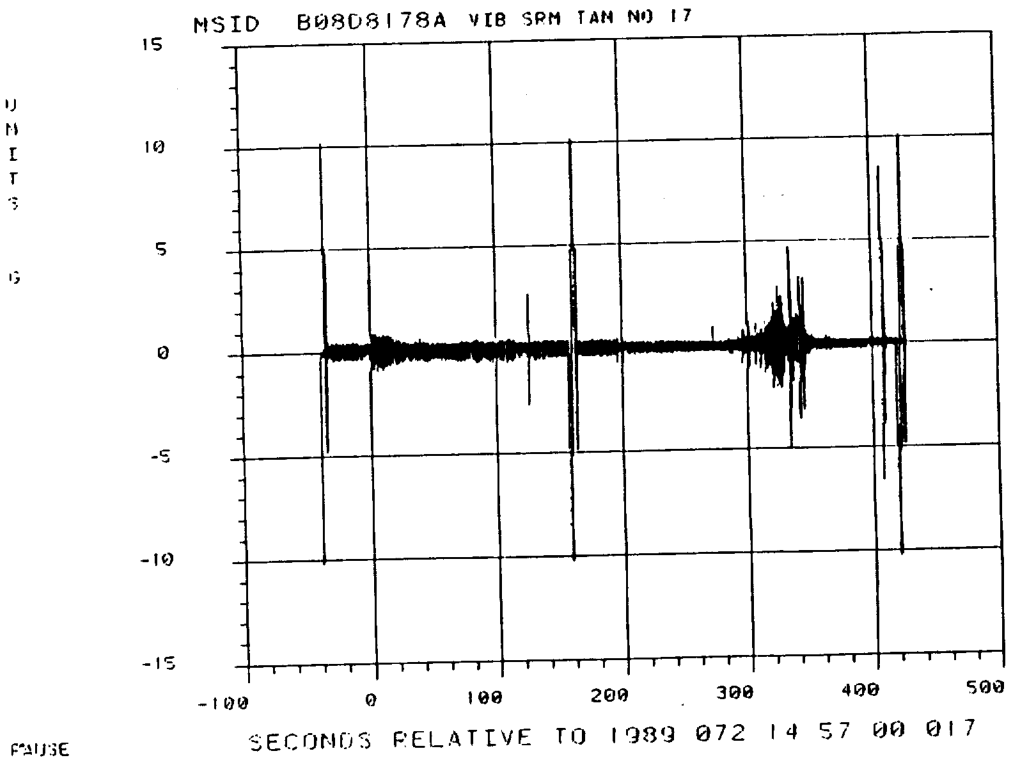

Figure 4.7-35. Acceleration Time History (Gage B08D8178A)

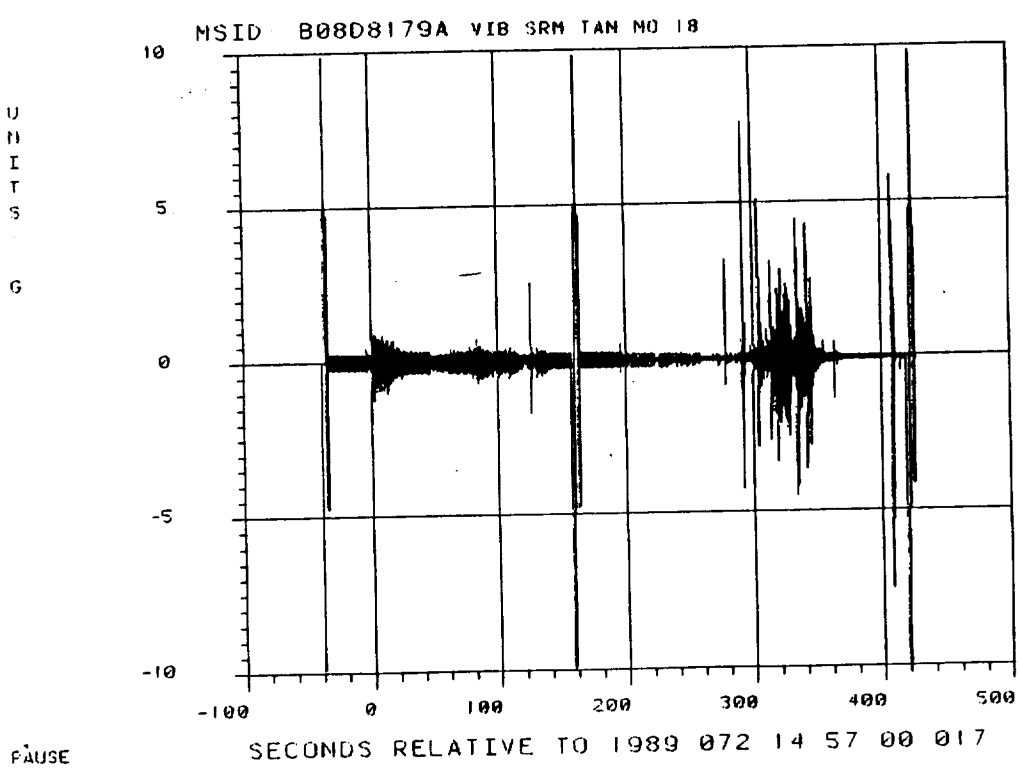

Figure 4.7-36. Acceleration Time History (Gage B08D8179A)

Another important loading event is water impact. Accelerometer data can be used directly to estimate the shock loading during impact. Currently, this task is also in work.

4.7.3 Predicted Versus Actual Results

To compare the predicted and measured results, the accelerometer data from 0 to 5 sec were selected (the analytical model used for the predictions is valid only for the first few seconds after ignition). These data were then filtered at 40 Hz (which is the cutoff frequency of the residual modes of the NASTRAN analytical finite element model). The predictions at the nozzle area are not available, since the finite element model resolution is not fine enough in this region to make accurate predictions. The available prediction results were compared with the measured 360L003 (STS-29) values and are presented in Tables 4.7-1 and 4.7-2.

In reading Table 4.7-1, it must be realized that the NASTRAN model acceleration predictions include the rigid body accelerations, while the accelerometer gages cannot detect this low-frequency dc movement. In addition, the force values used in the prediction model are preflight predicted values from previous experiences. These values are not accurate when the loading environment is random. Further comparisons will be made when the updated forces (reconstructed loads) are available and will be included in Volume XI of this report.

4.7.4 Modal Frequencies

To identify the modes of SRM structural vibration, the method of discrete Fourier transform (FT) is used. This method selects the data from a short time period (such as 2 sec) and performs the fast Fourier transform (FFT). The resulting frequency spectra are plotted in a stacking manner for different time periods to form a waterfall plot. The waterfall plots for each channel are shown in Figures 4.7-37 through 4.7-68. If the excitation sources are wide-band noises, the discrete FT will show the characteristics similar to that of transfer function.

It is believed that the frequency of the SRB modes during burn will increase with time due to the decreasing of mass. However, evaluation of the waterfall plots from flight data, unlike those from static firing, does not shown such increasing frequency trends. This was also experienced on 360L002 (STS-27R). (Motor set 360L001 (STS-26R) did not have enough instrumentation to evaluate this.) After evaluation of the accelerometer data from 360L002 and 360L003, it is concluded that identifying the SRM modal frequencies using only accelerometer data is extremely difficult.

4.7.5 Conclusions and Recommendations

The dynamic data from 360L002 and 360L003 (flights STS-27 and STS-29), unlike the static firing data, show some degree of unpredictability. For example, 360L002 (STS-27R) showed unpredicted high amplitudes of vibration in the radial direction during the ignition transient (measured on STS-27 Channels B08D8166A and B08D7166A). For STS-29, 12g of vibration under 160 Hz is also

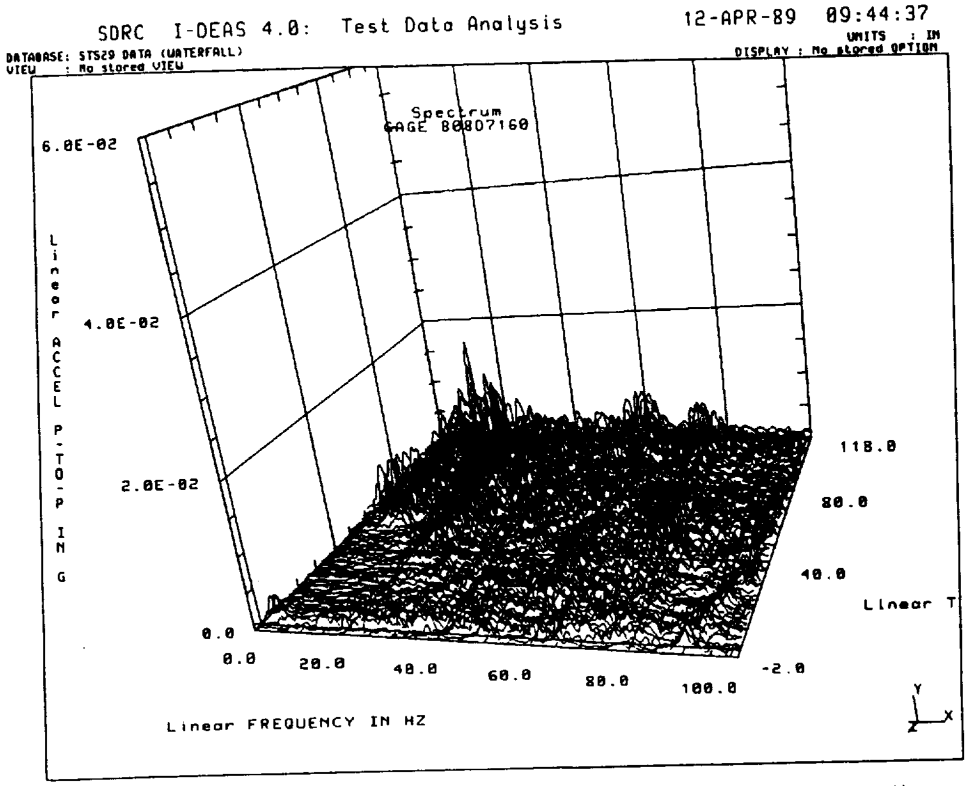

Figure 4.7-37. Random Decrement Waterfall Plot (Gage B08D7160)

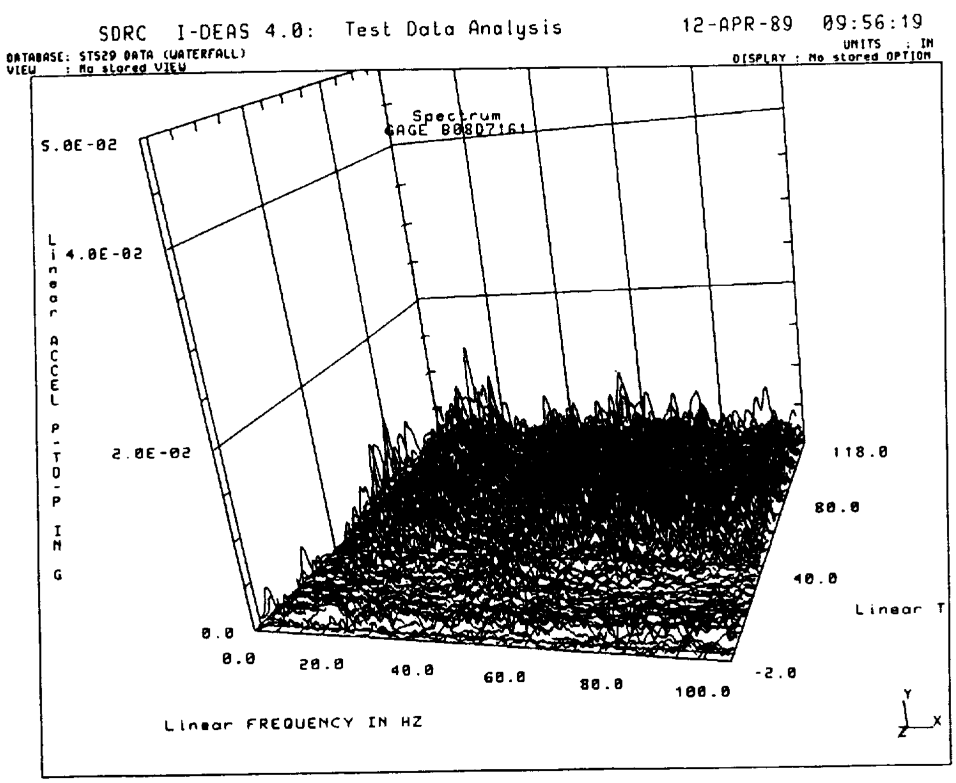

Figure 4.7-38. Random Decrement Waterfall Plot (Gage B08D7161)

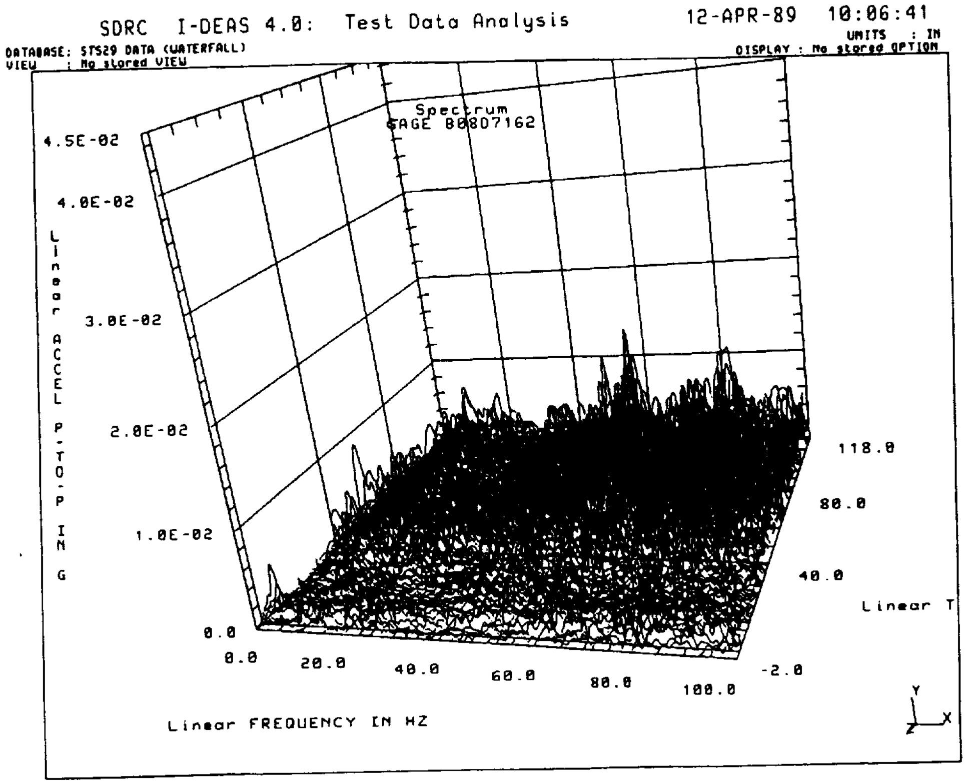

Figure 4.7-39. Random Decrement Waterfall Plot (Gage B08D7162)

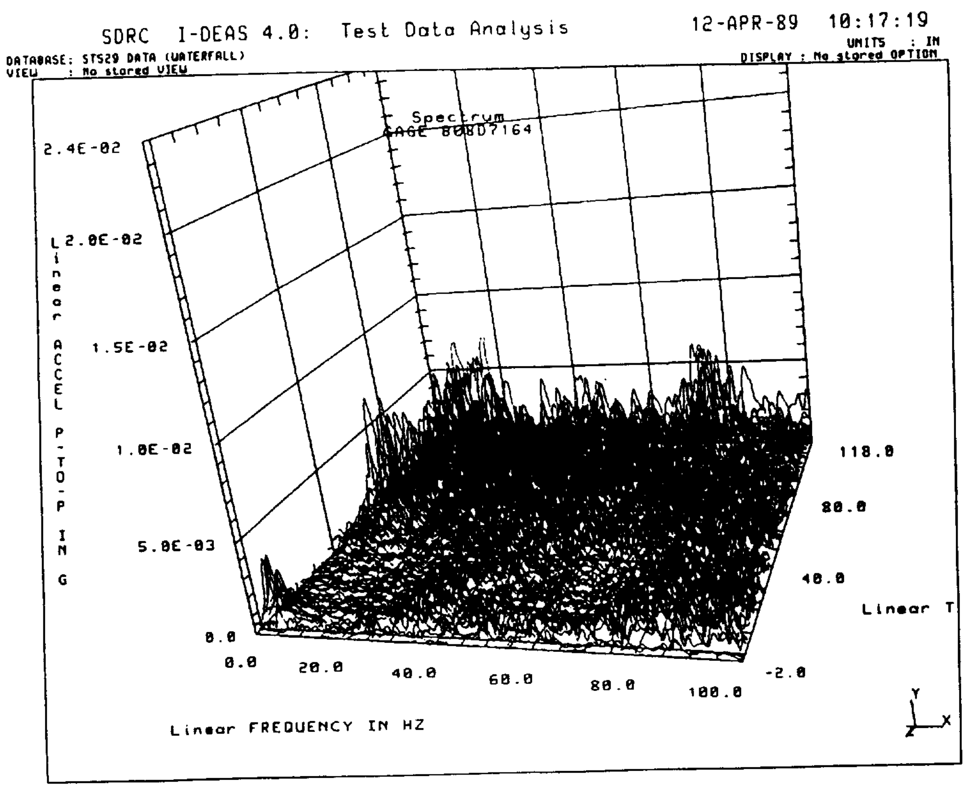

Figure 4.7-40. Random Decrement Waterfall Plot (Gage B08D7164)

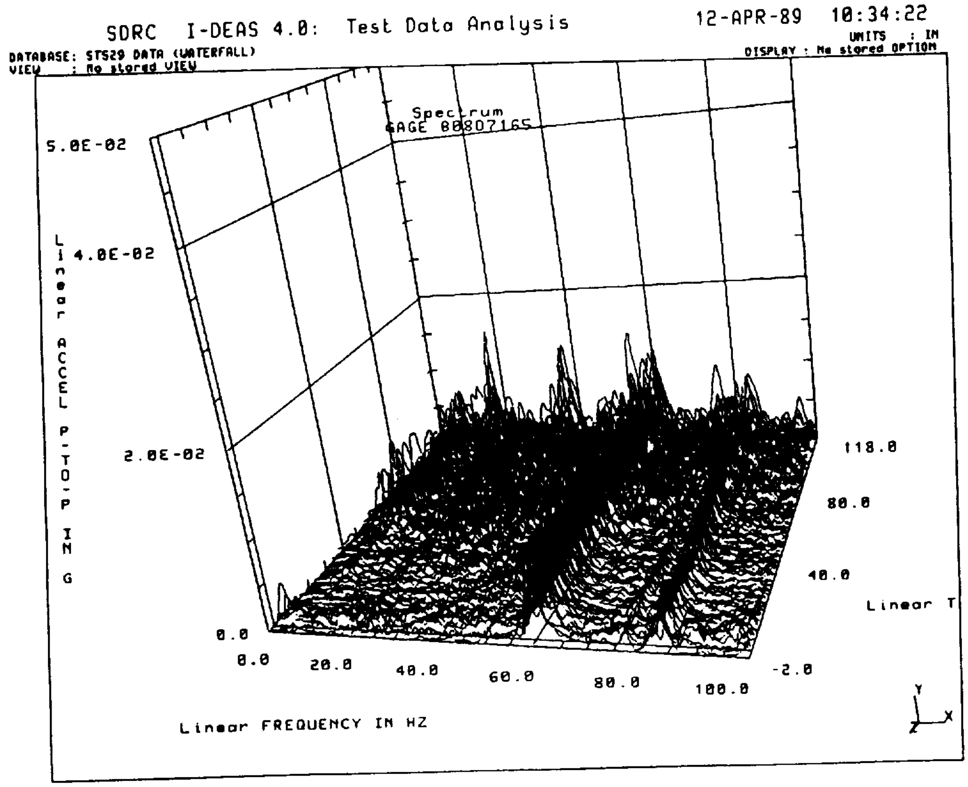

Figure 4.7-41. Random Decrement Waterfall Plot (Gage B08D7165)

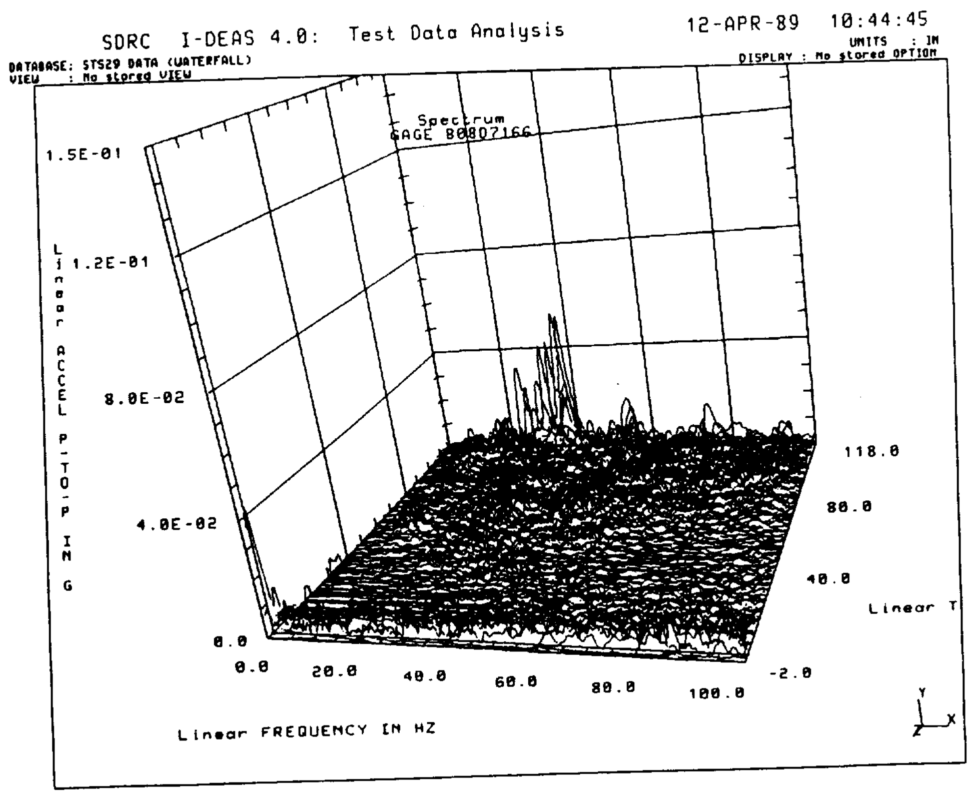

Figure 4.7-42. Random Decrement Waterfall Plot (Gage B08D7166)

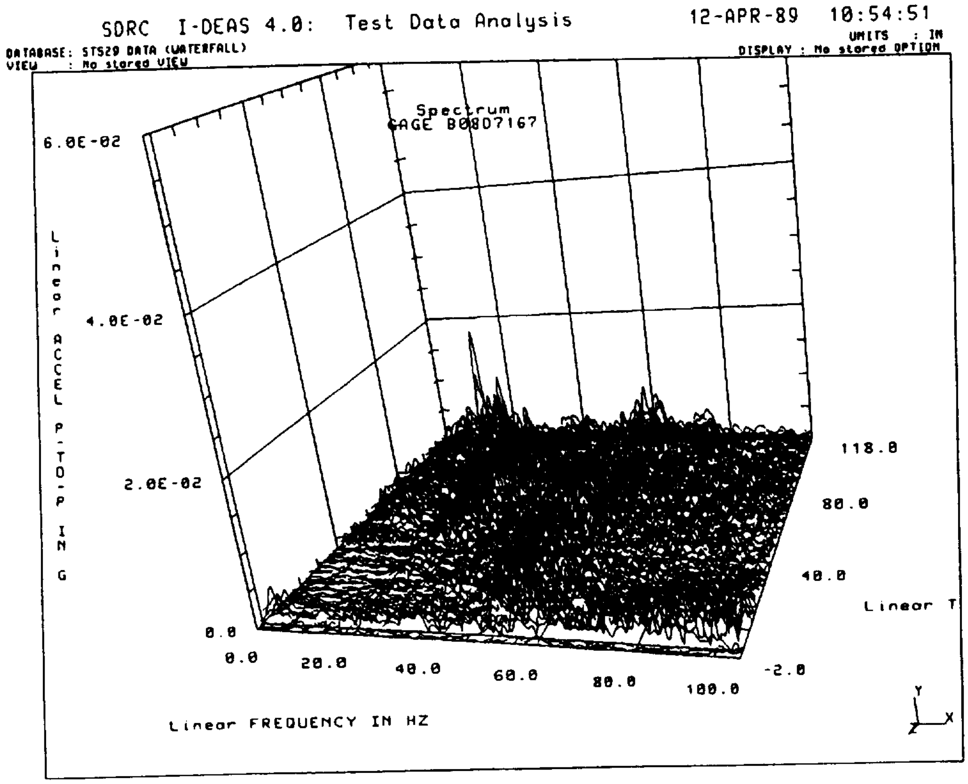

Figure 4.7-43. Random Decrement Waterfall Plot (Gage B08D7167)

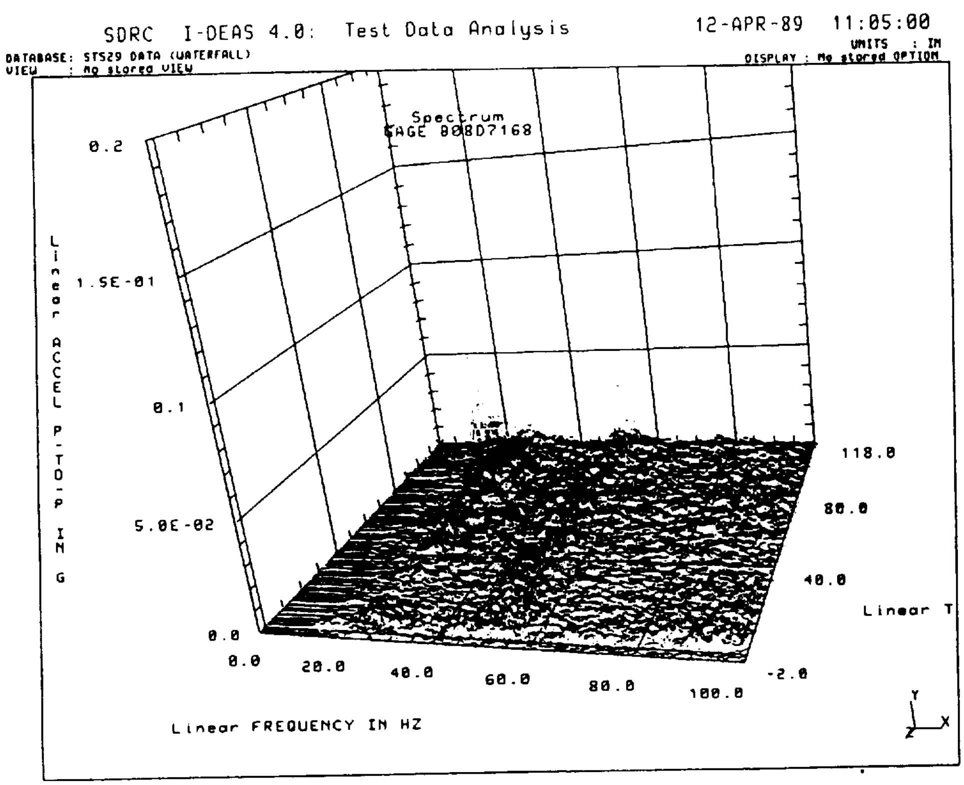

Figure 4.7-44. Random Decrement Waterfall Plot (Gage B08D7168)

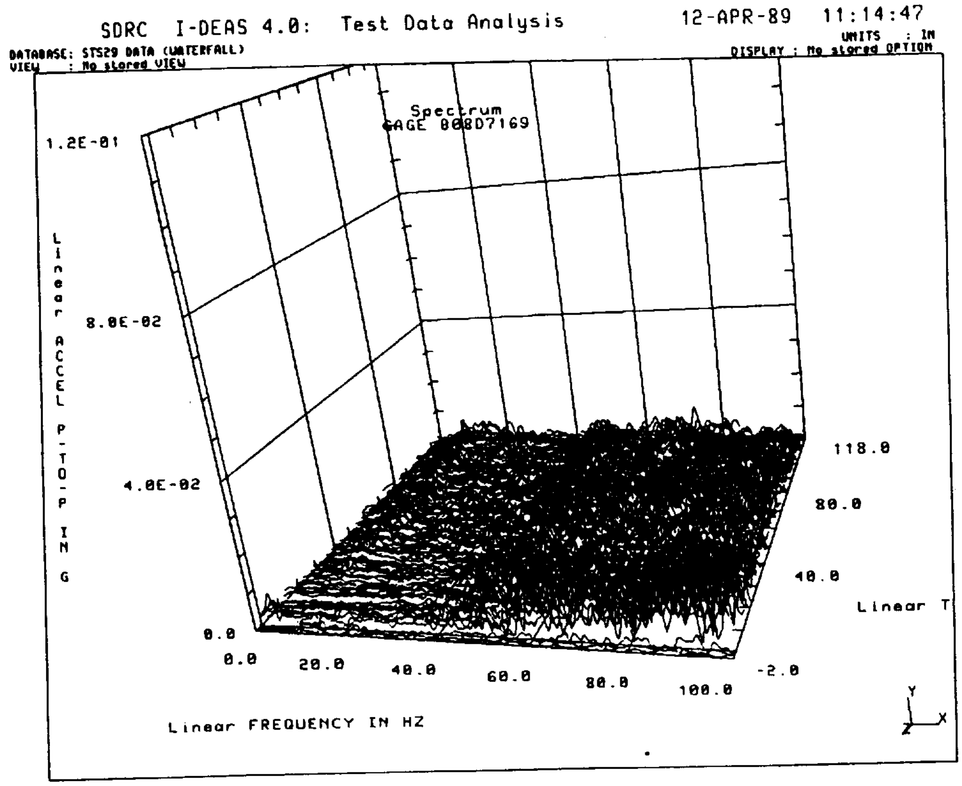

Figure 4.7-45. Random Decrement Waterfall Plot (Gage B08D7169)

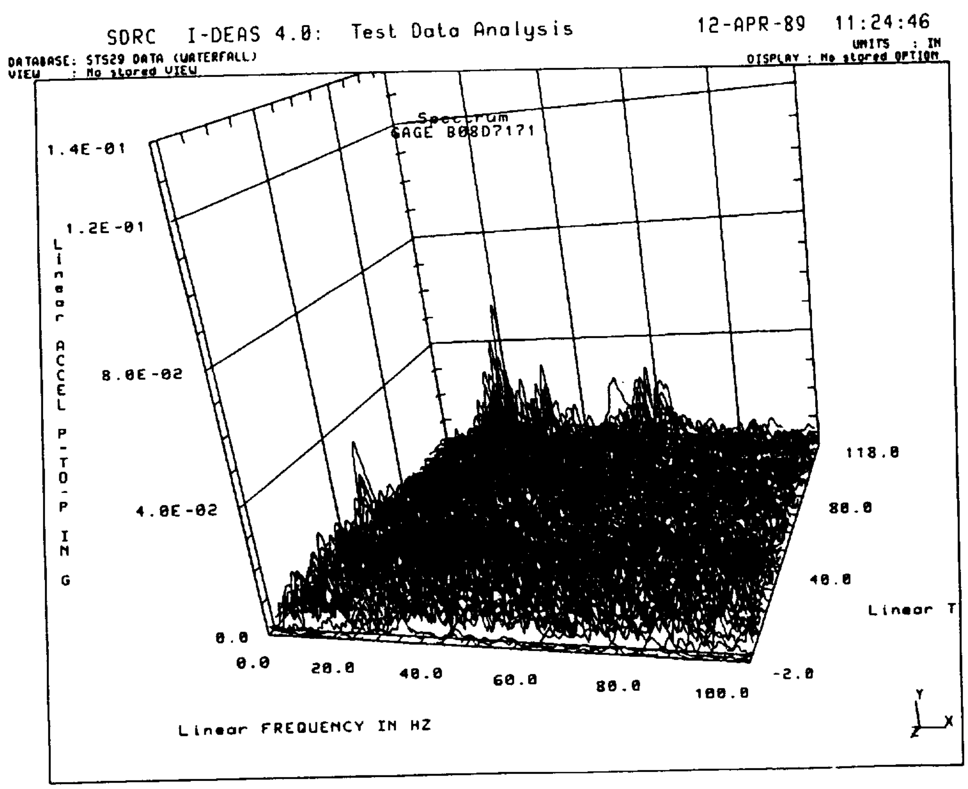

Figure 4.7-46. Random Decrement Waterfall Plot (Gage B08D7171)

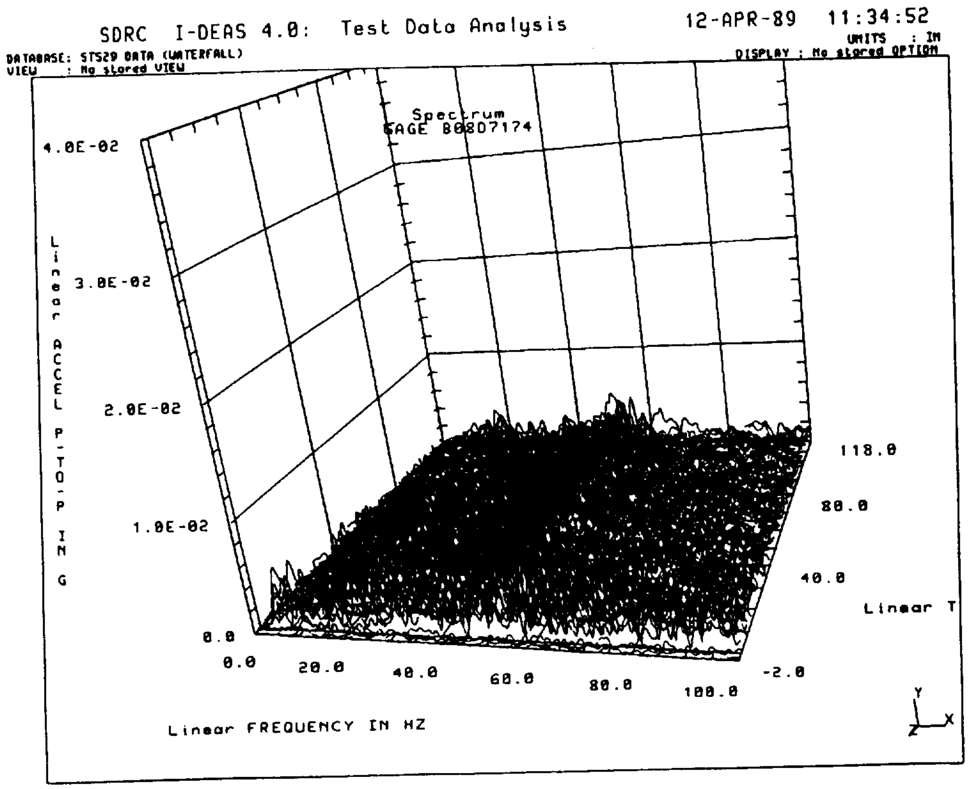

Figure 4.7-47. Random Decrement Waterfall Plot (Gage B08D7174)

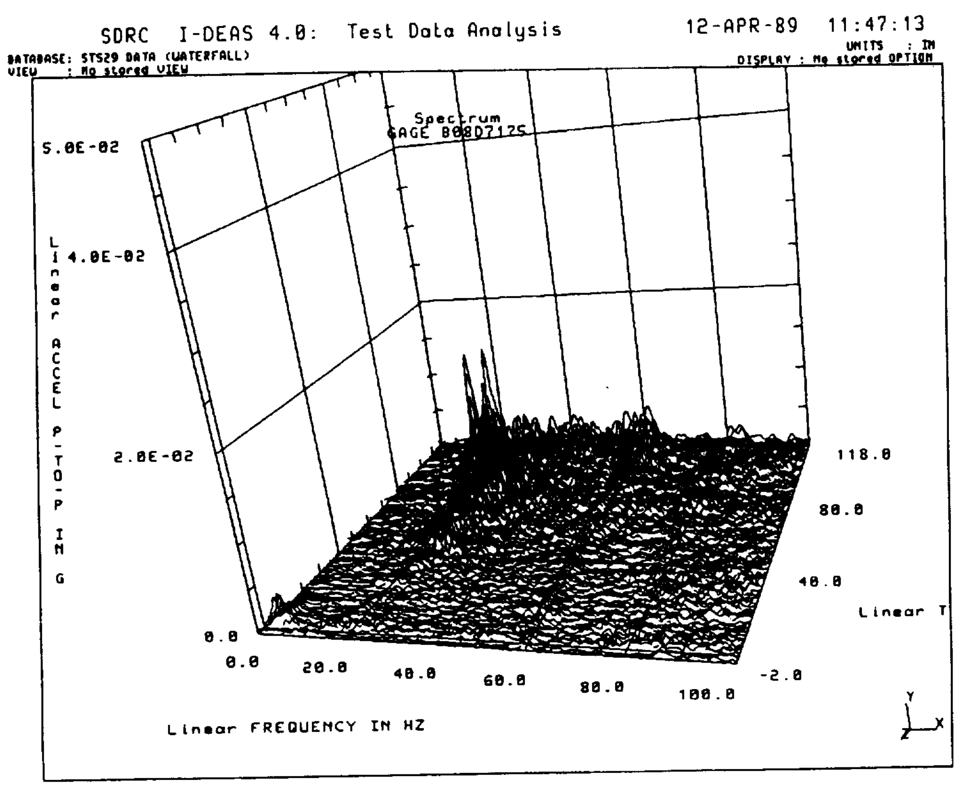

Figure 4.7-48. Random Decrement Waterfall Plot (Gage B08D7175)

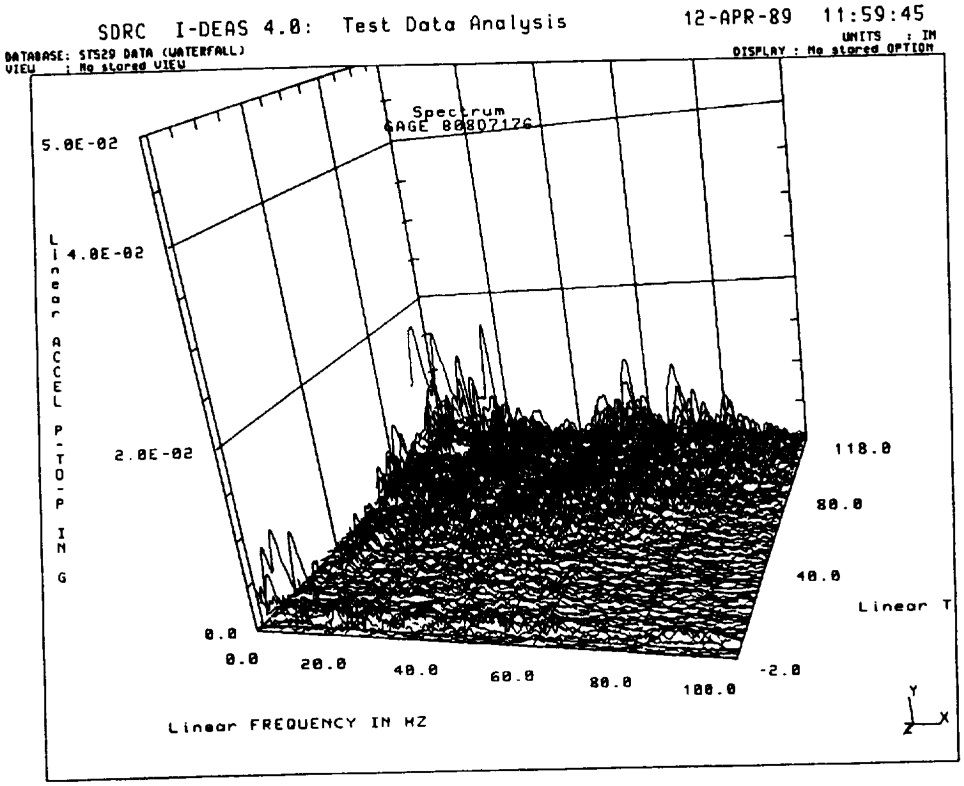

Figure 4.7-49. Random Decrement Waterfall Plot (Gage B08D7176)

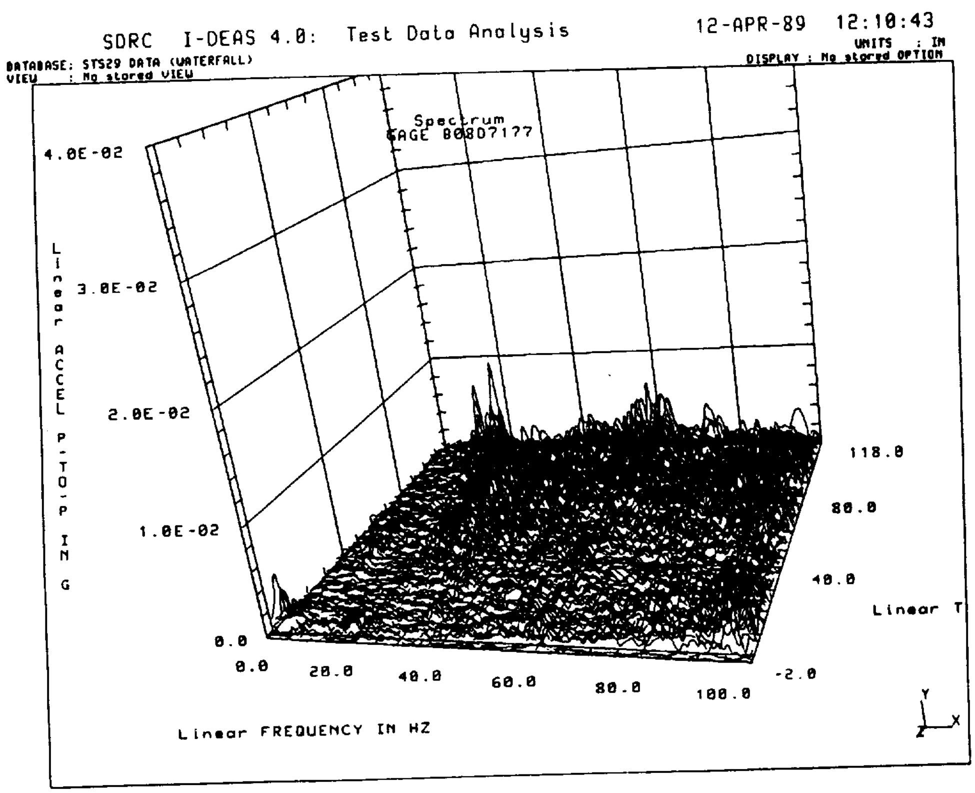

Figure 4.7-50. Random Decrement Waterfall Plot (Gage B08D7177)

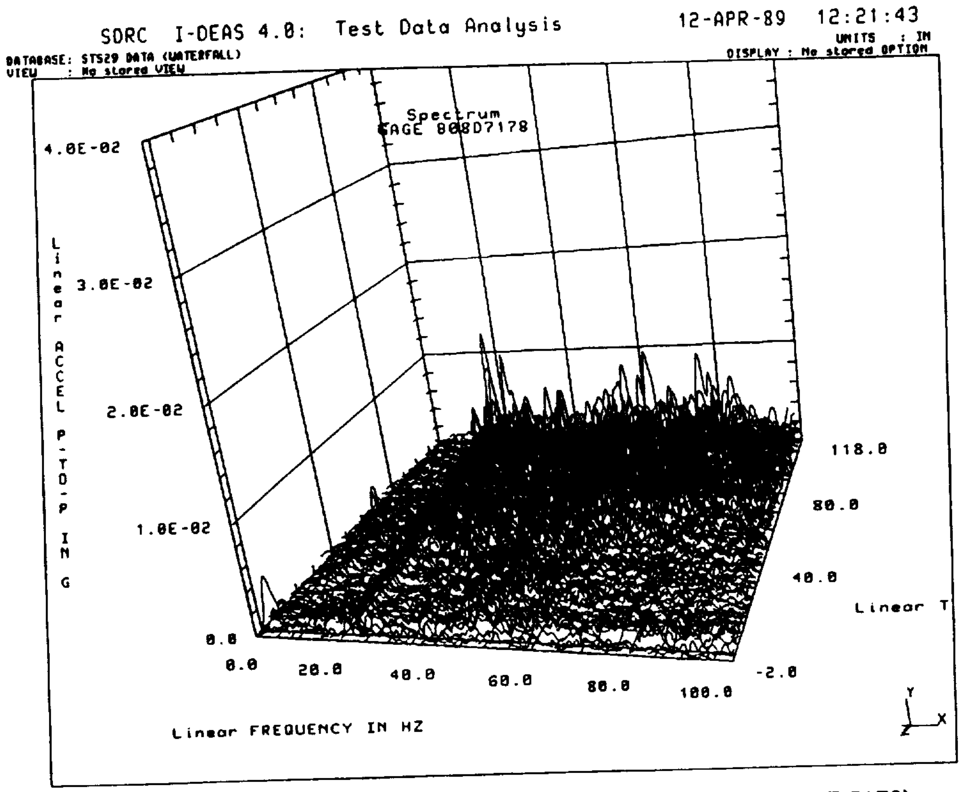

Figure 4.7-51. Random Decrement Waterfall Plot (Gage B08D7178)

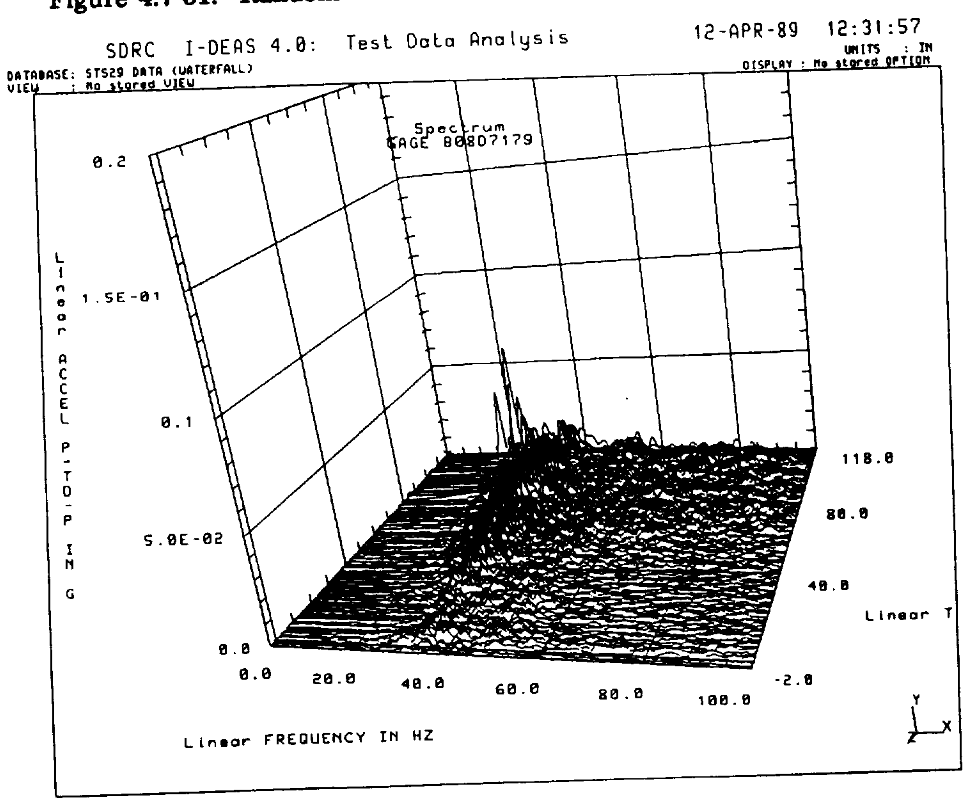

Figure 4.7-52. Random Decrement Waterfall Plot (Gage B08D7179)

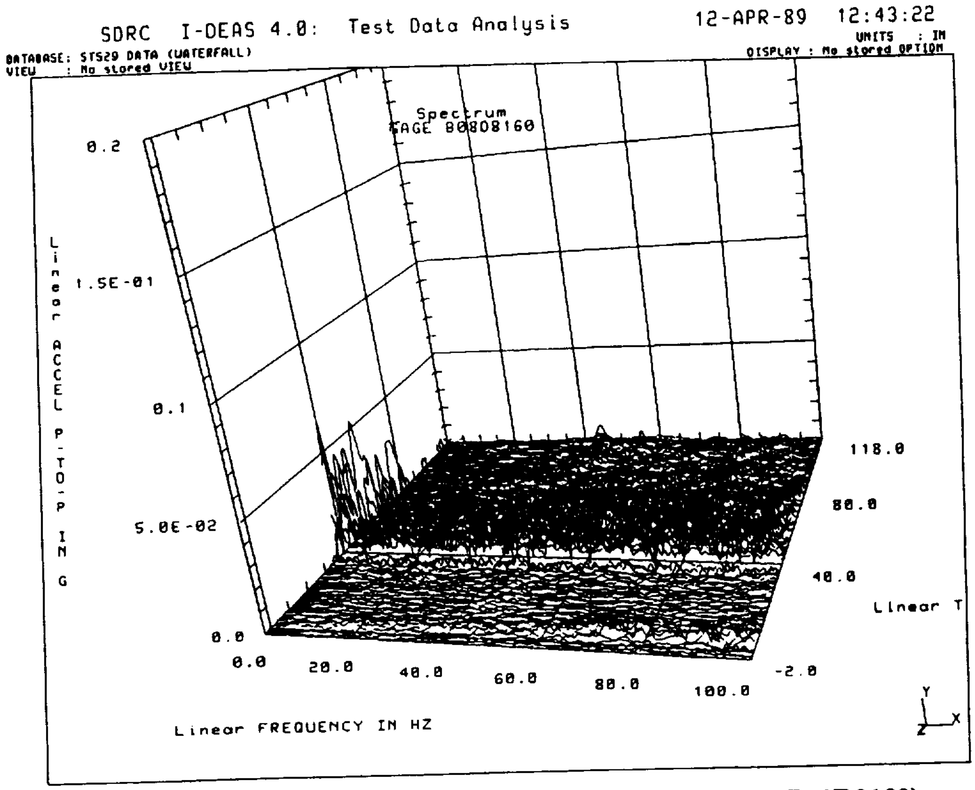

Figure 4.7-53. Random Decrement Waterfall Plot (Gage B08D8160)

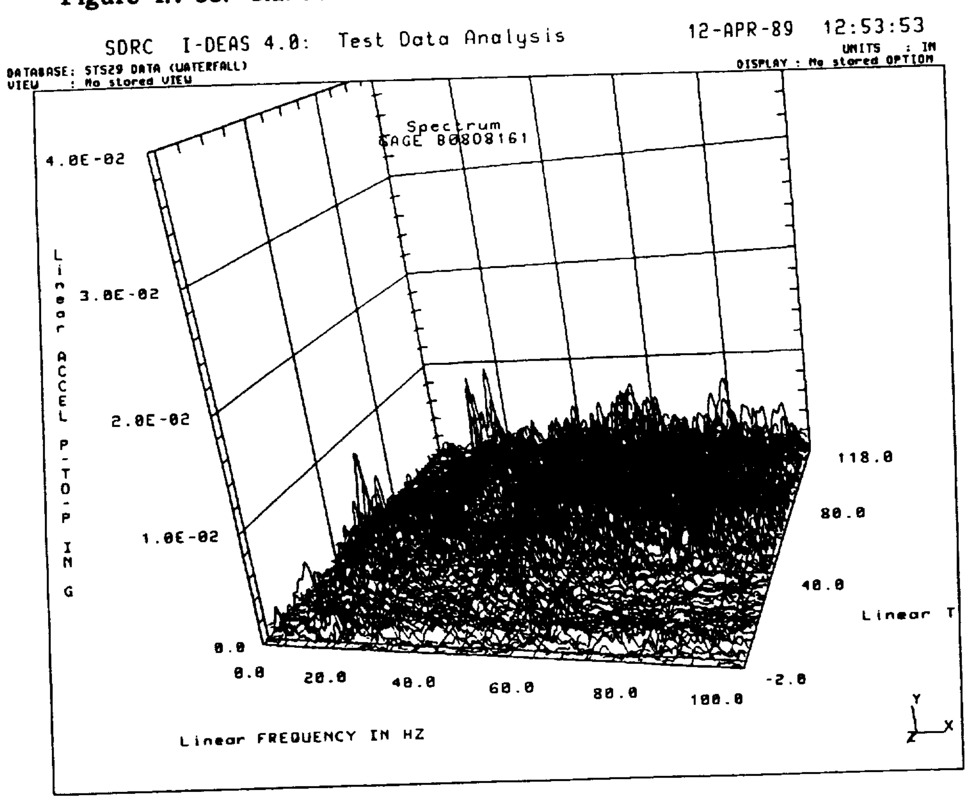

Figure 4.7-54. Random Decrement Waterfall Plot (Gage B08D8161)

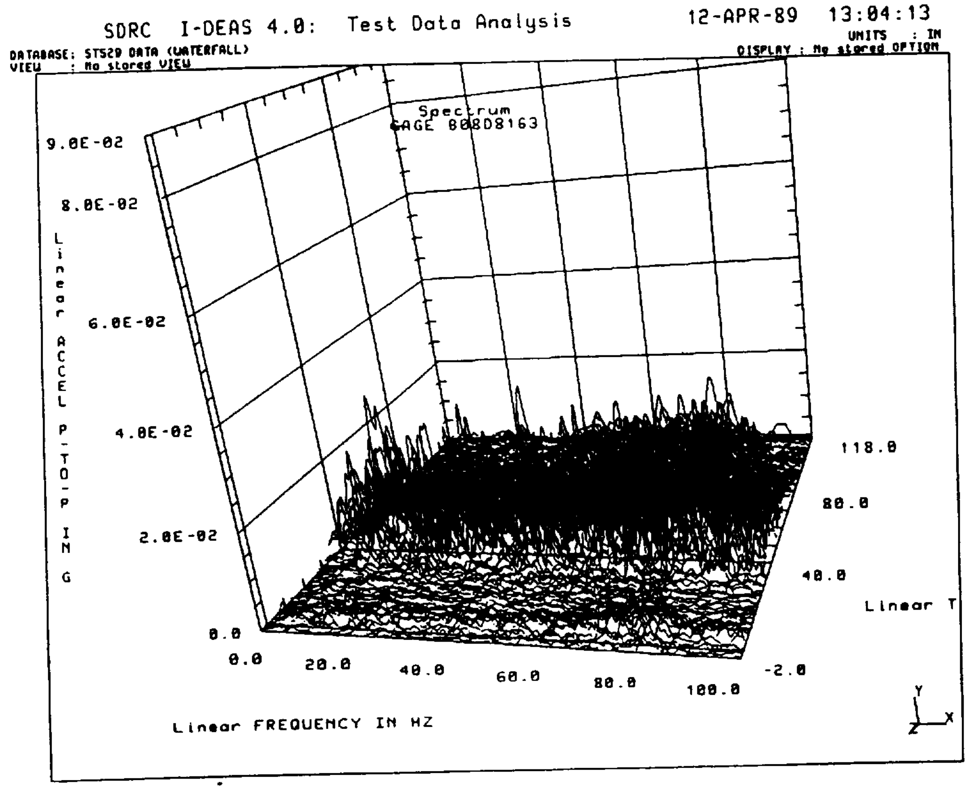

Figure 4.7-55. Random Decrement Waterfall Plot (Gage B08D8163)

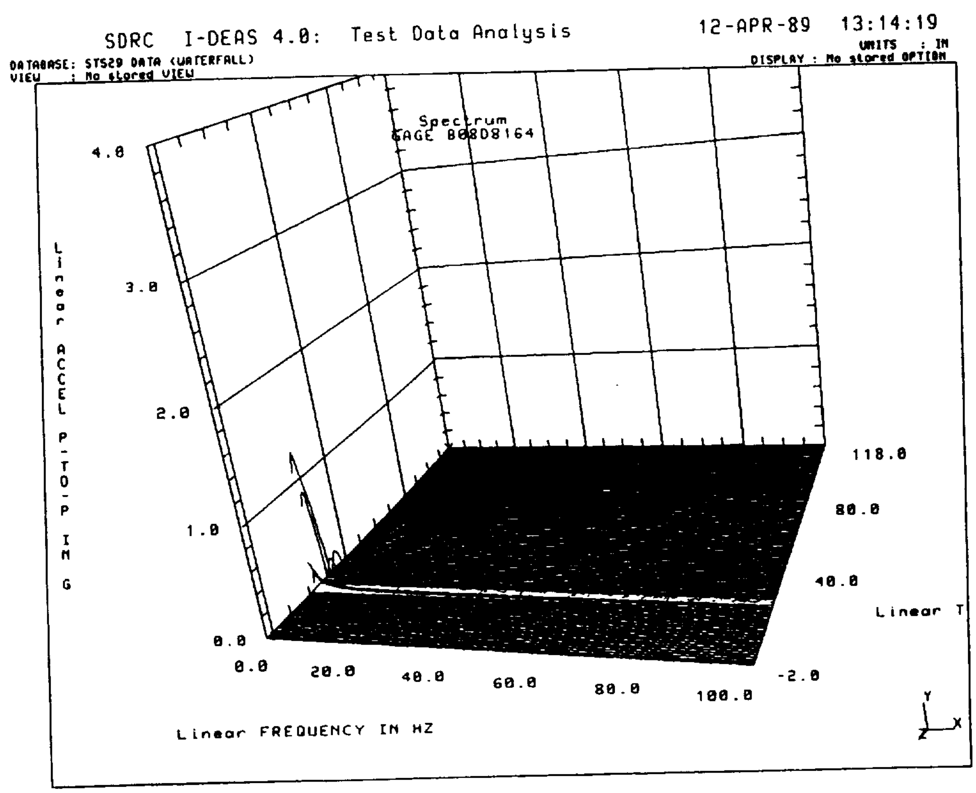

Figure 4.7-56. Random Decrement Waterfall Plot (Gage B08D8164)

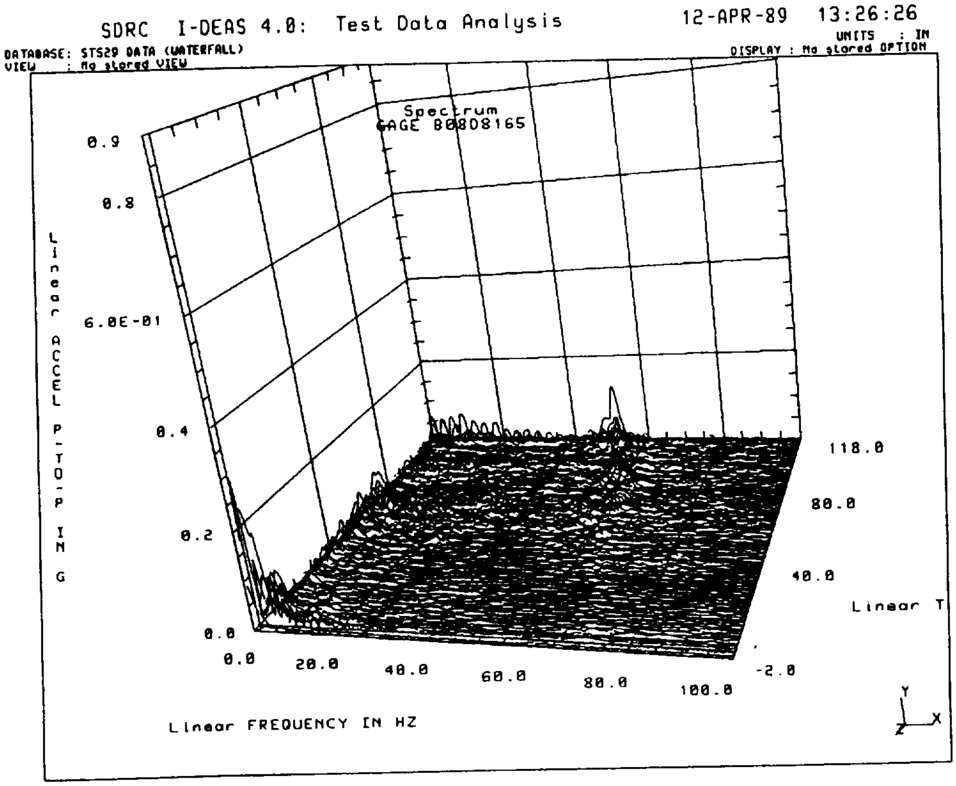

Figure 4.7-57. Random Decrement Waterfall Plot (Gage B08D8165)

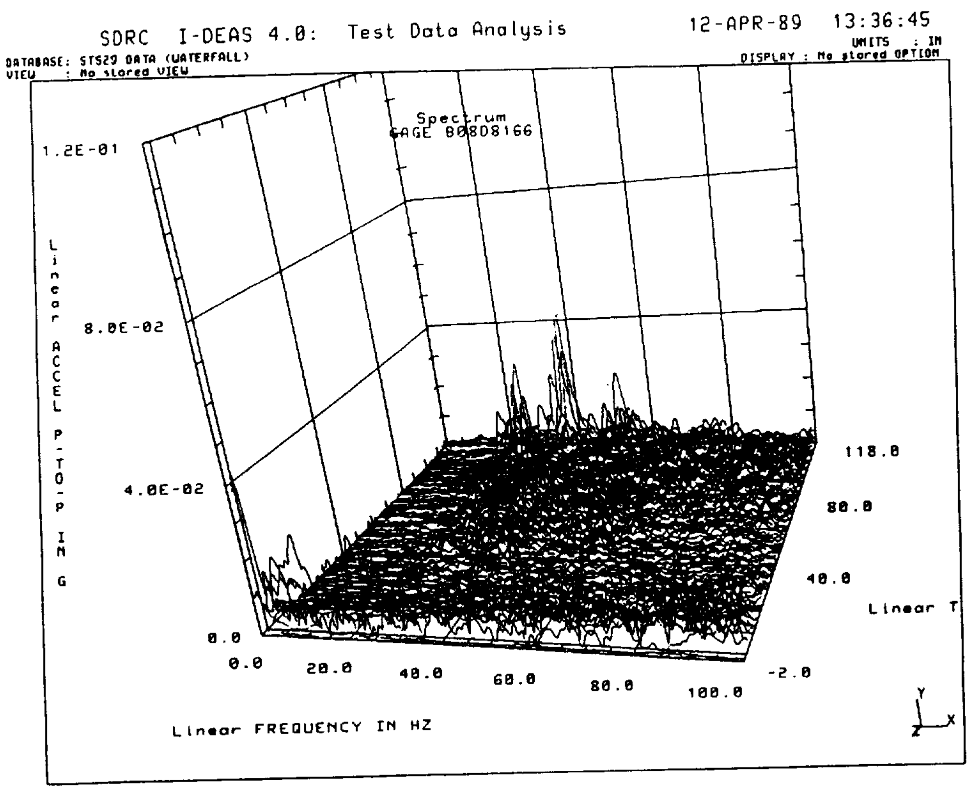

Figure 4.7-58. Random Decrement Waterfall Plot (Gage B08D8166)

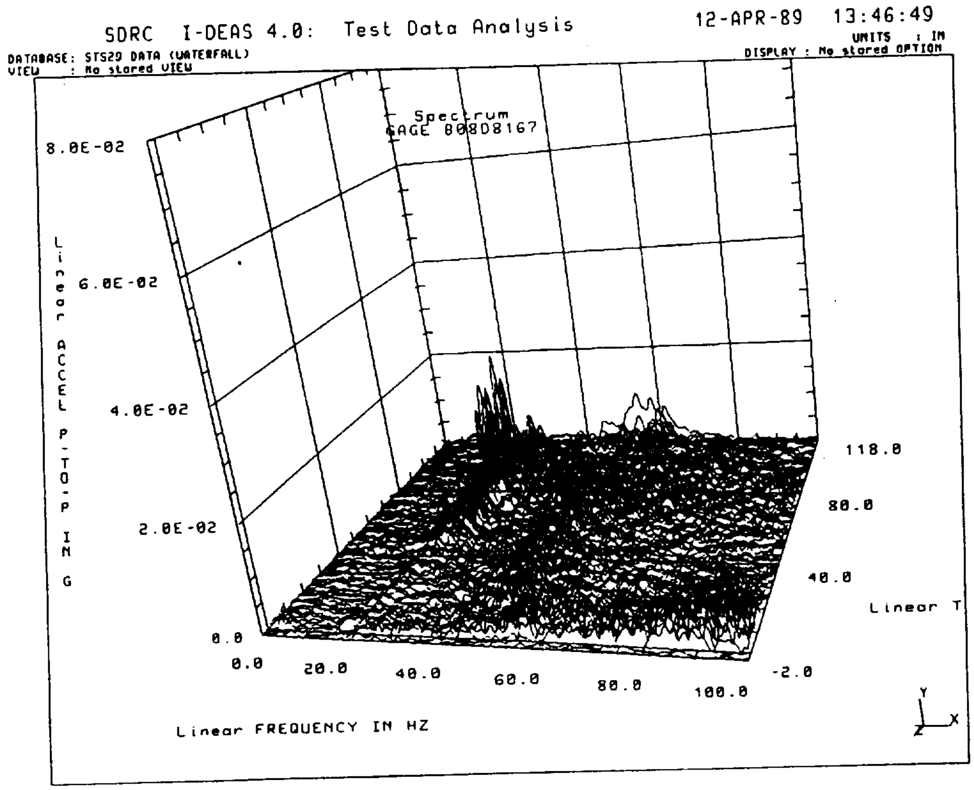

Figure 4.7-59. Random Decrement Waterfall Plot (Gage B08D8167)

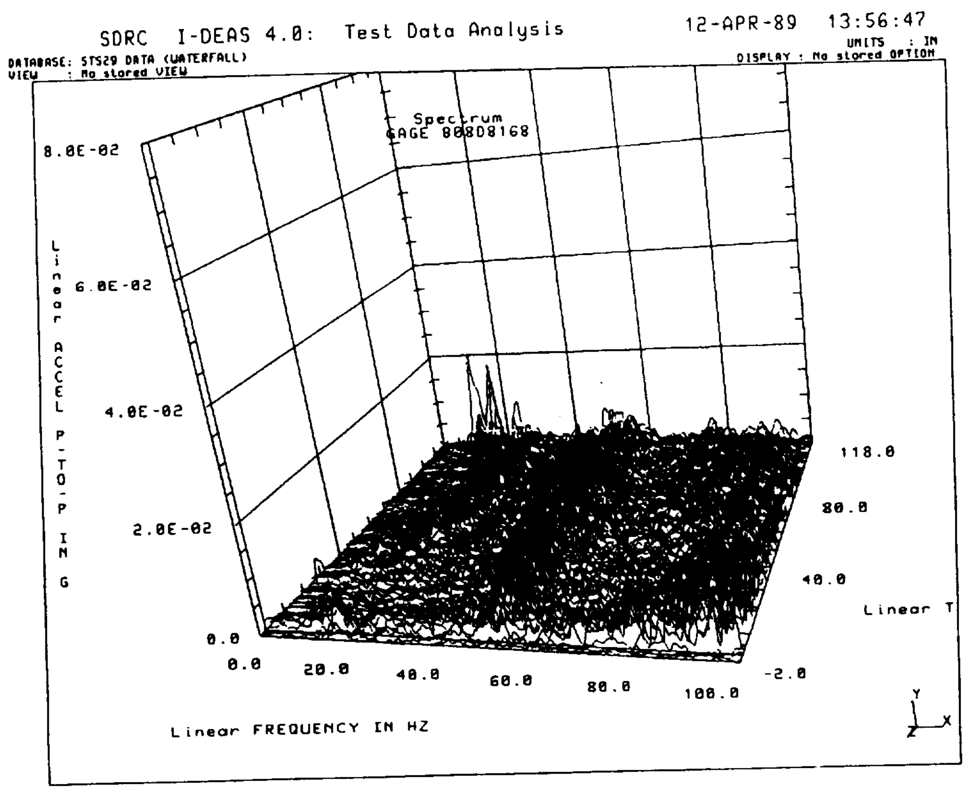

Figure 4.7-60. Random Decrement Waterfall Plot (Gage B08D8168)

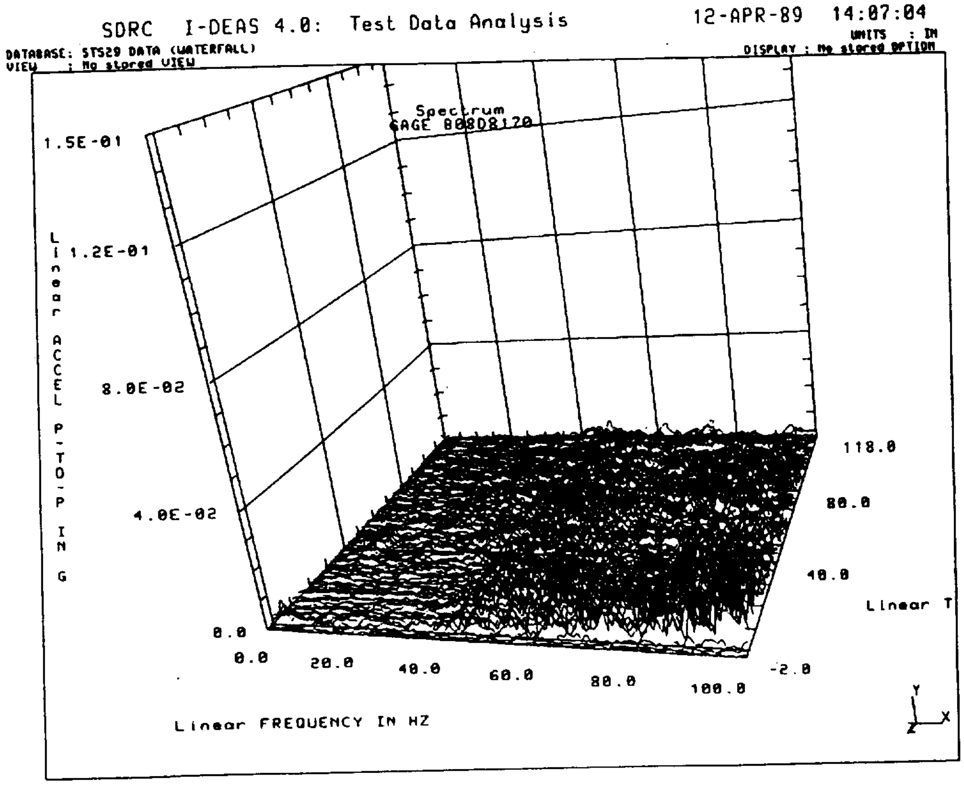

Figure 4.7-61. Random Decrement Waterfall Plot (Gage B08D8170)

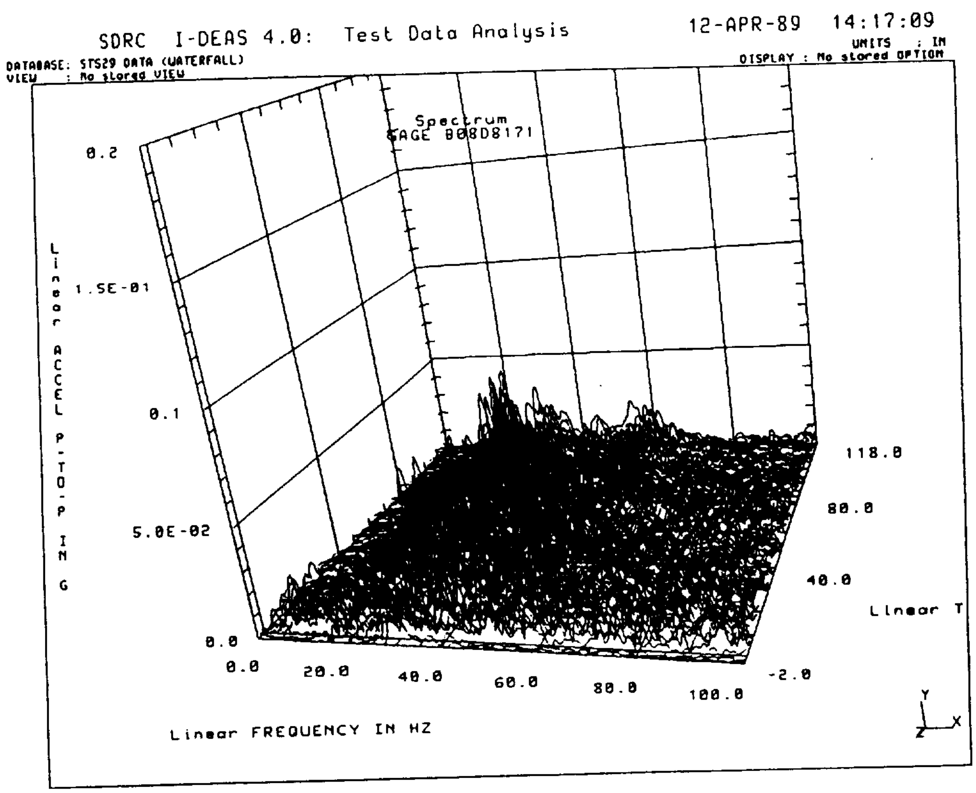

Figure 4.7-62. Random Decrement Waterfall Plot (Gage B08D8171)

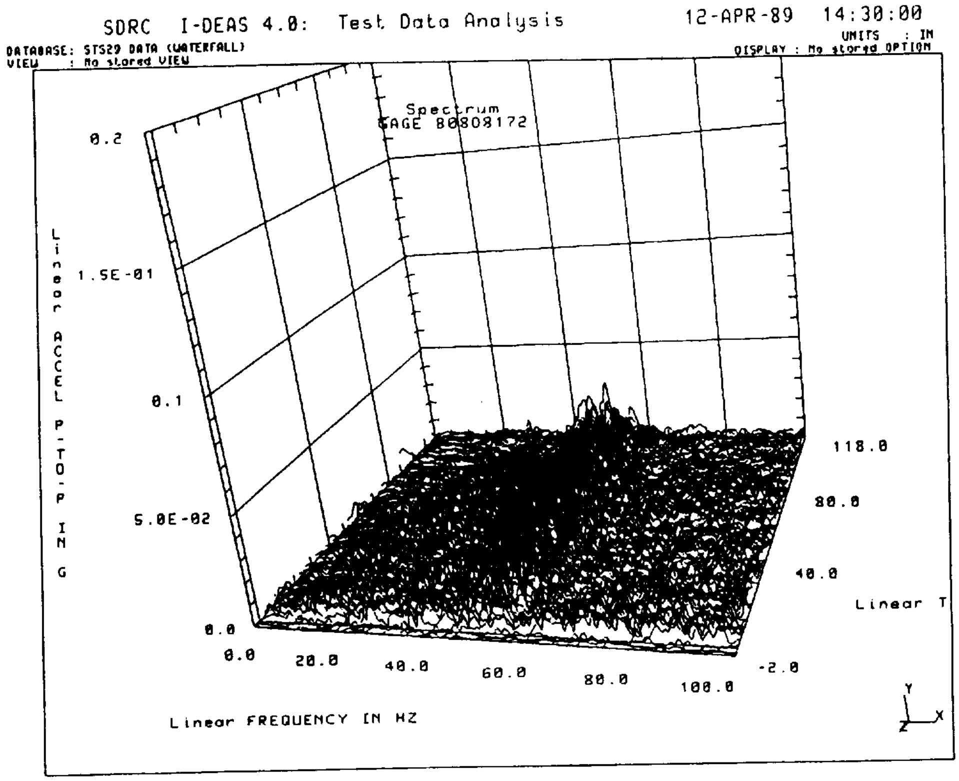

Figure 4.7-63. Random Decrement Waterfall Plot (Gage B08D8172)

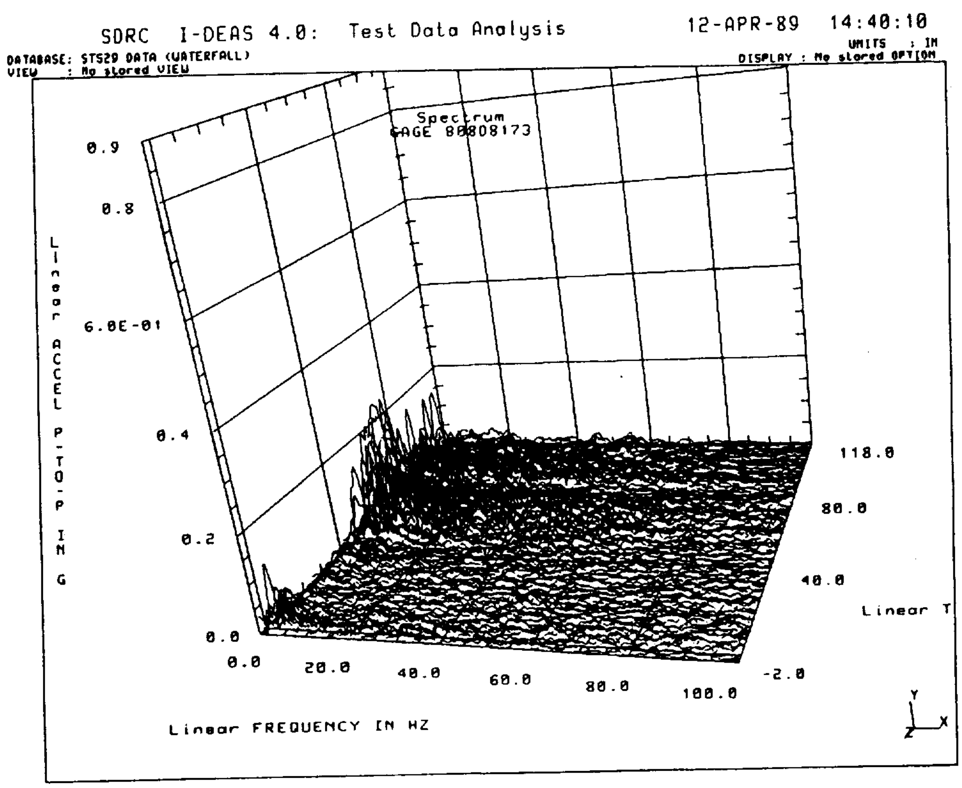

Figure 4.7-64. Random Decrement Waterfall Plot (Gage B08D8173)

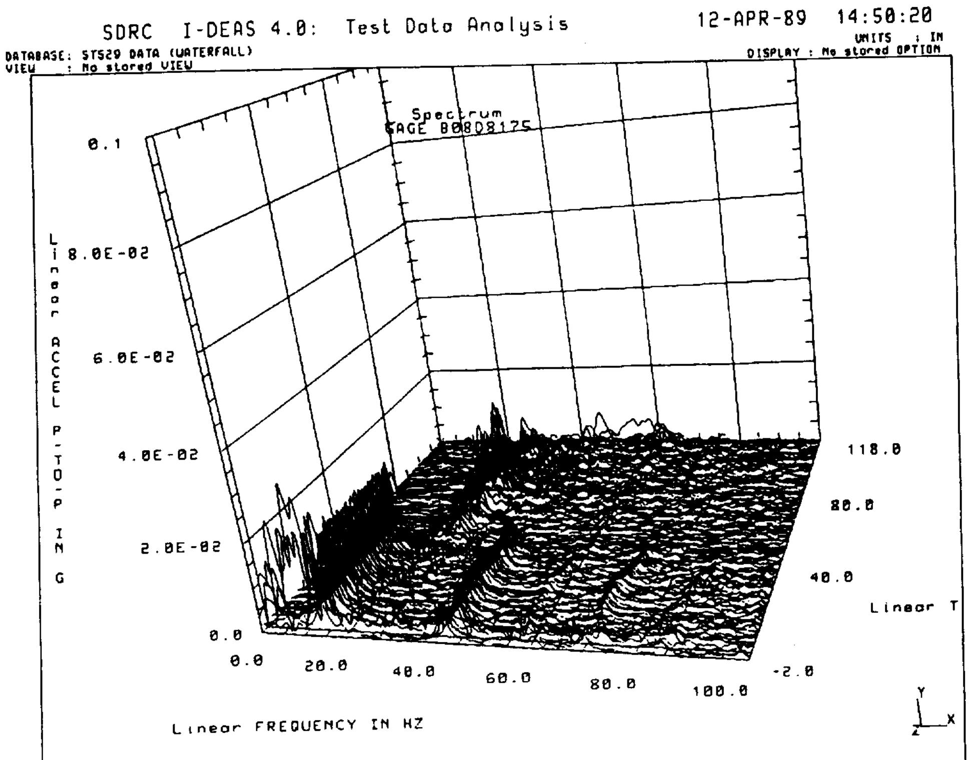

Figure 4.7-65. Random Decrement Waterfall Plot (Gage B08D8175)

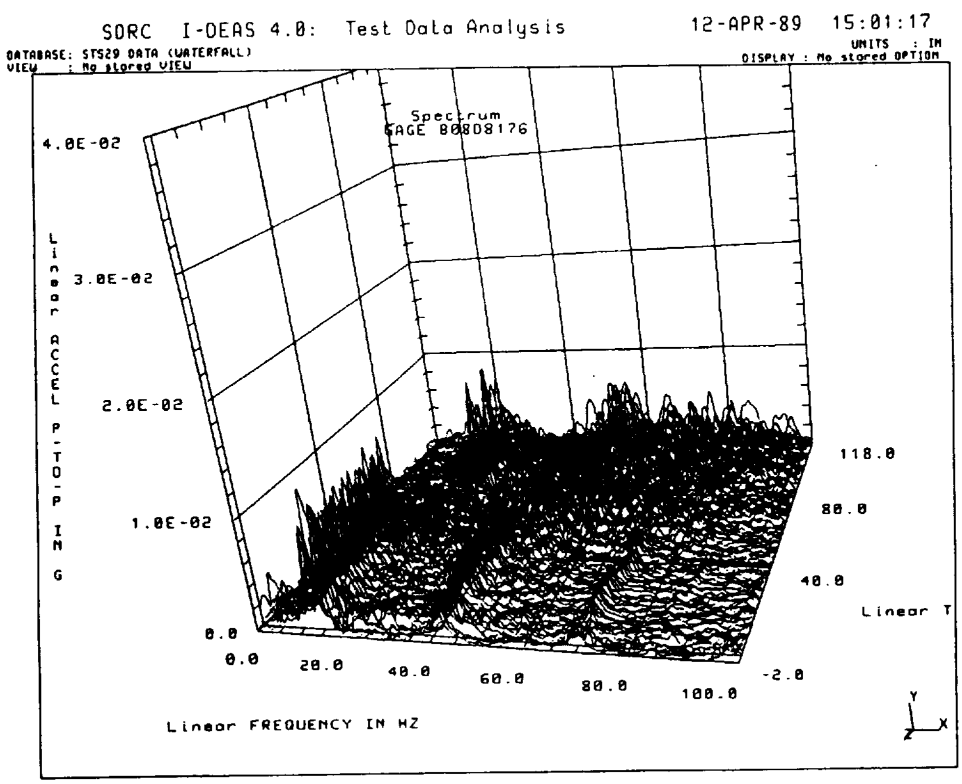

Figure 4.7-66. Random Decrement Waterfall Plot (Gage B08D8176)

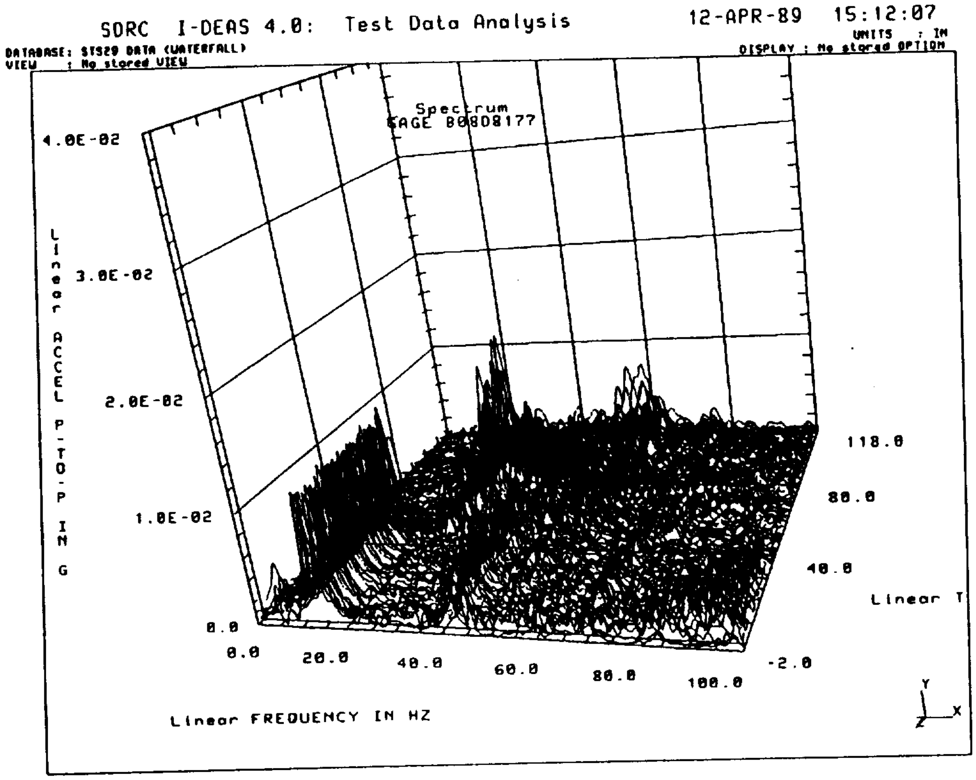

Figure 4.7-67. Random Decrement Waterfall Plot (Gage B08D8177)

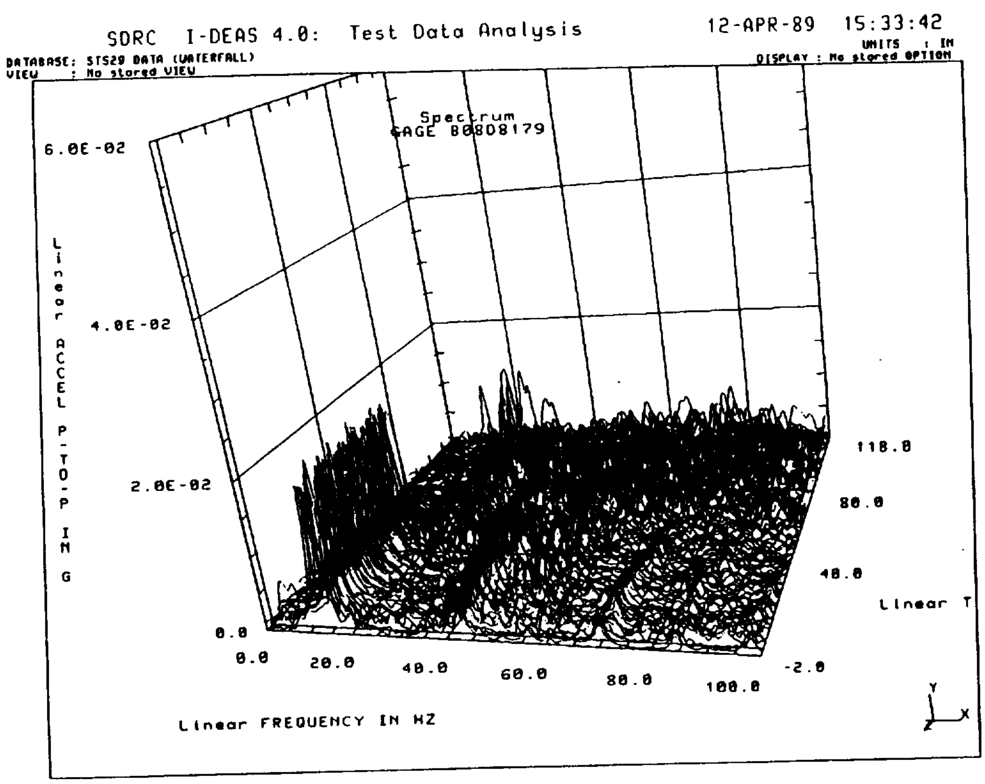

Figure 4.7-68. Random Decrement Waterfall Plot (Gage B08D8179)

observed for some other channels (B08D8175A, Station 839.5, axial) in addition to the large radial direction vibration amplitudes. Analytical models cannot predict such short-duration, high-amplitude vibrations.

Additional confidence and knowledge must be gained through more measurements and analyses. The current data bank for flight dynamic data is limited to two flights (STS-27 and STS-29). STS-1 through STS-6 did not have adequate measurements in the center area of the SRB--the area where extreme vibration was observed on STS-27 and STS-29. It is recommended that accelerometers be mounted at or near the center area on at least four additional flights to monitor and further understand the SRB vibrations.

4.8 RSRM TEMPERATURE AND TPS PERFORMANCE (FEWG REPORT SECTION 2.8.2)

4.8.1 Introduction

This section documents the thermal performance of the 360L003 (STS-29R) SRM external components and TPS as determined by postflight hardware inspection. Assessments of DFI, mean bulk temperature predictions, on-pad ambient/local induced environments, LCC, and GEI/joint heater sensor/thermal imaging data have also been included. Performance of SRM internal components (insulation, case components, seals, and nozzles) is reported in Section 4.11 of this volume.

4.8.2 Summary

4.8.2.1 Postflight Hardware Inspection. Postflight inspection revealed no unexpected problems resulting from flight heating environments. The condition of both SRMs was similar to that of previous flight motors. A complete external heating evaluation of postflight hardware is given in Section 4.8.3.1 of this volume. Nozzle erosion is discussed in Section 4.11.4 of this volume.

4.8.2.2 DFI Thermal Data Evaluation. For the most part, DFI thermal data were well within the estimated values derived from worst-case Integrated Vehicle Baseline Configuration-3 (IVBC-3) design trajectory analyses. Design estimates were exceeded on two different locations within the SRB aft skirt base region (both SRM nozzle throat steel housings and both SRM nozzle aft exit cone aluminum shells). A complete DFI thermal data evaluation is given in Section 4.8.3.2 of this volume. A summary of the two locations where design estimates were exceeded follows.

Nozzle Throat. Similar to STS-27R DFI response, measured data on the nozzle throat exceeded the design estimate by a few degrees. The response was not due to internal soakout heating through the nozzle ablatives. Temperatures decreased during late reentry instead of continually increasing until splashdown, as would be evident of internal soakout heating. The higher response is attributed to the fact that there are some minor reentry heating effects within this inner nozzle region forward of the nozzle snubber. Present external heating design environments are not defined for this region. This occurrence appears not to be a problem, since actual hardware response is still well within the general reuse temperature criteria of a steel structure (500°F as reported in the SRB Thermal Design Data Book, SE-019-068-2H).

Nozzle Aft Exit Cone. Measured data on the aft exit cone exceeded the design estimate by as much as 73°F (reaching 295°F) for an approximate 100-sec period up to splashdown. A probable explanation is that additional heating was imparted to the components in the base region due to hydrazine fires, which have also occurred in some of the past flights.

The additional heating from this hydrazine fire phenomenon is not accounted for in present external heating design environments. The occurrence of hydrazine fires can only be confirmed by the instrumentation installed by USBI on the hydrazine tubes supplying the fuel to the auxiliary power units (APU) within the base region. General reuse temperature criteria of an aluminum structure is 300°F as reported in the SRB Thermal Design Data Book (SE-019-068-2H). The appropriate reuse criteria will be evaluated concerning this hardware.

4.8.2.3 Mean Bulk Temperature Predictions. A discussion of day of launch predictions, made at different timeframes, is presented in Section 4.8.3.3 of this volume. Final postflight predictions from reconstructed data are as follows:

1. The PMBT was 62°F.
2. The flex bearing mean bulk temperature (FBMBT) was 74°F.

4.8.2.4 On-Pad Environment Evaluations. A complete environment evaluation is given in Section 4.8.3.4 of this volume. A summary of key observations follows.

Ambient Conditions. Ambient temperature data (47° to 78°F) exceeded the range of the average March historical data (61° to 73°F), the lower or cooler side showing the most deviation. Cooler than average temperatures, representative of the March historical -1 sigma value, were also evident during the final 12 hr prior to launch. Windspeeds were high (reaching 30 kn) a couple of days prior to launch but were within the historical average the day of launch.

SRM Local. The local prelaunch environment due to March historical predictions suggested as much as a 1°F temperature suppression while the ET was loaded for winds from the southeast direction. Actual winds were consistently from the southwest by west direction. After assessing GEI, there was no apparent evidence of extreme temperature suppression due to ET cooling effects--only minor 1° to 2°F chilling on the inboard region of the RH SRM.

4.8.2.5 Launch Commit Criteria. No LCC thermal violations were noted. Measured GEI and heater sensor data, as compared to the LCC requirements, are discussed in Section 4.8.3.5 of this volume. Highlights of heating operations are summarized below.

Igniter Joint. The heaters performed as expected, with cooldown occurring over an approximate 8-hr period. During this period the temperature dropped from 99°F (T - 4 hr) to 70°F (T - 5 min).

Field Joint. Five of the six field joint heaters performed adequately and as expected. However, the RH aft field joint primary heater circuit failed at approximately T - 10 hr. The operations and maintenance requirements and specification document (OMRSD) maximum heater current limit of 19.5 amp was exceeded and a waiver was approved. The secondary heater circuit was initiated and performed nominally for the remainder of the countdown. Additional information on the heater failure can be found in Sections 4.1 (IFA STS-29-M-1) and 4.8.3.5 of this volume.

Nozzle Region. The SRB aft skirt conditioning system performed satisfactorily and as expected. However, similar to 360L002 (STS-27R), there was a 30°F temperature differential between conditioning gas and SRM hardware response, suggesting significant heat loss between the heater and aft skirt compartment. There was also evidence of circumferential temperature differences within the aft skirt compartment (as much as 5°F on the RH flex bearing aft end ring).

4.8.2.6 Prelaunch Thermal Data Evaluation. A complete assessment of prelaunch thermal data is given in Section 4.8.3.6. A summary of key observations follows.

GEI and Joint Heater Sensors. Data were somewhat in agreement with March historical on-pad thermal predictions, deviating for the most part on the cooler side because the average ambient temperature fell below the -1 sigma value. The LCC time period (T - 6 hr to T - 5 min) real-time predictions, which incorporated an environmental update for the last 24 hr prior to launch, were also somewhat in agreement with GEI. GEI deviated for the most part on the warmer side due to higher than anticipated ambient temperatures.

Infrared Temperature Measurements. IR readings were taken for the T - 3 hr timeframe from the portable STI. No IR gun readings were taken due to a malfunction during pad walkdown. Measurements from a fixed STI were verbally reported for the outboard area of the LH SRB. These measurements, between 59° and 61°F, were comparable with GEI data.

4.8.3 Results Discussion

4.8.3.1 Postflight Hardware Inspection. Following the recovery of the STS-29R SRBs, a postflight inspection of the external hardware was conducted at the SRB disassembly facility (Hangar AF). TPS performance was considered to be excellent in all areas, with external heating and recession effects being less than predicted (Table 4.8-1). Predictions from the worst-case design trajectory environments (Table 4.8-2) will be documented in the SRB Thermal Design Data Book, SE-019-068-2H.

The condition of both motors appeared to be similar to previous flight motors, with most of the heat effects seen on the aft segments on the inboard sides of the SRBs. The aft segment inboard regions facing the ET experience high aerodynamic heating normal to protuberance components. They also receive the high plume radiation and recirculation heating of aft-facing surfaces induced by the adjacent SRB and SSMEs. In this area there was slight ablation to the TPS over the factory joints, the stiffener rings and stubs, and DFI runs. A concise summary of the external hardware condition is shown in Table 4.8-3.

Field Joints. All field joints on both motors were in excellent condition. There were no signs of ablation on any of the JPSs and only slight paint blistering on the cork cover. The paint on the K5NA closeout aft of the cork was also slightly darkened and blistered, with occasional pitting. This was probably due to aerodynamic heating and the result of aft edge hits from water impact and nozzle severance debris.

Table 4.8-1. 360L003 RSRM External Performance Summary (TPS erosion) (LH and RH motors)

Component	TPS Material	Maximum Erosion (in.) Predicted	Maximum Erosion (in.) Measured
Field Joints	Cork	0.003	None
Factory Joints	EPDM	0.014	Not measurable*
Systems Tunnel	Cork	0.014	None
Stiffener Rings	EPDM	0.009	Not measurable*
DFI, Cables	Cork	0.036	Not measurable*
	Silica phenolic	0.000	None
Nozzle Exit Cone	Cork	0.104	NA**

*All evidences of erosion were apparent only on the inboard region of the aft segment, where the flight induced thermal environments are the most severe
**Nozzle exit cones are not recovered

Table 4.8-2. SRB Flight-Induced Thermal Environments

1. Ascent Heating

   Document No. STS 84-0575, dated 24 May 1985
   Change Notice 2, SE-698-D, dated 30 Apr 1987
   Data on computer tapes No. DN 4044 and DN 9068
   Change Notice 3, SE-698-D, dated 30 Oct 1987
   Tape No. DP 5309

2. Base Recirculation Heating

   Document No. STS 84-0259, dated October 1984
   Change Notice 1, SE-698-D, dated 30 Sep 1987

3. SSME and SRB Plume Radiation

   Document No. STS 84-0259, dated October 1984
   Change Notice 1, SE-698-D, dated 30 Sep 1987

4. SSME Plume Impingement After SRB Separation

   Document No. STS 84-0259, dated October 1984
   Change Notice 1, SE-698-D, dated 30 Sep 1987

5. Reentry Heating

   Document No. SE-0119-053-2H, Rev D, dated August 1984,
   and Rev E dated 12 Nov 1985

Table 4.8-3. 360L003 RSRM External Performance Summary (LH and RH motors)

Component	TPS Material	Performance	Recovered Hardware Performance Assessment
Field Joints	Cork	Typical	All field joints in excellent condition; slight paint blistering
Factory Joints	EPDM	Typical	All factory joints in very good condition; slight ablation of EPDM on aft segment joints on inboard side of both motors (approximately 220 to 320 deg); multiple debonds on aft edge of LH aft center weatherseal
Systems Tunnel	Cork	Typical	Cork TPS adjacent to tunnel floor plate in excellent condition; very little paint discoloration and no measurable cork ablation
Stiffener Rings	EPDM	Typical	Normal thermally, only significant ablation was on stub tips and leading edge of tee sections on inboard side of motors; stiffener ring on RH motor were fractured at approximately 210 deg due to water impact
DFI, Cables	Cork	Typical	Generally in good condition, with slight paint blistering; some areas of cork missing on phenolic DFI cable runs
Nozzle Exit Cone	Cork	Typical	Normal based on temperature sensor data
Motor Case	NA	Typical	No hot spots or discoloration of the motor case paint due to external or internal heating; intermittent paint blistering on either side of forward stubs

Factory Joints. The factory joints on each of the motors were in very good condition. The only signs of heat effects found on the factory joints were located on the aft segments of each motor. There was only slight ablation, charring, and discoloration on the inboard regions of the aft segment factory joints. This occurred between approximately 220 and 320 deg circumferentially on each motor. Again, these are all normal occurrences that have been consistently observed on previous flight motors. The weatherseal over the aft center factory joint of the LH SRB was unbonded at 11 locations, with the largest unbond (about 58 in. long) located between 320 and 360 deg circumferentially. The unbonds appeared to be due to adhesive failure occurring at splashdown. Additional discussion of the unbonds is in Section 4.1 of this volume (IFA-STS-29-M-2).

Systems Tunnel. The cork TPS adjacent to the systems tunnel floor plate was in excellent condition. There was very little paint discoloration and blistering. All K5NA closeouts over cables and tunnel seams were in excellent condition.

Stiffener Rings. The stiffener ring TPS was generally in very good condition, with only slight thermal degradation. The major heat-affected area was again predominantly in the 220- to 320-deg sector, with the ethylene-propylene-diene monomer (EPDM) on the outer flange showing signs of brown charring. This region was subjected to aeroheating along the outboard tip forward face, while the aft face and top surfaces experienced radiant heating. The K5NA TPS on the forward side of the stubs was also slightly charred in the same regions, with intermittent pitting around the whole circumference. The three stiffener rings on the RH SRB were fractured during water impact, typically at about the 210- to 220-deg location.

DFI and GEI Cables. The cork and K5NA TPS covering the DFI, GEI, and cableways was generally in good condition. Very little heat effect was observed, consisting of only slight paint discoloration and blistering. Some of the DFI and GEI cable runs had small areas of missing cork at intermittent regions. These minor cork losses were all attributed to debris impact during reentry or at splashdown. The largest sections missing were a 6- by 4-in. section at Station 539 and a 10- by 4-in. section at Station 1751, both on the LH SRB. All other sections were less than 2 square inches.

Nozzle. The external appearance of the nozzles was typical compared to other flights. The CCP on the exit cone was either fractured or completely missing due to linear shaped charge (LSC) firing and water impact. In many areas the GCP insulator was also missing, exposing the aluminum shell. The aluminum shell showed no signs of heat damage, however. The internal parts of both nozzles had the appearance of previous postflight hardware. There were intermittent impact marks located circumferentially around both of the nozzles. There were a few instances of charred, popped-up CCP and postfire wedgeouts, which have been observed on previous postfire nozzles. Additional nozzle assessment is given in Section 4.11.4 of this volume.

4.8.3.2 DFI Thermal Sensor Assessments. DFI was installed on STS-29R to obtain the pressure, strain, vibration, and thermal data reflecting the effects of the actual flight environments. It was intended to compare the flight test data with the corresponding information obtained analytically by using the design flight environments to verify the design. The DFI consisted of pressure transducers, strain gages, girth gages, accelerometers, and RTDs.

This part of the report presents the comments pertaining to the data recorded by the RTDs. RTDs were installed by both Morton Thiokol and USBI to confirm their respective designs. This discussion will address the RTDs which were installed by Morton Thiokol.

The STS-29R flight trajectory was a lofted trajectory as compared to the IVBC-3 worst-case design trajectory. Consequently the flight aerodynamic heating and plume heating pulses during ascent would be lower than the corresponding heat pulses for the design trajectory. Therefore, the measured DFI thermal data, barring some unforeseen circumstance, would be lower than the analytically predicted data. The predicted data are based on the results of computer-aided thermal analysis using the thermal environments provided by MSFC (Table 4.8-2).

During the STS flights, two phenomena have been historically observed during the reentry phase of the SRBs. These phenomena have been identified as hydrazine fires in the base region and flame radiation from the nozzle plume. Both occur during the reentry phase of the SRBs at about 280 sec into flight when the boosters reenter the earth's atmosphere. The effects of these two phenomena augment the effects of the normal reentry aerodynamic heating.

Hydrazine fires have been observed on 6 of the first 24 flights, and the nozzle flame heating has been observed on practically all of the flights. The reentry thermal environments (Item 5, Table 4.8-2) include the effects of the nozzle plume radiation environments, and these have been taken into consideration in the design of the base region equipment. In other words, the effect of the plume radiation is already shown in the predicted data. Since the hydrazine fires have occurred sporadically, it is doubtful that their effects are included in the reentry thermal environments. Their occurrence can be confirmed from the readings of the RTDs installed by USBI on the hydrazine equipment and by postflight hardware inspection of the base region.

The RTDs were installed on both the LH and RH SRMs on the igniter adapter, the forward and aft field joints, the nozzle fixed housing flange, the nozzle nose inlet aluminum housing, the nozzle throat steel housing, the nozzle aft exit cone aluminum supporting structure, and the aft exit cone near the exit plane under the cork (Figures 4.8-1 through 4.8-4). Most of the instrumentation was installed to detect any possible leakage of combustion gases through the igniter joint, the field joints and the case-to-nozzle joint. Furthermore, the RTDs were to record the time of certain events such as the severance of the aft exit cone and the blowing away of the thermal curtain which protects the equipment in the base region. It should be noted that the predicted temperatures do not consider the leakage of combustion gases.

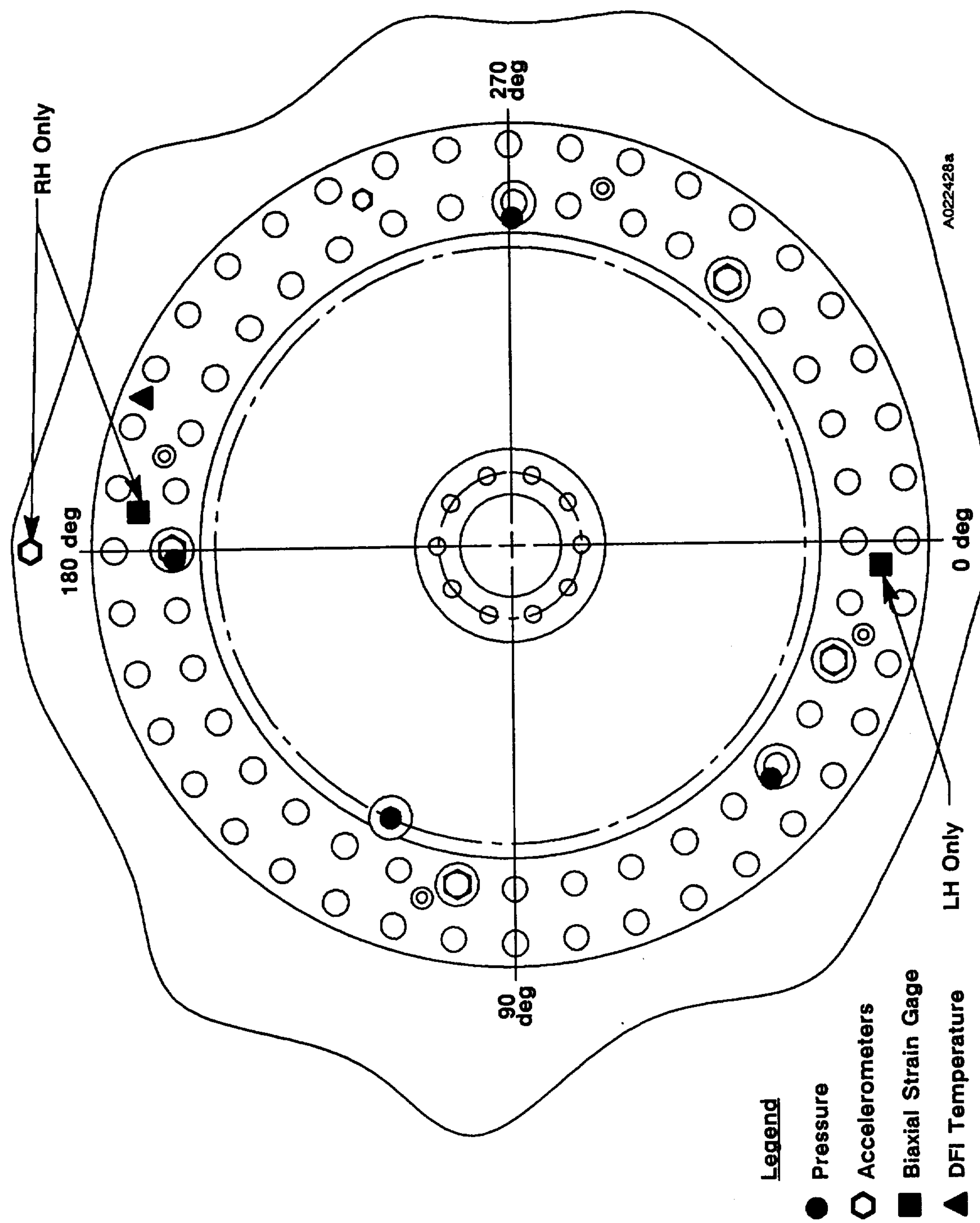

Figure 4.8-1. Forward Dome DFI

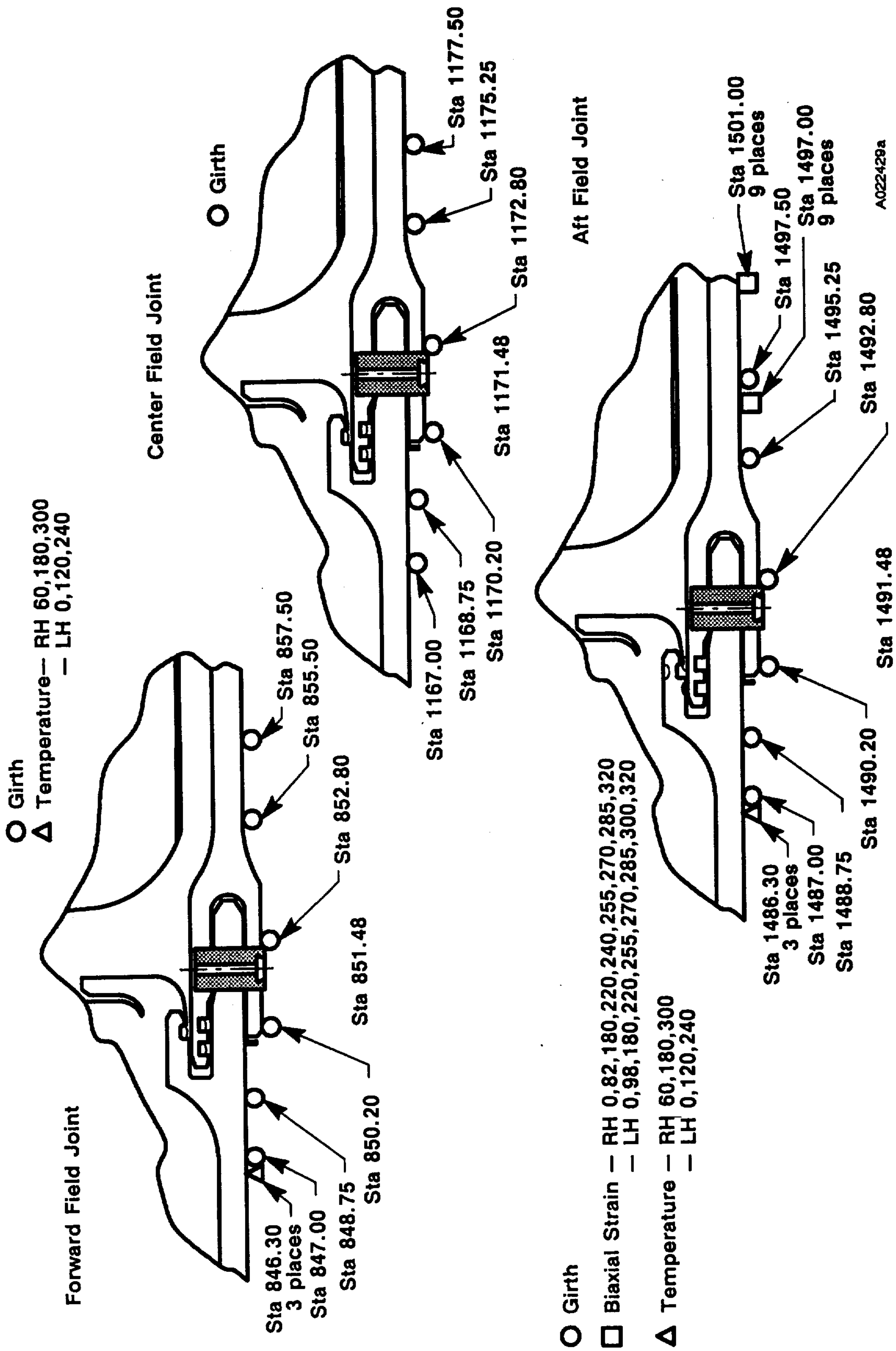

Figure 4.8-2. Field Joint DFI

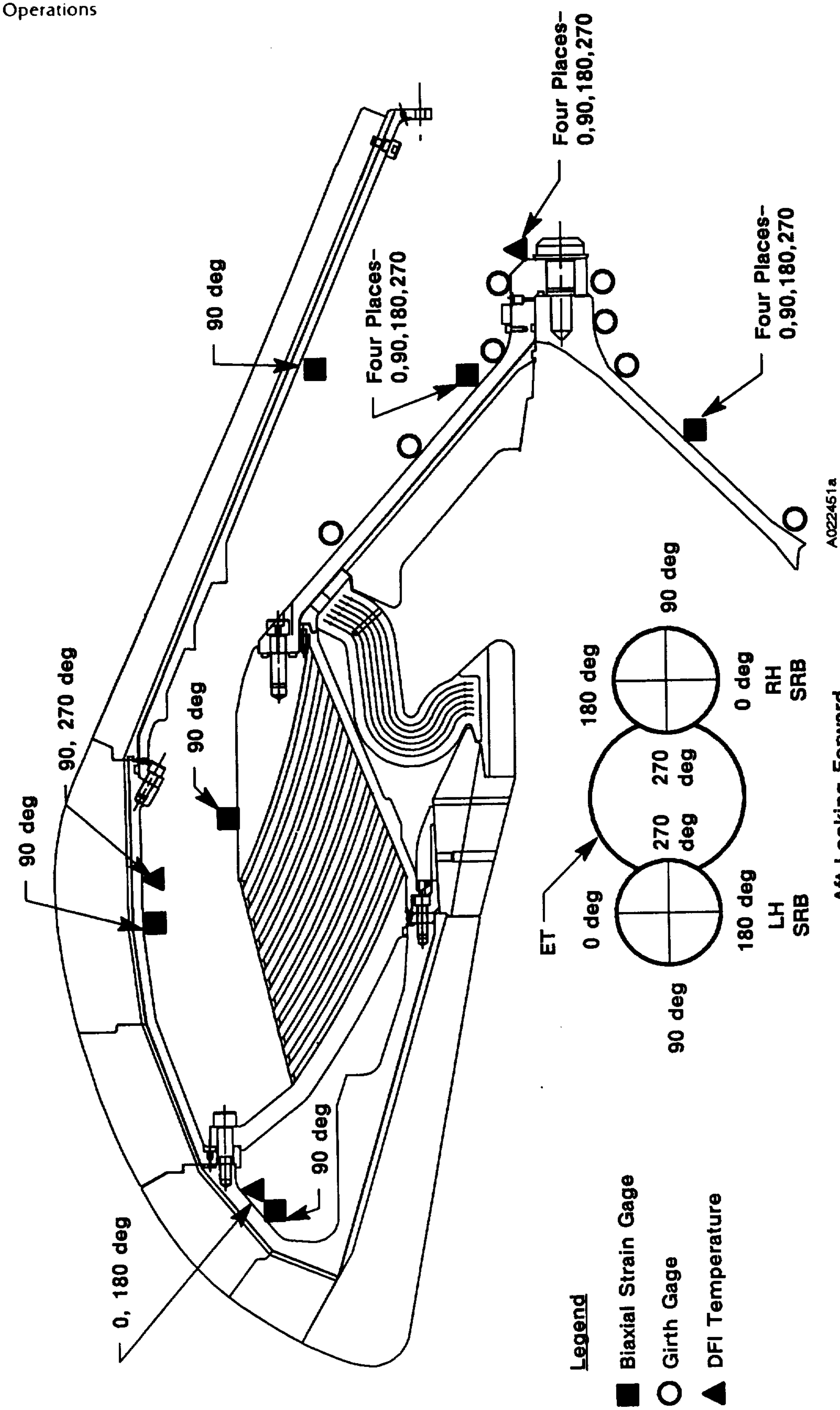

Figure 4.8-3. Nozzle DFI

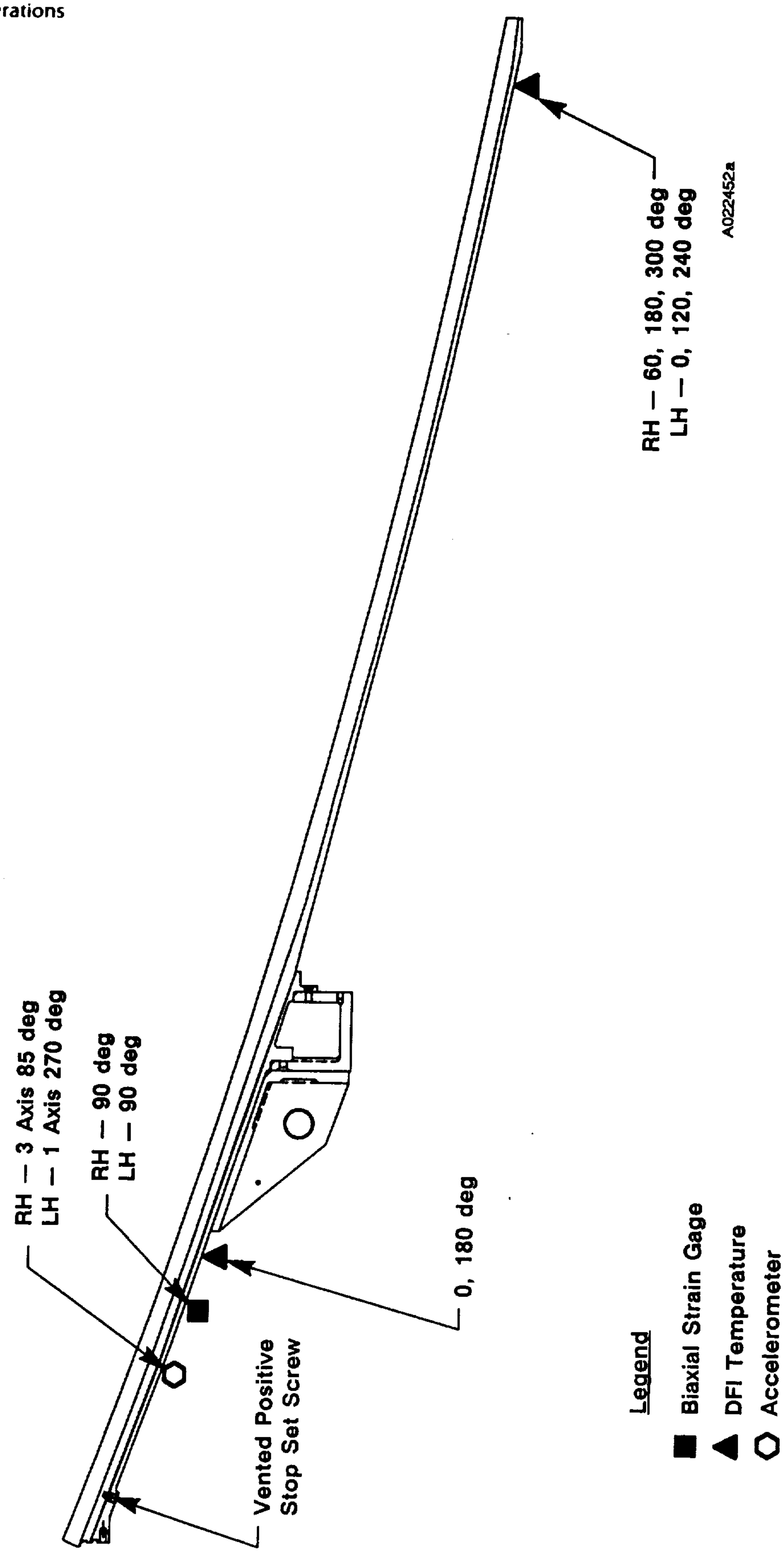

Figure 4.8-4. Aft Exit Cone DFI

Table 4.8-4 presents the list of DFI thermal gages, their locations, the maximum predicted temperatures, and the actual maximum temperatures recorded at the time of SRB separation and later during reentry. Figures 4.8-5 through 4.8-20 detail actual DFI thermal histories. The following general comments provide observations and concerns:

a. All the measured data showed oscillations around the mean values, indicating that the RTDs were picking up stray signals due to vibrations or that a problem existed in the data acquisition system.

b. All of the measured data registered normal temperatures during the ascent of the STS, indicating that there was no leakage around the igniter joints, the field joints, or the case-to-nozzle joint.

c. The RTDs on the aft exit cone near the exit plane dropped their data at about 195 sec after lift-off. This suggests that the aft exit cone was severed from the SRBs at about 195 sec into flight. The aft exit cone is severed by the LSC, which, when ignited, produces high-velocity debris under vacuum conditions.

   Since the thermal curtain is tied to the compliance ring, which is very close to the LSC, the inner edge of the thermal curtain will more than likely tear off when bombarded with the pieces of high-velocity debris. It is therefore highly probable (a fair assumption) that the thermal curtain lost its protective shield to the base region at the time of aft exit cone severance.

d. The RTD (MSID B07T7621A) located on the steel structure of the LH SRM nozzle throat failed the system checkout test in the VAB and was not repaired. Therefore, no data were available for this location. The RTD (MSID B07T7623A) located on the aft exit cone at the nozzle exit on the LH SRM did not register any temperature rise during flight; its performance is therefore questionable. The RTD (MSID B07T8607A) located on the forward field joint of the RH SRM dropped its data at 320 sec into flight for a period of approximately 18 sec.

e. The RTDs on the LH SRM (MSID BO7T7620A) and on the RH SRM (MSID BO7T8620), all located on the steel structure of the nozzle throat, showed higher-than-predicted temperatures during reentry. All of these temperatures could have been influenced by the entry through the nozzle snubber of the reentry hot air, the products of the burning hydrazine, or the products of combustion from the nozzle. Snubber clearance is only 0.25 inch. The predicted temperatures do not consider this extra heating caused by the inflow of the gases. The reentry thermal environments (Item 5, Table 4.8-2) do not prescribe any environments for this region. However, a maximum measured steel temperature at the nozzle throat of 115°F during reentry, as compared to the predicted temperature of 90°F, should not be objectionable.

f. The RTDs (MSIDs B07T8619A and B07T8622A) located on the aluminum structure of the aft exit cone of the RH SRM registered maximum temperatures of 295° and 270°F, respectively,

Table 4.8-4. 360L003 Flight Design Trajectory Estimates Versus Actual Ascent and Reentry DFI Data

Component and Location/MSID	Axial Station (in.)	Angular Location (deg)	Maximum Temperature (°F) Design Estimate*	Measured Ascent	Measured Reentry
Igniter Adapter	486.4				
RH SRM/B07T8606A		205	200	69	76
LH SRM/B07T7606A		205	200	68	75
Forward Field Joint	846.3				
RH SRM/B07T8607A**		180	120	92	92
B07T8608A		60	120	92	92
B07T8609A		300	120	85	85
LH SRM/B07T7607A		0	120	89	91
B07T7608A		120	120	92	92
B07T7609A		240	120	87	88
Aft Field Joint	1486.3				
RH SRM/B07T8610A		180	132	95	95
B07T8611A		60	125	99	99
B07T8612A		300	128	89	90
LH SRM/B07T7610A		0	132	92	92
B07T7611A		120	125	101	101
B07T7612A		240	128	90	92
Case-to-Nozzle Joint	1876.6				
RH SRM/B07T8613A		180	172	89	132
B07T8614A		90	172	85	117
B07T8615A		0	172	88	124
B07T8616A		270	172	89	134
LH SRM/B07T7613A		0	172	89	125
B07T7614A		90	172	86	130
B07T7615A		180	172	86	137
B07T7616A		270	172	86	138
Nozzle Nose Housing, Aluminum	1828.1				
RH SRM/B07T8617A		180	90	73	77
B07T8618A		0	90	73	73
LH SRM/B07T7617A		0	90	73	74
B07T7618A		180	90	73	74

*Estimates from worst-case induced heating design trajectory
**Temporary data dropout at 320 sec

Table 4.8-4. 360L003 Flight Design Trajectory Estimates Versus Actual Ascent and Reentry DFI Data (cont)

Component and Location/MSID	Axial Station (in.)	Angular Location (deg)	Maximum Temperature (°F) Design Estimate*	Measured Ascent	Measured Reentry
Nozzle Throat Housing, Steel	1845.0				
RH SRM/B07T8620A		90	90	86	111**
B07T8621A		270	90	80	101**
LH SRM/B07T7620A		0	90	86	115**
B07T7621A		270	90***	NA	NA
Nozzle Aft Exit Cone, Aluminum	1905.0				
RH SRM/B07T8619A		180	222	83	295†
B07T8622A		0	222	82	270†
LH SRM/B07T7619A		0	222	82	250†
B07T7622A		180	222	82	286†
Nozzle Exit--Under Cork	1996.5				
RH SRM/B07T8623A		180	236	62	73††
B07T8624A		60	236	62	73††
B07T8625A		300	236	60	73††
LH SRM/B07T7623A		0	236	73	73††
B07T7624A		120	236	61	73††
B07T7625A		240	236	63	73††

*Estimates from worst-case induced heating design trajectory

**Gage response exceeded design estimate. The higher response is attributed to the fact that there are some minor reentry heating effects within this inner nozzle region past the nozzle snubber. Present external heating design environments are not defined for this region

***Gage was not operative--failed system test

†Gage response exceeded design estimate. A probable explanation is that additional heating was imparted to the components in the base region due to hydrazine fires, which have also occurred on some of the past flights. The environment from this phenomenon is not accounted for in present external heating design environments

††Readings were taken at the time of nozzle severance--approximately 195 sec

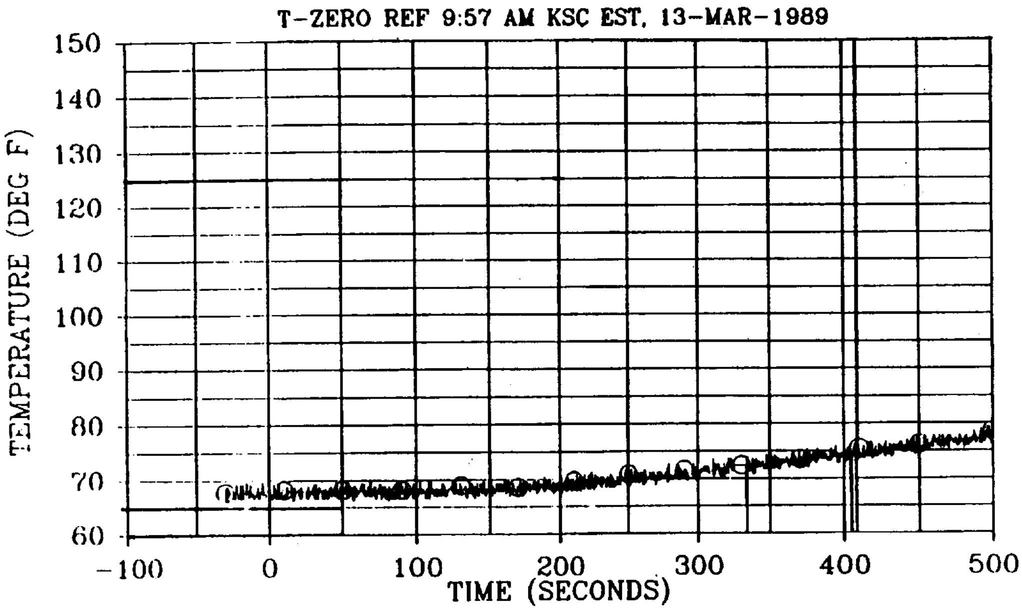

*NOTE: T-0 SRB IGNITION 072:14:57:00.017
DFI DATA (5 SPS)
ALL REF INSTR BASED ON SRM ORIENTATION
PLOTTED 27-MAR-1989

LEGEND
B07T7606A (205 DEG)

Figure 4.8-5. LH Motor Temperature (Station 486.40)

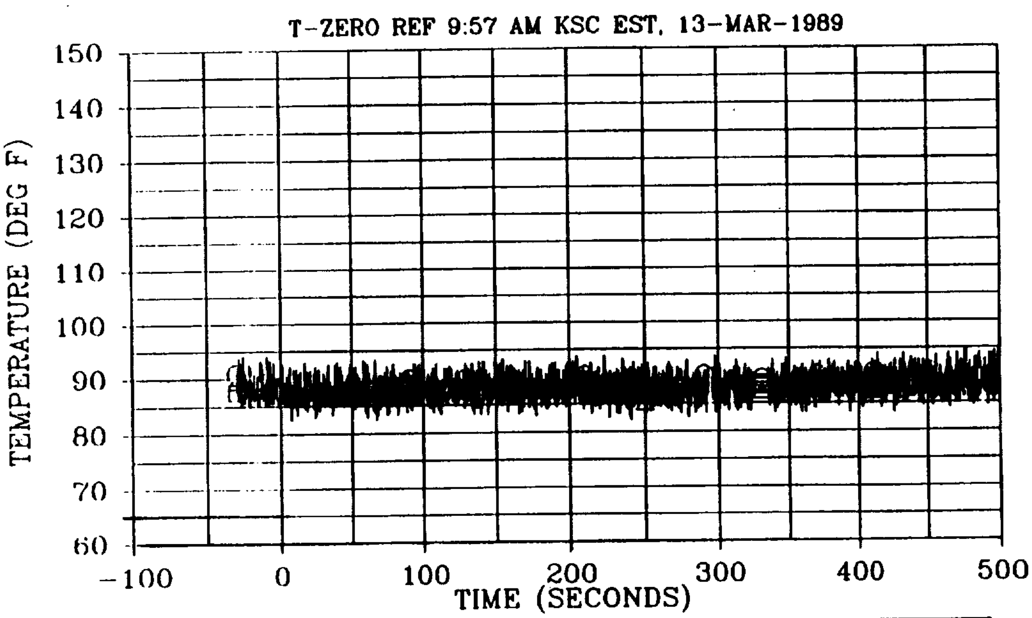

*NOTE: T-0 SRB IGNITION 072:14:57:00.017
DFI DATA (5 SPS)
ALL REF INSTR BASED ON SRM ORIENTATION
PLOTTED 27-MAR-1989

LEGEND
B07T7607A (0 DEG)
B07T7608A (120 DEG)
B07T7609A (240 DEG)

Figure 4.8-6. LH Motor Temperature (Station 846.30)

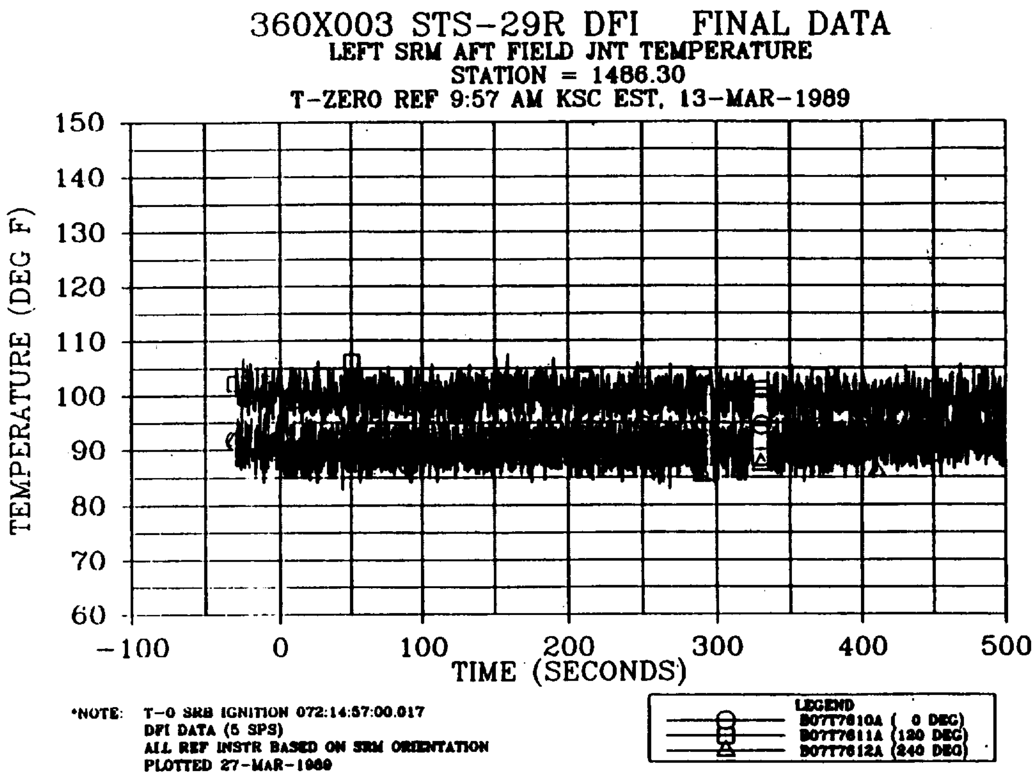

Figure 4.8-7. LH Aft Field Joint Temperature (Station 1486.30)

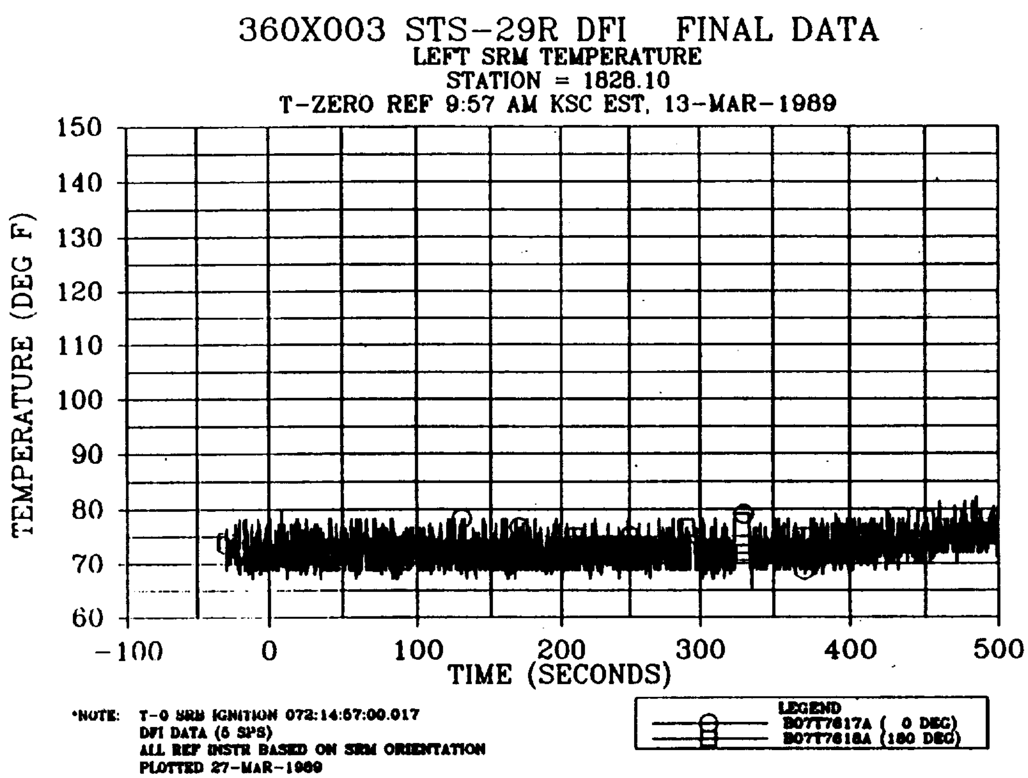

Figure 4.8-8. LH Motor Temperature (Station 1828.10)

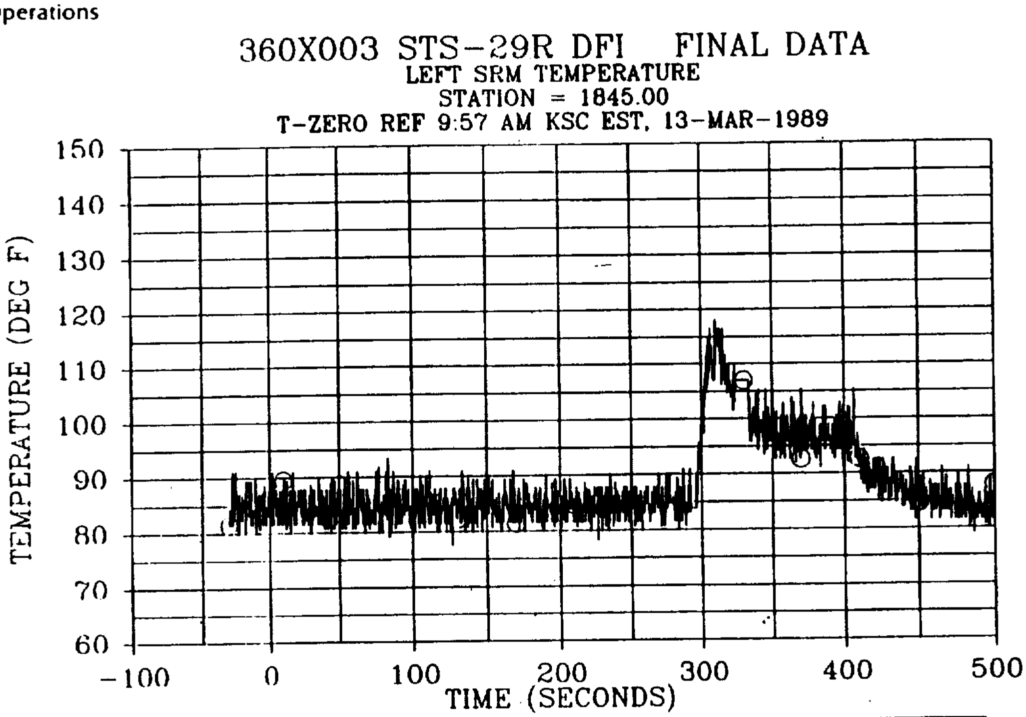

*NOTE: T-0 SRB IGNITION 072:14:57:00.017
DFI DATA (5 SPS)
ALL REF INSTR BASED ON SRM ORIENTATION
PLOTTED 27-MAR-1989

LEGEND
B07T7620A (90 DEG)

Figure 4.8-9. LH Motor Temperature (Station 1845.00)

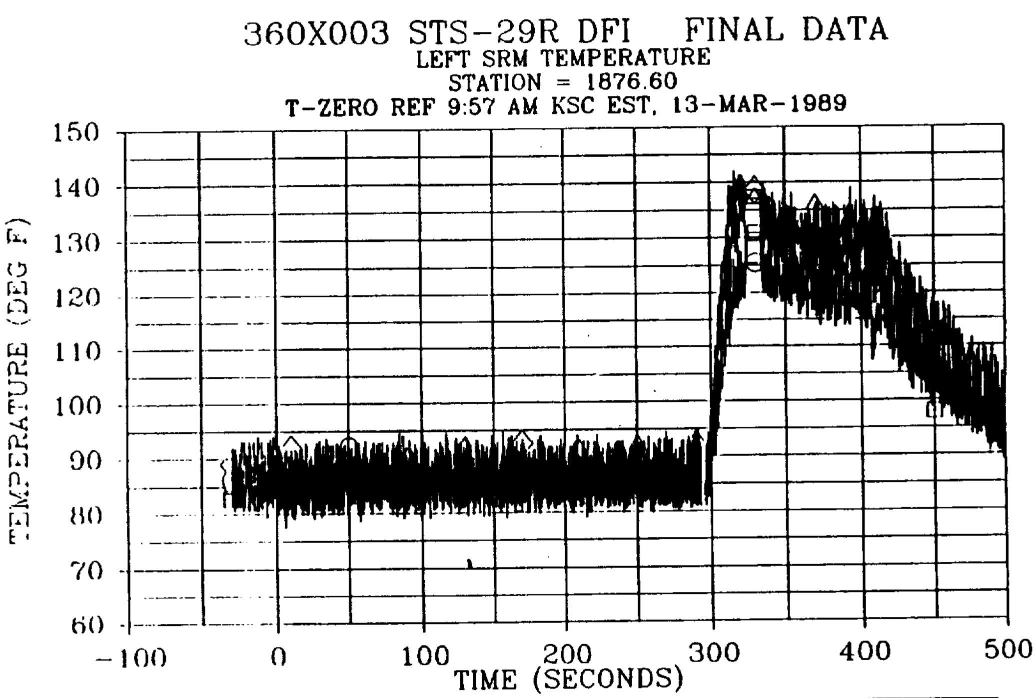

*NOTE: T-0 SRB IGNITION 072:14:57:00.017
DFI DATA (5 SPS)
ALL REF INSTR BASED ON SRM ORIENTATION
PLOTTED 27-MAR-1989

LEGEND
B07T7613A (0 DEG)
B07T7614A (90 DEG)
B07T7615A (180 DEG)
B07T7616A (270 DEG)

Figure 4.8-10. LH Motor Temperature (Station 1876.60)

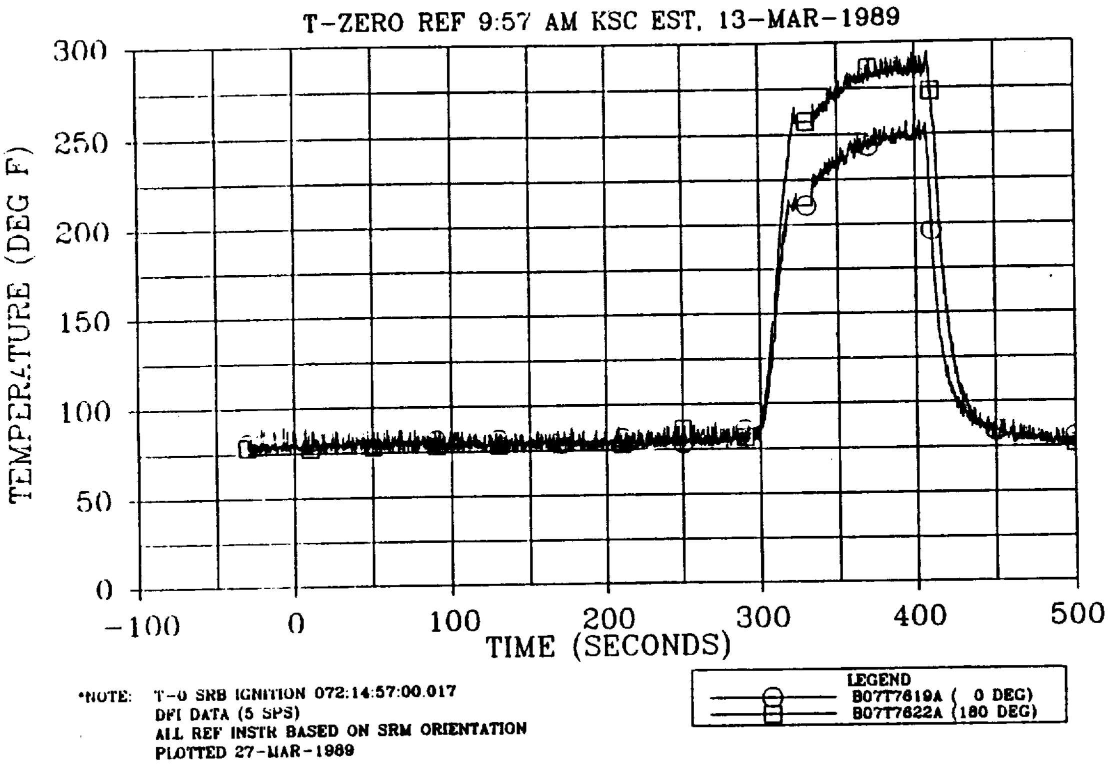

Figure 4.8-11. LH Nozzle Exit Cone Temperature (Station 1905.00)

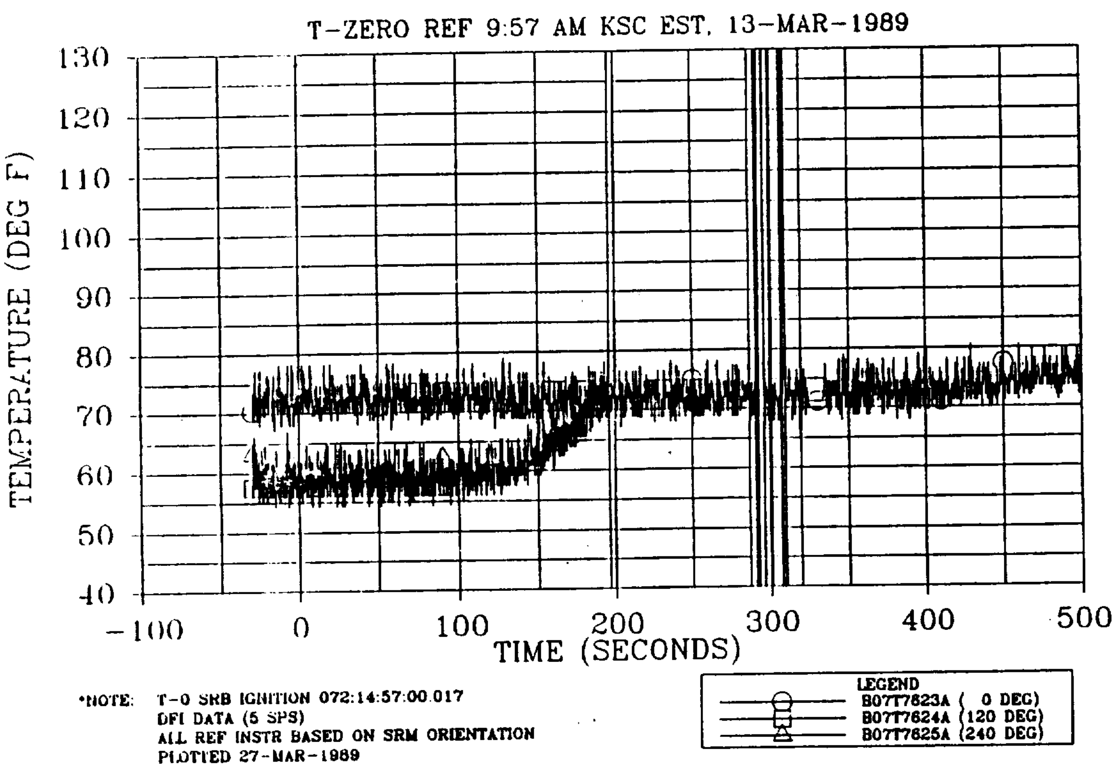

Figure 4.8-12. LH Nozzle Exit Cone Temperature (Station 1996.50)

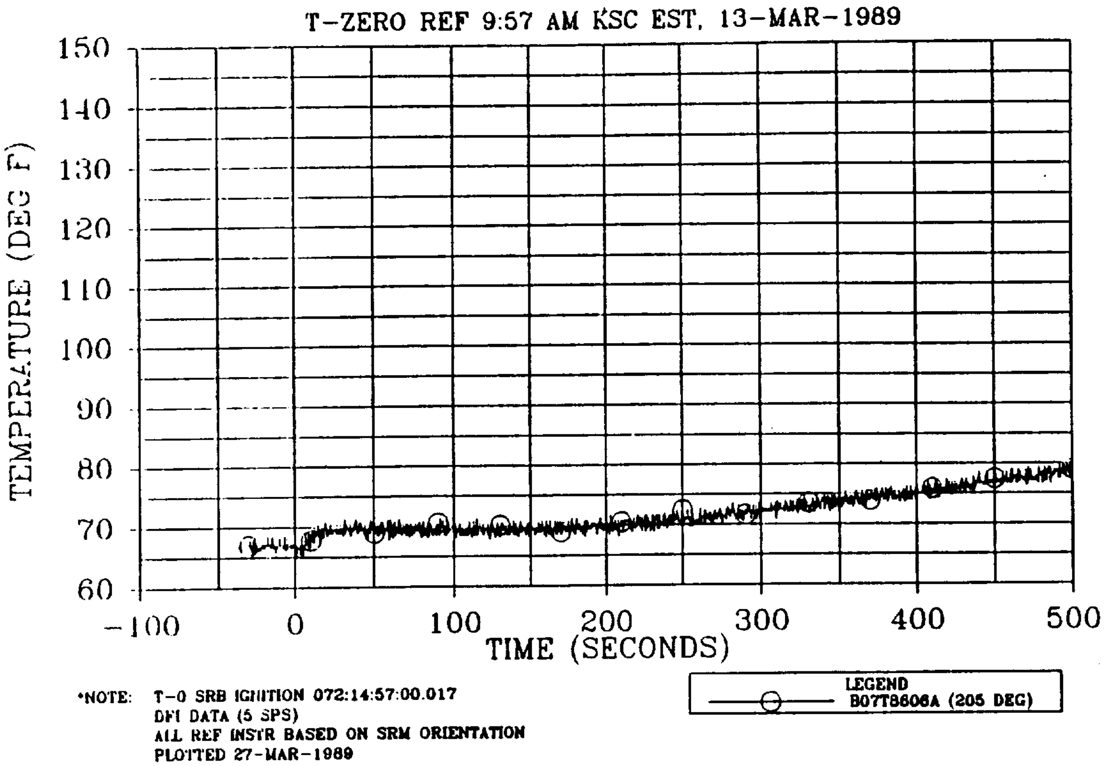

Figure 4.8-13. RH Motor Temperature (Station 486.40)

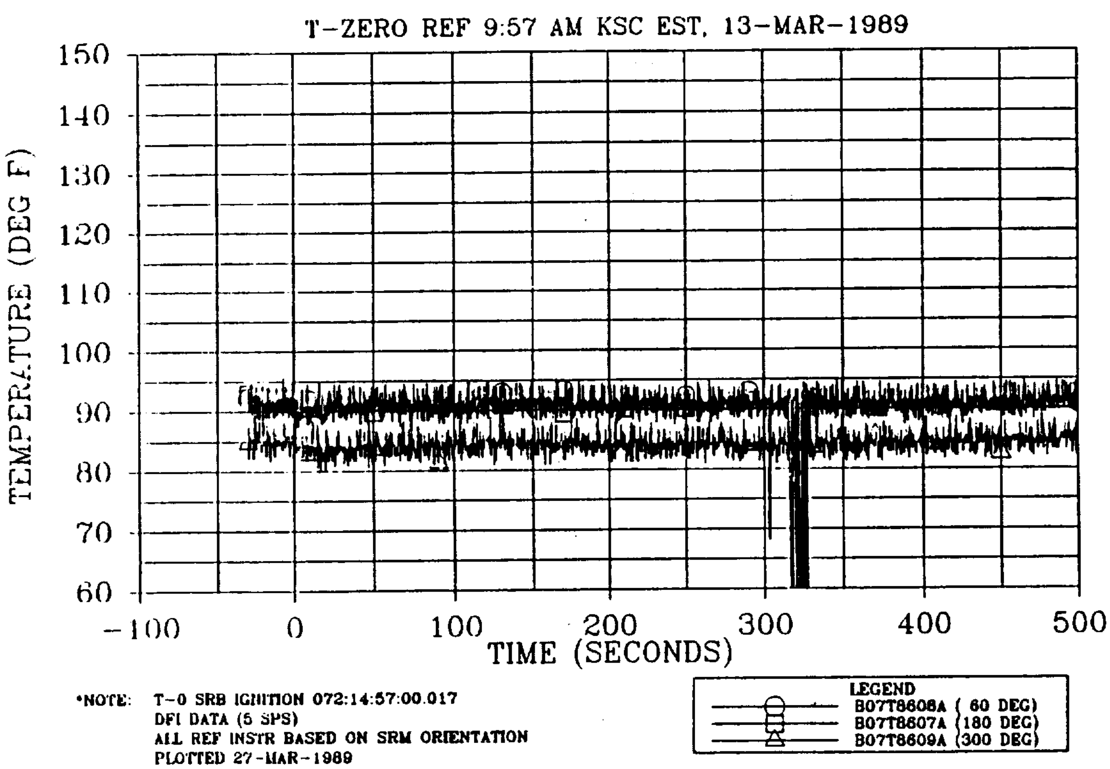

Figure 4.8-14. RH Motor Temperature (Station 846.30)

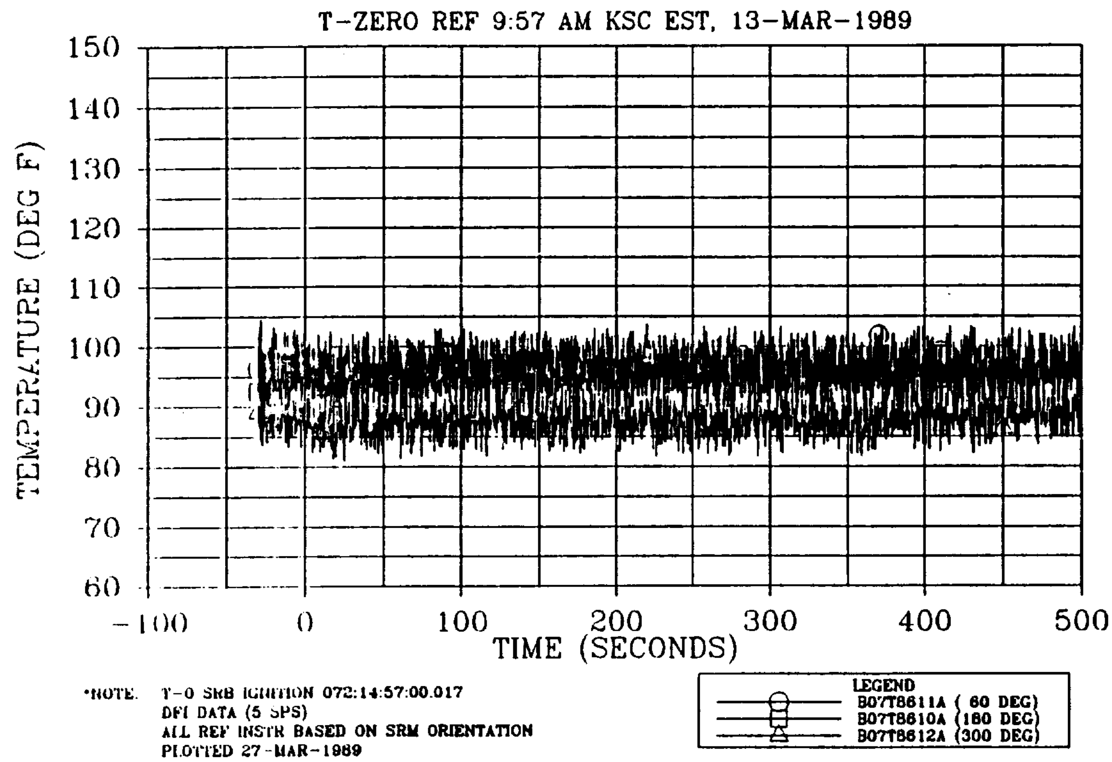

Figure 4.8-15. RH Aft Field Joint Temperature (Station 1486.30)

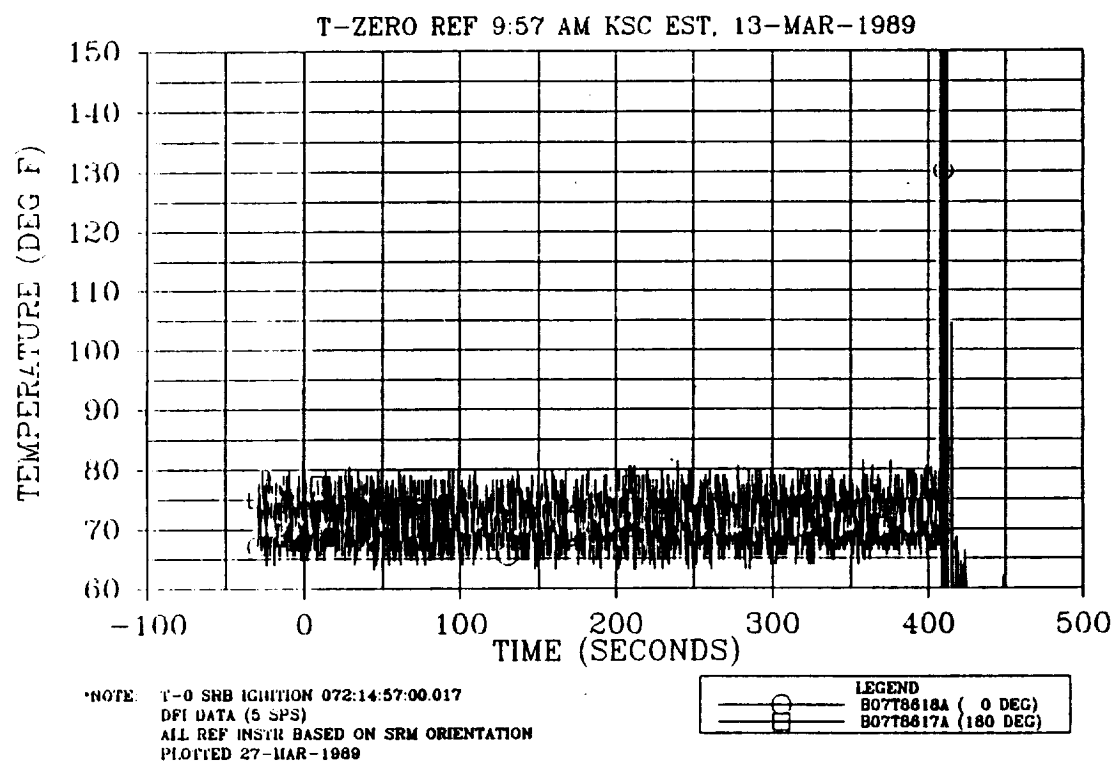

Figure 4.8-16. RH Motor Temperature (Station 1828.10)

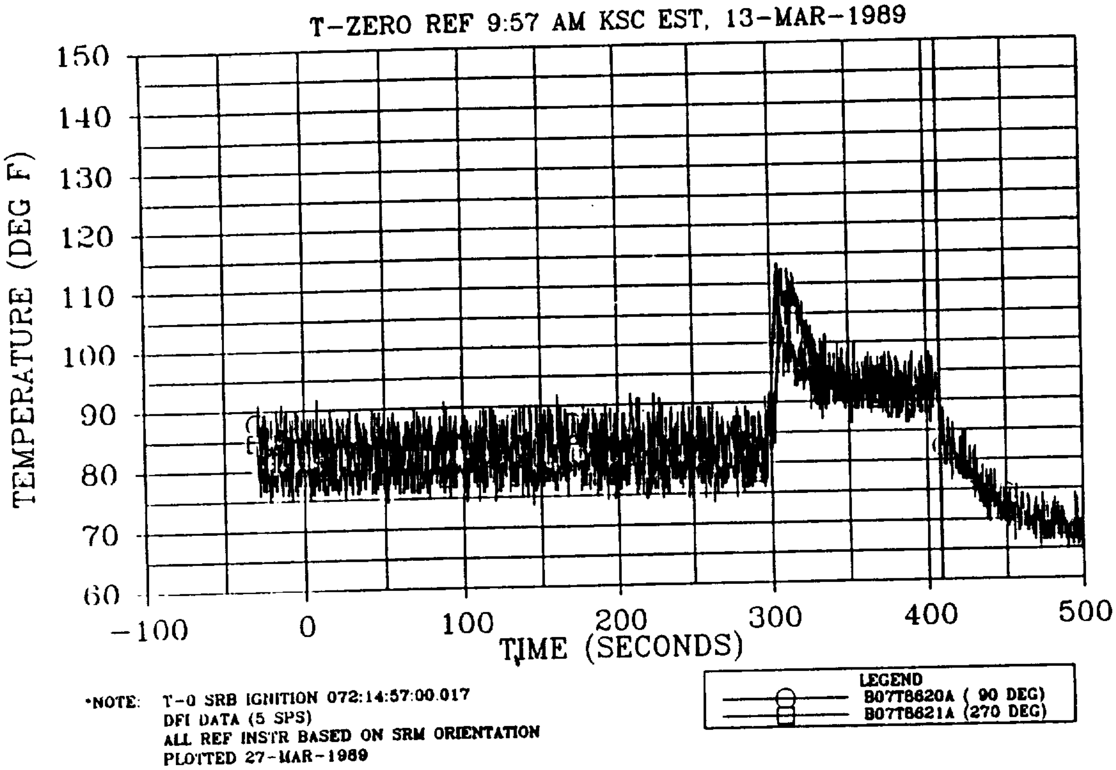

Figure 4.8-17. RH Motor Temperature (Station 1845.00)

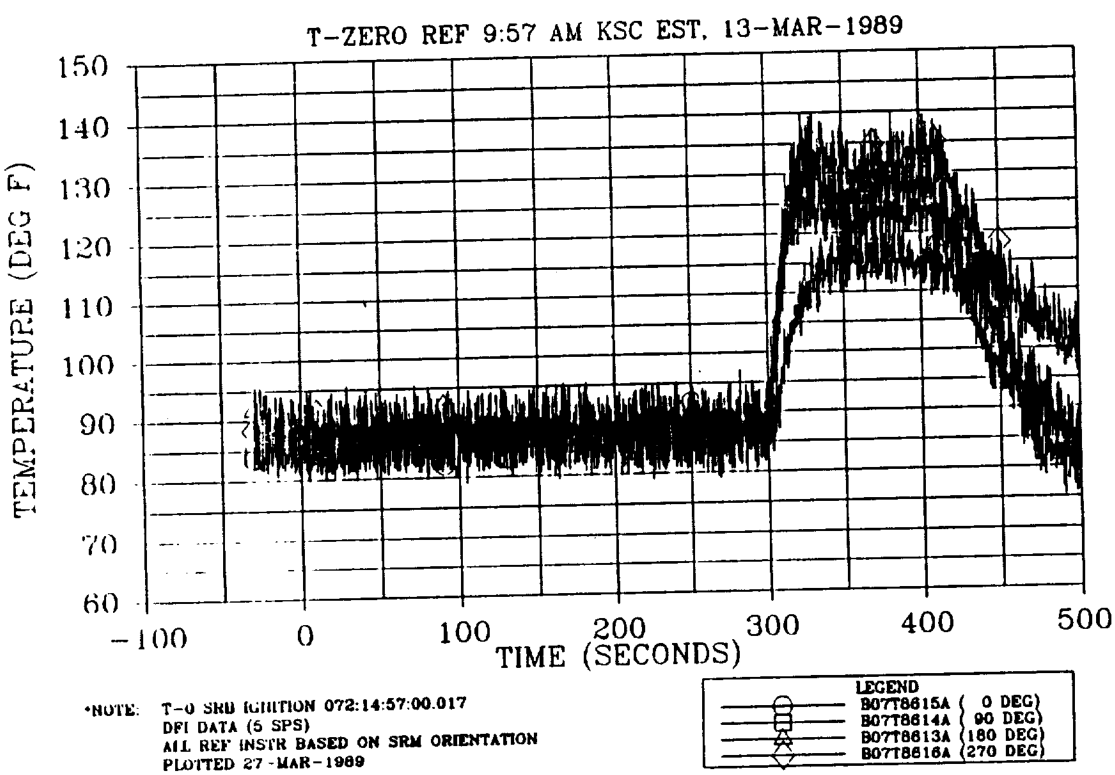

Figure 4.8-18. RH Motor Temperature (Station 1876.60)

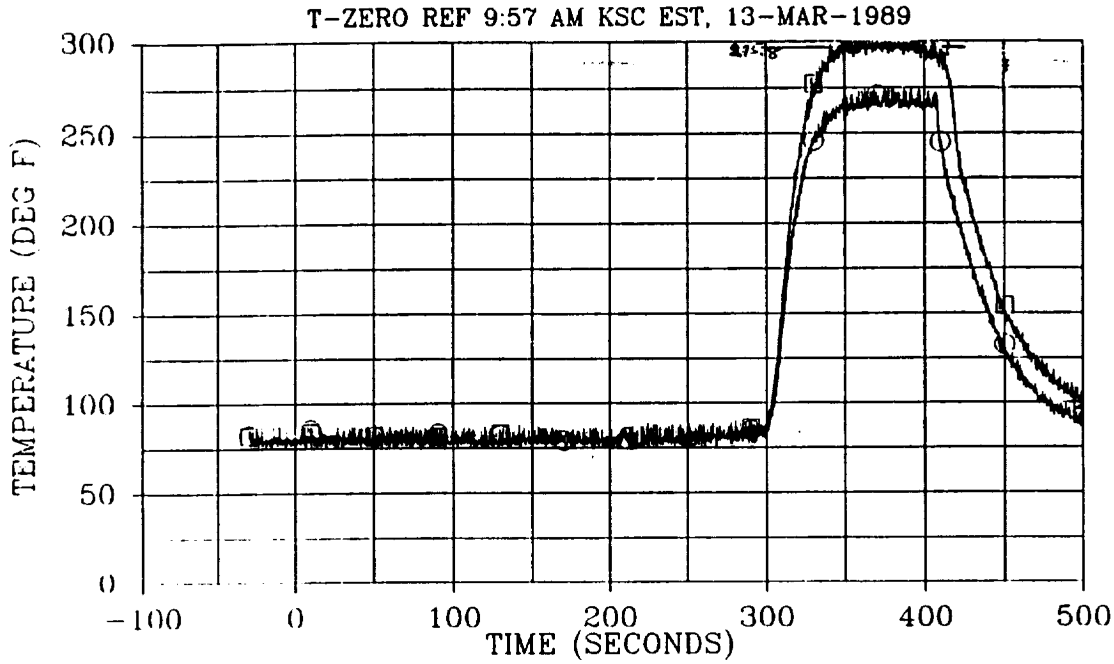

*NOTE: T-0 SRB IGNITION 072:14:57:00.017
DFI DATA (5 SPS)
ALL REF INSTR BASED ON SRM ORIENTATION
PLOTTED 27-MAR-1989

Figure 4.8-19. RH Nozzle Exit Cone Temperature (Station 1905.00)

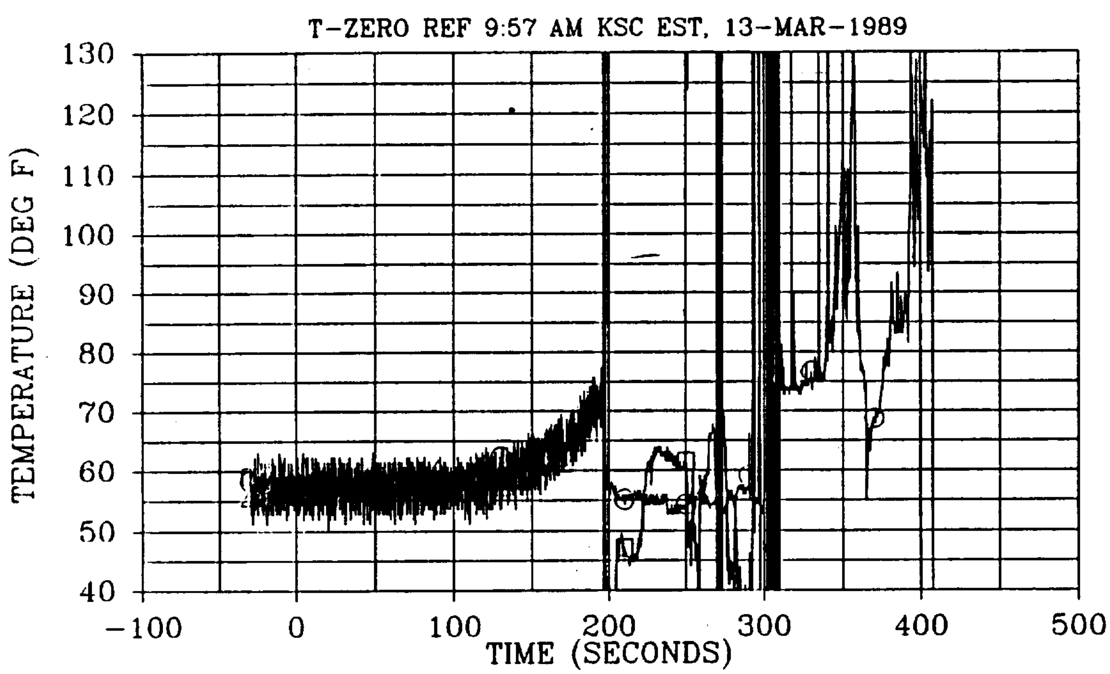

*NOTE: T-0 SRB IGNITION 072:14:57:00.017
DFI DATA (5 SPS)
ALL REF INSTR BASED ON SRM ORIENTATION
PLOTTED 27-MAR-1989

Figure 4.8-20. RH Nozzle Exit Cone Temperature (Station 1996.50) as compared to the predicted temperature of 222°F at these locations. Similar RTDs (MSIDs B07T7619A and B07T7622A) on the LH SRM registered maximum temperatures of 250° and 286°F, respectively. All these temperatures are rather high based on previous flight experience. For example, these same RTDs for STS-26R and STS-27R registered maximum temperatures in the range of 130° to 200°F.

There is a difference between the flight of STS-29R and the flights of STS-26R and STS-27R in that STS-29R had nozzle severance at apogee, while the latter two had nozzle severance just before splashdown. Analytically calculated temperatures for these two conditions are not that different.

The reason that the maximum measured temperatures for STS-29R are higher than the maximum predicted temperatures is because that additional heating was imparted, unaccounted for in the design, to the components in the base region by hydrazine fires. The probability of hydrazine fires can be confirmed by the instrumentation installed by USBI on the hydrazine tubes supplying the fuel to the APUs in the base region.

Apart from the two anomalies discussed in items e and f above, it can reasonably be stated that the majority of the DFI thermal gages recorded temperature data well within the predictions. Upon comparing the data (prediction versus actual measurements), it appears that the thermal environments, as presented in Table 4.8-2, are overly conservative. Undefined environments for hydrazine fires in the base region would be an exception to this.

4.8.3.3 PMBT and FBMBT Predictions. Temperature predictions (°F) were performed at various times with respect to the launch of STS-29R. They are predictions for the time of launch and are summarized as follows:

	Historical	L - 8 Days March 3	L - 2 Days March 11	L - 24 Hours March 12	L - 24 Hours Post
PMBT	62	66	62	--	62
FBMBT	70	74	--	75	74

The change in predicted PMBT can be attributed to the differences between the weather predictions used for the L - 8 day prediction and the actual ambient environment available for the L - 2 day prediction (Figure 4.8-21). Predicted average daily ambient temperature for the period from 3 to 11 March, which was used in the L - 8 day prediction, was 70°F. The actual average daily ambient temperature for this same time period, which was used in the L - 2 day prediction, was 64°F.

The L - 8 day prediction of 66°F was based on three sources of data: 1) tapes sent to Morton Thiokol from KSC for the period from 4 to 15 February, 2) ambient weather data from

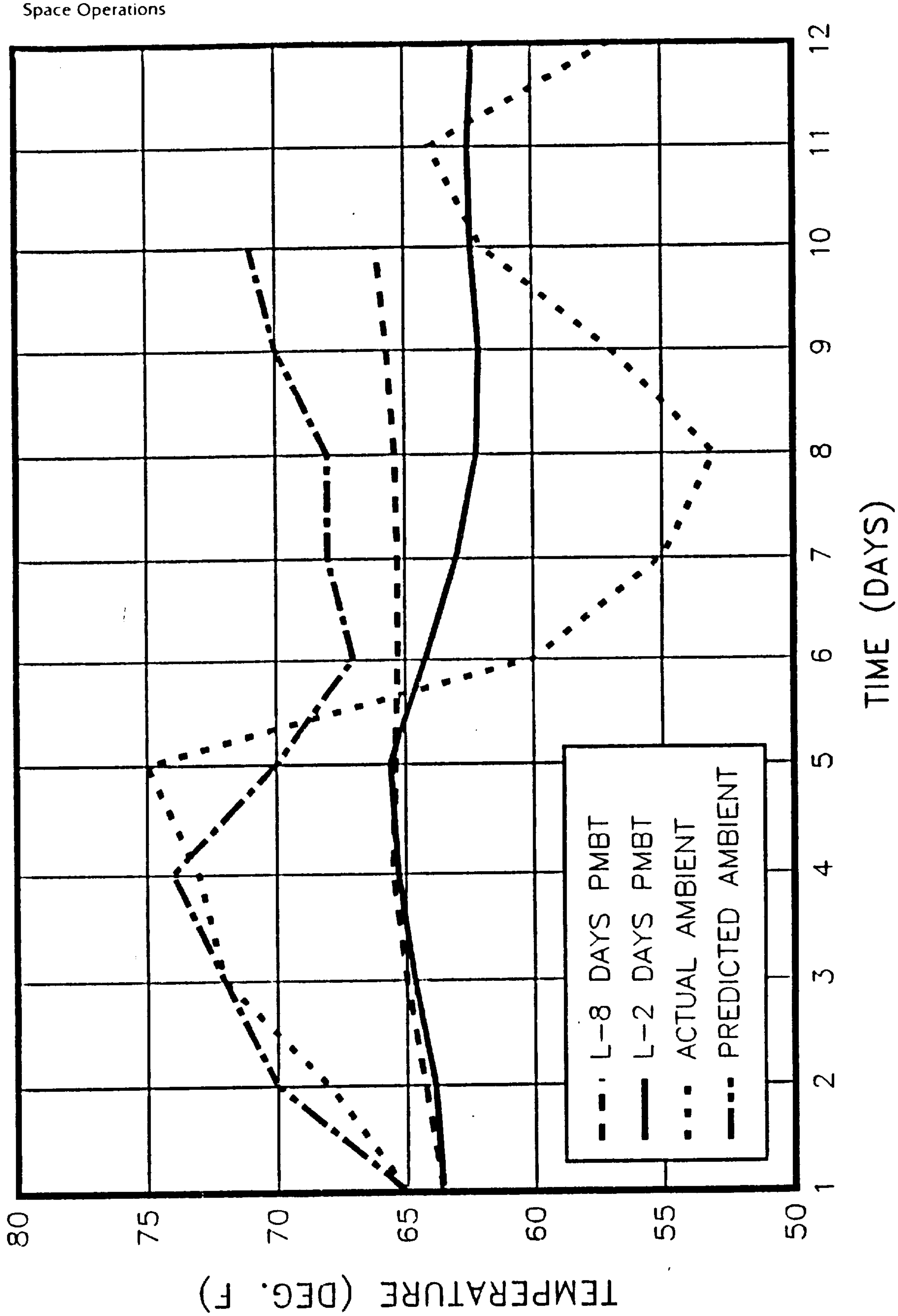

Figure 4.8-21. Daily Temperature From 2 March to Launch

KSC weather station from 16 to 2 March, and 3) weather predictions from MSFC for 3 to 11 March (scheduled day of launch at that time). The data sent by tapes contained periodic lapses which were resolved by: 1) contacting the KSC weather station, 2) using a linear interpolation scheme which incorporated data prior to and after the lapse, and 3) consulting the newspaper USA Today for the high and low temperatures of the day.

The L - 2 day prediction of 62°F was based on the same three sources of data. However, since no additional data tapes were available because of delays in receiving the tapes and difficulty in reading the tapes, the ambient weather data from the KSC weather station became the primary source of data due to reliability. Weather predictions from MSFC were used for the last 48 hr prior to launch.

Figure 4.8-22 presents the FBMBT predictions for both SRMs using reconstructed GEI average flex bearing aft end ring data as boundary conditions for the analysis. Time periods of aft skirt conditioning purge operation are evident in the figure. Prior to launch, a 12°F rise in FBMBT resulted from the 14- to 15-hr conditioning period. It should be noted that the conditioning system was used early in the countdown when GEI fell below 61°F during the cold front of late February. This was performed as a precaution according to OMRSD recommendations to maintain the flex bearings above 60°F.

4.8.3.4 On-Pad Environment Evaluations. Actual environmental data for the final 24 hr prior to launch are detailed in Figures 4.8-23 through 4.8-27 and summarized together with GEI in Table 4.8-5. Ambient temperature data (47° to 78°F) exceeded the range of the average March historical data (61° to 73°F), the lower or cooler side showing the most deviation. Cooler-than-average temperatures representative of the March historical -1 sigma value were also evident during the final 12 hr prior to launch. Windspeeds were high (reaching 30 kn) a couple of days prior to launch, but were within the historical average the day of launch.

The SRM local prelaunch environment due to March historical predictions suggested as much as a 1°F temperature suppression while the ET was loaded for winds from the southeast direction. Actual winds were consistently from the southwest-by-west direction. After assessing GEI, there was no apparent evidence of extreme temperature suppression due to ET cooling effects--only minor 1° to 2°F chilling on the inboard region of the RH SRM (Table 4.8-5).

4.8.3.5 Launch Commit Criteria. No LCC thermal violations were noted. Measured GEI and heater sensor data, as compared to the LCC requirements, are presented in Table 4.8-6. The igniter joint heaters performed as expected, with cooldown occurring over an approximate 8-hr period. During this period, the temperature dropped from 99° (T - 4 hr) to 70°F (T - 5 min).

Five of the six field joint heaters performed adequately and as expected. However, the RH aft field joint primary heater circuit failed at approximately T - 10 hr. The OMRSD maximum

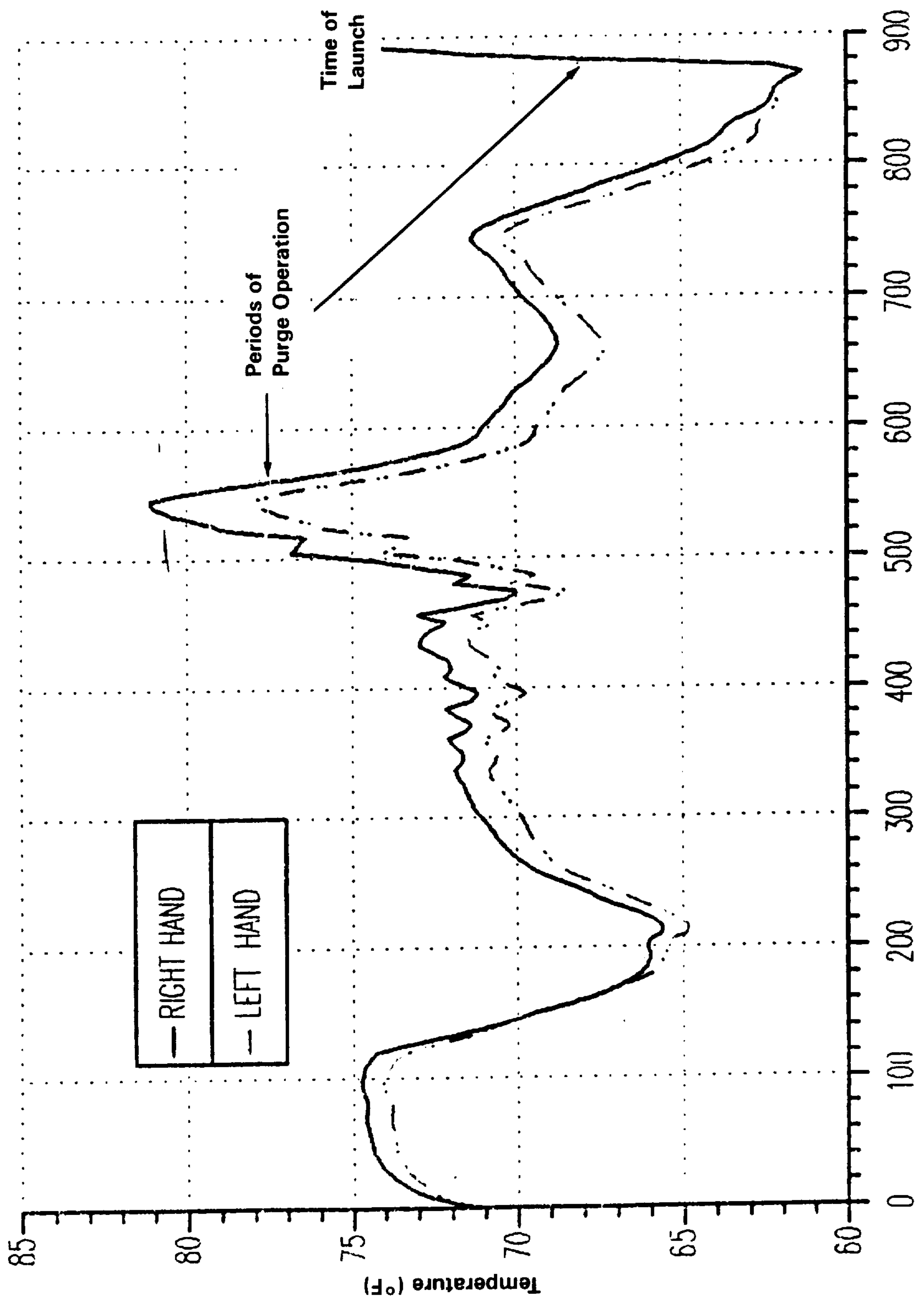

Figure 4.8-22. Flex Bearing Mean Bulk Temperature

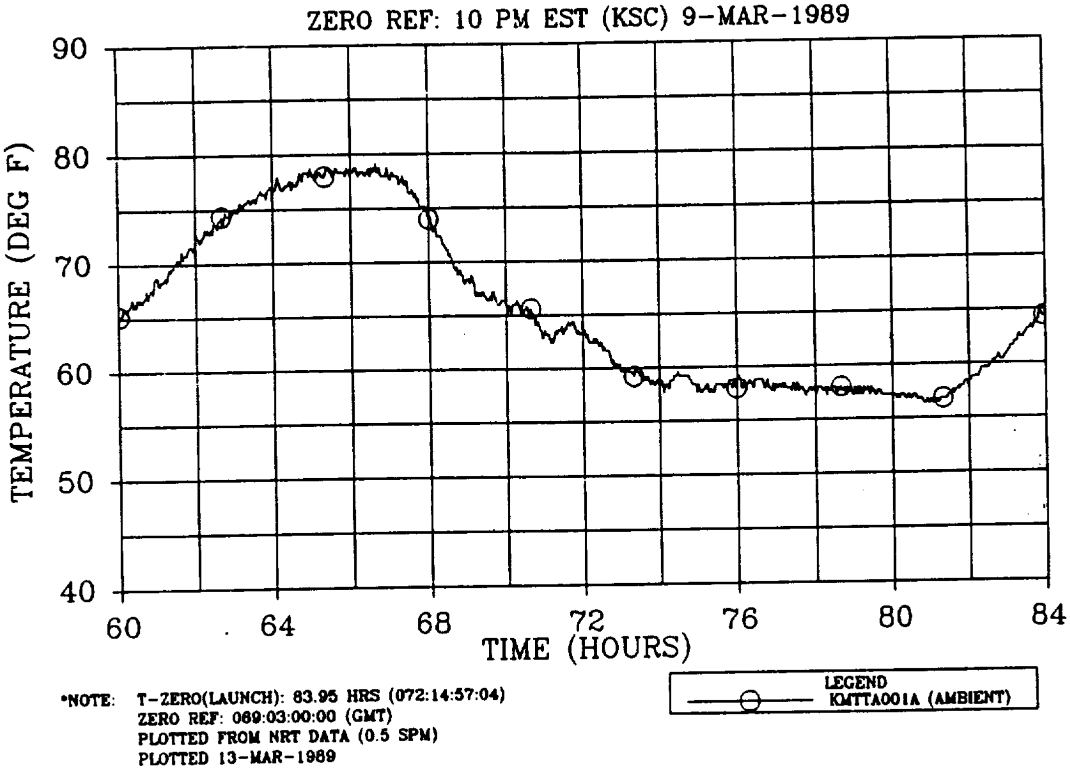

Figure 4.8-23. Prelaunch Ambient Temperature at Camera Site No. 3

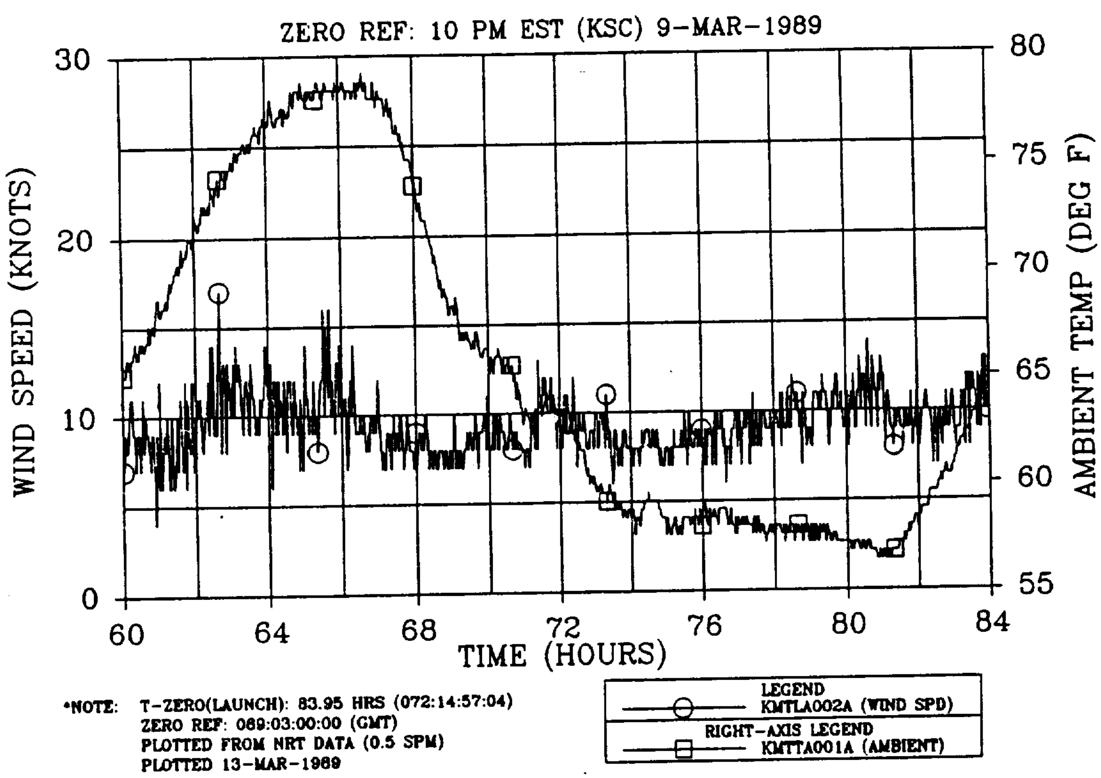

Figure 4.8-24. Prelaunch Windspeed at Camera Site No. 3 (overlaid with ambient)

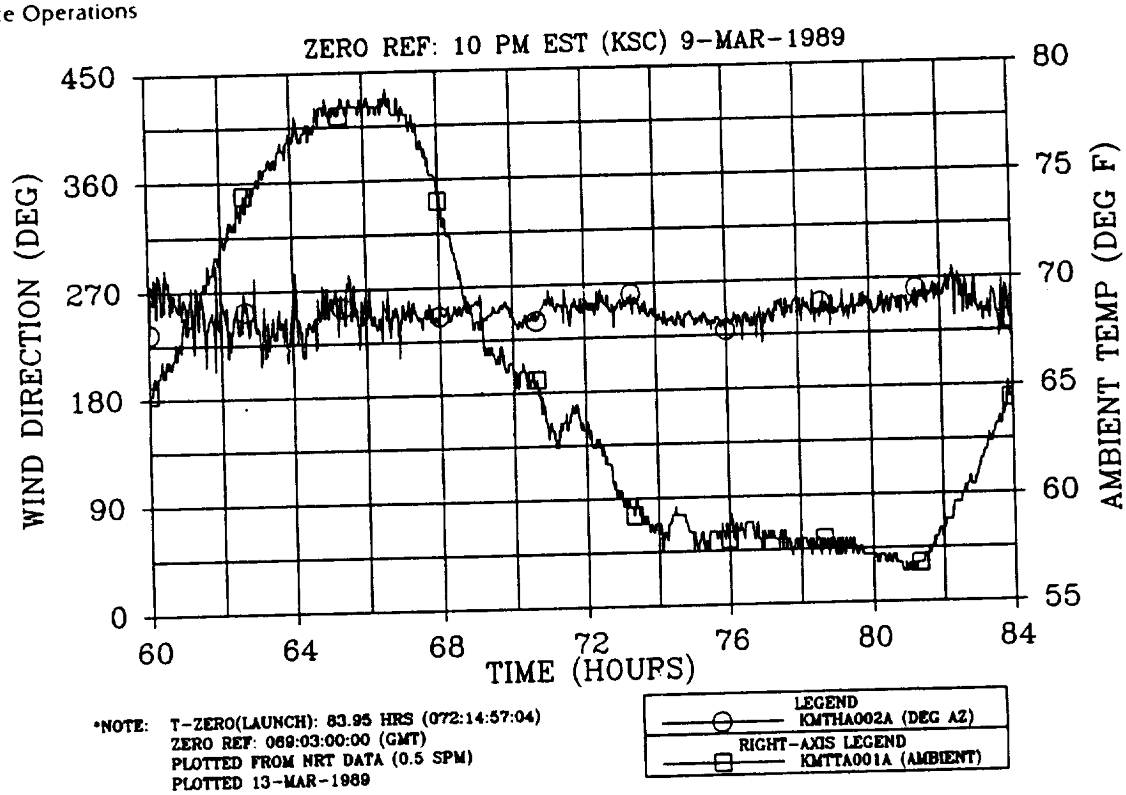

Figure 4.8-25. Prelaunch Wind Direction at Camera Site No. 3 (overlaid with ambient)

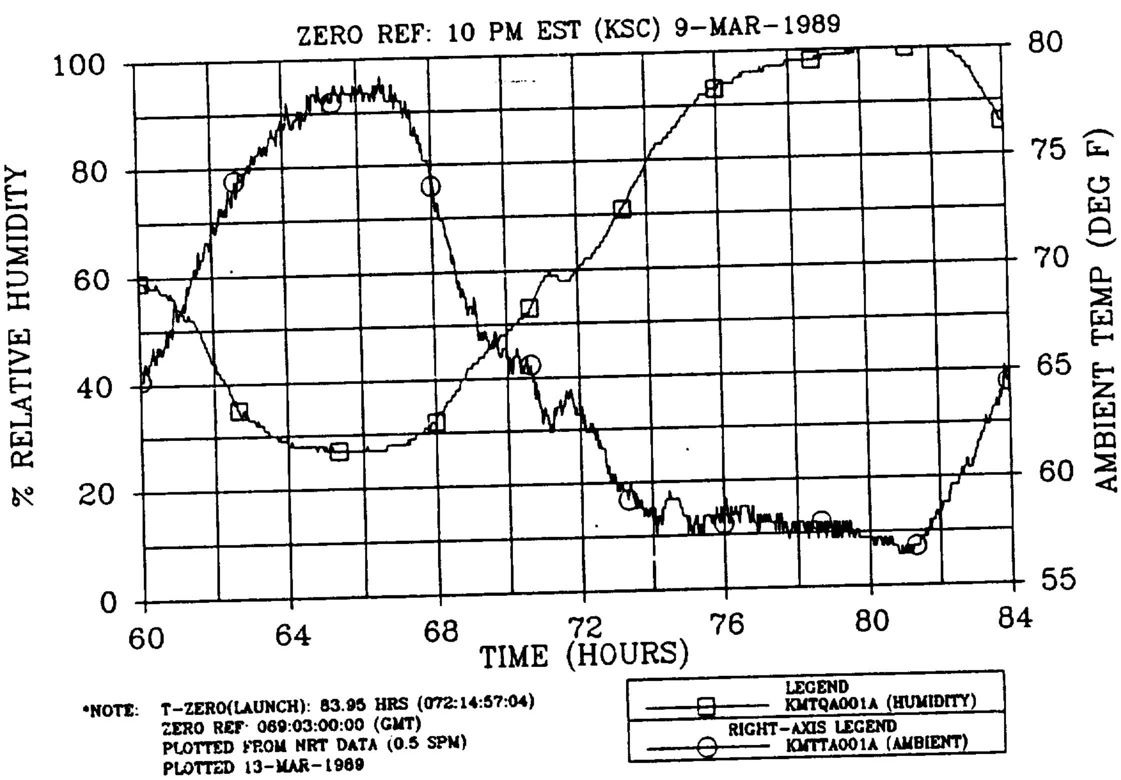

Figure 4.8-26. Prelaunch Humidity at Camera Site No. 3 (overlaid with ambient)

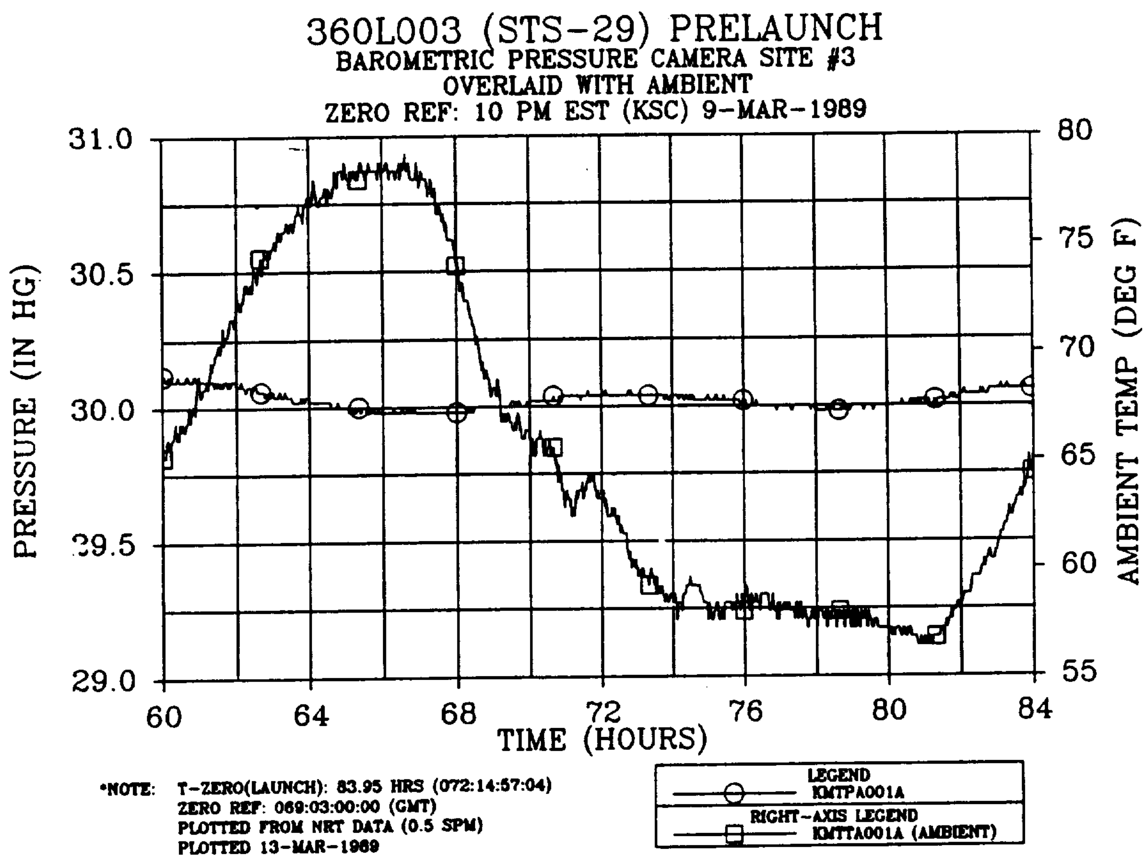

Figure 4.8-27. Prelaunch Barometric Pressure at Camera Site No. 3 (overlaid with ambient)

Table 4.8-5. 360L003 March Historical On-Pad Temperature Predictions Versus Actual GEI/Joint Heater Sensor Data (°F)

Component	Daily Cycling		T - 6 Hr to T - 5 Min		T - 5 Min	
	Historical	Actual	Historical	Actual	Historical	Actual
Igniter Joint						
RH	66-74	59-66	72-100	72-101	73-77	72-74
LH	66-74	61-67	72-100	70-101	73-77	70-72
Field Joint						
RH Forward	60-78	58-70	97-108	94-107	98-108	97-107
LH Forward	60-78	56-67	97-103	94-100	97-103	95-100
RH Center	60-77	56-67	97-107	93-108	98-107	95-106
LH Center	60-79	55-65	97-102	94-101	97-102	96-98
RH Aft	60-76	55-63	97-106	94-109	98-106	97-109
LH Aft	60-78	55-64	97-102	94-104	97-101	94-96
Case-to-Nozzle Joint						
RH	62-71	49-63*	71-77	75-88*	75-77	82-88*
LH	62-71	56-64	71-77	78-88	75-77	85-88
Flex Bearing Aft End Ring						
RH	62-71	61-64	71-77	76-93	75-77	86-93
LH	62-71	60-64	71-77	78-90	75-77	88-90
Case Acreage (deg)						
RH 45	60-75	52-74	60-75	57-72	72-73	64-72
135	61-79	53-78	61-79	58-80	77-78	70-80
215	62-76	53-75	62-76	58-72	73-74	61-72
270	62-76	53-77	62-76	56-66	72-73	58-61
325	61-75	52-77	61-75	56-66	72-73	58-62
LH 45	61-79	53-73	61-74	59-66	73-74	61-64
135	61-74	53-75	61-73	59-68	72-73	61-64
215	61-74	53-73	61-73	58-69	72-73	61-69
270	62-76	53-76	62-74	59-69	73-74	61-66
325	62-78	53-75	62-76	59-67	73-76	61-62
Local Environment						
Temperature (°F)**	61-73	47-78	61-70	56-65	70	65
Wind Speed (kn)	13	2-30	13	7-12	13	8-9
Wind Direction***	SE	SW-N	SE	SW-W	SE	SW-W
Cloud Cover		Scattered-clear		Foggy		Clear

*Sensor B06T8049A read consistently low during all monitoring periods
**Actual temperatures representative of March historical (-1 sigma value)
***Predominant wind direction

Table 4.8-6. 360L003 LCC Time Period (T - 6 hr to T - 5 min) On-Pad Temperature Predictions Versus Actual GEI/Joint Sensor Data (°F)*

Component	T - 6 Hr to T - 5 Min Predicted	T - 6 Hr to T - 5 Min Actual	T - 5 Min LCC	T - 5 Min Actual
Igniter Joint				
RH	70-75	72-101	66-123	72-74
LH	70-75	70-101	66-123	70-72
Field Joint				
RH Forward	94-108	94-107	85-122	97-107
LH Forward	94-102	94-100	85-122	95-100
RH Center	94-106	93-108	85-122	95-106
LH Center	94-102	94-101	85-122	96-98
RH Aft	94-104	94-109	85-122	97-109
LH Aft	90-102	94-104	85-122	94-96
Case-to-Nozzle Joint				
RH	82-88	75-88	75-115	82-88
LH	82-88	78-88	75-115	85-88
Flex Bearing Aft End Ring				
RH	85-90	76-93	NA-115	86-93
LH	85-90	78-90	NA-115	88-90
Case Acreage (deg)				
RH 45	52-58	57-72	35-NA	64-72
135	--	58-80	--	70-80
215	--	58-72	--	61-72
270	51-58	56-66	35-NA	58-61
325	--	56-66	--	58-62
LH 45	52-58	59-66	35-NA	61-64
135	--	59-68	--	61-64
215	--	58-69	--	61-69
270	51-58	59-69	35-NA	61-66
325	--	59-67	--	61-62
Local Environment				
Temperature (°F)**	50-56	56-65	38-99	65
Wind Speed (kn)	13	7-12	24	8-9
Wind Direction***	W	SW-W	SW-SE	SW-W
Cloud Cover		Foggy		Clear

*Predictions for anticipated launch window at T - 5 min
**Actual temperatures representative of March historical (-1 sigma value)
***Predominant wind direction

heater current limit of 19.5 amps was exceeded and a waiver was approved. The secondary heater circuit was initiated and performed nominally. IFA STS-29-M-1 was generated as a result of the heater failure.

Prior to flight (after booster stacking at KSC) this heater failed the dielectric working voltage (DWV) test. (This heater had previously passed continuity, insulation, and DWV tests at the vendor and had also passed inspection after installation.) The K5NA ablative compound was chipped off the cable and the cable was removed. It is hypothesized that, during replacement of the cable, 1) the Kapton® insulation was damaged during handling and installation, 2) moisture penetrated the cable or connector, or 3) the workmanship was defective. Postrecovery examination revealed that an electric short between the conductor and backshell had burned away approximately 0.5 to 1 in. of each of the four conductors, as well as the potting compound inside the connector. Corrective action and disposition of this anomaly were discussed in Section 4.1 of this volume.

The SRB aft skirt conditioning system performed satisfactorily and as expected. However, as on STS-27R, there was a 30°F temperature differential between conditioning gas and SRM hardware response, suggesting significant heat loss between heater and aft skirt compartment. There was also evidence of circumferential temperature differences within the aft skirt compartment (as much as 5°F on the RH flex bearing aft end ring).

4.8.3.6 Prelaunch Thermal Data Evaluation. Figures 4.8-28 through 4.8-32 show locations of the GEI and joint heater sensors for the igniter adapters, field joints, case acreage, nozzle region, and aft exit cone, respectively. Figures 4.8-33 through 4.8-62 present March historical predictions. These predictions are based upon event sequencing, as specified in Table 4.8-7. Figures 4.8-63 through 4.8-119 present actual STS-29R countdown data.

Actual GEI and joint heater sensor data were somewhat in agreement with March historical on-pad thermal predictions, deviating for the most part on the cooler side because the average ambient temperature fell below the -1 sigma value (Table 4.8-5). The LCC time period (T - 6 hr to T - 5 min) real-time predictions, which incorporated an environmental update for the last 24 hr prior to launch, were also somewhat in agreement with GEI. GEI deviated for the most part on the warmer side due to higher than anticipated ambient temperatures (Table 4.8-6).

Postflight reconstructed predictions of GEI and joint heater sensor response have been performed using the actual environmental data of the final 24 hr prior to launch. A few examples of these predictions, compared with actual measured sensor data, are found in Figures 4.8-120 through 4.8-135. Reasonable agreement is evident for all areas except the ETA ring, systems tunnel, and case-to-nozzle joint regions. Modeling considerations (environment and detail) for these regions need to be examined closely. Future modeling will check these and incorporate updates as solutions are found.

A022311a

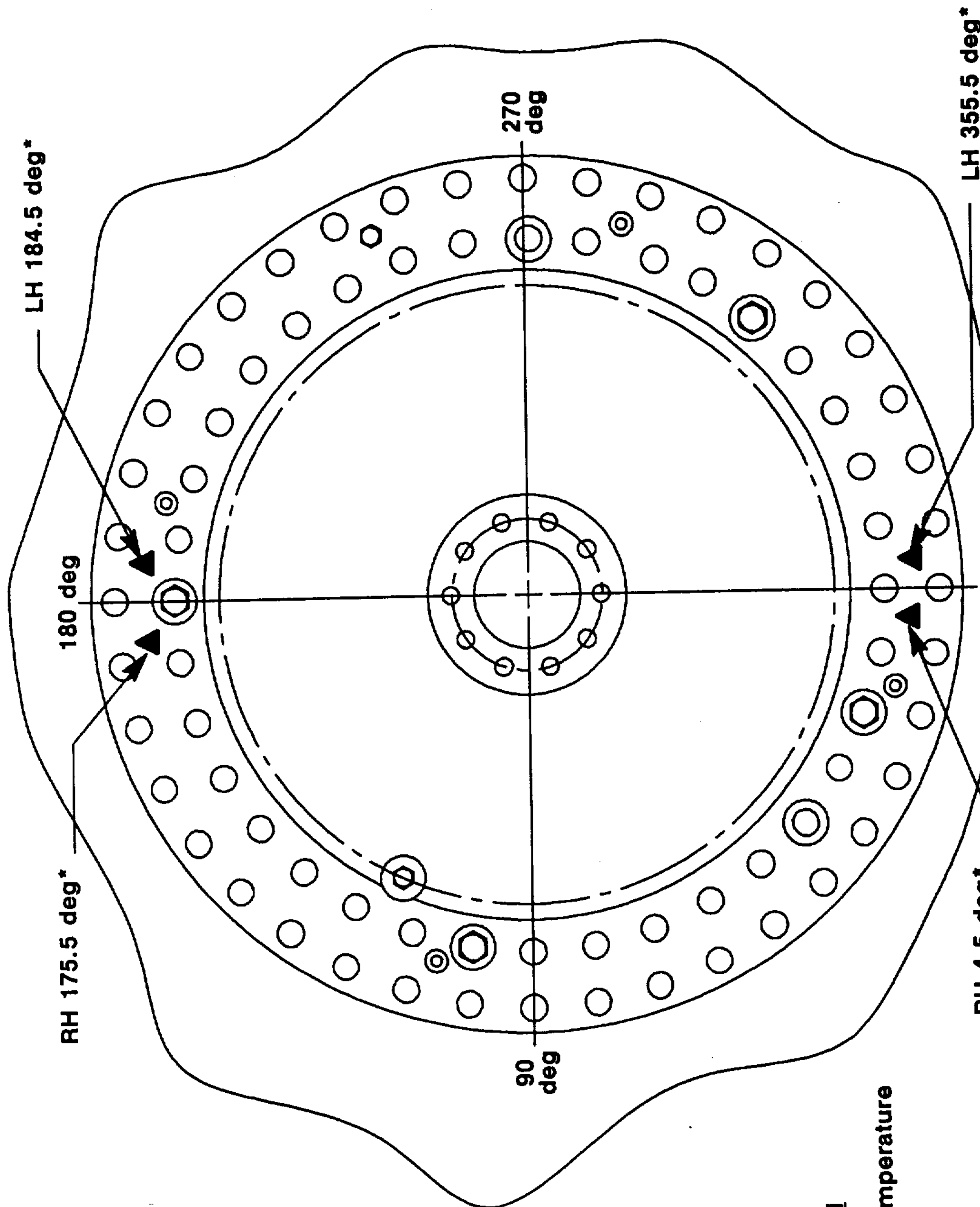

Legend

▲ GEI Temperature

*1 of 2 per each booster required for LCC compliance

Figure 4.8-28. Forward Dome GEI

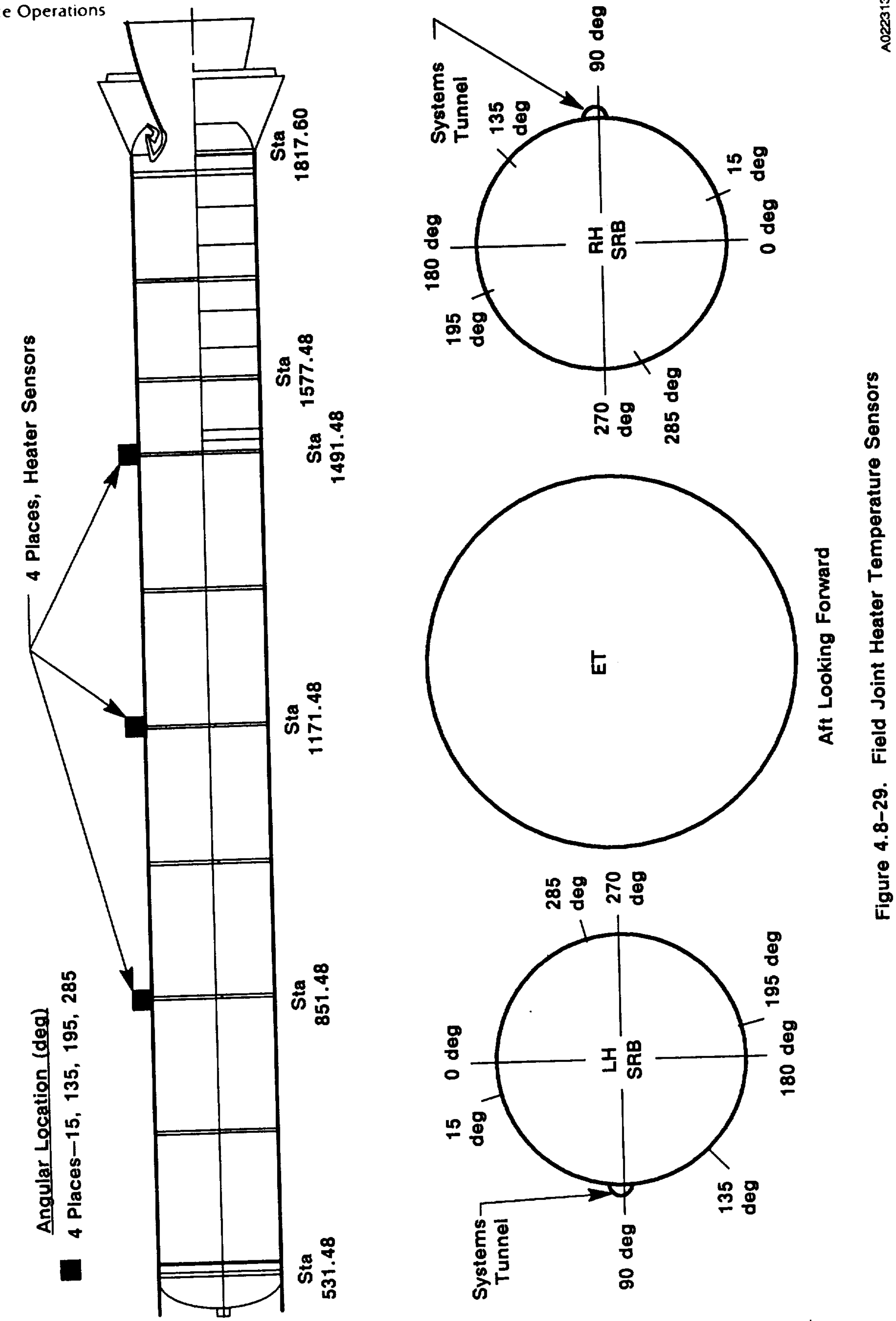

Figure 4.8-29. Field Joint Heater Temperature Sensors

A022312a

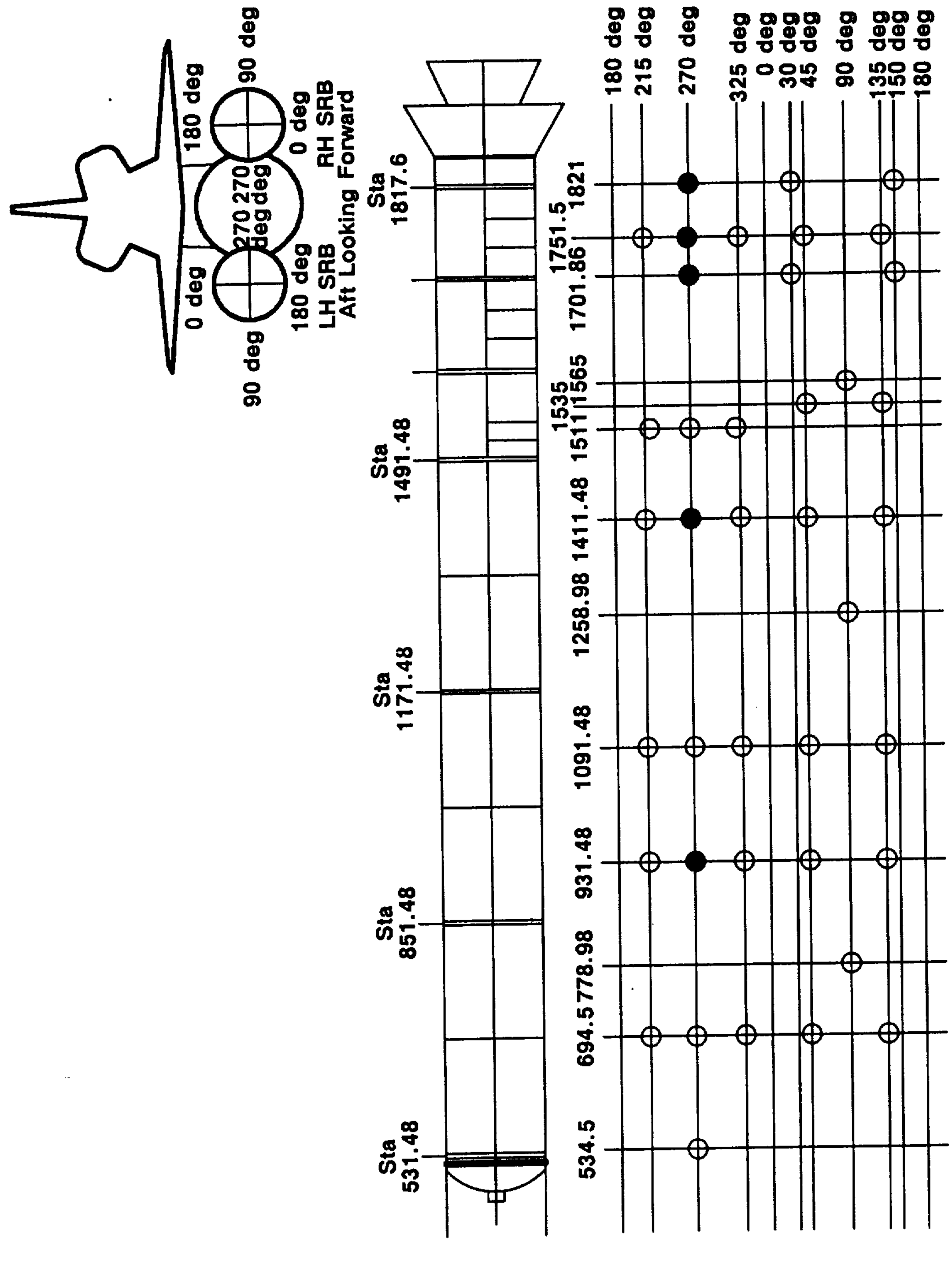

○ Denotes case GEI temperature sensors
● Denotes case GEI temperature sensors required for LCC
* 4 of 6 per flight set required for LCC compliance

Figure 4.8-30. Case GEI

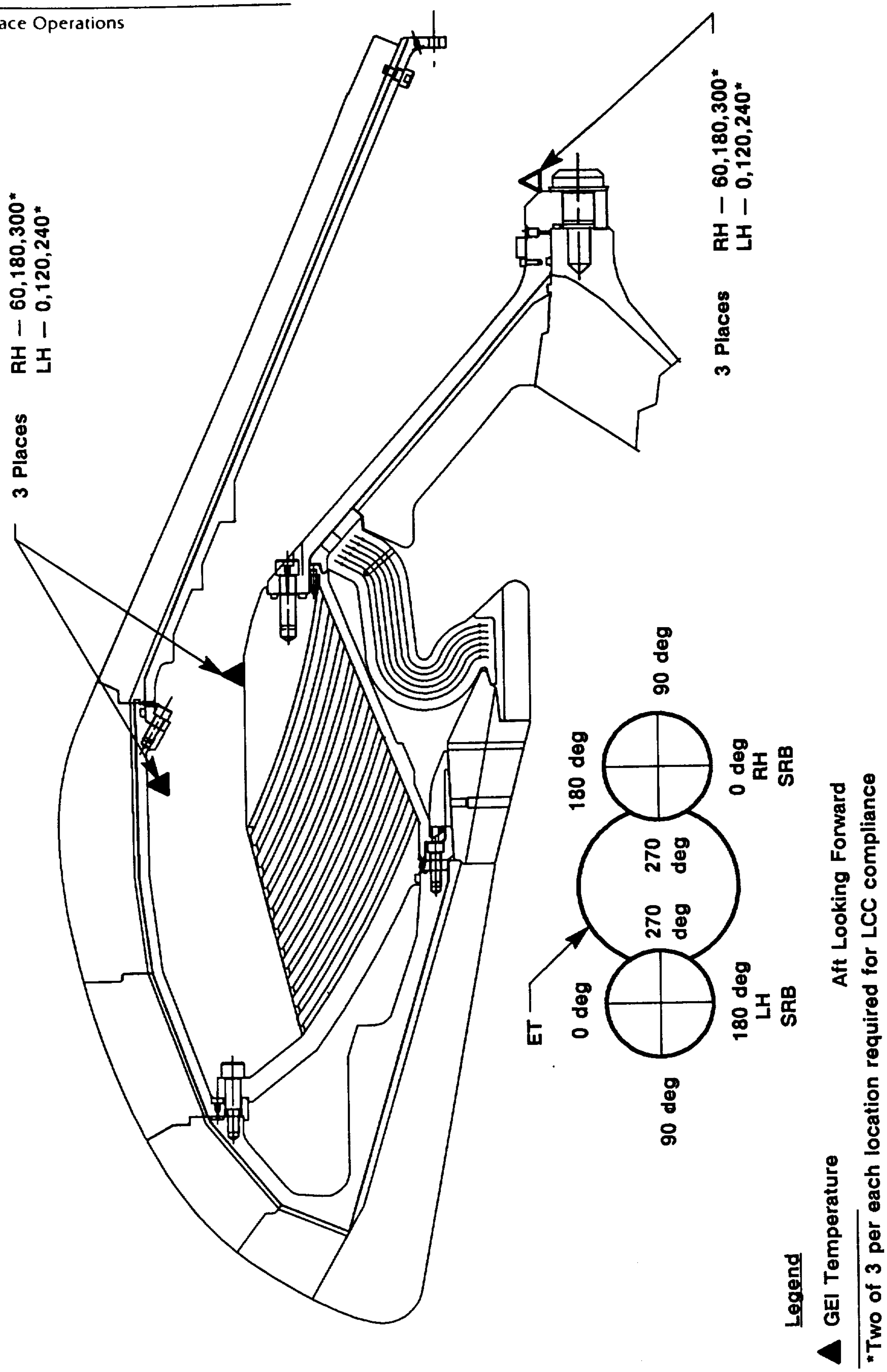

A022480a

Figure 4.8-31. Nozzle GEI

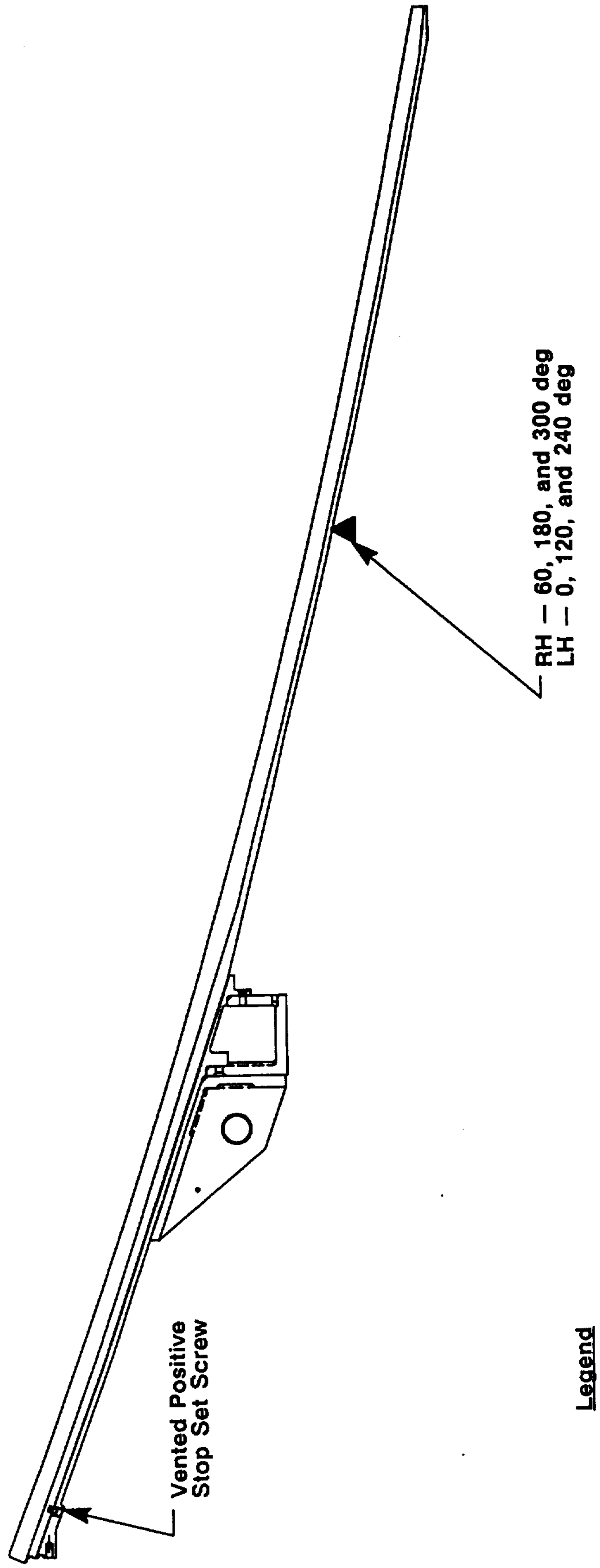

Legend

▲ GEI Temperature

Figure 4.8-32. Aft Exit Cone GEI

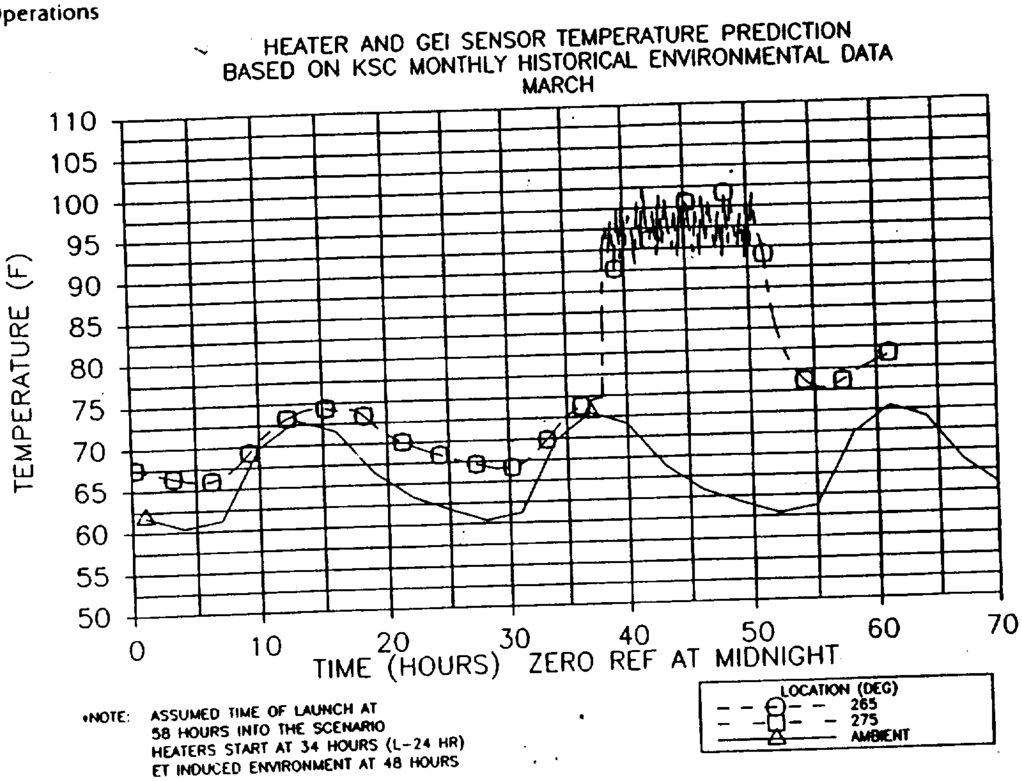

Figure 4.8-33. Temperature Prediction--RH Motor Ignition System Region

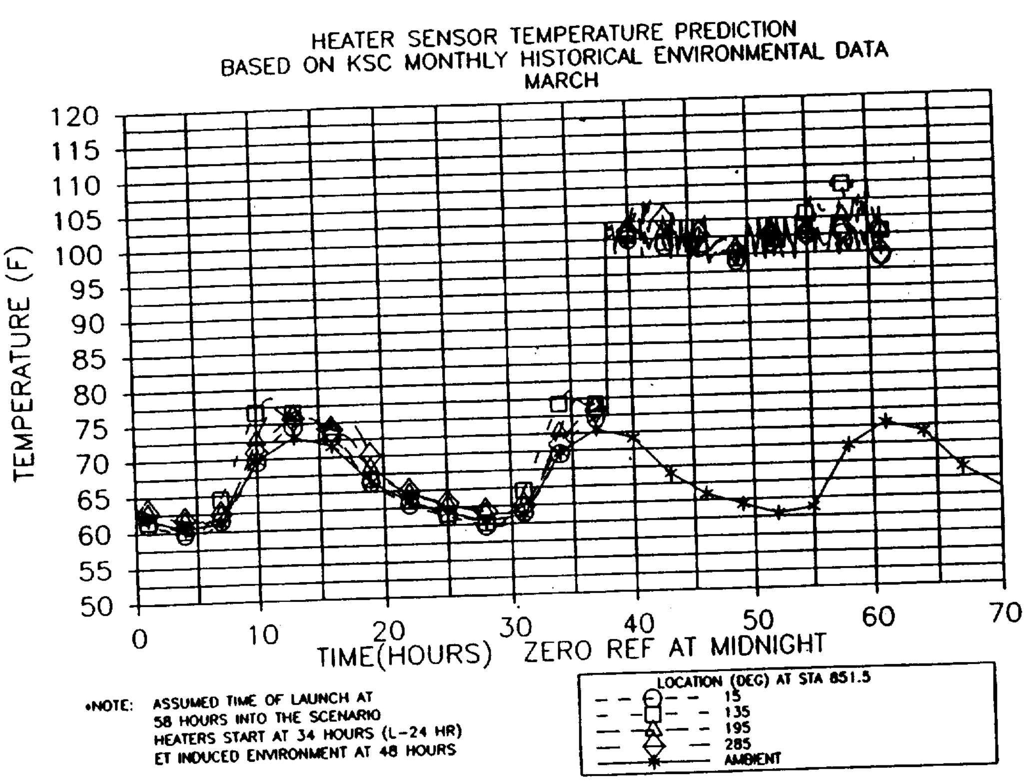

Figure 4.8-34. Temperature Prediction--RH Motor Forward Field Joint

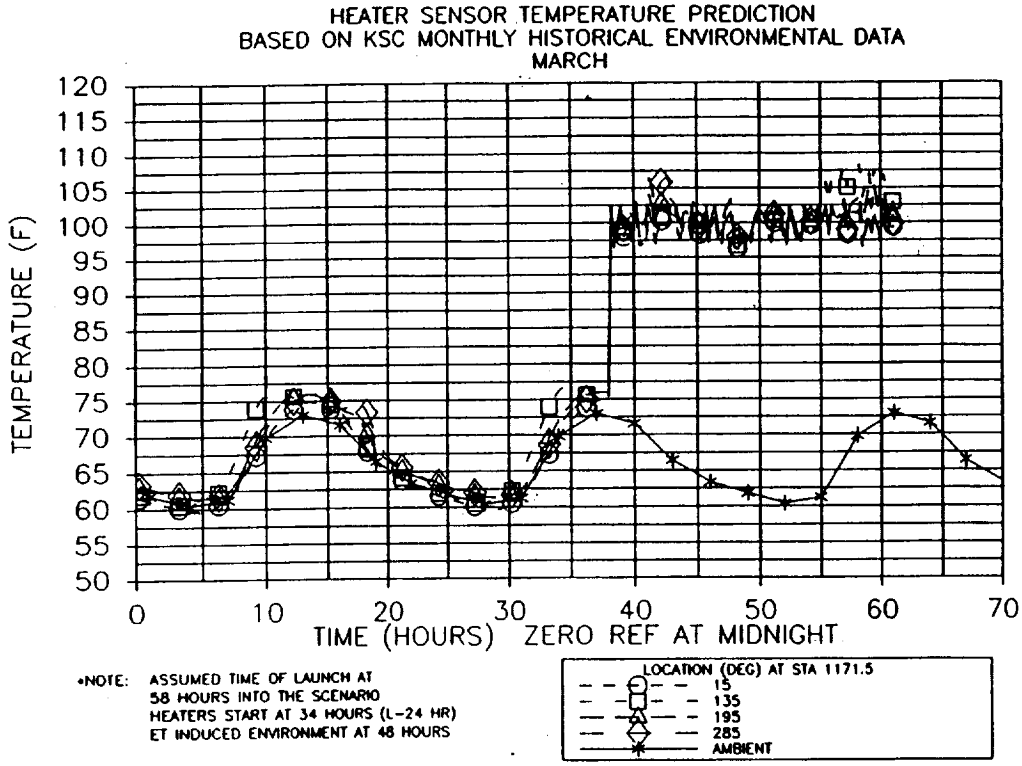

Figure 4.8-35. Temperature Prediction--RH Motor Center Field Joint

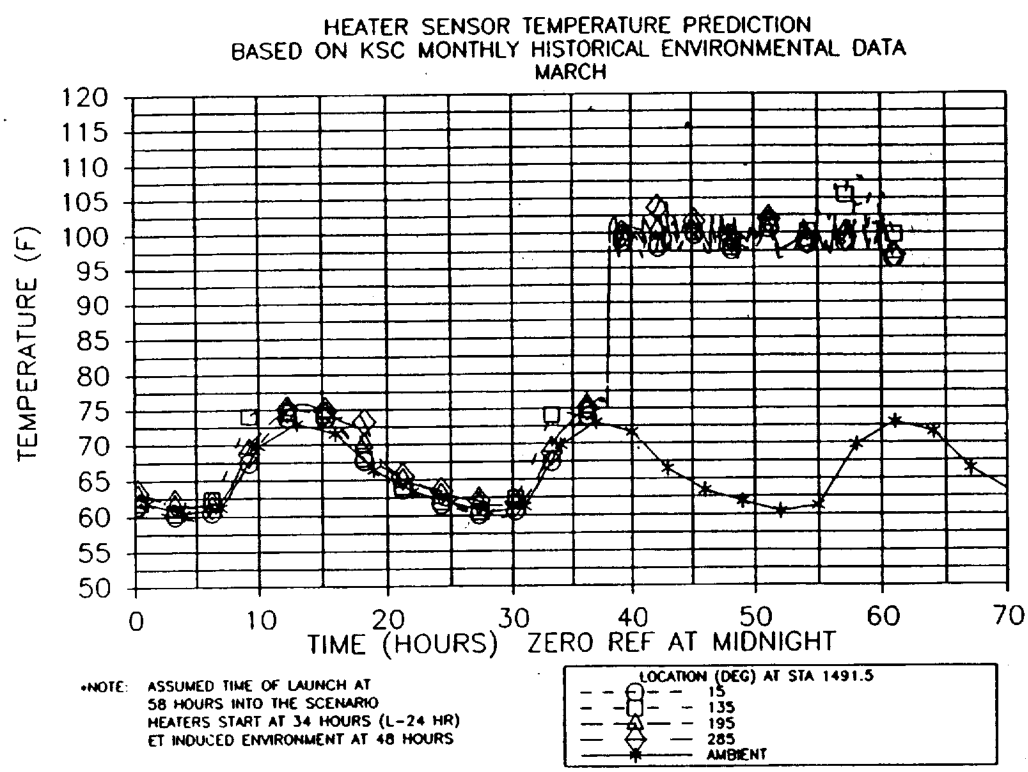

Figure 4.8-36. Temperature Prediction--RH Motor Aft Field Joint

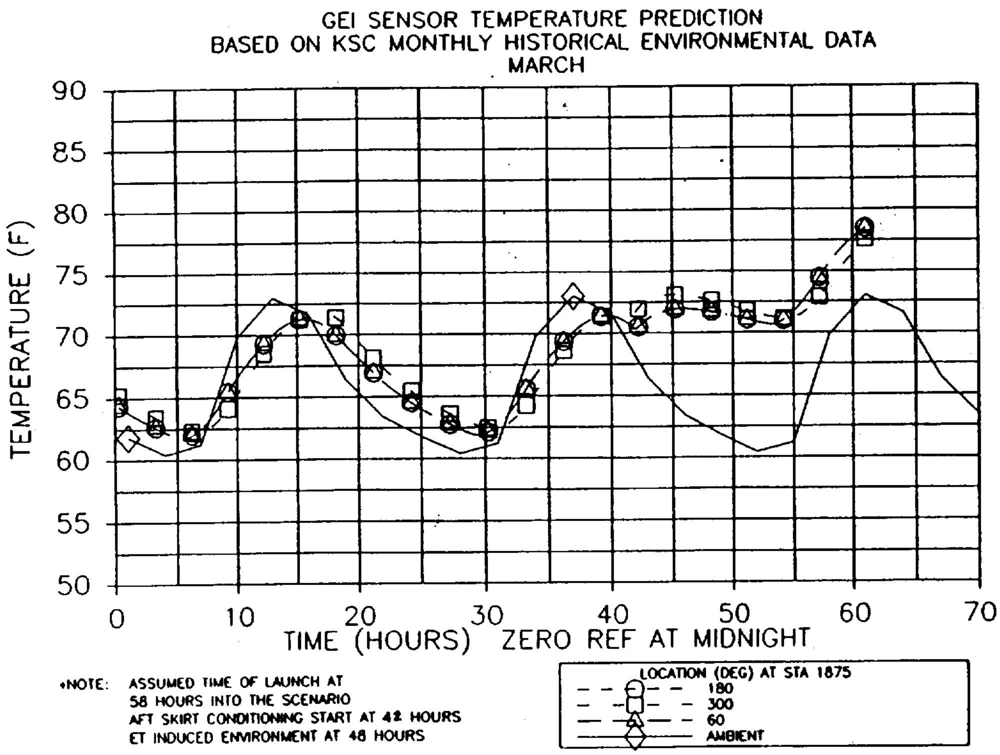

Figure 4.8-37. Temperature Prediction--RH Motor Nozzle Region

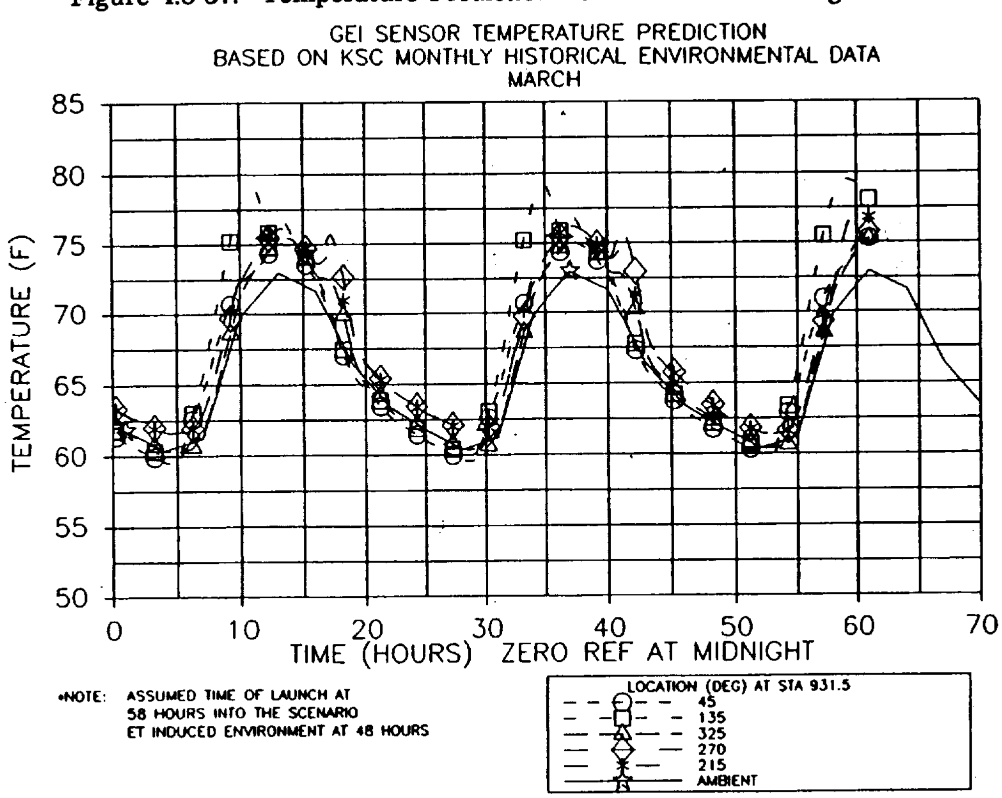

Figure 4.8-38. Temperature Prediction--RH Motor Forward Case Acreage

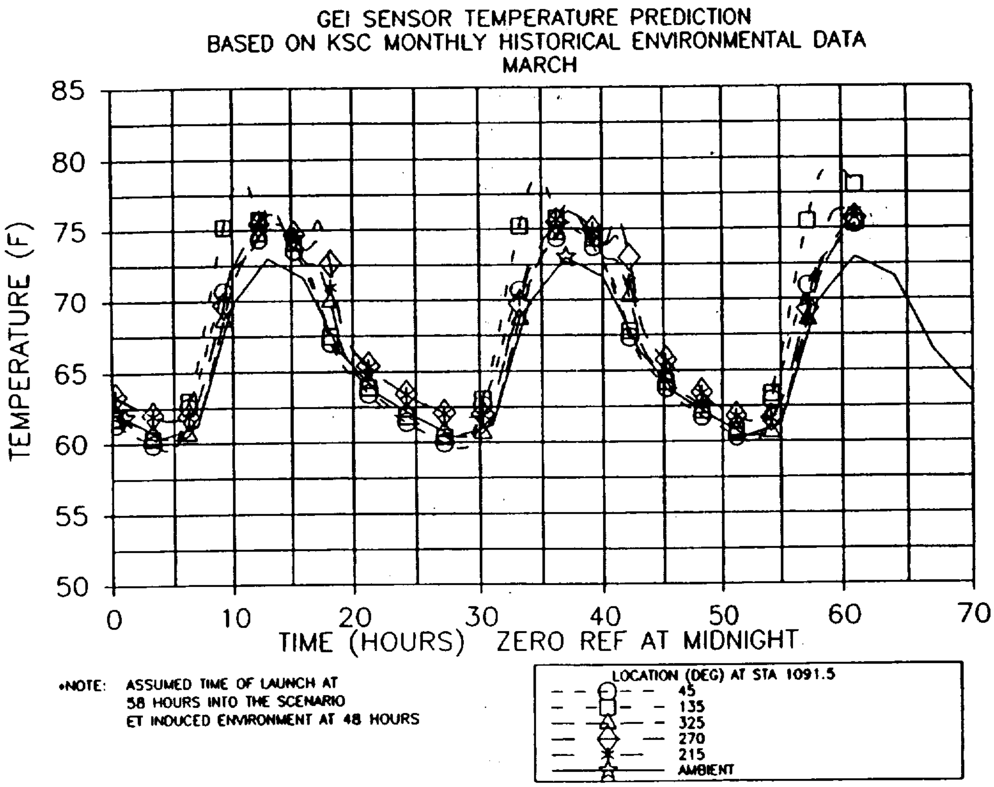

Figure 4.8-39. Temperature Prediction--RH Motor Forward Center Case Acreage

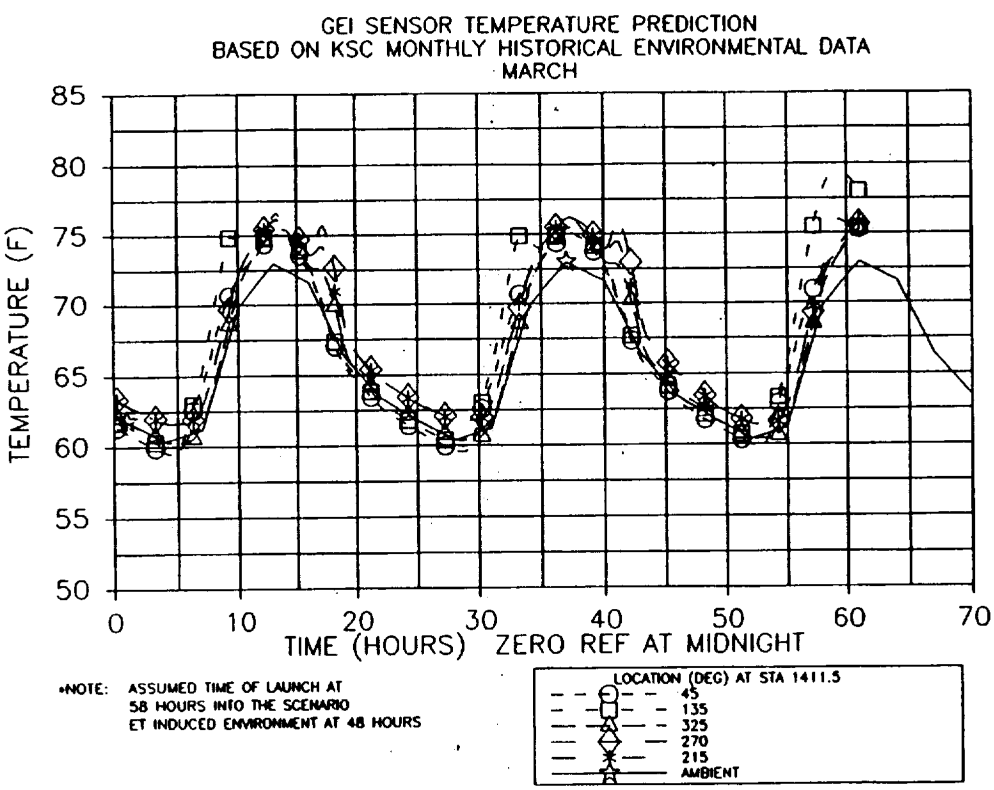

Figure 4.8-40. Temperature Prediction--RH Motor Aft Center Case Acreage

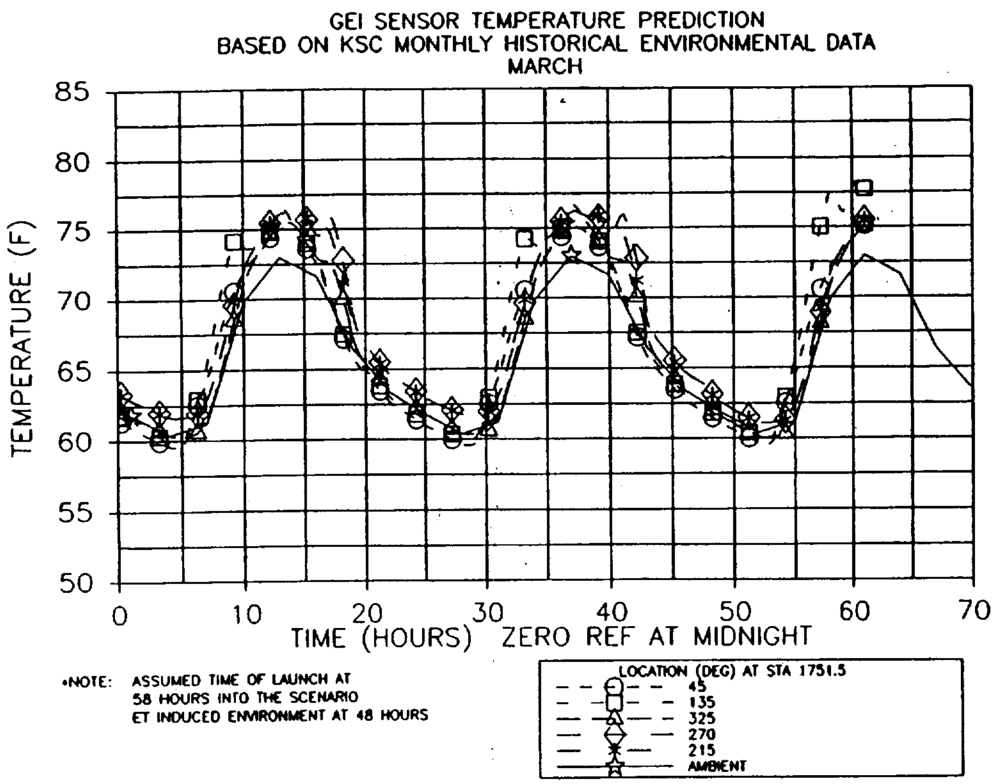

Figure 4.8-41. Temperature Prediction--RH Motor Aft Case Acreage

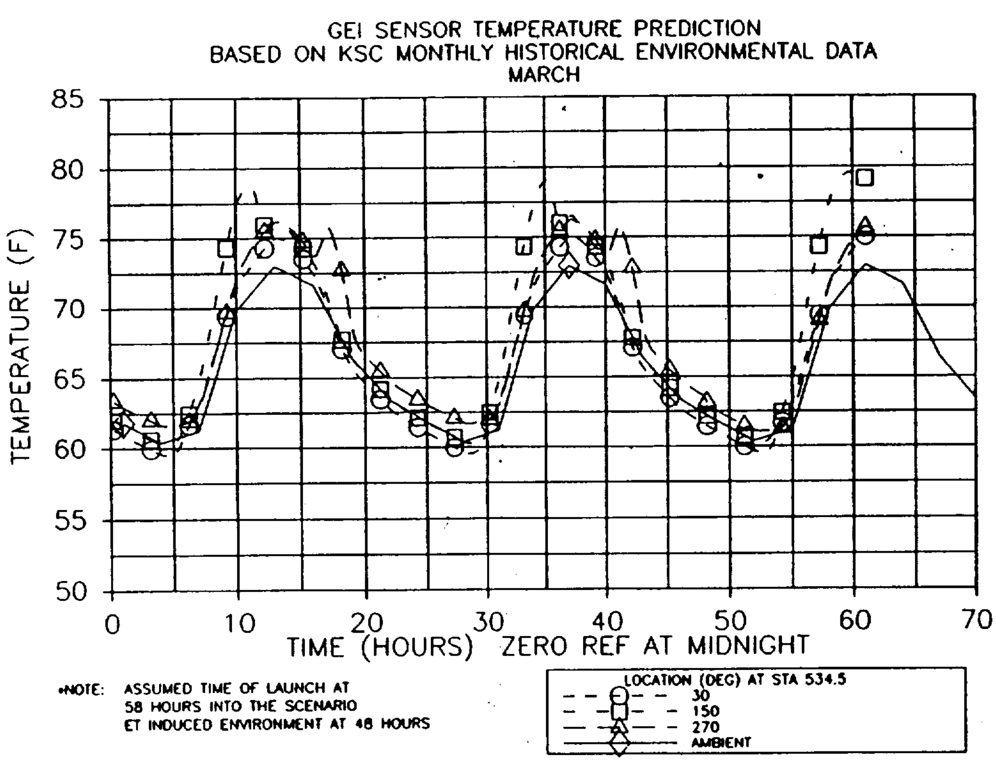

Figure 4.8-42. Temperature Prediction--RH Motor Forward Dome Factory Joint

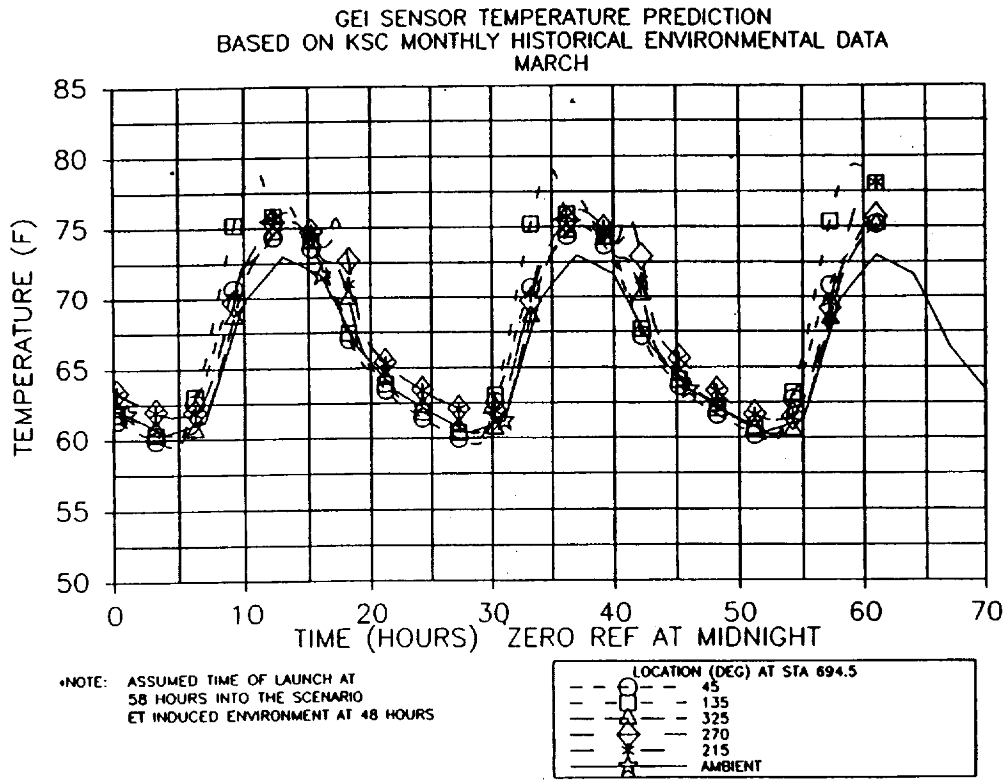

Figure 4.8-43. Temperature Prediction--RH Motor Forward Factory Joint

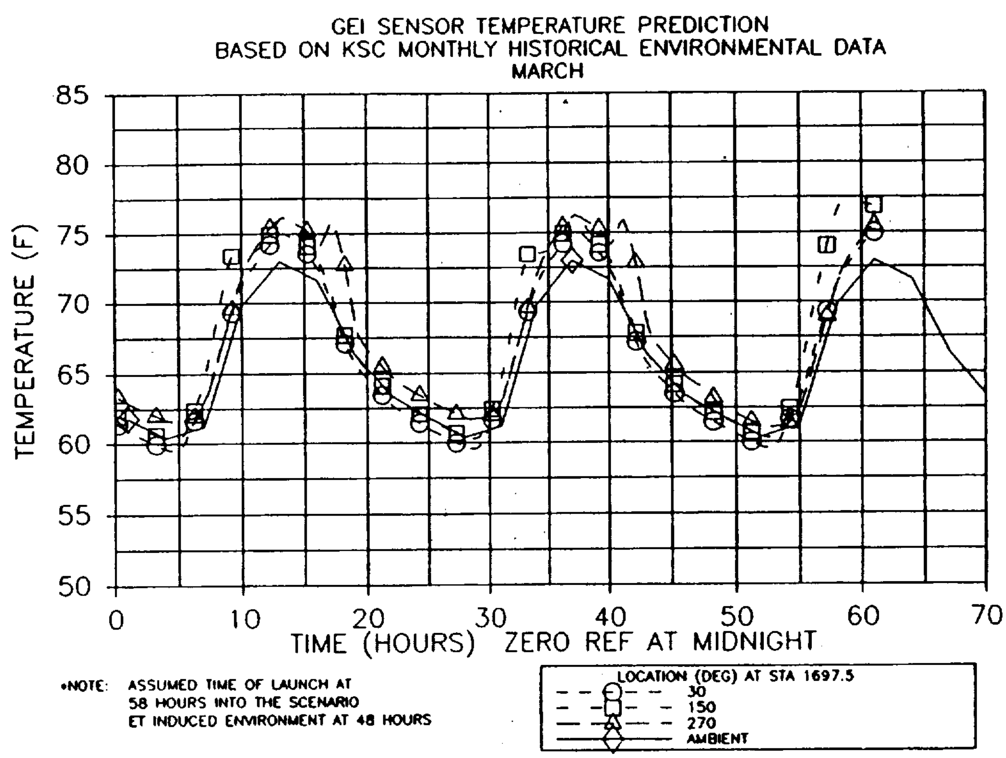

Figure 4.8-44. Temperature Prediction--RH Motor Aft Factory Joint

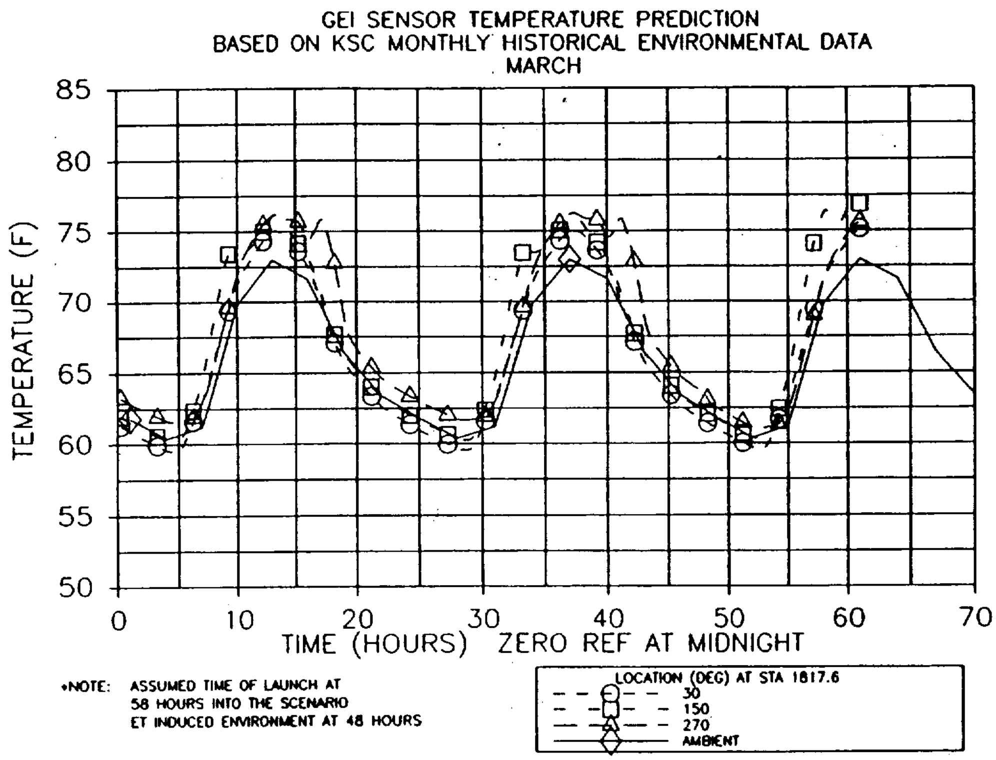

Figure 4.8-45. Temperature Prediction--RH Motor Aft Dome Factory Joint

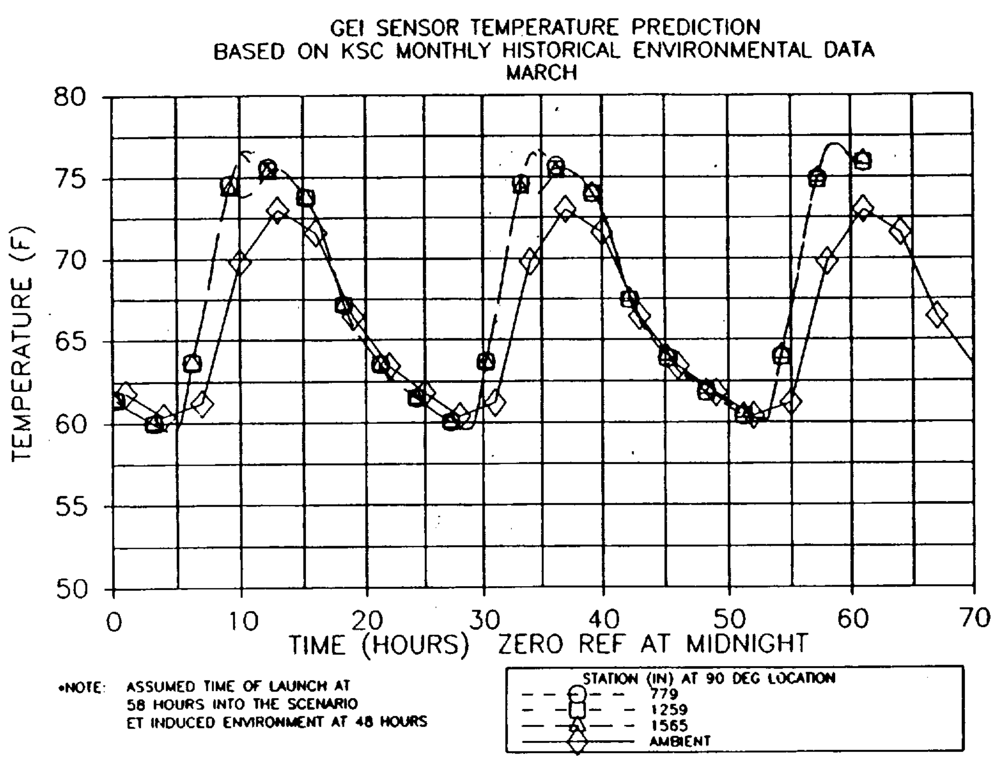

Figure 4.8-46. Temperature Prediction--RH Motor Tunnel Bondline

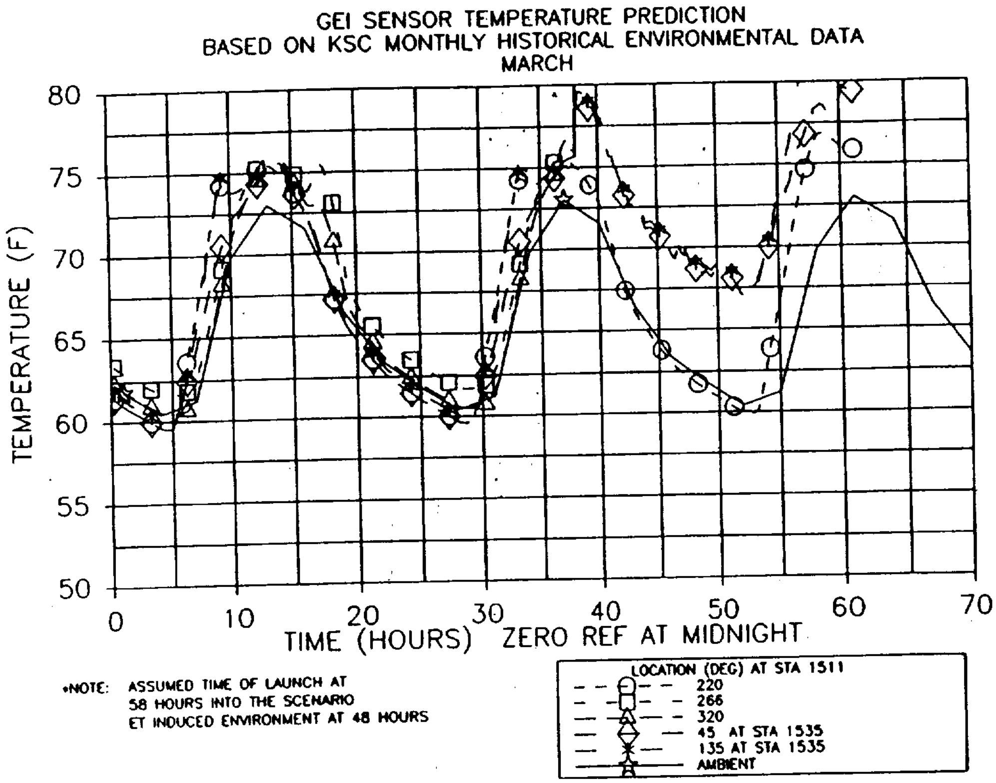

Figure 4.8-47. Temperature Prediction--RH Motor ETA Region

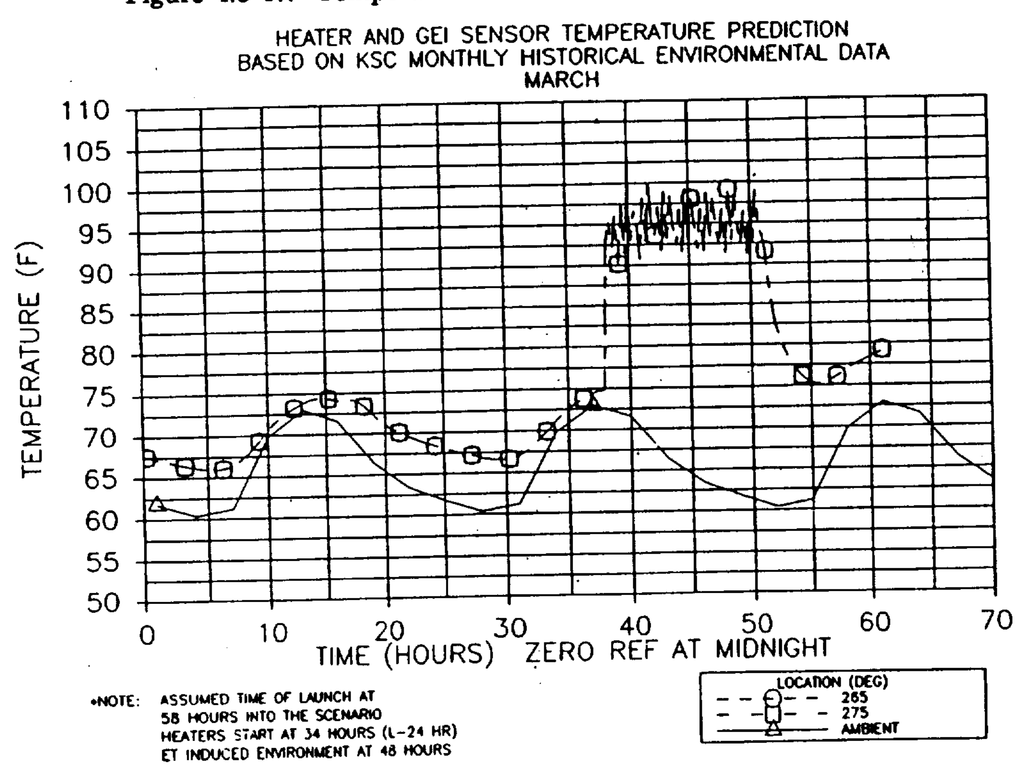

Figure 4.8-48. Temperature Prediction--LH Motor Ignition System Region

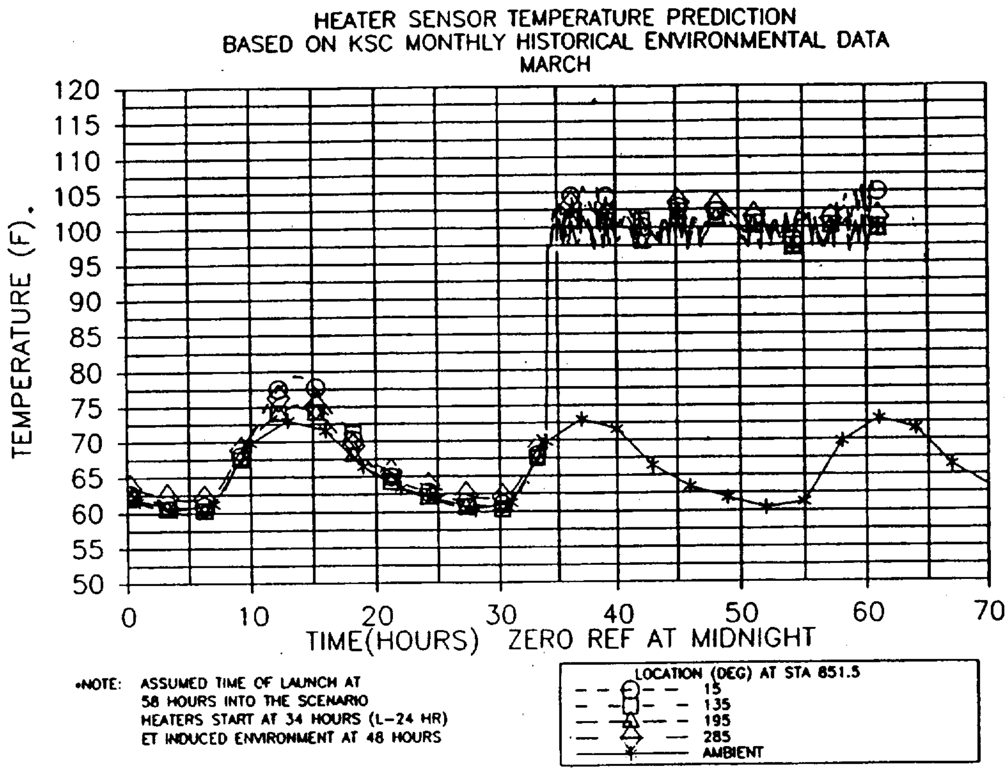

Figure 4.8-49. Temperature Prediction--LH Motor Forward Field Joint

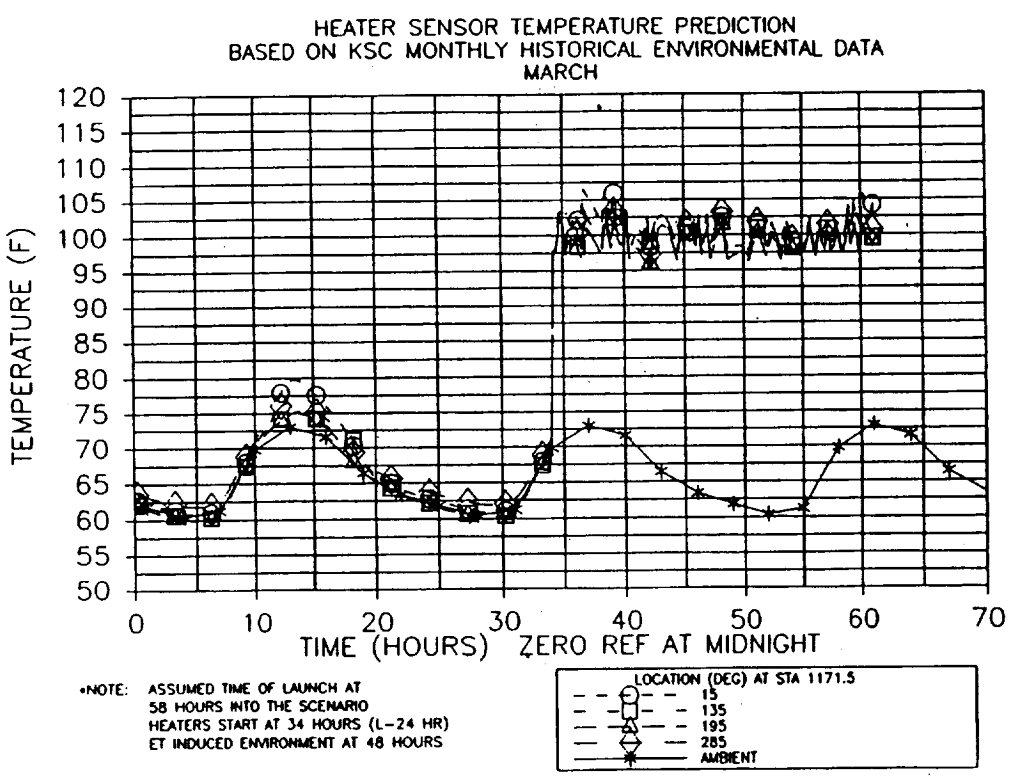

Figure 4.8-50. Temperature Prediction--LH Motor Center Field Joint

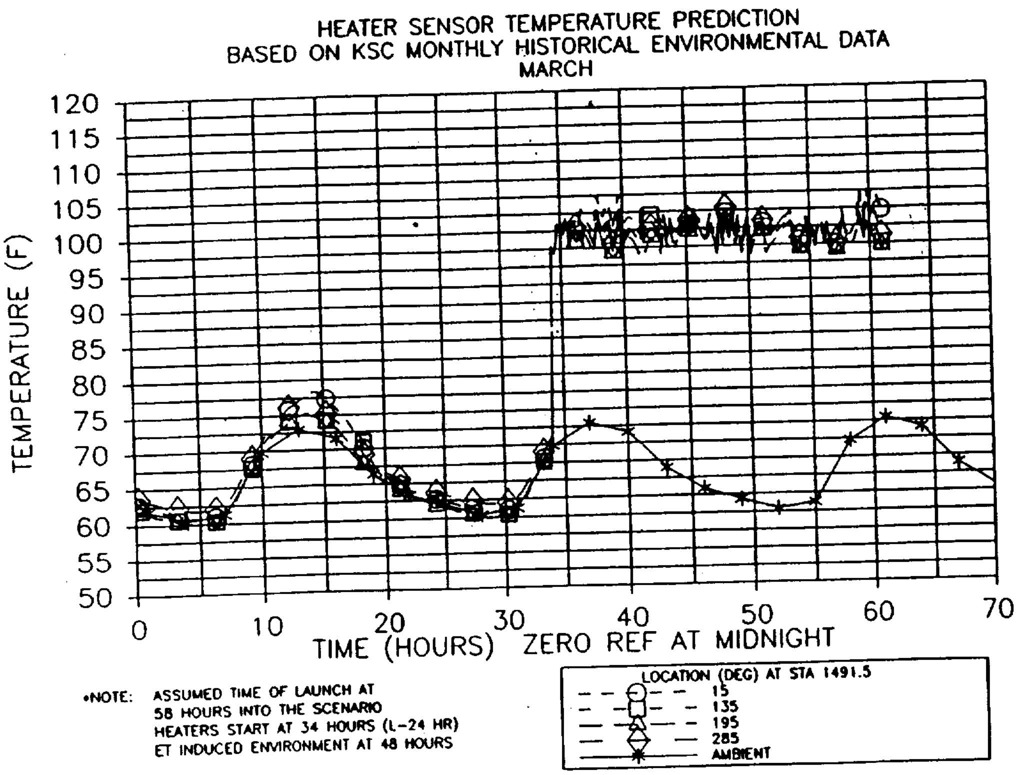

*NOTE: ASSUMED TIME OF LAUNCH AT 58 HOURS INTO THE SCENARIO
HEATERS START AT 34 HOURS (L-24 HR)
ET INDUCED ENVIRONMENT AT 48 HOURS

Figure 4.8-51. Temperature Prediction--LH Motor Aft Field Joint

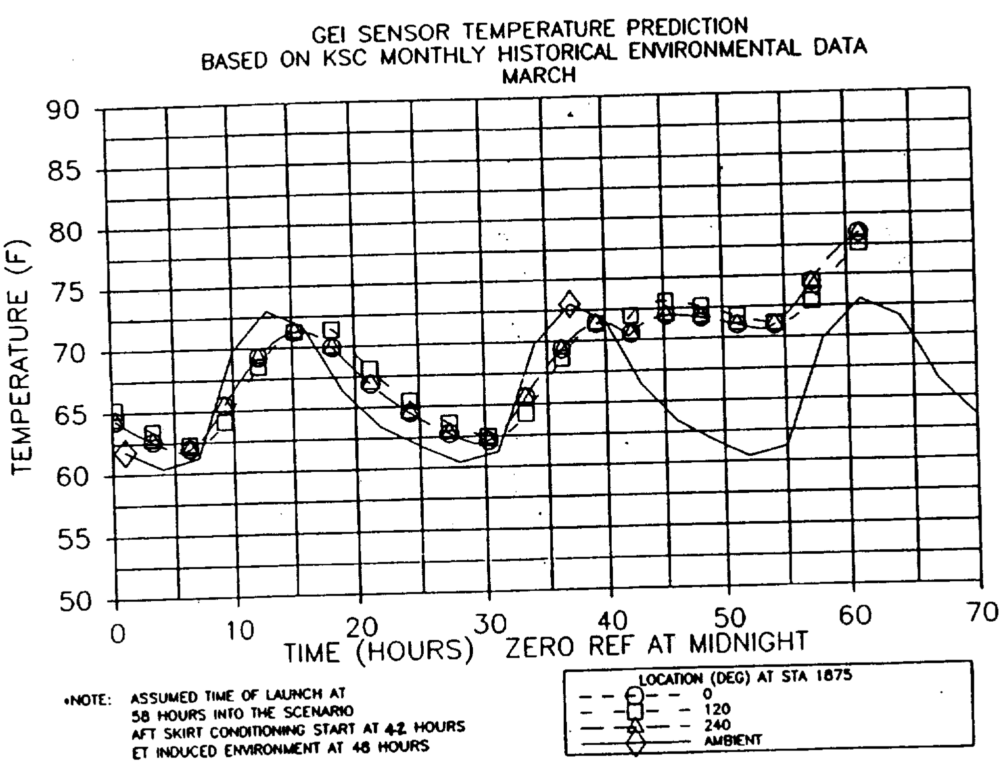

*NOTE: ASSUMED TIME OF LAUNCH AT 58 HOURS INTO THE SCENARIO
AFT SKIRT CONDITIONING START AT 42 HOURS
ET INDUCED ENVIRONMENT AT 48 HOURS

Figure 4.8-52. Temperature Prediction--LH Motor Nozzle Region

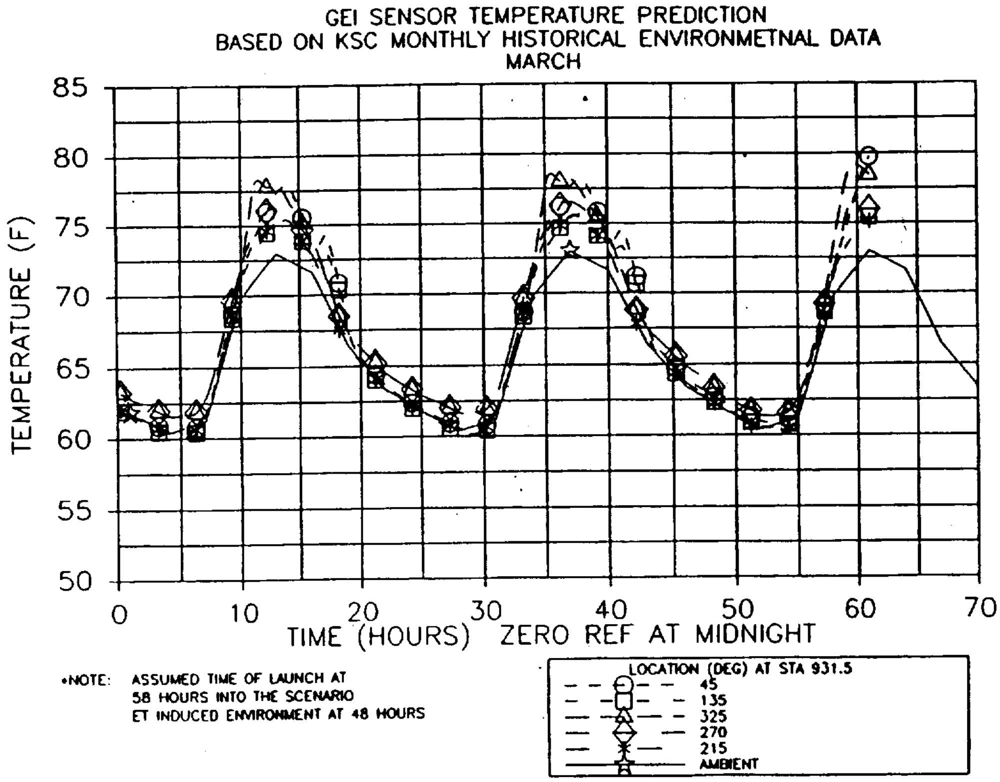

Figure 4.8-53. Temperature Prediction--LH Motor Forward Case Acreage

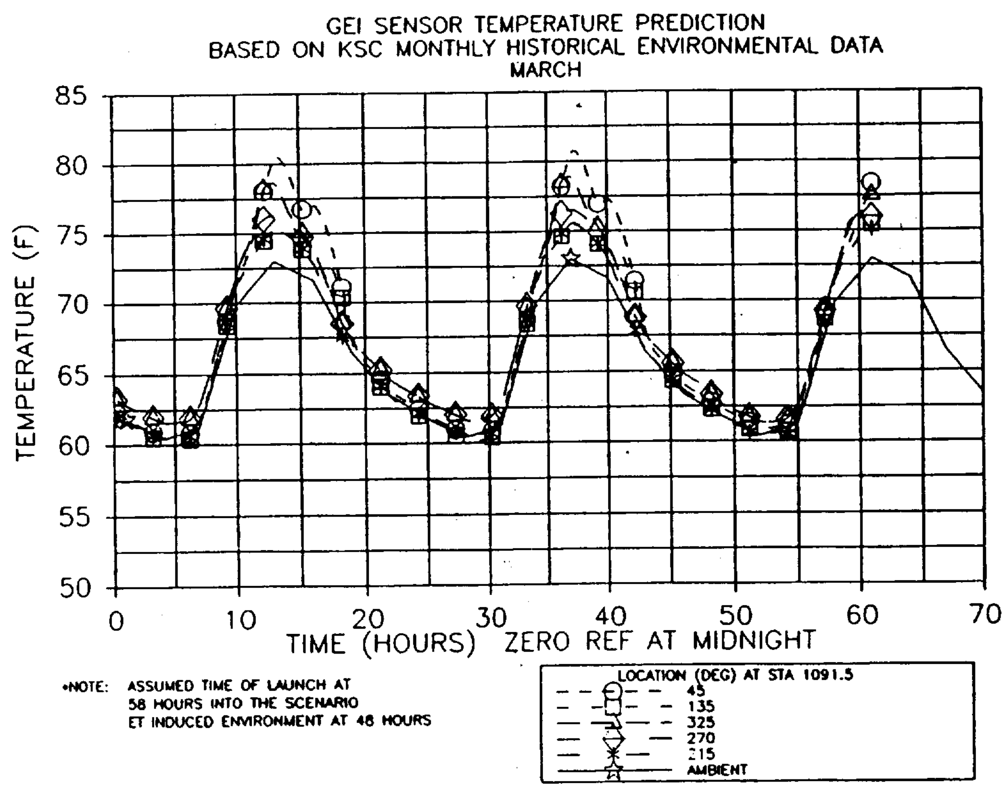

Figure 4.8-54. Temperature Prediction--LH Motor Forward Center Case Acreage

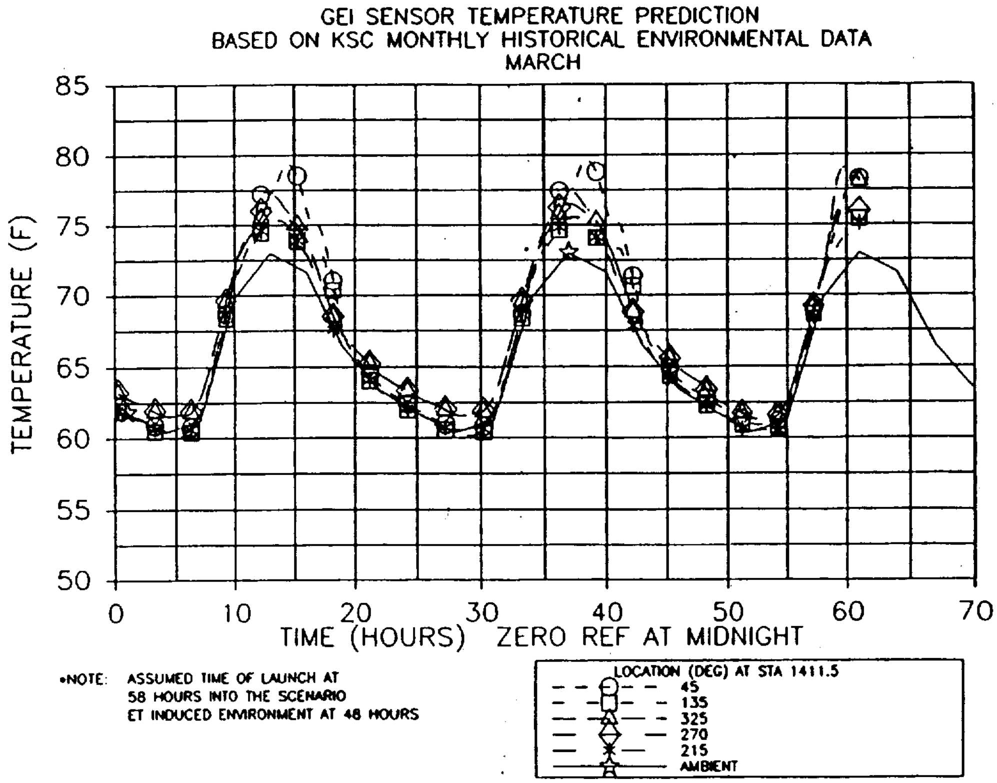

Figure 4.8-55. Temperature Prediction--LH Motor Aft Center Case Acreage

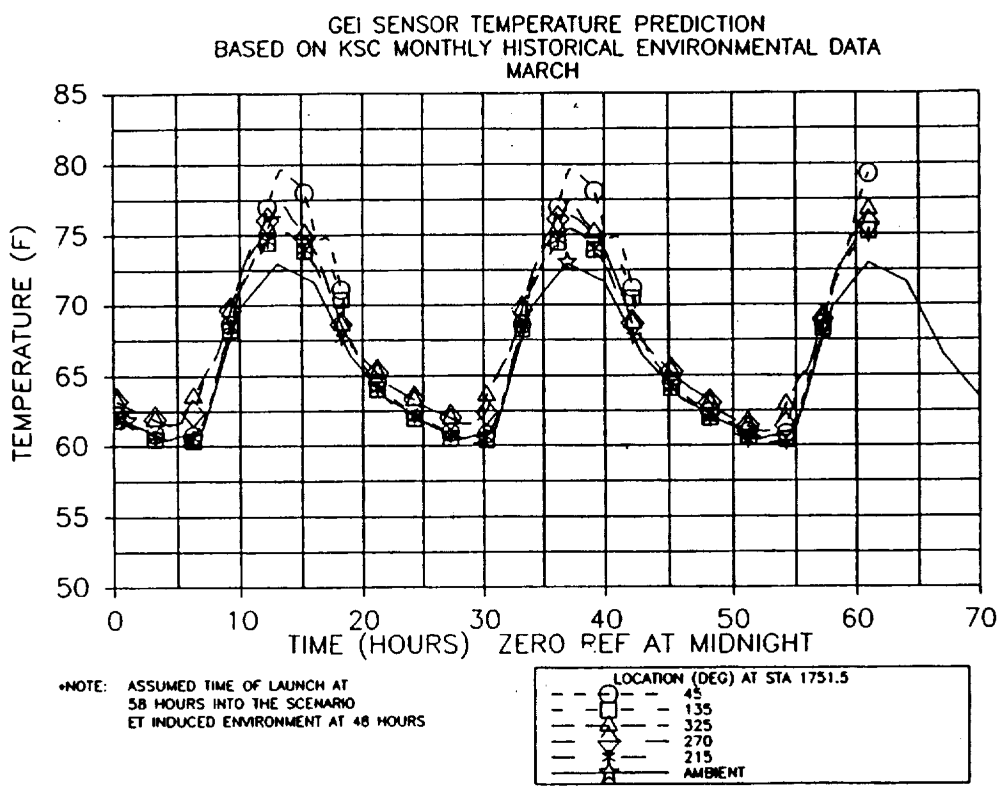

Figure 4.8-56. Temperature Prediction--LH Motor Aft Case Acreage

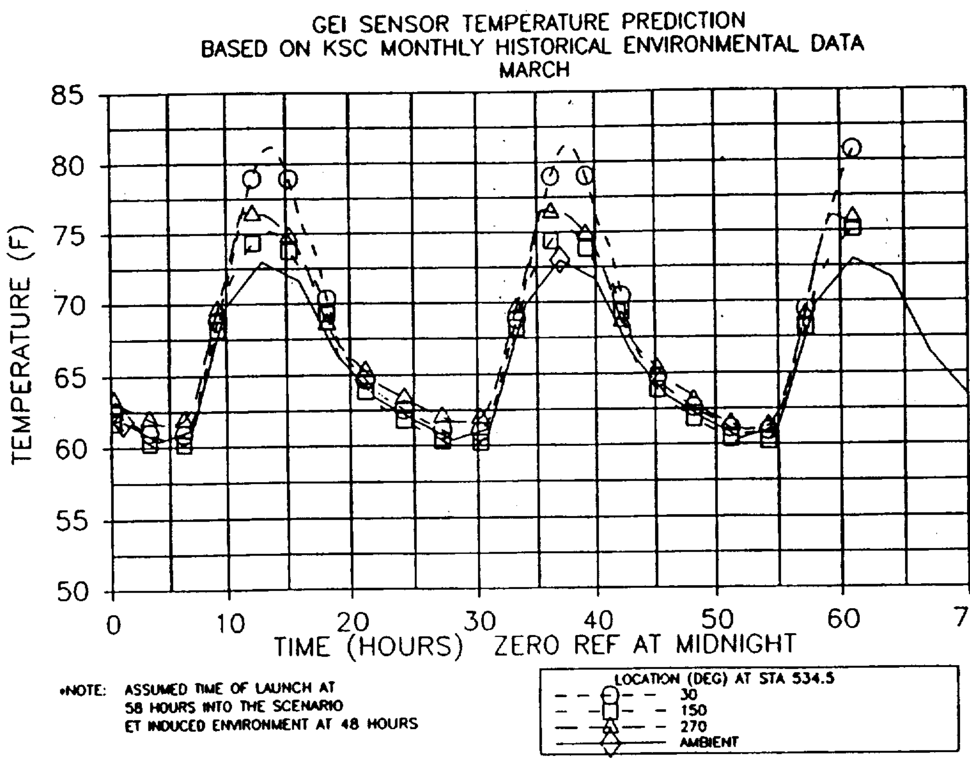

Figure 4.8-57. Temperature Prediction--LH Motor Forward Dome Factory Joint

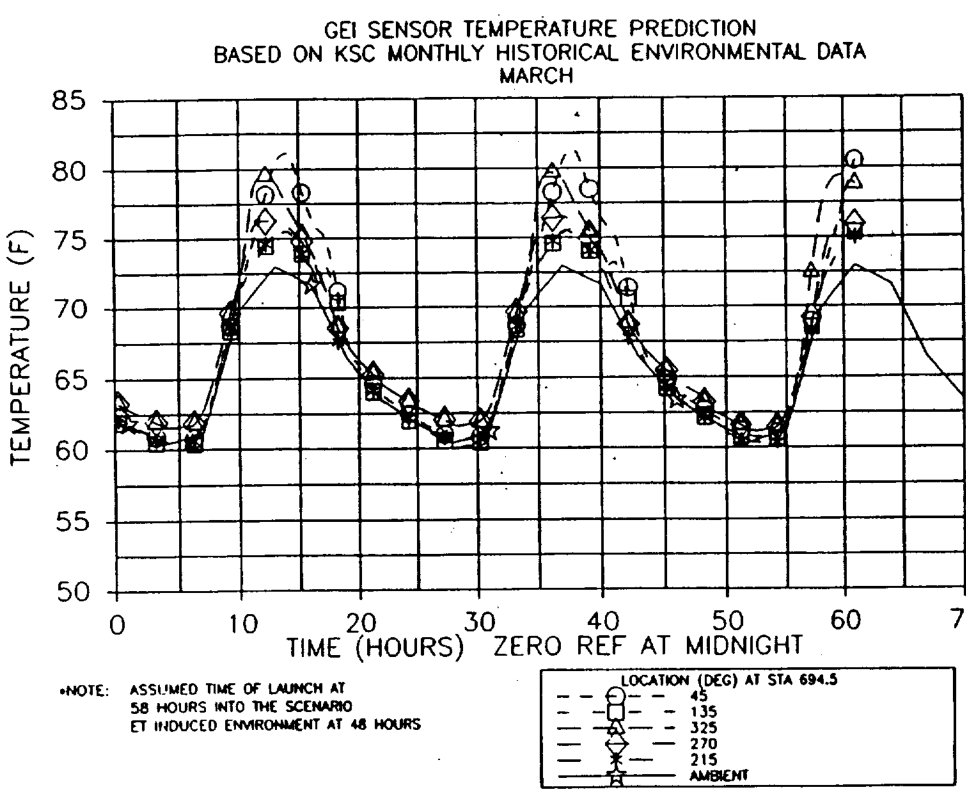

Figure 4.8-58. Temperature Prediction--LH Motor Forward Factory Joint

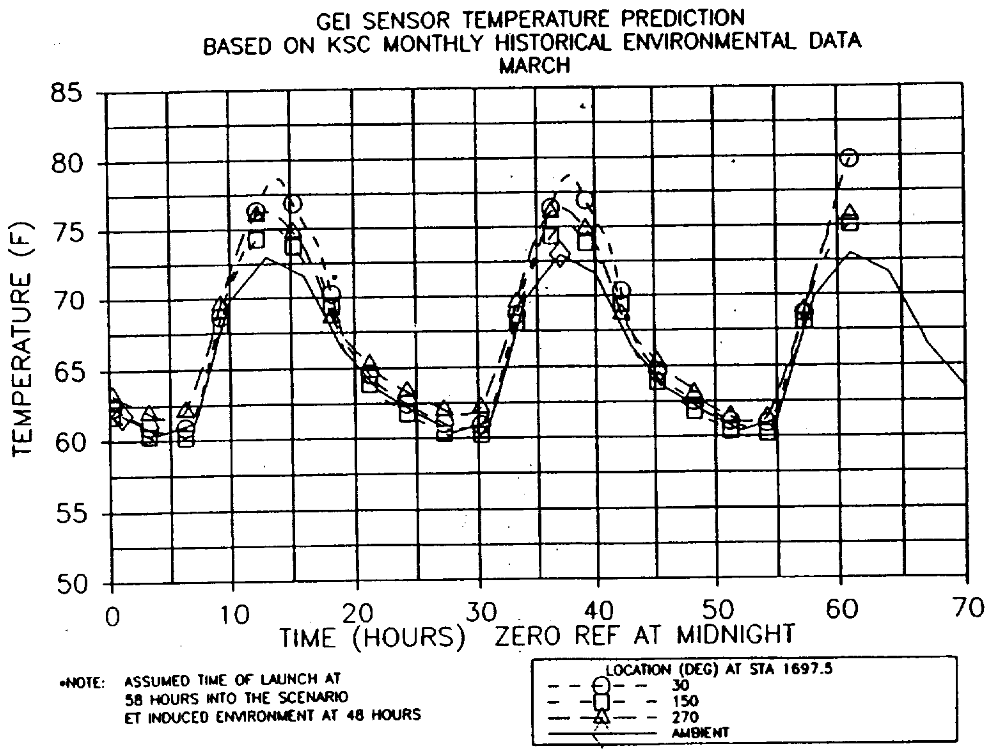

Figure 4.8-59. Temperature Prediction--LH Motor Aft Factory Joint

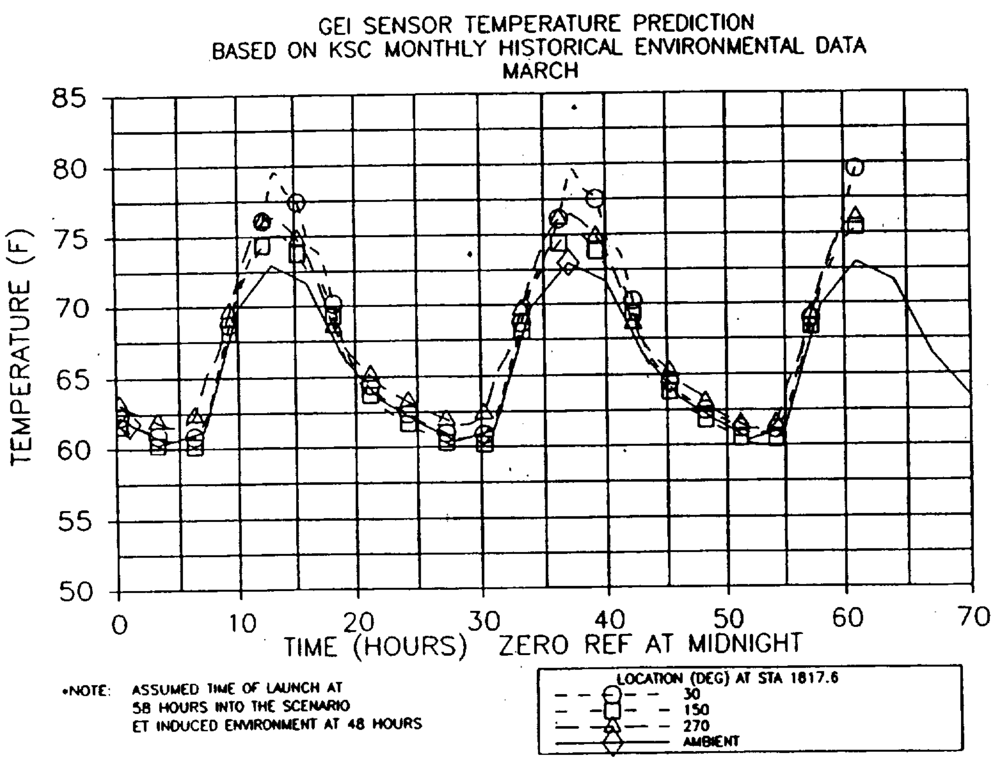

Figure 4.8-60. Temperature Prediction--LH Motor Aft Dome Factory Joint

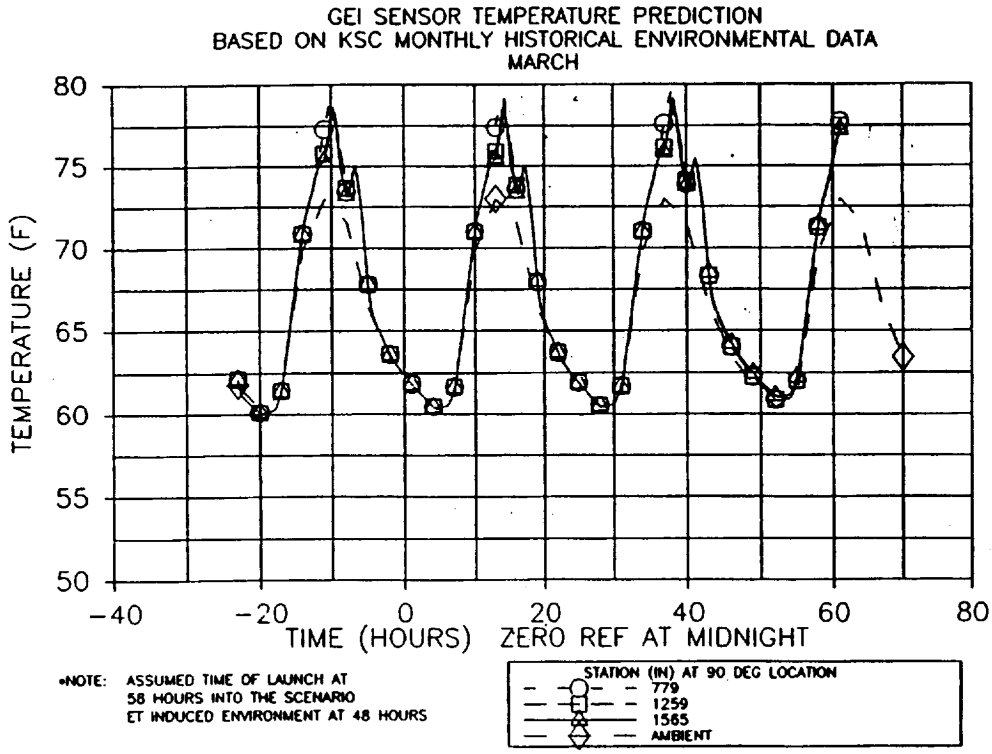

Figure 4.8-61. Temperature Prediction--LH Motor Tunnel Bondline

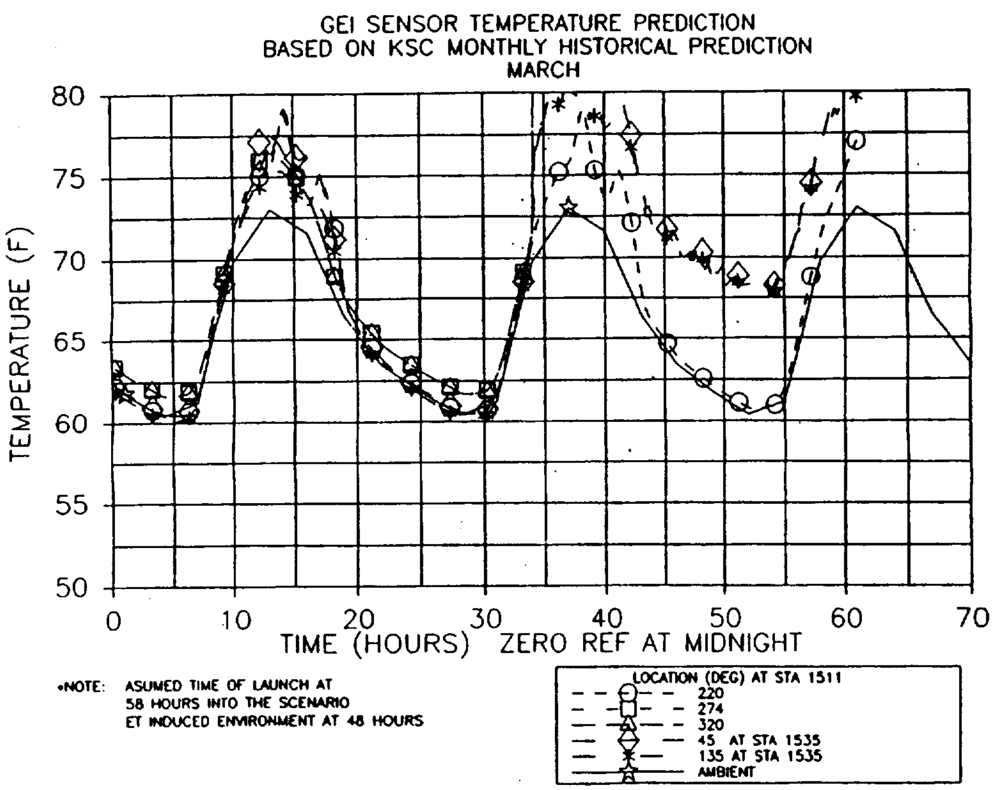

Figure 4.8-62. Temperature Prediction--LH Motor ETA Region

Table 4.8-7. 360L003 Analytical Timeframes for Estimating Event Sequencing of March Historical Joint Heater and GEI Sensor Predictions

Time (hr)	Countdown Events in Analysis
0	Midnight KSC EDT (11 Mar 1989)
34	Joint heater operation begins on 12 Mar 1989 (L - 24 hr)
42	Aft skirt conditioning operation begins on 12 Mar 1989 (T - 12 hr plus 4 hr for holds)
48	Induced environments due to ET refrigeration effect begins early on 13 Mar 1989 (T - 6 hr plus 4 hr for holds)
51	Igniter heater shutoff/start cooldown (T - 4 hr plus 3 hr for holds)
58	Assumed time of launch (13 Mar 1989)
61	Up to an early afternoon launch on 13 Mar 1989 (allowing for some delay)

Note: Figures 4.8-33 through 4.8-62 consist of a 2-day plus 13-hr scenario.

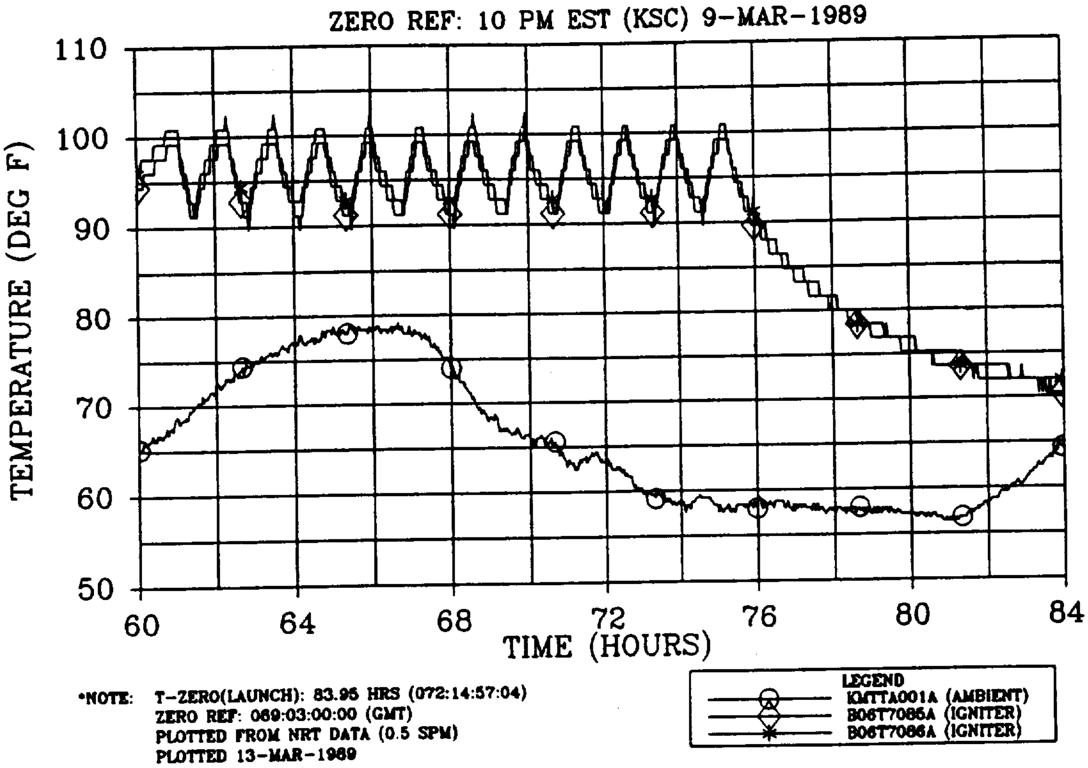

Figure 4.8-63. Prelaunch LH Igniter Joint Temperature (overlaid with ambient)

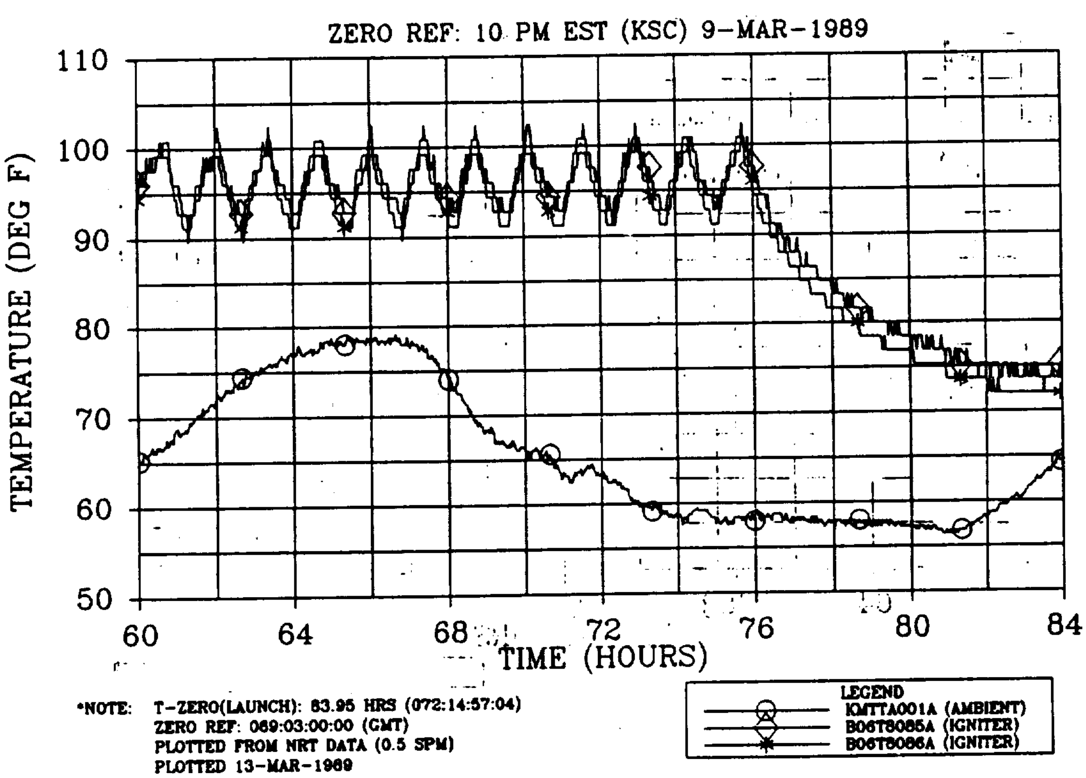

Figure 4.8-64. Prelaunch RH Igniter Joint Temperature (overlaid with ambient)

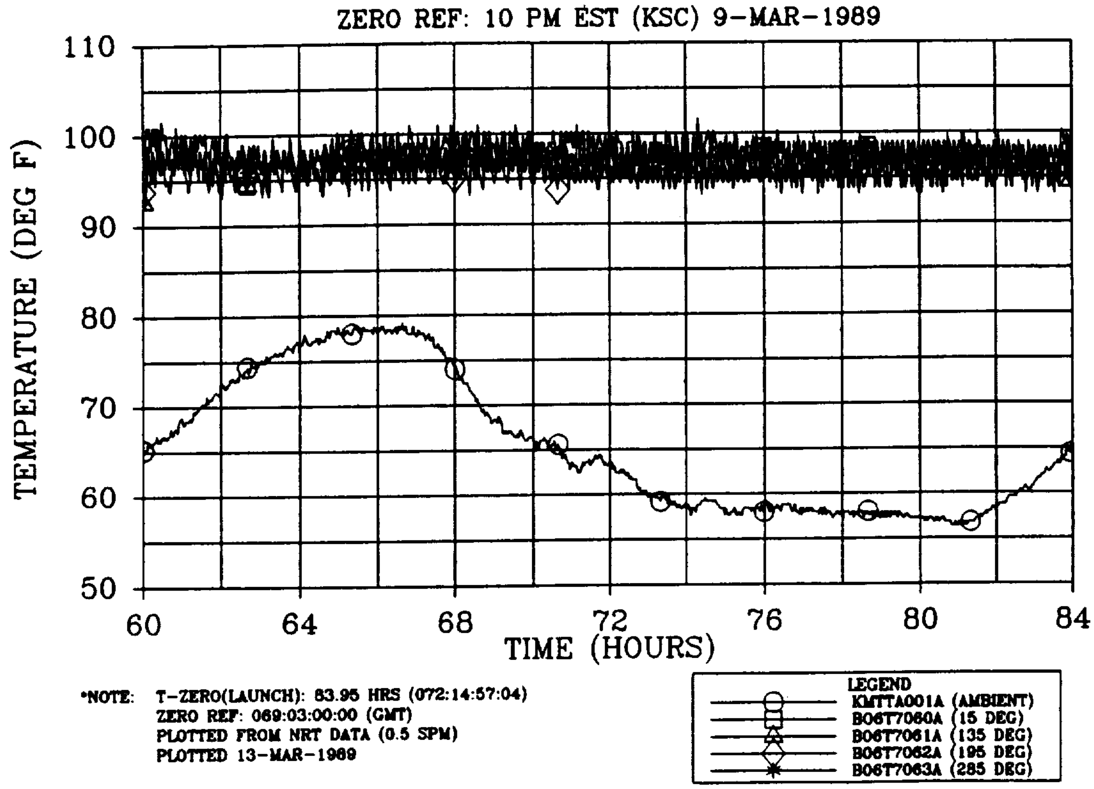

*NOTE: T-ZERO(LAUNCH): 83.95 HRS (072:14:57:04)
ZERO REF: 069:03:00:00 (GMT)
PLOTTED FROM NRT DATA (0.5 SPM)
PLOTTED 13-MAR-1989

Figure 4.8-65. Prelaunch LH Forward Field Joint Temperature (overlaid with ambient)

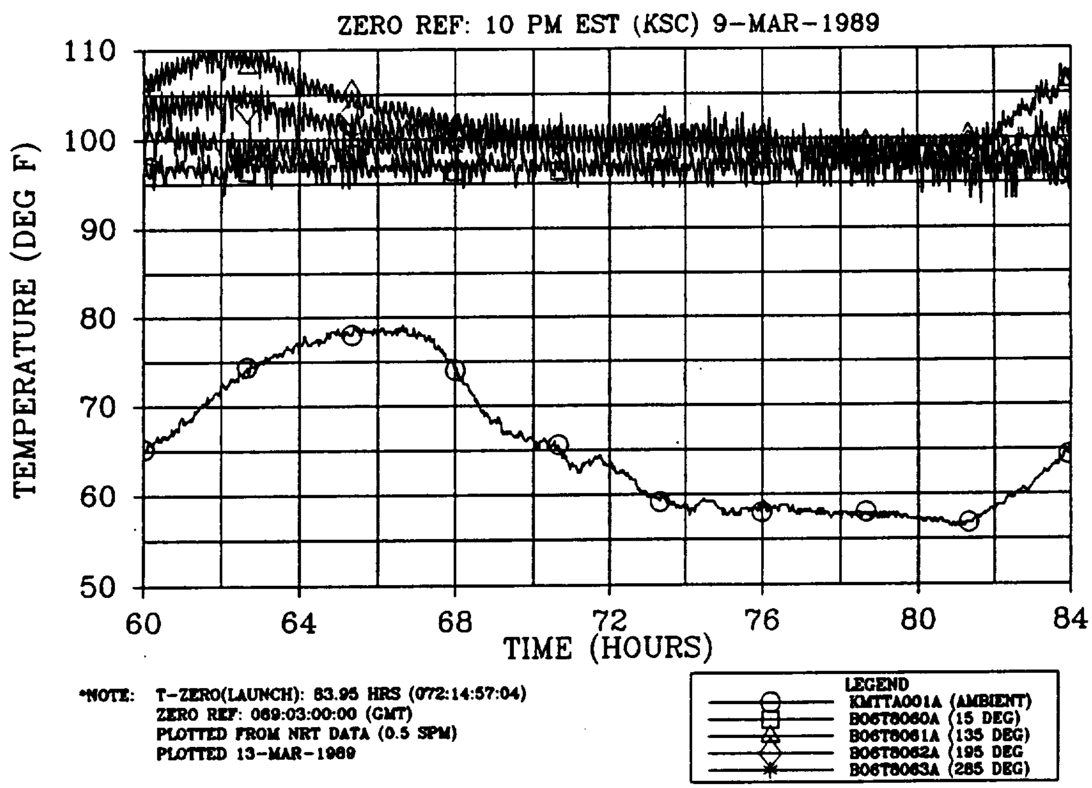

*NOTE: T-ZERO(LAUNCH): 83.95 HRS (072:14:57:04)
ZERO REF: 069:03:00:00 (GMT)
PLOTTED FROM NRT DATA (0.5 SPM)
PLOTTED 13-MAR-1989

Figure 4.8-66. Prelaunch RH Forward Field Joint Temperature (overlaid with ambient)

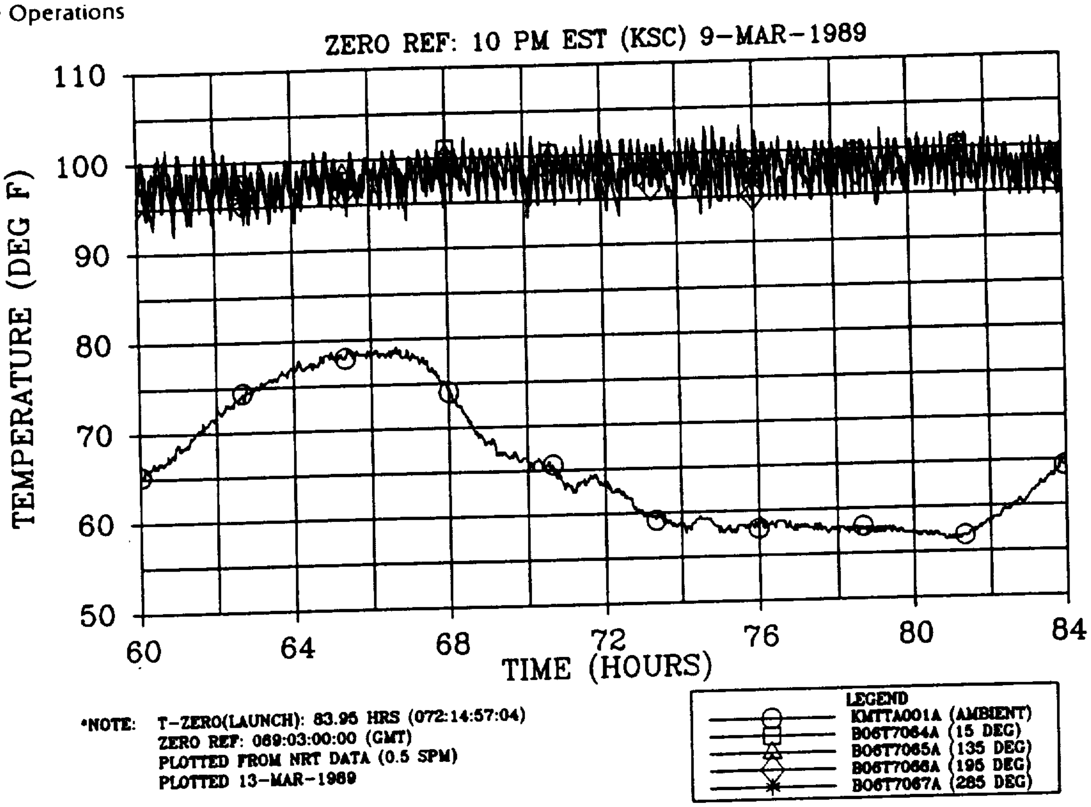

Figure 4.8-67. Prelaunch LH Center Field Joint Temperature (overlaid with ambient)

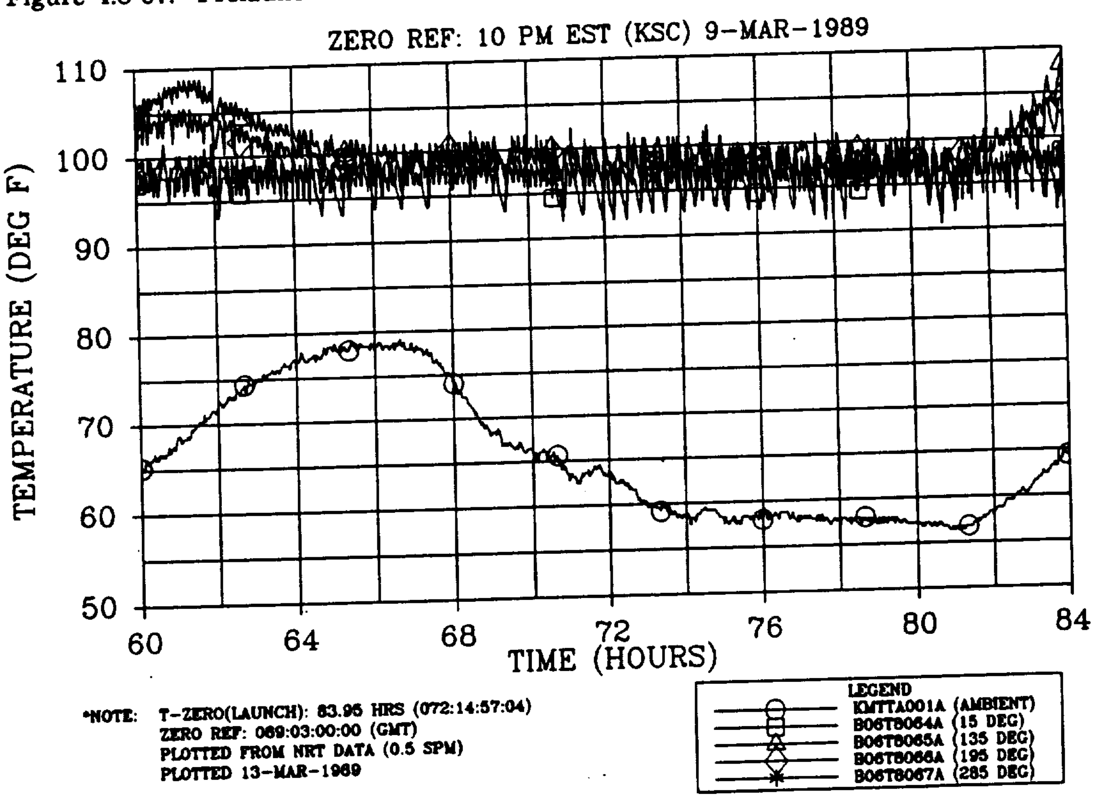

Figure 4.8-68. Prelaunch RH Center Field Joint Temperature (overlaid with ambient)

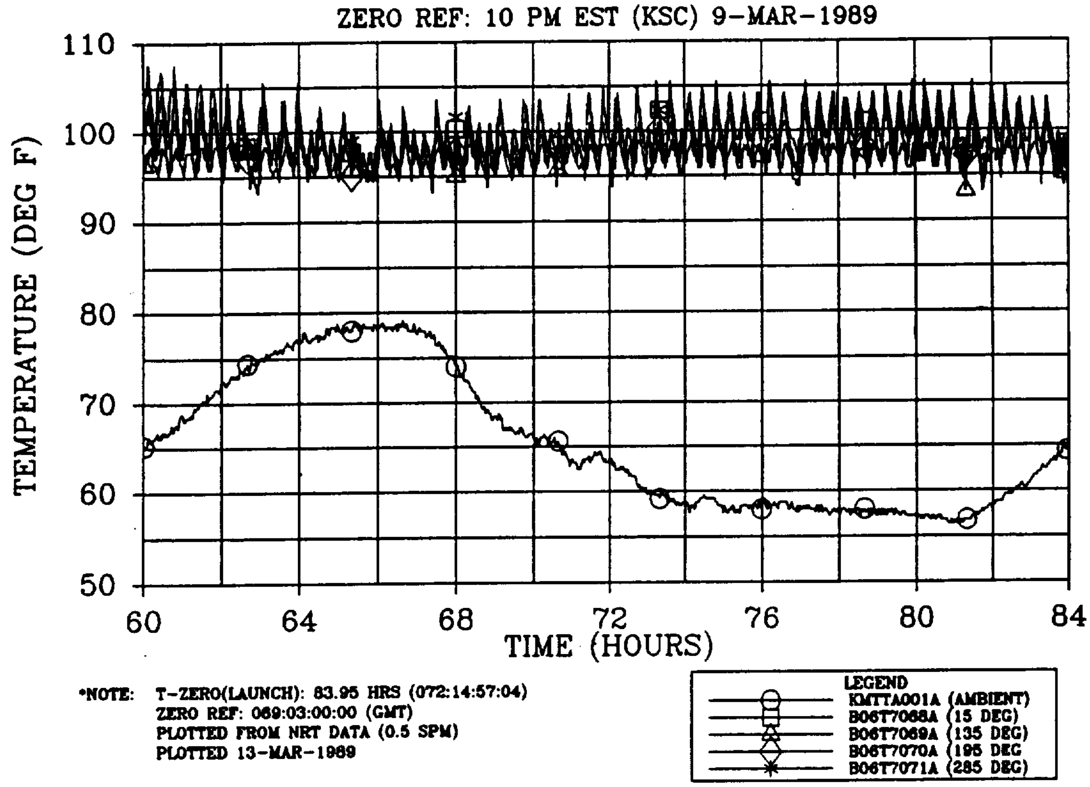

Figure 4.8-69. Prelaunch LH Aft Field Joint Temperature (overlaid with ambient)

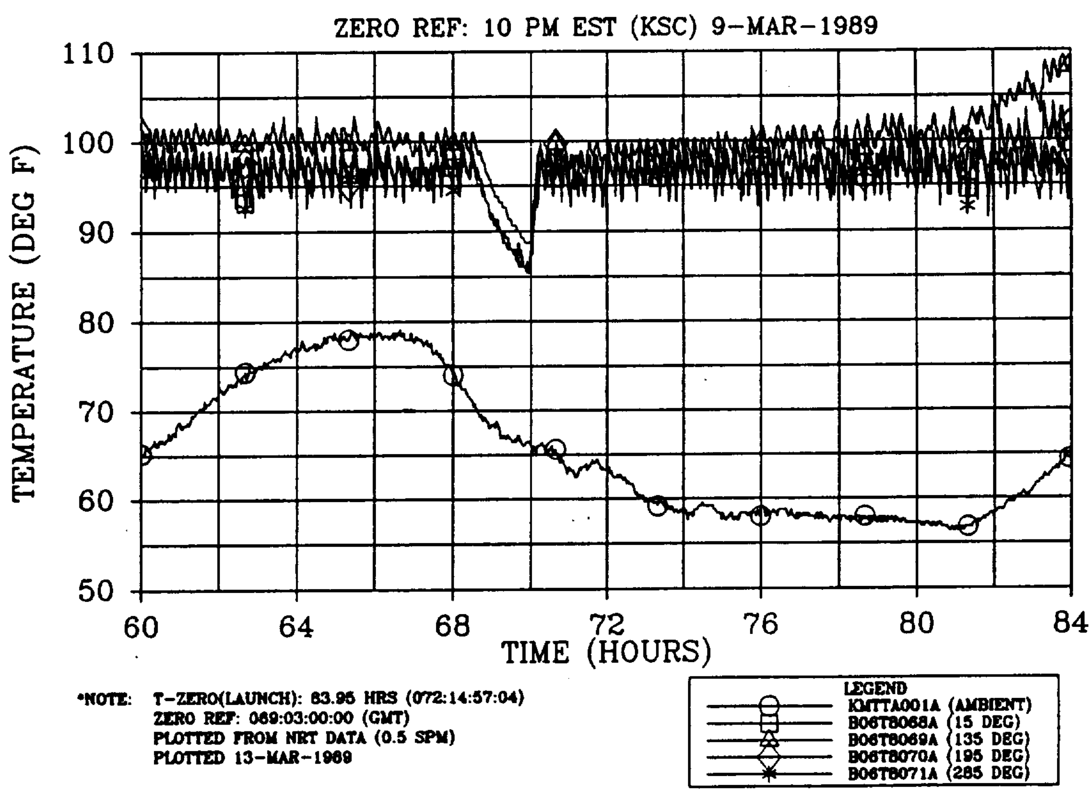

Figure 4.8-70. Prelaunch RH Aft Field Joint Temperature (overlaid with ambient)

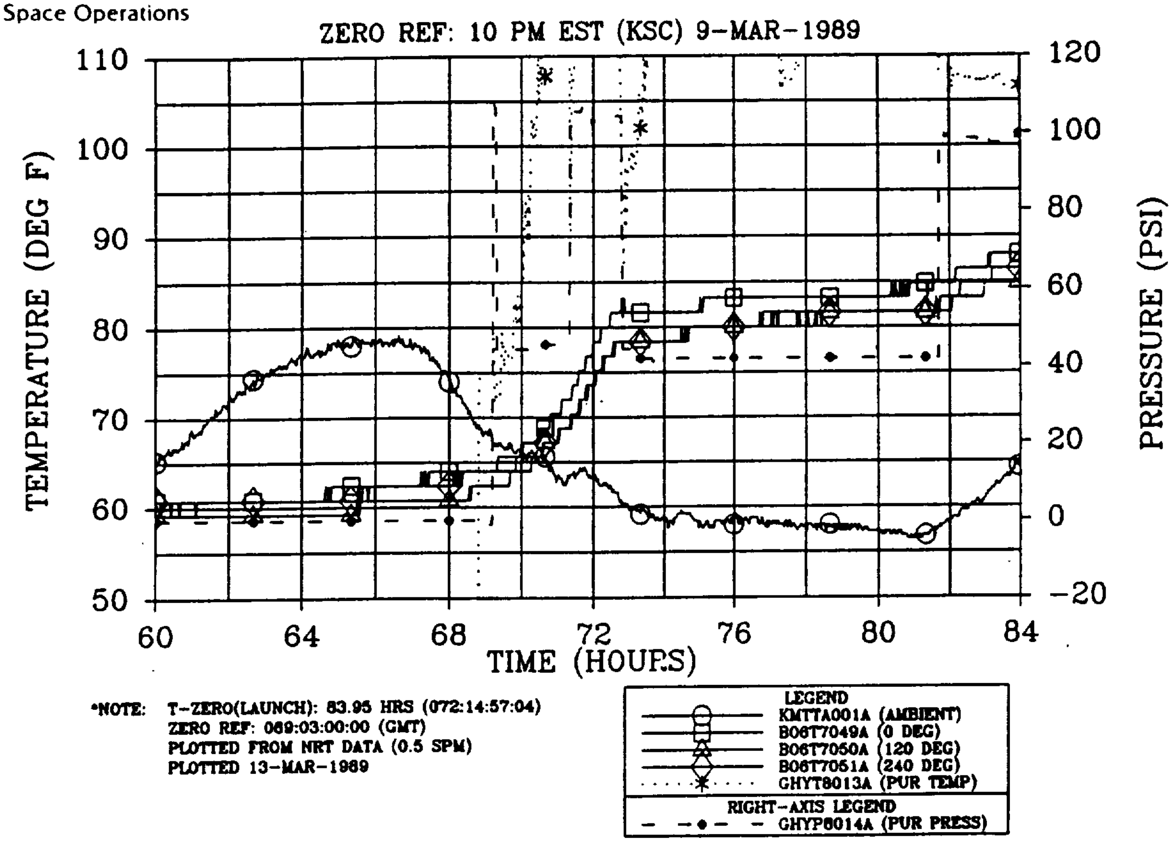

Figure 4.8-71. Prelaunch LH Case-to-Nozzle Joint Temperature (overlaid with ambient)

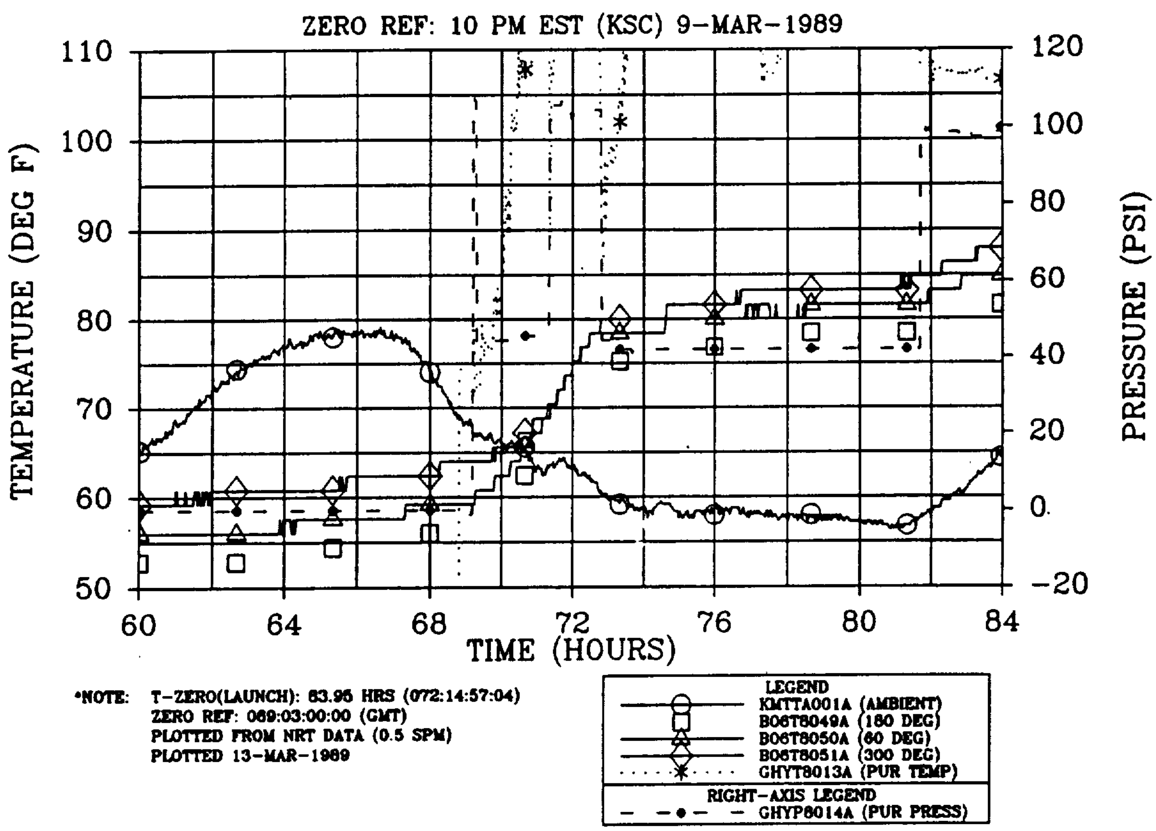

Figure 4.8-72. Prelaunch RH Case-to-Nozzle Joint Temperature (overlaid with ambient)

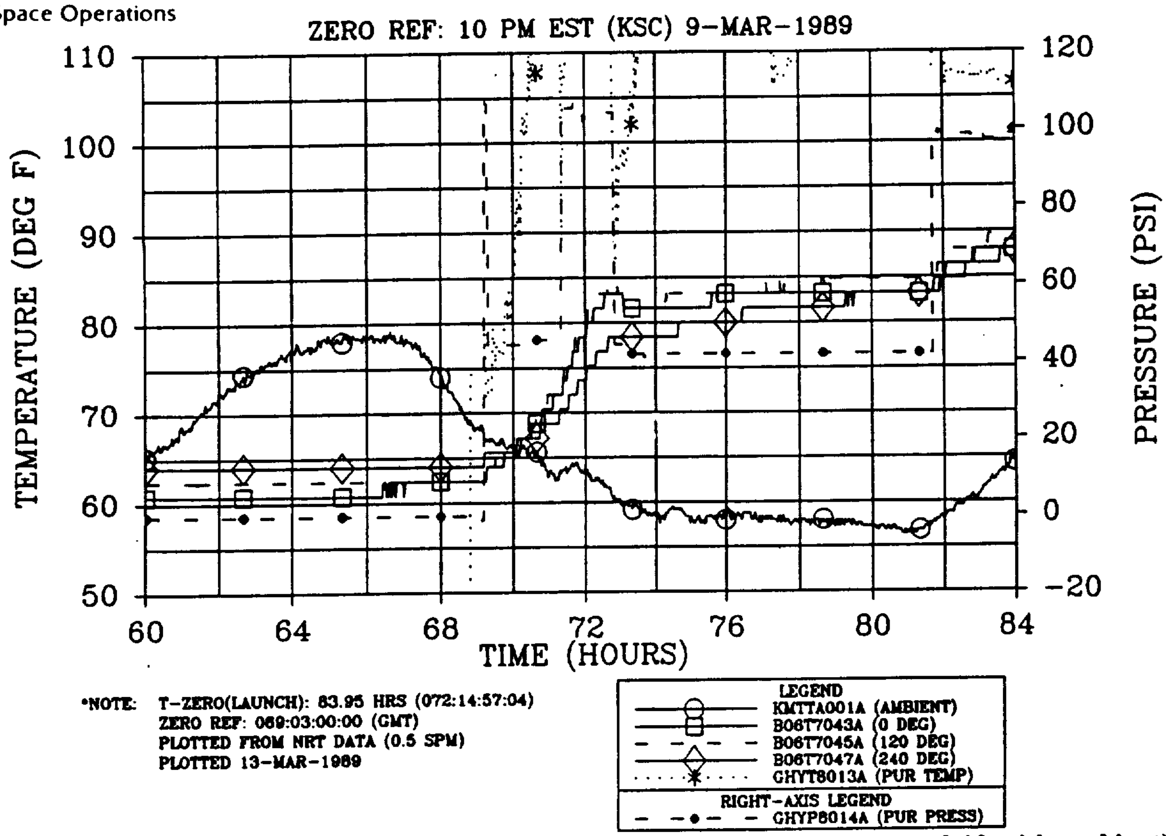

Figure 4.8-73. Prelaunch LH Flex Bearing Aft End Ring Temperature (overlaid with ambient)

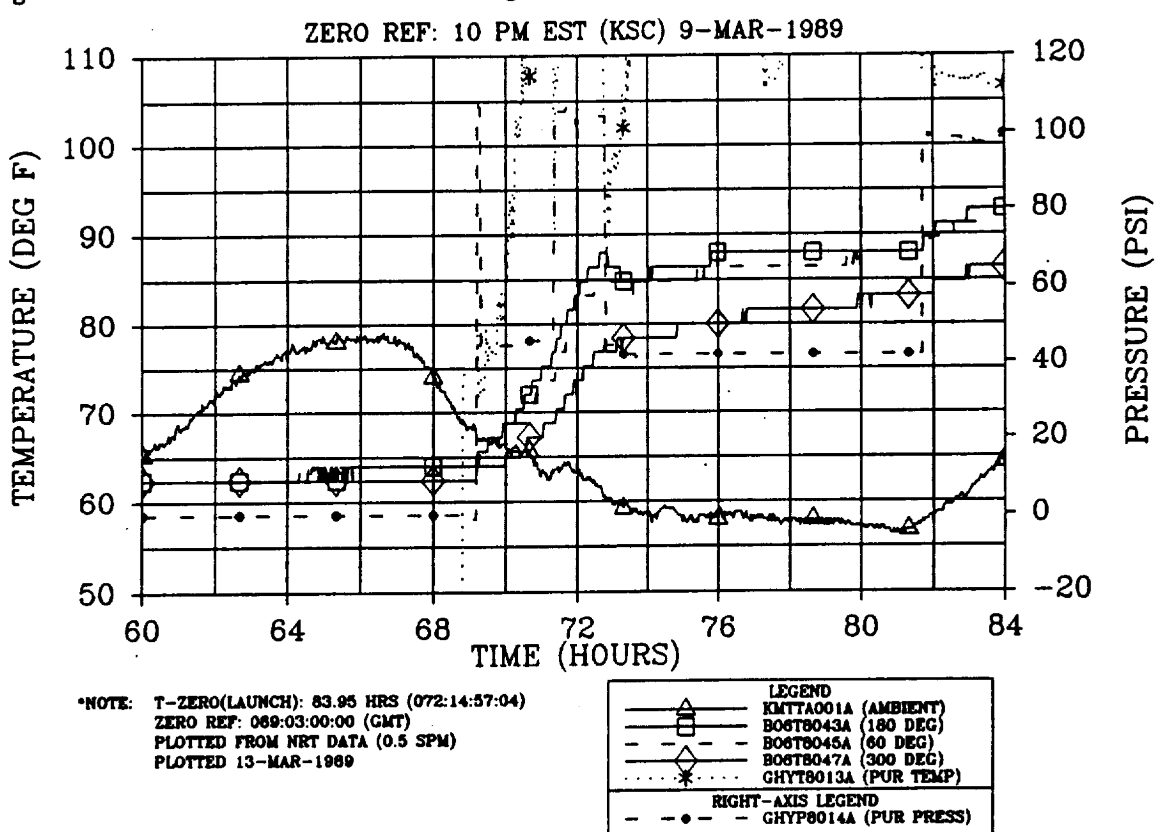

Figure 4.8-74. Prelaunch RH Flex Bearing Aft End Ring Temperature (overlaid with ambient)

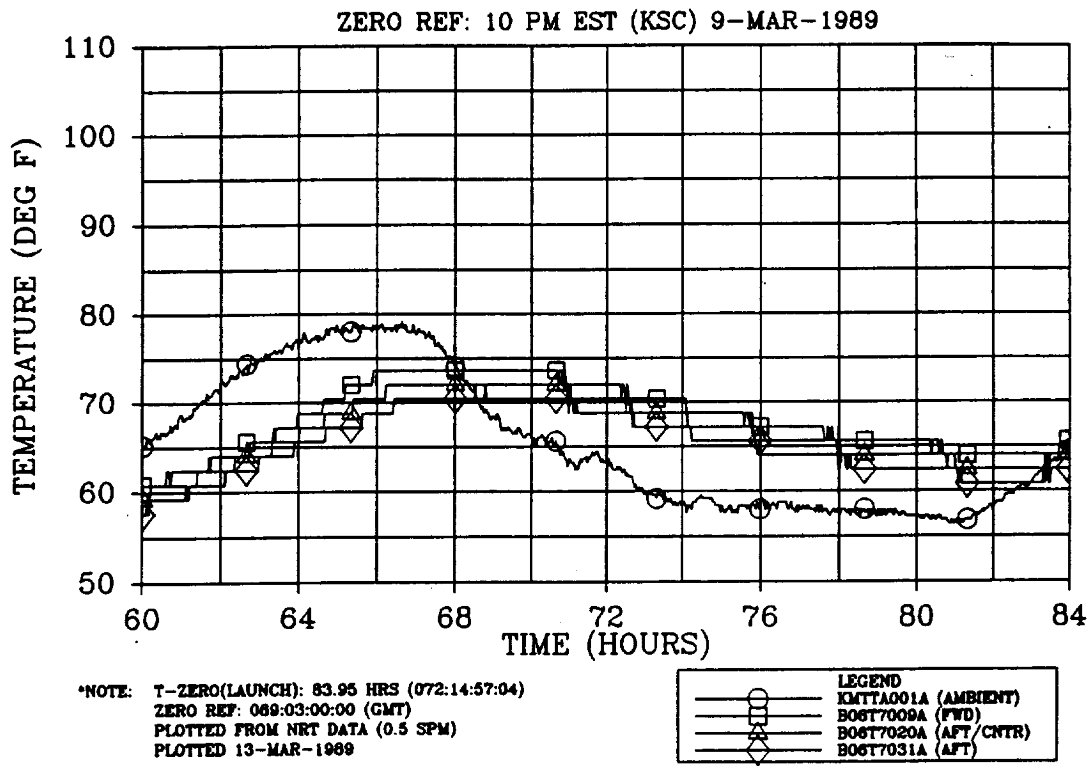

Figure 4.8-75. Prelaunch LH Tunnel Bondline Temperature (overlaid with ambient)

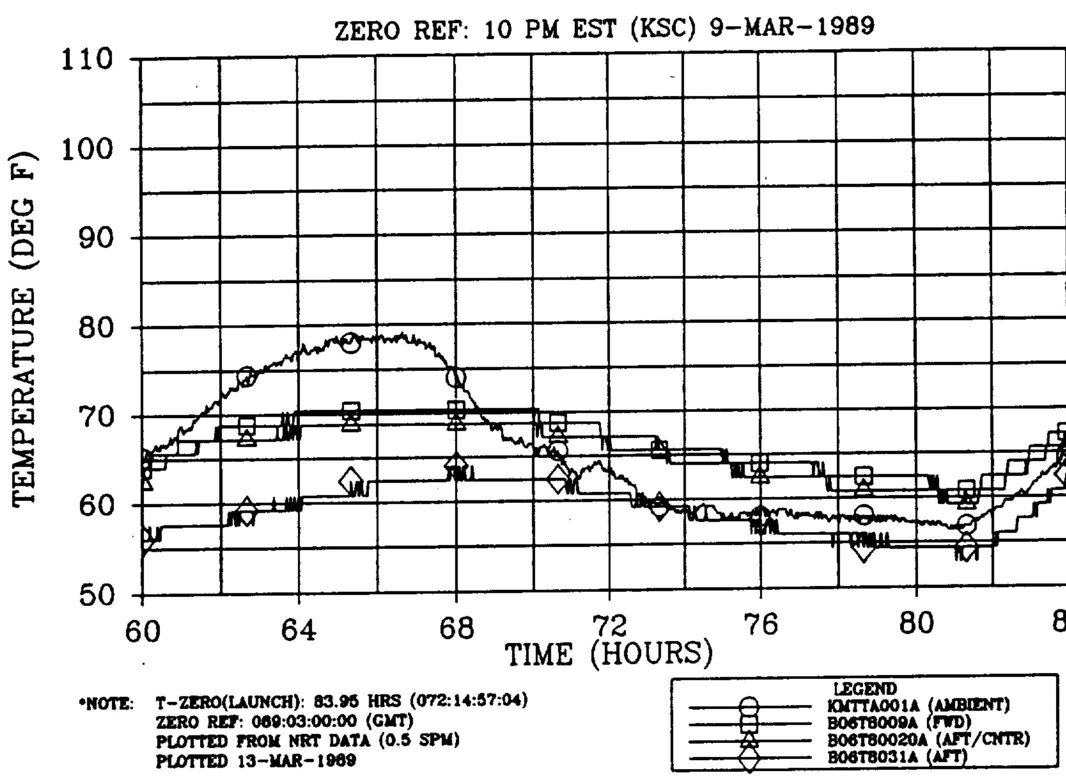

Figure 4.8-76. Prelaunch RH Tunnel Bondline Temperature (overlaid with ambient)

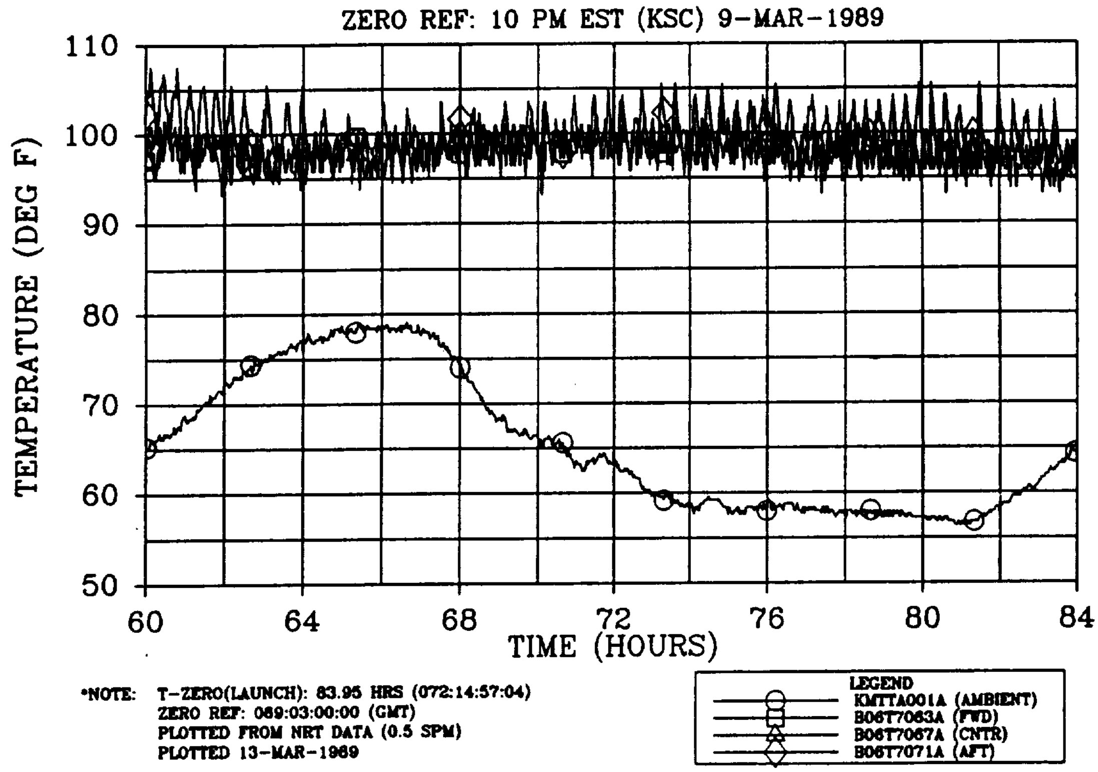

Figure 4.8-77. Prelaunch LH Field Joint Temperature at 285 Deg (overlaid with ambient)

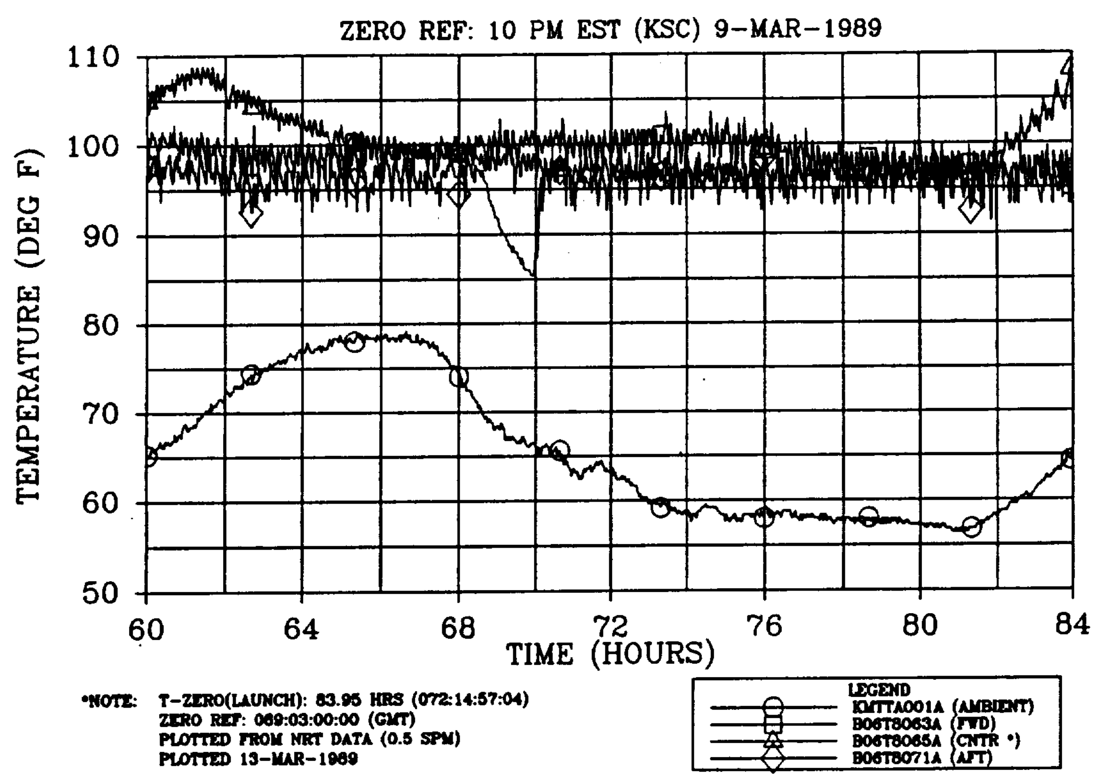

Figure 4.8-78. Prelaunch RH Field Joint Temperature at 285 Deg (overlaid with ambient)

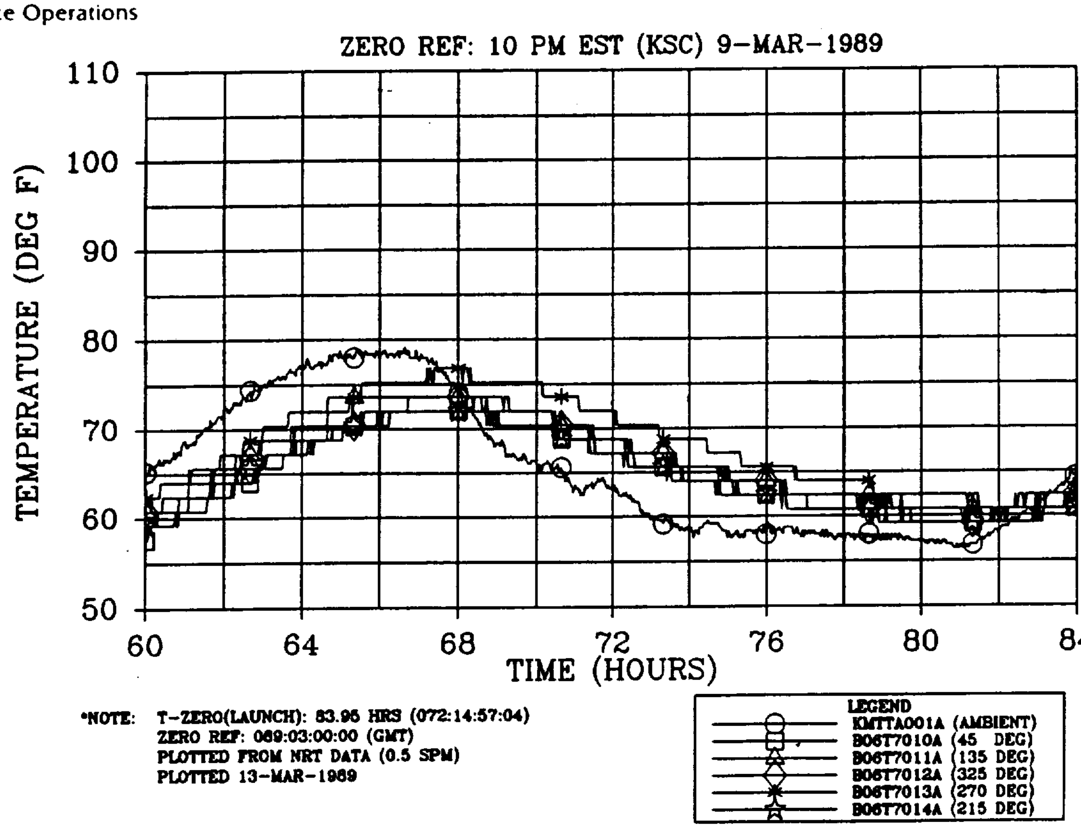

Figure 4.8-79. Prelaunch LH Case Acreage Temperature at Station 931.5 (overlaid with ambient)

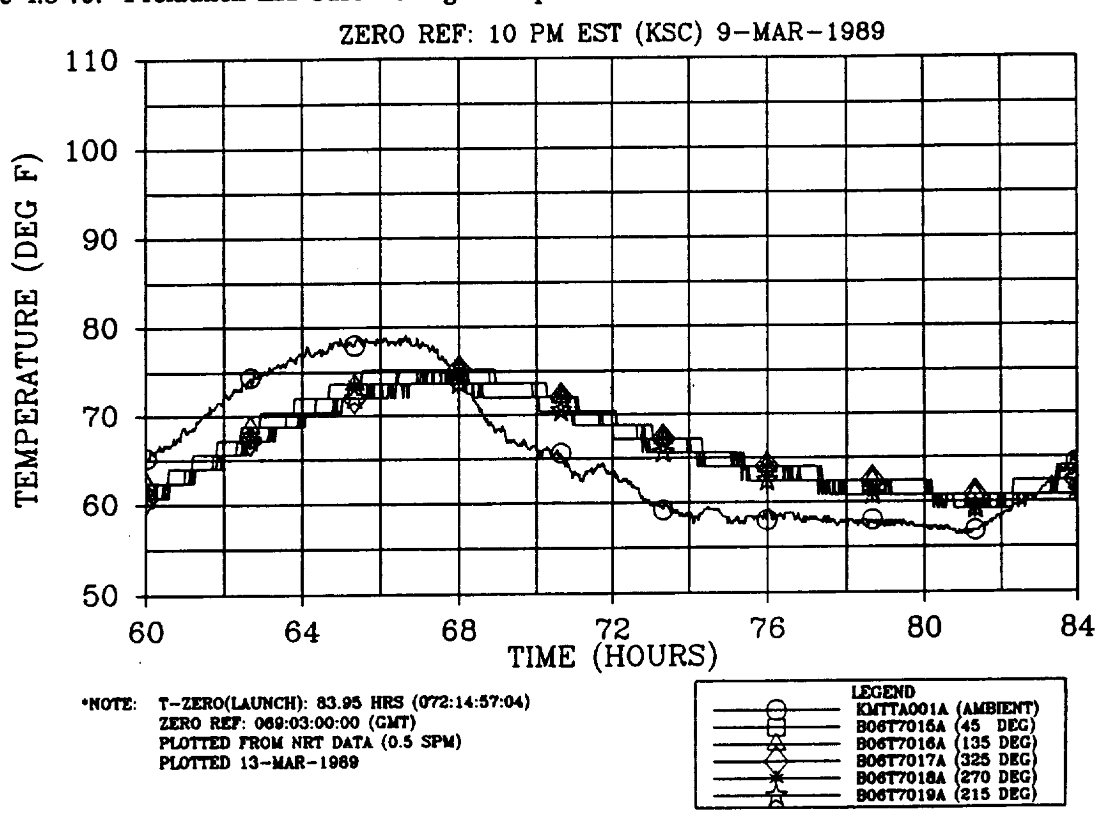

Figure 4.8-80. Prelaunch LH Case Acreage Temperature at Station 1091.5 (overlaid with ambient)

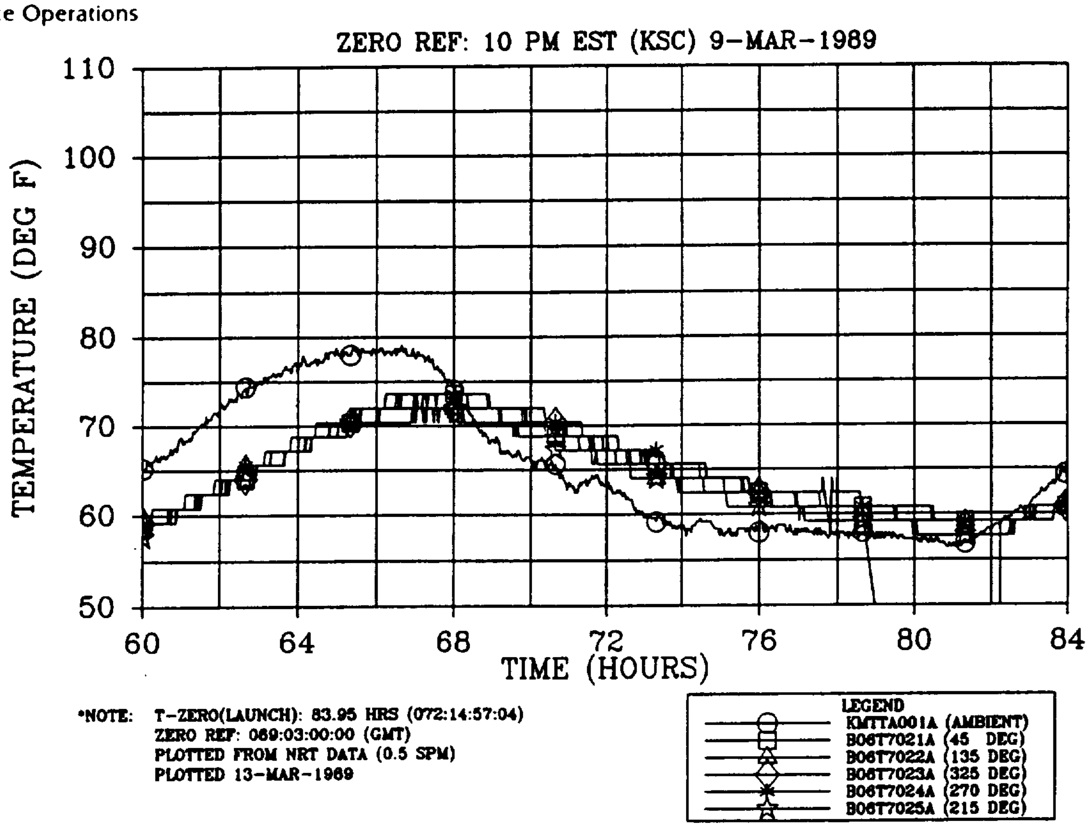

Figure 4.8-81. Prelaunch LH Case Acreage Temperature at Station 1411.5 (overlaid with ambient)

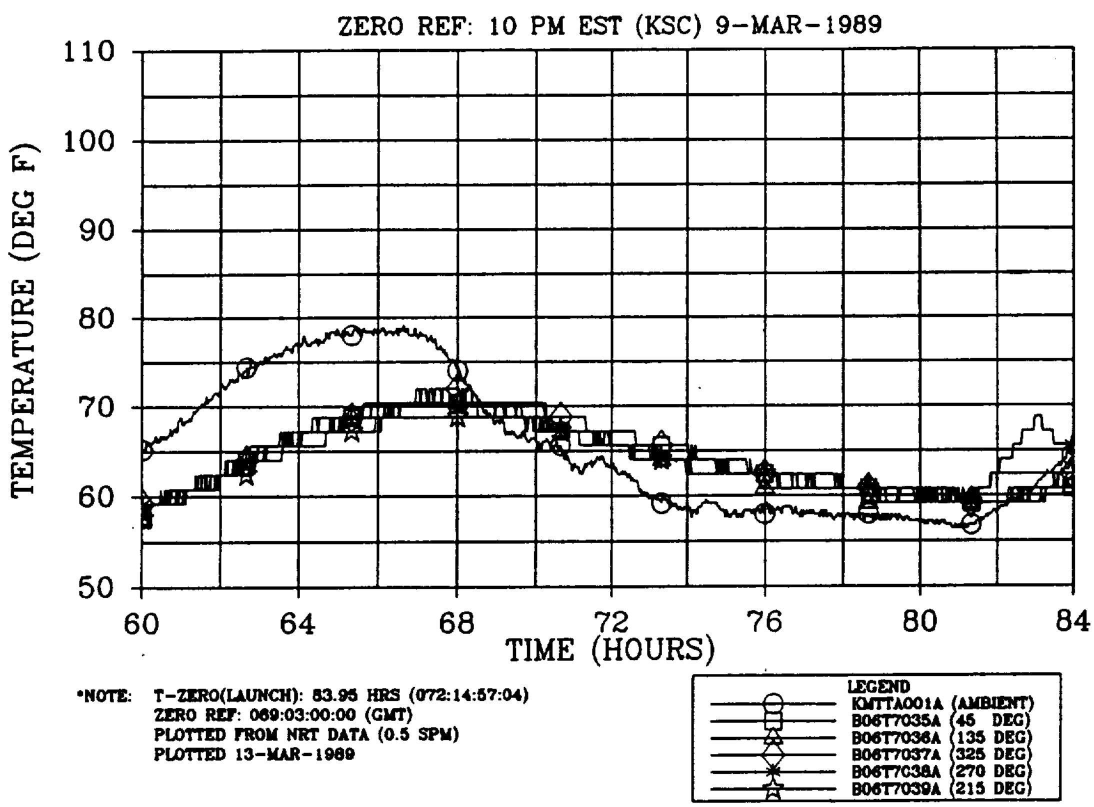

Figure 4.8-82. Prelaunch LH Case Acreage Temperature at Station 1751.5 (overlaid with ambient)

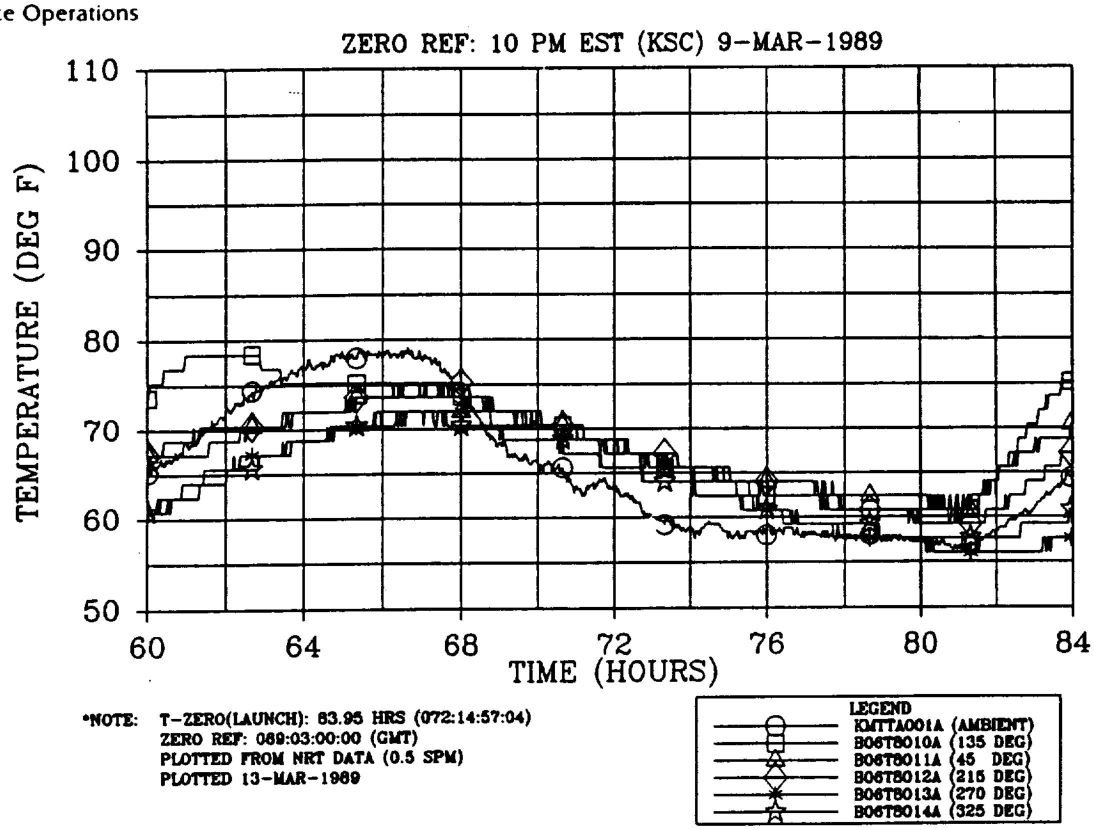

Figure 4.8-83. Prelaunch RH Case Acreage Temperature at Station 931.5 (overlaid with ambient)

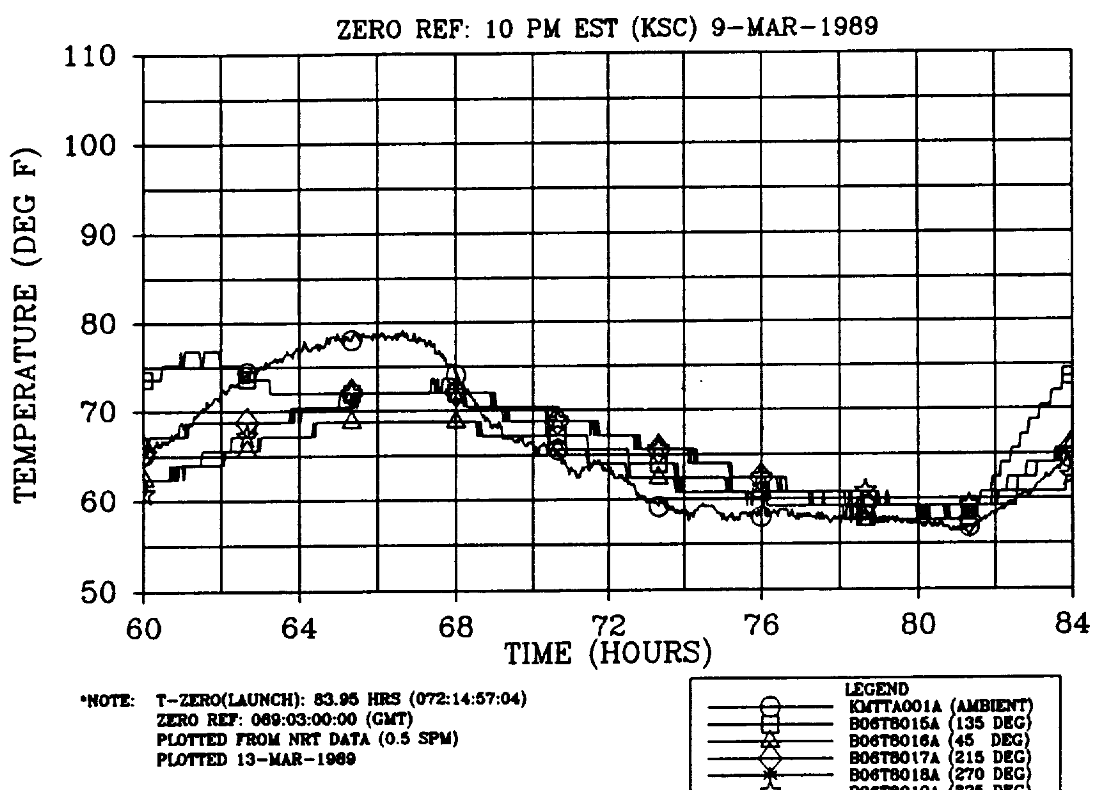

Figure 4.8-84. Prelaunch RH Case Acreage Temperature at Station 1091.5 (overlaid with ambient)

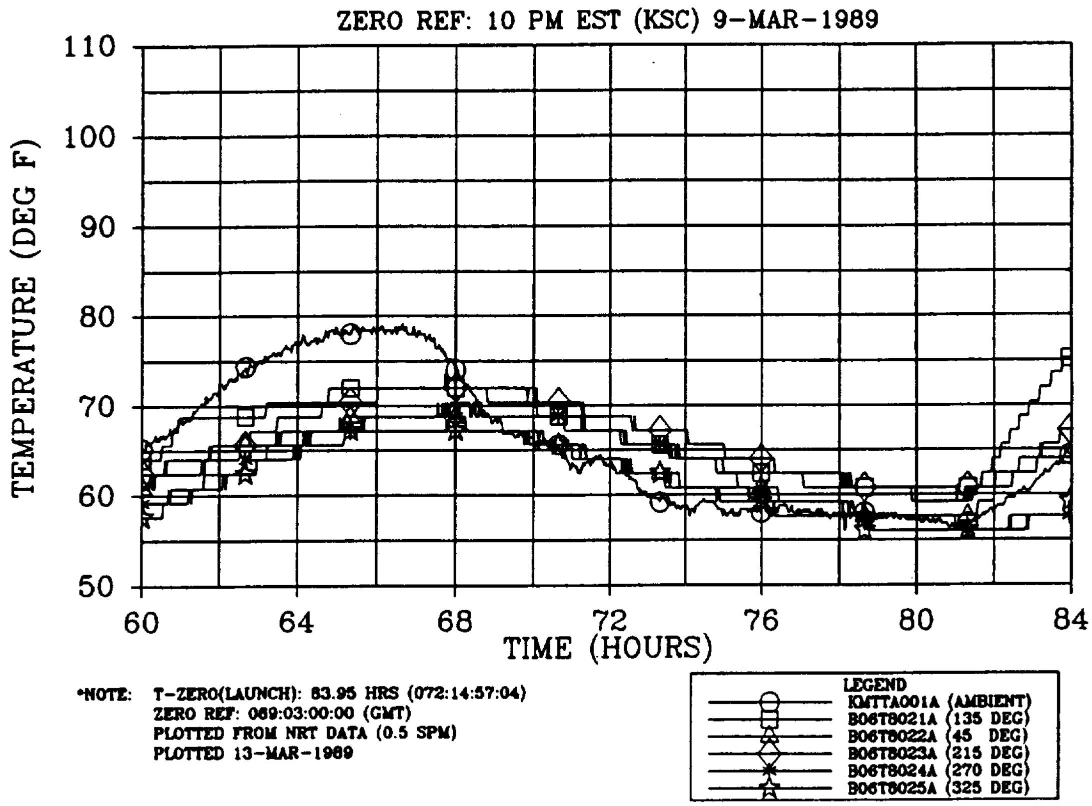

Figure 4.8-85. Prelaunch RH Case Acreage Temperature at Station 1411.5 (overlaid with ambient)

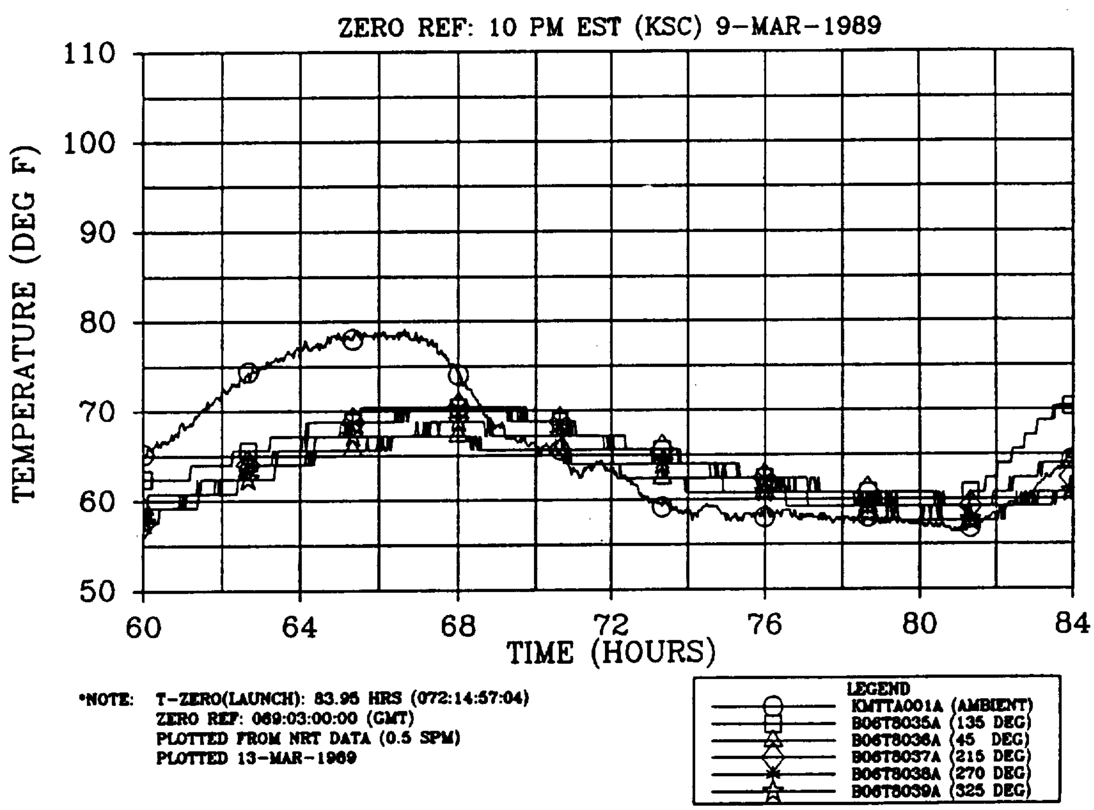

Figure 4.8-86. Prelaunch RH Case Acreage Temperature at Station 1751.5 (overlaid with ambient)

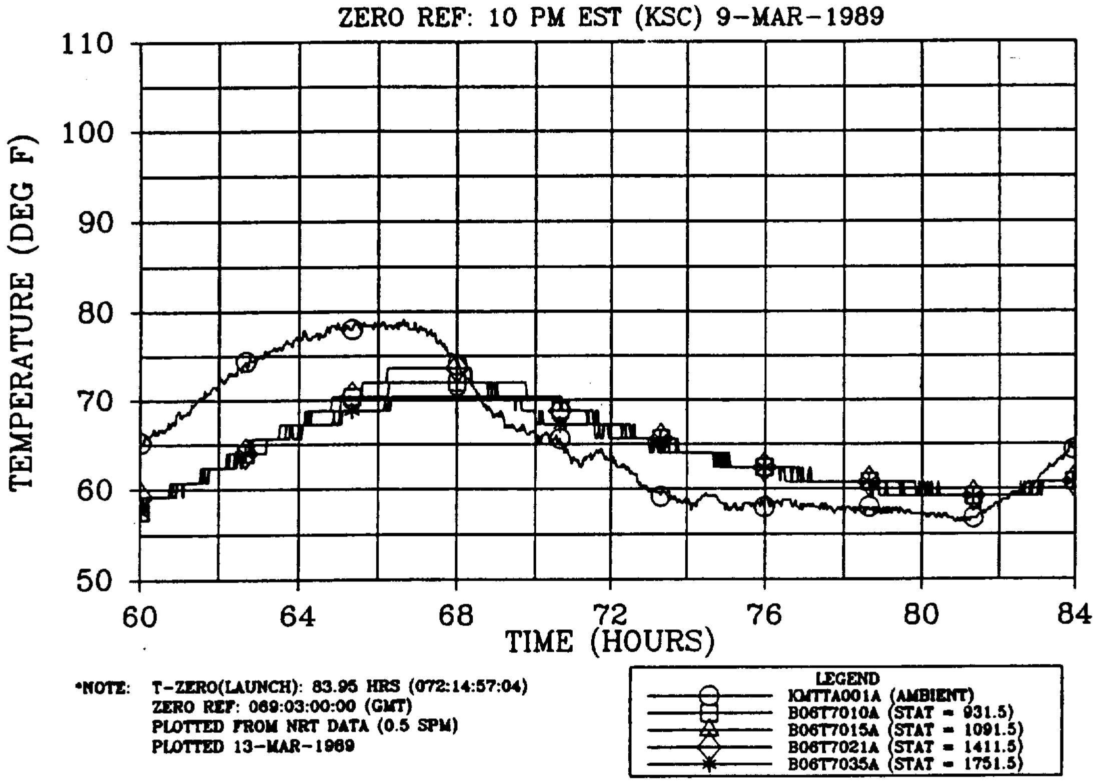

Figure 4.8-87. Prelaunch LH Case Acreage Temperature at 45 Deg (overlaid with ambient)

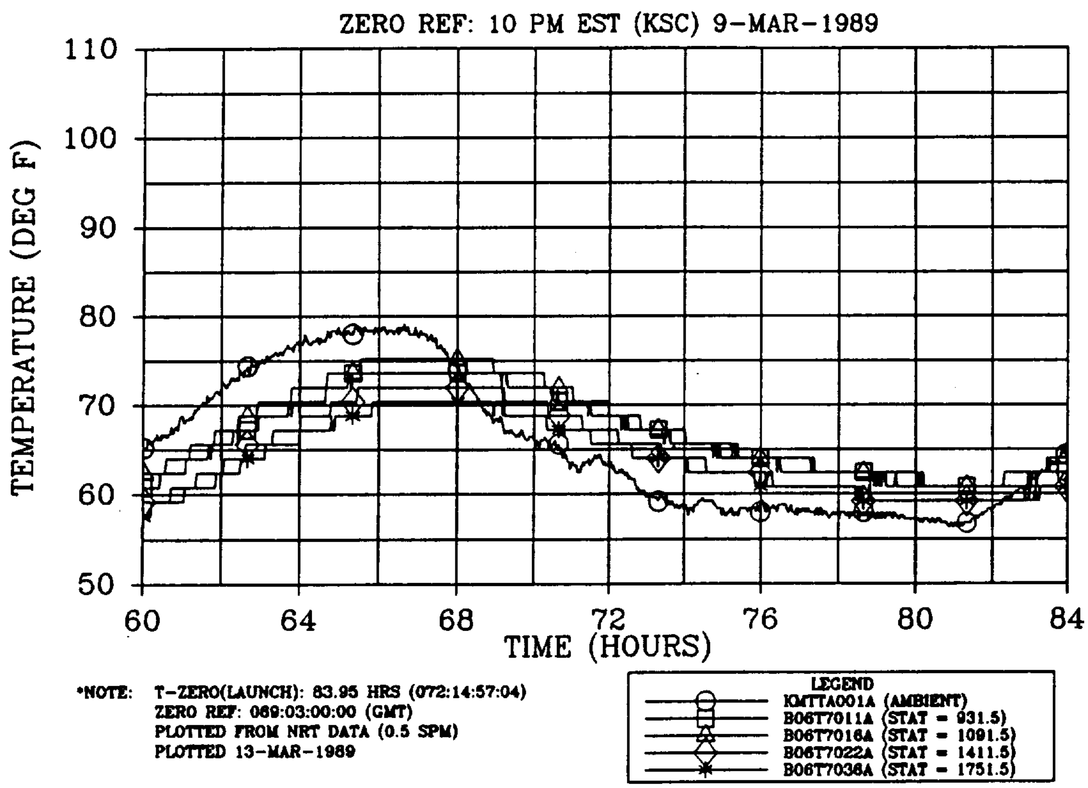

Figure 4.8-88. Prelaunch LH Case Acreage Temperature at 135 Deg (overlaid with ambient)

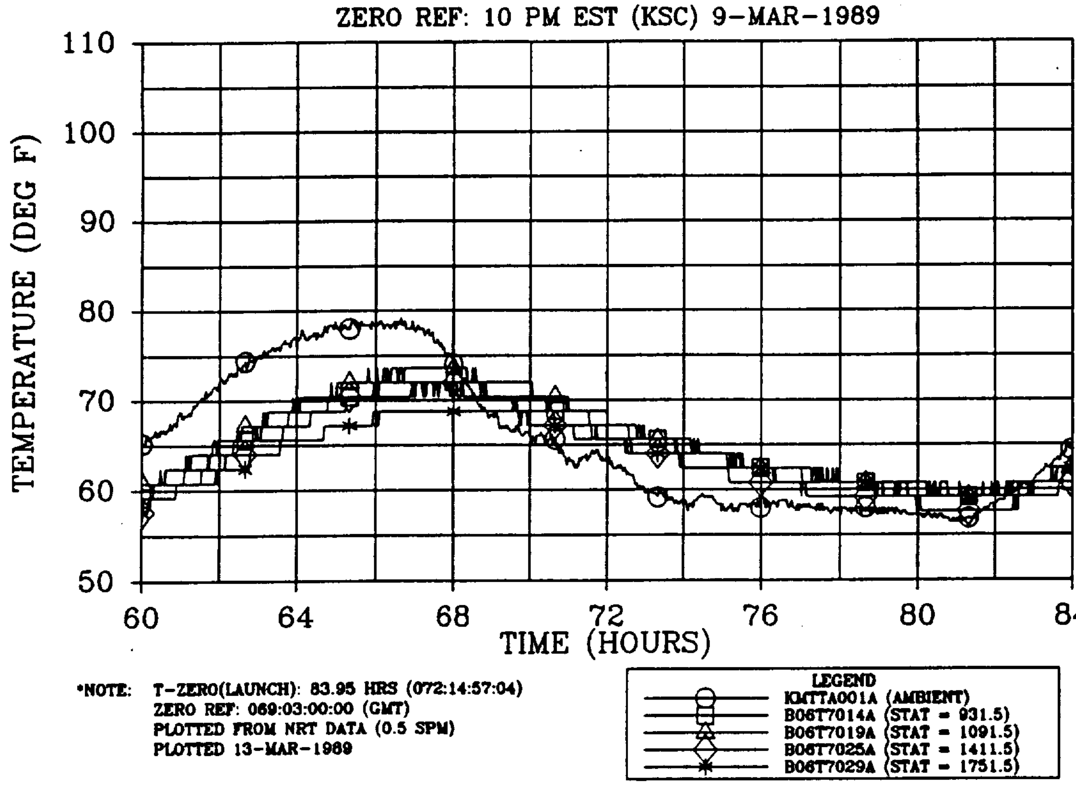

Figure 4.8-89. Prelaunch LH Case Acreage Temperature at 215 Deg (overlaid with ambient)

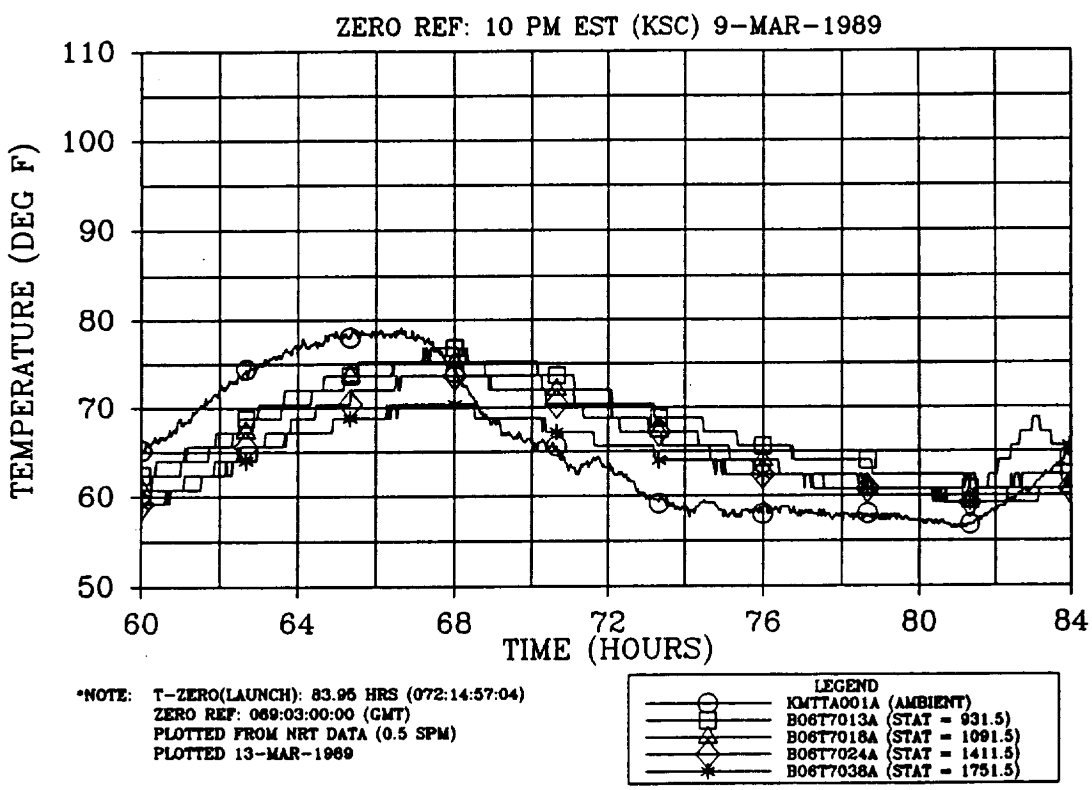

Figure 4.8-90. Prelaunch LH Case Acreage Temperature at 270 Deg (overlaid with ambient)

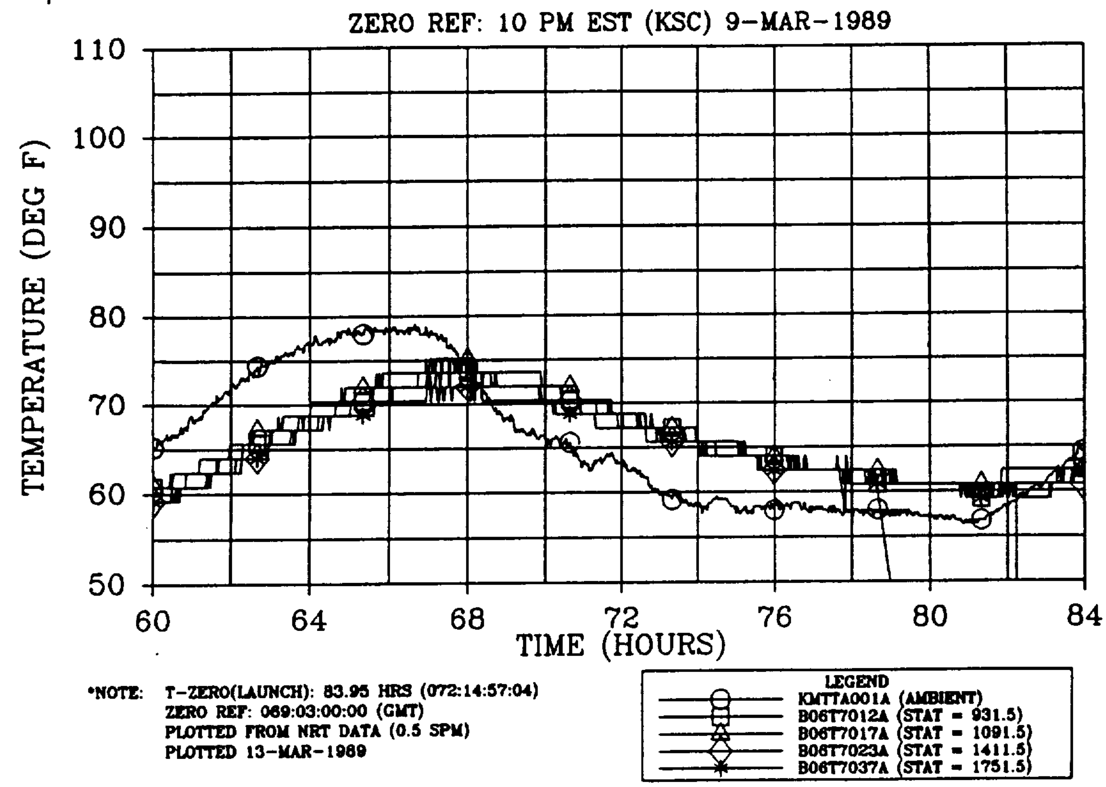

Figure 4.8-91. Prelaunch LH Case Acreage Temperature at 325 Deg (overlaid with ambient)

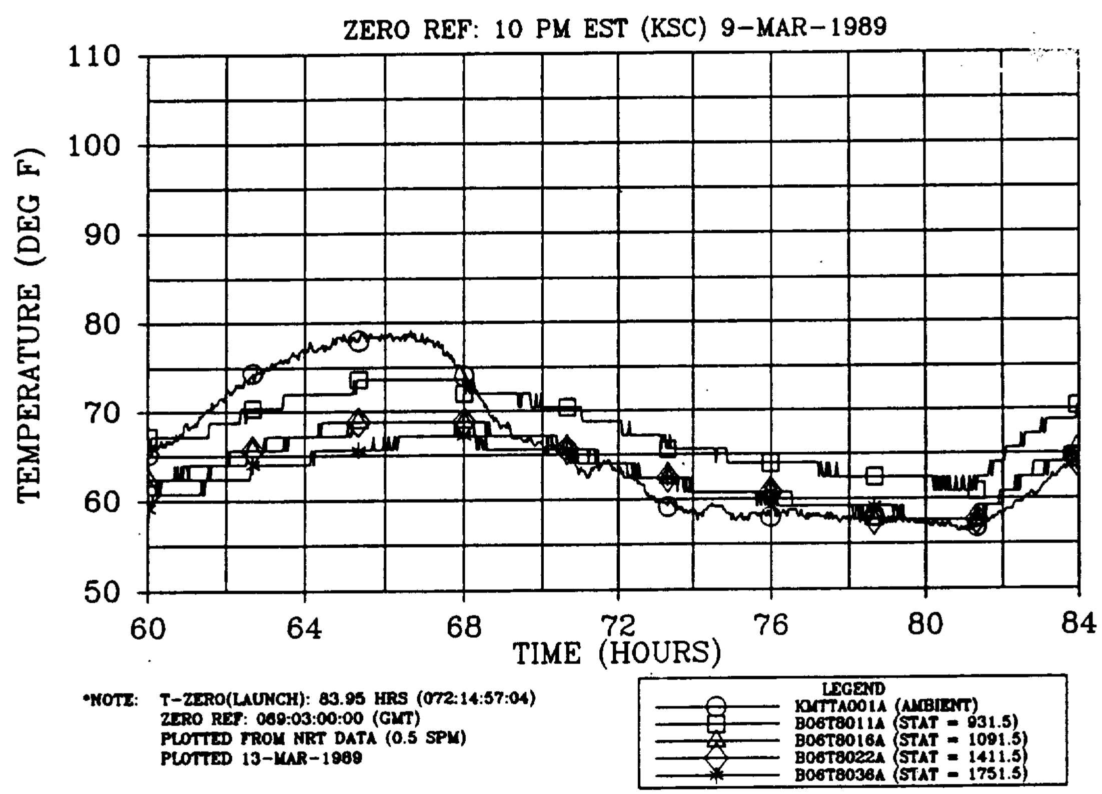

Figure 4.8-92. Prelaunch RH Case Acreage Temperature at 45 Deg (overlaid with ambient)

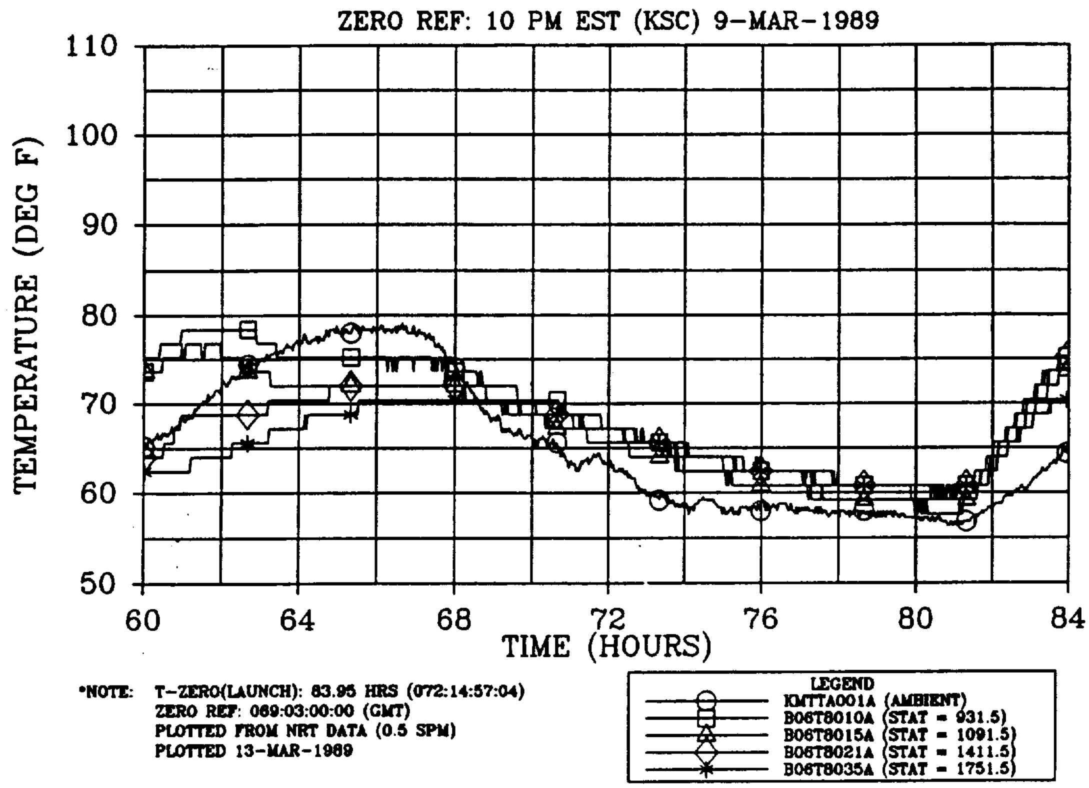

Figure 4.8-93. Prelaunch RH Case Acreage Temperature at 135 Deg (overlaid with ambient)

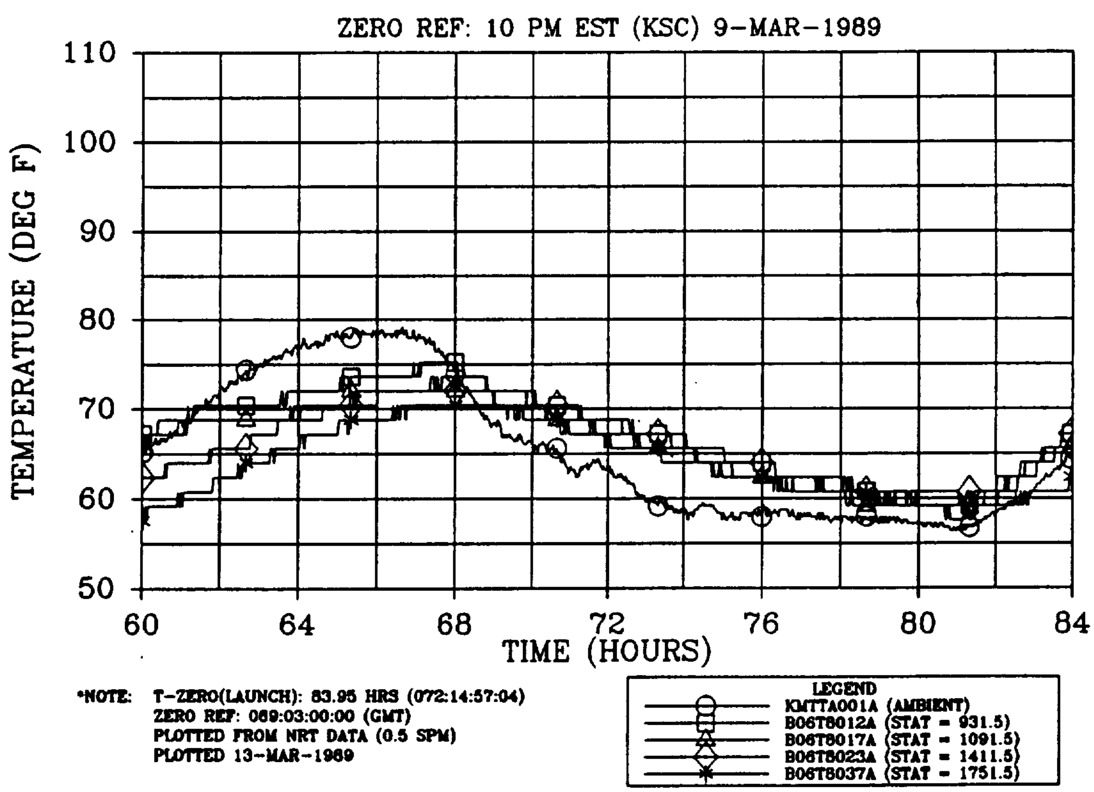

Figure 4.8-94. Prelaunch RH Case Acreage Temperature at 215 Deg (overlaid with ambient)

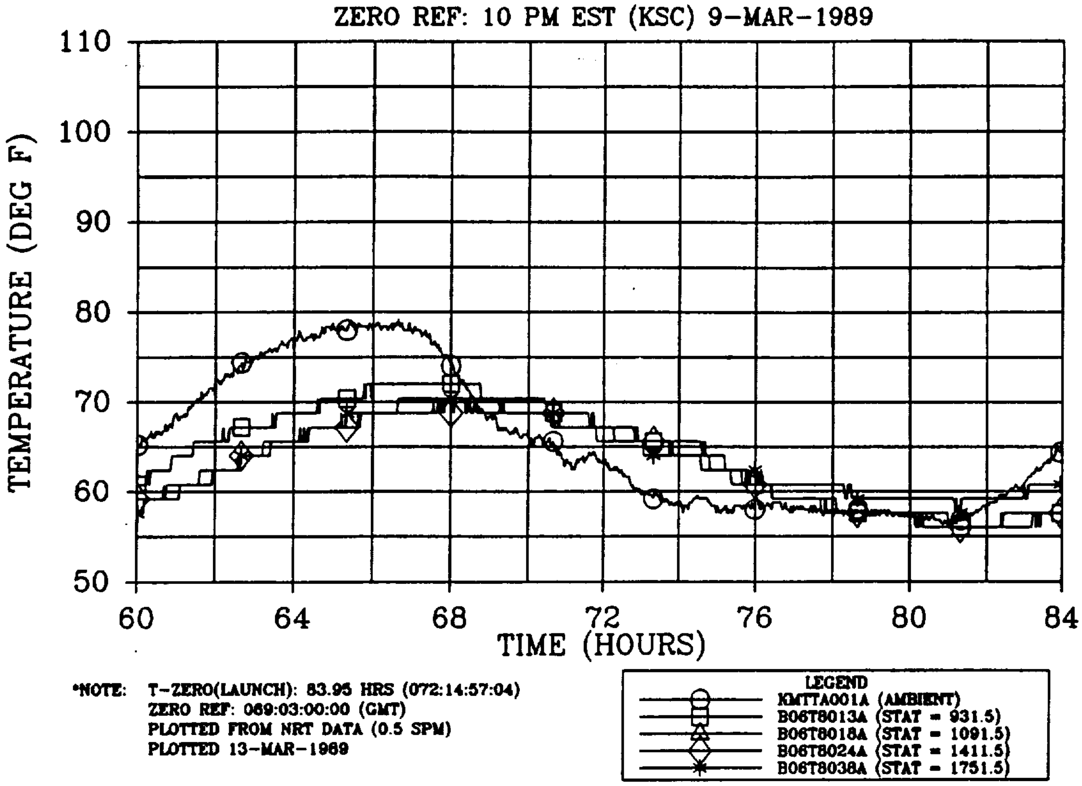

Figure 4.8-95. Prelaunch RH Case Acreage Temperature at 270 Deg (overlaid with ambient)

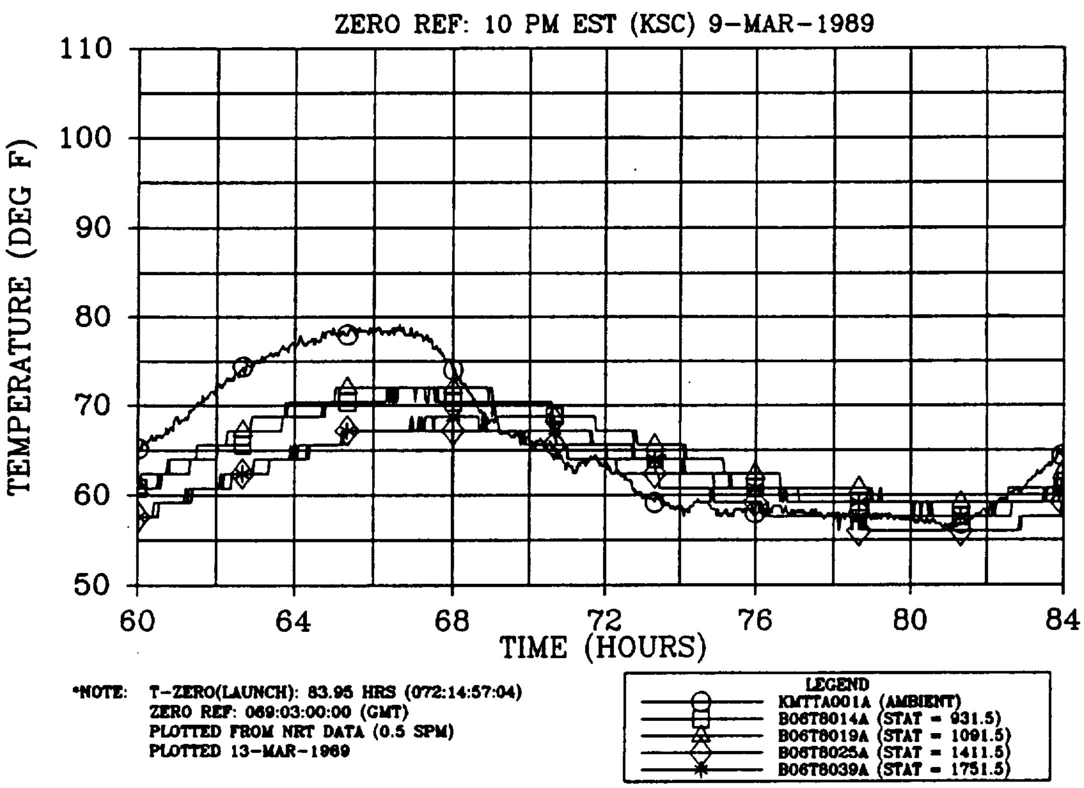

Figure 4.8-96. Prelaunch RH Case Acreage Temperature at 325 Deg (overlaid with ambient)

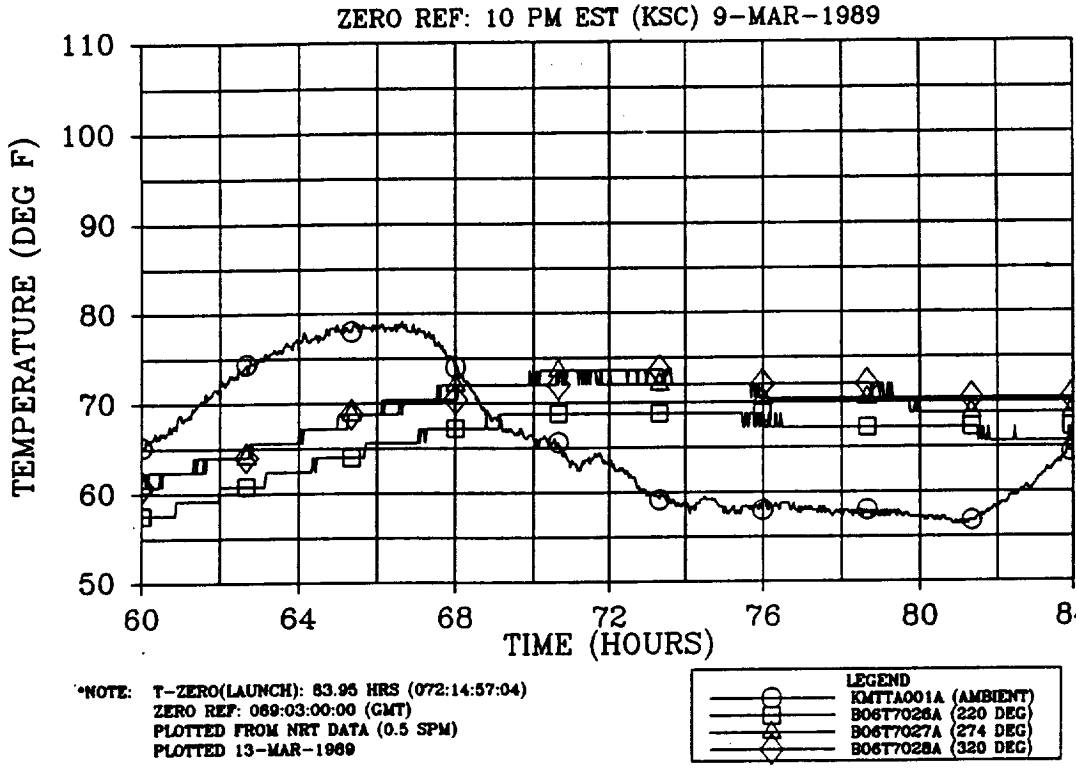

Figure 4.8-97. Prelaunch LH ETA Region Temperature at Station 1511.0 (overlaid with ambient)

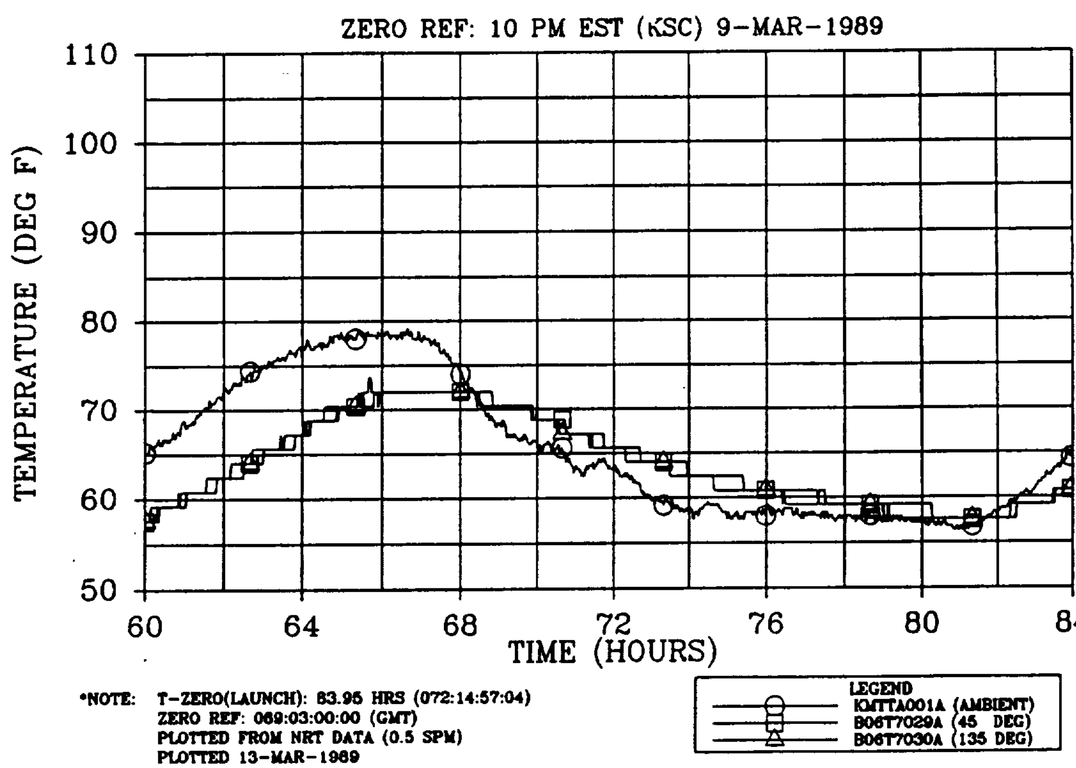

Figure 4.8-98. Prelaunch LH ETA Region Temperature at Station 1535.0 (overlaid with ambient)

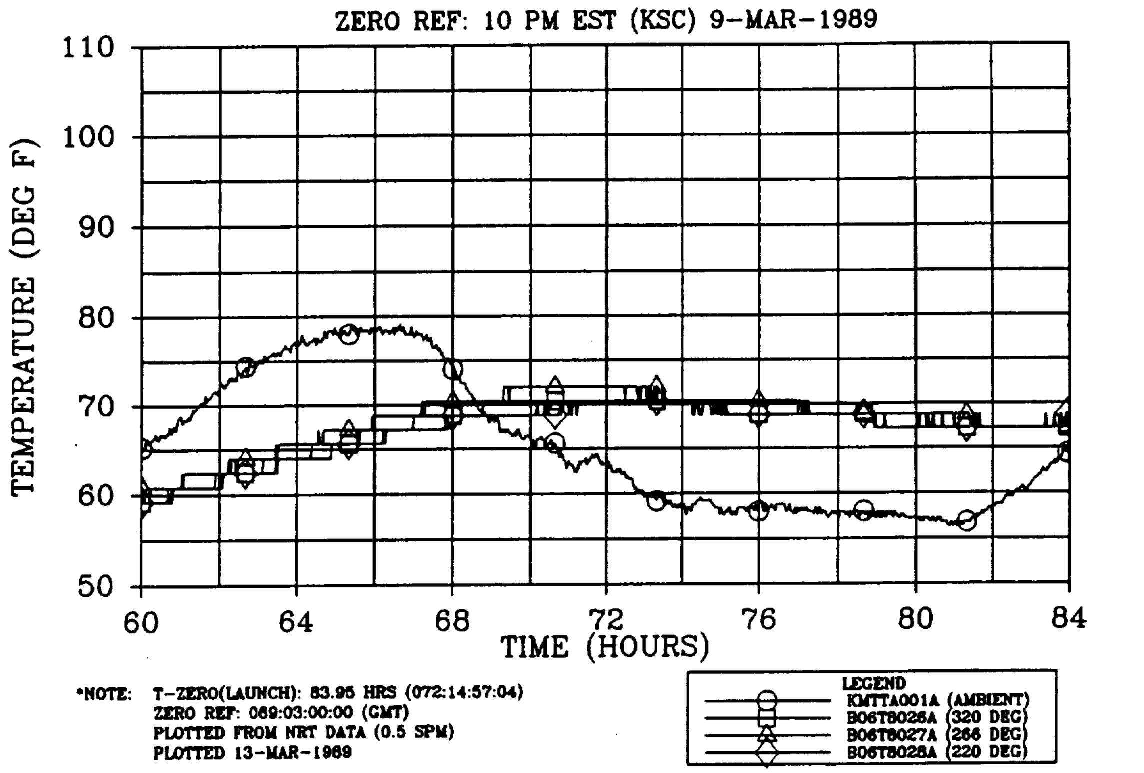

Figure 4.8-99. Prelaunch RH ETA Region Temperature at Station 1511.0 (overlaid with ambient)

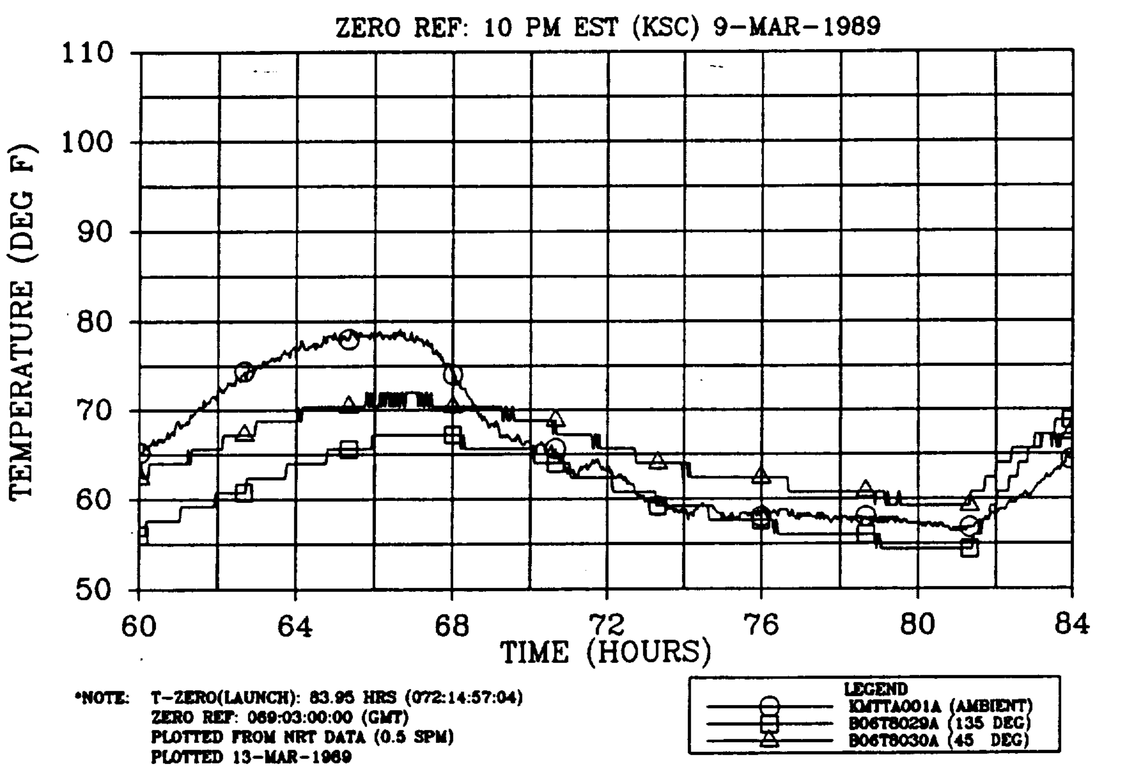

Figure 4.8-100. Prelaunch RH ETA Region Temperature at Station 1535.0 (overlaid with ambient)

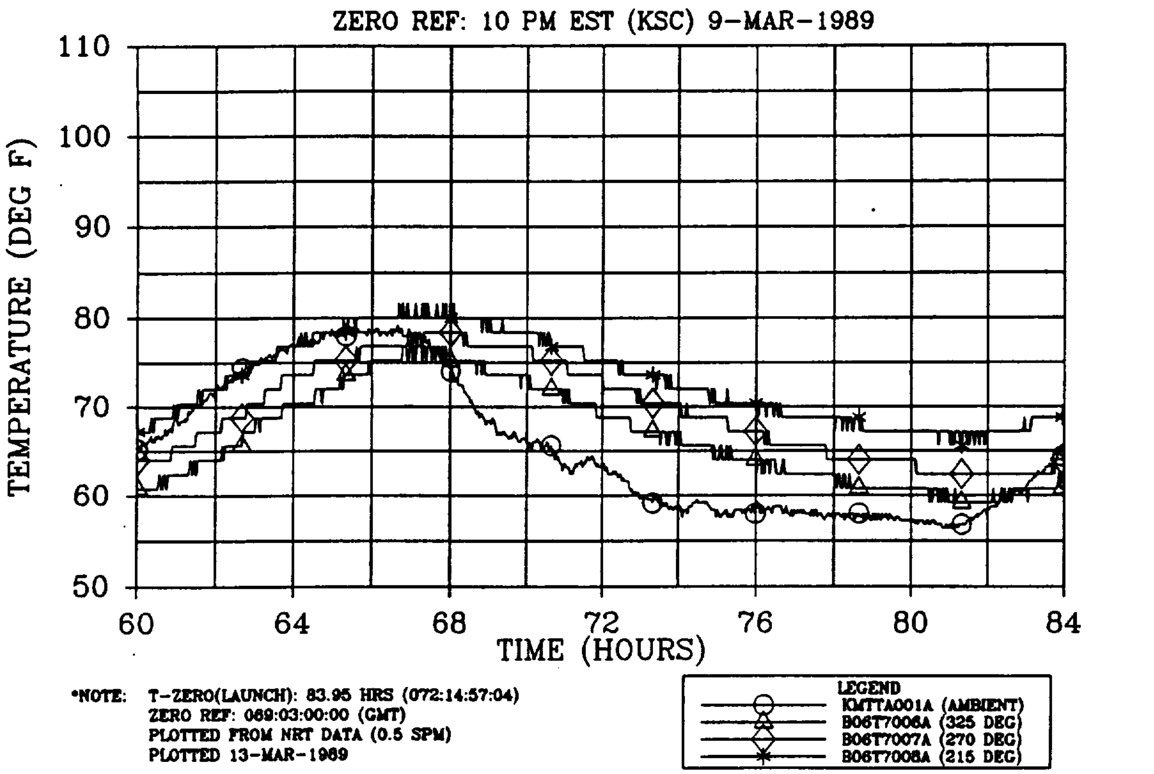

Figure 4.8-101. Prelaunch LH Forward Factory Joint Temperature at Station 691.4 (overlaid with ambient)

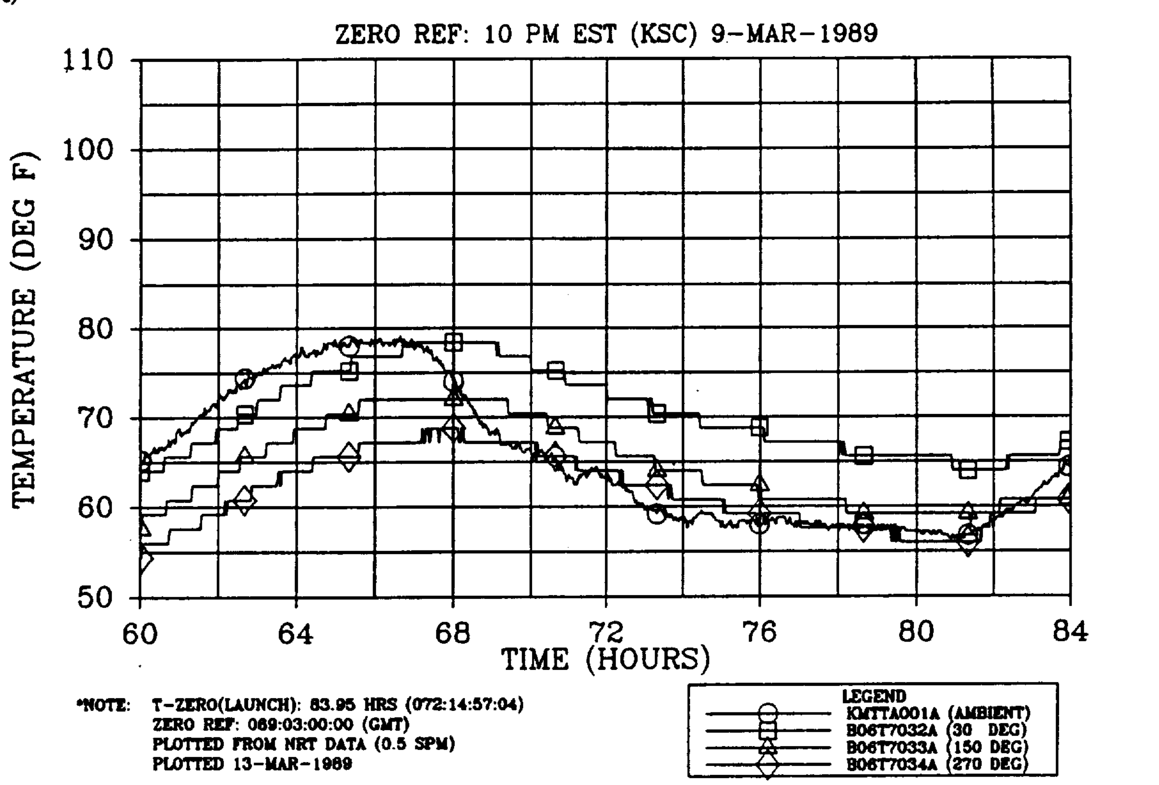

Figure 4.8-102. Prelaunch LH Aft Factory Joint Temperature at Station 1701.9 (overlaid with ambient)

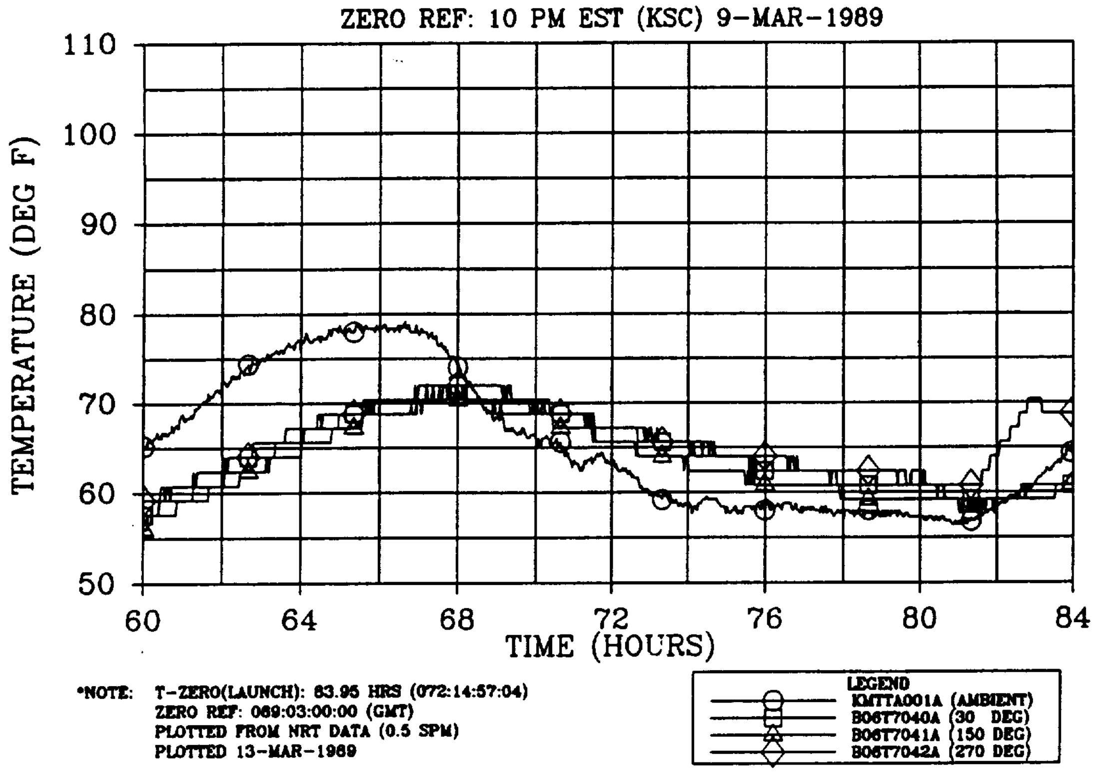

Figure 4.8-103. Prelaunch LH Aft Factory Joint Temperature at Station 1821.0 (overlaid with ambient)

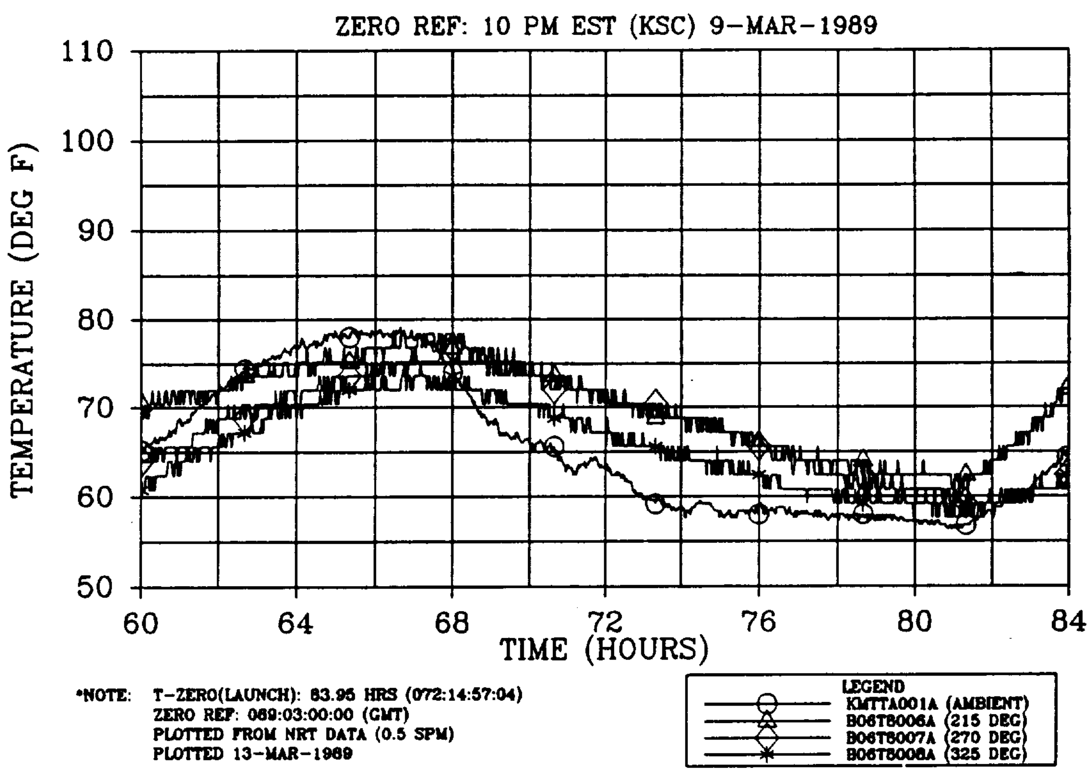

Figure 4.8-104. Prelaunch RH Forward Factory Joint Temperature at Station 691.4 (overlaid with ambient)

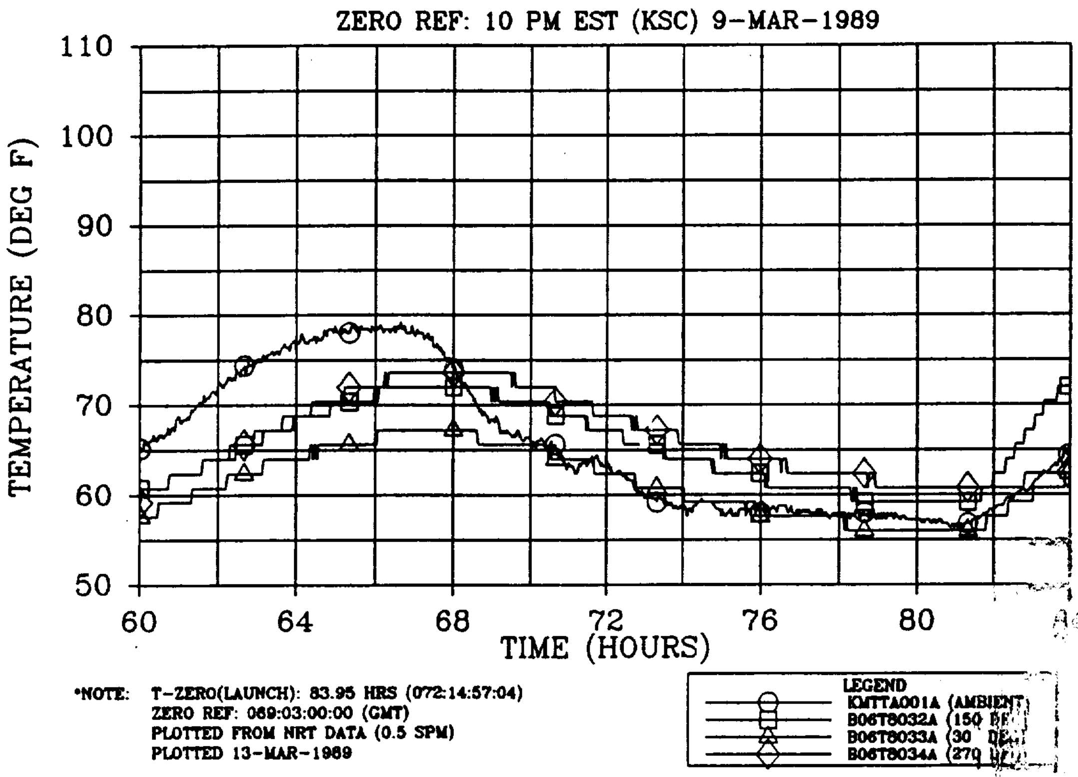

Figure 4.8-105. Prelaunch RH Aft Factory Joint Temperature at Station 1701.9 (overlaid with ambient)

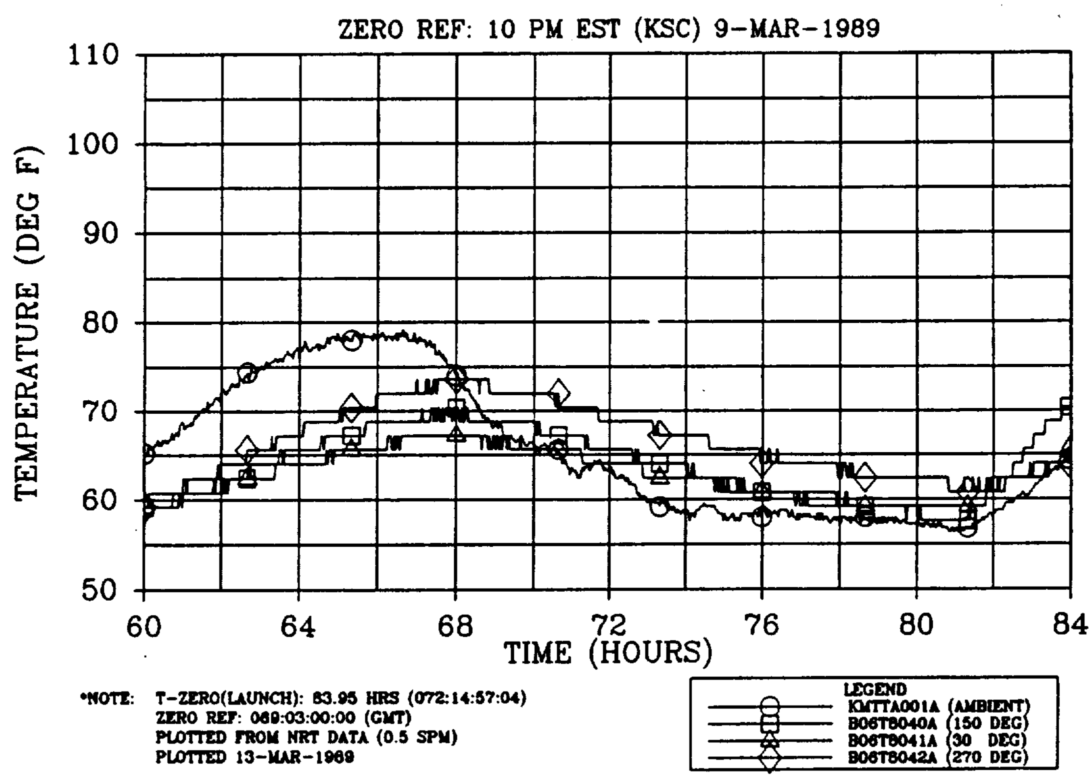

Figure 4.8-106. Prelaunch RH Aft Factory Joint Temperature at Station 1821.0 (overlaid with ambient)

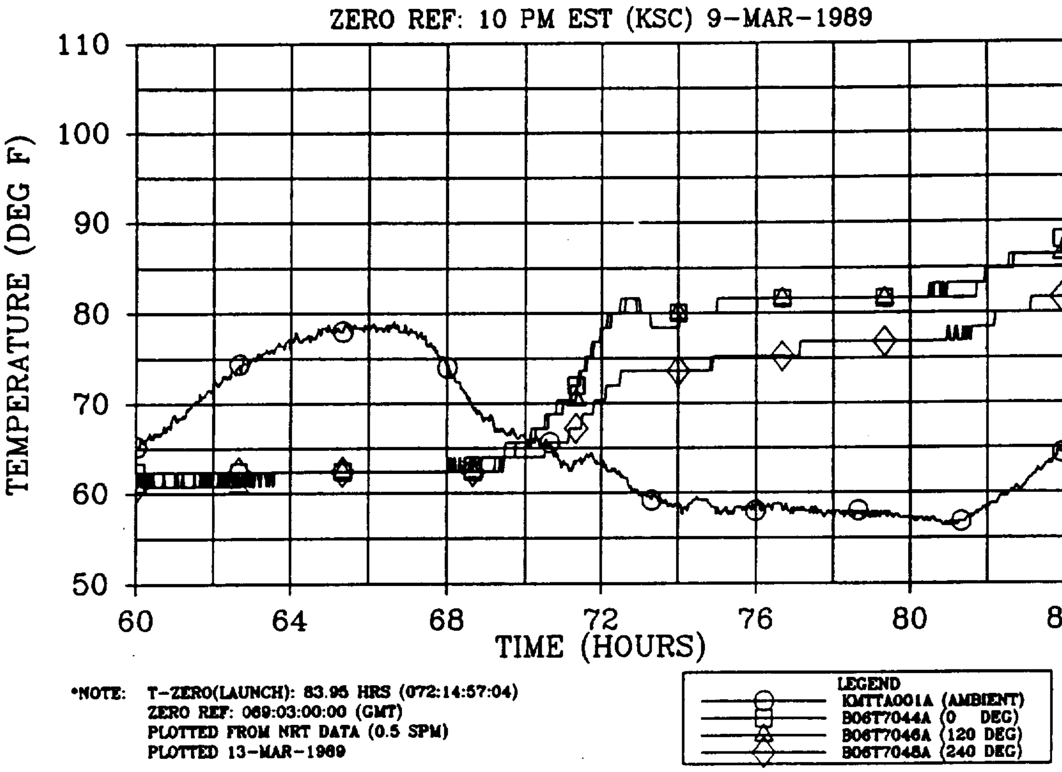

Figure 4.8-107. Prelaunch LH Nozzle Region Temperature at Station 1845.0 (overlaid with ambient)

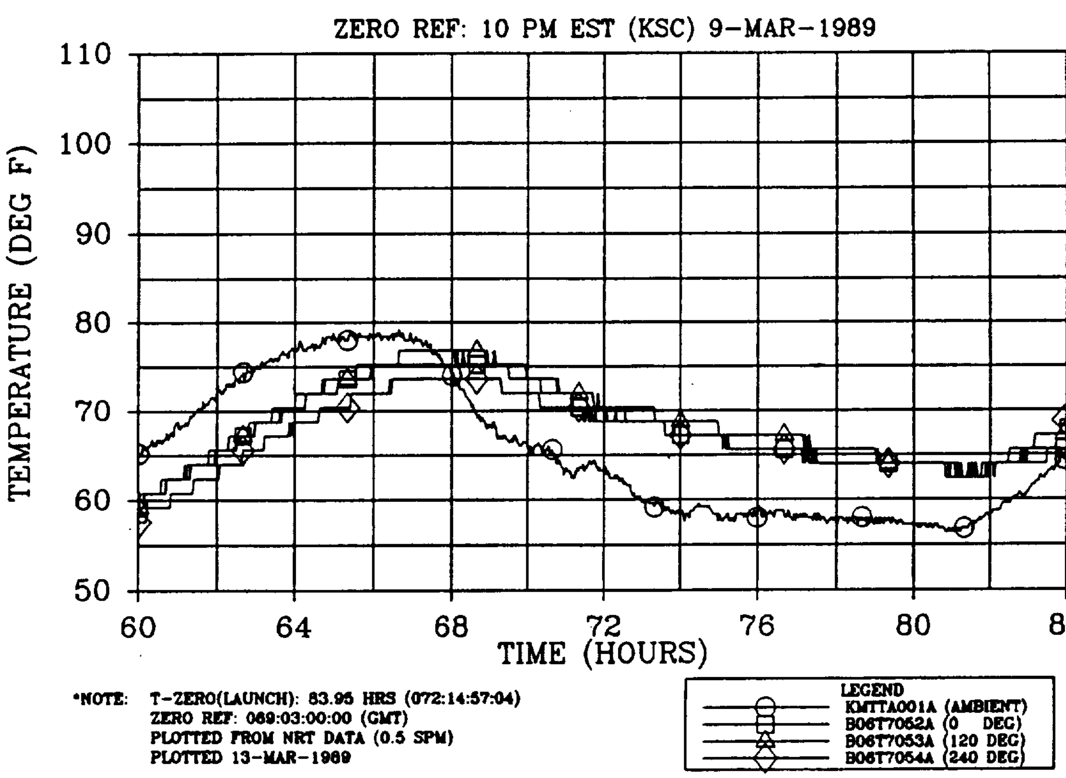

Figure 4.8-108. Prelaunch LH Nozzle Region Temperature at Station 1950.0 (overlaid with ambient)

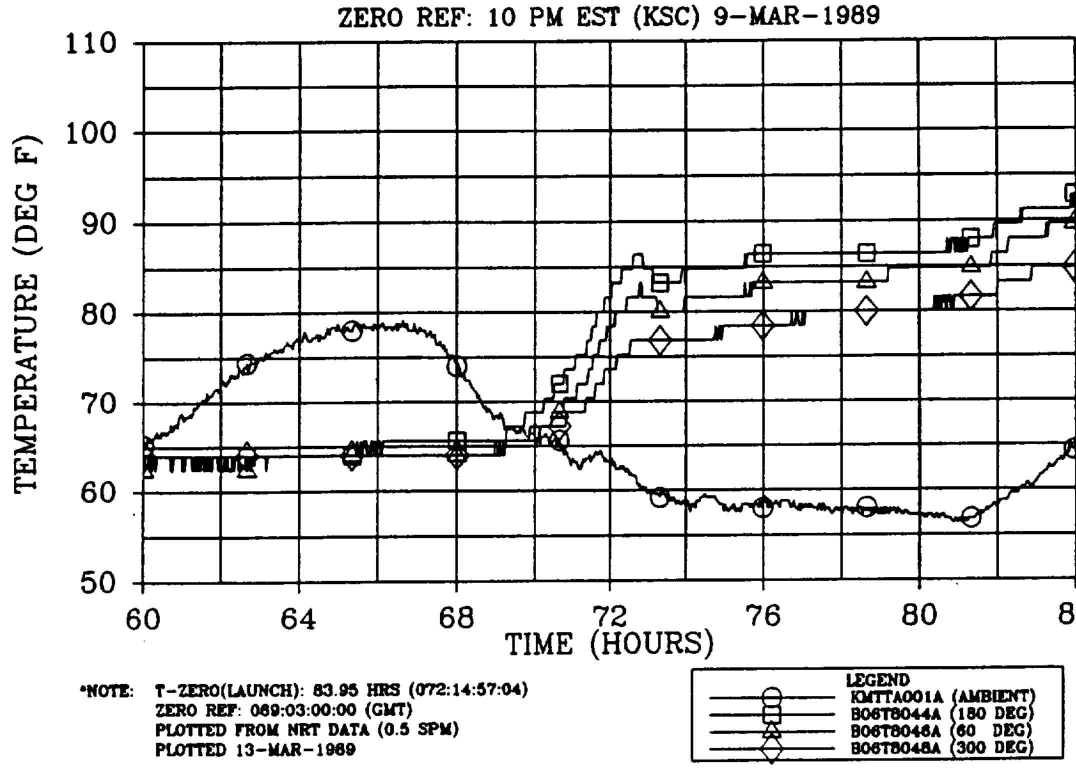

Figure 4.8-109. Prelaunch RH Nozzle Region Temperature at Station 1845.0 (overlaid with ambient)

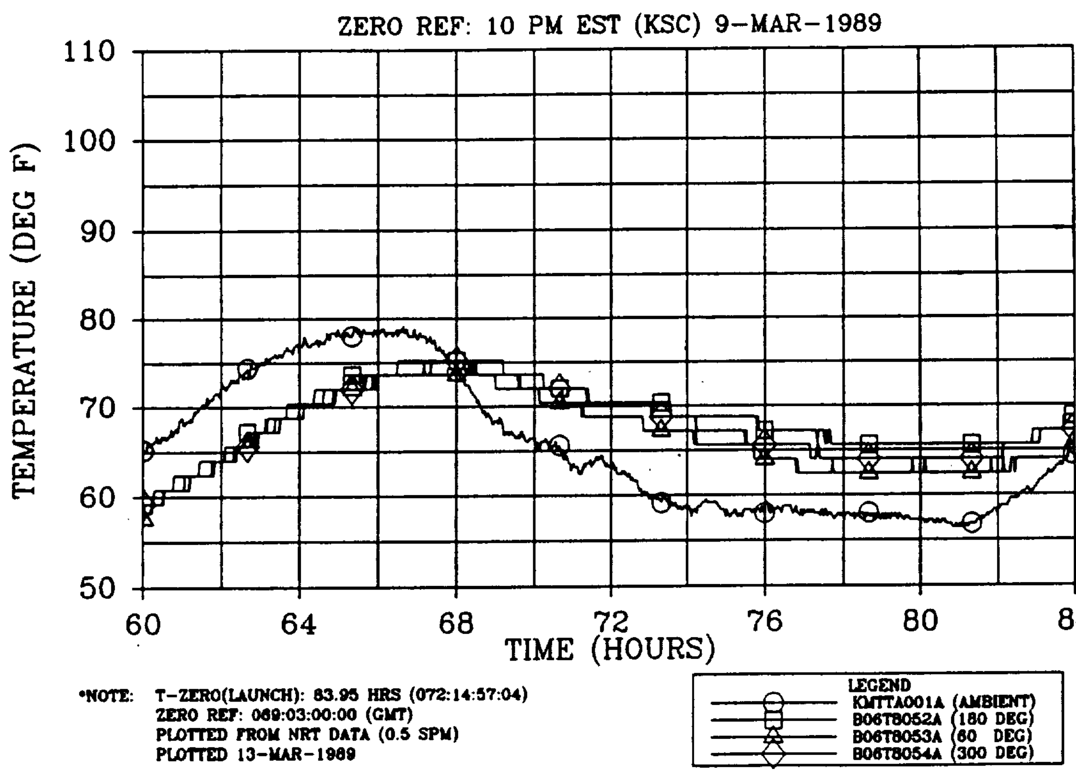

Figure 4.8-110. Prelaunch RH Nozzle Region Temperature at Station 1950.0 (overlaid with ambient)

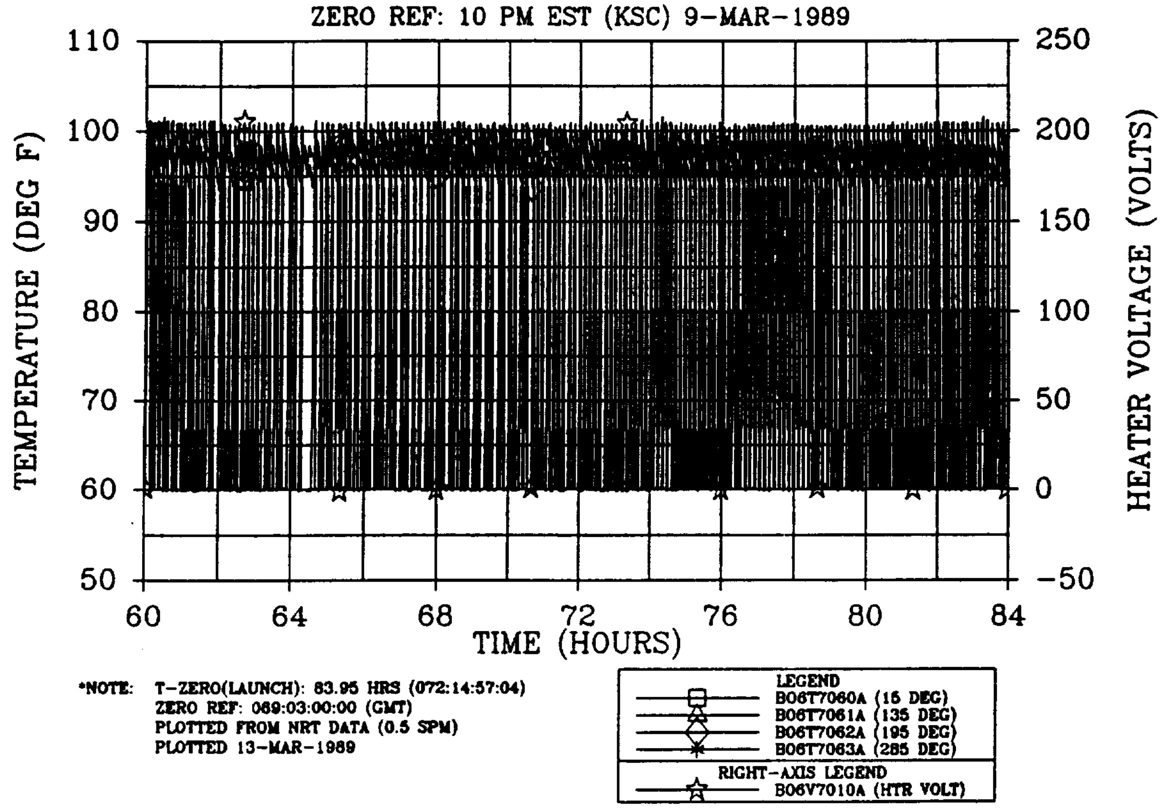

Figure 4.8-111. Prelaunch LH Forward Field Joint Temperature (overlaid with heater voltage)

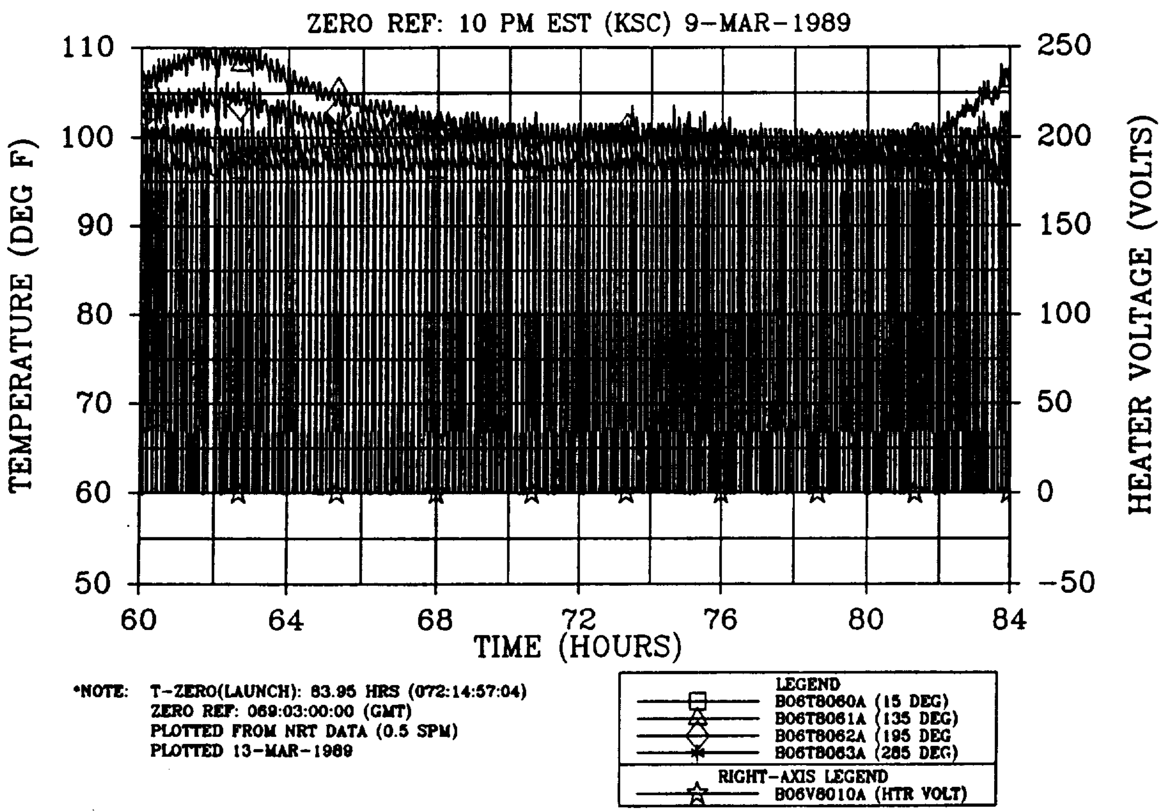

Figure 4.8-112. Prelaunch RH Forward Field Joint Temperature (overlaid with heater voltage)

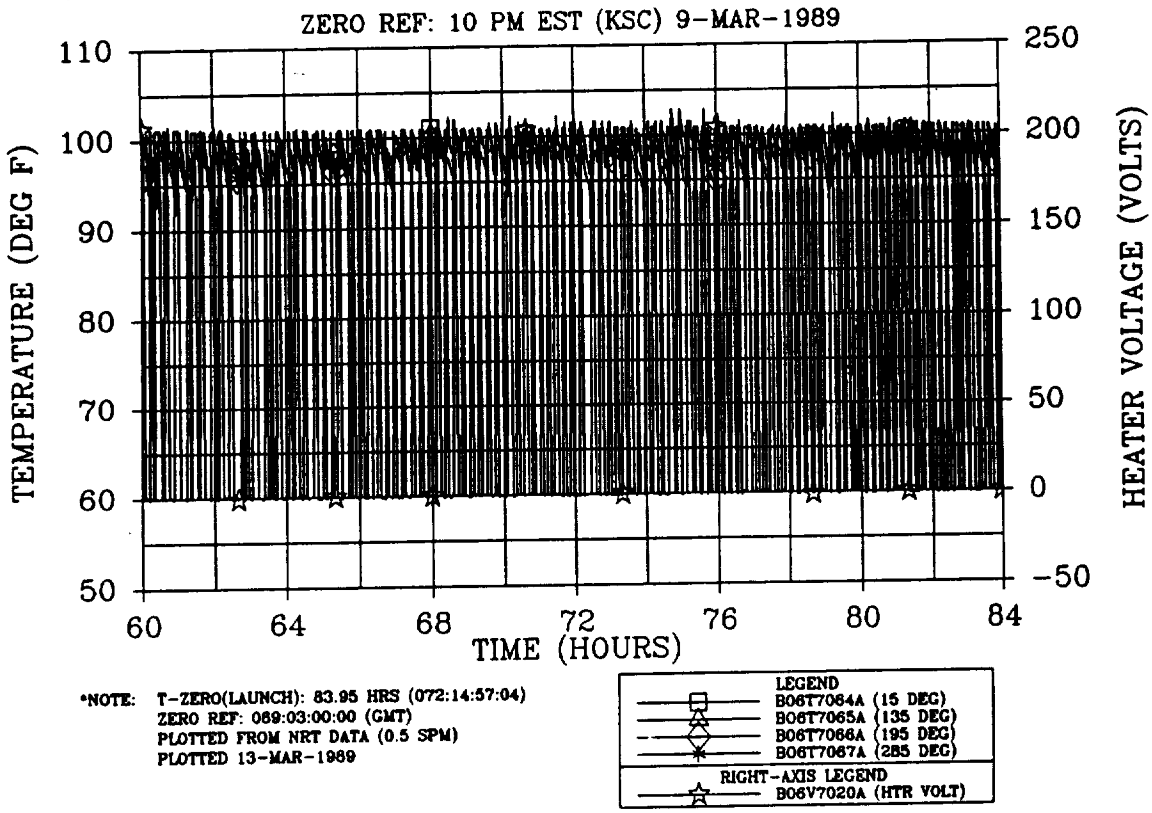

*NOTE: T-ZERO(LAUNCH): 83.95 HRS (072:14:57:04)
ZERO REF: 069:03:00:00 (GMT)
PLOTTED FROM NRT DATA (0.5 SPM)
PLOTTED 13-MAR-1989

Figure 4.8-113. Prelaunch LH Center Field Joint Temperature (overlaid with heater voltage)

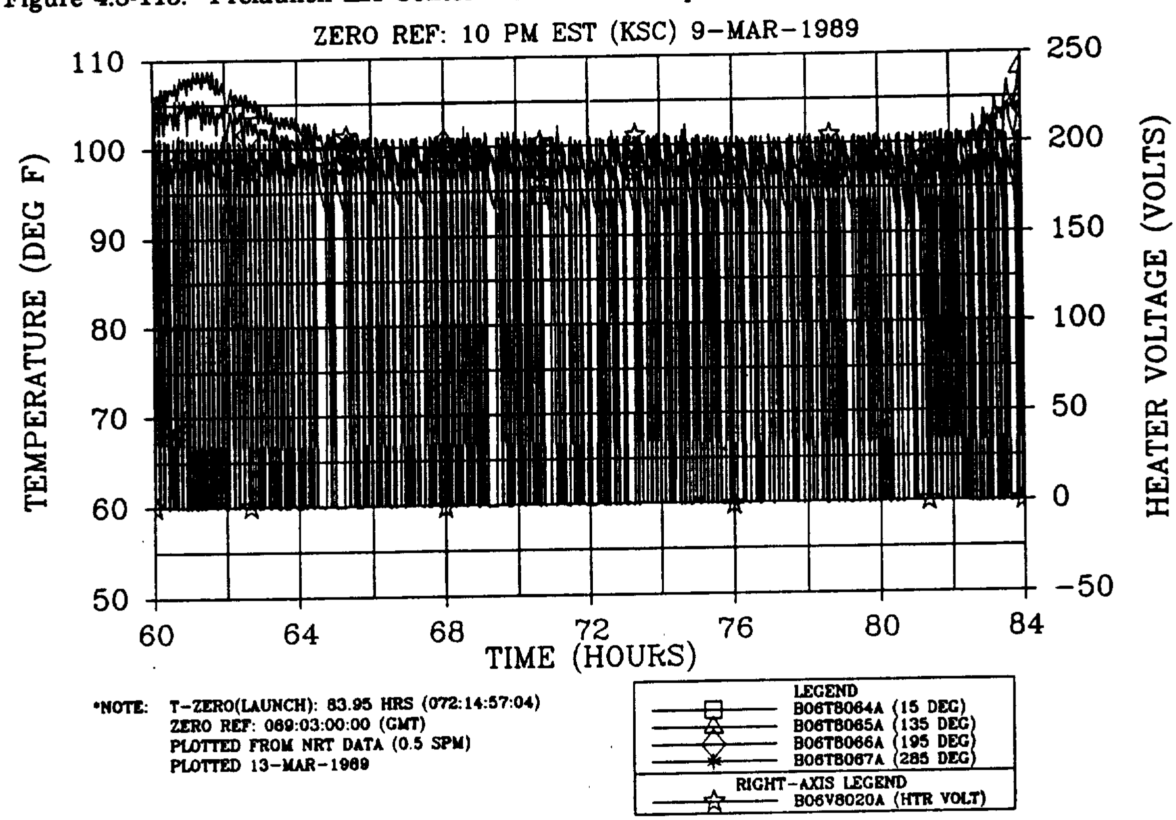

*NOTE: T-ZERO(LAUNCH): 83.95 HRS (072:14:57:04)
ZERO REF: 069:03:00:00 (GMT)
PLOTTED FROM NRT DATA (0.5 SPM)
PLOTTED 13-MAR-1989

Figure 4.8-114. Prelaunch RH Center Field Joint Temperature (overlaid with heater voltage)

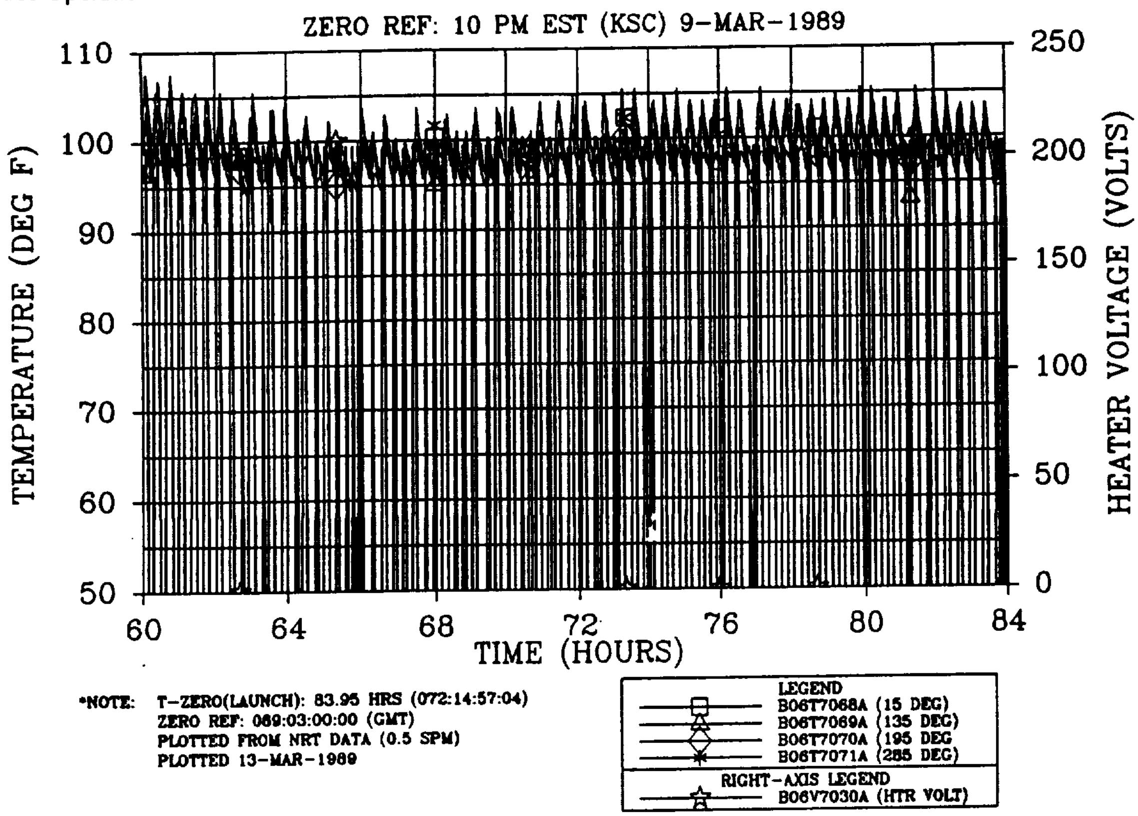

Figure 4.8-115. Prelaunch LH Aft Field Joint Temperature (overlaid with heater voltage)

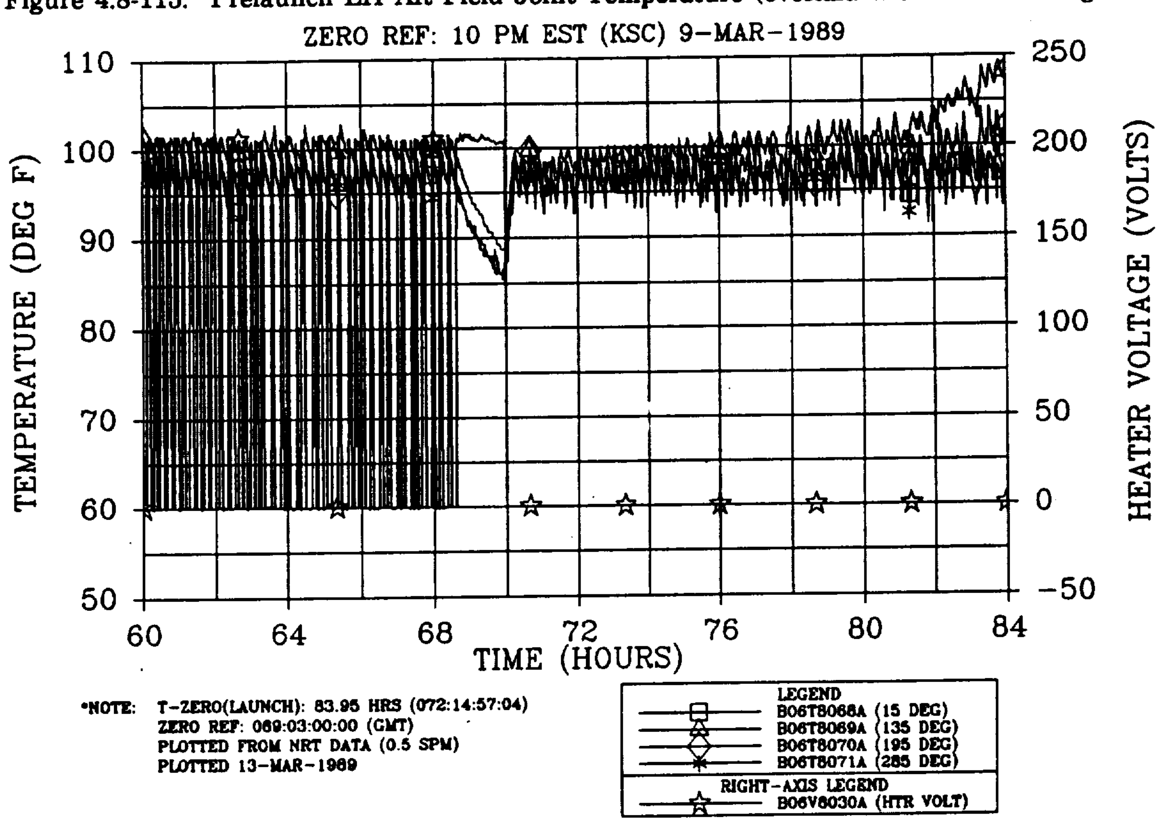

Figure 4.8-116. Prelaunch RH Aft Field Joint Temperature (overlaid with heater voltage)

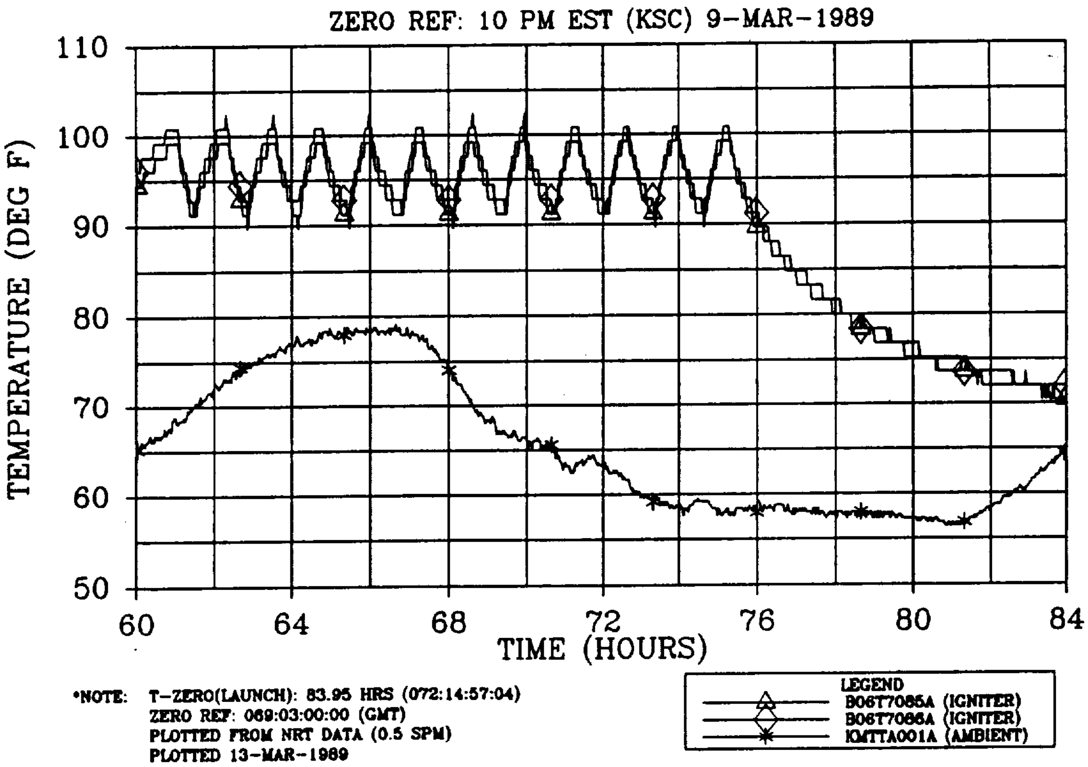

Figure 4.8-117. Prelaunch LH Igniter Joint Temperature (overlaid with ambient)

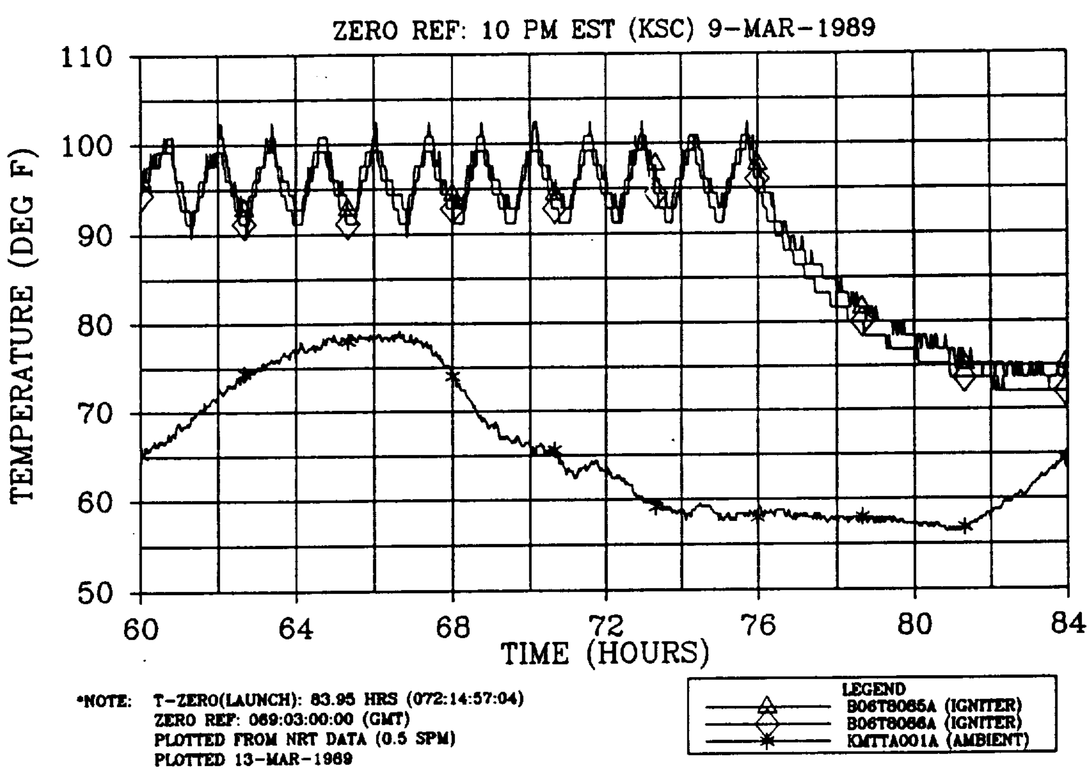

Figure 4.8-118. Prelaunch RH Igniter Joint Temperature (overlaid with ambient)

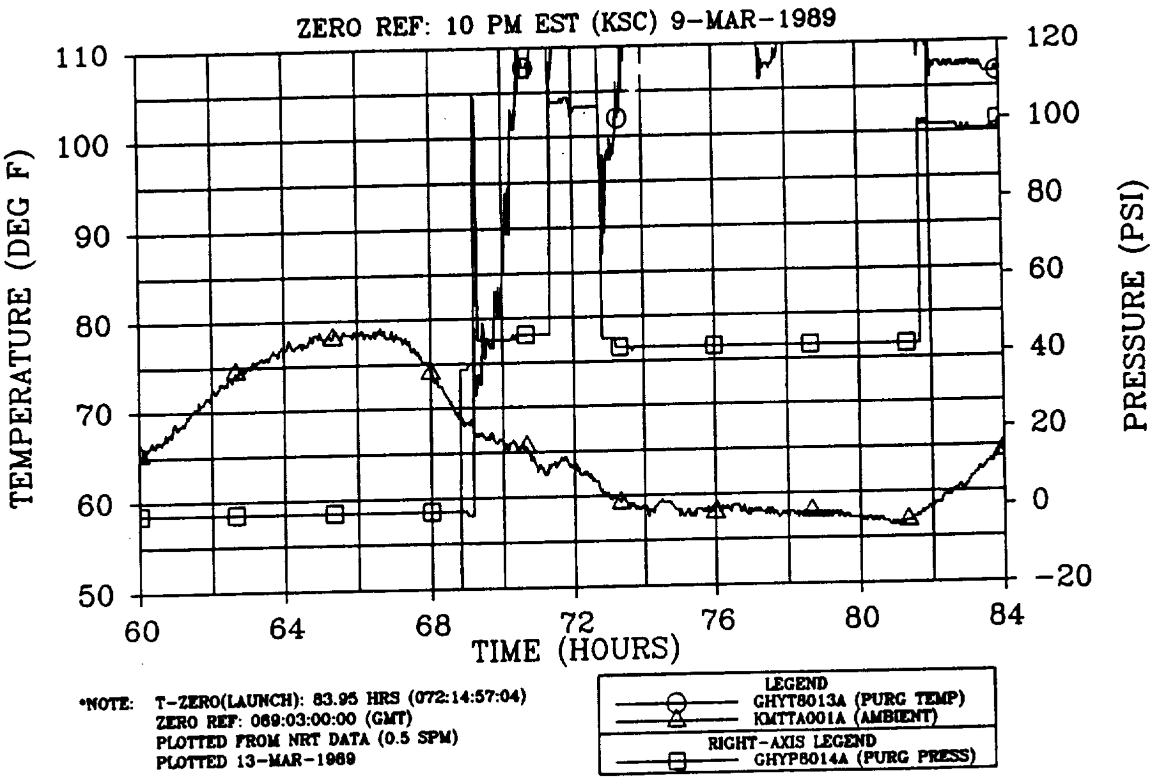

Figure 4.8-119. Prelaunch Aft Skirt Purge Temperature and Pressure (overlaid with ambient)

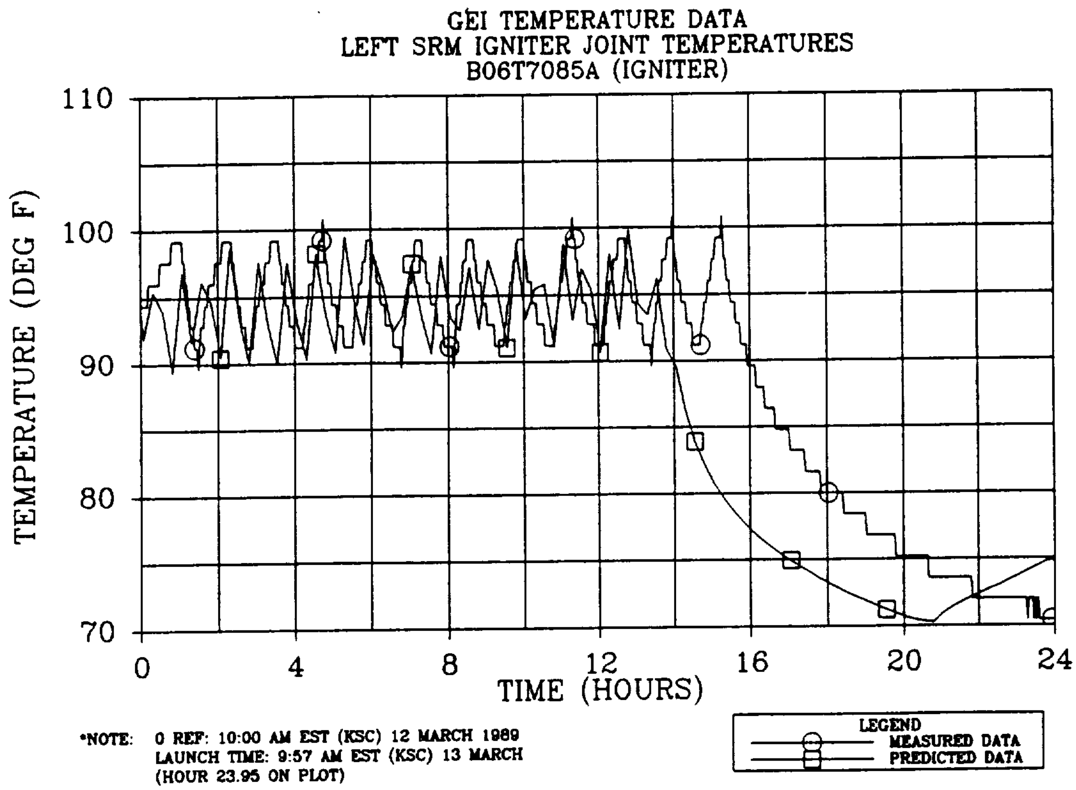

Figure 4.8-120. Measured Versus Predicted Temperature--LH Igniter Joint

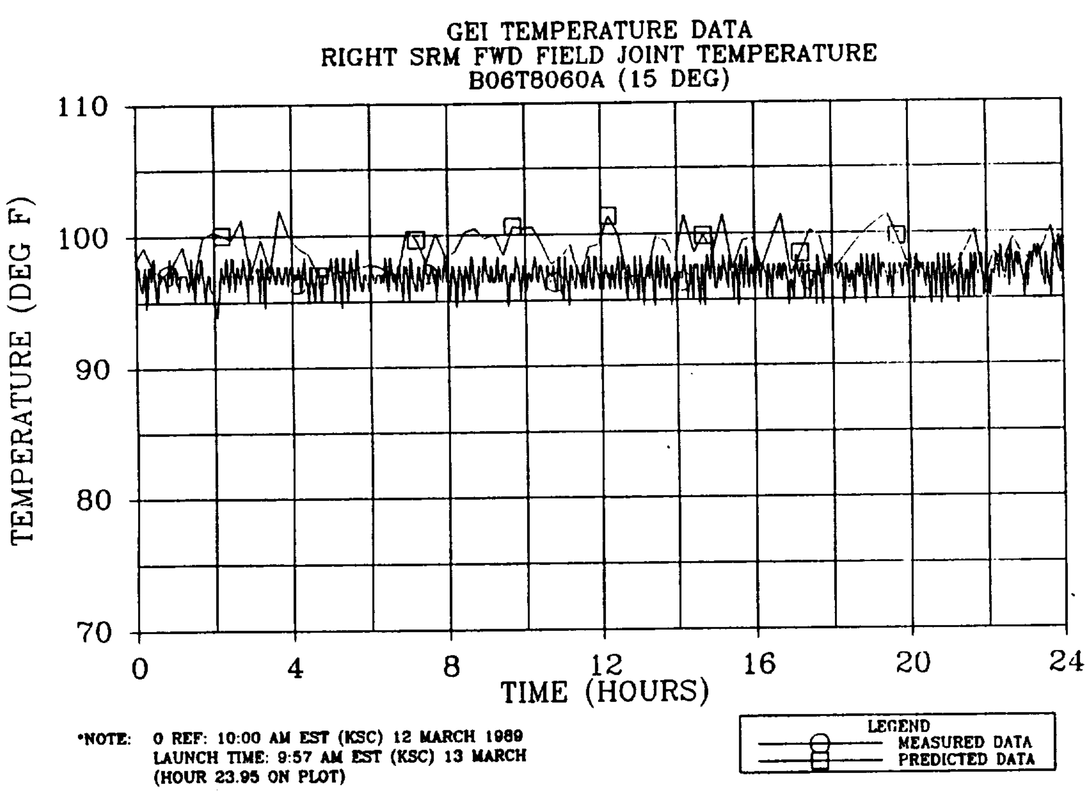

Figure 4.8-121. Measured Versus Predicted Temperature--RH Forward Field Joint (15-deg location)

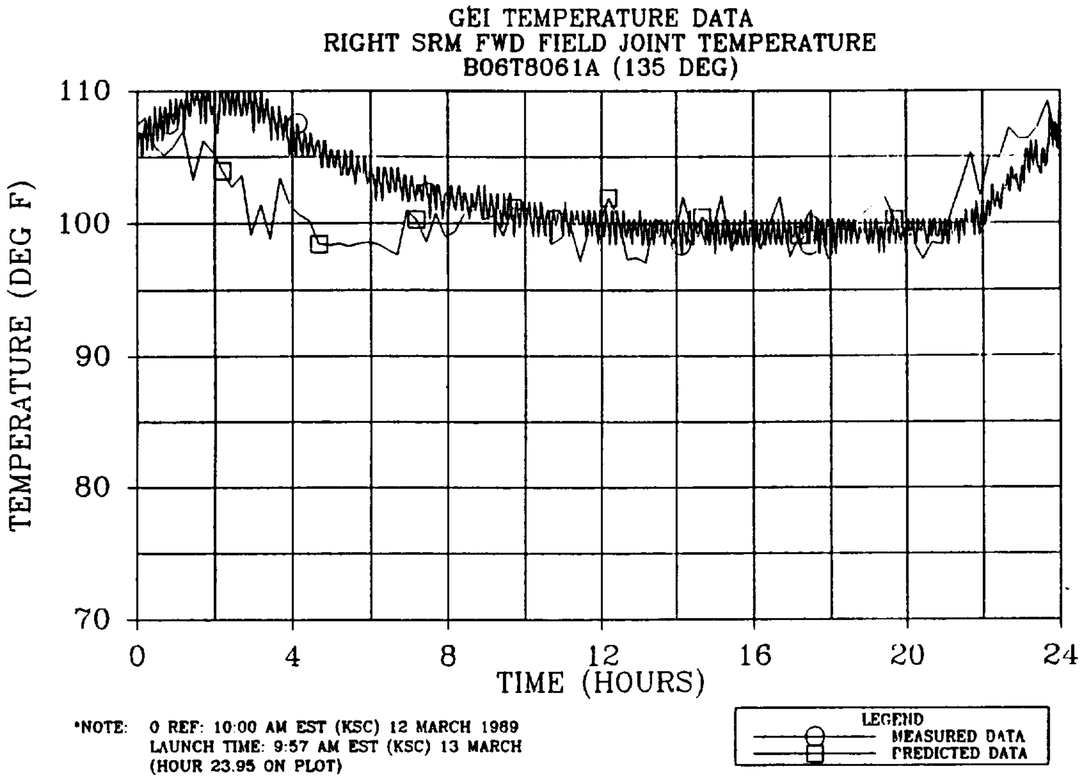

Figure 4.8-122. Measured Versus Predicted Temperature--RH Forward Field Joint (135-deg location)

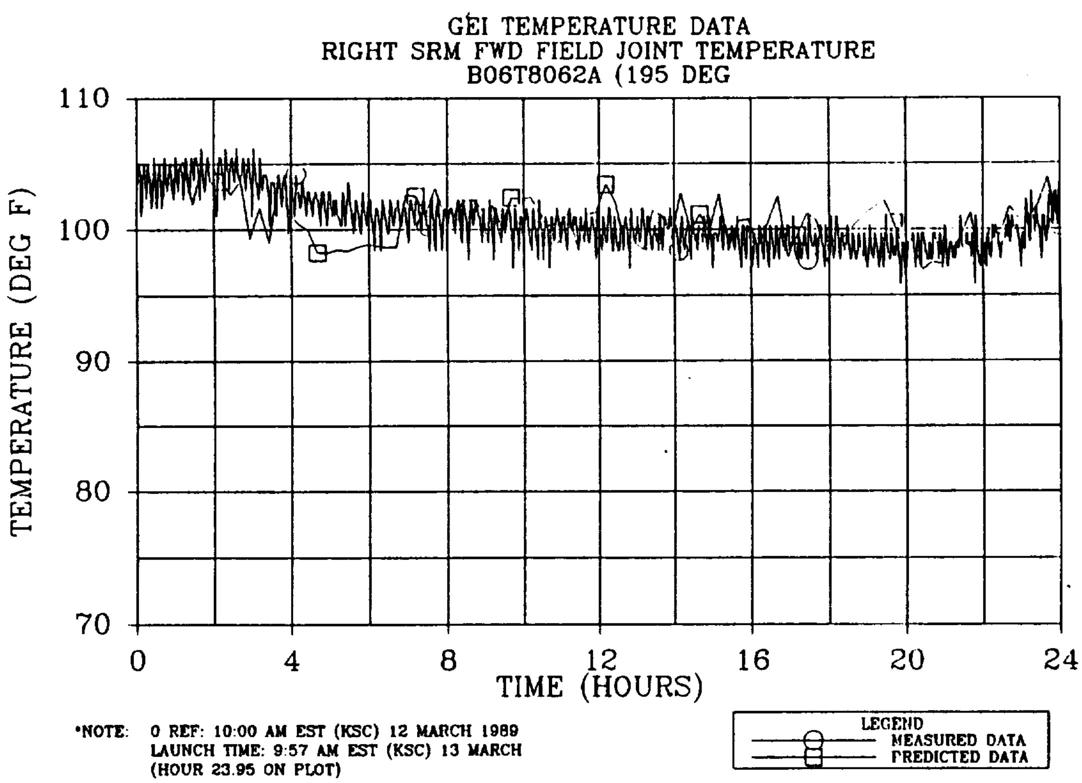

Figure 4.8-123. Measured Versus Predicted Temperature--RH Forward Field Joint (195-deg location)

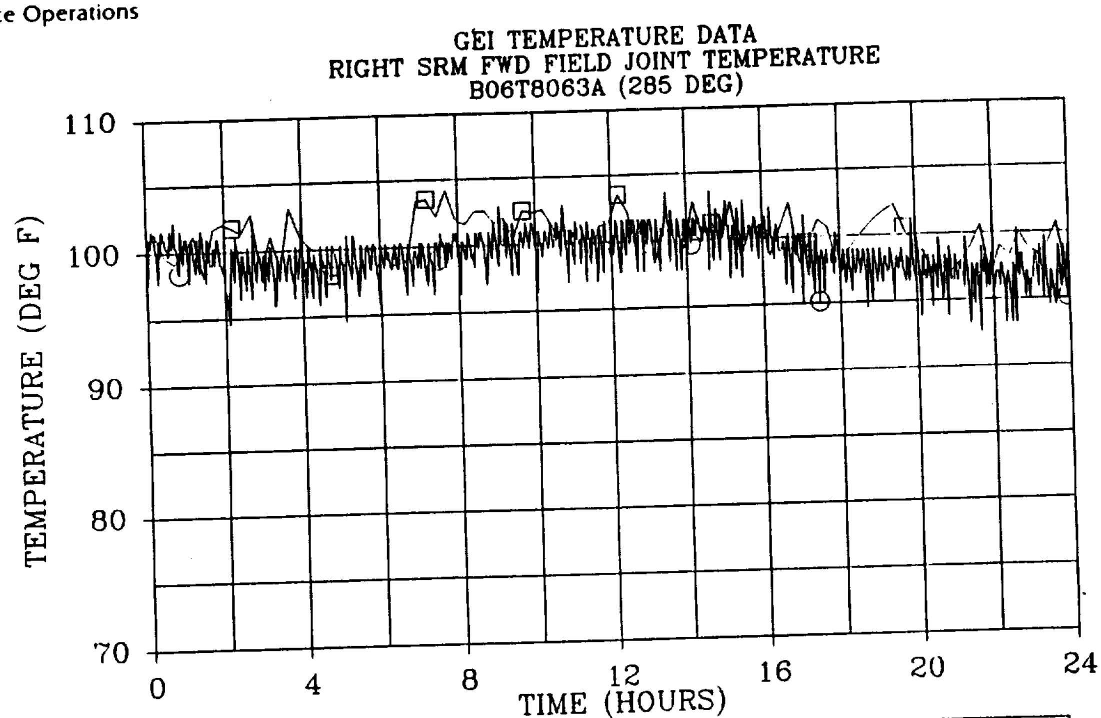

*NOTE: 0 REF: 10:00 AM EST (KSC) 12 MARCH 1989
LAUNCH TIME: 9:57 AM EST (KSC) 13 MARCH
(HOUR 23.95 ON PLOT)

Figure 4.8-124. Measured Versus Predicted Temperature--RH Forward Field Joint (285-deg location)

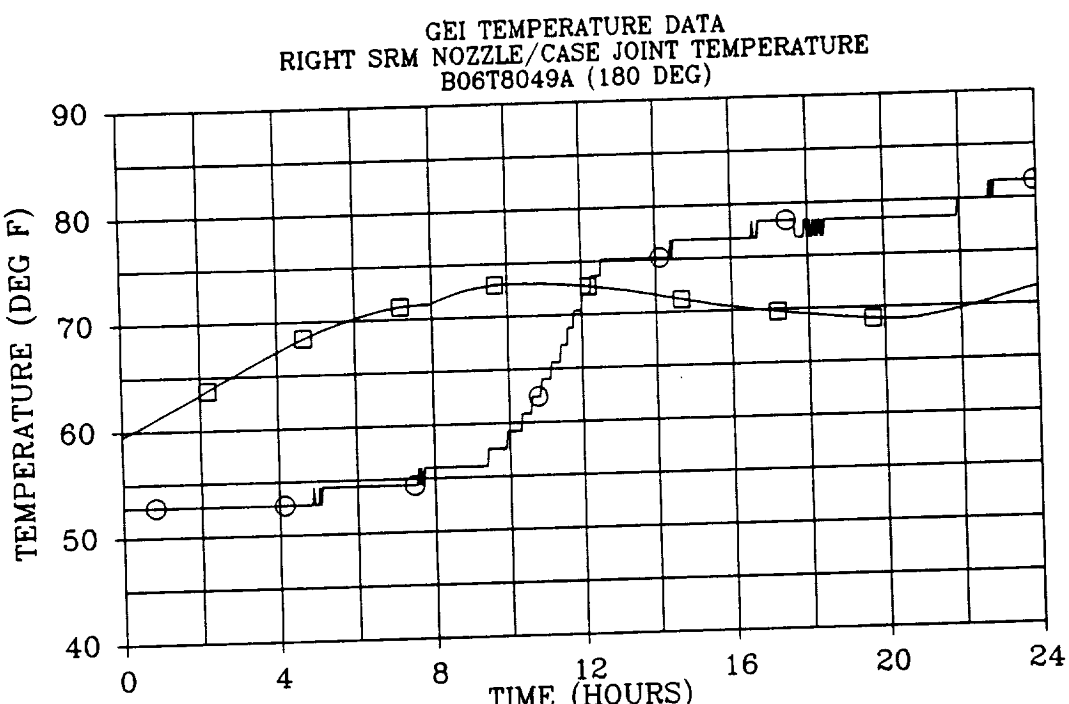

*NOTE: 0 REF: 10:00 AM EST (KSC) 12 MARCH 1989
LAUNCH TIME: 9:57 AM EST (KSC) 13 MARCH
(HOUR 23.95 ON PLOT)

Figure 4.8-125. Measured Versus Predicted Temperature--RH Case-to-Nozzle Joint (180-deg location)

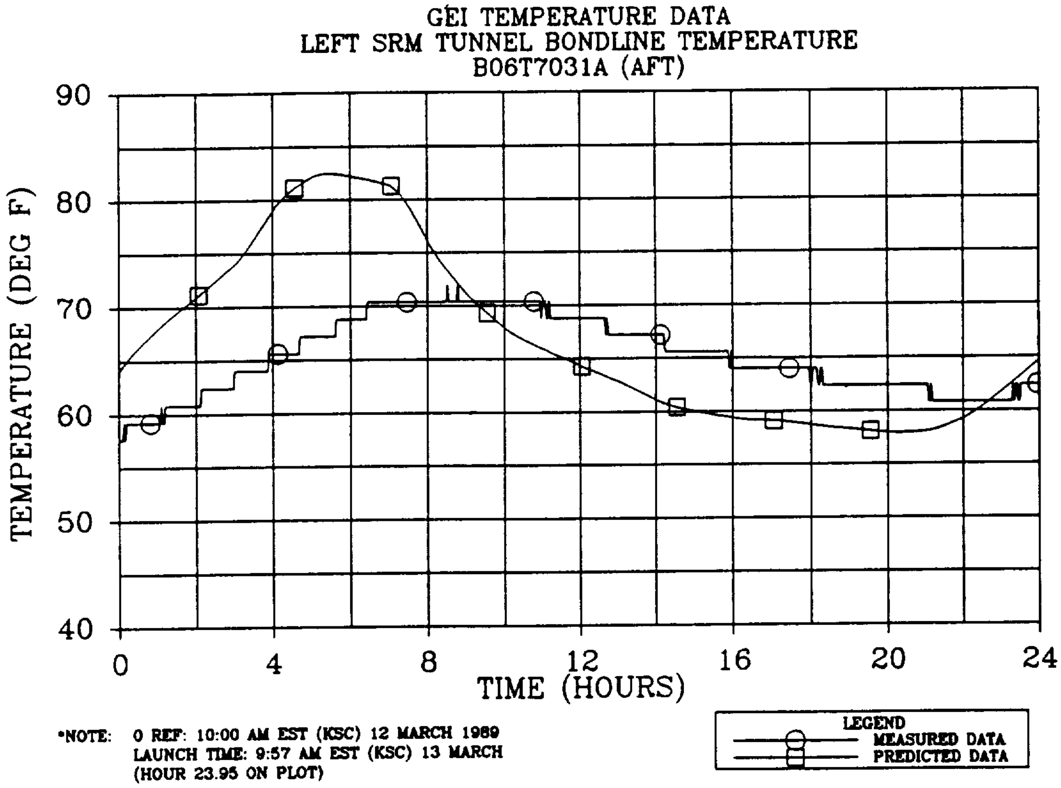

Figure 4.8-126. Measured Versus Predicted Temperature--LH Tunnel Bondline

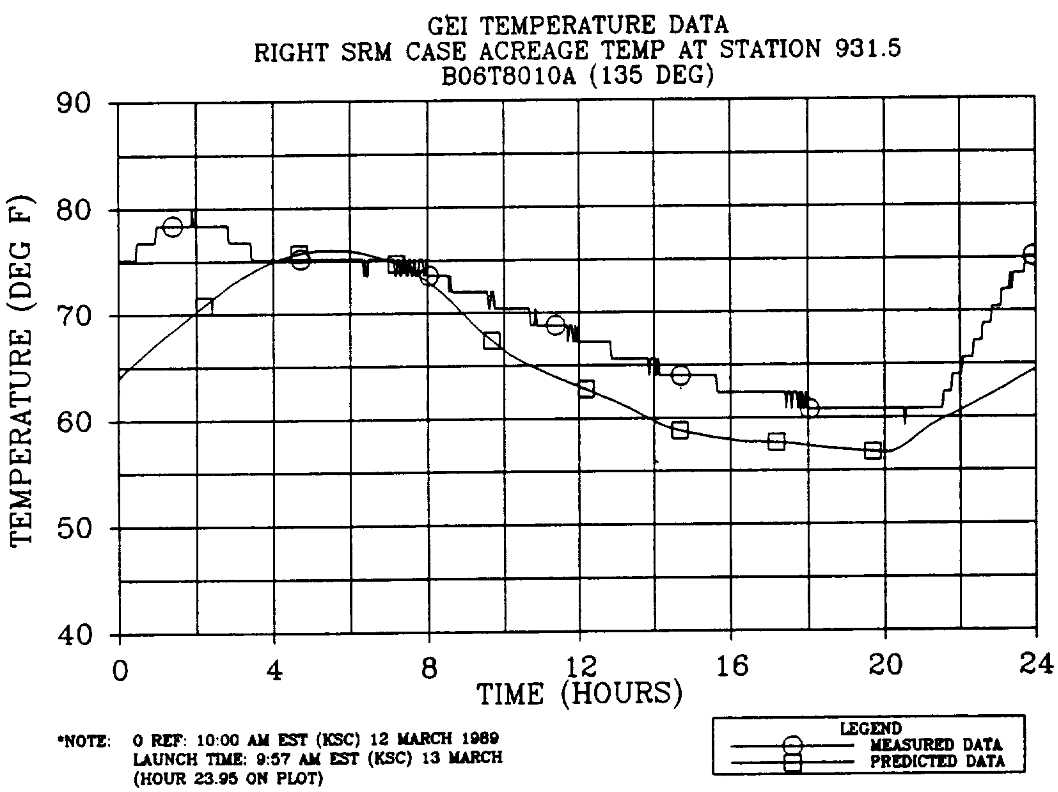

Figure 4.8-127. Measured Versus Predicted Temperature--RH Case Acreage at Station 931.5 (135-deg location)

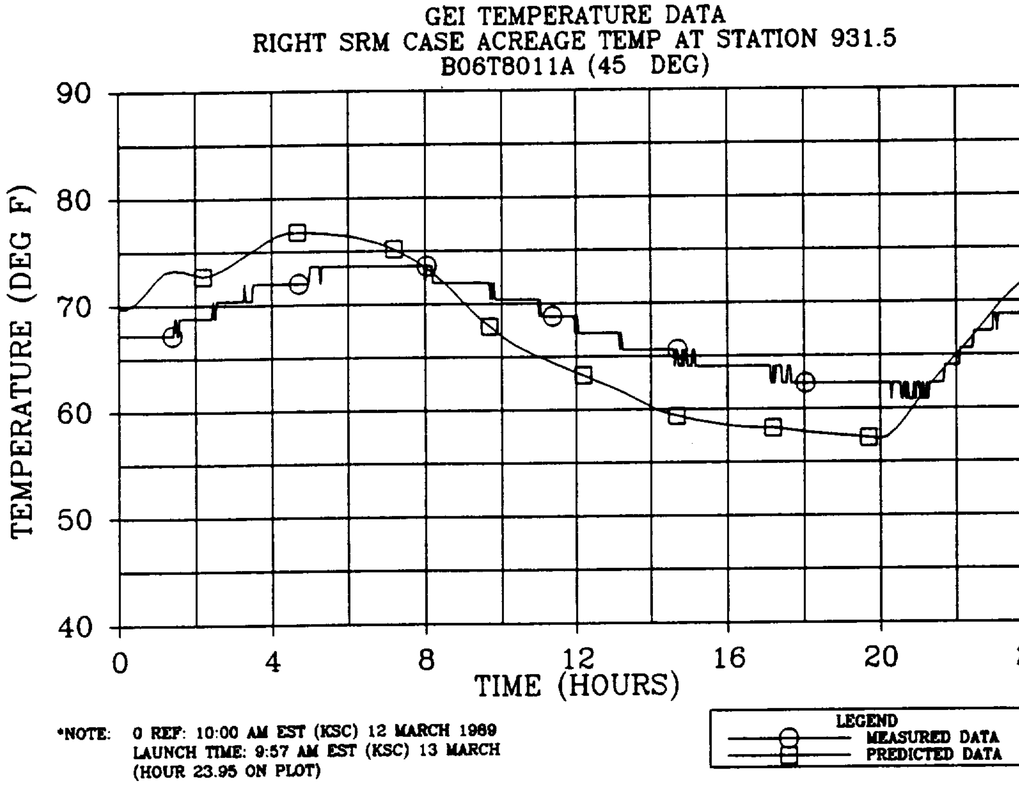

Figure 4.8-128. Measured Versus Predicted Temperature--RH Case Acreage at Station 931.5 (45-deg location)

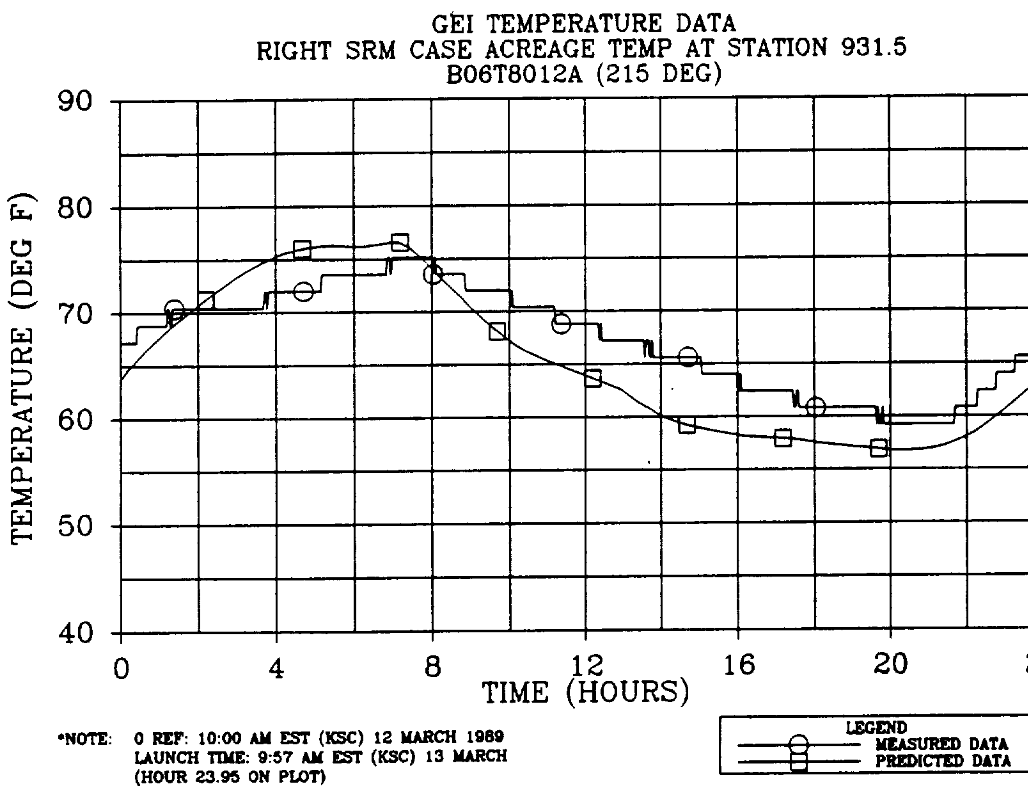

Figure 4.8-129. Measured Versus Predicted Temperature--RH Case Acreage at Station 931.5 (215-deg location)

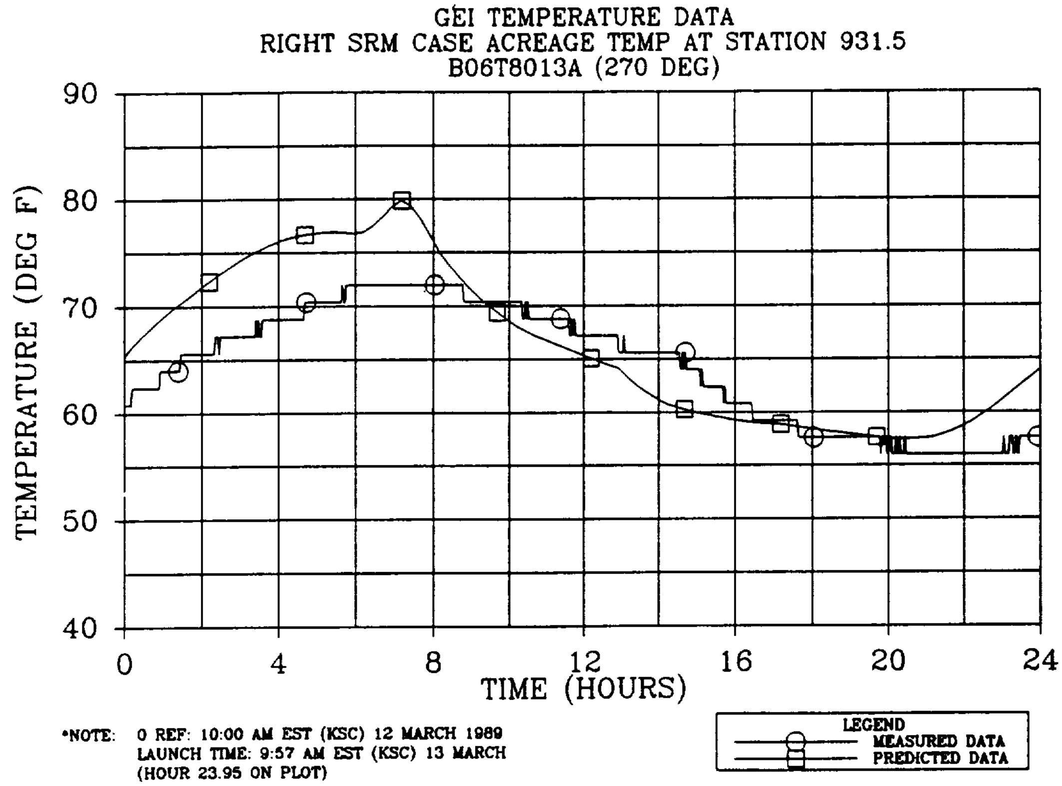

Figure 4.8-130. Measured Versus Predicted Temperature--RH Case Acreage at Station 931.5 (270-deg location)

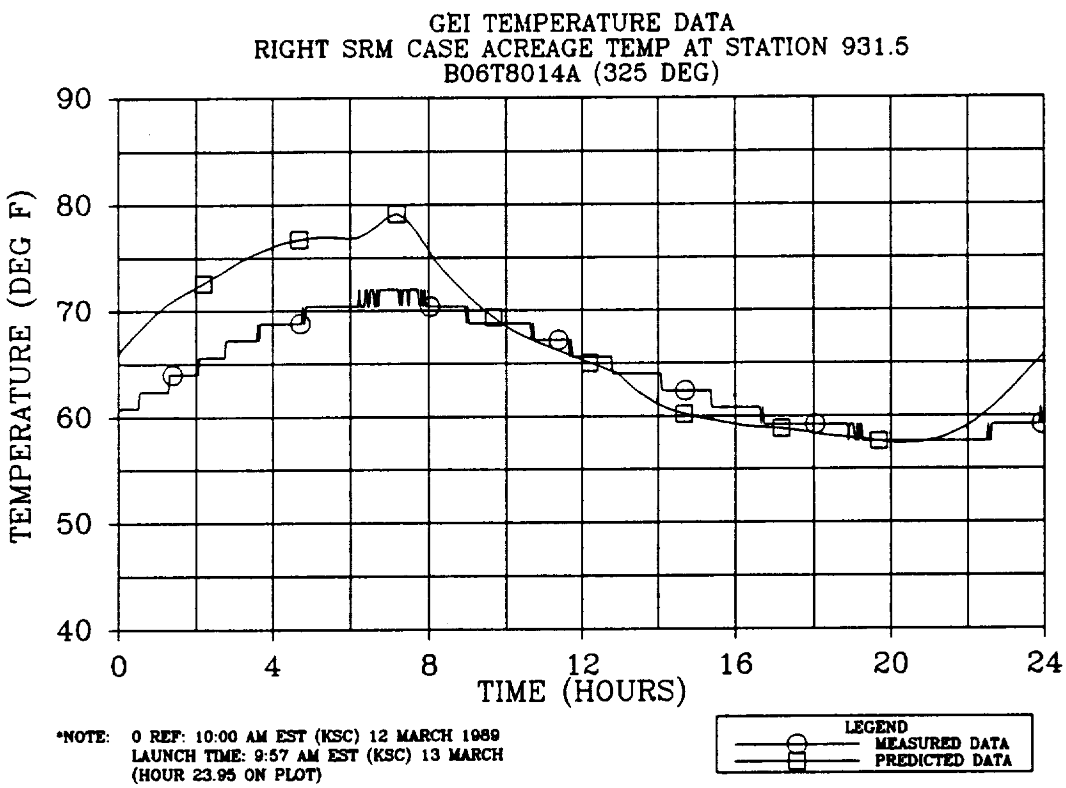

Figure 4.8-131. Measured Versus Predicted Temperature--RH Case Acreage at Station 931.5 (325-deg location)

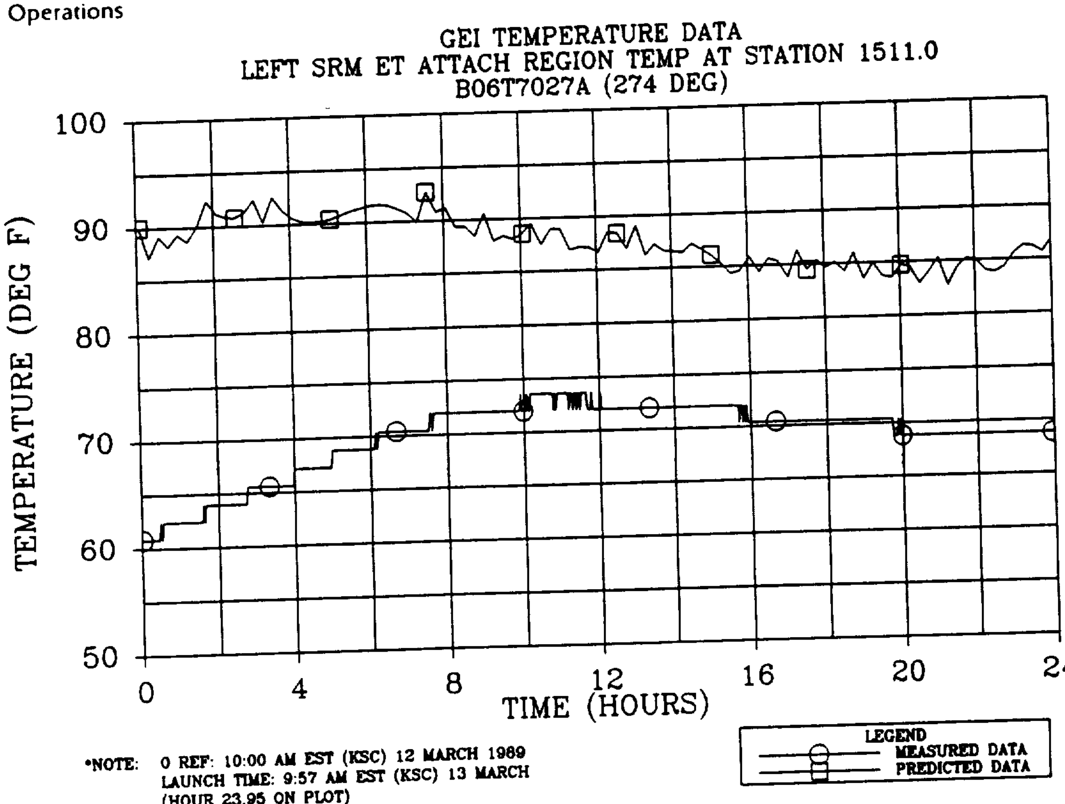

Figure 4.8-132. Measured Versus Predicted Temperature--LH ETA Region at Station 1511.0 (274-deg location)

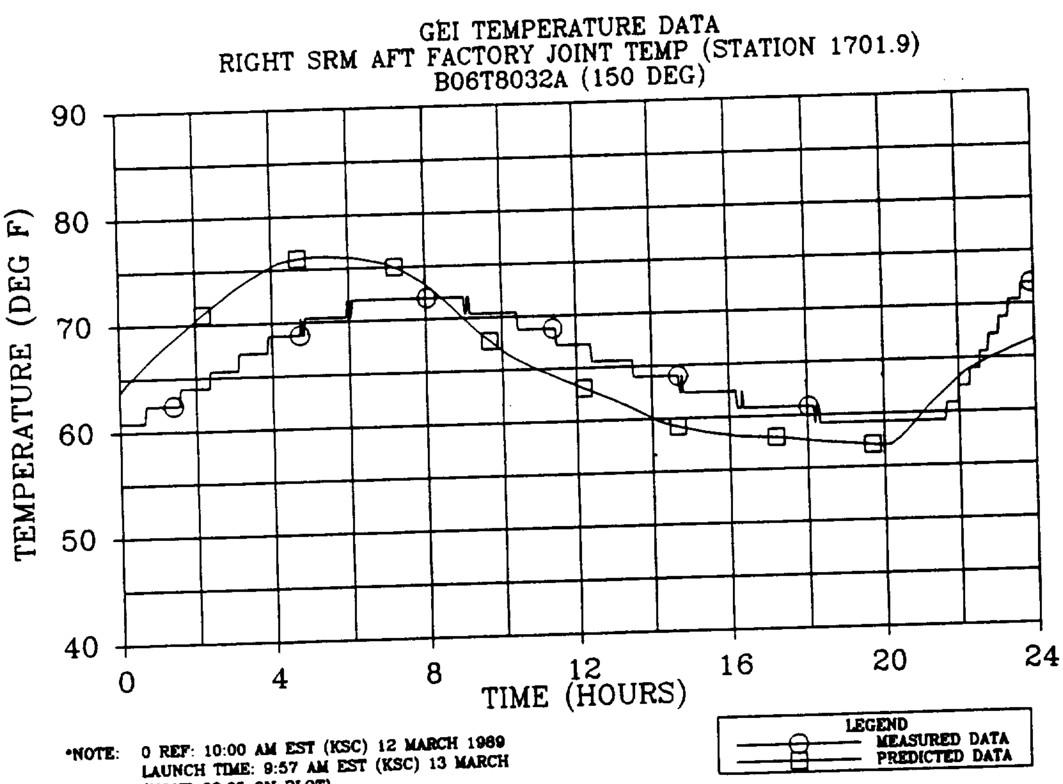

Figure 4.8-133. Measured Versus Predicted Temperature--RH Aft Factory Joint at Station 1701.9 (150-deg location)

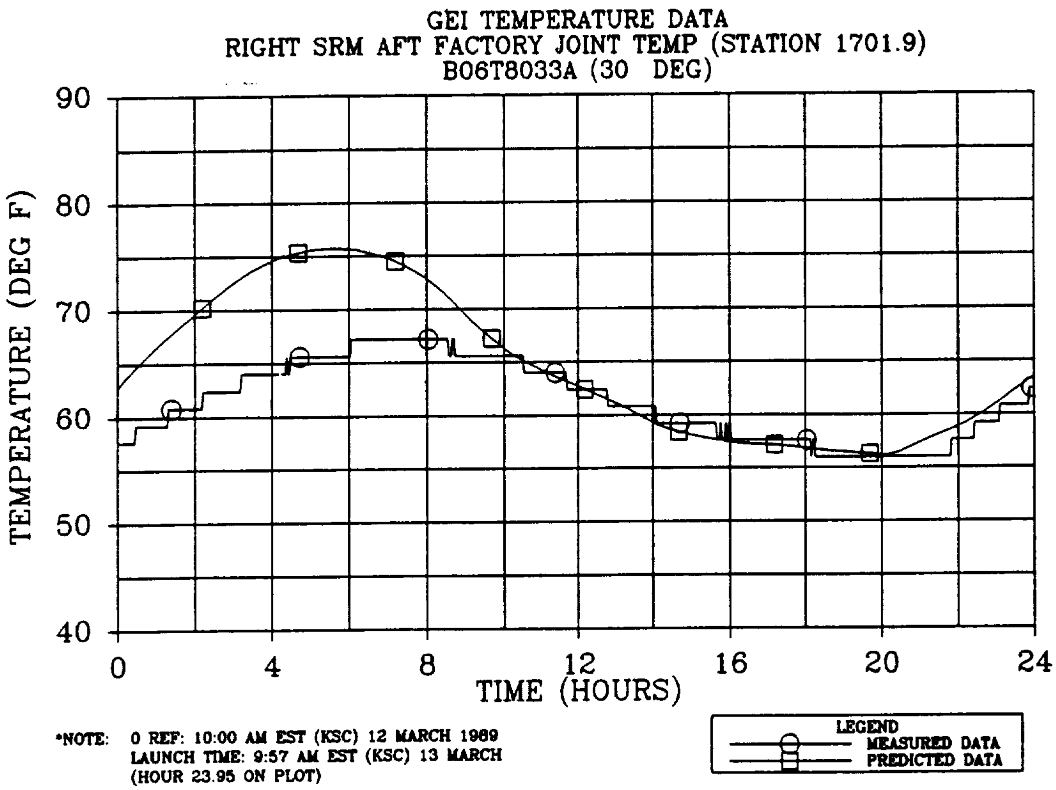

Figure 4.8-134. Measured Versus Predicted Temperature--RH Aft Factory Joint at Station 1701.9 (30-deg location)

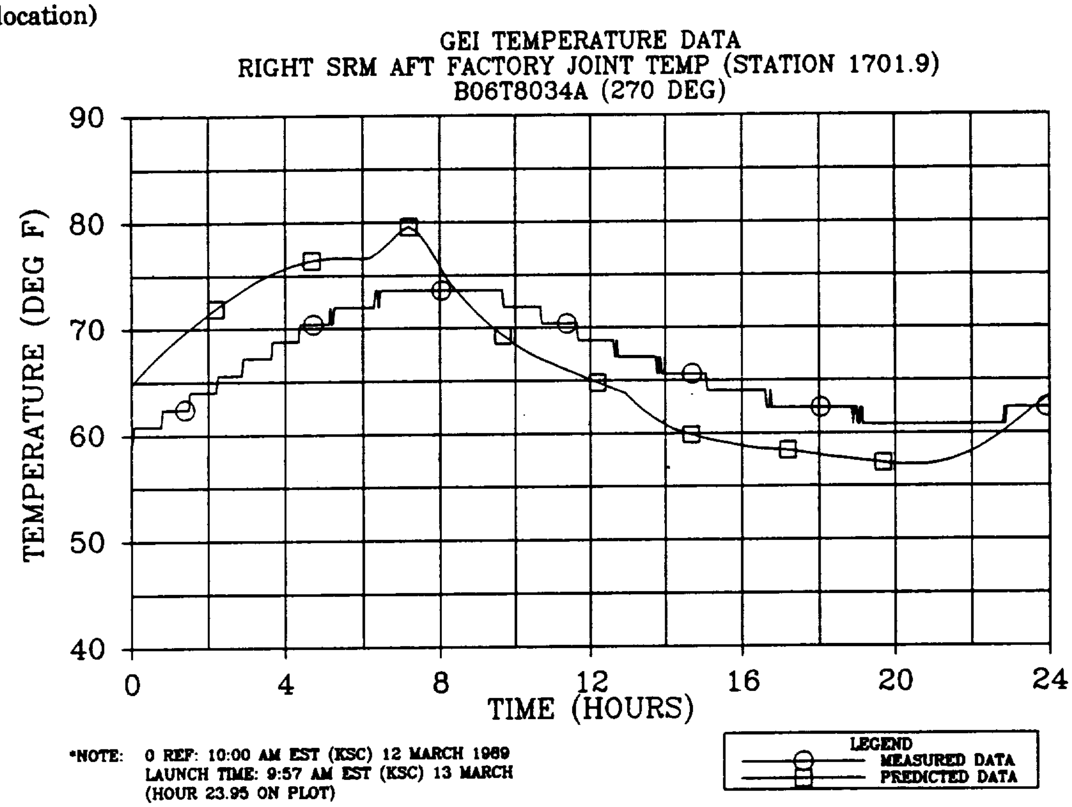

Figure 4.8-135. Measured Versus Predicted Temperature--RH Aft Factory Joint at Station 1701.9 (270-deg location)

IR temperature measurements were taken for the T - 3 hr timeframe from the portable STI. No IR gun readings were taken due to a malfunction during pad walkdown. Measurements from a fixed STI were verbally reported for the outboard area of the LH SRB. These measurements, between 59° and 61°F, were comparable with GEI data.

4.8.4 Conclusions and Recommendations

4.8.4.1 Postflight Hardware Inspection. Based on the quicklook external inspection, the SRM TPS performed adequately on STS-29R. The problem of losing TPS cork caps covering the instrumentation cables due to poor cork bonds appears to have been alleviated. Those areas that were found to be unbonded were vented prior to launch by drilling ventholes through the cork. Some of the instrumentation cable runs on STS-29R were filled with K5NA, as recommended following cork losses experienced on STS-26R. The K5NA performed well, as expected, and provided the necessary thermal protection to the cables, which have a temperature limit of 500°F.

4.8.4.2 Flight Thermal Design Environments. It is evident, based upon STS-29R nozzle region DFI response, that additional body points and environments for hydrazine fires need to be incorporated into the reentry design environments for the SRB base region. It is recommended that NASA consider incorporating these data into the next revision of the reentry thermal design environment data book.

4.8.4.3 GEI Prediction. Additional model development is recommended for modeling regions that require more emphasis and detail in order to improve predictions. Submodels of the ETA ring, field joint, factory joint, systems tunnel, igniter, and nozzle regions are anticipated to be incorporated into the global thermal effort. It is also recommended that all these models, including the 3-D SRM model, be made available for use at MSFC. This would allow Morton Thiokol thermal personnel the opportunity to support launch countdowns at the HOSC with real-time PMBT, GEI, and component prediction updates. This would also allow MSFC thermal personnel the same modeling capabilities for their needs.

4.8.4.4 Aft Skirt Conditioning. It is apparent, based on the STS-29R GEI sensor steady state response to the operation of the aft skirt conditioning system, that substantial gas cooling occurs in the ducting system before the gas enters the aft skirt. It is recommended that the gas temperature be monitored as it enters the aft skirt compartment. During cold weather this would allow the use of a higher operating temperature and at the same time not violate the 115°F maximum within the compartment.

4.8.4.5 GEI Accuracy. It is recommended that GEI data collection accuracy be increased by reducing the gage range and increasing the digital word length.

4.8.4.6 Real-Time Data Acquisition. It is recommended that near-real-time on-pad GEI and environmental data be available to Morton Thiokol after pad validation. These data, collected hourly, need to be transmitted electronically at weekly intervals until 2 weeks prior to scheduled launch dates. From this point until launch, daily transmittals are necessary. These data are necessary to help meet the requirement of PMBT updates prior to launch and to aid in predicting the local SRM environment by building a variable conditions data base.

4.8.4.7 Nozzle Severance

Based on the severe reentry heating environments of STS-29R, it is recommended that nozzle severance occur just prior to splashdown rather than at apogee. Reentry nozzle flame heating was significant for this flight, exceeding the 95-percent design environments.

It is also recommended that Thiokol obtain formal contract direction concerning hydrazine fires before the redesign of the nozzle severance cable.

4.8.5 Thermal Prediction Methodology

Methodology will be presented for PMBT, GEI, and component predictions due to on-pad natural and induced environments. Also, methodology will be presented for DFI and component predictions, including TPS recession, due to flight-induced environments.

4.8.5.1 Flight Induced DFI and Component Predictions. Component design analyses due to current flight-induced thermal loads were performed during the redesign effort and will be documented in the SRB Thermal Design Data Book, SE-019-068-2H. Estimates for DFI locations were inferred from these analyses and summarized.

The current design loads were developed for a conservative trajectory which is not included in presently planned flight trajectories. Since thermal loads data were not available for the trajectory of STS-29R, there will be no direct correlation possible with actual DFI data.

Actual DFI data were used for determining if design predictions were exceeded. If they were exceeded, the design analyses and environments were to be readdressed to identify problem areas and to update and/or modify analytical models.

4.8.5.2 On-Pad PMBT and Flex Bearing Predictions. PMBT and flex bearing predictions were performed using on-pad environmental and GEI measurements. However, these data were limited due to availability and access problems. From these data, boundary conditions were derived for a coarse 3-D global thermal model in predicting PMBT and for a 2-D axisymmetric model of the aft end in predicting FBMBT.

Two possible methods were considered in making the predictions. The first involved using the environmental data (convecting to the ambient and adding solar heating where appropriate). The predicted surface temperatures from this method could then be compared to the case acreage GEI in an attempt to perfect modeling techniques. The second method was to apply the GEI data directly to the model as imposed surface temperatures. This method will be considered when time permits.

4.8.5.3 On-Pad GEI and Component Predictions. Four methods were considered. Three of the four are concerned with predicting boundary conditions using March historical data. Results from these three were applied to a coarse 3-D SINDA global thermal model of the SRM for predicting case acreage GEI and joint heater sensor response. 2-D axisymmetric and planar models were considered for other regions, such as the systems tunnel and the aft end components. The fourth method was an estimation based upon near-real-time GEI and environmental data, and this method was used to supplement and update the results of the other three during HOSC support. The four methods are detailed below.

a. Historical ambient correlations using natural environments--This method was used to predict historical average monthly boundary conditions for the month of March based upon solar heating, predominant windspeeds, and ambient temperature cycling.

   Monthly averaged heat transfer coefficients were calculated using the NASA large cylinder correlation for every hour of the day. Solar heating input was calculated using the methods described in standard solar heating texts for a single, monthly averaged daily insolation profile to represent all days of the month. Shading aspects were also considered through experimental use of a model representing the STS on the MLP with service structures. This model was mounted on a heliodon, and shading factors were visually estimated.

b. 3-D flow/thermal modeling using natural and induced environments--This method was used to predict boundary conditions due to ET cooling effects (local air temperatures and heat transfer coefficients) during final countdown while the ET was loaded.

   The geometry that was used consisted of the STS on the MLP, the orbiter support structure, the concrete hardstand, and the flame trenches. It can be used for modeling winds originating from the north, northeast, east, southeast, and south. Historically, March winds are predominantly from the southeast, and this was considered for STS-29R.

c. Experimental with near-real-time data--This method is used to experimentally predict local heat transfer coefficients at GEI locations during preflight activities and at IR locations during postflight activities.

   This task has not been accomplished at this time but will be considered in future correlations in an attempt to data base heat transfer coefficients for a given wind direction, windspeed, and ambient temperature. The task will consist of calculating local heat transfer coefficients by measuring the change in skin and ambient air temperature over a period of time. This will be correlated to the average weather conditions existing over this time period (windspeed, wind direction, and ambient air temperature). It would also be advantageous to correlate it with the internal bore temperature. Response due to solar heat flux to the surface will be taken into consideration. A calculated solar component will be removed from the measured value.

For future efforts after development flights, a data base of overall local heat transfer coefficients could be generated for a spectrum of windspeeds, wind directions, and ambient air temperatures. Heat transfer models will access and extrapolate from this data base. These coefficients will also take into account the complex airflow pattern around the motors, the specific locations on the motors, radiation interchange with the surrounding surfaces, and radiation to the sky.

d. Estimates from near-real-time and projected weather data--This method is used to estimate GEI response at the time of launch by interpreting previously collected (prior week) GEI and environmental data and projecting with day-of-launch weather predictions.

   This determination was based upon having a near-real-time update available prior to HOSC support. This update was at two intervals--one week's worth of data before leaving Morton Thiokol for the HOSC supplemented with T - 36 to T - 6 hr data at the HOSC. Results from the previously discussed methods and projected weather data were taken into consideration. This effort provided the final T - 6 hr to T - 5 min predictions.

4.9 MEASUREMENT SYSTEM PERFORMANCE (DFI) (FEWG REPORT SECTION 2.9.5)

4.9.1 Developmental Flight Instrumentation Performance

Of the 417 SRM DFI measurements, 389 were operative at lift-off. Of those that were operative at lift-off, 375 (96 percent) performed properly throughout their respective mission phases. Table 4.9-1 lists the DFI measurements that failed prior to or during flight. Additional information on the DFI performance is contained in Volume IX of this report.

4.9.2 Girth Gage Spiking

As was mentioned previously in Section 4.6.3 of this volume, the data of the center and aft field joints of the RH SRM contained spikes similar to those seen on 360L001 and 360L002. There were also a few other gages that showed similar spiking behavior. Table 4.9-2 contains a list of the gages that showed some degree of spiking. (It should be noted that Table 4.9-2 is not a comprehensive list of all spiking gages.)

An engineering spiking investigation team concluded that the girth gage spikes were an instrumentation phenomenon and are not representative of actual case movement or behavior. This conclusion was partially based on the fact that there were locations where the girth gages showed some spiking and biaxial gages that were placed very close to the girth gage showed no evidence of spiking.

Another significant point that indicates this is an instrumentation phenomenon is the spike timing. As can be seen in Table 4.9-2, all the spike events occur around 0.25 sec (with the exception of two that are noted to be data acquisition system "glitches").

Table 4.9-1. Questionable/Bad DFI

Instrument No.	Location (deg)	Station	Measurement Direction	Measurement Type	Case Location	Instrument Condition
B08G7261A	270.0	1330.00	Axial	Strain, Biaxial	Aft Center Segment	Bad--Data clipped, switched with B08G7262A
B08G7262A	270.0	1330.00	Tangential	Strain, Biaxial	Aft Center Segment	Good--Switched with B08G7261A
B08G7278A	NA	857.28	Hoop	Strain, Girth	Forward Center Segment	Gage lost at VAB
B08G7284A	NA	1168.53	Hoop	Strain, Girth	Forward Center Segment	Lost during heater installation, bad
B08G7287A	NA	1175.03	Hoop	Strain, Girth	Aft Center Segment	Gage bad at VAB
B08G7288A	NA	1177.28	Hoop	Strain, Girth	Aft Center Segment	Gage bad at VAB
B08G7292A	NA	1411.48	Hoop	Strain, Girth	Aft Center Segment	Gage bad at VAB
B08G7294A	NA	1488.53	Hoop	Strain, Girth	Aft Center Segment	Bad--isol at VAB
B08G7295A	NA	1490.17	Hoop	Strain, Girth	Aft Segment	Bad--isol at VAB
B08G7296A	NA	1492.58	Hoop	Strain, Girth	Aft Segment	Bad--isol at VAB
B08G7311A	NA	1872.45	Hoop	Strain, Girth	Aft Dome	Bad--Noisy
B08G7312A	NA	1872.95	Hoop	Strain, Girth	Fixed Housing	Bad--Noisy
B08G7335A	0.0	1196.48	Tangential	Strain, Biaxial	Aft Center Segment	Bad
B08G7348A	270.0	1466.00	Axial	Strain, Biaxial	Aft Center Segment	Gage bad at VAB
B08G7349A	270.0	1466.00	Tangential	Strain, Biaxial	Aft Center Segment	Gage bad at VAB
B08G7374A	320.0	1497.00	Axial	Strain, Biaxial	Aft Segment	Good--Switched with B08G7375
B08G7375A	320.0	1497.00	Tangential	Strain, Biaxial	Aft Segment	Good--Switched with B08G7374
B08G7392A	320.0	1501.00	Axial	Strain, Biaxial	Aft Segment	Good--Switched with B08G7393
B08G7393A	320.0	1501.00	Tangential	Strain, Biaxial	Aft Segment	Good--Switched with B08G7392 and offset
B08G7396A	285.0	1501.00	Axial	Strain, Biaxial	Aft Segment	Gage bad at VAB
B08G7400A	255.0	1501.00	Axial	Strain, Biaxial	Aft Segment	Bad--Lost at VAB, switched with B08G7401
B08G7401A	255.0	1501.00	Tangential	Strain, Biaxial	Aft Segment	Good--Switched with B08G7400
B08G7405A	0.0	1797.00	Tangential	Strain, Biaxial	Aft Segment	Gage bad at VAB
B08G7413A	0.0	1871.80	Tangential	Strain, Biaxial	Fixed Housing	Bad--Noisy
B08G7423A	180.0	1871.80	Tangential	Strain, Biaxial	Fixed Housing	Bad--Noisy
B08G7450A	90.0	1834.00	Axial	Strain, Biaxial	Throat Assembly	Bad--Lost at VAB
B08G7460A	220.0	1511.00	Axial	Strain, Biaxial	Aft Segment	Bad--Lost in flight
B08G7461A	220.0	1511.00	Tangential	Strain, Biaxial	Aft Segment	Bad--Lost in flight
B08G7464A	285.0	1511.00	Axial	Strain, Biaxial	Aft Segment	Gage bad at VAB
B08G7467A	320.0	1511.00	Tangential	Strain, Biaxial	Aft Segment	Bad--Lost in flight
B07P7399A	79.0	763.50		Pressure, SRM	Forward Segment	Bad--Lost during flight
B07T7621A	270.0	1845.00		Temperature, SRM	Throat Assembly	Gage bad at VAB
B47P1302A		487.00		OPT	Igniter	Bad--Noisy
B08D8174A	270.0	1914.00	Tangential	Vibration, SRM	Exit Cone	Gage bad at VAB
B08G8261A	270.0	1330.00	Axial	Strain, Biaxial	Aft Center Segment	Gage bad at VAB
B08G8274A	NA	848.53		Strain, Girth	Forward Segment	Bad--isol at VAB
B08G8278A	NA	857.28		Strain, Girth	Forward Center Segment	Gage bad at VAB
B08G8284A	NA	1168.53		Strain, Girth	Forward Center Segment	Bad--isol at VAB
B08G8293A	NA	1486.78		Strain, Girth	Aft Center Segment	Bad--isol at VAB

89857-7.9

Table 4.9-1. Questionable/Bad DFI (Cont)

Instrument No.	Location (deg)	Station	Measurement Direction	Measurement Type	Case Location	Instrument Condition
B08G8294A	NA	1488.53		Strain, Girth	Aft Center Segment	Bad–Lost during heater installation
B08G8305A	NA	1834.75		Strain, Girth	Aft Segment	Gage bad at VAB
B08G8306A	NA	1836.20		Strain, Girth	Aft Segment	Gage bad at VAB
B08G8308A	NA	1861.00		Strain, Girth	Fixed Housing	Bad–Noisy
B08G8421A	90.0	1874.18	Axial	Strain, Biaxial	Aft Dome	Bad
B08G8462A	285.0	1511.00	Axial	Strain, Biaxial	Aft Segment	Bad–Data clipped, switched with B08G8463
B08G8463A	285.0	1511.00	Tangential	Strain, Biaxial	Aft Segment	Good–Switched with B08G8462
B07T8607A	180.0	846.30		Temperature, SRM	Forward Segment	Bad–Data dropout
B47P2301A		487.00		OPT	Igniter	Bad–Noisy

89857-7.10

Table 4.9-2. Summary of Girth Gages That Contain Spiking

Gage	Station	Time (sec)	Direction	Comments
LH SRB				
B08G7269	611.5	0.2625	Hoop (girth)	Small spike on the way up--does not exceed overall maximum
B08G7298	1497.5	0.11875	Hoop (girth)	Big spike shortly after ignition--does not exceed overall maximum; may be a glitch in the data acquisition system
B08G7410	1797.0	0.2875	Hoop (girth)	Small spike on the way up--does not exceed overall maximum
RH SRB				
B08G8283	1168.8	0.225	Hoop (girth)	Noisy at ignition with a small negative spike
B08G8285	1170.2	0.225	Hoop (girth)	Same as above
B08G8286	1172.6	0.225	Hoop (girth)	Same as above
B08G8287	1175.0	0.26875	Hoop (girth)	Spikes similar to those seen on 360L001 and 360L002; exceeds overall maximum of the gage
B08G8288	1177.3	0.26875	Hoop (girth)	Same as above
B08G8342	1466.0	0.11875	Axial	Big negative spike; one data point only--may be a "glitch" in the data acquisition system
B08G8295	1490.2	0.29375	Hoop (girth)	Spikes similar to those seen on 360L001 and 360L002; exceeds overall maximum of the gage
B08G8296	1492.6	0.29375	Hoop (girth)	Same as above
B08G8297	1495.0	0.29375	Hoop (girth)	Same as above
B08G8298	1497.5	0.29375	Hoop (girth)	Same as above
B08G8301	1637.5	0.2875	Hoop (girth)	Same as above, except there are two spike points of equal magnitude very close together.
B08G8410	1797.0	0.2875	Axial	Spikes on the way up, does not exceed overall maximum.
B08G8307	1859.19	0.09375	Hoop (girth)	Negative spike right at ignition, followed by some noise.

Figure 4.9-1 is a comparison plot that shows four girth gages on the RH aft field joint overlaid with motor pressure. Normally, the girth gage readings track the motor pressure; in other words, the girth gage is expected to peak at the same time that the motor pressure peaks. However, as can be seen in Figure 4.9-1, peak motor pressure is not reached until about 0.6 sec, whereas the girth gage spiking and peaks all occur at about 0.25 sec. A preliminary evaluation indicates that this 0.25-sec time may be associated with the gage natural frequency and/or configuration.

As was also mentioned previously in Section 4.6.3.3, some girth gages on the RH SRB also showed a response delay of about 0.25 sec. This delay phenomenon is also believed to be related to the above-mentioned girth gage spiking phenomenon.

It is recommended that additional investigation be conducted to more fully understand the girth gage spiking phenomenon, including the addition of DFI on future flight motors.

4.10 MEASUREMENT SYSTEM PERFORMANCE (GEI) (FEWG PARAGRAPH 2.9.7)

A total of 105 GEI measurements that were on flight set 360L003 performed properly. Therefore, of the total 108 GEI measurements, 97 percent performed properly throughout their respective mission phases. Table 4.10-1 lists the GEI measurements that failed prior to flight. (All GEI are disconnected by breakaway umbilicals at SRB ignition and are not operative during flight.) A complete listing and evaluation of all the GEI are contained in Volume IX of this report.

Table 4.10-1. GEI Losses

MSID No.	Angular Location	Station	Comments	Instrument Condition
BO6T7015A	45.0	1091.48	Forward/Center Segment	Shorted at VAB
BO6T8018A	270.0	1091.48	Forward/Center Segment	Shorted at VAB
BO6T8049A	180.0	1876.60	Case-to-Nozzle Joint	Read consistently low

4.11 RSRM HARDWARE ASSESSMENT (FEWG REPORT SECTION 2.11.2)

4.11.1 Insulation Performance

4.11.1.1 Summary. Postflight evaluation showed excellent insulation performance. No evidence of motor combustion gas was found past the insulation in the six field joints or two case-to-nozzle joints. No gas paths or severe erosion was identified in any acreage insulation. All external insulation was in good condition, with the exception of the LH aft center segment factory joint. Complete insulation evaluation is contained in Volume III of this report.

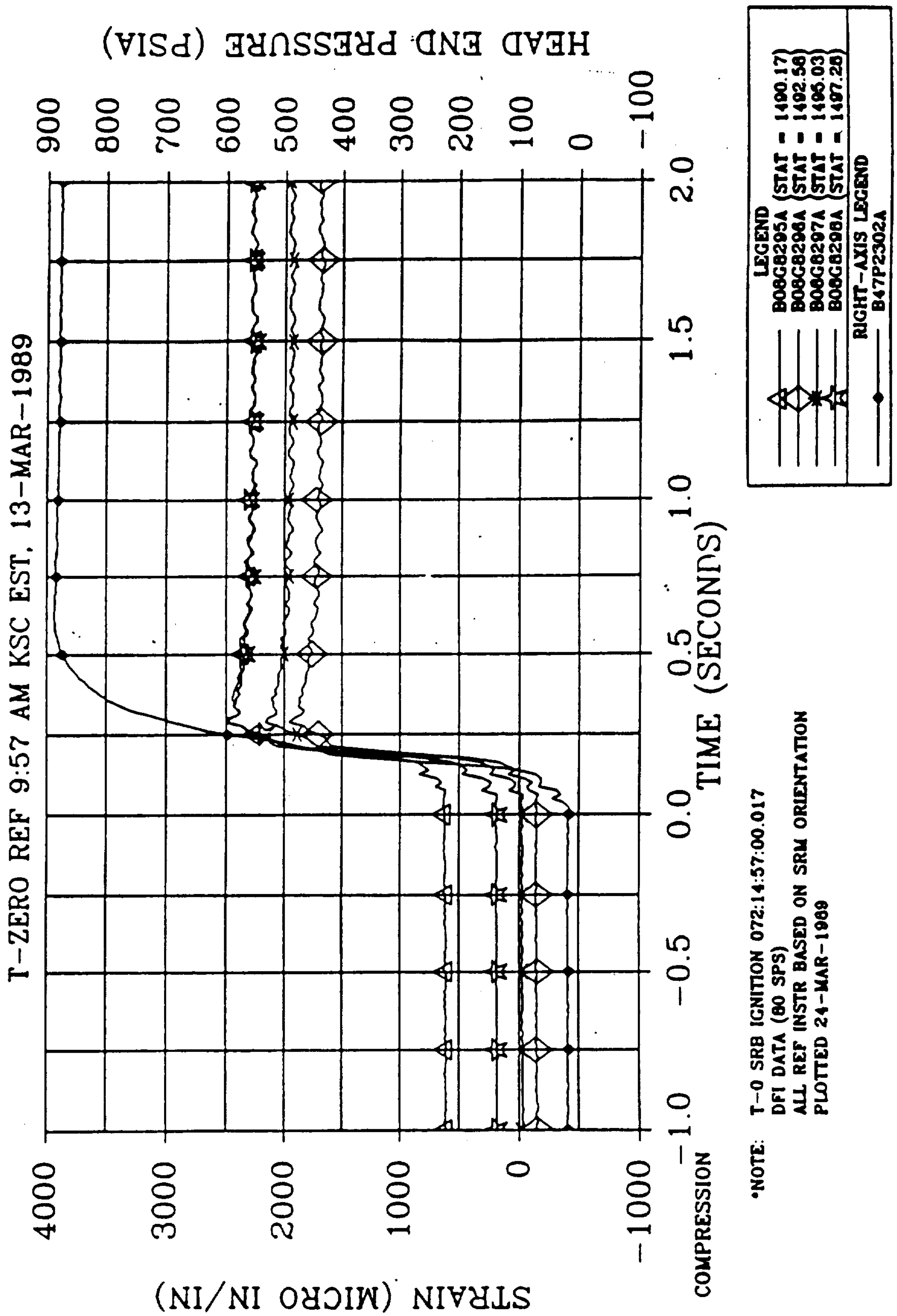

Figure 4.9-1. RH Motor Hoop Strain (girth) Overlaid With Motor Pressure

4.11.1.2 External Insulation

Factory Joint Weatherseals. The factory joint weatherseals and exterior motor cases appeared to be in good condition. However, the weatherseal on the 360L003A aft center segment was unbonded on the aft edge in 11 places. The largest unbond extended 58.3 in. circumferentially and exhibited adhesive failure at the Chemlok® 205-to-case interface. The pin retainer band was also stretched, and the pins were visible. The total unbond area covered approximately 57 percent of the circumference on the aft edge. The unbonding appears to be the result of bondline contamination and is being further evaluated.

Moisture was found dripping from under the weatherseal on the 360L003B forward center segment factory joint. The water appeared to have entered the weatherseal at the locations where DFI instrumentation wires or insulation cure thermocouple wires were routed between the weatherseal and the case. The weatherseal was very well bonded in all other areas.

This same condition was noted on multiple segments of the 360L002 flight set. The closeout of the wire exit locations is being reevaluated to eliminate problems on future flights. No significant areas of missing EPDM insulation were noted on any factory joint weatherseal.

Stiffener Stubs and Rings. The insulation over the stiffener stubs and rings was in good condition. Normal heat effects and discoloration were evident on all surfaces, with no significant areas of missing material. The EPDM was well bonded to the stiffener stubs and appeared to be well bonded to the stiffener rings, as evidenced by a tap test of all exposed surfaces prior to hydrolazing. The only exceptions were on the 360L003B RH motor, where the stiffener rings were buckled due to impact loads and the insulation was visibly unbonded.

After the rings were removed from the case, separations were noted between the insulation and stiffener rings on approximately a third of the 18 ring segments. A similar condition was noted on the 360L002 flight set. Most of the unbonds occurred on the 360L003B motor, which was more thoroughly hydrolazed than the 360L003A. The largest separation measured the full length of the ring segment. Pieces of K5NA ablation compound were found under the EPDM as much as 39 in. from the end of the ring segment. Insulation Design believes that hydrolazing is the major contributor to these unbonds.

4.11.1.3 Case-to-Nozzle Joint. Based on the visual evaluation, both case-to-nozzle joints performed well. No gas paths through the polysulfide adhesive or any other anomalous conditions were identified. The polysulfide adhesive had only two measurable voids aft of the insulation step on the 360L003A joint.

The largest void was 0.85 in. axially by 0.50 in. circumferentially. There were three voids on the 360L003B joint forward of the insulation step. All three voids were eroded as a result of the normal ablation process. However, no hot gas penetrated beyond the insulation step. The largest of the three voids measured 2.8 in. circumferentially and extended to the step. The 360L003A motor exhibited a high amount of adhesive failure upon disassembly (75 percent). This can be attributed to inadequate NBR abrasion prior to joint assembly. The high amount of adhesive failure had no effect on the function of the joint.

The 360L003B joint had good cohesive failure of the polysulfide (95 percent). The average polysulfide vent slot fill was 11 percent on 360L003A and 5 percent on 360L003B.

4.11.1.4 Field Joints. The internal insulation in all six of the case field joints performed as designed, and no anomalous conditions were identified.

J-leg tip contact was evident over the full circumference at each joint. Wet soot deposits extending down the bondline were noted on all of the 360L003 field joints to a fairly uniform depth (0.3 to 0.6 in.). The most extreme condition was on the 360L003A forward field joint, with soot extending a maximum of 0.9 in. into the bondline (outboard from the remaining material). The initial appearance of these areas could have been construed to be chamber gas leakage into the joint bondline, but the soot was readily removable with solvent and showed no heat-affected insulation. Wet sooting was noted further into the bondline on the 360L001 forward field joints and extended to the radius region. This sooting is believed to have occurred at splashdown during joint flexing in conjunction with the phenomena which generates the radial tears in the NBR inhibitor stubs.

An area that appeared to be dry soot was also noted in the 360L003B aft field joint outboard of the wet sooted region. The soot was visible in an adhesive glossy region approximately 1 in. outboard of the J-leg tip. The soot did not fill the entire glossy noncontact area and left no indication of heat effects after solvent cleaning. A theory for this occurrence is that, during motor reentry, the internal pressure is decreasing and increasing ("chugging"). During this process, partial joint insulation contact may be lost. When the motors splash down, wet sooting occurs, as discussed above. In this instance, the wet sooting did not penetrate to the depth that the joint had opened during reentry.

The deepest clevis edge separation noted measured 0.21 in. axially by 1.1 in. circumferentially on the 360L003A aft center segment. Only two segments had recordable (over 0.1 in.) edge separations, and the total separation count was only five. This was significantly less than on the previous two flights. This hardware was the first flight set to incorporate grit blasting of the inner clevis leg. The process appears to have significantly improved the postfire edge separation condition.

4.11.1.5 Internal Acreage Insulation. The acreage insulation, including the internal insulation over each of the factory joints, appeared in good condition during the preliminary evaluation. No evidence of gas paths through the insulation or severe erosion was identified.

Center Segments. A few tears greater than 3 in. radially were noted in the aft center segment inhibitor stubs (four on 360L003A and three on 360L003B). Some radial tears were also noted in the forward center segment NBR inhibitor stubs (3 on 360L003A and 22 on 360L003B). The largest tear measured 18.5 in. radially, but most of the tears ranged from 12.0 to 14.0 in. radially. One of the tears extended radially outward to approximately 5.0 in. inboard from the clevis inside diameter (ID). The radial extent and frequency of the tears identified in the inhibitor stubs are within the range of tears noted on past flight motors. The edges of the tears appeared rough and could be placed together, demonstrating no material loss or erosion. This indicates that the tears occurred after motor burn.

Forward Segments. The stress relief flap was present over the full circumference on both forward segments but was severely heat affected. Up to half of the flap length was eroded for part of the circumference. The castable inhibitors were completely missing over the full circumference. Some axial tears were identified on the remaining heat-affected flap, similar to 360L001, which had numerous flap tears. A final evaluation of the thermal performance of the insulation will be accomplished after the remaining material is measured at the Clearfield H-7 facility.

4.11.2 Case Component Performance

4.11.2.1 Summary. Fretting was observed on five of the six field joints. Overall, this flight exhibited fretting comparable to 360L002 (STS-27). A few of the pits measured slightly deeper (as deep as 0.013 in.) than those from 360L002. Figure 4.11-1 shows the relative location of the fretting. The 360L003 fretting was worse on the LH motor, while on 360L002 the RH motor fretting was worse. (On 360L001 (STS-26R) the fretting was relatively even.) Based on the last three flights, there is a bias towards the center and aft regions of the motors.

All three RH stiffener rings had cracks and buckles. There were a total of five outer ligament cracks on the boltholes of the corresponding stiffener case stubs. No metal damage was noted on the LH stiffener rings and stubs. The crack that was in the LH forward stiffener stub (at 24 deg) did not propagate during flight. A complete case evaluation is given in Volume II of this report.

4.11.2.2 Stiffener Rings and Stubs. All three RH stiffener rings had cracks and buckles. There were a total of five outer ligament cracks on the boltholes of the corresponding stiffener case stubs. The affected lightweight stiffener case segments are Part 1U50715, serial numbers 50 (aft position) and 54 (forward position).

The LH booster showed only hairline circumferential cracks in the K5NA closeout of the stiffener attach bolts. This was seen in the region where the ramp-up foam was torn away due to water impact centerline loads.

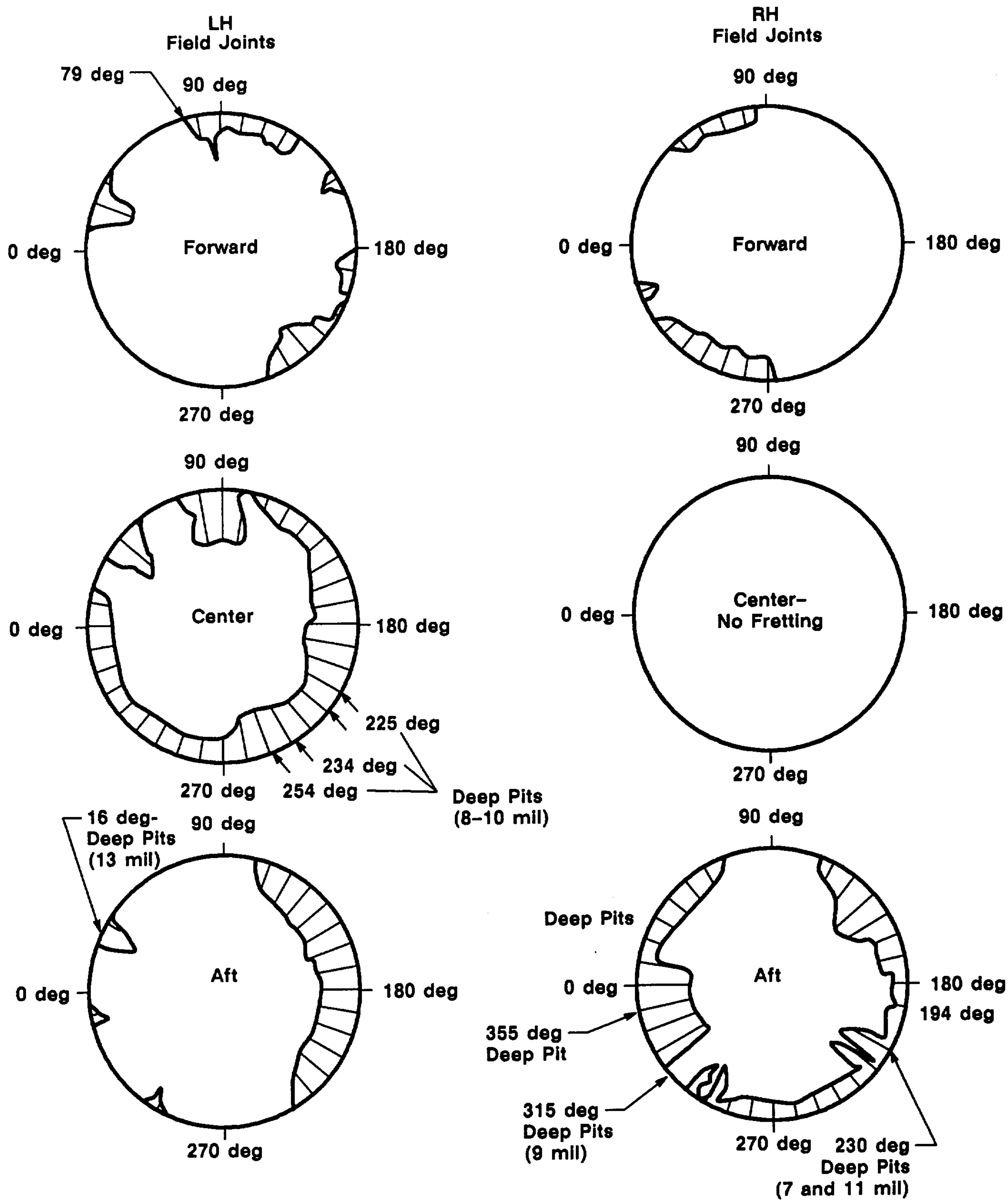

Figure 4.11-1. Fretting Summary

A022525a

The water impact damage on the RH booster was centered at approximately the 210-deg splice plate. "Knuckling" points are at about 180 and 240 deg. No inner ligament stubhole cracks were detected during this KSC assessment. However, significant stubhole elongation occurred in the 210-deg splice region. In three previous flights where water impact centered on a splice, inner ligament cracks were found. Magnetic particle inspection during the refurbishment of this flight's hardware will be more conclusive in detecting cracks in the stiffener cases. The 210-deg splice adapter plates (connecting the webs) were broken on each ring at about 211 deg. Boltholes--particularly in the ring--were elongated, or at least noticeably thickened, so that some load patterns could be discerned.

Water impact loads on the LH booster were centered at about 140 deg. A hairline crack on the K5NA closeout was evident on the aft faces of the center and aft rings. No new metal damage was noted. This booster flew with an outboard ligament crack at the 24-deg position under the forward stiffener ring. This crack was located. The paint on the forward face of the stub was unbroken, indicating no growth took place.

4.11.2.3 RH Aft Stiffener Ring and Stub. The RH aft stiffener ring damaged area extends from about 186 to 236 deg. Compression buckles (bent forward) in the ring web occurred at 190, 195, and 235 deg. The buckle at 195 deg was also cracked. A tension crack in the ring web was observed at 216 deg. The adapter plate was broken through the boltholes at approximately 211 deg.

There were 19 broken bolts in a span from 190 deg through 234 deg. The three bolts at 212, 214, and 216 deg were intact. The RH aft stiffener stub outer ligament cracks were located at 188 and 234 deg.

4.11.2.4 RH Center Stiffener Ring and Stub. The center stiffener ring damaged area extends from 178 to 250 deg. Compression buckles in the ring web were found at 180, 189, 231, 236, and 248 deg. The buckle at 189 deg was also cracked. The tension crack occurred at 218 deg. The adapter plate was broken at the 211 deg location, as above.

There were 29 bolts broken in a span from 180 through 248 deg. Again, there were three bolts in the center of the impact load which did not break (212, 214, and 216 deg). In addition, two "lone" bolts in the knuckling region did not break. These were at 188 and 238 deg. These two bolts were involved in the mechanism which caused outboard stub cracks.

The stiffener case stub under the center ring had two broken outer ligaments. One was at 238 deg--the exact location of one of the lone unbroken bolts. The other broken outer ligament was at 186 deg--the next bolt over from the lone unbroken bolt at 188 deg. As pointed out in the stiffener stub summary diagram, the hole at 188 deg was necked down and, therefore, close to cracking the outer ligament.

4.11.2.5 RH Forward Stiffener Ring and Stub. The forward stiffener damage extends from 174 to 248 deg. Compression buckles in the ring web occur at 188 and 244 deg. The tension crack in the ring occurred at 220 deg. In addition to cracking through the web, the crack extended through the flange at about 214 deg. The adapter plate was broken as in the rings above.

In this ring, 31 bolts were found to be broken. This breakage span was from 176 through 246 deg. Bolts at 212, 214, 216, and 218 deg were intact.

Only one stub outer ligament crack was noted at this ring location. This occurred at 240 deg.

4.11.2.6 Field Joint Fretting. Fretting was observed on five of the six field joints. Overall, this flight exhibited fretting comparable to the last flight (STS-27). A few of the pits measured slightly deeper (as deep as 0.013 in.) than those from the last flight. The relative locations of the frets are shown in Figure 4.11-1. Notice that this time the fretting was worse on the LH motor. On flight 360L002 (STS-27R), the RH motor fretting dominated. On 360L001 (STS-26) it was about even. No circumferential bias has been established yet. There may be a slight bias towards the aft ends of the motors based on the last three flights.

The RH motor had locally severe fretting on the aft joint. The center joint of that motor had no fretting. The forward joint had minimal fretting.

The LH motor was considerably affected. The center joint of this motor showed the most severe extent of fretting of any of the joints. The forward and aft joints had regions of moderate fretting.

Fretting is established as such for documentation if it can be felt (however lightly) by rubbing a fingernail across the pits or scratches. Depths of the deeper pits were determined by a plunging needle pit gage and by impression molds which were measured with an optical scanner.

Several small particles of metallic debris were collected this time. Some were embedded in the capture feature O-ring (due to disassembly). Some were scraped off the pitted areas of the inner clevis leg. Metallurgical test results indicate this metal debris reached temperatures of at least 1,500°F and possibly melting. Grease samples in the fretted region were also collected for testing of heat and chemical degradation.

4.11.2.7 LH Center-Aft Factory Joint Pin Retainer Band. After booster recovery from the ocean, it was noticed that the EPDM weatherseal on this joint was unbonded in several places around the case. This rubber adheres quite well to the pin retainer band. In the 340 to 0 to 20 deg region, the seal and metal retainer or hat band was lifted up enough at the aft edge to see the top of the joint pins. It was suspected that the hat band might be broken, stretched, or that the turnbuckle bolts might be stripped.

This seal was removed and the retainer band disassembled and inspected. No damage of any kind was found on any of the buckle components. It is now suspected that the band may simply have been stretched due to water impact, when the weatherseal probably debonded.

4.11.3 Seals Performance

4.11.3.1 Summary. All seals performed as expected during flight. All fluorocarbon seals, including the redesigned field joint and case-to-nozzle joint seals, performed well, with no heat effects, erosion, or hot gas leakage evident. A complete seal evaluation is contained in Volume IV of this report.

4.11.3.2 External Field and Factory Joints. There was no evidence of combustion product leakage at any joint.

4.11.3.3 Aft Exit Cone Field Joints. The LH aft exit cone field joint components suffered extensive damage. The primary O-ring became dislodged and cut at splashdown. A 3-in. piece was found between the GCP and the metal housing at aft exit cone demate, and other pieces were found within the motor during field joint disassembly. The secondary O-ring also was cut at splashdown. A piece was missing from 70 to 197 deg. There was no evidence of hot gas within or past the sealing area.

The RH aft exit cone field joint components were in good condition. The O-rings were free from erosion, heat effect, or any other damage, and the sealing surfaces and O-ring glands were devoid of soot, debris, or damage.

4.11.3.4 Case Field Joints. The case field joint O-rings, V_2 filler, and sealing surfaces appeared to be in excellent condition, with no evidence of heat effect or assembly damage. The grease application appeared to be per design. Typical corrosion was noted on unpainted surfaces of the joints outside of the sealing areas. The capture feature O-rings on the LH center and RH aft field joints were scuffed by fretting marks during disassembly. A fiber was found on the land between the primary and secondary O-ring grooves at 263 deg, probably due to disassembly.

4.11.3.5 OPT Special Bolt and Special Bolt Plug Seals. The OPTs, special bolts, and special bolt plugs were removed from the LH and RH motors. The seals all performed as designed, with no evidence of gas leakage past the primary seals. Three of the RH motor special bolts had soot on the bottom of the bolts and the fourth bolt had corrosion below the primary O-ring groove.

4.11.3.6 Ignition System Joints. Both S&A gaskets were in nominal condition, with no evidence of gas leakage past the primary seals. There was no evidence of heat or damage to the gaskets or S&A sealing surfaces.

The igniter inner and outer gaskets on both motors were in excellent condition. All seals performed as expected, with no evidence of heat effect or blowby. The RH outer gasket had soot on the retainer inboard of the primary seal on both the forward and aft faces. Soot was in contact with the primary seal on the forward face intermittently from 280 to 0 deg. This soot was in line with a blowhole through the putty, which is typical. No damage was found on the forward dome boss, adapter, or chamber sealing surfaces of either motor. All igniter inner joint Stat-O-Seals® showed typical disassembly damage to the fluorocarbon portions.

4.11.3.7 Case-to-Nozzle Joints. The overall joint condition was excellent on both motors. Motor pressure was halted at the polysulfide adhesive, leaving the fluorocarbon O-rings untouched. The polysulfide passed the wiper O-ring at 122 deg on the RH motor but did not reach the primary O-ring. All case-to-nozzle joint sealing surfaces and O-ring glands were devoid of heat effect, soot, foreign material, or damage. The only O-ring damage noted was a gouge (0.25 in. circumferentially by 0.125 in. axially by 0.025 in. deep) at 334 deg on the RH wiper O-ring. The gouge was caused by a radial bolthole plug during disassembly. The aft edge of the fixed housing assembly phenolic groove was also damaged at this location. A similar gouge was noted on the wiper O-ring on the previous flight. Ten radial bolthole plugs on the LH motor and 17 on the RH motor were broken or damaged during disassembly.

4.11.3.8 Vent Port Plugs. The case field joint and case-to-nozzle joint vent port plugs and seals on both motors were in excellent condition. There was no evidence of soot or heat effect on any vent port plug O-rings. Possible extrusion damage was found on the outside diameter of the RH aft field joint vent port plug around the full circumference.

4.11.3.9 Leak Check Port Plugs. The case field joint and case-to-nozzle joint leak check port plugs and seals on both motors were in good condition. There was no evidence of soot, heat effect, or damage on any leak check port plug O-rings. Slight surface corrosion was found on the spotface on one of the plugs.

4.11.4 Nozzle Performance

4.11.4.1 Summary. Postflight evaluation indicated both nozzles performed as expected during flight, with typical smooth and uniform erosion profiles. The 360L003A (LH) nozzle aft exit cone and joint suffered excessive splashdown damage. A complete nozzle evaluation is contained in Volume V of this report.

4.11.4.2 360L003A (LH) Nozzle

Aft Exit Cone. The 360L003 LH aft exit cone showed missing CCP liner and GCP insulator over the majority of the shell due to splashdown. The exposed aluminum shell showed no signs of heat effect. The primary O-ring was also missing due to splashdown (refer to aft exit cone field joint section). Traces of polysulfide remained on the forward end of the shell, but most was torn off at splashdown. GCP plies remained on the aft 6 in. of the shell around the entire circumference.

Spots of EA 946 adhesive remained on the exposed shell at 98, 153, 168, 205, and 235 deg. These spots of adhesive showed glossy finishes, which indicated that bondline voids were present prior to flight. Adhesive voids are expected due to assembly procedures and are not considered anomalous. The 45- and 135-deg actuator brackets were not damaged. All actuator bracket screws were still tight.

Forward Exit Cone Assembly. The forward exit cone showed missing CCP liner over the center 20 in. of the cone. This was due to splashdown and diver-operated plug (DOP) insertion. The GCP insulator exposed by the missing liner showed no signs of heat effect. The remaining CCP liner showed smooth erosion, with typical dimpled erosion appearing on the aft 7 inches.

Impact marks due to DOP insertion and loose phenolics at splashdown were also observed on the forward end of the remaining liner.

The forward 0.75 in. of the forward exit cone liner showed postburn wedgeouts at 5, 15, 65, 110, and 150 deg. The maximum radial depth of the wedgeouts was 0.65 inch.

The aft end of the forward exit cone showed separations between the EA 946 adhesive and the steel housing intermittently around the circumference. The maximum radial separation was 0.06 inch. Separations were also observed from 330 to 0 to 15 deg and at 120 deg between the CCP and GCP. These were a maximum of 0.08 in. wide radially. There were no cohesive separations or separations between the adhesive and GCP.

Throat Assembly. Erosion of the throat and throat inlet rings was smooth and uniform. Typical popped-up, charred CCP material was observed on the forward 1.5 in. of the throat ring at 312 and 357 deg.

Impact marks due to DOP insertion and loose phenolics at splashdown were observed on the throat ring liner. Popped-up, charred CCP material was also observed on the forward 0.8 in. of the throat inlet ring at 72 and 188 deg. Throat diameter measurements will be taken at the Clearfield H-7 facility.

Forward Nose (-503) and Aft Inlet (-504) Rings. The forward nose and aft inlet rings showed smooth erosion with no wedgeouts, pockets, or wash areas observed. The forward 1.3 in. of the -503 ring showed typical popped-up charred CCP material at 13, 119, 204, and 270 deg.

Nose Cap. The nose cap showed smooth erosion, with no pockets or major washes observed. Impact marks due to DOP insertion and loose phenolics at splashdown were observed on the forward end of the nose cap. The aft 2.4 in. of the nose cap showed postburn wedgeouts of charred liner from 122 to 161 and 220 to 360 to 40 deg. Popped-up, charred CCP material was also observed intermittently around the nose cap aft end.

Cowl Ring. The cowl ring showed smooth erosion, with no wedgeouts observed. Typical erratic erosion was observed on the cowl ring intermittently around the circumference. All cowl ventholes appeared to be plugged with soot and slag.

Outer Boot Ring. The outer boot ring (OBR) showed smooth erosion, with no wedgeouts. The forward 2 in. showed typical popped-up, charred CCP material at 90, 123, 165, 180, and 245 deg. The aft tip adjacent to the flex boot showed fractured, charred CCP material from 43 to 135 and 155 to 360 to 20 deg. The cowl-to-OBR bondline remained intact.

Fixed Housing Assembly. Fixed housing insulation erosion was smooth and uniform. Postburn wedgeouts were observed on the forward 2 in. at 97, 204, 240, 270, and 338 deg. The maximum radial depth of the wedgeouts was 0.45 inch. Slag deposits were minimal on the aft end of the fixed housing insulation (less than observed on 360L001 (STS-26) and 360L002 (STS-27)).

The fixed housing assembly aft end showed no bondline separations and no metal corrosion. The alignment pin (case-to-nozzle joint) showed two cracks. It is not known whether the cracks occurred before assembly, during assembly, or during disassembly.

Aft Exit Cone Field Joint. The backfilled RTV extended below the joint char line 360 deg circumferentially. RTV reached the high-pressure side of the primary O-ring intermittently around the joint. One unfilled void area was observed at 225 deg (0.20 in. radially by 0.25 in. circumferentially). There was no blowpath extending from the flow surface to the unfilled void area. The remainder of the joint circumference also showed no blowpaths.

The 360L003A (LH) aft exit cone field joint suffered damage as a result of splashdown. A separation from 80 to 180 deg (0.25 in. maximum) was observed between the forward and aft exit cones before disassembly. The majority of the primary O-ring was lost with the aft exit cone phenolics at splashdown. Following joint disassembly, a 3-in. section of the primary O-ring was found caught in a bondline separation on the forward exit cone aft end. The remainder of the primary O-ring was located inside the aft segment. The secondary O-ring was severed in two places, with the 71- to 197-deg arc completely missing.

Metal and bolt damage within the joint was observed from 56 to 206 deg. Helicoils® were pulled from the aft exit cone threaded holes from 71 to 198 deg. The aft exit cone aluminum threads were stripped in this range. The forward end of the aft exit cone shell also showed displaced metal at threaded hole locations. This damage may be cause for rejection of the aluminum shell. Three bolts were broken at 131, 135, and 142 deg. The remaining screws in the 56- to 206-deg range showed bending, flattened threads, and dings. The bolts and Helicoils® from 210 to 360 to 52 deg showed no damage. Half of the 91.8-deg alignment pin was fractured and missing. The forward exit cone aft flange throughholes showed displaced metal at 75, 78.75, 82.5, 183.75, and 195 deg. The 91.8-deg alignment pinhole also showed displaced metal. This damage is not cause for rejection of the steel forward exit cone housing.

Rust and aluminum oxide corrosion were observed within the joint outboard of the primary O-ring intermittently around the circumference. Severe rusting was observed on the aft end of the forward exit cone housing from 80 to 210 deg. Minor pitting was observed after the rust was scrubbed off, but the depth of the pitting did not exceed refurbishment repair specifications limits (0.010 in.). The aluminum oxide and rust observed around the remainder of the joint circumference was similar to that observed in the STS-26 (RH) aft exit cone field joints.

4.11.4.3 360L003B (RH) Nozzle

Aft Exit Cone. The 360L003B aft exit cone showed the entire CCP liner missing and portions of the GCP insulator torn and missing due to splashdown. The aft exit cone aluminum shell was exposed from 70 to 90 deg (2.5 ft circumferentially by 10 in. axially) forward of the compliance ring. The exposed GCP plies and aluminum shell showed no signs of heat effect. The missing CCP liner and GCP insulator are typical postflight observations and occurred during exit cone severance and at splashdown.

The 45- and 135-deg actuator brackets were not damaged. Minor paint scratches were observed. All actuator bracket screws were tight. Separations between the polysulfide and the aft exit cone shell were observed intermittently around the circumference. The maximum radial separation was 0.04 inch. Postflight measurements of the polysulfide groove radial width showed that the GCP insulator did not pull away from the aluminum shell during cooldown. The average postflight radial width of the groove was 0.20 inch. The polysulfide appeared to shrink axially aft up to 0.13 inch.

Forward Exit Cone Assembly. The 360L003B forward exit cone showed missing CCP liner over the center 20 in. of the cone. This was due to splashdown and DOP insertion. The GCP insulator exposed by the missing liner showed no signs of heat effect. The remaining CCP liner showed the typical dimpled erosion pattern seen on all previous postburn nozzles. The maximum depth of the dimpled erosion was 0.15 inch. Postburn wedgeouts of charred CCP were observed on the forward 0.5 in. at 50, 80, 160, 190, 260, and 290 deg. The maximum radial depth of the wedgeouts was 0.4 in. at the forward end.

The aft end of the forward exit cone showed bondline separations between the EA 946 adhesive and the steel housing, and cohesive separations within the CCP intermittently around the circumference. The maximum radial separations were 0.02 and 0.01 in., respectively.

Throat Assembly. Erosion of the 360L003B throat and throat inlet rings was smooth and uniform. Typical popped-up, charred CCP material was observed on the forward 1.5 in. of the throat ring intermittently around the circumference and on the forward 0.65 in. of the throat inlet ring from 200 to 265 deg. Intermittent impact marks were also noted on the throat ring. Throat diameter measurements will be taken at the Clearfield H-7 facility during internal joint disassembly operations.

<u>Forward Nose (-503) and Aft Inlet (-504) Rings</u>. The 360L003B forward nose and aft inlet rings showed smooth erosion, with no wedgeouts, pockets, or wash areas observed. Popped-up, charred CCP material was observed on the forward 1.35 in. of the -504 ring at 175 deg (3.5 in. wide circumferentially) and on the forward 1.0 in. of the -503 ring at 75 deg (8 in. wide circumferentially). These are typical postburn occurrences.

<u>Nose Cap</u>. The 360L003B nose cap showed smooth erosion with no pockets or major washes observed. Minor slag deposits were observed on the forward 1.5 ft. of the flow surface. The nose cap aft 2 to 3 in. showed typical postburn wedgeouts of charred CCP material from 17 to 35, 105 to 128, 150 to 186, 220 to 245, and 250 to 275 deg. No wedgeouts were observed on the forward end of the nose cap. Popped-up, charred CCP was also observed on the aft end intermittently around the circumference.

<u>Cowl Ring</u>. The 360L003B cowl ring showed the typical erratic erosion seen on previous postburn RSRM cowl rings. The forward portion of the ring eroded a maximum of 0.15 in. more than the aft end. Typical postburn wedgeouts of charred CCP were observed on the aft 3.0 in. from 25 to 65, 240 to 300, and 352 to 0 to 10 deg. The maximum radial depth of the wedgeouts was 0.85 inch. All cowl ventholes appeared plugged with soot and slag except those at wedgeout locations.

<u>Outer Boot Ring</u>. The 360L003B OBR showed smooth erosion with no wedgeouts. The aft tip adjacent to the flex boot was intact 360 deg circumferentially. The cowl-to-OBR bondline remained intact.

<u>Fixed Housing Assembly</u>. The 360L003B fixed housing insulation erosion was smooth and uniform. The forward 2 in. of the fixed housing showed typical postburn wedgeouts of charred CCP from 52 to 59, 65 to 72, 80 to 95, 130 to 135, 203 to 213, 300 to 305, and 325 to 332 deg. The maximum radial depth of the wedgeouts was 0.4 inch. Minor slag deposits were observed on the aft portion of the liner surface. There were no bondline separations observed on the aft end of the fixed housing.

The fixed housing aft flange showed no damage to the metal surfaces, boltholes, or O-ring grooves. All metal surfaces were greased, and no corrosion was observed.

<u>360L003B Aft Exit Cone Field Joint</u>. The backfilled RTV extended below the joint char line 360 deg circumferentially. RTV reached the high-pressure side of the primary O-ring groove intermittently around the circumference. There were no distinct blowpaths observed within the joint. The primary O-ring did not see pressure during motor operation and showed no signs of blowby, erosion, heat effect, or assembly damage.

The aft exit cone field joint bolts were not bent, broken, or damaged. Raised metal was observed on the forward exit cone aft end 91.8-deg alignment pin hole due to the aft exit cone demate. The maximum dimensions were 0.02 in. circumferentially, 0.01 in. axially, and 0.10 in. radially.

The aft exit cone shell forward face showed aluminum oxide corrosion intermittently around the circumference between the O-ring grooves. No pitting was observed. Rust corrosion was observed on the forward exit cone aft flange intermittently around the circumference, with the worst condition located from 200 to 215 deg. No pitting was observed.

5

APPLICABLE DOCUMENTS

The latest revisions of the following documents are applicable to the extent specified herein.

Document	Title
TWR-15723C	Redesign Development and Verification Plan, Rev C
TWR-18984	Engineering Requirements Document for RSRM Third Flight (Flight Set 360L003)
TWR-16340	Nondestructive Criteria for the Nozzle Phenolic Component
TWR-16961	RSRM Grain and Insulation Structural Analysis Summary
TWR-19001a	Redesigned Solid Rocket Motor Flight Readiness Review (MSFC Level III)
TWR-10211-88	5 September 1988 Mass Properties Quarterly Status Report
TWR-17338	Mass Properties History Log Space Shuttle 360L003--Left Hand
TWR-17339	Mass Properties History Log Space Shuttle 360L003--Right Hand
TWR-19197	Structural Preflight Predictions for 360L003 (STS-29) DFI Instrumentation
TWR-19092	Predicted Ballistic Performance Characteristics for RSRM-3
TWR-17272-1	Flight Motor Set 360L001 (STS-26R) Final Report, Volume I
TWR-17541-1	Flight Motor Set 360L002 (STS-27R) Final Report, Volume I
CPW1-3600A	Prime Equipment Contract End Item Detail Specification, Rev A (including Addendum G)

DISTRIBUTION

Recipient	No. of Copies	Mail Stop
L. Allred	1	L10
C. Bacon	1	L34
L. Bailey	1	L10
B. Baugh	1	L36
N. Black	1	L36
R. Buttars	1	L21
V. Call	1	L22
C. Chang	1	L22
M. Cox	1	L30
R. George	1	L23
T. Gregory	1	L10
D. Gurney	1	L22D
S. Henderson	1	L36
S. Hicken	1	L21
H. Huppi	1	L21
T. Johnson	1	L34
S. Julkarni	1	L00
B. Jurewicz	1	E05
J. Kapp	1	L20
K. Kobayashi	1	L10
G. Lasley	1	L10
B. Laubacher	1	L21
B. MacBeth	1	L10
R. Mackley	1	L22
S. Manz	1	L21
J. Maw	1	L21
B. McQuivey	1	L10
S. Medrano	1	L10
S. Meyer	1	L23
T. Morgan	1	L10
S. Morris	1	L10
D. Nisonger	1	E16
R. Papasian	15	E05
D. Peterson	1	L10
P. Petty	1	L10
C. Richards	1	L21
G. Ricks	3	L36
R. Riley	1	E16
D. Roth	1	L10
D. Rowsell	1	L22D
C. Saderholm	1	E16
K. Sanofsky	1	851
T. Seigler	1	851
J. Seiler	1	L10
K. Speas	1	L21
J. Sutton	1	L10
D. Wagner	1	L10
M. Williams	1	L36
Data Management	5	L23E
Print Crib	5	K23B1